COMPOSITE STEEL AND CONCRETE STRUCTURAL MEMBERS

Fundamental Behaviour

by

Deric J. Oehlers

The University of Adelaide, Australia

and

Mark A. Bradford

University of New South Wales, Australia

Preface

This book deals with the analysis and behaviour of composite structural members that are made by joining a steel component, such as an I-section beam, to a concrete component, such as a reinforced concrete slab. The behaviour of these composite members is first described in general terms, and then methods of analysis are given for determining the behaviour under all loading conditions. These analysis techniques can, if required, be used in a design mode. However, factors of safety or resistance factors will not be included specifically in the analysis procedures, and it will be left to the designers to include their own national values. When material properties are required, such as the local buckling strength of thin plates or the fatigue endurance of shear connectors, then the mean strengths and standard deviations or characteristic values are given. If for example, the national standard in use requires the characteristic compressive strength of the concrete at 28 days, then this should be substituted for the strength of the concrete in the analysis procedure that is given. This book is therefore not oriented towards national codes or standards. Instead, it aims to give the reader a basic understanding of the structure irrespective of where it is built, because it is suggested that the region in which the structure is built does not affect significantly its fundamental behaviour.

It is not the object to provide quick design procedures for composite members, as these are more than adequately covered by recourse to such aids as safe load tables. The emphasis in writing this book is to impart a *fundamental* understanding of how composite structures work, so that the engineer will develop a *feel* for the behaviour of the structure that is often missing when design is based solely by using codes of practice or by the direct application of prescribed equations. The subject should therefore be of interest to practising engineers, particularly if they are involved in the design of non-standard or unusual composite structures for buildings and bridges, or are involved in upgrading, strengthening or repairing existing composite structures. However, this book has been written specifically for teaching the basic behaviour of composite structures to undergraduate students, and the more advanced sections can be used in postgraduate courses.

In order to help in the teaching procedure, the contents have been divided into nineteen relatively short self-contained chapters, many of which can be taught in single one hour lectures. By using this format, the instructors can choose chapters according to their interest and the length of the course. It is suggested that in order to cover the fundamentals in composite construction in an undergraduate course, Chapters 1, 2, 4, 6, 7, 9 and 10 need to be covered, with the inclusion of Chapters 15 and 18 if there is time. More advanced topics or specialisation courses, particularly in building construction, could be based on Chapters 5, 8, 11-14, 16 and 17. Chapters 3 and 19 would be of particular interest to bridge design engineers.

The chapters have been grouped into six Parts. The subject is introduced in Part 1, which covers the fundamental behaviour of composite beams and columns in purely qualitative terms, and in particular the terminology peculiar to composite construction. Part 2 covers the material properties, and no attempt is made to discuss these properties in depth except for those related specifically to shear connectors and shear bond, as there are many specialised books that cover the material properties and these are referred to. Instead, only the material properties that are required for the analysis techniques used in this book are described. Both static and fatigue behaviour, and idealised values suitable for the analysis techniques, are described. It is worth noting that the behaviour of mechanical shear connectors, and the shear resistance between steel decking or profiled sheets and the concrete, have been included as material properties. Part 3 covers geometric dimensions or effective sizes of the actual structure that should be used in the analysis procedures. This part treats both shear lag and local buckling of thin steel plates or sheets. At this stage, the designer has defined the material and geometric properties of the structure for use in the ensuing analysis procedures.

The subsequent parts refer either to general types of structures or types of forces. Part 4 describes the behaviour of possibly the simplest and most common form of composite structure, namely that of a hot-rolled steel section that is composite with the reinforced concrete slab that it supports. The behaviour of such a member under flexure and shear at both service and ultimate loads is described for both the simply supported and continuous cases. Having ascertained in Part 4 that the structure is strong enough to resist both the applied flexural and shear forces, the next step is to ensure that the concrete slab portion can resist the highly concentrated loads that are exerted on it by the shear connectors. This is covered in Part 5 for the four possible modes of failure. At this stage the complete behaviour of a composite flexural member has now been described, and so the most important fundamental basics of composite construction have been covered.

Part 6 applies the fundamental basics to the analysis of specific forms of construction such as composite beams with service ducts in the web of the steel element. The analysis of this special form of construction requires a thorough understanding of the first five parts of the book, and is useful in consolidating the theory covered in these parts. Also considered are composite structures that are made from cold formed profiled sheets, such as the familiar composite floor slab made with steel decking that is designed to act as a permanent formwork and to act integrally with the concrete slab. Also covered here is the use of steel decking as permanent and integral formwork to the sides of reinforced concrete beams, known as composite profiled beams. Part 6 covers the analysis of composite columns, and considers the steel section encased in concrete and also concrete-filled steel hollow sections. Finally, the effect of fatigue loads on composite bridge beams is considered and techniques are developed for assessing the remaining life and endurance of existing composite bridge beams, as well as assessing the effect of remedial work on these structures.

The authors' interest in composite construction of steel and concrete stems from their associations with Professor R.P. Johnson while they were working at different times at The University of Warwick. Professor Johnson's enthusiasm for teaching, research and practice of composite construction is infectious, and inspired the authors to embark on the writing of this book. The subject matter has been influenced by the authors' own areas of research and teaching experiences at the Universities of Warwick, Cork, Adelaide, Sydney, New South Wales, Minnesota and Edinburgh.

We would like to acknowledge with thanks the facilities made available at our universities for the writing of this book. Especially acknowledged is the support provided by Professor R.I. Gilbert at The University of New South Wales and by Professor J.M. Rotter for the second author during a period of study leave at the University of Edinburgh. Jan Hutchinson is also acknowledged for typing portions of the text.

During the period of writing, it is the authors' families who invariably suffer most, and their patience, support and understanding has been most valuable to us. Thanks then are due to Bernie, Suzanne and the children, for whom this book is dedicated.

Contents of Examples

Notation

The following notation is used in this book. Generally, only one meaning is assigned to each symbol, but in cases where more than one meaning is possible, then the correct one will be evident from the context in which it is used.

A	= area; area of free body; residual strength constant or fatigue damage;
A_b	= area of bottom transverse reinforcement that crosses shear plane;
A_{conc}	= cross-sectional area of concrete element;
A_d	= cross-sectional area of dowel;
A_e	= used life parameter for experimentally determined endurances;
A_{free}	= area of free body of slab;
A_{hoop}	= cross-sectional area of hooped reinforcement;
A_m	= area of moment diagram;
A_p	= patch load area;
A_{prism}	= area of concrete prism in splitting analysis;
A_r	= area of transverse reinforcement per longitudinal length of crack plane;
A_{rc}	= area of compressive reinforcement;
A_{reinf}	= area of reinforcement;
A_{rib}	= area of concrete between ribs;
A_{rt}	= area of tensile reinforcement;
A_{sh}	= cross-sectional area of the shank of a stud shear connector;
A_{shear}	= area of axial force diagram;
A_{st}	= area of tensile reinforcing bars;
A_{steel}	= cross-sectional area of steel element;
A_t	= area of top transverse reinforcement that crosses shear plane;
A_{void}	= area of individual void encompassed by rib;
a	= half-length of crack;
a_o	= length of web opening;
B	= lateral spacing of steel elements; width of steel column; probability of occurrence of vehicle weight;
B_{limit}	= minimum beam load required to apply a shear force onto the connector after overload;
B_{peak}	= peak of cyclic load being applied to the beam;
B_{trough}	= trough of cyclic load being applied to the beam;

B_{zero} = minimum beam load required to apply a shear force onto the connector after cyclic loading;

b = breadth of slab to one side of the steel element; width of plate transverse to applied load;

b_a = width of bar connector;

b_c = width of concrete element;

$(b_c)_{o,i}$ = effective width of haunch;

b_e = effective width of plate;

b_{eff} = effective breadth of slab to one side of the steel element;

b_f = flange breadth;

b_h = average breadth of haunch in profiled slab;

b_{haunch} = mean breadth of haunch;

b_r = reinforcement distance;

C = flexibility coefficient; ratio of characteristic to mean strengths; constant in endurance equation;

c = reduction factor;

c_b = cover to hooped reinforcement;

c_{do} = splitting side cover;

D = depth of section; standard deviation; shear force in dowel;

D_a = standard deviation of asymptotic endurances;

D_c = dowel strength after fatigue loading; concrete slab flexural rigidity parameter;

D_{crack} = postcracking dowel strength of mechanical shear connector;

D_e = standard deviation of experimentally derived endurances;

$(D_e)_{emb}$ = embedment failure strength;

D_{max} = maximum dowel strength when concrete element does not fail prematurely; dowel strength prior to fatigue loading;

$(D_{max})_{push}$ = maximum dowel strength from push tests;

$(D_{max})_{beam}$ = maximum dowel strength of shear connectors in beams;

D_Z = standard deviation of parameter Z;

d = depth of web; width of connector; diameter of circular column; effective depth;

d_{hd} = diameter of head of stud;

d_n = depth to neutral axis;

d_r = depth of rectangular stress block; depth to reinforcement; diameter of reinforcement;

d_{sh} = diameter of the shank of a stud shear connector;

d_w = depth of web;

E	= endurance;
E_a	= asymptotic endurance; maximum endurance associated with stage 2 gradual crack propagation;
$(E_a)_{ch}$	= characteristic asymptotic endurance;
E_{beam}	= endurance of bridge beam;
E_c	= concrete modulus of elasticity;
E_e	= effective modulus; experimentally determined endurance;
$\bar{E}_e$	= age-adjusted effective modulus;
$(E_e)_{mean}$	= mean endurance; endurance from prediction equation through mean of fatigue data;
$(E_e)_{ch}$	= characteristic endurance at two standard deviations;
$(EI)_e$	= effective flexural rigidity;
$(EI)_s$	= flexural rigidity of steel element;
$(EI)_{st}$	= strain hardening flexural rigidity;
E_r	= stage 3 endurance; endurance associated with rapid reduction in strength through rapid crack propagation;
E_s	= elastic modulus of steel;
E_{sr}	= elastic modulus of reinforcing bars;
E_{st}	= strain hardening modulus of steel;
e	= eccentricity of load;
e_b	= eccentricity at balanced failure;
F	= force; internal axial forces; force profile; creep function;
{F}	= load vector;
F_b	= force in bottom portion of web opening;
F_{comp}	= resultant compressive force;
F_{conc}	= resultant force in concrete element;
FD	= fatigue damage;
F_{dowel}	= force to cause fatigue damage of shear connector;
F_{emb}	= embedment force;
F_f	= force constant;
F_{fric}	= frictional force;
F_{fsc}	= full shear connection force;
F_h	= force on head of stud;
F_m	= minimum of applied cyclic load;
F_{nf}	= sum of normal forces on shear plane per unit length;
F_{norm}	= normal force across steel/concrete interface;
F_o	= maximum force due to overload;
F_p	= peak of cyclic load;

F_{point}	= load to cause step change in shear flow;
F_{psc}	= partial shear connection force;
F_r	= resultant force;
F_s	= shear force on shank;
F_{shear}	= longitudinal shear force at steel/concrete interface; longitudinal shear in composite profiled beam;
F_{steel}	= resultant force in steel element;
F_t	= trough of cyclic load; force in top portion above opening;
F_{ten}	= resultant tensile force;
f	= stress;
f_c	= compressive cylinder strength of concrete;
f_{cb}	= Brazilian tensile strength of concrete;
$(f_{cb})_{eq}$	= equivalent tensile strength of concrete;
f_{cf}	= modulus of rupture strength of concrete;
f_{ct}	= direct tensile strength of concrete;
f_{cu}	= compressive cube strength of concrete;
f_d	= lateral stress at shear flow discontinuity;
f_{emb}	= axial stress at shank needed to form conical failure plane;
f_{fy}	= flexural stress to cause yield in the presence of shear;
f_{mean}	= mean stress;
f_r	= lateral stress;
f_u	= ultimate tensile strength;
$(f_u)_{eq}$	= equivalent tensile strength;
$(f_u)_{step}$	= minimum strength requirement in standard;
f_y	= yield strength of steel;
f_{yp}	= proof yield stress;
f_{yr}	= yield strength of reinforcing bars;
G	= shrinkage time function; energy release rate; sustained dead load;
[G]	= elastic geometric or stability matrix;
H	= horizontal frictional force; force in shear connector normal to interface; parameter that controls the magnitude of the endurance;
H_a	= intercept on vertical axis of regression analysis of asymptotic endurances;
H_e	= intercept on vertical axis of regression analysis of experimental data;
h	= distance; height of shear connector;
h_a	= height of bar connector;
h_b	= depth of bottom section below opening;
h_c	= distance from centroid of concrete element to steel/concrete interface;

$(h_c)_e$	= effective height of prism;
h_{conc}	= depth of concrete element;
h_{eq}	= equivalent height of connector;
h_h	= neutral axis distance for composite columns;
h_o	= depth of opening;
h_r	= height of rib; height of reinforcement above base of shear connection;
h_{rib}	= height of profiled rib;
h_s	= distance from centroid of steel element to steel/concrete interface;
h_{sh}	= height of shank;
h_{solid}	= height of solid part of concrete element;
h_{steel}	= depth of steel element;
h_t	= depth of top section above opening;
h_v	= effective height of shear connector;
h_{wc}	= mean height of weld collar;
I	= second moment of area; second moment of area about weaker axis;
I_c	= second moment of area of uncracked concrete encasement; second moment of area of concrete element;
I_F	= second moment of area of steel flange;
$(I')_{hog}$	= hogging second moment of area;
I_{nc}	= second moment of area of transformed concrete section;
I_s	= second moment of area of steel section;
$(I')_{sag}$	= sagging second moment of area;
K	= stiffness of a shear connector;
K_c	= critical stress intensity factor;
K_{ch}	= characteristic strength parameter;
K_{cov}	= coefficient of variation;
K_d	= lateral force parameter;
K_h	= embedment strength ratio;
K_s	= true secant stiffness;
K_{sh}	= stress ratio;
K_{si}	= initial secant stiffness;
K_{tc}	= tangent stiffness during unloading or cyclic loading;
$[K]$	= elastic stiffness matrix;
$[K^e]$	= element elastic stiffness matrix;
$[K_o]$	= linear stiffness matrix;
$[K_1]$	= nonlinear stiffness matrix;
k	= local buckling coefficient;
k_m	= parameter that reflects non uniform moment distribution;

k_u	= neutral axis parameter;
L	= distance along beam; span of beam; length between pin ends in column; length of continuous beam between supports; buckling half-wavelength;
L_c	= distance between points of contraflexure;
L_E	= effective length of U-frame strut;
L_e	= effective length of column;
L_f	= load constant;
L_p	= length of perimeter of shear plane;
L_s	= longitudinal spacing of shear connectors placed in a single line;
L_{sp}	= distance from support; length of shear span;
ℓ_a	= lever arm;
M	= applied moment; bending moment distribution; magnification of range of load in propped construction;
M_a	= moment at centre of opening;
M_b	= moment in bottom portion below opening;
M_{bs}	= buckling strength;
M_{conc}	= moment in concrete element;
M_{frac}	= moment to cause the shear connectors to fracture;
M_{fsc}	= moment capacity with full shear connection;
M_{init}	= moment capacity at opening;
M_{linear}	= flexural capacity based on linear interpolation;
M_{Lsp}	= moment capacity at shear span L_{sp};
M_m	= maximum moment in a column;
M_{max}	= maximum applied moment;
M_{od}	= elastic lateral-distortional buckling moment;
M_p	= plastic moment capacity;
M_{pur}	= pure moment capacity;
$(M_P)_{hog}$	= hogging plastic moment capacity of composite beam;
$(M_P)_{sag}$	= sagging plastic moment capacity of composite beam;
M_{Ps}	= plastic moment of steel element;
M_{psc}	= moment capacity with partial shear connection;
M_{PsN}	= plastic moment reduced due to axial load;
M_s	= moment about plastic centroid;
M_{steel}	= moment in steel element; moment capacity of steel element;
M_t	= moment in top portion above opening;
M_{top}	= moment about top fibre of column section;
M_u	= ultimate moment at crushing;
M_{ub}	= balanced failure moment of a reinforced concrete column;

M_x	= moment about x-axis of column;
M_y	= moment to cause first yield; moment about y-axis of column;
m	= exponent in endurance equation;
m_a	= slope of regression analysis of asymptotic endurances;
m_e	= slope of regression analysis of experimentally determined endurances;
N	= number; number of connectors in a shear span; axial load in column; number of cycles; number of cycles to cause axial failure; axial load; number of profiled ribs;
N-A	= position of neutral axis;
N_b	= block of cyclic loads;
N_c	= buckling load of concrete or composite column under axial force; depth to neutral axis in reinforced concrete element;
N_{cr}	= Euler buckling load;
N_{crit}	= critical load;
N_{init}	= number of cycles to initiate the crack;
N_L	= limiting failure load;
N_o	= axial strength; squash load of column;
N_{oc}	= Euler buckling load;
N_{om}	= axial strength at maximum moment;
N_p	= depth to neutral axis is a composite profiled beam;
N_{prop}	= number of cycles to propagate a crack to fracture;
N_s	= net axial force;
n	= number of shear connectors in a group; modular ratio; ratio of height of stud to diameter of stud;
P	= strength of section; applied load; strength of shear connector;
P^*	= splitting strength;
P_b	= axial strength of shear connection in composite profiled beam;
P_c	= strength of component that has been subjected to cyclic loads;
$(P_{ch})_{bri}$	= characteristic strength of brittle shear connectors;
$(P_{ch})_{duc}$	= characteristic strength of ductile shear connectors;
P_{conc}	= axial strength of concrete element; $0.85f_cA_{conc}$;
P_d	= dowel strength of individual shear connector;
P_{fi}	= shear connection strength required for full interaction;
P_{fri}	= frictional resistance;
P_{fsc}	= full shear connection strength;
P_m	= mean strength;
P_o	= force exerted by maximum overload;
P_{of}	= static strength prior to cyclic loading;

P_p	= load for plastic mechanism to form; yield strength of profiled sheeting;
P_{prop}	= maximum strength associated with stage 2 crack propagation;
P_r	= yield strength of reinforcing;
P_s	= static strength; strength of component not subjected to cyclic loads;
P_{shear}	= strength of longitudinal shear connection in shear span;
$(P_{shear})_{fsc}$	= strength of shear connection required to achieve full shear connection;
P_{split}	= load to cause concrete element to split;
P_{steel}	= axial strength of steel element; $A_{steel}f_y$;
P_{strip}	= strip load;
P_t	= transverse force;
P_{weak}	= weaker of the element axial strengths;
P_y	= split load in y-direction;
P_z	= split load in z-direction;
p	= area of reinforcement as proportion of area of the shear plane;
Q	= shear flow strength; longitudinal shear strength per unit length; increase in strength due to vertical dispersal; short-term live load;
$\{Q\}$	= vector of global buckling displacements;
Q_{ch}	= characteristic shear flow strength;
Q_m	= mean shear flow strength;
Q_r	= longitudinal shear strength of rib per unit length;
Q_{res}	= residual shear flow strength;
q	= shear flow; shear flow force; longitudinal shear force per unit length;
q_{dowel}	= shear flow force on mechanical connector;
q_f	= shear flow force at longitudinal shear plane;
q_m	= mean shear flow;
q_r	= range of shear flow forces;
q_t	= shear flow force applied to slab by shear connection;
q_V	= shear flow force due to load V;
R	= stress resultant; profile of stress resultants; range of cyclic load; reservoir range;
R_{ET}	= temperature reduction factor for elastic modulus;
R_{fu}	= multiplication factor for ultimate strength of stud steel;
R_{two}	= reduction in strength for two lines of connectors;
R_{wc}	= reduction factor for height of weld collar;
R_{yT}	= temperature reduction factor for yield stress;
R_ρ	= variation in concrete density multiplication factor;
r	= radius of gyration; axial line force per unit length;
r_t	= percentage of reinforcement crossing lateral splitting zone;

r_y	= radius of gyration;
S	= fatigue parameter such as range or peak of cyclic load; plastic section modulus of steel element;
S_{set}	= incremental set; increase in set per cycle;
S_{ult}	= slip at fracture;
s	= longitudinal slip; longitudinal spacing of connectors;
s_{max}	= maximum slip;
T	= total number of load traversals;
T_{adj}	= distance between centre line of webs; lateral spacing of beams;
T_{edge}	= distance between centre line of web and edge of slab;
t	= time; thickness of plate;
t_f	= flange thickness;
t_w	= web thickness;
u	= longitudinal displacement at interface; out of plane displacement;
V	= transverse shear load;
V_a	= shear at centre of opening;
V_b	= shear in bottom portion below opening;
V_c	= shear force in concrete element;
V_{conc}	= shear load in concrete element;
V_{init}	= shear capacity of opening;
V_{mat}	= maximum shear capacity;
V_{pur}	= pure shear capacity;
V_{steel}	= shear load in steel element;
V_t	= shear in top portion above opening;
v	= lateral deflection of column;
v_{dow}	= contribution of transverse reinforcement to shear strength of shear plane;
v_{fric}	= shear resistance through active friction;
v_{full}	= deflection with full interaction;
v_{lock}	= shear resistance through interface interlock;
v_{no}	= deflection with no interaction;
v_{part}	= deflection with partial interaction;
v_{steel}	= deflection of steel element;
$(v_u)_{ch}$	= characteristic shear strength;
W	= weight of vehicle;
W_{SFV}	= weight of standard fatigue vehicle;
w	= width of concrete element; uniformly distributed load;
w_{eff}	= effective width;
w_{split}	= uniformly distributed load to cause splitting;

X_a	= applied axial load to cause connector to fail;
X_{emb}	= load to cause conical failure plane in determining embedment strength;
x	= distance along beam; horizontal distance from result to regression line; lateral plate coordinate;
x_t	= length of lateral zone on one side of connector;
y	= vertical distance from result to regression line; distance; distance from neutral axis to stress point;
y_n	= distance to neutral axis;
$\bar{y}$	= distance between centroid of free body and centroid of whole section;
Z	= property; elastic section modulus;
Z_{ch}	= characteristic value;
$(Z')_{hog}$	= hogging elastic section modulus;
Z_{mn}	= mean strength;
$(Z')_{sag}$	= sagging elastic section modulus;
α	= initial curvature and residual stress parameter for local buckling; stress gradient; index for column strength; angle in W-s response;
α_c	= plastic neutral axis parameter;
α_t	= stiffness of U-frame;
β	= ratio of smaller to larger eccentricities; column strength parameter; angle in W-s response;
β_d	= sustained loading factor;
γ	= neutral axis parameter; flexural stiffness ratio; angle in W-s response;
γ_{conc}	= specific weight of concrete;
Δ	= increment; eccentricity of shear in composite profiled beam;
δ	= maximum lateral deflection of plate; deflection; neutral axis parameter;
δ_b	= amplification factor;
δ_o	= initial maximum out-of-flatness of plate;
ε	= strain; strain profile;
ε_{cr}	= creep strain;
ε_e	= instantaneous strain;
ε_{fr}	= strain at fracture;
ε'_o	= strain at maximum compressive strength;
ε_r	= strain in reinforcing bars;
ε_{sh}	= shrinkage strain;
ε_{st}	= strain hardening strain;
ε_u	= ultimate concrete strain at crushing;
ε_y	= yield strain;
ε_{yp}	= proof strain;

ε^*	= strain developed as time approaches infinity;
ζ	= relative strength parameter;
η	= degree of shear connection; reduction factor for lightweight concrete; imperfection parameter;
η_{Lsp}	= degree of shear connection at shear span L_{sp};
η_{max}	= degree of shear connection at maximum moment section;
θ	= angle; angle of shear plane; angle in degrees between direction of the profiled rib and that of the composite beam; rotation at plastic hinge;
θ_e	= 'elastic' beam rotation;
θ_p	= 'plastic' beam rotation;
κ	= curvature;
κ_P	= 'elastic' curvature at M_P;
κ_{st}	= curvature at strain hardening of steel element;
κ_y	= curvature at first yield of steel element;
λ	= load factor; slenderness; constant of proportionality;
λ_1, λ_2	= limiting slendernesses;
λ_{cr}	= critical value of load factor at which buckling occurs;
λ_d	= modified distortional buckling slenderness;
μ	= coefficient of friction; frictional resistance;
μ_d, μ_k	= abscissae in column interaction diagram;
ν_c	= Poisson's ratio for concrete;
ν_s	= Poisson's ratio for steel;
ξ	= slenderness term;
ρ	= density of concrete in kg/m^3; range of cyclic stress;
ρ_{step}	= concrete density of original specimens;
σ	= stress; stress profile;
σ_a	= axial applied stress;
σ_{cr}	= elastic critical or local buckling direct stress;
σ_{cro}	= direct stress to cause local buckling in the absence of shear;
σ_ℓ	= longitudinal stress;
σ_{nc}	= stress in transformed concrete section;
σ_{nf}	= lateral stress; external active normal stress;
σ_o	= constant sustained stress;
$\sigma_{o\ell}$	= local buckling stress;
σ_r	= radial confining pressure;
σ_{ult}	= average post buckling failure stress in plate;
σ_1, σ_2	= edge stresses;
τ	= time at first loading;

τ_{cr}	= elastic critical or local buckling shear stress;
τ_{cro}	= shear stress to cause local buckling in the absence of bending;
τ_w	= uniform shear stress in web;
τ_y	= shear yield stress;
ϕ	= creep coefficient; strength parameter;
χ	= aging coefficient; ductility parameter; capacity reduction parameter;
χ_d	= non-dimensional applied load;
χ_n	= non-dimensional ordinate in strength interaction envelope;
ψ	= degree of interaction;
Ω	= cracking factor for columns;
ω	= stress ratio for column post-local buckling.

1   Composite Construction

1.1   Types of composite construction

1.1.1   UNIQUENESS OF STEEL AND COMPOSITE CONSTRUCTION

Composite steel and concrete structural members are formed by bonding a steel component, such as an I-section, to a concrete component, such as a reinforced concrete slab, so that the two components now act as one. In order to standardise the terminology used in this book, the steel component of a composite member will be referred to as the *steel element*, while the concrete component of the composite member will be referred to as the *concrete element*.

Engineers are all too familiar with the problems involved in constructing in either steel or concrete, as each of these materials has its own peculiarity. For example, steel structural members are generally fabricated as components consisting of thin plate elements, so they are prone to local and lateral buckling, as well as to fatigue. Therefore, steel standards are concerned predominantly with the prevention of failure by instability or buckling. Conversely, concrete structural members are generally thick and unlikely to buckle. However, concrete is very weak in tension, and is inclined to creep and shrink with time. In order to overcome the problem of weak tensile strength, a major effort in design is in placing steel reinforcing bars as a substitute for the weak concrete.

Steel and concrete composite structural members are also subjected to the possibility of buckling of the steel element and tensile cracking of the concrete. However, they are also prone to failure of the bond between the steel element and the concrete element, which is often referred to as *debonding*. It is the behaviour of this bond between the concrete and steel elements that gives composite construction its unique peculiarity. Hence, in the design of composite steel and concrete structures, the engineer not only has to understand the behaviour of the individual components of the steel and concrete, but also the bond between these components.

Composite structures also have other unique characteristics. For example, a prismatic steel beam can be considered to have a flexural strength that is constant at any section of the beam, and so in design it is sufficient to ensure that the flexural strength is larger than the maximum applied moment. The same can be said of a reinforced concrete beam, except at positions that are very close to the ends of the reinforcing bars. However, unlike steel beams or reinforced concrete beams, the strength of a composite beam varies along its length, and so the strength at all sections of a composite beam must be compared with the applied load along the beam. Steel plates in steel members can buckle locally in either direction transverse to the plane of the plate. However in composite members, a steel plate adjacent to a concrete element can only buckle away from the concrete element and hence these plates are less prone to buckling than those in steel members. Such an example is the steel skin in a

concrete-filled tubular composite column, which can only buckle away from the enclosed concrete core.

1.1.2 USE OF COMPOSITE FORMS OF CONSTRUCTION

There are several reasons for combining steel and concrete elements to form composite members. Most structural slabs are made from reinforced concrete, as this has good sound and fire insulation properties, and a common form of construction is to use steel beams to support the slab as shown in Fig. 1.1. The applied flexural forces in this unbonded system are therefore resisted solely by the steel beam, with the top half being subjected to compression with the possibility of buckling, and with the bottom half being in tension. When the steel/concrete interface is bonded together so that the two elements act as one, then the steel element will be subjected to tension and the concrete element will resist the compressive forces. Best use is therefore being made of the two materials, as concrete is effective in compression and steel is effective in tension. The depth of the beam resisting flexure has now increased from that of the steel beam acting by itself to that of the composite beam, and this can double both the flexural strength and stiffness of the beam, and consequently lead to reduced span to depth ratios. Reducing span to depth ratios may only give a small saving in beam materials, and thus appear only to achieve a small overall saving in costs. However, it is worth noting that this reduction in depth affects the whole building and will lead to reduced floor heights, with consequent savings in column heights, glazing and cladding, and will eventually lead to reduced foundation loads.
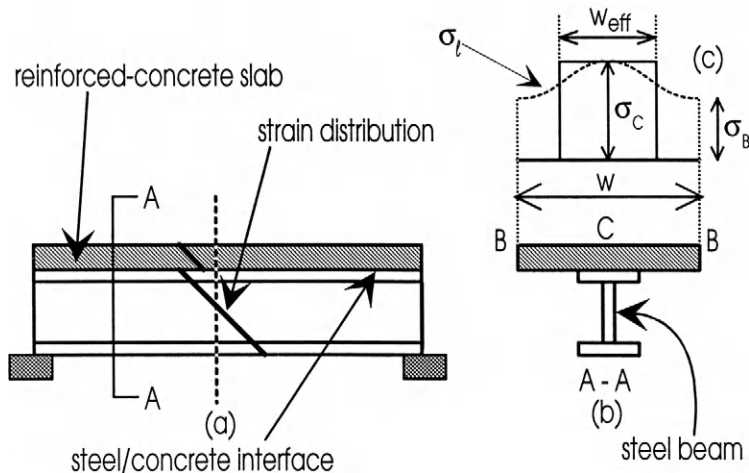
Fig. 1.1 Steel and concrete elements

Steel sections used as both beams and columns are often encased in concrete for fire protection, as in Fig. 1.2. The concrete encasement also helps resist local and overall buckling of the steel section, as well as being capable of resisting compressive forces. Hence a smaller steel section can be used when the steel section is encased in concrete, and this will offset in part the extra cost of encasement.

(a)   (b)
encased column   encased beam
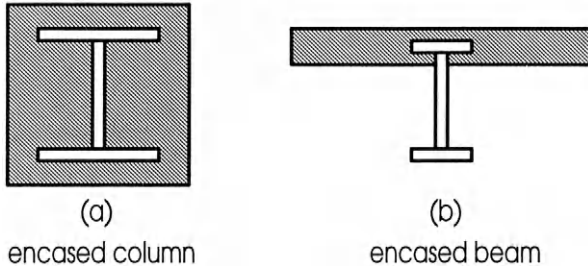
Fig. 1.2 Fire protection

Composite structures are also formed when steel sections are used as permanent formwork for the concrete portion, and are designed to act integrally with the concrete so that the two components act as one. An interesting long-standing and efficient form of construction is to use composite columns made from circular steel tubes as in Fig. 1.3(b). Using the steel tube externally to the concrete element may appear to defeat the object of using composite construction for fire prevention, but this technique has many other advantages which may well offset the additional cost of fire protecting the exposed steel. For example, the concrete element is now fully encased by the steel element so that the concrete is less prone to shrinkage, has a higher compressive strength as it is now triaxially restrained, and acts integrally with the steel element. Furthermore, the steel element is restricted to buckling away from the concrete element, so that it is less likely to buckle locally. A further advantage of this type of construction is obtained when the steel column is designed to withstand several stories of construction load, so that concreting of the steel tube does not delay the steel construction sequence and occurs well below the steel construction zone. Concrete-filled hollow steel elements are now used extensively in high-rise office building construction.

concrete   cold formed ribs

(a)   (b)   steel decking or profiled sheet
composite   composite
tube   column   (c)composite slab
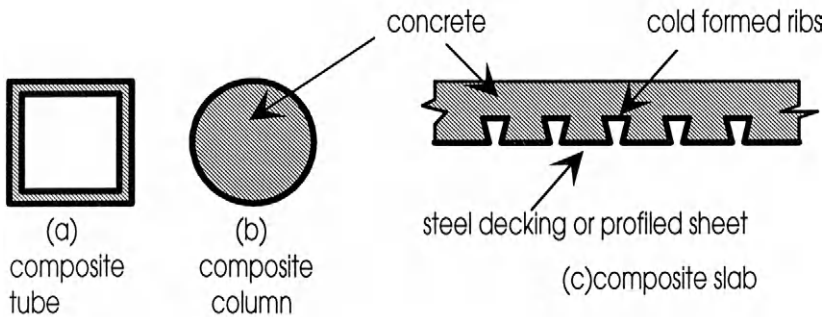
Fig. 1.3 Permanent and integral shuttering

A further example of permanent and integral shuttering is the use of steel decking in the construction of composite slabs in Fig. 1.3(c). The steel decking, which is made by cold rolling ribs into galvanised sheets, is designed to support the construction loads during concrete casting, and is also designed to act compositely with the hardened concrete, so reducing the amount of reinforcing bars required. A

very common form of construction is to substitute a composite profiled slab for the solid slab in Fig. 1.1, and then to bond the two elements together with mechanical shear connectors forming a double composite action, so that the composite slab now acts as part of the composite beam. Steel decking can also be used as permanent and integral shuttering to the sides of reinforced concrete beams, and also in the construction of reinforced concrete walls.

Steel plates can be bonded to the surface of existing reinforced concrete beams as in Fig. 1.4. The composite action between the steel plate and the reinforced concrete flexural member increases both the shear and flexural strength, and hence this form of construction can be used to upgrade existing reinforced concrete structures.

steel plates   reinforced-concrete beam
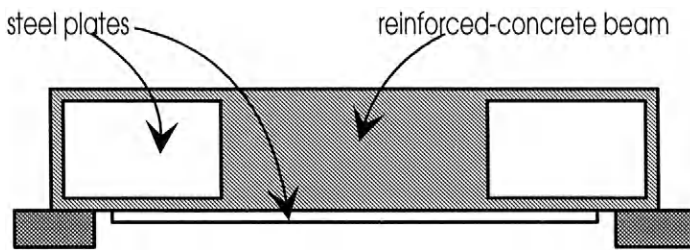
Fig. 1.4 Strengthening and stiffening

1.1.3   BOND BETWEEN STEEL AND CONCRETE ELEMENTS

The bond which must be achieved between the steel element and the concrete element in a composite member is crucial to the composite action. When the two elements only touch at an interface such as shown in Fig. 1.1, then they are often tied together using mechanical forms of shear connection, examples of which are given in Fig. 1.5. When one element encases the other element as in the columns and tube in Figs. 1.2(a) and 1.3(a) and (b), then the two elements are tied together by interface forces induced by the geometry of the encasement and any bond strength. In the case of composite plated beam construction in Fig. 1.4, the plate can be bonded to the existing reinforced concrete beam by gluing or bolting, or by a combination of gluing and bolting. In all cases, the bond must be designed to resist the longitudinal shear forces at the steel/concrete interface. However, the bond must also be designed to prevent separation between the steel and concrete elements in order to ensure that the curvature in the steel and concrete elements is the same. Hence the interface bond must be able to resist both tensile forces normal to the steel/concrete interface, and shear forces parallel to the steel/concrete interface.

Stud shear connectors, as shown in Fig. 1.5(a), are probably the most common type of mechanical shear connector used, and consist of a bolt that is electrically welded to the steel member using an automatic welding procedure. The shank and the weld-collar adjacent to the steel flange are designed to resist the longitudinal shear load, whereas the head is designed to resist the tensile loads that are normal to the steel/concrete interface. Studs of 19 mm diameter are used frequently, and have a shear strength of around 120 kN. Bolts can also be attached directly to the flange,

prior to casting the concrete, through friction welding by spinning the bolt whilst in contact with the flange, or by bolting as shown in Fig. 1.5(b). Alternatively, the steel and concrete elements can be bolted together after casting as in (g) and (h). A further form of attaching shear connectors is to use explosively driven pins as in (d). In hand welded channels (c), the longitudinal shear load is resisted mainly by the bottom flange of the channel whilst the top flange resists the tensile loads normal to the steel/concrete interface. Angle sections (f) behave in a similar fashion, except that the normal tensile loads are resisted by reinforcing bars that are threaded through holes in the leg. Block connectors (e) form a very stiff and strong shear connection, and the hooped bars resist the normal tensile loads.
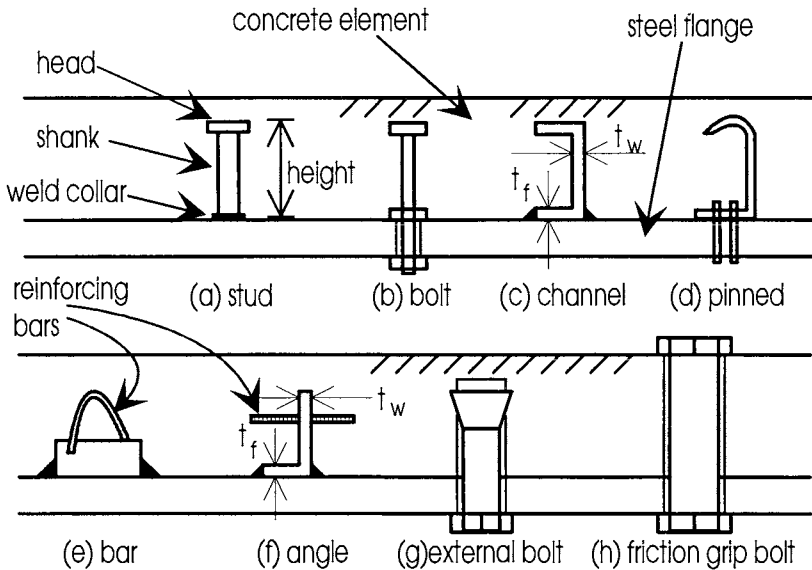
Fig. 1.5 Mechanical shear connectors

There is an enormous variety of mechanical shear connectors varying in shape, size and methods of attachment. However, they all have the following important similarities. They are steel dowels embedded in a concrete medium, they have a component that is designed to transmit longitudinal shear forces, they have a component that is designed to resist normal tensile forces and hence prevent separation at the steel/concrete interface, and they all impart highly concentrated loads onto the concrete element.

When mechanical shear connectors are not used, such as occurs when one element is encased by another as in Figs. 1.2 and 1.3, then the two elements are tied together by interface forces that are induced by the geometry of the encasement. Full encasement, as in the columns in Fig. 1.2(a) and 1.3(b), ensures that there is no separation, and the longitudinal shear is now transmitted by interface friction and chemical bond, and it is often assumed that the strains in the steel and concrete at the interface are the same. A similar action occurs in composite slabs, as in Fig. 1.3(c), but in this case it is the encasement of the rib that prevents interface separation.

There are numerous types of profiled sheeting, some of which are shown in Fig. 1.6. Their shapes are generally chosen as a compromise between enhancing the bond at the steel/concrete interface, and enhancing the performance of the permanent shuttering to resist the construction load and any instability effects due to the wet concrete. In all cases, the longitudinal shear is transmitted by the encased ribs, so this form of shear connection will be referred to as *rib shear connectors*. The bond performance of these ribs is improved by rolling indentations and protrusions into the rib, so that the longitudinal shear is also transmitted by mechanical action that is analogous to the transfer of shear in cracked reinforced concrete sections by aggregate interlock.
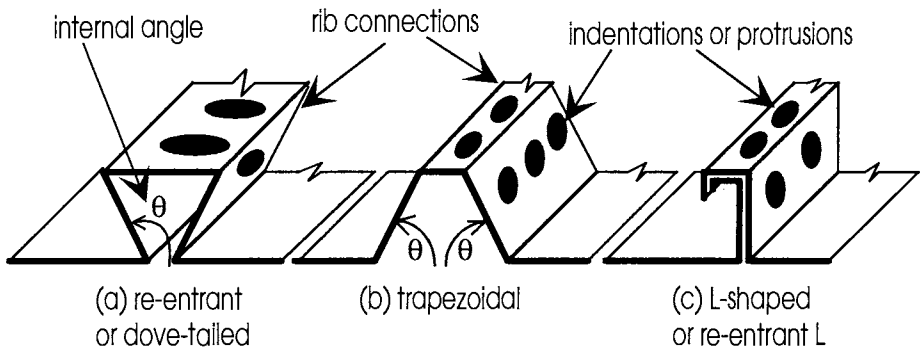
Fig. 1.6 Steel decking from profiled sheets

1.1.4 SHAPES OF COMPOSITE SECTIONS

The shapes of composite sections are as varied as the imagination of the designer. Composite sections can be made from hot-rolled steel sections by encasing the steel sections in concrete as in Fig. 1.7(a), or by encasing the concrete element with steel (b), (c) and (d), or by encasing the concrete within two skins of steel to form a composite tube as in (e).

Mechanically bonded sections have a variety of forms as shown in Fig. 1.8. T-beams, that are made from standard hot-rolled sections as shown in (a), are a common form of construction. Because the top flange of the steel element of the T-beam contributes very little to the overall strength and is mainly present to hold the shear connectors in place, the composite section can be made more efficient by welding a plate to the bottom flange and reducing the size of the top flange as shown in the plate beam in (b), thereby making the steel section monosymmetric. In fact, the top flange can be removed altogether and the connectors welded to the web, as in the hybrid beam in (c). The depth of the composite section can be increased with the addition of haunches in (d), and when the steel element is at the edge of the slab or adjacent to a service duct a composite L-beam is formed, as in (e). Composite beams in bridges are often formed from steel box sections (g) instead of I-sections, and can also be formed from open box girder sections (f) where the connectors are concentrated over the webs.
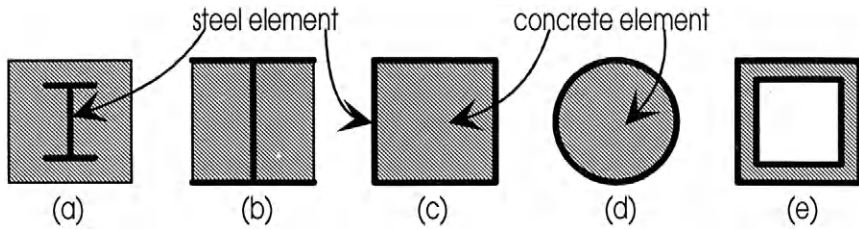
Fig. 1.7 Hot rolled steel elements
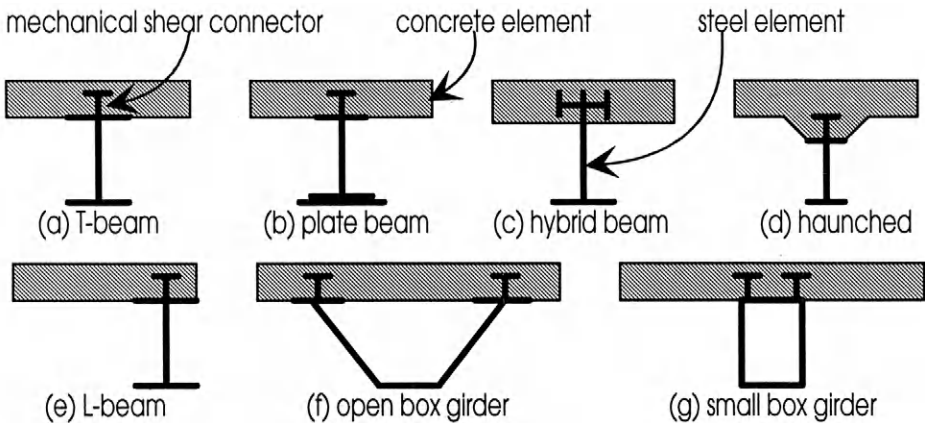
Fig. 1.8 Mechanically bonded sections

Composite beams are often constructed with openings in the webs to allow for the passage of services, as in Fig. 1.9(a). Openings are also formed in stub girder construction (b) to allow for the passage of services, to accommodate secondary transverse composite beams, and to increase the depth of the main section and hence allow for greater spans. Composite truss girders (c) and (d) are another form of open web construction.

As mentioned earlier, composite sections are also formed when steel decking, which is made from cold rolled profiled sheets, is used as permanent and integral shuttering for reinforced concrete members. Examples of this form of construction are shown in Fig. 1.10. Composite profiled slabs (a) are a very common form of construction in steel framed structures, and are now often used in concrete framed structures as well. Profiled sheets can also be used as permanent and integral shuttering in the construction of reinforced concrete walls (c) and beams (b). In advanced forms of construction, fully braced box girders (d) can be constructed from profiled sheeting, and then infilled with concrete.
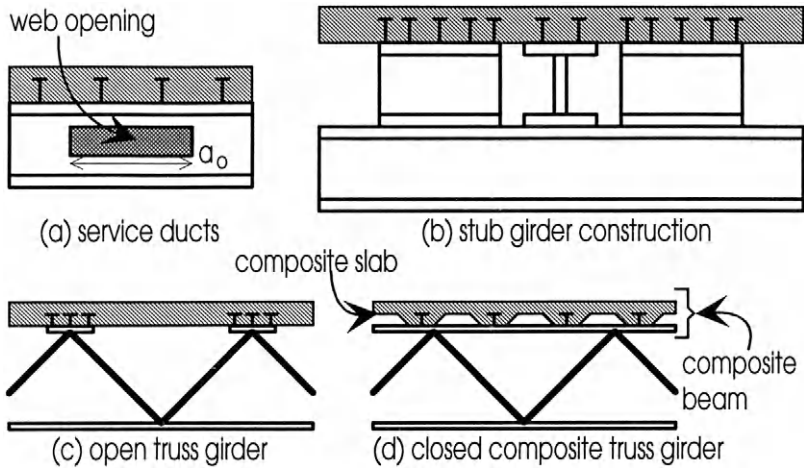
Fig. 1.9 Open web girders
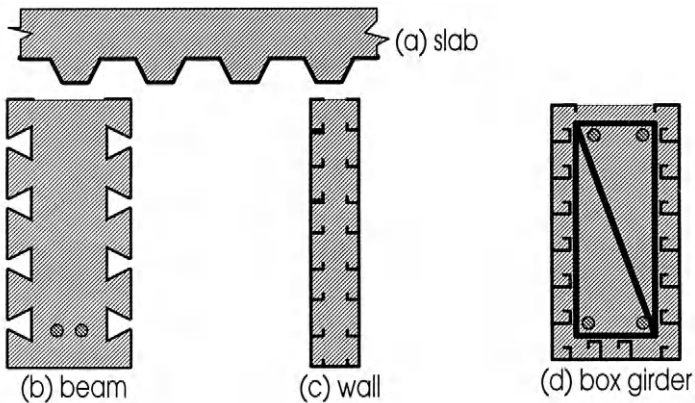
Fig. 1.10 Profiled sections

Examples of double composite action are shown in Fig. 1.11. The composite slab can be made to act integrally with the steel section by welding connectors through the troughs of the profiled section. The ribs of the profiled section can be parallel to the steel element (b), or transverse to the steel element (c), or even diagonal to the steel element. When the ribs of the profiled section are parallel to the steel element as in (b), then a haunched composite beam is formed. This type of construction, in which there is a double composite action, can also be used where there are web openings, as in Fig. 1.9(a), and also in composite stub girders (b) and in trusses (c) and (d). In the closed box girder section in Fig. 1.11(a), the shear connectors tie the steel girder to the concrete slab along the length of the beam. However, the shear connectors also tie the top flange of the steel girder to the concrete slab, so that this plate is acting compositely with the slab in the transverse direction. Hence composite actions in two directions are occurring within the composite beam. The flange plate

acting compositely with the slab in Fig. 1.11(a) is an example of composite plate girder construction. This form of construction also occurs in composite plated beams, as in Fig. 1.4, where the shear connection between the plate element and the reinforced concrete element can be provided by gluing or bolting.
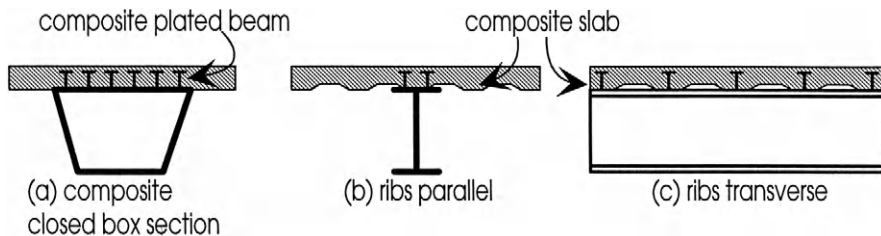
Fig. 1.11 Double composite action

Finally, in order to illustrate the versatility of composite construction, it is worth noting that the composite truss in Fig. 1.9(d) is an example of triple composite action, as the composite truss girder incorporates composite beams between the joints as well as transverse composite slab action. This form of construction is especially popular in North America.

1.2   General behaviour of composite beams

1.2.1   INTRODUCTION

The deformation of a continuous composite beam under gravity loads is sketched in Fig. 1.12(a). The distribution of forces in the positive or sagging region between the points of contraflexure is completely different from the behaviour in the negative or hogging region between a point of contraflexure and the adjacent support.

Between points of contraflexure, the composite beam can be visualised as being simply supported, as shown in Fig. 1.12(b). The resultant of the flexural forces in the concrete element of the composite beam is compressive, and the resultant forces in the steel element is tensile, so that the cross-section of the beam can be considered to consist of both a steel and concrete element as in (c). The concrete fibre adjacent to the steel/concrete interface is trying to expand under the flexural forces as shown in (b), whereas the steel fibre adjacent to the interface is trying to contract under the flexural loads. This relative deformation distorts the connectors, causing them to bear onto the concrete in the zones marked with an asterisk. The connectors are therefore applying a thrust onto the concrete that is directed towards the midspan of the beam, and are themselves subjected to horizontal shear forces. The flexural distortion of the composite beam also tries to induce vertical separation between the steel and concrete elements, and the tensile component of these forces is resisted by the shear connectors.
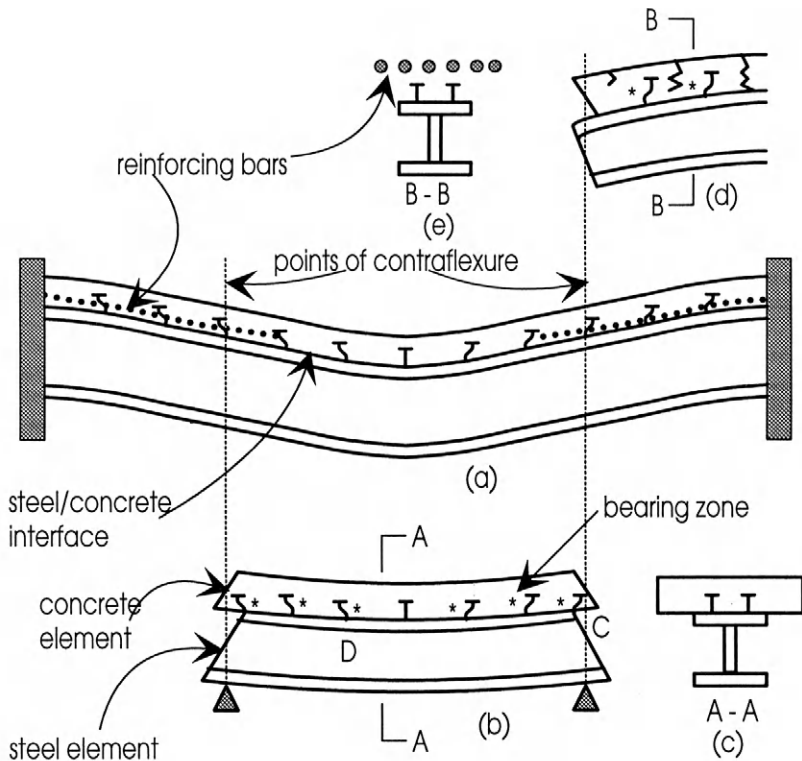
Fig. 1.12 Deformation of composite beam

In most simply supported composite beams in buildings, the neutral axis lies in the concrete element, so that all of the steel is in tension and hence buckling does not occur once the concrete has hardened. When the neutral axis lies in the steel element, the top flange may be totally or partially in compression. However, the steel top flange is less likely to buckle than a compression flange in a steel beam because it can only buckle away from the concrete element, and even then this buckle may be restrained by the ability of the shear connectors to resist the normal tensile forces across the interface.

In the negative moment region adjacent to the supports as in Fig. 1.12(d), the composite beam acts as a cantilever. The concrete is in tension and is generally fully cracked, so it does not contribute directly to the strength of the structure. The beam can therefore be considered to consist of two steel components, these being the steel element and the reinforcing bar elements as in (e). The section is therefore no longer composite but a steel structure, although it is still referred to as a composite beam as the concrete is required to transfer the load to the reinforcing bars, in the same way as the load is transferred through cracked concrete to the reinforcing bars in concrete structures. The flexural deformation of the steel and concrete elements causes the same distortion in the shear connectors as occurs in the positive region, so that these connectors are also applying a thrust onto the concrete directed towards the centre of

the beam as shown in (d). The bottom flange and much of the web of the steel element is subjected to compression, so that the negative moment region is prone to buckling. This behaviour is described in Section 1.2.3.

1.2.2 INTERFACE BEHAVIOUR

The deformations, stress distributions and modes of failure of composite beams depend on the behaviour of the shear connection between the steel and concrete elements. The behaviour of this bond is represented by the relationship between the interface longitudinal shear-load and slip as shown in Fig. 1.13. It can be seen that this bond behaviour varies from extremely brittle as in curve A, to extremely ductile as in curve B.
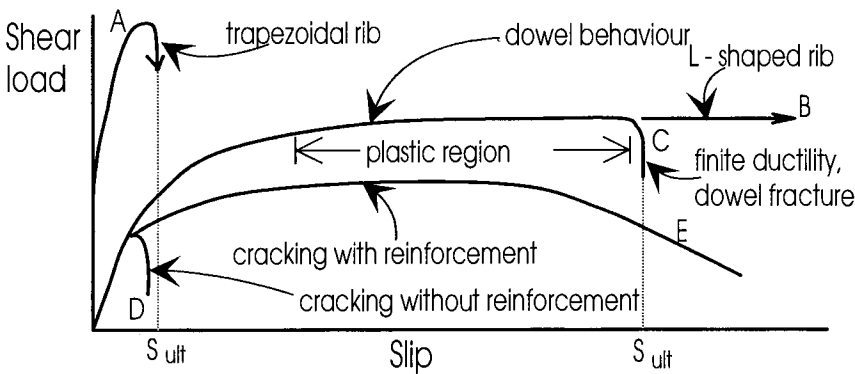
Fig. 1.13 Interface shear behaviour

The rib in a profiled sheet, as shown in Fig. 1.6, in composite profiled sheet construction transfers most of the longitudinal shear and prevents interface separation as it is encased by the concrete. This form of shear connection will therefore be referred to as rib shear connectors to distinguish them from mechanical shear connectors as in Fig. 1.5. The bond characteristics of rib shear connectors depends on the shape of the profiled rib. Composite beams made with L-shaped ribs, as in Fig. 1.6(c), exhibit extremely good ductile bond characteristics, as in curve B in Fig. 1.13. This is because the rib is fully encased by the concrete, and so can slide through the concrete without detaching. L-shaped rib connectors can therefore sustain almost unlimited slip before failure, and hence are well suited for composite construction. However, beams made with the trapezoidal ribs as in Fig. 1.6(b) tend to exhibit very brittle bond characteristics, as in curve A of Fig. 1.13, because the rib is not fully encased. After the chemical bond at the interface is broken, the trapezoidal rib tends to detach from the concrete, although embossments do help to make the rib more ductile. The bond in composite beams with trapezoidal ribs tends to fail at small finite slips S_{ult}, as in curve A in Fig. 1.13, which may prevent the composite beam from achieving its flexural capacity.

Mechanical shear connectors have a similar range of bond characteristics as rib shear connectors. The stud, bolt and angle connectors in Fig. 1.5 exhibit substantial

plastic regions, but will fracture at a finite slip as in curve C in Fig. 1.13. This is because the slip capacity is now controlled by the deformation capacity of the connector, as compared to profiled L-shaped ribs which simply slide through the concrete. Block connectors, (e) in Fig. 1.5, have very limited plastic regions as in curve A in Fig. 1.13 and can therefore be considered as non-ductile. All mechanical shear connectors have finite slip capacities, and fracture of the connector at this finite slip S_{ult} can cause premature failure of the composite beam if this limited slip capacity is not designed against.

Unlike profiled-rib connectors, mechanical connectors tend to impose very high concentrations of load onto the concrete element. This concentrated load is transferred from the steel element to the concrete element through the dowel action of the connectors. All mechanical connectors are simply steel dowels embedded in a concrete medium as illustrated in Fig. 1.14(a). The resistance of a connector to this dowel action is referred to as the *dowel strength*, and this strength is often quoted in national standards. The concentrated load is dispersed into the concrete element and the action of this dispersal can induce tensile cracking, as shown in the plan view of the concrete element in Fig. 1.14(b). These tensile cracks are induced by ripping, shear and splitting actions. Tensile cracking can also be induced by the dowel action, particularly when the connector is also resisting separation at the steel/concrete interface of the composite beam, and these cracks are referred to as *embedment cracks* as shown in (a). These four forms of tensile failure of the slab can affect both the dowel strength and ductility of the shear connection. When there are no reinforcing bars crossing the planes of cracking, then the strength of the dowel reduces immediately cracking occurs and the slip capacity is also reduced, as in D in Fig. 1.13. The presence of reinforcement across a crack plane makes failure much more ductile, as in curve E, and can even allow increases in load after cracking.
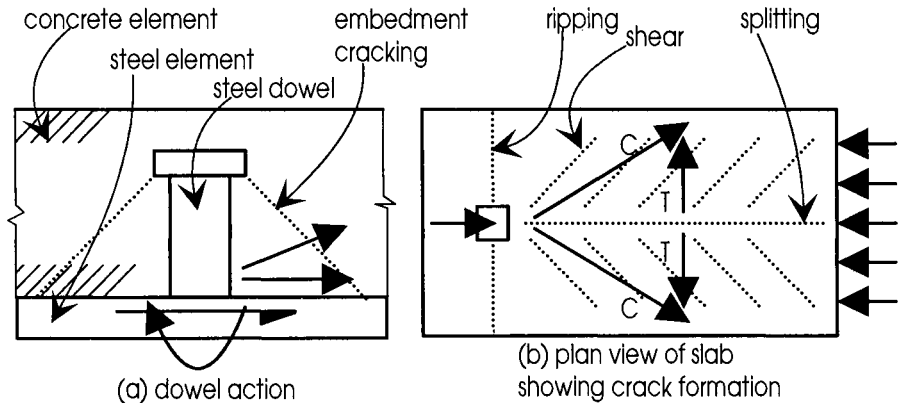
Fig. 1.14 Transfer of connector force

1.2.3   BUCKLING BEHAVIOUR

1.2.3.1   *General*

A governing strength limit state in the design of structural steelwork is that of buckling, and the phenomenon is devoted very considerable attention in national steel standards. Buckling can generally be attributed to the thin-walled nature and large elastic range of structural steel members.

Modes of buckling can generally be considered to be *overall*, as described in Section 1.2.3.2., and as *local*, as described in Section 1.2.3.3 and Chapter 5. As the term implies, overall buckling takes place when the whole member becomes unstable, and shifts sideways and twists to an adjacent equilibrium position, with the half-wavelength of the buckle being the order of the member length. On the other hand, local buckling takes place when there are localised distortions of the cross-sectional shape, with the buckling half-wavelength being of the order of the depth or width of the section. Many textbooks, such as Bleich (1952), Timoshenko and Gere (1961), Galambos (1968) and Trahair and Bradford (1991) treat these buckling modes in detail.

1.2.3.2   *Overall Buckling*

Both in the construction phase and when the concrete has hardened, overall buckling of the steel element must be designed against. Under the action of wet concrete during construction, the top flange of the steel is subjected to compressive stresses in the positive bending region, and instability may take place by the usual *lateral-torsional buckling* that is treated in national codes of practice for structural steelwork. Lateral-torsional buckling, as shown in Fig. 1.15(a), occurs when each cross-section of the steel element displaces and twists as a rigid body. Fortunately, this mode of failure is relatively easy to predict, and cross-bracing such as that shown in Fig. 1.15(b) or propping is often used.
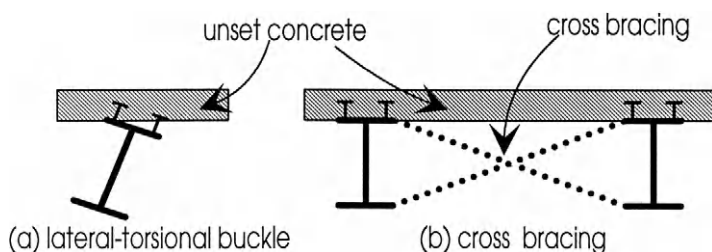
Fig. 1.15 Lateral - torsional buckling

On the other hand, the steel in the negative moment region of a hardened composite beam may buckle in what is called a *lateral-distortional* mode (Bradford 1992), as shown in Fig. 1.16. This is because the shear connection between the top flange of the steel element and the concrete slab prevents the twist of this flange during buckling, rendering the stiffness of the web to provide resistance to buckling of the bottom compressive flange of the steel element. The cross-section thus distorts in

its plane during buckling. Clearly in this case, lateral-torsional buckling such as that shown in Fig. 1.15(a) is not possible, although many national composite standards consider this as the limit state to be designed for, and accordingly cross-bracing is often specified. Lateral-distortional buckling strengths are greater in composite beams than lateral-torsional buckling resistances, and there is both theoretical and experimental evidence that the cross-bracing shown in Fig. 1.15(b) is unnecessary to prevent lateral-distortional buckling in the majority of cases when a universal section steel element is used.

web distortion   set concrete
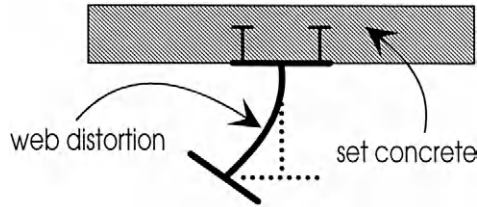
Fig. 1.16 Lateral - distortional buckle

1.2.3.3 *Local buckling*

In many cases, local buckling of the compression flanges and web is an instability possibility that must be prevented. Local buckling of a steel cross-section, as shown in Fig. 1.17, takes place when the component plates of the section distort out-of-plane, but with the straight line junctions at the intersections of the component plates remaining straight. The steel element in a composite beam may buckle locally in both the positive and negative bending regions.

Under positive bending and when the neutral axis lies in the steel web, the top flange is subjected to compressive stresses. This flange may buckle locally, but the restraint offered by the shear connectors, and the presence of the rigid concrete slab, contribute towards suppressing this mode of buckling. Such a buckling mode is usually unlikely to occur in many situations prior to the attainment of the full plastic moment.

line junction
set / remains straight
concrete
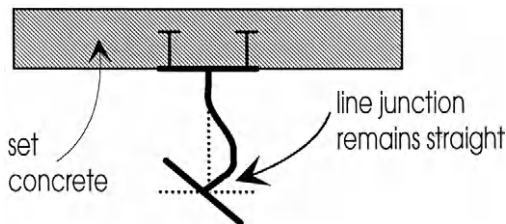
Fig. 1.17 Local buckling

In the negative moment region, local buckling can and often occurs. It is characterised by distortion of the web and rotation of the usually stocky flange, as shown in Fig. 1.17. To quantify local buckling, national composite codes of practice place limits on the depth to thickness ratios of the web which depend on the position

of the neutral axis. Limits are also placed on flange width to thickness ratios. Compact sections are defined as having web depth to thickness ratios d_w/t_w such that a plastic hinge will form prior to local buckling, as well as requiring limits on the flange breadth to thickness ratio b_f/t_f. Non-compact sections will yield before local buckling, but will buckle locally before full plasticity of the beam is achieved. On the other hand, slender sections will buckle locally before first yield of the bottom flange. Some composite bridge girders are made from slender steel components, and reduced bending moments must be used. Recent research (Azhari and Bradford 1993) has shown that the provision of a longitudinal stiffener attached to the web near the bottom flange may increase the local buckling capacity. Whilst not greatly deployed yet in practice, a longitudinal stiffener should serve to obtain a more favourable section classification, so that the flexural capacity of the composite beam prior to local buckling may be increased. A more detailed discussion of section classifications in both steel and composite cross-sections is deferred until Chapter 5.

1.2.4 EQUILIBRIUM

1.2.4.1 *General*

The behaviour of the composite beam will be illustrated in terms of the positive moment region in Fig. 1.12(b). Even though the cross-section in the negative moment region (e) appears different to that in the positive moment region (c), the interaction between the two elements in each section in the same, and hence the behaviour of the negative region can be considered to be the same as that in the positive region.

#### 1.2.4.2 *Equilibrium of forces within the composite beam*

Consider a simply supported beam with the cross-section shown in Fig. 1.18(a) and elevation (b). The beam has been cut at section A-A which is at a distance L_{sp} from the support. The shear load V is resisted by both the concrete contribution V_{conc} and by the steel contribution V_{steel}, although in many design procedures it is assumed that $V_{conc} = 0$. Let us assume that the section is subjected to the arbitrary flexural stress profile σ in (d) that has a neutral axis N-A in the steel element, so that there is compression in both the concrete and steel elements.

The flexural forces within the beam, that is along the length of the beam, can be derived by integrating the stress in Fig. 1.18(d) over the cross-section in (a). For example, the cross-section could be divided into the seven elements shown in (c), the mean stress within each element can be determined from (d), and if as a first approximation it can be assumed that these forces act at the mid-depth of their element, then the magnitude and distribution of the internal forces F is known, as shown in (e). Equilibrium requires that $\Sigma F = 0$, as it is assumed that there are no external longitudinal forces being applied such as occurs in post-tensioning.

There are numerous ways of visualising the stress resultants R in Fig. 1.18(f) of the internal force distribution F in (e). For example, the internal forces in (e) can be visualised as simply the internal couple in (f). The compressive forces F_1 to F_5 in (e)

can be summed to give the total compressive force in the beam F_{comp} in (f) and the position at which this acts, say h_1, can be determined by equating the moments of F_1 to F_5 and F_{comp} about the steel/concrete interface. Similarly, the total tensile force F_{ten} can be determined by summing F_6 and F_7, and its position h_2 can be determined by taking moments about the interface. From horizontal equilibrium, $F_{comp} = F_{ten} = F_r$, and from rotational equilibrium with the external applied moment $VL_{sp} = F_r(h_1+h_2)$.
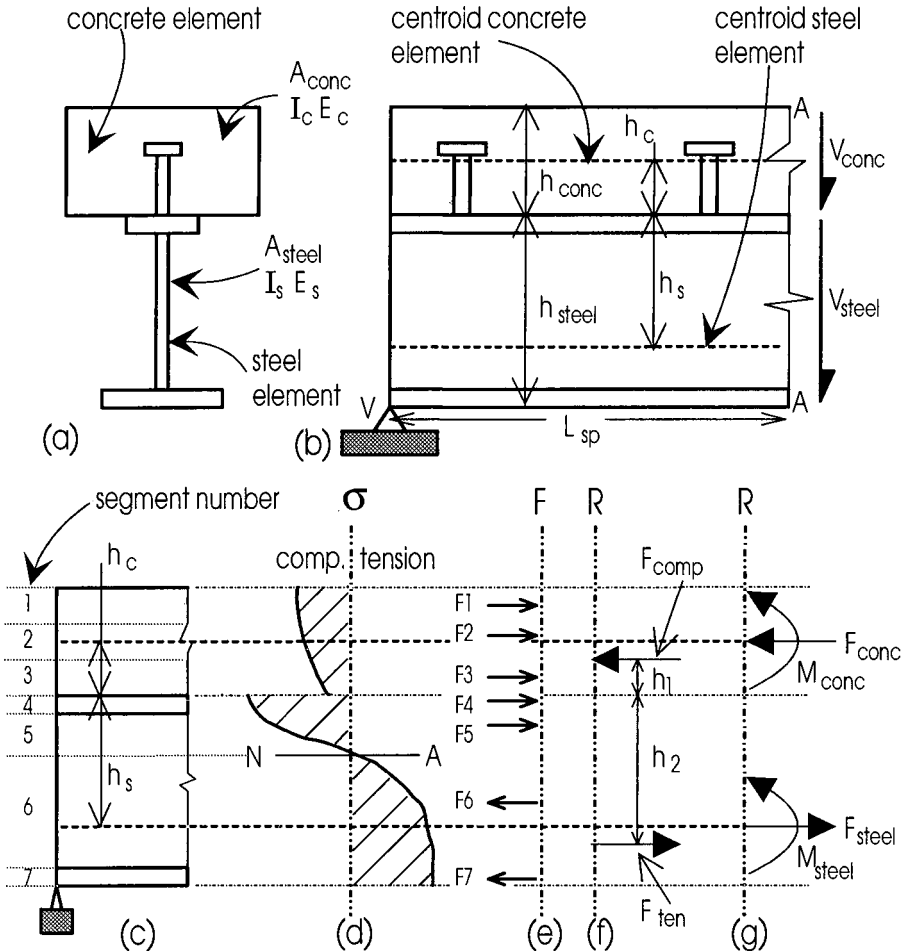
Fig. 1.18 Steel and concrete elements

Alternatively, F_1 to F_3 can be summed to determine the resultant force in the concrete element F_{conc} in Fig. 1.18(g). The force F_{conc} can be assumed to act at the centroid of the concrete element at a distance h_c from the steel/concrete interface, and hence the moment about this plane M_{conc} can be determined by summing the moments of F_1 to F_3 about this centroid. In a similar fashion, the stress resultants F_{steel} and

M_{steel} at the centroid of the steel section at a distance h_s from the interface can be determined. From horizontal equilibrium

$$F_{conc} = F_{steel} \qquad\qquad (1.1)$$

and from rotational equilibrium of the internal moment

$$M = M_{conc} + M_{steel} + F_{conc}\left(h_s + h_c\right) \qquad\qquad (1.2)$$

The internal moment is therefore the sum of three components, these being the moment resisted by the concrete element M_{conc}, the moment resisted by the steel element M_{steel} and a moment resisted by the longitudinal axial forces in each element $F_{conc}\left(h_s + h_c\right)$. However, in many ultimate strength design procedures it is assumed that the concrete element is not reinforced in the longitudinal direction, so that M_{conc} = 0.

1.2.4.3   *Equilibrium of forces within the concrete element*

The distribution of forces in the shear connectors in Fig. 1.18(b) can be determined by detaching the concrete element from the steel element as in Fig. 1.19.   The longitudinal force in the concrete on the left hand side is zero as this section has specifically been chosen to occur at a section of zero moment, namely at the support of a simply supported beam or at a point of contraflexure in a continuous beam. Hence from simple horizontal equilibrium, the total force on the shear connectors F_{shear} must equal the force in the concrete element, so that

$$F_{shear} = F_{conc} \qquad\qquad (1.3)$$

The concrete element is still subjected to a couple, $F_{conc}h_c$ in Fig. 1.19, which is in equilibrium with the couple formed by the resultant of the normal forces across the interface $F_{norm}L_1$ and the moment in the concrete element M_{conc}. As mentioned earlier, in most applications M_{conc} is assumed to be zero, particularly when dealing with sections near their ultimate strength. It can therefore be seen that the rotation of the concrete element is resisted by normal forces across the interface. The normal tensile forces across the interface can only be provided through the shear connectors, whilst the normal compressive forces can be resisted by both the shear connectors and bearing at the interface. Hence the importance of designing shear connectors to resist normal tensile forces now becomes clear.

It is worth noting that as $F_{conc} = F_{shear}$ from Eq. 1.3, the third component of the internal moment in Eq. 1.2 is also equal to $F_{shear}\left(h_s + h_c\right)$. This third component of the internal resisting moment is therefore directly dependent on the shear force on the connectors in a shear span, which is often governed by the shear strength of the connectors in the shear span P_{shear}. For example, when there are no shear connectors so that $F_{shear} = P_{shear} = 0$, then this third component is zero. The internal resistance

$F_{shear}\left(h_s + h_c\right)$ is therefore the direct contribution of the shear connectors, and can thus be considered to be the internal resistance due to the composite action.
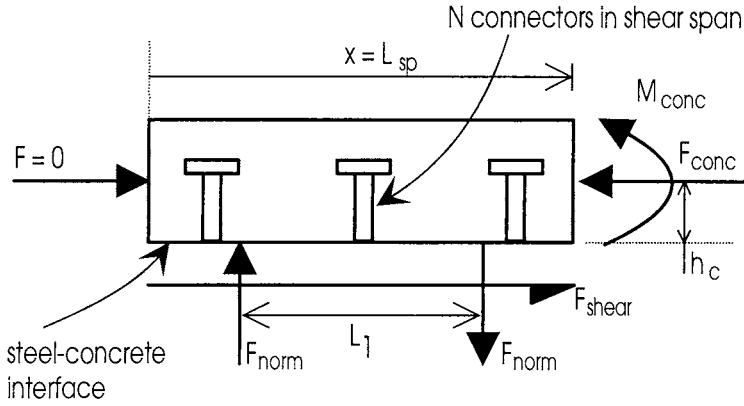
Fig. 1.19 Concrete element

An analytically convenient method for describing the longitudinal interface shear force F_{shear} is the shear force per unit length, which is called the *shear flow* q. This will sometimes be referred to in the text as the shear flow force when it is necessary to distinguish between the shear force per unit length and the shear strength per unit length. The distance from the section being considered to the point of contraflexure is also an important parameter in analyses, and this will be referred to the shear span L_{sp} as shown in Fig. 1.19. Hence the mean shear flow q_m in this figure is F_{shear}/L_{sp}.

1.2.4.4 *Degree of shear connection*

The force in the concrete element F_{conc} in Fig. 1.19 is governed by the relative strengths of the steel element, the concrete element, and the longitudinal shear strength of the shear connectors in the shear span L_{sp}. We will define the axial strength of the steel element P_{steel} as the cross-sectional area of the steel element, A_{steel} in Fig. 1.18(a), multiplied by the yield strength of the steel element f_y. The axial strength of the concrete element P_{conc} is the cross-sectional area of the concrete element A_{conc} multiplied by the equivalent yield strength of the concrete, that is often taken as 85% of the compressive cylinder strength f_c or about 72% of the cube strength f_{cu}.

The longitudinal shear strength of the shear connectors P_{shear} is the dowel strength of the individual connectors P_d multiplied by the number of connectors N in the shear span. A convenient analytical tool is to deal with the strength of the shear connectors per unit length, and this is referred to as the shear flow strength Q, as compared with the shear flow force q. For example, the mean shear flow strength Q_m of the shear connectors in the concrete element in Fig. 1.19 is NP_d/L_{sp}. Using shear

flow strengths in the analyses is useful because it allows the choice and sizing of the shear connectors to be done in the final stages.

There are three possible stress distributions that can occur in composite beams at their maximum strength, and these are illustrated in Fig. 1.20 for the beam in Fig. 1.18. It has been assumed in Fig. 1.20 that $M_{conc} = 0$, as we are dealing with the maximum flexural strength, where the contribution to M_{conc} through the tensile strength of the concrete is negligible. We are also assuming that there are no longitudinal reinforcing bars at the soffit of the concrete element to contribute to M_{conc}, which is the normal case in design. In case 1, in Fig. 1.20, the strength of the steel section P_{steel} is less than the strength of the concrete section P_{conc}. As $P_{steel} < P_{conc}$, the steel element must be fully yielded as shown in (b), and as $P_{conc} > P_{steel}$, only part of the area of the cross-section of the concrete element A_{conc} can be fully stressed, and so the neutral axis must lie in the concrete element as shown in (c). As the steel section is fully yielded, the force in the steel element $F_{steel} = P_{steel}$, that is the axial strength of the steel element, and for horizontal equilibrium across the section being considered, the force in the concrete element $F_{conc} = P_{steel}$. Hence the stress resultants across the section are both equal to P_{steel} as shown in (a). It is also necessary to ensure that the concrete element is in equilibrium. For case 1 in Fig. 1.20, F_{conc} in Fig. 1.19 is equal to P_{steel}. Therefore, the force in the shear connectors $F_{shear} = P_{steel}$. If the strength of the shear connectors $P_{shear} > P_{steel}$, then the shear connectors can resist the force in the concrete which is P_{steel}, and hence can maintain equilibrium. The distribution of forces in (a) in Fig. 1.20 can therefore be maintained, and this is referred to *full shear connection* as the strength of the shear connectors does not affect the stress resultants in the composite beam in (a). The moment capacity of the composite beam with full shear connection is thus given by

$$M_{fsc} = P_{steel} h_1 \qquad\qquad (1.4)$$

as M_{steel} in Eq. 1.2 is zero since the stress distribution in the steel element in (b) is uniform and M_{conc} is assumed to be negligible.

If on the other hand in case 1 in Fig. 1.20, $P_{shear} < P_{steel}$, then from equilibrium of the concrete element in Fig. 1.19 the force in the concrete element F_{conc} must be reduced from P_{steel}, as shown in Fig. 1.20(a), to P_{shear} as shown in case 3 in Fig. 1.20(g). For equilibrium, F_{steel} in (g) must also equal P_{shear}, so that the moment capacity of the composite section is now given by

$$M_{psc} = M_{steel} + P_{shear} h_2 \qquad\qquad (1.5)$$

as M_{steel} in Eq. 1.2 is no longer zero since the stress distribution in the steel element in (b) is no longer uniform. This condition is referred to as *partial shear connection*, since the strength of the shear connectors now controls the strength of the composite beam. As P_{shear} is less than P_{steel}, the steel must be partly in compression and partly in tension, and the concrete must be partly stressed as shown in (h). Hence the

distribution of stresses shown in (h) with two neutral axes is typical of composite beams with partial shear connection.

Case 1: $P_{steel} < P_{conc}$; $P_{shear} > P_{steel}$; full shear connection

(a)   (b)   (c)
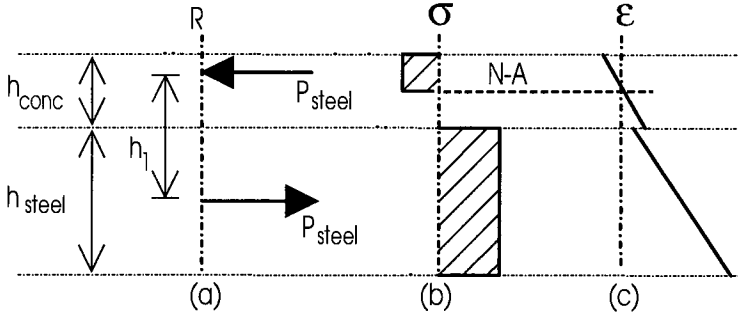
Case 2: $P_{conc} < P_{steel}$; $P_{shear} > P_{conc}$; full shear connection

(d)   (e)   (f)
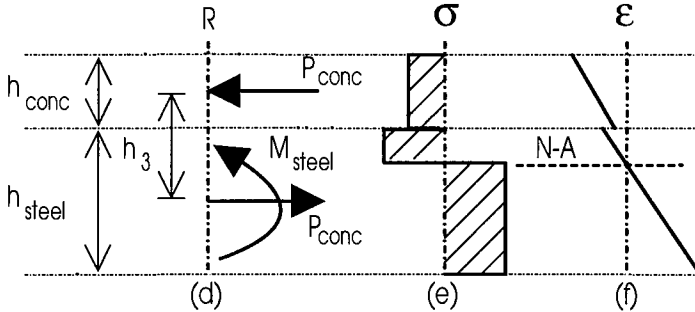
Case 3: $P_{shear} < P_{conc}$; $P_{shear} < P_{steel}$; partial shear connection

(g)   (h)   (i)
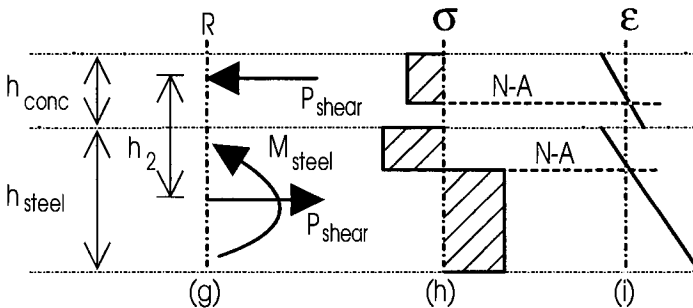
Fig. 1.20 Degree of shear connection

A similar rationale can be applied to case 2 in Fig. 1.20, as has already been applied to case 1. When $P_{conc} < P_{steel}$ and $P_{shear} > P_{conc}$, so that we are dealing with full shear connection, then the neutral axis must lie in the steel element as in (e) and the stress resultant must be P_{conc} as in (d). Because of this, the moment capacity for full shear connection is now given by

$$M_{fsc} = M_{steel} + P_{conc}h_3 \tag{1.6}$$

When $P_{shear} < P_{conc}$, then equilibrium of the concrete element can no longer be maintained, so that the equilibrium condition reverts to that for partial shear connection (g) which has already been discussed. It can be seen from a comparison of the three possible stress distributions (b), (e) and (h) that *there is always one neutral axis when there is full shear connection, and that there are always two neutral axes when there is partial shear connection.* Moreover, full shear connection is always associated with one of the elements being fully stressed and hence achieving its full axial yield strength P.

1.2.4.5 *Flexural capacity*

The strength of the shear connection that is just sufficient to achieve full shear connection $(P_{shear})_{fsc}$ can be deduced from cases 1 and 2 in Fig. 1.20. In case 1, when $P_{steel} < P_{conc}$, then $(P_{shear})_{fsc} = P_{steel}$. Similarly in case 2, when $P_{conc} < P_{steel}$ then $(P_{shear})_{fsc} = P_{conc}$. The *degree of shear connection* η is often defined as the strength of the shear connection in a shear span, as a proportion of the strength required for full shear connection, so that

$$\eta = \frac{P_{shear}}{\left(P_{shear}\right)_{fsc}} \tag{1.7}$$

A typical example of the variation of the flexural capacity of the composite beam with the degree of shear connection is shown in Fig. 1.21. When there are no shear connectors, that is when $\eta = 0$, then $P_{shear} = 0$ in Fig. 1.20(g) and in Eq. 1.5 and hence the strength of the composite beam is simply the flexural strength of the steel element M_{steel} in Fig. 1.21. When $P_{shear} > \left(P_{shear}\right)_{fsc}$, that is when $\eta > 1$, then the flexural capacity is constant at M_{fsc} in Fig. 1.21, which is the flexural capacity for full shear connection and is given by either (a) or (d) in Fig. 1.20 or by Eqs. 1.4 and 1.6. Between these two extreme values, at M_{steel} at $\eta = 0$ and at M_{fsc} at $\eta = 1$, the flexural capacity of the composite beam is given by M_{psc} in Fig. 1.21. This is the flexural capacity for partial shear connection and is given by both (g) in Fig. 1.20 and Eq. 1.5. When $\eta > 1$, the strength of the composite section is controlled by either P_{conc} or P_{steel}, and when $\eta < 1$ the strength is controlled by P_{shear}. In all of these analyses, we are assuming that the shear connection never reaches its finite slip S_{ult} in Fig. 1.13.

Fig. 1.21 can also be viewed as the variation in flexural strength of a simply supported composite beam along its length. In this case, the abscissa is the distance measured from a support L_{sp} as a proportion of the distance L where the maximum moment in the beam occurs. Hence at $L_{sp} = 0$, $\eta = 0$ and at $L_{sp} = L$, $\eta = 1$. When the connectors are uniformly distributed along the beam, then the degree of shear connection at a section at L_{sp} from the support is given by $\eta_{Lsp} = L_{sp}/L$, so that the flexural strength at L_{sp} is equal to M_{Lsp} in Fig. 1.21. It can now be clearly seen that

unlike steel beams and concrete beams, the moment capacity of a composite beam varies along its length from M_{steel}, at a support or point of contraflexure, to M_{fsc} should there be enough shear connectors in the shear span.
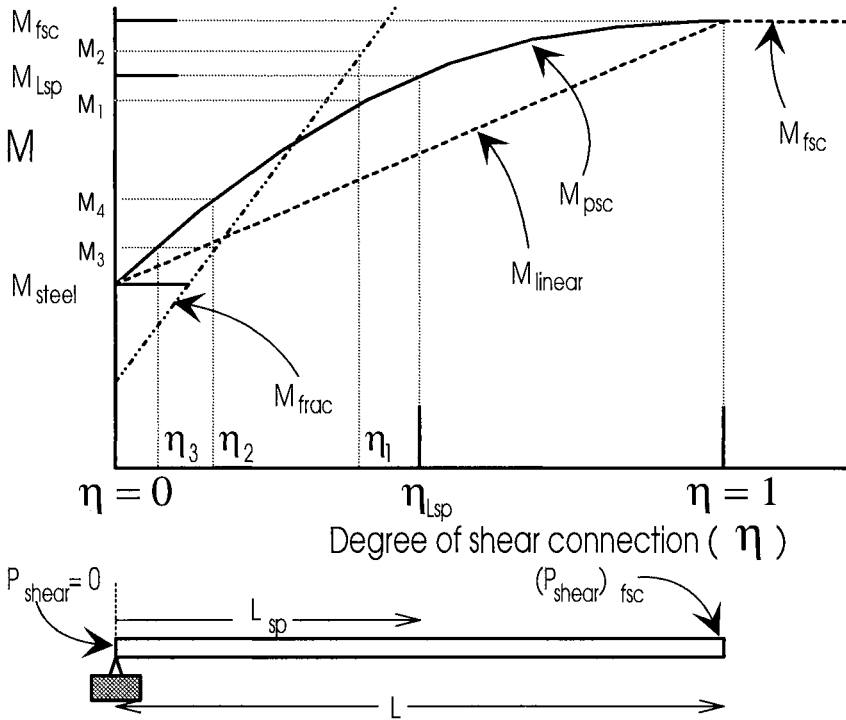
Fig. 1.21 Variation of flexural capacity

It can also be seen that even though this beam may have full shear connection at the section at L in Fig. 1.21, that is at $\eta = 1$, the degree of shear connection at any other section η is less than 1, so that the beam has partial shear connection everywhere except at the section at L. However, it is normal practice to categorise a beam according to its degree of shear connection at the maximum moment section, and this will be referred to as η_{max}.

1.2.5 COMPATIBILITY

1.2.5.1 *General*

The behaviour of composite beams is directly affected by the slip of the shear connection at the steel/concrete interface. The form of the slip characteristic, examples of which are shown in Fig. 1.13, is very important because it can affect both the method of analysis and the flexural capacity of the composite beam.

1.2.5.2 *Slip and slip strain*

The elevation of a simply supported composite beam is shown in Fig. 1.22(a). Consider the section A-B-C-D. The section A-B is in the concrete element, where B is adjacent to the steel/concrete interface, and C-D is in the steel element, where C is adjacent to the interface. When the composite beam is unloaded, both of these sections are in line and at a distance L from some reference axis. After a load P is applied, the section deforms as shown in (b). The flexural forces tend to cause the top fibres of both the concrete and steel elements to contract and the bottom fibres of these elements to expand as shown, causing a sliding action across the interface. The relative movement across the interface that is induced by this sliding action is referred to as the *slip* s. If the new position of B in the concrete element is at $L + u_c$, and the new position of C in the steel element is at $L + u_s$, then the interface slip is given by s $= u_c - u_s$. This slip is resisted by the interface longitudinal shear forces.
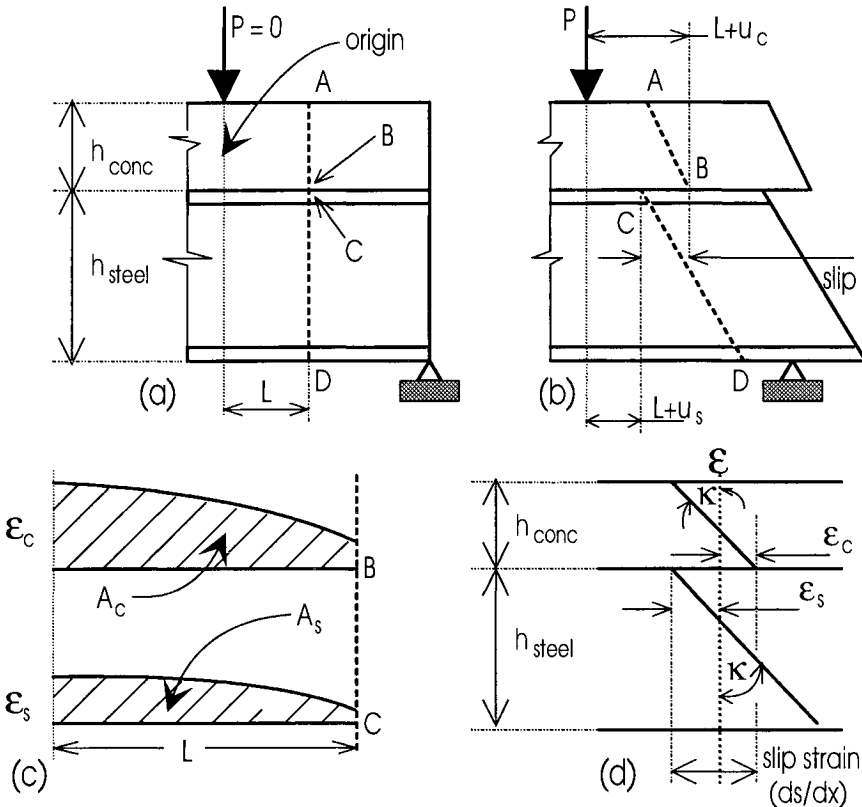
Fig. 1.22 Slip and slip strain

The slip at the interface can be derived by considering the longitudinal strains in the concrete and steel elements adjacent to the interface, that is at levels B and C in Fig. 1.22(b). Let us assume that the applied load causes a strain distribution ε_c in the

concrete element adjacent to the interface that varies over the length L as shown in (c), and that the origin of the reference axis, that is the left hand side of L, is chosen to occur at a position of zero slip. The integral of this strain distribution ε_c over L is equal to the movement of B relative to the origin of the axis, that is $\int_L \varepsilon_c \, dx = A_c = u_c$

where A_c is the area shown in (c). Similarly the strain in the steel element adjacent to the interface ε_s varies over the length L as shown in (c), so that $\int_L \varepsilon_s \, dx = A_s = u_s$. As

it has already been shown that $s = u_c - u_s$, then $s = \int_L \varepsilon_c \, dx - \int_L \varepsilon_s \, dx$. Differentiating

gives

$$\frac{ds}{dx} = \varepsilon_c - \varepsilon_s \tag{1.8}$$

where the derivative of the slip ds/dx is referred to as the *slip strain*.

The slip strain induced by the interface slip is shown diagrammatically in Fig. 1.22(d). There are now two strain profiles which are parallel because it is assumed that there is no separation at the steel/concrete interface, and hence the curvatures κ in each strain profile are the same. The slip strain ds/dx is the step change between the two strain profiles and occurs at the steel/concrete interface.

1.2.5.3 *Degree of interaction*

Consider the case of a composite beam in which the interface is greased so that there are no interface shear forces to restrict the interface slip. However, it will still be assumed that there is no separation between the two elements so that the curvatures are the same. In this case $F_{conc} = F_{steel} = 0$ in Fig. 1.18(g), so that the composite component of the flexural resistance $F_{conc}(h_c + h_s)$ in Eq. 1.2 is zero. We are now simply dealing with two flexural members which happen to have the same curvature and the external moment is now resisted by pure flexure in the concrete beam M_{conc}, and by pure flexure in the steel beam M_{steel}. The strain profile for this configuration is shown in Fig. 1.23(a). Because there is no resistance to the shear at the interface, this condition is referred to as *no-interaction*.

Consider now the case of a composite beam in which interface slip is totally prevented, such as occurs when the two elements are glued together or when the frictional bond at the interface has not been overcome. In this case $\varepsilon_c = \varepsilon_s$ in Fig. 1.23(b) and the slip strain ds/dx = 0. This condition is referred to as *full-interaction*. *Partial-interaction*, as shown in (c), simply refers to bond conditions between no-interaction and full-interaction.

It must be emphasised that the *degree of interaction* is not the same as the degree of shear connection that has already been described in Section 1.2.4.4. The degree of shear connection is governed by the strength of the shear connectors in a composite beam, and deals with failure when one of the components of strength,

namely P_{conc}, P_{steel} or P_{shear} is exceeded. On the other hand, the degree of interaction is governed by the stiffness of the shear connectors in a composite beam and, as will be shown, deals with failure when a component does not have sufficient ductility. However, the degree of shear connection and the degree of interaction are directly related because increasing the number of connectors in a beam both increases the shear strength and the shear stiffness of the shear connection.
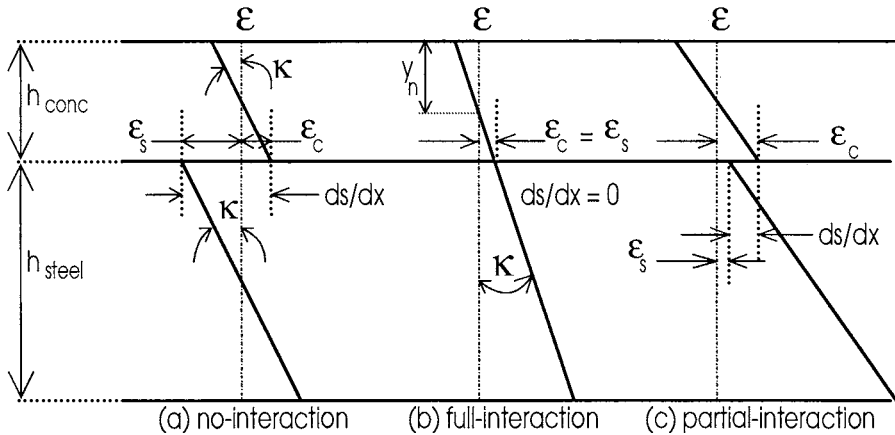
Fig. 1.23 Degree of interaction

The interrelationship between the degree of shear connection and the degree of interaction is further illustrated in Fig. 1.20. In case 1 for full shear connection, the neutral axis lies in the concrete element as shown in (b). Therefore, both the concrete and steel below the neutral axis are in a region of tensile strain as shown in (c), so that the slip strain is associated with a step change in strains of the same sign, in this case tensile. In case 2, which is also dealing with full shear connection, but where the neutral axis is now in the steel element, the slip strain is also associated with a step change in strains of the same sign, but this time compressive. In contrast, when dealing with partial shear connection, the slip strain is always associated with a step change in strains of different signs, as shown in (i). As the strains change sign at the interface when there is partial shear connection, the slip strain tends to be larger than that associated with full shear connections. Hence the slip strains in beams with partial shear connection tend to be significantly larger than those in beams with full shear connection.

It is also worth re-emphasising the different shapes of strain profiles associated with the degree of shear connection. A comparison of Figs. 1.20(c) and (f) and (i) shows that full shear connection is associated with one neutral axis and a step change within the same sign, whereas partial shear connection is associated with two neutral axes and a step change with different signs.

1.2.5.4 *Behaviour of a composite beam*

A simply supported composite beam is shown in Fig. 1.24(a). The beam is loaded at midspan, and so both shear spans act in an identical fashion. On applying a load, the slip strain varies as shown in (b). When there is no interaction, the strain profile in Fig. 1.23(a) applies. At the supports in Fig. 1.24, the moments are zero, so that the curvature $\kappa = 0$ in both elements, hence $\varepsilon_c = \varepsilon_s = 0$ and the slip strain $ds/dx = 0$, as shown in Fig. 1.24(b). The curvature κ in Fig. 1.23(a) is largest at midspan, where the moment in the beam is largest, and hence the slip strain along the beam for no-interaction is as shown in Fig. 1.24(b), being maximum at midspan and zero at the supports. When there is full-interaction the strain profile in Fig. 1.23(b) applies throughout the length of the beam, and hence the slip strain is zero throughout as shown in Fig. 1.24(b). The distribution for partial-interaction simply lies between these two extremes.
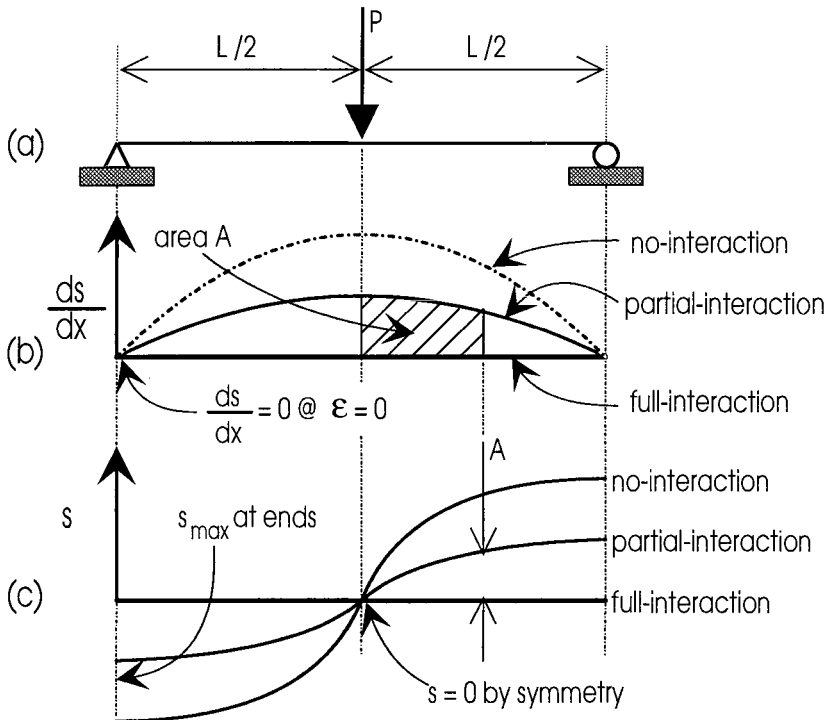
Fig. 1.24 Variation in slip and slip strain

Once the variation of the slip strain along the beam has been determined, it is a simple procedure to calculate the variation of slip in the beam by integrating the slip strain along the beam and allowing for known boundary conditions. As an example of a boundary condition, it can be deduced that the slip at midspan in the beam in Fig. 1.24 is zero because the beam and loading conditions are symmetrical about the midspan. The integration procedure is shown diagrammatically in (b) and (c), where the area A in (b) is the height A in (c) and where A has been determined from midspan

as the slip at midspan is zero. It can be seen that the maximum slip s_{max} occurs at the supports, s_{max} increases as the degree of interaction reduces, and s_{max} increases as the span length L increases, as it has been derived by integrating the slip strain along the half-span.

1.2.5.5   *Flexural capacity*

The flexural capacity of a composite beam can be limited by the finite slip capacity of the shear connection, shown as S_{ult} in Fig. 1.13. A shear connector with a finite ductility will therefore fracture when the maximum slip $s_{max} = S_{ult}$, and the maximum applied moment at which this occurs will be referred to as the *moment capacity at fracture* M_{frac}. It has already been shown that the maximum slip in a composite beam depends on the degree of interaction, and that the degree of interaction is also proportional to the degree of shear connection. Therefore for a composite beam of fixed cross-section, span and connector slip capacity S_{ult}, the moment at which fracture occurs M_{frac} varies with the degree of shear connection as shown in Fig. 1.21.

Consider a beam with a degree of shear connection η_1 in Fig. 1.21 where $M_{frac} > M_{psc}$ as shown. The beam will fail at M_1 due to a lack of strength in the connectors before they have the chance to fracture at the moment M_2 due to the limited slip of the connectors. When the degree of shear connection is η_2, the connectors will fracture at a moment M_3. The beam will therefore fail prematurely before its partial shear connection capacity M_4, which was derived from the strength of the connectors, is reached. At η_3 the connectors will fracture at a moment less than M_{steel}, but this will not prevent the composite beam acting as a steel beam and achieving a moment capacity of M_{steel}. Finally when $\eta > 1$, failure of the beam is governed by the axial strength of either the steel or concrete element.

1.3   General behaviour of composite columns

1.3.1   GENERAL

As mentioned in Section 1.1.2, composite columns are generally classified as encased columns or concrete-filled steel tubes. Encased columns are formed by surrounding a structural steel shape, generally one or more I-sections, with concrete. They are usually rectangular or sometimes circular in shape, and conventional longitudinal reinforcing bars are often included. On the other hand, concrete-filled steel tubes are manufactured by filling either rectangular or circular hot-rolled tubing, or larger diameter fabricated steel tubes, with unreinforced concrete. For both types of column, the steel and concrete share in carrying the loads. Concrete-filled tubes are susceptible to local buckling and the concrete within the tube is subjected to triaxial forces, so that the behaviour of encased members and the behaviour of concrete-filled tubes are substantially different as ultimate conditions are reached.

The usual definition of a column is a structural member which carries only concentric axial compression. If the member is a steel element and is subjected to bending as well as axial compression, as occurs when the load is applied eccentrically, it is referred to as a *beam-column*, and the various national standards present load-moment interaction equations which are slenderness-dependent, and which must be satisfied for the strength limit state. The behaviour of steel beam-columns is treated in texts such as Trahair and Bradford (1991). Reinforced concrete elements in frameworks are also subjected to bending as well as axial compression, but such elements are still referred to as 'columns'. Although slenderness is often a factor in their design, the strength of reinforced concrete members is usually governed by their cross-section capacity in bending and compression. Texts such as Warner, Rangan and Hall (1989) and Nawy (1990) treat the behaviour of reinforced concrete columns in depth.

In this book, composite members subject to both compression and bending will be referred to as *columns*. Because of the presence of both steel and concrete in a composite column, the behaviour of such a member is akin both to a steel beam-column and a reinforced concrete column. Both approaches to design are, in fact, adopted by researchers, and these are treated in depth in Chapter 18. Generally speaking, short or stocky composite columns are treated by the reinforced concrete approach based on section material strengths. Slender composite columns, which do not contain appreciable bending actions, are treated by the steel approach which is based on a design strength that is affected by the slenderness of the column.

In all column analysis approaches used at both ultimate and serviceability limits, it is assumed that there is full interaction between the concrete element and the steel element. This implies that the strain profile across the section remains uni-linear, so that there is no step change or slip-strain across the steel/concrete interface, as is often assumed in composite beam design. This assumption is reasonable, since the area of the interface is generally fairly large and hence good bond is provided at relatively low bond stresses. It is also worth noting that the bond stresses in composite columns are generally lower than those in beams, because the columns are normally symmetrical. For example, in linear elastic analyses, the shear flow q at the steel/concrete interface is given by the well-known equation (Hall 1984)

$$q = VA\frac{\bar{y}}{I} \tag{1.9}$$

where V is the shear force, A is the area of a free body cut away from the section, q is the shear flow at the cut, and $\bar{y}$ is the distance between the centroid of the free body and the centroid of the whole section. Because of the symmetry of the steel and concrete elements within the composite column, as shown in Fig. 1.7, the distance $\bar{y}$ between the centroid of say the free body steel-element and the centroid of the whole section is generally zero, and hence the shear flow is zero. Once nonlinearity occurs, such as due to tensile cracking in the concrete, $\bar{y}$ increases and a shear flow is induced which is generally less than in a beam.

1.3.2   MODES OF FAILURE

Composite columns are usually categorised by their modes of failure. Short or *stocky columns* usually attain the cross-sectional strength, so that their failure is governed by the yield strength f_y of the steel and the cylinder strength f_c of the concrete. Stocky columns are therefore material-dependent.

Long or *slender columns*, on the other hand, fail by so-called flexural buckling in much the same way as a slender steel column. Under such conditions, the composite column becomes unstable, and buckles sideways with the buckling half-wavelength being the order of the length of the column.

As noted in Section 1.2.3.3, local buckling may also occur. Fully encased columns will not buckle locally, owing to the restraint provided by the concrete encasement. However, if any of the steel element is free, as in Figs. 1.7(b), (c), (d) and (e), then the steel element may buckle locally. However, the rigid concrete medium forms a restraint against the free formation of buckles (Wright 1993, Uy and Bradford 1994), so that local buckling is less likely than if the concrete element was absent, as in a pure steel member.

1.3.3   STOCKY COLUMNS

A short or stocky column is so short that flexural buckling will not occur, although local buckling must in some cases be designed against. Stocky columns are designed primarily on the material strengths of the concrete and steel elements.

Consider the encased column shown in Fig. 1.25(a). The neutral axis is arbitrarily positioned $k_u D$ below the top fibre, where k_u is the neutral axis parameter under ultimate conditions. The resulting strain diagram is shown in (b), where it is assumed that the ultimate or crushing strain at failure in the concrete is 0.003 (Warner, Rangan and Hall 1989, Nawy 1990). The strain profile is thus determined, and by invoking the relevant material constitutive properties in Chapter 2, we can find the resulting force F_{conc} in the concrete, and that in the steel F_{steel}, by integrating over the area of each element. If F_{steel} is positioned h_s from the plastic centroid (Hall 1984) and F_{conc} is positioned h_c from the plastic centroid of the section, then the net axial force, N_s, may be obtained from

$$N_s \;=\; F_{steel} + F_{conc} \tag{1.10}$$

while the moment about the plastic centroid may be obtained from

$$M_s \;=\; F_{steel} h_s + F_{conc} h_c \tag{1.11}$$

Of course, N_s and M_s represent the ultimate strengths of the stocky column, and they may plotted, by varying k_u as a path parameter, as in Fig. 1.26. This interaction curve is referred to as a *material failure envelope*, and is treated more fully in Chapter 18. The interaction curve is analogous to that for reinforced concrete

columns, and national standards reduce the (N_s, M_s) combinations for design by using reduction or safety factors.
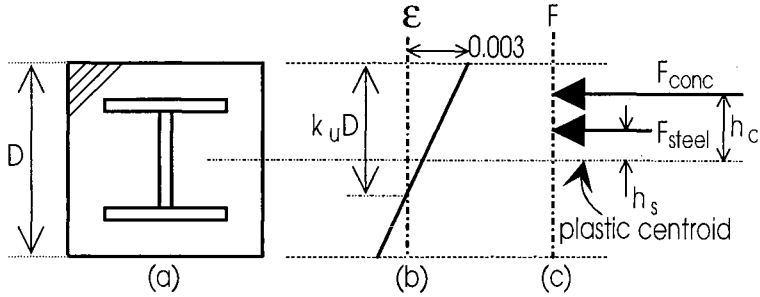
Fig. 1.25 Encased column
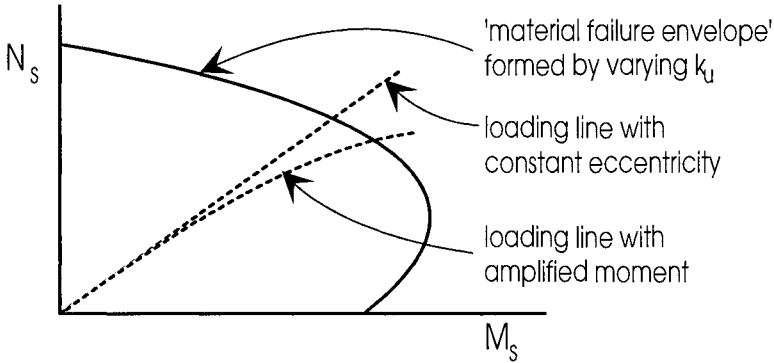
Fig. 1.26 Interaction diagram

1.3.4 SLENDER COLUMNS

1.3.4.1 *Reinforced concrete approach*

Under the reinforced concrete approach to slender columns, the member is assumed to be loaded by an axial force N at end eccentricities e_1 and e_2. Consider such a column shown in Fig. 1.27, where the moment M varies from Ne_1 at end 1 to Ne_2 at end 2. By assuming M is initially linear, we may calculate the deflection v along the column, but this produces a secondary moment Nv so that the moments and deflections are magnified. The behaviour is thus nonlinear, owing to the amplification of the moment and deflection due to the axial force N, and in braced columns this is commonly referred to as the P-δ *effect*.

The P-δ effect is primarily due to geometric nonlinearity, but it is accentuated by material nonlinearities such as yielding of the steel element, or cracking and shrinkage of the concrete. The behaviour of the column is thus difficult to quantify

rigorously, and certain simplifications have to be made. For example, if $e_2 > e_1$ so that the largest moment Ne_2 occurs at end 2, then the maximum moment M_m may be approximated by

$$M_m = \frac{k_m Ne_2}{1 - \dfrac{N}{N_c}} \tag{1.12}$$

where N_c is the buckling load under axial force which incorporates the different materials and concrete cracking, and where

$$k_m = 0.6 + 0.4\beta > 0.4 \tag{1.13}$$

reflects the non-uniform moment distribution, in which β is the ratio of the smaller to larger end eccentricities $(-1 \leq \beta \leq 1)$ and is positive if the column is bent in single curvature.
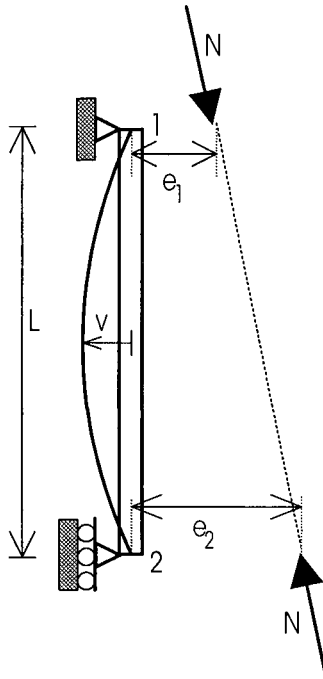
Fig. 1.27 Eccentrically loaded column

The nonlinearity in the column behaviour is represented by the term $1/(1-N/N_c)$ which is termed the *amplification factor*. Its effect on reducing the axial capacity is illustrated in Fig. 1.26, and the ultimate strength is reached where the loading line corresponding to Eq. 1.12 intersects the cross-section failure envelope

derived from Eqs. 1.10 and 1.11. For very short composite columns, N_c is large so that the amplification factor is close to unity, and $M_m = k_m N e_2$.

1.3.4.2 *Steel column approach*

The basis of the design of a concentrically loaded steel column in the elastic range of structural response is its so-called Euler buckling load N_{cr} which is akin to N_c in Eq. 1.12, and is given by

$$N_{cr} = \frac{\pi^2 E_s I}{L^2} \tag{1.14}$$

in which E_s is the elastic modulus of the steel, I is its second moment of area about the weaker axis, and L is the length between pin ends. In reality, a real steel column is not perfectly straight, the loads are applied eccentrically, the material yields and residual stresses are present. Because of this, design is usually based on the strength of a column at first yield, which has been modified empirically to allow for all of the other imperfections. This equation is known as the *Perry curve*, and its derivation is given in texts such as Trahair and Bradford (1991), and briefly in Chapter 18. The most important parameter in the Perry curve is the slenderness ratio $\lambda = L_e / r$, where L_e is the effective length of the column and r is its radius of gyration (Hall 1984).

A typical relationship between the column buckling load N_0 and the slenderness λ is shown plotted in Fig. 1.28. It can be seen for stocky columns for which λ is small, that N_0 approaches the squash load Af_y where A is the cross-sectional area of the column, while for slender columns for which λ is large, N_0 approaches the Euler buckling load N_{cr}. The reduction in N_0 below Af_y and N_{cr} is greatest at the intersection of the latter two loads, and is indicative of material and geometric imperfections.

Fig. 1.28 Perry curve for steel column

The alternate method for the design of slender composite columns is thus to model the strength by a curve similar to the Perry curve used for steel design. Tests on quite slender encased composite columns and concrete-filled steel tubes shown that a Perry-type representation of the strength is satisfactory. There are, however, two major problems which result from this approach. Firstly, the imperfection parameter used for steel columns in the Perry curve must be changed to an appropriate value for composite columns, but this can be achieved through an analysis o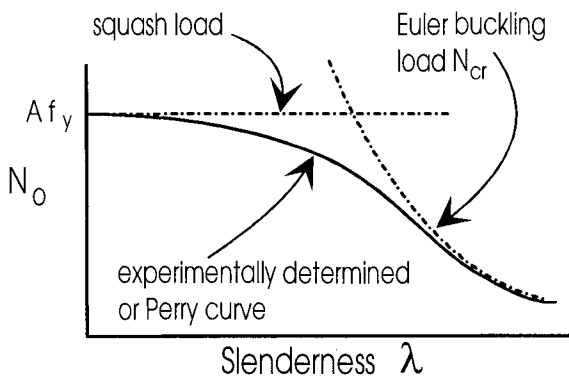f available test results. The second, and most important problem associated with the Perry curve representation, is in the definition of the column slenderness λ. This is because the radius of gyration r must be calculated for two different materials, and elastic modular ratio theory (Hall 1984) is inappropriate for calculating r owing to the material nonlinearity involved.

Since the buckling stress or strength of a composite column is dependent on materials with different moduli, any strength derived from an equation of the form of the Perry curve must refer to only one of the two materials. One way of circumventing this problem was proposed by Basu and Somerville (1969), who expressed the radius of gyration r as

$$r = \sqrt{\frac{I_s f_y + 0.43\, I_c f_c}{N_s}} \qquad (1.15)$$

where N_s is the squash load of the encased column, I_s its the second moment of area of the steel and I_c is the second moment of area of the uncracked concrete encasement. Other studies on slender composite columns using a strength versus slenderness curve have been undertaken by several researchers, such as Virdi and Dowling (1976) and Rotter (1982). These are treated more fully in Chapter 18.

1.4   References

Azhari, M. and Bradford, M.A. (1993). "Local buckling of tee-beams with longitudinal stiffeners", Canadian Journal of Civil Engineering, Vol. 20, No. 6, 923-930.

Basu, A.K. and Somerville, W. (1969). "Derivation of formulae for the design of rectangular composite columns", Proceedings of the Institution of Civil Engineers, London, Supp. Volume, 233-280.

Bleich, F. (1952). *Buckling Strength of Metal Structures*, McGraw Hill, New York.

Bradford, M.A. (1992). "Lateral distortional buckling of steel I-section members", Journal of Constructional Steel Research, Vol. 23, 97-116.

Galambos, T.V. (1968). *Structural Members and Frames*, Prentice Hall Inc., New Jersey.

Hall, A.S. (1984). *An Introduction to the Mechanics of Solids*, John Wiley and Sons, Sydney.

Nawy, E.G. (1990). *Reinforced Concrete*, 2nd edn., Prentice Hall, New Jersey.

Rotter, J.M. (1982). Chapter 7 of *Composite Structures of Steel and Concrete*, Postgraduate Lecture Course, School of Civil and Mining Engineering, The University of Sydney.

Timoshenko, S.P and Gere, J.M. (1970). *Theory of Elastic Stability*, 3rd edn., McGraw Hill, New York.

Trahair, N.S. and Bradford, M.A. (1991). *The Behaviour and Design of Steel Structures*, revised 2nd edn., Chapman and Hall, London.

Uy, B., and Bradford, M.A. (1994). "Slenderness limits for thin steel plates when restrained by concrete", Australian Structural Engineering Conference 1994, Sydney, 613-618.

Virdi, K.S. and Dowling, P.J. (1976). "A unified design method for composite columns", Publications, IABSE, 36-II, 165-184.

Warner, R.F., Rangan, B.V. and Hall, A.S. (1989). *Reinforced Concrete*, 3rd edn., Longman Cheshire, Melbourne.

Wright, H.D. (1993). "Buckling of plates in contact with a rigid medium", The Structural Engineer, Vol. 71, No. 12, 209-215.

2 Material Properties under Static Loads

2.1 Introduction

It is assumed in structural design that the frequency distribution of the predicted properties, such as the structural or material strengths and stiffnesses Z, will be of a Normal or Gaussian type (Walpole and Myers 1978) as shown in Fig. 2.1. This Normal Distribution is defined by the mean strength Z_{mn} and the standard deviation D_Z. In order to allow for this scatter of properties, design is often simplified by basing it on the upper or lower *characteristic values* Z_{ch}. For properties derived from static loading, the characteristic values are defined as either the value of the property at which 5% of the values lie below or 5% lie above.

Frequency

5%   5%

$\leftarrow 1.64\,D_z \rightarrow | \leftarrow 1.64\,D_z \rightarrow$

$(Z_{ch})_{lower}$ Z_{mn} $(Z_{ch})_{upper}$
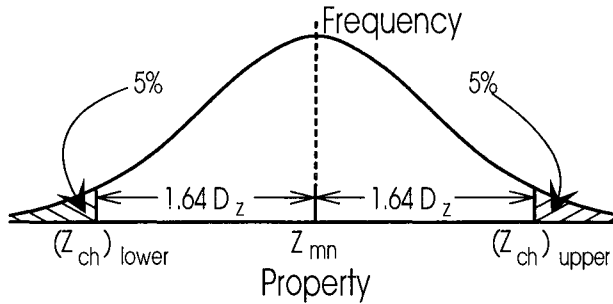
Property

Fig. 2.1 Distribution of static properties

In mathematical terms, and when we are dealing with large normally distributed populations, this characteristic value Z_{ch} is given by the equation (Walpole and Myers 1978)

$$Z_{ch} = Z_{mn} \pm 1.64\, D_Z \qquad (2.1)$$

The conservative value of the characteristic property is used in design. For most design procedures, such as strength and deflection calculations, this will be given by the lower characteristic value, that is $(Z_{ch})_{lower} = Z_{mn} - 1.64\,D_Z$ as shown in Fig. 2.1. Occasionally, the upper characteristic value should be used, such as in crack width predictions.

Wherever possible in this book, and where prediction equations have been validated experimentally, the mean and characteristic values of the prediction equations will be given. It is left to designers to apply their national procedures to these equations. For example, it is common practice in limit states design to insert characteristic material properties into the characteristic value of the prediction equation, in order to allow for the normal scatter of both the material properties and

37

the prediction equation. The result obtained from the prediction equation is then multiplied by a capacity reduction factor, or factor of safety, to reduce the probability of failure to within acceptable levels. The statistical methods by which this is achieved have been outlined by Pham and Bradford (1988).

It is worth noting that it is only by convention that the 5% characteristic value is used in static design. In fatigue design, as in Chapter 3, the characteristic property is often defined as the value at two standard deviations, and so 2.3% of the values lie beyond this characteristic value.

2.2   Steel component

As mentioned in Chapter 1, the primary purpose of the steel element in a composite beam is to carry tensile stresses, while in composite columns the steel shares in the carrying of compressive stresses with the concrete. It is the high strength of the steel, coupled with its ductility, which makes it such a vital component of a composite member.

The steel section is usually made from so-called *mild* or *structural steel*. The real stress-strain curve for a tensile coupon of such a steel is shown in Fig. 2.2. Initially, the stress-strain curve is linear with an elastic modulus E_s. For most mild steels, the modulus E_s is close to 200×10^3 N/mm^2, and this is the value generally used in design. If the stress is removed in the elastic zone, the steel recovers perfectly on unloading. The linear elastic behaviour continues until the yield stress f_y is reached, at a yield strain ε_y of f_y/E_s. Further straining results in plastic flow with little or no increase in stress until the strain hardening strain ε_{st} is reached. The stress in the steel then increases until its ultimate tensile strength f_u is attained. The cross-section then begins to neck down, with large reductions in the cross-sectional area, until the steel finally fractures.
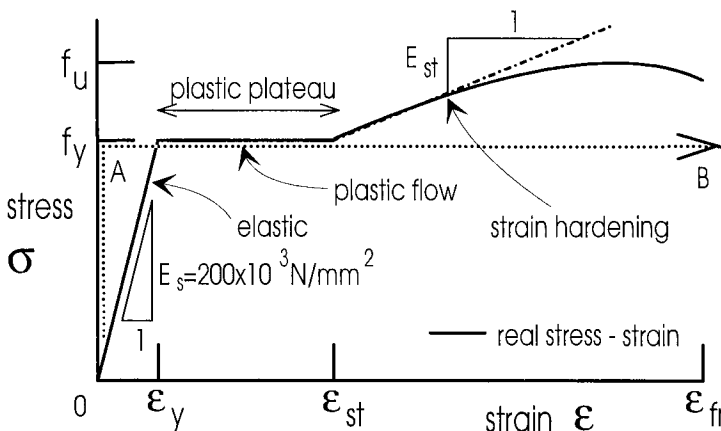
Fig. 2.2 $\sigma - \varepsilon$ curve for structural steel (not to scale)

Undoubtably, the most important strength property of the steel element is its yield strength f_y. In most composite applications, this value is usually between about 250 and 350 N/mm^2, although in some columns it may be higher, and it depends largely on the chemical constituents of the steel, primarily carbon and manganese. The yield stress is increased with increased amounts of these elements, as well as the amount of working which takes place during the rolling process. Higher yield stresses are also observed under higher strain rates $d\varepsilon/dt$ of loading. Generally speaking, the higher the yield stress, the less is the plastic plateau in Fig. 2.2 and consequently the ductility is decreased. Because of this, many structural steel standards place limits on the yield stress of the steel that may be used, since ductility is a desired requirement in structural design.

Under uniaxial compression, the stress-strain characteristics of the steel section are roughly the same as those in tension up to the plastic range. The yield stress f_y determined from a tensile strength test is generally accepted as being the same for compression, along with the elastic modulus E_s. However, the steel section under compression is often subjected to buckling or instability effects as was discussed in Section 1.2.3, and these are treated in more detail in Chapters 5 and 10.

Quite often, it is appropriate to treat the stress in the steel section as being uniaxial. However, the general state of stress at a point in the steel section is in fact biaxial, as shown in Fig. 2.3, which uses the notation of Trahair and Bradford (1991). The most accepted theory of two-dimensional yielding under biaxial stresses acting in the 1'2' plane is the von Mises' maximum distortion energy theory, for which the stresses at yield satisfy

$$f_{1'}^2 - f_{1'}f_{2'} + f_{2'}^2 + 3f_{1'2'}^2 \;=\; f_y^2 \tag{2.2}$$

where $f_{1'}$ and $f_{2'}$ are the normal stresses and $f_{1'2'}$ is the shear stress at the point.
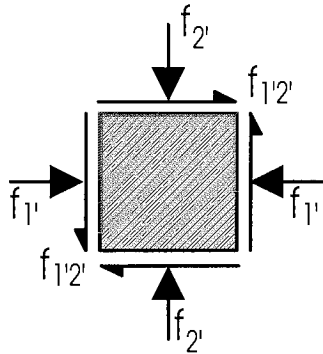
Fig. 2.3 Notation for biaxial loading

If the directions 1' and 2' are the principal stress directions 1 and 2, then Eq. 2.2 takes the form

$$f_1{}^2 - f_1 f_2 + f_2{}^2 = f_y{}^2 \tag{2.3}$$

and the subsequent yield surface ellipse is shown in Fig. 2.4. For the case of pure shear, $f_1 = -f_2 = f_{1'2'}$, so that the shear yield stress τ_y is given by

$$\tau_y = f_{1'2'} = \frac{f_y}{\sqrt{3}} \tag{2.4}$$

so that the close approximation $\tau_y = 0.6f_y$ is often used in design.
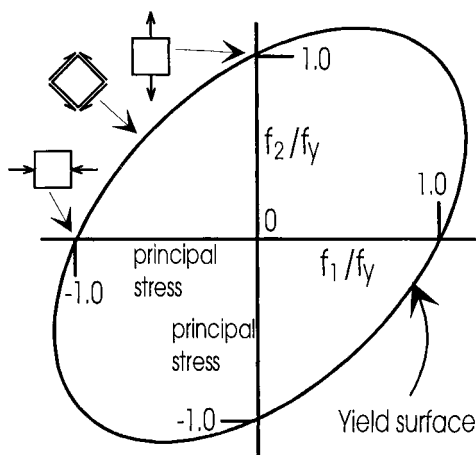
Fig. 2.4 Von Mises' yield criterion

Residual steel stresses are established during the cooling of a hot-rolled or welded steel element, and influence the buckling behaviour and fatigue endurance as well as having some bearing on the redistribution of bending moments in continuous beams. The shrinking of late-cooling regions of the section induces residual compressive stresses in the early-cooling regions, and these are balanced by equilibrating tensile stresses in the late-cooling regions. Typical residual stress patterns for a hot-rolled I-section are shown in Fig. 2.5, while those for a welded I-section are shown in Fig. 2.6.

While mild or structural steel elements contribute greatly to the ductility of a composite member, sudden and catastrophic *brittle fracture* may occur at comparatively low stress levels. Brittle fracture is initiated by the presence of a small crack in a region of high local stresses, such as at the corner of a service opening in the web. This crack may be produced by load cycling, as treated in Chapters 3 and 19. Ductile or stable crack propagation occurs when external forces must supply energy to tear the steel. On the other hand, unstable brittle fracture takes place when some of the internal elastic strain energy stored in the steel is released, and is used to fracture the steel with crack propagation taking place at high speed.
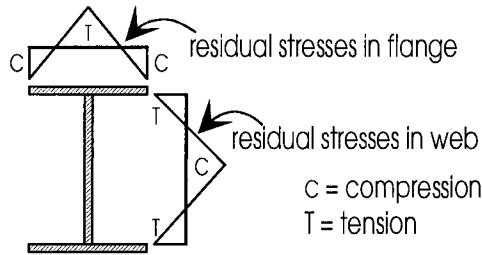
Fig. 2.5 Residual stresses in hot rolled I-section
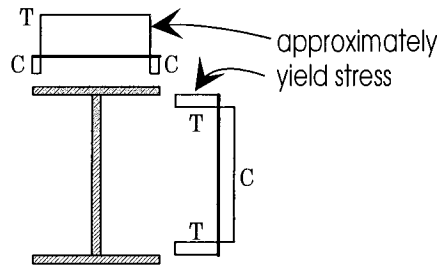
Fig. 2.6 Residual stresses in welded I-section

In some national standards, minimum service temperatures are given for various steels which increase with the thickness. This reflects the dependence of brittle fracture on the ambient temperature, and the phenomenon may be of some concern if the composite member is subjected to an excessively cold climate. The reader is referred to Lay (1982) for more guidance on brittle fracture.

2.3   Reinforced concrete component

2.3.1   GENERAL

The second major component contributing to the strength and stiffness of a composite member is the reinforced concrete. The concrete is produced by mixing cement powder with coarse aggregate (gravel), fine aggregate (sand) and water. Quite often, fly ash and slag waste from steel blast furnaces are added to increase the workability of the wet concrete mix, and to reduce the cost of the cement which in terms of mass is the most expensive major component of the concrete mix.

The strength of hardened concrete varies inversely with its water/cement ratio. Because the workability of the concrete is reduced as this ratio decreases, it is not uncommon to introduce various organic admixtures, apart from slag and fly ash, such as lignosulphonates to the mix. A water/cement ratio (by weight) of at least 0.25 is

required to hydrate the cement properly, and water/cement ratios in the range 0.35 to 0.50 are commonly used for normal strength concretes.

Normal concretes have compressive strengths generally less than 40 N/mm^2, however much research is currently underway into so-called high-strength concrete. These concretes are produced using silica fume cement, and strengths in excess of 100 N/mm^2 have been obtained both in the laboratory and in the lower storey columns of recently constructed high-rise office buildings. The stresses in the concrete part of beam members in buildings are not very large, so that normal strength concretes may be used. It is in the construction of composite bridge beams, and in particular composite columns, that economies may be gained by the use of higher strength concretes.

In addition to the steel element in a composite member, steel reinforcement is usually added to the concrete. In continuous beams, the longitudinal reinforcement carries the tensile stresses over the internal supports, where the concrete has cracked and the beam is subjected to negative bending, while the provision of reinforcement in both beams and columns usually increases the ductility. In addition, reinforcement is very often used to control the in-service cracking which takes place in the concrete portion of the composite member.

Limit states or load and resistance factor design necessitate that both strength and stiffness requirements be met. In achieving these requirements, it must be noted that the properties of reinforced concrete are time-dependent. Because of this, both the short-term and time-dependent properties of reinforced concrete under static loads must be addressed. These properties are considered in the following.

2.3.2   SHORT-TERM PROPERTIES

Concrete is a variable material, and identical strength tests undertaken at a given time after casting show significant variability. However, the mean strength f_{cm} in uniaxial compression increases with concrete age. The major shortfall of the concrete portion of a composite member is its low tensile strength, so that strengths usually quoted for concrete are in terms of the uniaxial compressive strength.

Concrete compressive strengths are determined by testing specimens of identical shape, which have been cured under the same conditions, in a stiff hydraulic testing machine. In North America and in Australia, the standard test specimen is a 150 mm diameter cylinder, which is 300 mm high with its top capped with sulphur. On the other hand, British practice is to use a 150 mm sided cube. Because of the shape effects, the cube strengths f_{cu} are higher than the cylinder strengths f_c. Generally throughout this book, reference will be made to cylinder strengths, however a standard conversion is to assume

$$f_c = 0.85 f_{cu} \tag{2.5}$$

Typical distributions of f_c are Normal or Gaussian, and are given in Fig. 2.1.

The tensile strength of concrete is very much lower than the compressive strength of concrete, and like the compressive strength it depends on the method of testing. The direct tensile strength f_{ct} as obtained from simple pull tests, can be assumed to be proportional to $\sqrt{f_c}$ for normal density concrete, and given by the commonly used empirical expression

$$f_{ct} = 0.4\sqrt{f_c} \tag{2.6}$$

where f_c and f_{ct} are both in N/mm^2. The mechanical shear connectors in composite beams transfer the longitudinal shear between the concrete and steel elements by imposing very high concentrations of load onto the concrete portion of the member. For example, a 19 mm by 100 mm stud shear connector may have a design load of about 120 kN, and this load is concentrated in an area at the base of the connector equal to the width of 19 mm and a height of about 40 mm. The dispersal of this highly concentrated load into the concrete slab induces lateral tensile stresses that can cause the slab to split. The resistance of the concrete to splitting stresses f_{cb} is usually obtained from cylinder split tests, also known as Brazil tests, and is given by the expression

$$f_{cb} = 0.5\sqrt{f_c} \tag{2.7}$$

where both strengths are also in N/mm^2. When the concrete is subjected to flexural tensile stresses, then its cracking resistance can be determined by testing an unreinforced concrete prism in flexure. This tensile strength is referred to as the modulus of rupture strength f_{cf}, and is given by

$$f_{cf} = 0.6\sqrt{f_c} \tag{2.8}$$

As a guideline to the tensile strength of lightweight concrete, it is suggested that f_{ct}, f_{cb} and f_{cf} should be multiplied by the reduction factor given in Eq. 13.5.

The stress-strain relationship for concrete under uniaxial compression differs significantly in shape from that of steel. Up to about $0.4f_c$, the stress-strain curve is close to linear, with a modulus of elasticity E_c. However, as illustrated in Fig. 2.7, the tangent modulus then decreases, until the maximum stress $\sigma = f_c$ is obtained at a strain ε of approximately 0.002. It can be seen that the shape of the stress-strain curve is dependent on the concrete strength f_c. It is also dependent on the strain rate $d\varepsilon/dt$, with higher strains being observed for slower loading rates. The strain rate $d\varepsilon/dt$ in Fig. 2.7 was at a constant value of 100 microstrain per minute.

There have been various empirical expressions presented to approximate the stress-strain curve for concrete in uniaxial compression. One of the early expressions is the Hognested parabola (Hognested 1951). For the ascending part of the curve, this takes the form

$$\frac{\sigma}{f_c} = 2\left(\frac{\varepsilon}{\varepsilon'_o}\right) - \left(\frac{\varepsilon}{\varepsilon'_o}\right)^2 \tag{2.9}$$

in which ε_o' is the strain at which $\sigma/f_c = 1$, typically about 0.002. A commonly used expression for both the ascending and descending parts of the stress-strain curve is that of Desayi and Krishnan (1964). This expression is written as

$$\frac{\sigma}{E_c} = \frac{1}{1 + \left(\dfrac{\varepsilon}{\varepsilon'_o}\right)^2} \tag{2.10}$$

where E_c is the initial slope $d\sigma/d\varepsilon$ curve, taken as $2f_c/\varepsilon'_o$. Perhaps the most widely used representation is that published by the CEB-FIP (1970). The relationship between stress and strain in this formulation is

$$\frac{\sigma}{f_o} = \frac{\varepsilon(a - 206,600\varepsilon)}{1 + b\varepsilon} \tag{2.11}$$

where

$$a = 39,000(f_o + 7.0)^{-0.953} \tag{2.12}$$

$$b = 65,6000(f_o + 10.0)^{-1.085} - 850.0 \tag{2.13}$$

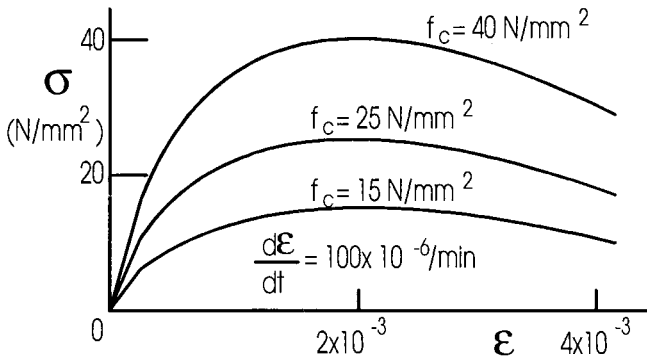and in which $f_o = 0.85f_c$, with f_c being in N/mm^2.

Fig. 2.7 Typical σ - ε curves for concrete

The elastic modulus E_c is often taken as the secant modulus of the stress-strain curve measured from the origin to $0.45f_c$. This has been determined empirically, with the expression

$$E_c = 0.043\rho^{1.5}\sqrt{f_c} \tag{2.14}$$

being often quoted, where E_c and f_c are in N/mm^2, and ρ is the density of the concrete in kg/m^3. For normal weight concretes, ρ is usually taken as 2400 kg/m^3, so that

$$E_c = 5050\sqrt{f_c} \tag{2.15}$$

while an alternative expression which provides a better estimate over the full range of concrete strengths is

$$E_c = 3500\sqrt{f_c + 7000} \tag{2.16}$$

where again E_c and f_c are in N/mm^2.

The stress-strain curve for concrete in tension is elastic-brittle, and the elastic modulus is very close to that for compression.

For ultimate strength analyses that deal with the material failure of concrete, the stress-strain relationship is often assumed to have the idealised γ stress distribution shown in Fig. 2.8, where the tensile strength of the concrete is assumed to be zero. The concrete in compression is assumed to be either not stressed at all in the region A-B, or fully stressed at 0.85f_c along C-D, and to fail by crushing at a strain E of around 0.003. The range of strain, as a proportion of the maximum strain, in which the concrete is assumed to be fully stressed in compression is given by γE, where γ is often assumed to be a function of f_c given by

$$\gamma = 0.85 - 0.007(f_c - 28) \le 0.85 \tag{2.17}$$

in which f_c is measured in N/mm^2.

This idealised rectangular stress distribution has been adopted in analysis and design because it simplifies considerably flexural strength calculations, as the depth of the rectangular stress block can now be determined from simple equilibrium procedures. As an example, this procedure is often applied to the analysis of so-called under-reinforced concrete flexural members such as that shown in Fig. 2.9(a). Noting that the reinforcement has yielded, and using equilibrium of the axial forces in (b), the depth of the rectangular stress in the concrete d_r in (c) can be determined. Hence the position of the resultant compressive force in the concrete, namely $d_r/2$ from the top fibre is now known, and therefore the moment capacity is $A_{st}f_y\ell_a$. This is the moment capacity if the reinforcing steel is fully yielded. The type of analysis such as this, in which the materials are either fully yielded or not stressed at all, and which is based purely on equilibrium requirements, is often referred to as *rigid plastic analysis*.
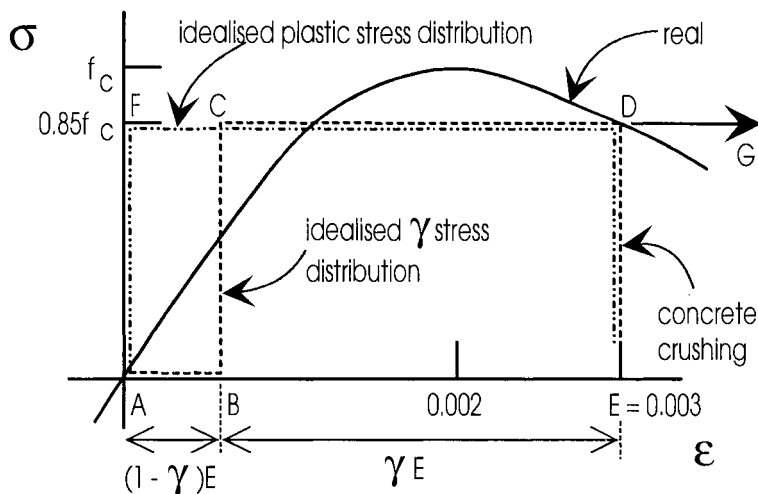
Fig. 2.8 Idealised properties for ultimate strength
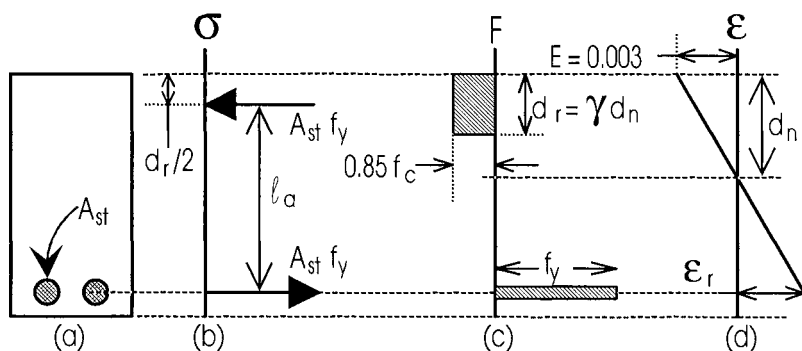
Fig. 2.9 Flexural strength of reinforced concrete beam

In order to determine whether the steel has indeed yielded, it is necessary to check the compatibility requirements. The rectangular stress block in Fig. 2.9(c) occurs in the region where the strain varies from B to E in Fig. 2.8. The change in strain is γE, and hence the depth of the rectangular stress block $d_r = \gamma d_n$, as shown in Fig. 2.9(c) where d_n is the depth to the neutral axis as in (d). Because d_r is now known as well as γ (from Eq. 2.17), the depth d_n to the neutral axis can be calculated and hence the strain distribution plotted as shown in Fig. 2.9(d). It is now a simple procedure to calculate the strain in the reinforcing bar ε_r to determine whether the bar has yielded.

It can be seen from the previous analysis that the reason for using the γ-concept for the stress distribution A-B-C-D-E in Fig. 2.8, where the concrete that is

subjected to compressive strain is either fully stressed or not stressed at all, is to ensure that the steel has yielded. This is done by using the neutral axis factor γ, and by then considering compatibility. It is necessary to undertake this compatibility analysis when dealing with reinforced concrete flexural members, as the concrete occupies the full depth of the section. It is thus theoretically possible, when applying a rigid plastic analysis, for the neutral axis to be very close to the reinforcing bars so that the concrete will fail by crushing before the steel has yielded. Such reinforced concrete sections are said to be over-reinforced, and are not ductile.

For typical composite beams of the types shown in Fig. 1.8, the concrete portion is always above the steel element, which is unlike reinforced concrete beams where the concrete occupies the full depth of the section. Moreover, as explained previously in Section 1.2, the bottom flange of the steel element gives the greatest contribution to the flexural strength. Because of this, the probability of the bottom steel flange not yielding before the concrete crushes is unlikely. Also as explained previously in Section 1.2, the contribution of the top flange to the flexural strength is negligible, so that if this portion does not yield, the effect on the flexural strength is minimal. Hence, for this type of composite beam, it is unnecessary to check for compatibility using the neutral axis depth factor γ, and so the plastic stress distribution A-F-D-E in Fig. 2.8 can be used in design where the neutral axis is now considered to be at the edge of the stress block. Some national design procedures even assume this plastic stress distribution for reinforced concrete members, but restrict the depth of the stress block to about one half of the effective depth of the beam to ensure that yielding occurs. In other forms of composite construction, where the concrete extends throughout the full depth of the section such as in Figs. 1.7 and 1.10, it may be necessary to ensure that the steel yields in a rigid plastic analysis. In this case it may be necessary to use the γ stress distribution shown in Fig. 2.8.

2.3.3 LONG-TERM PROPERTIES

2.3.3.1 *General*

The long-term time-varying properties of concrete affect the behaviour of composite members under service loads. Whilst not affecting greatly most ultimate strengths, they can have a significant effect on both composite columns and on the flexural capacity of composite beams with non-ductile connectors. This is because the concrete creeps and shrinks during the hydration process over a very long period of time, and long-term deformations under typical sustained service loads may be many times greater than their short-term values. In addition, variations in temperature also affect the properties of the concrete in the long-term, with consequent ramifications on the behaviour of composite members.

Under sustained service loads, the stress in the concrete element is usually less than about 40 percent of its compressive strength f_c. As noted in the previous subsection, the instantaneous response may then be assumed to be linear and elastic, so that if the stress is removed, the instantaneous strain ε_e is recovered. However, if the stress is sustained over a period of time, then an additional *creep strain* ε_{cr} will develop. Even when it is unstressed, the concrete component of a composite member

will be subjected to *shrinkage strains* ε_{sh}, and these begin to develop when the concrete starts to dry.

Figure 2.10 shows schematically the time-dependent deformation of a simply supported composite beam subjected to a sustained service load, which is first applied at a time $t = \tau$. Under constant temperature, the total strain ε at any time t may be taken as the sum of the instantaneous strain ε_e, creep strain ε_{cr} and shrinkage strain ε_{sh} components, so that

$$\varepsilon(t) = \varepsilon_e(t) + \varepsilon_{cr}(t) + \varepsilon_{sh}(t) \tag{2.18}$$

In order to predict the time-varying response of composite members, it is necessary to predict the magnitude and rate of development of each of these components. For values of these predictions to be used in the design of composite members, recourse should be made to the appropriate national concrete standard, as variations in the ambient conditions usually make the creep and shrinkage strains regional-dependent.
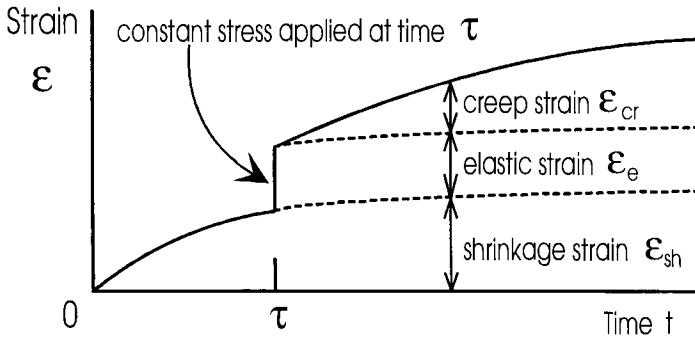
Fig. 2.10 Deformation under constant sustained stress

2.3.3.2 *Creep strain*

Soon after first loading, the creep strains develop rapidly, but the rate of increase $d\varepsilon_{cr}/dt$ slows down with increasing time, as shown in Fig. 2.11. Under sustained load, about 50 percent of the final creep strain developed as time approaches infinity, ε_{cr}^*, occurs in the first three months under load, while about 90 percent of ε_{cr}^* develops in the first two years (Neville, Dilger and Brooks 1983, Gilbert 1988).

Generally, better quality concretes tend to creep less. Higher strength concretes creep less than low strength concretes, so that factors which increase the concrete strength such as a reduction in the water/cement ratio cause a decrease in creep. The magnitude of the creep strain also depends on the age of the concrete τ when the stress is first applied as shown in Fig. 2.11, and the load history has a marked effect on the final creep strain ε_{cr}^*. The usual observation is that concrete loaded at an early age creeps more than the same concrete loaded at a later age.
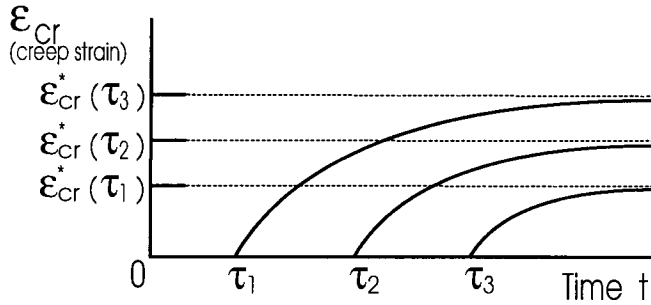
Fig. 2.11 Age at first loading on creep strain

A constant sustained stress σ_o first applied at time $t = \tau$ causes a monotonic increase in creep strain, as noted earlier. This relationship is of the form

$$\varepsilon_{cr}(t,\tau) \;=\; F(t,\tau)e_{cr}^{*}(\tau) \tag{2.19}$$

where $F(t,\tau)$ is a time function, dependent on both the duration of the load t and the age of first loading τ. It varies from zero at time $t = 0$ to unity as the time t approaches infinity. In dealing with concrete creep, it is usual to deal with the so-called creep coefficient $\phi(t,\tau)$, which is the ratio of the creep strain ε_{creep} caused by the constant sustained stress σ_o to the elastic strain $\varepsilon_e = \sigma_o / E_c$. Thus

$$\phi(t,\tau) \;=\; \frac{\varepsilon_{cr}(t,\tau)}{\varepsilon_e(t)} \tag{2.20}$$

and substituting Eq. 2.19 gives

$$\phi(t,\tau) \;=\; F(t,\tau)\phi^{*}(\tau) \tag{2.21}$$

where ϕ^* is the final creep coefficient as the time t approaches infinity, namely $\varepsilon^{*}_{cr} / \varepsilon_e$, and usually lies between 1.0 and 4.0.

Owing to the proportionality of both the creep and elastic strains to the stress σ_o, $\phi^{*}(\tau)$ is independent of σ_o and hence the creep coefficient ϕ is independent of stress, and has the same shape as the creep function $F(t,\tau)$. Approximate numerical values for $\phi(t,\tau)$ may be obtained from various national concrete design standards and other specifications, and these have been summarised in the text by Gilbert (1988).

Under the action of the constant stress σ_o, the load-dependent strains ε_e and ε_{cr} will be given by

$$\varepsilon_e(\tau) + \varepsilon_{cr}(t,\tau) = \frac{\sigma_o}{E_c}(\tau)\{1 + \phi(t,\tau)\} = \frac{\sigma_o}{E_e(t,\tau)} \tag{2.22}$$

where the elastic strain $\varepsilon_e(\tau)$ is now assumed to be a function of the modulus E_e at the time of loading τ and where $E_e(t,\tau)$ is known as the *effective modulus*, and is given by

$$E_e(t,\tau) = \frac{E_c(\tau)}{1 + \phi(t,\tau)} \tag{2.23}$$

Of course, σ_o is usually not constant in the concrete element of a composite member, and so the effect of concrete aging should be considered for a varying stress history. The creep strains for concrete loaded at the different ages τ_1, τ_2 and τ_3 are shown in Fig. 2.11. The relevant creep strain for loading at the time τ_1 must therefore be calculated using the appropriate creep coefficient $\phi(t,\tau_1)$. A simple method which allows for such a calculation, accounting for aging of the concrete, has been given by Gao and Bradford (1993). Generally throughout this book, it is assumed that the stress σ_o is gradually applied over a reasonably short period compared with the design life and then held constant, and that only one $\phi(t,\tau_1)$ relationship is used.

When a stress increment $\Delta\sigma$ is applied gradually to the concrete, the effects of aging can be accounted for by using a reduced creep coefficient. If $\Delta\sigma$ is the gradually applied stress increment in the concrete portion, then

$$\Delta\varepsilon_e(\tau) + \Delta\varepsilon_{cr}(t,\tau) = \frac{\Delta\sigma}{\overline{E}_e(t,\tau)} \tag{2.24}$$

where $\overline{E}_e(t,\tau)$ is known as the *age-adjusted effective modulus* (Bazant 1972) given by

$$\overline{E}_e(t,\tau) = \frac{E_c(\tau)}{1 + \chi\phi(t,\tau)} \tag{2.25}$$

in which χ is the *aging coefficient* (Trost 1967) which is dependent on both t and τ, and varies usually between about 0.6 and 1.0. Although numerical values of χ have been determined (Bazant 1972, Neville *et al* 1983), a value of $\chi = 0.8$ is usually appropriate when the long-term effects of creep are to be determined. The much used *Age-Adjusted Effective Modulus Method* (Bazant 1972) is based on the above, as is the predictive method for the time-dependent behaviour of composite members used in this book.

2.3.3.3 Shrinkage strain

The shrinkage strains $\varepsilon_{sh}(\tau)$ are the time-dependent strains measured at constant temperature in an unloaded and unrestrained concrete specimen, as shown in Fig.

2.12. Their magnitude and rate of development depend on such characteristics as the relative humidity, temperature, mix proportions and shape and size of the member.
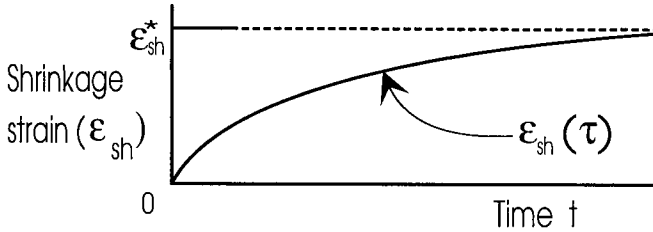
Fig. 2.12 Development of shrinkage strain

As time increases, the rate of shrinkage $d\varepsilon_{sh}/dt$ decreases, and the shrinkage strain approaches its limiting value ε_{sh}^* as the time $t \rightarrow \infty$. At any time t after drying has commenced

$$\varepsilon_{sh}(t) \;=\; G(t)\varepsilon_{sh}^* \tag{2.26}$$

where $G(t)$ is a shrinkage time function, not to be confused with that for creep, which varies from zero at $t = 0$ to unity as $t \rightarrow \infty$. Again, numerical values for ε_{sh}^* and $G(t)$ may be obtained from national concrete design standards, and a summary of some of these has been given by Gilbert (1988).

2.3.3.4 *Thermal expansion*

The coefficient of thermal expansion for concrete is dependent on a number of factors, including the aggregate type and mix proportions. It usually lies in the range $5x10^{-6}/^\circ C$ to $13x10^{-6}/^\circ C$. A value often quoted in design is $10x10^{-6}/^\circ C$.

2.3.4 REINFORCING STEEL

The behaviour of reinforcing steel used in the reinforced concrete element of a composite member differs slightly from that of the steel component already shown in Fig. 2.2. The reinforcement is generally manufactured to comply with the provisions of the relevant national design standards. Typically, *deformed bars* are used as the main longitudinal reinforcement in composite members. Figure 2.13 shows a typical idealised stress-strain curve for such a bar. Reinforcement yield strengths f_{yr} are usually greater than 400 N/mm^2, which is higher than those generally quoted for mild steel. In addition, it is usual to assume that the behaviour is elastic-perfectly plastic, with large elongations at failure, as in Fig. 2.13. The elastic modulus of deformed bars E_{sr} is assumed to be $200x10^3 \text{ N/mm}^2$.

Reinforcing fabric or mesh, manufactured from hard-drawn reinforcing wire, is used most frequently in composite slabs. It is produced by welding the hard-drawn wires into an orthogonal grid. The yield stress of reinforcing fabric is usually about

450 N/mm^2, and because of the welding, the mesh tends to have somewhat brittle characteristics.
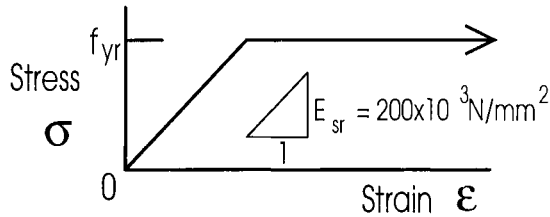
Fig. 2.13 Assumed σ-ε curve for reinforcement

2.4 Mechanical shear connectors

2.4.1 GENERAL

Three forms of bond transfer at the steel/concrete interface in composite members have been identified in Section 1.1.3. They can be categorised as *full interaction connections, mechanical shear connections* and *rib shear connections*. As the name suggests, there is no interface slip with full interaction connections. Therefore for full interaction to occur, the bond stresses have to be transferred either by friction or by chemical bonding at the interface. Composite columns as in Fig. 1.7 are generally assumed to have full interaction connections at both serviceability and ultimate loads, as the encasement of one material element by the other provides a very large interface contact area, and hence good bond. Rib shear connectors as in Fig. 1.6 rely on friction and on an aggregate interlock effect, described in Section 2.5, to transfer the shear. Mechanical shear connectors as in Fig. 1.5 do not rely on friction, nor chemical bonding nor aggregate interlock at the interface to transfer shear. Instead, the shear is transferred by the mechanical deformation of a steel dowel that connects the steel element to the concrete element of the composite member.

Examples of mechanical shear connectors are shown in Fig. 1.5. There is an enormous variety of shapes, sizes and methods of fixing, and the choice is perpetually increasing to cater for changing demands. Because of both the variety and the complex mechanism by which the shear is transferred, the material properties of mechanical shear connectors are always determined empirically. However, as they are all steel dowels embedded in a concrete medium, they all have certain fundamental behavioural similarities. For example, they all have limited ductility, and they all apply a highly concentrated load into the concrete element.

2.4.2 MECHANISM OF DOWEL ACTION

When flexural forces are applied to a composite member, slip is induced at the interface of the steel and concrete elements which is resisted by the dowel action of the mechanical shear connectors, as shown by the deformation of the connectors in Fig. 1.12. It is therefore worth noting that mechanical shear connectors only resist the

longitudinal shear after they slip, as compared with full interaction and rib connections that can resist shear without interface slip.

The transfer of longitudinal shear by the dowel action of mechanical shear connectors is illustrated in an idealised and simplified form in Fig. 2.14(a). The stress resultants in (a) are induced by the relative slip movement shown. In this example, the steel dowel is trying to move to the right which causes it to bear onto the concrete to the right of the dowel. For the dowel action to work, the concrete adjacent to the bearing zone has to withstand compressive stresses of about seven times the cylinder strength of the concrete f_c, and this can only be achieved by the triaxial restraint imposed on this region by the steel element, the dowel and the surrounding concrete.
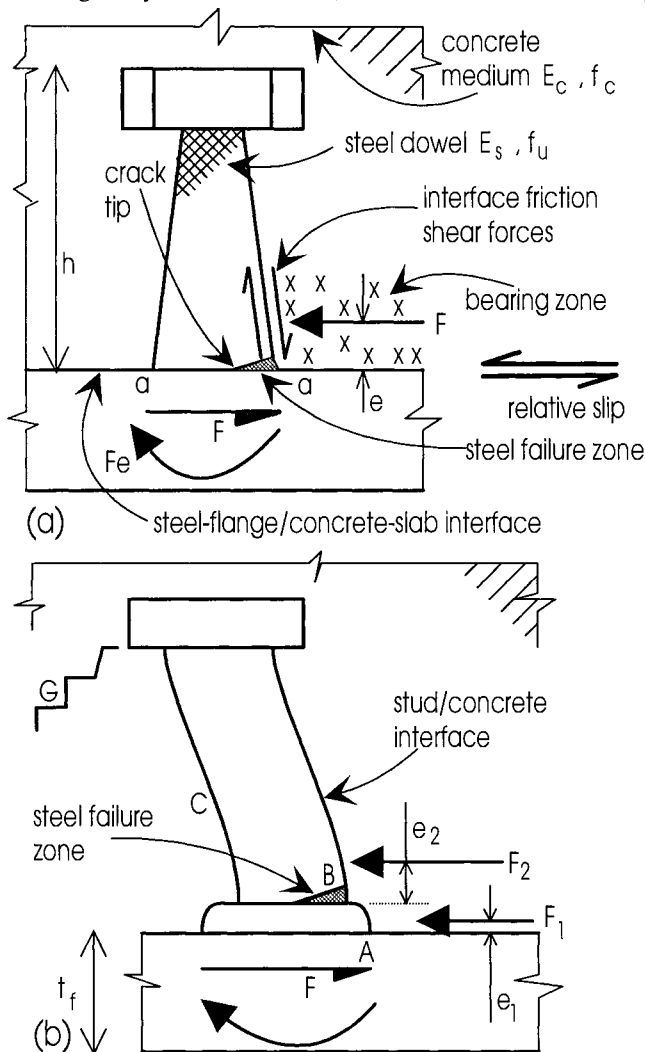

Fig. 2.14 Dowel mechanism

The resultant force in the bearing zone in Fig. 2.14(a) is F, and occurs at an eccentricity e from the steel/concrete interface. This force is in horizontal equilibrium with the shear force in the steel element as shown, and in order to maintain rotational equilibrium a moment Fe is induced at the base of the dowel. The steel dowel must therefore resist both flexural and shear forces, and these forces cause high tensile stresses in the steel failure zone shown. The concrete can therefore crush in the bearing zone, and the steel can fracture in the steel failure zone. It must be further emphasised that this is a highly idealised model of a very complex stress distribution and mechanism of failure. For example, we have ignored the interface friction shear forces between the dowel and the concrete in the bearing area as shown in Fig. 2.14(a), which allows high shear forces to coincide with high flexural forces in the steel failure zone of the dowel. The mechanism of dowel failure is therefore governed by the interaction between the steel and concrete failure zones, and this can best be described by considering the equivalent dowel mechanism in Fig. 2.15.
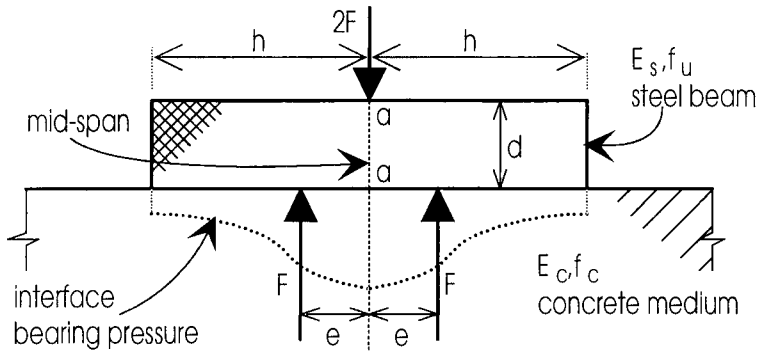
Fig. 2.15 Equivalent dowel mechanism

The dowel behaviour can be considered to be analogous to a steel beam resting on a concrete medium, where section a-a at midspan of the steel beam in Fig. 2.15 is equivalent to section a-a at the steel/concrete interface in Fig. 2.14(a). Consider the distribution of pressure at the steel/concrete interface in Fig. 2.15, for a constant applied force 2F and for different configurations of the material properties. When the steel modulus E_s approaches infinity, the pressure at the interface can be considered to be uniform and hence the resultant force F in one shear span will act at an eccentricity e = h/2. The section at midspan has therefore to resist a shear force F and a moment Fh/2. Conversely, when E_s approaches zero, the steel beam can be visualised as a layer of paper such that the resultant interface force in one shear span is now almost in line with the applied load so that e tends to zero, and so the midspan of the beam now only resists a shear load F. It can therefore be seen that as E_s increases relative to the concrete modulus E_c, the strength of the dowel reduces because the flexural component Fe at midspan increases.

The same argument applies when E_c is changed relative to E_s. In this case, increasing E_c is equivalent to reducing E_s, which reduces e, which consequently leads

to a reduction in the flexural component Fe and thus an increase in dowel strength. In conclusion, it can be expected that the dowel strength is proportional to the modular ratio parameter E_c/E_s, no matter what the shape or size of the steel dowel.

Consider now the mechanism of failure of the dowel in Fig. 2.14(a). It has been shown that the eccentricity e depends on the parameter E_c/E_s. As the shear load F is increased, e will remain constant whilst E_c/E_s remains constant, and the stress in both the concrete and steel failure zones will increase with F. If the concrete starts to fail before the steel, this will reduce E_c and hence increase e, thereby causing an increase in the flexural component Fe and increased flexural stresses in the steel failure zone. Further increases in F will lead to further reductions in E_c and both the increase in F and the reduction in E_c will further increase the stress in the steel failure zone, until eventually the dowel will crack in the steel failure zone. Cracking in the dowel is equivalent to reducing E_s. This reduction in E_s leads to a reduction in e, which consequently leads to an increased bearing pressure and hence further concrete failure. Further concrete failure will lead to a reduced E_c, and thus the cycle continues.

The description of the failure mechanism given previously helps to illustrate the strong interaction between the steel and concrete elements on the dowel action. Sometimes when a large volume of concrete fails, the steel dowel does not fracture but is bent over because e is large. Exactly the same mechanism of failure occurs when the steel starts to fail before the concrete. Cracking in the dowel is equivalent to a reduced E_s which will lead to a reduced e, which in turn will cause an increased bearing pressure and eventually failure of the concrete. Therefore, it is simply not a case of the steel dowel failing by itself or the concrete crushing by itself as some standards suggest, except in exceptional and unusual cases such as splitting of the concrete when there is no reinforcement present (and this will be discussed in Chapters 11 and 12), or when the dowel is extremely rigid and strong as might occur in a block connector.

It can also be expected that the strength of the dowel shear connection is proportional to the compressive strength of the concrete f_c, as stronger concrete can withstand a larger force F before it starts to fail and reduce in stiffness. The strength of the dowel connection will also be proportional to the tensile strength of the steel dowel f_u and cross-sectional area of the dowel A_d, as the greater the axial strength of the dowel, which is $A_d f_u$, then the greater the shear load and flexural force that can be resisted before fracture. It has already been shown that the dowel strength depends on the parameter E_c/E_s. Therefore, it is to be expected that the dowel strength D_{max} is a function of the following parameters, that is

$$D_{max} = f\left(A_d, f_u, f_c, E_c/E_s\right) \tag{2.27}$$

In reality, the dowel strength is only dependent on four parameters, as E_s can be assumed to be constant at 20×10^3 N/mm^2. Should the concrete element fail prematurely in tension by splitting or shear, then this will reduce the triaxial restraint

to the concrete bearing zone and be equivalent to a reduced compressive strength f_c with a subsequent reduced dowel strength. Methods of determining these reduced dowel strengths are described in Chapter 12. When the concrete element does not fail prematurely in tension, then the triaxial restraint is at its largest, and this will lead to the maximum dowel strength which will be referred to herein as D_{max}.

2.4.3 DERIVATION OF DOWEL BEHAVIOUR

2.4.3.1 *Push-tests*

Because of the large variety of mechanical shear connectors, and because of the complexity of the dowel action, the strength and ductility of shear connectors are always determined experimentally. It is very difficult, if not impossible, to determine the behaviour of shear connectors from composite beam tests. This is because the connectors are loaded indirectly from the flexural forces within the beam, as indicated by the deformations in Fig. 1.12. It is clear that the force on a connector is not directly proportional to the load applied to the beam, but depends on the stiffness of various components of the composite beam. Furthermore, residual stresses in the steel element and further material nonlinearity in the concrete element make it practically impossible to determine the forces in the connectors through measuring the longitudinal strains in either element. Even if it could be done, composite beam tests are expensive and this would prohibit the development of shear connectors.

Instead of beam tests, the behaviour of mechanical shear connectors is determined from so-called *push-tests* in which the connectors are loaded directly. Push specimens are inexpensive to manufacture and easy to test, and this has allowed the development of the wide variety of connectors now available. However, the forces induced in the shear connections in push specimens are, unfortunately, not the same as those in composite beams, and this can lead to different strengths as well as different modes of failure. The results from push-tests should thus be interpreted with some caution.

2.4.3.2 *Push specimens*

An example of a push specimen is shown in Fig. 2.16(a). The specimen is made by first attaching the shear connectors to the steel section, and then casting a concrete slab around the shear connectors, so that the steel section is sandwiched by the concrete sections. The connectors are then loaded directly by applying a vertical downward displacement to the steel section. There are several adaptations of this system. For example, it is possible to test half the push specimen (Slutter and Fisher 1966, Terazkiewicz 1965) (that is specimens with connectors only embedded in one slab), or to test specimens with a central concrete core sandwiched by two steel elements. Each of the systems described will work, but each system will give different dowel strengths, and even these strengths will be different to the dowel strengths of the connections in composite beams.

Experimental research has shown that the geometry and layout of the push specimens can also have a significant effect on the dowel strengths of the connections. For example, the height of the connectors above the base (h_1 in Fig. 2.16(a)), the

number of levels of connectors shown in (a), the number of connectors per concrete section shown in (b) and the restraints applied to the base (c) (namely whether the specimen is bedded directly onto the floor or free to slide), will affect the strength of the connection in the push specimen. Furthermore, the width of the concrete section in the push specimen in (b) is often much less than the width of the slab supported by the composite beam, so push specimens are more prone to slab failure through splitting, shear or embedment forces. It is therefore essential that the width of the concrete section in push specimens be chosen so that these forms of premature slab failure do not occur before the dowel strength is reached. The procedures for doing this are given in Chapters 11 to 14.
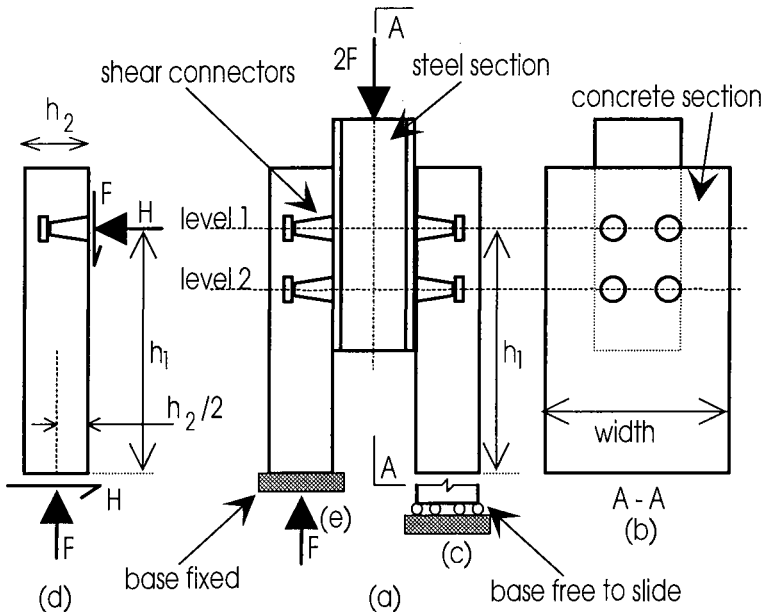
Fig. 2.16 Push specimen

In spite of this, it is still possible to deduce the dowel strength of shear connections in composite beams from the dowel strength in push tests by considering the forces involved in both systems. These are discussed in the following.

2.4.3.3 *Forces in push specimens*

The forces induced in the shear connection in push specimens are illustrated in Fig. 2.16(d). The load applied to the steel section in (a) is transmitted through the dowel action of the shear connector as a force F in the concrete element at an eccentricity e, as shown in Fig. 2.14(a). As the eccentricity e in Fig. 2.14(a) is much less than the depth of the slab h_2 in Fig. 2.16(d), then it can be assumed that the force F acts at the surface of the concrete element and is dispersed to the base of the element at a distance $h_2/2$ from the surface, as shown. The external forces F form a couple $Fh_2/2$. In order to resist this couple, a horizontal frictional force H is induced in the base and

in the shear connection as shown, causing an opposing couple Hh_1, where h_1 is the height of the connection from the base.   Equating the couples, the horizontal component H is given by

$$H = F \frac{h_2}{2h_1} \tag{2.28}$$

Hence the push-test induces a compressive force in the shear connection H that does not occur in a composite beam. It has already been shown that dowel failure is caused by tensile stresses in the steel failure zone shown in Fig. 2.14, and thus the compressive force H in the dowel will increase the dowel strength. As the dowel strengths determined from push tests are greater than those in composite beams, their magnitude should be reduced before they are used in design. Alternatively, the push specimen could be allowed to slide using rollers as in Fig. 2.16(c), so that the resultant force across the steel/concrete interface is zero.

It is also worth noting that the load applied to the push specimen in Fig. 2.16(a) is carried by the shear connections in two slabs, so that the strength of the push specimen depends on the interaction between these two sides. Consider, for example, the mechanism of failure if there was just one level of shear connections, instead of the two shown in Fig. 2.16(a), and that the shear connection could be considered to act as pinned joints between the steel and concrete sections.   The structure would then be statically determinate and would fail when the strength of the weaker of the two sides was attained. We would therefore be dealing with the statics of the minimum of a pair of results. Alternatively, if the shear connections could be considered to be moment resisting joints, instead of pinned joints, then the push specimen can redistribute load from the weaker side to the stronger side and fail at the mean strength of both sides.   An analysis of the mechanism of failure of push specimens (Oehlers and Johnson 1987) showed that two criterion were necessary for push specimens to fail at the average strength of both sides. These were that the shear connection had to have a good rotational stiffness which is achieved when there are two levels of shear connection as shown in Fig. 2.16(a), and the shear connection has to be ductile so as to have a plastic region as in load/slip curve C in Fig. 1.13. Both of these conditions have to be satisfied before the push specimen can be considered to fail at the mean strength of the shear connections on both sides of the push specimen.

2.4.4   CHARACTERISTIC STRENGTHS OF SHEAR CONNECTORS

It was shown in the previous section that the strength of the shear connection in push specimens depends on the ability of the shear connections to redistribute loads among themselves. The strength of shear connectors in composite beams also depends on their ability to redistribute the shear load from weaker to stronger connectors, and this depends on the load/slip characteristics of the shear connectors. Mechanical shear connectors can be described as brittle when their ability to resist load diminishes rapidly after their peak carrying capacity has been achieved, as shown in the 'brittle connectors' in Fig. 2.17. Alternatively, they are often referred to as ductile when they can maintain their peak carrying capacity over large displacements.   A ductile connector therefore has a large plastic plateau, whereas a brittle connector has no plastic plateau. However, in reality, the performance of connectors lies between these

two extremes. It should be emphasised that ductility and stiffness are not the same concept. Stiffness refers to the increase in load per unit slip as given by K in Fig. 2.17, whilst ductility refers to the plastic plateau. A connector can be both flexible and brittle, or stiff and ductile.
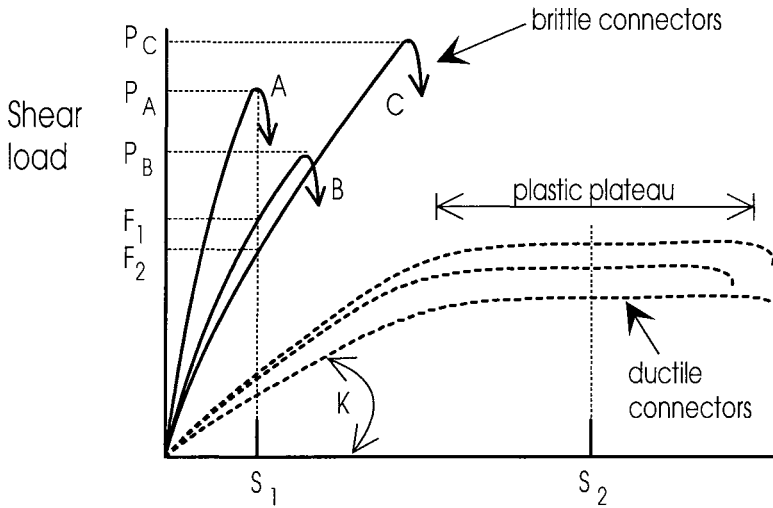
Fig. 2.17 Load/slip characteristics

Consider now the behaviour of a group of three brittle connectors in a composite beam. The load/slip characteristics of the three connectors are given as A, B and C in Fig. 2.17. Even though the three connections might appear to be identical, their strengths and stiffnesses will vary slightly due to the variability of both the material properties and the geometry of the connections. Let us assume that the mean strength P_m of the three connections is $P_m = (P_A + P_B + P_C)/3$, that the standard deviation of the strengths is D_p, and that these three shear connections are in close proximity to each other so that they are all subjected to the same displacement, that is the same slip.

As the composite beam is loaded, the slip on the connectors will increase, increasing the shear loads on the connectors. At slip S_1 in Fig. 2.17, the mean load on the connectors is $(P_A + F_1 + F_2)/3$, and will be less than the mean strength of the connectors P_m. Increasing the slip S_1 will cause connector A to fracture and redistribute its load to the other two connectors, which in turn will fracture. Hence, the failure load of the three connectors is less than their mean strength and is controlled by the strength of the weakest connection, which is the strength of an individual connector. Therefore, for brittle connectors, design should be based on the characteristic strength of an individual connector $(P_{ch})_{bri}$, which for 95% exceedence is given by

$$\left(P_{ch}\right)_{bri} = P_m - 1.64 D_p \tag{2.29}$$

where D_p is the standard deviation of the strengths of individual connectors in the total population, and P_m is the mean strength of the total population.

The behaviour of a group of three ductile connectors in a composite beam that are subjected to the same slip is now considered. The load/slip characteristics of these shear connectors are shown in Fig. 2.17. When the slip on the connectors S_2 lies within the plastic plateau of each connector, then each connector has reached its maximum strength, and the failure load is equal to the mean strength of the three connectors. The mean strength can only be achieved because the connectors have plastic plateaux. Therefore, for ductile connectors, design should be based on the characteristic strength of a group of n connectors that are subject to similar displacements $(P_{ch})_{duc}$. Standard basic statics gives the characteristic strength as

$$\left(P_{ch}\right)_{duc} \quad = \quad P_m \quad - \quad \frac{1.64 D_p}{\sqrt{n}} \tag{2.30}$$

It can be seen that Eq. 2.29 is simply a specific case of Eq. 2.30 at n = 1. Hence, the characteristic strength of brittle connections can be determined from Eq. 2.30 by inserting n = 1 in order to derive the characteristic strength of the individual connection. It is also worth noting that when n approaches infinity in Eq. 2.30, then $(P_{ch})_{duc} = P_m$, which is the mean strength of the shear connection. It is not always clear what value of n to substitute into Eq. 2.30, because n is the number of connectors that have simultaneously reached their plastic plateaux. For certain types of structures, it is fairly obvious what value of n to choose. For example, when the connectors are placed in groups, as over the stubs in the stub girder in Fig. 1.9(b) or over the diagonals in the composite truss girder in (c), then n can safely be taken as the number of connectors in the group. For connectors distributed over a shear span, n can be taken as equal to the number of connectors in the shear span only when the composite beam has been designed against fracture of the shear connection, as described in Section 1.2.5.5 and Chapter 8. This criterion will ensure that a connector does not fracture, at S_{ult} in Fig. 1.13, before all the other connectors in the group of n have reached their plastic plateau.

2.4.5 IDEALISED BEHAVIOUR

Examples of the load/slip characteristics of mechanical shear connectors are shown in Fig. 2.17. The main properties of these characteristics are the plastic plateau and the stiffness K. These load/slip characteristics can be idealised as shown in Fig. 2.18. It can be seen that these idealised characteristics form two groups, namely those based on the plastic plateau, and hence the ductility of the mechanical shear connector, and those based on the stiffness K. Ultimate strength analyses are usually based on the plastic plateau, whereas serviceability analyses are usually based on the stiffness K.

In serviceability analyses, K is normally taken as the connector stiffness per mm length of the composite beam. Linear elastic techniques are used, in which it is assumed that the three materials in the composite beam have constant stiffnesses E_s, E_c and K. When there is no shear connection, and thus no resistance to slip, then K = 0 and the analysis is referred to as *no interaction* as shown in Fig. 2.18. When the

analysis assumes no slip, then K approaches infinity, and this is referred to as *full interaction*. When the analysis assumes a finite value for K, this is referred to as *partial interaction*, and the classical solution to partial interaction analyses was developed by Newmark, Siess and Viest (1951).
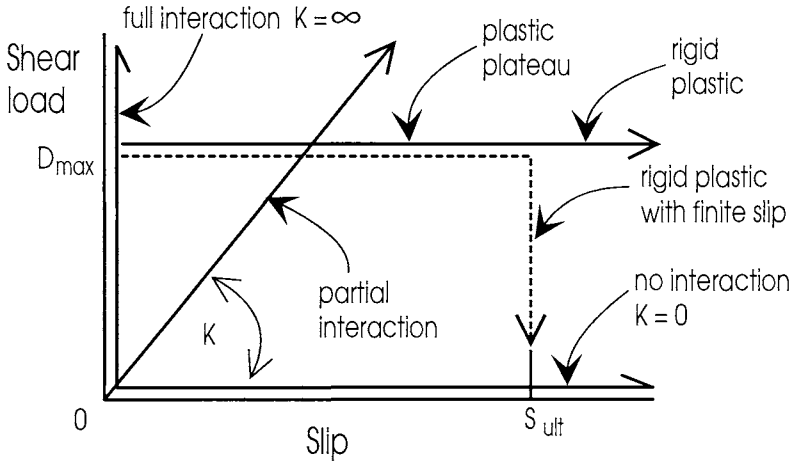
Fig. 2.18 Idealised load/slip characteristics

Ultimate flexural strength analyses are based on the assumption that the three material components of the composite beam are fully stressed. This condition is often referred to as rigid plastic, and allows the flexural strength to be determined purely from equilibrium equations as described in Chapter 7. The connectors are therefore always fully loaded at D_{max} in Fig. 2.18. Additional compatibility analyses are then required to ensure that the slip capacity of the connector S_{ult} is not exceeded, and procedures for doing this are described in Chapter 8.

2.4.6 STUD SHEAR CONNECTIONS

2.4.6.1 *General*

The stud shear connection shown in Fig. 1.5(a) is probably the most common form of mechanical shear connection, and is certainly the most researched and understood form of shear connection. These connections can be bonded to the steel element in seconds using an automatic welding procedure. The most important dimension is the diameter of the shank d_{sh} which varies from about 13 mm to about 22 mm, and a very common size is 19 mm. The diameter of the head is usually about $1.5d_{sh}$, and the height of the connector is usually greater than $4d_{sh}$ in order to ensure that the connector does not pull out of the concrete element. The weld collar has a diameter of about $1.3d_{sh}$, and a height of about $0.3d_{sh}$.

The weld collar at the shank/flange interface, shown in Fig. 2.14(b), increases the dowel strength by increasing the bearing surface at the stud/concrete interface, and

so reduces the stresses in the concrete for a given force F. The weld collar also increases the dowel strength by raising the steel failure zone, so that the steel failure zone now occurs at the weld-collar/shank interface. Raising the steel failure zone means that the zone is now only subjected to a portion F_2 of the shear load F. Furthermore, the eccentricity e_2 of F_2 in (b) is less than the eccentricity e of F in (a), so that the weld collar also reduces the flexural stresses at the failure zone.

An example of dowel failure at the raised steel failure zone, which occurs at the weld-collar/shank interface, is shown in both Figs. 2.19 and 2.20. Figure 2.19 shows the weld collar side of the failure zone and Fig. 2.20 shows the stud shank side of the failure zone. It can be seen in Fig. 2.19 that the steel failure zone is immediately above the weld collar, and is on an almost horizontal plane. The zone of damaged concrete, around the bearing zone in Fig. 2.14(a) can clearly be seen in Fig. 2.20. This concrete failure zone is confined to a small region in front of the stud. The minimum spacing of connectors in a composite beam is controlled by this concrete bearing zone because it is necessary to ensure that these zones do not overlap, otherwise the dowel strengths of the connectors will be reduced. This is achieved in design through detailing rules which require that the longitudinal spacing of stud shear connectors is greater than about $5d_{sh}$, and that the lateral spacing is greater than about $4d_{sh}$. It is also necessary to ensure that the steel element to which the stud is welded, is strong enough to resist the dowel action and this is achieved in design by ensuring that both the flange thickness $t_f > 0.40d_{sh}$, and the distance from the edge of the stud to the edge of the flange is greater than about d_{sh}.

Fig. 2.19 Weld collar failure zone

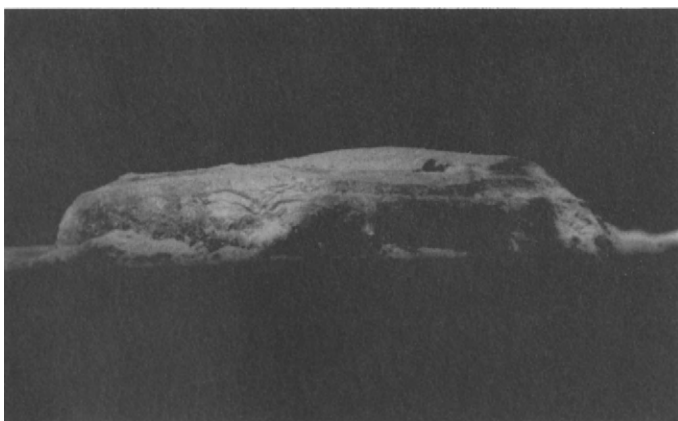### 2.4.6.2 *Load/slip characteristics of stud shear connections*

It has been shown in Section 1.2 that the ultimate strength of composite beams depends not only on the strength of the shear connection, but also on its ductility and slip capacity. Furthermore, it has also been shown in Section 2.4.4 that the characteristic strength for use in design also depends on both the ductility and slip

capacity of the connection. Hence the load/slip behaviour of stud shear connections is an important characteristic in design.
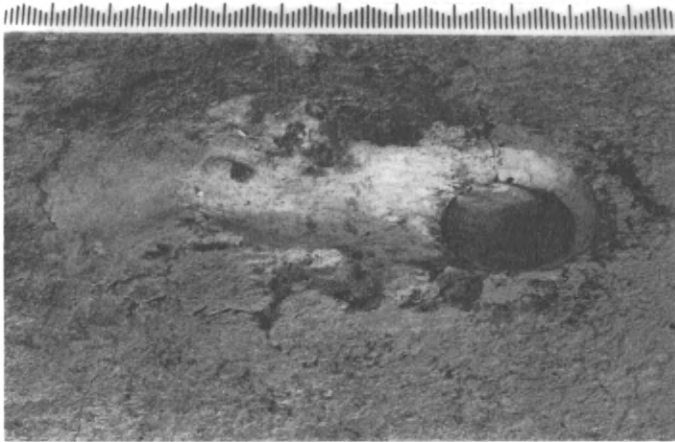

Fig. 2.20 Concrete failure zone

A typical example of the load/slip characteristic of a stud shear connector (Oehlers and Coughlan 1986) is shown in Fig. 2.21. When a displacement is applied to the connector, there is an almost linear variation up to point A which occurs at about $0.5D_{max}$. Further increases in displacement cause the stiffness to reduce until the plastic plateau is reached at point B, after which the slip increases (at fairly constant load) up to point C. There is then a gradual reduction in strength with slip, until the connector fractures at D at about 95% of its strength and at a slip of about 40% of its shank diameter. This is a typical load/slip characteristic of a stud shear connector that is embedded in a solid concrete element which does not fail prematurely by splitting, shear or embedment. It therefore represents the maximum dowel strength and stiffness of a stud shear connector. Should the concrete element fail prematurely, then this can reduce both the strength and stiffness, as indicated by line E in Fig. 2.21. However, premature failure of the concrete element does not necessarily reduce the ductility represented by the plastic plateau. The dowel behaviour after premature failure of the concrete element is discussed in detail in Chapter 12.

When a connector is unloaded at say point F in Fig. 2.21, it follows the path F-G with permanent set O-G. The unloading path F-G is never the same as the loading path O-F, even at very low values of the shear force at F. On further loading, the connector then follows the path G-F, the tangent stiffness of which (K_{tc}) is greater than the secant stiffness (K_{si}) of the initial loading path O-F, although in reality, the true secant stiffness K_s say at point J along the path G-F is less than that of the initial loading path K_{si}. This point is worth noting because engineers sometimes try to estimate the performance of stud shear connectors in bridge beams which have been in service for a long time by measuring their stiffness. They invariably measure K_{tc} which is an overestimation of the true stiffness K_s, and which is even larger than the

initial stiffness K_{si}. The only way to measure the true stiffness, namely the secant stiffness from the origin K_s, is to instrument the bridge when it is first constructed.
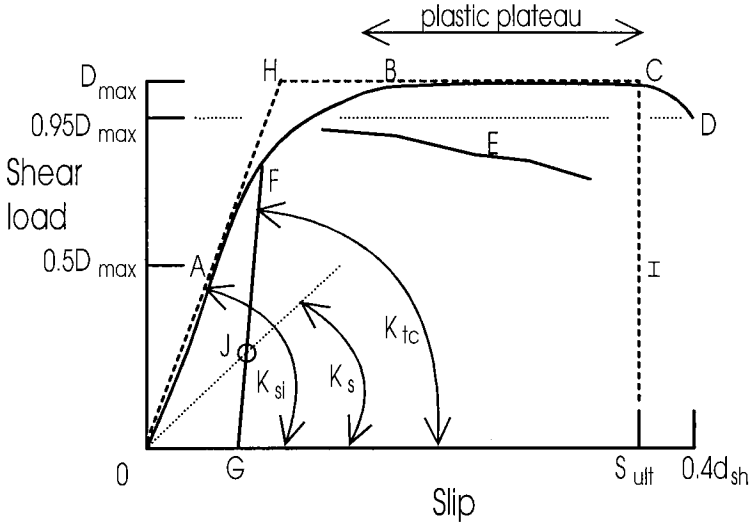
Fig. 2.21 Stud shear connection

     The load/slip characteristic of stud shear connectors can be idealised using the path O-H in Fig. 2.21 at stiffness K_{si}, followed by a plastic plateau of length H-C, and then fracture at C at a slip S_{ult}, as represented by the path I. The stiffness K_{si} is sometimes used to determine the force on connectors that are induced by shrinkage of the concrete or thermal changes in the steel and concrete elements. The slip capacity S_{ult} is used to determine the moment at which the connectors fracture as described in Chapter 8. The following values of K_{si} and S_{ult} were derived from the results of a statistical analysis (Oehlers and Coughlan 1986) of the load/slip characteristics of 116 push tests in which premature failure of the concrete element did not occur.

At a load of $0.5D_{max}$, the slip is given by

$$S_{0.5D_{max}} = \left(80 \times 10^{-3} - 86 \times 10^{-5} f_c\right) d_{sh} \qquad (2.31)$$

where the units are in N and mm, and the standard deviation is $0.026d_{sh}$. The initial tangent stiffness K_{si} can be assumed to be the stiffness at $0.5D_{max}$, and hence the mean stiffness is given by

$$K_{si} = \frac{D_{max}}{d_{sh}\left(0.16 - 0.0017 f_c\right)} \qquad (2.32)$$

where the units are N and mm. The upper 95% characteristic stiffness is given by substituting 0.08 for 0.16 in Eq. 2.32, and the lower characteristic stiffness can be

obtained by substituting 0.24 for 0.16 in this equation. The tangent stiffness during unloading, K_{tc} in Fig. 2.21, was found to be equal to $2.8K_{si}$. It can be seen in Eq. 2.32 that the initial tangent stiffness K_{si} increases with the cylinder strength f_c. The load along the plastic plateau in Fig. 2.21 does vary slightly, if point C is assumed to occur when the load has reduced by 1% from its peak, then the mean value of S_{ult} is given by

$$S_{ult} = (0.48 - 0.0042 f_c)d_{sh} \qquad (2.33)$$

where again the units are in N and mm. The lower 95% characteristic ultimate slip is given by substituting 0.42 for 0.48 in Eq. 2.33. It can be seen that the slip at fracture S_{ult} reduces as the cylinder strength f_c increases, and hence connectors encased in strong concrete are less ductile than those in weak concrete, and so are more prone to fracture. Both the stiffnesses K_{si} and K_{tc}, as well as the slip S_{ult}, were derived from experimental tests in which the compressive cylinder strengths f_c varied from 23 N/mm^2 to 82 N/mm^2.

2.4.6.3 *Strength of stud shear connections*

The strength of stud shear connectors is always derived empirically from push tests. However, the strength in composite beams that is required for design can be deduced from the strength in push specimens.

(a) Strength in push specimens

Ollgaard, Slutter and Fisher (1971) pioneered the research on the dowel strength of stud shear connectors, and identified the important parameters that control the dowel strength. Using statistical analyses, they derived an equation for determining the mean dowel strength of stud shear connectors in push specimens in which the concrete slab had not failed prematurely through splitting, shear or embedment. This equation can be represented as

$$(D_{max})_{push} = 1.83 A_{sh} f_c^{0.3} E_c^{0.44} \qquad (2.34)$$

where the units are in N and mm, and in which A_{sh} is the cross-sectional area of the shank of the stud and E_c is the Young's modulus for the concrete. They then changed the exponents to make the equation dimensionally correct, although this did lead to a loss of accuracy. The altered equation is

$$(D_{max})_{push} = 0.50 A_{sh} \sqrt{f_c E_c} \qquad (2.35)$$

It was shown in Section 2.4.2 and in Eq. 2.27 that $D_{max} = f(A_{sh}, f_u, f_c, E_c/E_s)$. As E_s can always be assumed to be constant, and as f_u was constant in Ollgaard's tests at 486 N/mm^2, then Ollgaard's equations contain all the remaining variables which affect the dowel strength.

Push tests by Hawkins (1973) showed that the dowel strength increases when the tensile strength of the stud material f_u is increased, and hence confirmed the hypothesis of the mechanism of failure described in Section 2.4.2. Oehlers and Johnson (1987) therefore modified Ollgaard's work to allow for variations in f_u. All the variables in Eq. 2.27 were included in a statistical analysis of the experimental data, and they were included so that $(D_{max})_{push}$ was proportional to $A_{sh}(E_c/E_s)^\alpha f_u^\beta f_c^\chi$. If in a linear or nonlinear analysis or simulation of the shear connection, the coordinates of the stress-strain relationships of the concrete and steel materials are increased by a factor k. Then because the shapes of the stress distributions, at connection failure, before and after factoring are the same, then the strength of the connection, as determined by material failure, must increase by the same factor k. Another way of visualising this statement is that $(kf_u)^\beta(kf_c)^\chi$ which is equal to $k^{\beta+\chi}\left(f_u^\beta f_c^\chi\right) = k\left(f_u^\beta f_c^\chi\right)$. In other words, increasing the individual material strengths by k to kf_u and kf_c, on the left hand side of the equation, causes an increase in the strength by k, on the right hand side of the equation. This can only be done if the exponents $\beta + \chi = 1$, and this will also make the equation dimensionally correct. Based on these parameters, a statistical analysis of the experimental data gave the following prediction equation for the dowel strength of stud shear connectors in push tests.

$$(D_{max})_{push} = \left(5.3 - \frac{1.3}{\sqrt{n}}\right)A_{sh}f_u\left(\frac{f_c}{f_u}\right)^{0.35}\left(\frac{E_c}{E_s}\right)^{0.40} \tag{2.36a}$$

where it can be seen that the dowel strength depends on the strength of the shank of the stud $A_{sh}f_u$ and the factors $(f_c/f_u)^{0.35}$ and $(E_c/E_s)^{0.40}$ allow for the interaction between the steel and the concrete. For analysis purposes, Eq. 2.36a can be written in the following form.

$$(D_{max})_{push} = \left(5.3 - \frac{1.3}{\sqrt{n}}\right)A_{sh}\,f_u^{0.65}\,f_c^{0.35}\left(\frac{E_c}{E_s}\right)^{0.40} \tag{2.36b}$$

The exponents of f_c and of E_c in Eq. 2.36 are almost identical to those derived by Ollgaard in Eq. 2.34, as would be expected since the populations from which they were derived were almost the same. The parameter $5.3 - 1.3/\sqrt{n}$ in Eq. 2.36 gives the characteristic strength in the form defined in Eq. 2.30, because it has been shown in the previous section that stud shear connections have a ductile plateau and hence are able to fail as a group.

Equations 2.34 to 2.36 are prediction equations that were derived from the strength of stud shear connections in push specimens, and are often used in standards for predicting the strength of stud shear connections in beams. It has been shown in Section 2.4.3.3 that the strengths derived from push specimens can be larger than those in beams, because the shear connection in beams are not subjected to the compressive forces H, in Fig. 2.16(d), that occur in push specimens. However, it is

worth noting that the strength of the shear connection in a composite beam is not a critical component of the strength of the composite beam. For example, it will be shown in Chapter 7 that a reduction of 25% in the shear connection strength may only lead to a 10% reduction in the strength of the composite beam. Hence, basing the strength of shear connections from push-specimens will only lead to a slightly unconservative design, and this unconservatism is often fully covered by factors of safety.

(b) Strength in composite beams

It was shown in Eq. 2.28 that the compressive force induced in push specimens, H in Fig. 2.16(d), is a function of the geometry of the specimen and the shear force F on the connector. From the geometry of Ollgaard's specimens, H/F is about 21%. Experimental tests on embedment failure, as described in Chapter 14, indicate a strong interaction between the shear force F and axial force H. If this interaction can be assumed to be linear, then the strength in beams, where H = 0, may be expected to be the reciprocal of 1 + 21%, that is 83% of the strength in push specimens. A limited number of experimental tests in which the axial force H was controlled (Oehlers and Johnson 1987) suggest that the strength in beams is 81% of that in push specimens, which is in close correlation with the theoretical value of 83%. If the strength in beams is assumed to be 81% of that in push specimens, then the strength of stud shear connections in composite beams $(D_{max})_{beam}$ is given by

$$\left(D_{max}\right)_{beam} = \left(4.3 - \frac{1.1}{\sqrt{n}}\right) A_{sh}\ f_u^{\ 0.65}\ f_c^{\ 0.35} \left(\frac{E_c}{E_s}\right)^{0.40} \tag{2.37}$$

(c) Range of variables

The prediction equations 2.36 and 2.37 should only be used within the range of variables from which they were determined statistically. The material properties varied within the ranges $10{,}000 < E_c < 33{,}000$ N/mm^2; $430 < f_u < 640$ N/mm^2; and $24 < f_c < 81$ N/mm^2. The heights of the studs were greater than or equal to $4d_{sh}$ and the weld collars had an average height of $0.31\ d_{sh}$.

It can be seen when applying Eqs. 2.36 and 2.37 that it is possible to have shear strengths close to or greater than $A_{sh}\ f_u$, and this is only possible because the weld collar ensures that the actual shear force at the failure zone is less than the total shear force as shown in Fig. 2.14(b). If the weld collar were removed, as in Fig. 2.22, then the steel failure zone will have to resist all of the shear force, as well as the flexural component Fe of the shear force, as shown in Fig. 2.14(a), and hence the strength would have to be less than $A_{sh}\ f_u$. Certain types of stud welding procedures produce very small or no weld collars, and it would be unsafe to use these equations directly to determine their strengths. There is a small amount of experimental and theoretical data (Johnson and Oehlers 1981) which indicates that the shear strength reduces by about one third when the size of the weld collar is reduced from $d_{sh}/4$ to zero. Reducing the strengths immediately when the height is less than $d_{sh}/4$ appears to be unduly conservative. It is therefore suggested that the shear strengths given by the

prediction equations should be reduced when the mean height of the weld collar is less than $d_{sh}/5$. A linear reduction factor R_{wc} could therefore be applied to the shear strength prediction equations when the mean height of the weld collar h_{wc}, in a group of n stud connectors, is less than $d_{sh}/5$. This reduction factor is

$$R_{wc} = \frac{2}{3} + \frac{5h_{wc}}{3d_{sh}} \tag{2.38}$$
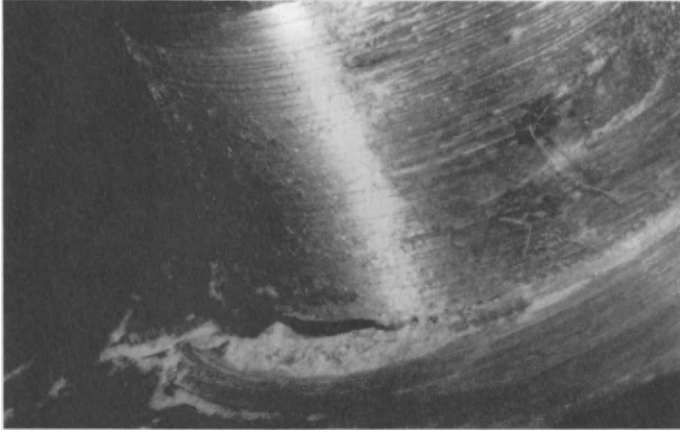

Fig. 2.22 Shank failure zone

(d) Characteristic strength

The statistical procedure of basing the characteristic strength on the number of connectors n, in a group with similar displacements, need not be a design difficulty and has certain benefits. Take, for example, the characteristic strength parameter K_{ch} = 4.3 - 1.1/$\sqrt{n}$ in Eq. 2.37, where n is the number of connectors in a group subjected to similar displacements, or is equal to the number of shear connectors in a shear span in which M_{frac} does not occur, that is where the analyses described in Chapter 8 have shown that the connectors will not fracture due to excessive slip. As n approaches infinity, K_{ch} = 4.3, and inserting this value into Eq. 2.37 will give the characteristic strength of a group that contains an infinite number of connectors, which is also the mean strength of the shear connectors. When n = 1, K_{ch} = 3.2 which produces the characteristic strength of an individual connector, which in this case is 26% weaker than the mean strength. The fewer connectors in a shear span, then the weaker will be their characteristic strength which will mean that more connectors will be required, so that the design force per connector will reduce. This is a reasonable design procedure, as the probability of connector failure, through variations in the material properties, is inversely proportional to the number of connectors.

It is noteworthy that it is usually only at the final stages of the design procedure when the type and number of connectors have to be chosen. Up until then, the analysis deals with shear flows. At this stage of choosing the connectors, the

simplest procedure is to first assume that n is infinite in deriving K_{ch}, that is to base the strength on the mean strength, and then determine the spacing and hence the number of connectors n_1 from the shear flow. This value of n_1 can then be used to determine a new value of K_{ch}, and this will give a new spacing and number n_2 from the shear flow. This iterative procedure can be repeated, and it will be found that n converges rapidly. It is a useful procedure, because it means that large composite beams with large numbers of connectors in a shear span will virtually be designed on their mean connector strength. For example, if n = 150 then K_{ch} = 4.21, which is only 2% less than the mean strength. Because of this, the connectors in large beams, such as bridges, can generally be designed on their mean strength. This is quite satisfactory because we are dealing with a large number of connectors, and the probability of them all being weak is very remote. However, when we are dealing with beams with small numbers of connectors, such as composite beams in buildings, and particularly when they are designed as partial shear connection, then there is a high probability that their mean strength is less than the population mean. For example, if in our initial analysis it was first assumed that n was infinite and this produced n = 8 after several iterations, then K_{ch} = 3.9 for 8 connectors, and this gives a strength that is 9% less than the mean. Hence, because there are only a few connectors in a shear span, we require approximately one extra connector than if the design were based on the mean strength.

(e) Multiplication factors

Not only do the design strengths of stud shear connectors vary from standard to standard, but the parameters which control the strength often vary between standards. Furthermore, standards often include step changes that require minimum material properties that can often cause a dilemma for designers. For example, if the standard requires a minimum value of the tensile strength of the stud material f_u of say 490 N/mm^2, what procedure does the designer adopt if the strength was found to be below this value? Similarly, if the standard requires that the strength be reduced by, say, 15% for lightweight concrete, then the question is what is lightweight concrete, and should this 15% reduction be applied to shear connections in concrete of density 2000 kg/m^3 as well as concrete of density 1200 kg/m^3. There is a proliferation of step changes in design standards that often define the bounds of knowledge that existed at the time of their drafting. Equations 2.36 and 2.37 can be used to augment these step changes.

When prediction equations are based on the strengths of stud shear connectors that had a constant value of the tensile strength of the stud, then standards often require that the stud material has a strength equal to or greater than this value, say $(f_u)_{step}$. As Eqs. 2.36 and 2.37 show that D_{max} is proportional to $f_u^{0.65}$ then the strengths given in the standard can be multiplied by the factor

$$R_{f_u} = \left(\frac{f_u}{(f_u)_{step}} \right)^{0.65} \tag{2.39}$$

to allow for variations in f_u. For example, Ollgaard's strengths given in Eqs. 2.34 and 2.35 were based on $(f_u)_{step} = 486$ N/mm^2 and thus increasing f_u to 640 N/mm^2 will produce $R_{fu} = 1.20$, so that it increases the strengths given by Eqs. 2.34 and 2.35 by 20%. Similarly, if a material 18% weaker were used, such that $f_u = 400$ N/mm^2, then the strengths should be reduced by 12% from those given in Eqs. 2.34 and 2.35. It can clearly be seen that the shear strength is not directly proportional to f_u.

Some national standards base the dowel strength on the density of the concrete ρ, or require reductions in strength when the connector is encased in lightweight concrete instead of normal density concrete. This dependence may appear to be slightly illogical, as the behaviour of shear connectors depends only on the material stress-strain relationships of which the density does not play a part directly. As an example, if the shear connection were being simulated using finite element models, then the geometry and material stress-strain relationships would have to be input. The density would almost certainly not be input. However, the density does affect the dowel strength, as it is proportional to E_c. Using the relationship between E_c and ρ given by Eq. 2.14, and the fact that D_{max} is proportional to $E_c^{0.40}$ in Eq. 2.37, gives the following factor R_ρ that allows for the variation in densities as

$$R_\rho = \left(\frac{\rho}{\rho_{step}} \right)^{0.60} \tag{2.40}$$

in which ρ_{step} is the density of the concrete in the push specimens from which the original prediction equations were derived. The density ρ_{step} is usually taken as the density of normal-density concrete, and as mentioned in Section 2.3.2, has a value of about 2400 kg/m^3. Thus if lightweight concrete of density 1800 kg/m^3 is used, then the strength reduces to 84% of the strength in normal density concrete. It should be noted that R_ρ should not be used when the design strengths already allow for the variations in E_c, as this factor was derived from the dependence of ρ on E_c.

2.5   Longitudinal shear strength of reinforced concrete element

2.5.1   GENERAL

It is necessary in the design of a composite structure, and in particular a composite beam, to ensure that the longitudinal shear, transmitted by the shear connection, can be resisted by the reinforced concrete element. The fundamental research on the in-plane shear strength of reinforced concrete was developed by Mattock and his colleagues (Hofbeck, Ibrahim and Mattock 1969, Mattock and Hawkins 1972) and their results are described in this section. The application of this research to the design of composite beams is given in Chapter 13.

2.5.2 MECHANISMS OF LONGITUDINAL SHEAR TRANSFER

2.5.2.1 *General*

The mechanisms by which the longitudinal shear is transferred from the shear connectors in a composite beam into the reinforced concrete element, depends on whether the element is initially cracked or not.

2.5.2.2 *Initially uncracked reinforced concrete element*

The transfer of shear into an initially uncracked reinforced concrete element is illustrated in Fig. 2.23, which shows the plan view of an element of a reinforced concrete slab. The force F represents the longitudinal shear forces applied by the shear connectors to the reinforced concrete element of the composite beam. When the shear force is first applied, the element distorts and induces diagonal tensile stresses, as sketched in region A. These tensile stresses crack the concrete in the well-known herringbone formation of parallel diagonal cracks, and hence form a series of concrete struts within these diagonal cracks. Further increases in the shear force F rotate the concrete struts in the direction indicated. This rotation increases the width of the element, B-B, and hence induces tensile stresses in the transverse reinforcement. Therefore, the shear strength of an initially uncracked reinforced concrete element depends on both the strength of the transverse reinforcement and on the strength of the concrete, as the shear is resisted by the formation of steel ties and concrete struts. This mechanism is analogous to the well-known 'truss action' associated with the shear resistance of reinforced concrete beams with stirrups.
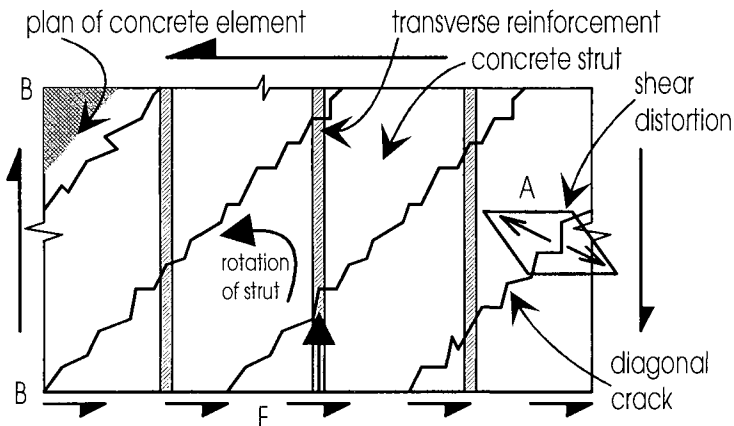
Fig. 2.23 Initially uncracked element

2.5.2.3 *Initially cracked reinforced concrete element*

The mechanisms by which shear is transferred across a crack in a reinforced concrete element is illustrated in Fig. 2.24. In this scenario, we are dealing specifically with slabs that have longitudinal cracks which are spanned by transverse reinforcement, as shown. These longitudinal cracks can be formed by transverse moments in the slabs of

composite beams, concrete shrinkage, the splitting action of mechanical shear connectors (as described in Chapter 11), or the misuse or mishandling of the concrete elements. The shear forces cause the crack faces in Fig. 2.24 to slip relative to each other, and this shear distortion is resisted along the line of the crack by a combination of dowel action, interface interlock and friction.
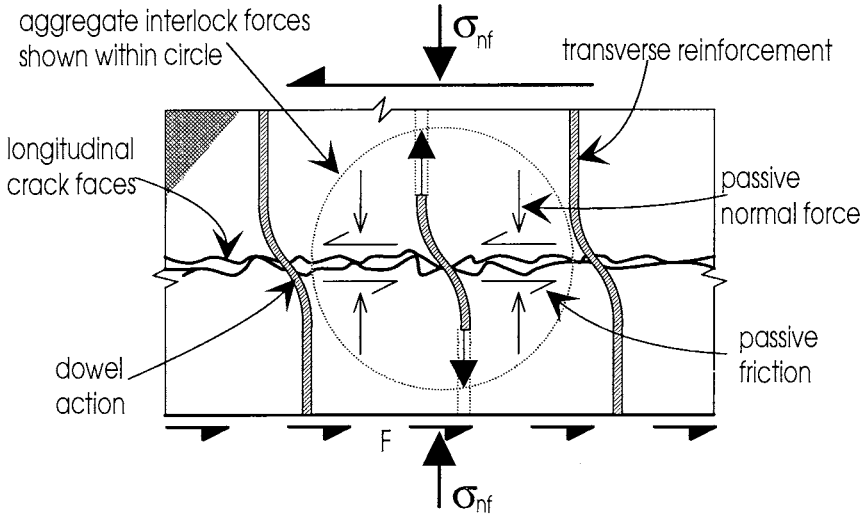

Fig. 2.24 Initially cracked element

The relative slip between the crack faces is resisted by bending of the transverse reinforcement across the crack front, as shown in Fig. 2.24. This resistance to shear is referred to as *dowel action*. The mechanism by which the dowel action of the transverse reinforcement resists the shear forces is similar to the dowel action associated with mechanical stud shear connections, that was described in detail in Section 2.4. It was shown in this section that the dowel strength of a stud shear connector is given by Eq. 2.37, which can be written in the form

$$v_{dow} = \left[3.4 \left(\frac{E_c}{E_s} \right)^{0.40} \left(\frac{f_c}{f_y} \right)^{0.35} \right] p f_{yr} \tag{2.41}$$

in which p is the area of reinforcement crossing the shear plane as a proportion of the area of the shear plane, f_{yr} is the yield strength of the reinforcement, and hence v_{dow} is the contribution of the transverse reinforcement to the shear strength of the shear plane. It was assumed in converting Eq. 2.37 to that for reinforcing bars in Eq. 2.41, that $f_u = 1.3 \, f_y$ and that $R_{wc} = 2/3$ in Eq. 2.38, as reinforcing bars do not have the equivalent of a weld collar. It can be seen in Eq. 2.41 that the main parameter that controls the dowel strength is the shear strength of the reinforcing bars $p f_{yr}$. The parameters E_c/E_s and f_c/f_y, in the brackets, can be visualised as allowing for the effect of the concrete properties on the dowel strength.

Shear is also resisted at the crack front by the *interlocking*, across the crack front, of the aggregate particles that protrude from each crack surface. This mechanism of shear transfer can only occur when the two crack surfaces are held together by transverse reinforcement or some external active normal stress σ_{nf}, as shown in Fig. 2.24. Otherwise, the concrete elements, on either side of the crack, would separate when a shear displacement is applied. When transverse reinforcement is present and $\sigma_{nf} = 0$, the slip across the crack interface can occur by fracture of the protruding aggregate particles or by the crack widening and allowing the particles to ride over each other. The axial stiffness pE_s of the transverse reinforcement restrains the widening of the crack. This passive restraint induces tensile forces in the reinforcement, and hence for equilibrium, compressive forces across the crack front form as shown, which in turn will allow a frictional force to resist the shear forces. This frictional force will be referred to as *passive friction*, as it is induced by passive restraints.

The transfer of shear across a crack front through interface interlock, v_{lock}, therefore depends on the passive restraint of the transverse reinforcement pE_s, that allows both fracture of the concrete protrusions at the interface and passive friction across the interface. Fracture of the interface protrusions will be mainly a function of the concrete tensile strength f_{ct}, although concrete crushing does also occur. The passive restraint of the transverse reinforcement, which is a function of the stiffness and hence area of the transverse reinforcement p, will only be of secondary importance to fracture of the interface protrusions, just as long as there is sufficient reinforcement to prevent the formation of wide cracks. Therefore, it may be expected that the shear resistance through interface interlock is a function of the following variables

$$v_{lock} \;=\; f(f_{ct}, p) \tag{2.42}$$

where f_{ct} is the tensile strength of concrete as given by Eq. 2.6. Whilst the passive restraint p is sufficient to allow interface interlock, the main parameter may be considered to be f_{ct}. It is also worth noting that both the dowel action v_{dow} and the interface interlock mechanism v_{lock} induce stresses in the reinforcing bars that can lead to their failure.

External active normal compressive forces to the reinforced concrete element, σ_{nf} in Fig. 2.24, will help develop the interface interlock mechanism, in the same way as the transverse reinforcement does, and will also allow the shear to be transferred by friction. Conversely, external active tensile normal forces will reduce the effect of the interface interlock mechanism, by allowing the crack width to widen and so reduce the amount of interlock, and also reduce the passive compressive normal forces and hence their ability to resist the shear through friction. The shear resistance, v_{fric}, associated with active normal forces applied to the crack face will be referred to as *active friction* in order to distinguish this shear resistance from the passive friction associated with the interface interlock mechanism. As in most frictional resistances, it will be assumed that

$$v_{fric} = \mu \rho_{nf} \tag{2.43}$$

where μ is the coefficient of friction.

Hence the total shear strength across a cracked plane v_u consists of the sum of the following three components

$$v_u = v_{lock} + v_{dow} + v_{fric} \tag{2.44}$$

2.5.3 PUSH SPECIMENS

The shear strength across cracked and uncracked shear planes was determined from the reinforced concrete push specimens shown in Fig. 2.25(a). The externally applied loads P are directly in line with the shear plane and thus induce the combination of stresses shown, where τ is the shear stress, σ_ℓ is the longitudinal stress and σ_{nf} is the lateral stress which in this push specimen is equal to zero. The stress σ_ℓ represents the longitudinal stress in the reinforced concrete element in a composite beam. In the push specimen in Fig. 2.25(a), P is compressive, and hence σ_ℓ is compressive, and so this represents the longitudinal stress in the positive or sagging region of a composite beam. When P and hence σ_ℓ are tensile, this represents the stress in the negative or hogging region of a composite beam.
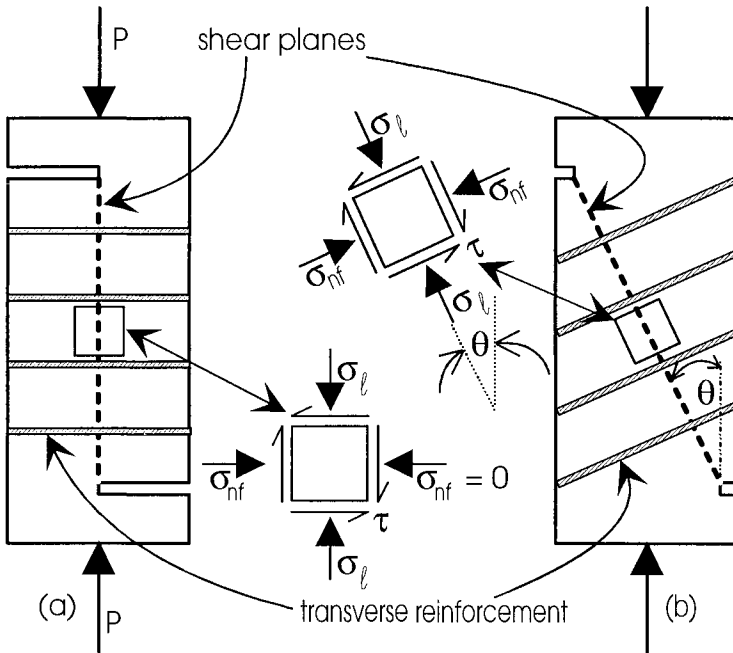

Fig. 2.25 Shear tests

The effect of active normal forces σ_{nf} was determined by inclining the shear plane by an angle θ as shown in Fig. 2.25(b), so that σ_{nf} is the active normal stress that induces friction. Mattock tested specimens in which σ_ℓ was either compressive or tensile, and in which the shear planes were either uncracked or initially pre-cracked by splitting.

2.5.4 LONGITUDINAL SHEAR STRENGTH

2.5.4.1 *Cracked shear plane*

Mattock proposed an equation to determine the shear strength of a cracked shear plane. This was a lower bound to his results and can therefore be considered to be the characteristic normal strength. The equation is

$$\left(v_u\right)_{ch} = 1.4 + 0.8pf_{yr} + 0.8\sigma_{nf} \tag{2.45}$$

where the units are in N and mm, σ_{nf} is positive when compressive and negative when tensile, and pf_{yr} is the axial strength of the reinforcement per unit area of the shear plane. The experiments also showed that the longitudinal stress σ_ℓ did not affect the shear strength of a cracked shear plane, and hence these results can be used in both the positive and negative regions of a composite beam.

Equation 2.45 can be compared with Eq. 2.44 where the parameters which affect the individual components are given in Eqs. 2.41 to 2.43. The first term in Eq. 2.45 ($v_{lock} = 1.4$ N/mm^2) can be considered to be the strength attributed to interface interlock. This term can be compared with Eq. 2.42, and hence can be considered to be the main parameter f_{ct} and not the minor parameter p. The second term ($v_{dow} = 0.8$ pf_{yr}) can be considered to be the dowel resistance. A comparison with Eq. 2.41 shows that the constant 0.8 is equivalent to the parameters in the square bracket in Eq. 2.41, that have already been shown to be of secondary importance, compared with the main parameter pf_{yr}. Finally, the third term ($v_{fric} = 0.8$ σ_{nf}) can be considered to be the active frictional resistance, and a comparison with Eq. 2.43 would suggest that $\mu = 0.8$. Mattock's Eq. 2.45 is therefore a credible simplification of a highly complex mechanism of failure, as it contains the main parameters that control the strength.

Equation 2.45 is plotted in Fig. 2.26 in terms of the individual shear strength components. The sum of the dowel and friction components, $v_{dow} + v_{fric}$, is shown as a line O-A with a slope of 0.8, and the interface interlock component, v_{lock}, is shown as a constant step change, so that the design equation is given by line B-C. It was found experimentally that when $pf_{yr} + \sigma_{nf} \leq 1.4$ N/mm^2, v_{lock} reduced along the line B-O, as shown. This is to be expected, as interface interlock cannot occur when the restraint across the crack, as measured by $pf_{yr} + \sigma_{nf}$, is removed. Mattock therefore proposed a lower limit to this restraint that is equal to the interface interlock factor of 1.4 N/mm^2. It was also found experimentally that the rate of increase in strength with $pf_{yr} + \sigma_{nf}$ reduced at higher shear strengths, because the large amounts of restraint ($pf_{yr} + \sigma_{nf}$) required at these high shear strengths changed the mode of failure. Therefore,

Mattock proposed an upper limit to the shear capacity of $0.3 f_c$. In order to make Eq. 2.45 dimensionally correct, the interface interlock factor of 1.4 N/mm^2 can be written in terms of the tensile strength of the concrete that was used in the tests, and this came to $0.66f_{ct}$, where the relationship between f_{ct} and f_c is given in Eq. 2.6.
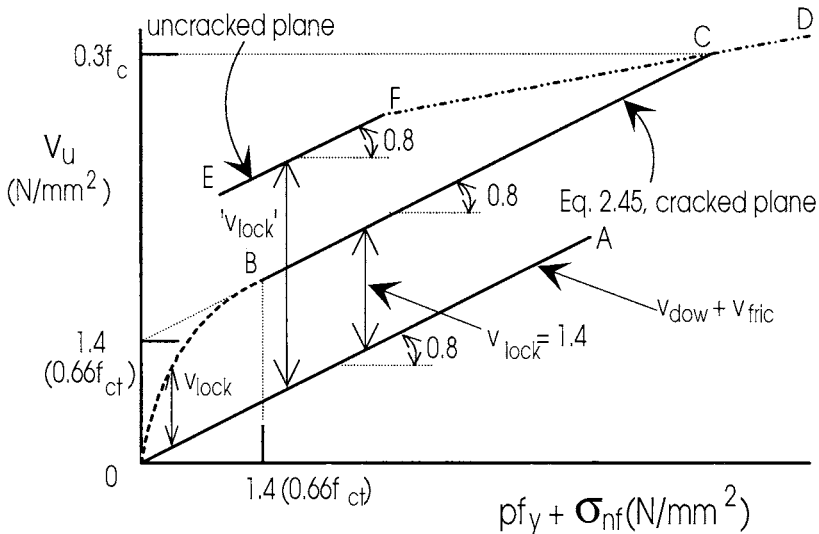
Fig. 2.26 Shear strength

The characteristic shear strength of a cracked shear plane is therefore given by the equation

$$(v_u)_{char} = 0.66f_{ct} + 0.8pf_{yr} + 0.8\sigma_{nf} \tag{2.46}$$

when both

$$pf_{yr} + \sigma_{nf} \geq 0.66f_{ct} \tag{2.47}$$

and

$$v_u \leq 0.3f_c \tag{2.48}$$

These are therefore the basic equations which can be used to derive the shear strength of cracked reinforced concrete elements, and most standards use some version of these equations. National standards also require that the transverse reinforcement is fully anchored on both sides of the crack front, although the anchorage length was not a parameter that was varied in these tests. It is also worth noting that the mean shear strengths, as opposed to the characteristic strengths, can be derived from Eq. 2.46 by substituting $v_{lock} = 1.1f_{ct}$ for $v_{lock} = 0.66f_{ct}$.

2.5.4.2 *Uncracked shear plane*

The shear strength in uncracked shear planes was found to be much higher than in cracked shear planes. However, the shear strength was also found to be dependent on the longitudinal stress in the concrete, σ_ℓ in Fig. 2.25. The longitudinal stress within a composite beam varies from tensile in the negative regions to compressive in positive regions, and so it would be difficult to allow for this variation in σ_ℓ along the length of the beam in design. Instead, design is based on the shear strength of initially cracked concrete, as it has been found to be independent of σ_ℓ. Magnitudes of shear strengths in uncracked regions will be given in this section, in order to give the engineer a feel for the margin of safety involved when using the shear strength of initially cracked planes for the design of initially uncracked planes.

The variation of the shear strength of an initially uncracked shear plane is shown as line E-F in Fig. 2.26. The dependence on the parameter $pf_{yr} + \sigma_{nf}$ is the same as in the cracked plane, and the upper bound also lies close to $0.3f_c$, as shown. The difference in strengths, between cracked and uncracked planes, occurs in the interface interlock factor v_{lock}, although it is worth bearing in mind that this term should not really be used when dealing with uncracked planes, as the shear is now transferred by a system of struts and ties, as shown in Fig. 2.23.

Experiments showed that when the longitudinal stress σ_ℓ, in Fig. 2.25, is both compressive and equal to the shear strength τ, then the mean shear strength is given by substituting $v_{lock} = 2.0f_{ct}$ for $v_{lock} = 0.66f_{ct}$ into Eq. 2.46. When the longitudinal stress σ_ℓ is tensile and approximately equal to half of τ, then the mean shear strength is given by substituting $v_{lock} = 1.4f_{ct}$. If we assume a linear variation in shear strength between these two values of longitudinal stress, then $v_{lock} = 1.6f_{ct}$ at $\sigma_\ell = 0$. Hence it would be reasonably safe to determine the shear strength of an uncracked plane in a positive region using $v_{lock} = 1.6f_{ct}$. As it has been shown that the mean shear strength of a cracked plane can be derived by substituting $v_{lock} = 1.1f_{ct}$ into Eq. 2.46, there is therefore a tendency to overdesign the shear strength in positive uncracked regions by $1.6f_{ct} - 1.1f_{ct} = 0.5 f_{ct}$.

2.6   Rib shear connectors

2.6.1   GENERAL

Three forms of bond transfer has been identified in Section 1.1.3, and have been referred to in Section 2.4.1 as full shear connection, mechanical shear connection and rib shear connection. Full shear connection requires that there is no slip at the steel/concrete interface, and hence no slip strain is induced during composite action. The strain profile induced by the composite action is therefore the uni-linear profile as shown in Fig. 1.23(b), compared with the bi-linear distribution in Fig. 1.23(c) where slip at the steel/concrete interface has induced a slip strain. The term full shear connection is not really a mechanism of bond transfer, but a prerequisite for an

analysis technique, and can only be achieved by chemical adhesion at the interface or where frictional resistances at the interface have not been exceeded. Composite columns and tubes in Figs. 1.3(a) and (b), and the encased beams in Fig. 1.2, are often designed as full shear connection.

Mechanical shear connections, examples of which are given in Fig. 1.5, consist of steel dowels embedded in a concrete medium. As the name suggests, they transfer the shear load by a mechanical deformation which causes the steel dowel to bear onto the concrete. Therefore, shear is only transmitted when there is slip at the steel/concrete interface, and so the strain profile induced by the composite action is never uni-linear, but always has a step change or slip strain.

Rib shear connectors are used in composite slab construction, as shown in Fig. 1.3(c). The rib extends the full length of the structure, so that it does not bear directly onto the concrete, as do mechanical shear connectors. Shear can be transferred across the steel/concrete interface by chemical adhesion. In this case, the structure acts as if it had full shear connection, and hence has a uni-linear strain profile. Alternatively, shear can be transferred by a mechanism similar to interface interlock, which was described in Section 2.5, where interface slip occurs at low loads and hence the strain profile is generally bi-linear.

2.6.2   RIB SHEAR CONNECTORS

Examples of rib shear connectors that are used in the construction of composite slabs are shown in Fig. 1.6, where it can be seen that the rib is formed as part of the steel decking. The rib has two main purposes. Firstly, it allows the steel decking to act as a steel beam, in order to support the unset concrete, in which case the steel decking is acting as permanent shuttering. Secondly, it provides bond between the hardened concrete and the steel decking, so that the two elements act as a single composite slab, in this case the steel decking is now acting as integral shuttering. Indentations and protrusions are formed in the ribs during the rolling process to enhance their bond characteristics, and hence the composite action. The ability to act as permanent shuttering and the ability to act as integral shuttering are controlled by the shape of the ribs.

Steel decking ribs can be categorised into the three types shown in Fig. 1.6, which consist of (i) L-shaped, or more correctly inverted L-shaped ribs, (ii) trapezoidal ribs, which will be defined as ribs in which $\theta < 90°$; and (iii) re-entrant or dove-tail ribs, in which $\theta > 90°$. L-shaped ribs have excellent bond characteristics, but are structurally weak. Therefore, steel decking that has L-shaped ribs are excellent as integral shuttering, because the composite behaviour is good, but are poor as permanent shuttering, because the steel beam behaviour of the decking is weak. Conversely, trapezoidal ribs tend to have very weak bond characteristics but are structurally strong, and so the steel decking is poor as integral shuttering but strong as permanent shuttering. Steel decking with re-entrant dove-tailed profiles tend to lie between these two extremes, having reasonable permanent and integral shuttering characteristics. It can therefore be seen that the choice of rib is a compromise between the behaviour as permanent shuttering and as integral shuttering.

Rib shear connectors are also used in the construction of composite beams as shown in Fig. 2.27. The rib is formed by welding a plate along the full length of the steel element, and the bond can be enhanced by roughening the surfaces of the rib or by drilling holes in the rib as shown.
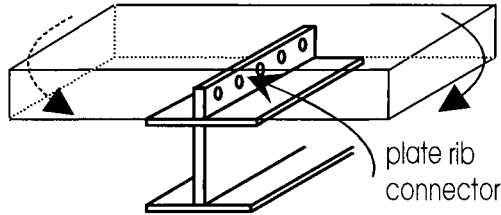

plate rib connector

Fig. 2.27 Plate rib shear connectors

2.6.3 MODES OF SHEAR TRANSFER

2.6.3.1 *General*

Rib shear connectors can transfer the shear by either chemical adhesion v_{chem}, interface interlock v_{lock}, or by active friction v_{fric}. Chemical adhesion acts separately from the other two mechanisms, whereas the shear resistance by interface interlock and active friction can be added.

2.6.3.2 *Chemical adhesion*

Chemical adhesive bond v_{chem} between the steel and concrete has a strength of about 0.1 N/mm^2 and occurs over the total interface area between the steel profile and the adjacent concrete. This contact area tends to be high for trapezoidal ribs, and low for L-shaped ribs. Chemical adhesion is lost as soon as slip occurs at the steel/concrete interface, and hence analysis techniques that are based on full interaction, such as the well-known $q = VA\bar{y} / I$ (Eq. 1.9), can be used to determine the forces on the structure that are required to break this bond.

2.6.3.3 *Interface interlock*

The mechanism of shear transfer by interface interlock, between the steel and concrete elements in a composite section, is similar to the interface interlock that occurs across a crack in a reinforced concrete element as described in detail in Section 2.5.2.3. Instead of the transverse reinforcement providing the passive restraint, as occurs in the cracked reinforced concrete, the passive resistance is provided by the rib acting as a compressed spring.

Consider the dove-tailed rib profile shown in Fig. 2.28, where there are protrusions on the sheet, and indentations in the concrete that were formed around these protrusions when the concrete was cast. Longitudinal slip at the interface is resisted by bearing between the steel protrusions and the concrete indentations. There will be a tendency for the two surfaces to ride over each other as shown, which is

resisted by the passive restraint of the rib that now acts as a spring. This passive restraint will induce passive normal forces across the interface, and hence the shear will be resisted by passive friction. The ability to transfer the longitudinal shear by bearing and passive friction depends on the passive resistance of the rib. For example, steel decking made with trapezoidal ribs have very little passive resistance, and the ribs tend to detach as shown in Fig. 2.29(a) because of the geometry of the section. However, thicker sheets and deeper and more frequent embossments will increase the passive resistance by both increasing the effective spring stiffness of the rib, and requiring larger interface separations to accommodate the slip.
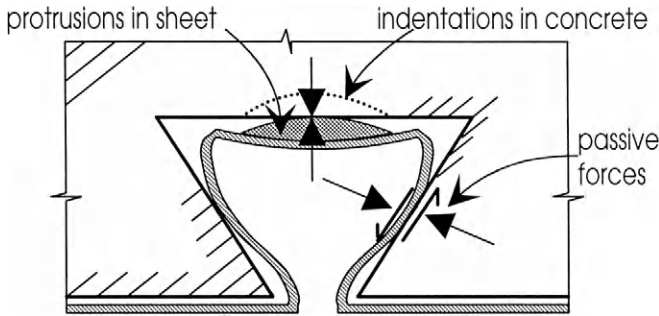

Fig. 2.28 Passive restraint in re-entrant or dove-tailed rib
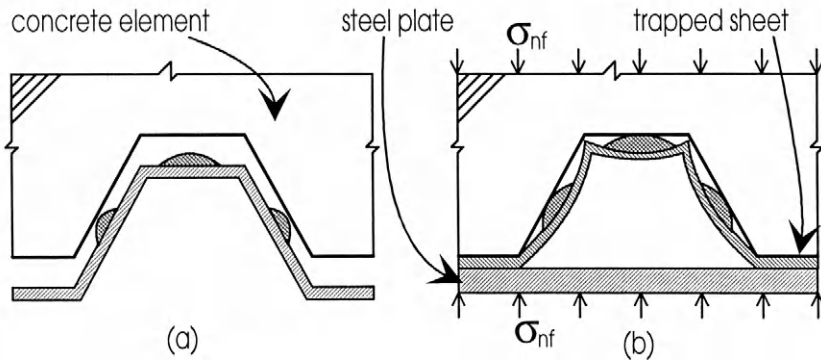
Fig. 2.29 Trapezoidal rib

The passive resistance of the rib therefore depends on the shape of the rib, thickness of the sheet and size and frequency of the embossments. When the passive resistance is low, then the transfer of shear through bearing and passive friction will be low, and there will be little or no damage to the steel rib and concrete adjacent to the interface when slip occurs. When the passive resistance is high, as occurs in the L-shaped ribs in Fig. 1.6, then the transfer of shear can be accommodated by localised failure of both the concrete and steel protrusions adjacent to the interface. It must be stressed that the longitudinal shear is transferred through the ribs in the interface interlock mechanism, and not through the steel sheet between the ribs that tend to detach because of the interface interlock mechanism, as shown in Fig. 2.28. It

is also worth noting that the plate rib connector, in Fig. 2.27, transfers shear in a similar way to the L-shaped rib connector.

The interface interlock shear strength v_{lock} can range from virtually zero for trapezoidal ribs without embossments to about 0.8 N/mm^2 for L-shaped ribs with embossments. These strengths are based on the area of the steel rib that is in contact with the concrete.

2.6.3.4 *Active friction*

The longitudinal shear can also be transferred by active friction which acts in conjunction with interface interlock shear. The active frictional shear resistance v_{fric} depends on the active normal force applied across the interface σ_{nf} and the coefficient of friction μ across the steel/concrete interface. The coefficient of friction between steel and concrete can range from virtually zero when the sheet is greased to about 0.6 when it is ungreased.

When concrete is poured onto steel decking, the pressure across the steel-decking/concrete-slab interface is equal to $h\rho$, where h is the height of the slab and ρ is the density of the concrete. Therefore, when the concrete has hardened, there is an active normal force across the interface that is equal to the dead weight pressure of the concrete $h\rho$. This active normal pressure is therefore available to provide a frictional resistance to the longitudinal shear of $v_{fric} = \mu h\rho$. For $\mu = 0.5$, h = 250 mm and $\rho = 2400$ kg/m^3, $v_{fric} = 0.003$ N/mm^2 which is two orders of magnitude less than both v_{chem} and v_{lock}. However, it should be remembered that its effect is larger as it acts over the whole contact surface and not just in the vicinity of the rib. The application of loads to the composite beam may also increase the interface normal force, but this increase in interface pressure tends to be concentrated over the supports where there is generally only a very small length of profile sheet, and so its contribution should be used with care.

Plate rib shear connectors, as in Fig. 2.27, also transfer shear by active friction that can be induced by transverse negative moments which are applied to the reinforced concrete slab as shown. However, positive transverse moments will remove this frictional resistance and also reduce the interlock strength, in the same say that active tensile stresses have been found to reduce the shear resistance of cracked reinforced concrete, as discussed in Section 2.5.4.1.

2.6.4 PUSH TESTS

The bond characteristics of rib shear connectors is determined from push specimens, in the same way that the bond characteristics of mechanical shear connectors are determined, as described in Section 2.4.3. As with mechanical shear connectors, the behaviour of the shear connection in a push specimen depends on the geometry and restraints on the push specimen, and furthermore this behaviour can be different from that in a beam. Hence bond characteristics determined from push specimens should be interpreted with care.

An example of a push specimen for rib shear connectors is shown in Fig. 2.30 (Burnet 1995). In this specimen, a concrete block is cast between two profiled sheets, and the specimen is tested by applying a load 2F to the concrete block, as shown. The forces and restraints imposed on this specimen are the same as those in the push specimen for mechanical shear connectors, as shown in Fig. 2.16(d), and so the horizontal force H is given by Eq. 2.28. In the rib connector push specimen in Fig. 2.30, h_2 is the sheet thickness, which is normally about 1 mm, and the distance h_1 to the resultant horizontal force H is approximately the distance to the centre of the concrete block, which can be about 200 mm. Therefore, $h_2 \ll h_1$ in Eq. 2.28 and hence the horizontal force H is much less than the longitudinal shear load F. Because of this, there will be virtually no increase in the bond strength due to the external restraint H that does not occur in a composite slab. Thus the behaviour of the bond in this type of push specimen should be similar to that in a composite beam.
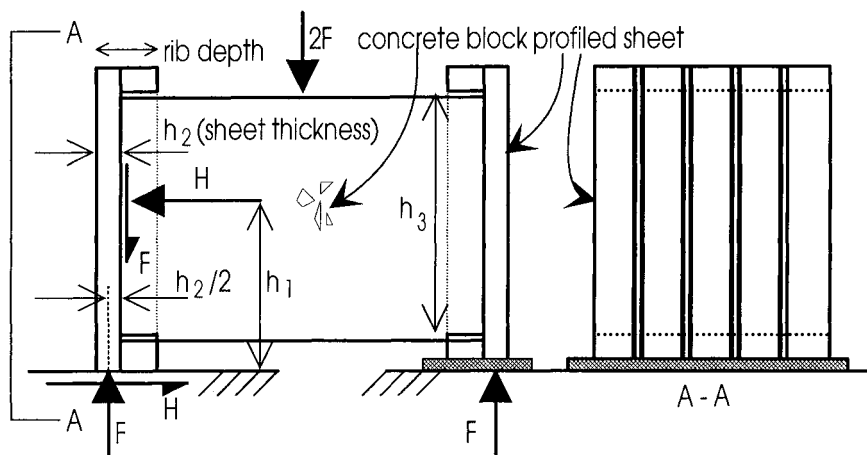

Fig. 2.30 Rib connector push specimen

This form of specimen is not easy to use, as there is a tendency for the sheet to buckle in the region between the soffit of the concrete block and support. Buckling can be prevented by embedding the sheet at the base, as shown on the right hand support in Fig. 2.30. Buckling can also be prevented by reducing the depth of the concrete block h_3 as the total bond strength and hence the load F is directly proportional to h_3.

In other forms of push specimens, the profiled sheet is fully supported and restrained by a steel plate, as shown in Fig. 2.29(b), so that the steel sheet in the soffit of the decking is now firmly trapped between the steel plate and the concrete element. A downwards compressive force σ_{nf} is then applied to the concrete element in order to simulate the dead weight pressure of the concrete on the profile sheet. Longitudinal shear is then applied to determine the bond characteristics. As discussed in Section 2.6.3.4, this active pressure is generally too small to affect the bond strength, and can be ignored. Of much greater significance is the fact that the trapped sheet will increase the passive restraint of the rib by preventing the rib from separating from the concrete

along the soffit, as shown in Fig. 2.29(b). This will increase the interface interlock bond and as this restraint does not occur in a composite beam, this form of testing will overestimate the bond strength particularly in trapezoidal ribs.

2.6.5 EXPERIMENTAL LOAD/SLIP CHARACTERISTICS

Typical load/slip curves for rib shear connectors are shown in Fig. 2.31. As with mechanical shear connectors, the shape of the curve is important as it determines the method of analysis and the mode of failure. For example, rib connectors that can sustain a shear load over an unlimited slip range can be used in rigid plastic ultimate strength analyses for all degrees of shear interaction.
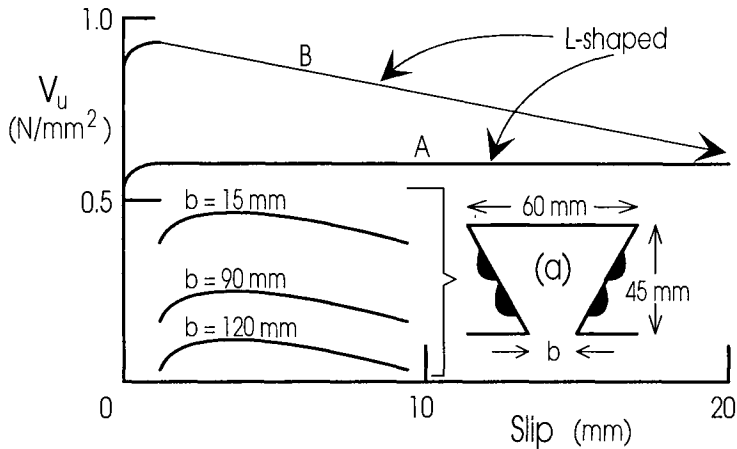

Fig. 2.31 Rib connector load/slip curves

Load/slip curve A in Fig. 2.31 was determined from an L-shaped rib shear connector (Burnet 1995) which had embossments and in which the rib was greased prior to casting the slab. The application of the shear load simply caused the rib to slide through the concrete while shear was being transferred by interface interlock. Because shear was being transferred by interface interlock, there is little to limit the slip capacity, just as long as the passive restraint of the rib is not reduced, and there is little damage to the concrete and steel that provide the interlock. This can be compared with mechanical shear connectors, in which there is always a finite slip because of the finite mechanical deformation capacity of the steel dowel. This rib connection, curve A, has the ideal characteristics required for rigid plastic analyses for all degrees of shear connection. The rib connection used in curve B was the same as in curve A, except that the rib was not greased prior to casting. The strength gradually reduced with slip until it approached that of the greased rib at high slips. The effect of varying the dimension of the opening of a dove-tailed rib (Burnet 1995), dimension b in Fig. 2.31(a), is also shown in Fig. 2.31. When b = 15 mm, the bond is ductile and can reach a maximum strength of 0.45 N/mm^2 when measured over the rib contact area. However, when b = 120 mm, which is equivalent to a trapezoidal rib, both the ductility and strength reduce considerably as shown.

2.7 References

Bazant, Z.P. (1972), "Prediction of creep effects using Age-Adjusted Effective Modulus Method", ACI Journal, Vol. 69, 212-217.

Burnet, M.J. (1995). *Partial Interaction Design of Composite Steel and Concrete Flexural Members*, Ph.D. Thesis, Department of Civil and Environmental Engineering, The University of Adelaide.

CEB-FIP (1970). *International Recommendations for the Design and Construction of Concrete Structures*, English Edition, CaCA, London.

Desayi, P. and Krishnan, S. (1964). "Equation for stress-strain curve for concrete", ACI Journal, Vol. 61, No. 3.

Gao, Z. and Bradford, M.A. (1993). "Time-dependent shortening of slender RC columns", Journal of Engineering Mechanics, ASCE, Vol. 119, No. 10, 2036-2051.

Gilbert, R.I. (1988). , *Time Effects in Concrete Structures*, Elsevier, Amsterdam.

Hofbeck, J.A., Ibrahim, I.O. and Mattock, A.H. (1969). "Shear transfer in reinforced concrete", ACI Journal, Feb., 119-128.

Hawkins, N.M. (1973). "The strength of stud shear connectors", Civil Engineering Transactions, Institution of Engineers, Australia, Vol. CE33, 46-52.

Hognested ,E. (1951). "A study of combined bending and axial load in reinforced concrete members", University of Illinois, Engineering Experimental Station Bulletin 399, Urbana, Illinois.

Johnson, R.P. and Oehlers, D.J. (1981). "Analysis and design for longitudinal shear in composite T-beams", Proceedings of the Institution of Civil Engineers, London, Part 2, Vol. 71, 989-1021.

Lay, M.G. (1982). *Structural Steel Fundamentals*, Australian Road Research Board, Melbourne.

Mattock, A.H. and Hawkins, N.M. (1972). "Shear transfer in reinforced concrete recent research", Precast Concrete Institute Journal, March-April, 55-75.

Neville, A.M., Dilger, W.H. and Brooks, J.J. (1983). *Creep of Plain and Structural Concrete*, Construction Press (Longman Group Ltd.).

Newmark, N.M., Siess, C.P. and Viest, I.M. (1951). "Tests and analysis of composite beams with incomplete interaction", Proceedings of Society for Experimental Stress Analysis, Vol. 9, No. 1, 75-92.

Oehlers, D.J. and Coughlan, C.G. (1986). "The shear stiffness of stud shear connections in composite beams", Journal of Constructional Steel Research, Vol. 6, 273-284.

Oehlers, D.J. and Johnson, R.P. (1987). "The strength of stud shear connections in composite beams", The Structural Engineer.

Ollgaard, J.G., Slutter, R.G. and Fisher, J.W. (1971). "Shear strength of stud connectors in lightweight and normal-density concrete", Engineering Journal, American Institute of Steel Construction, Vol. 8, 55-64.

Pham, L. and Bradford, M.A. (1988). "Safety index analysis of the design rules for webs and steel members under shear", Civil Engineering Transactions, Institution of Engineers, Australia, Vol. CE30, No. 1, 10-14.

Slutter, R.G. and Fisher, J.W. (1966). "Fatigue strength of shear connectors", Highway Research Record No. 147.

Teraskiewicz, J.S. (1965). "Tests on stud shear connectors", Road Research Laboratory Technical Note No. 36.

Trahair, N.S. and Bradford, M.A. (1991). *The Behaviour and Design of Steel Structures*, revised 2nd edn., Chapman and Hall, London.

Trost, H. (1967). "Auswrikungen des Superpositions prinzips auf Kriech-und Relaxations-Problem bei Beton und Spannbeton", Beton und Stahlbetonbau, Vol. 62, No. 10, 230-238.

Walpole, R.E and Myers, R.H. (1978). *Probability and Statistics for Engineers and Scientists*, Macmillan, New York.

3   Material Properties under Fatigue Loads

3.1   Introduction

Applying cyclic tensile stresses to materials can cause cracks to propagate that will eventually induce failure at stresses well below the static strengths of the material given in Chapter 2. It is the tensile cyclic stresses alone that cause fatigue failure, and not compressive cyclic stresses. However, it is worth bearing in mind that cyclic compressive forces can cause fatigue failure when they induce cyclic tensile stresses. This situation occurs in the welded girders in Fig. 2.6, where there are tensile residual stresses which may be near the yield stress.

It is standard practice to define the endurance of components that are subjected to fatigue loads in terms of their mean endurance and their characteristic endurance at two standard deviations from the mean, and not at 1.64 standard deviations as is commonly used in static behaviour. At two standard deviations, the characteristic endurance is defined as the 2.3% probability of not being exceeded, and it is this value that is quoted in this chapter.

Fatigue design is closely related to the method of fatigue testing. Two types of fatigue testing and their consequent fatigue procedures will be discussed in this chapter. The most common type of fatigue testing concentrates on determining how long a structural component will last under cyclic loading, and this will be referred to as endurance testing. A less common form of testing concentrates on determining the strength of a structure during cyclic loading, and this will be referred to as residual strength testing.

3.2   Endurance based procedures

3.2.1   METHOD OF TESTING

Most fatigue procedures in structural engineering are developed from tests in which cyclic loads are applied to structural components. This form of loading is shown in Fig. 3.1, where for example a cyclic load of range R_1 at a peak load $(F_p)_1$ and trough load $(F_t)_1$ is applied to a structural component. The static strength of the component, P_s, can be defined as the strength of a component that has not been subjected to cyclic loading. The strength of a component that has been subjected to cyclic loading will be referred to as P_c. When the peak and trough loads are of the same sign, such as $(F_p)_1$ and $(F_t)_1$, then this cyclic range of load will be referred to as a uni-directional range. When the peak and troughs of a cycle are of different signs, as in $(F_p)_2$ and $(F_t)_2$, then this cyclic range of load will be referred to as a reverse range. A component that is subjected to a reverse range of load is subjected to a total reverse cyclic load of magnitude R_2, that comprises two uni-directional ranges of opposite direction, of magnitudes $(F_p)_2$ and $(F_t)_2$.
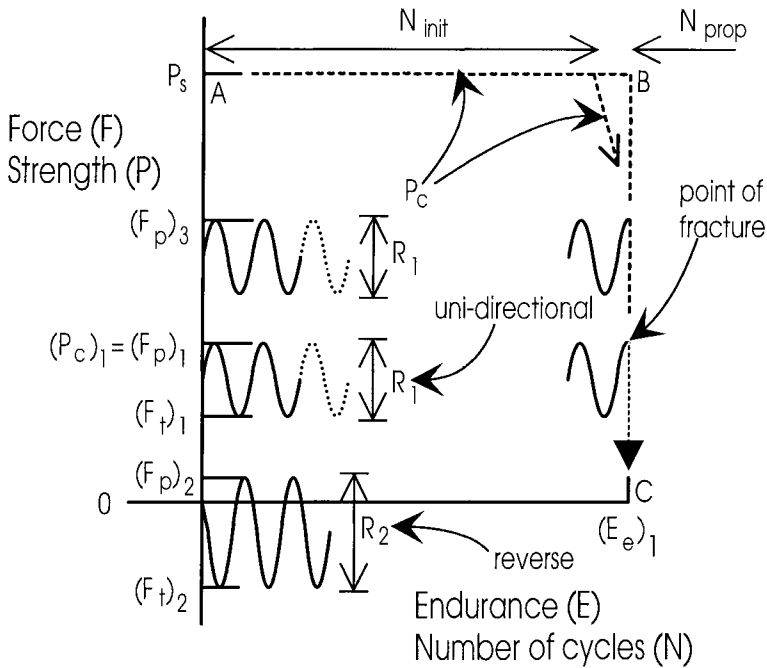
Fig. 3.1 Standard form of fatigue testing

It is normal practice in fatigue testing to keep cycling away at a constant peak load $(F_p)_1$ and a range of load R_1 in Fig. 3.1 until the strength of the structural component reduces to that of the peak load $(F_p)_1$, at which point the component fractures. The number of cycles N at which fracture occurs is referred to as the *endurance* $(E_e)_1$, noting that the endurance E_e is defined here as the endurance determined directly from experimental testing. We may repeat these tests on supposedly identical components, at range R_1 and peak $(F_p)_1$, and get slightly different endurances, and then use the mean or characteristic value of these endurances for the assessment of existing structures or the design of new structures. The independent variable in these tests is the range of cyclic load R, and the dependent variable is the endurance E_e. It can therefore be seen that the main purpose of this form of testing is to determine the endurance E_e of a structural component. What we know from this method of testing is that the strength of the structural component $(P_c)_1$ is equal to the peak load $(F_p)_1$ at fracture. We also know that the strength of the component has reduced from the static strength P_s to $(P_c)_1$ after $(E_e)_1$ cycles of load. There is, therefore, absolutely no doubt that the strength has reduced during cyclic loading, what we do not know from this form of testing is when this reduction in strength occurred, that is, what is the strength P_c during the period of cyclic loading.

Many steel design standards assume that the experimentally determined endurance E_e is dependent only on the range R and independent of the peak load F_p,

because of the presence within the steelwork of residual stresses that are close to the yield stress. Hence, it is assumed that increasing the peak load from $(F_p)_1$ to $(F_p)_3$ in Fig. 3.1 will lead to the same endurance $(E_e)_1$ when the same range R_1 is applied. Because of this, these design standards assume that part of the failure envelope is vertical, that is B-C as shown. Furthermore, as the strength is assumed not to change during cyclic loading, the remainder of the failure envelope, A-B, is horizontal. Therefore, the residual strength envelope, namely the failure envelope, is given by A-B-C in Fig. 3.1. In conclusion, this form of testing, and its associated analysis procedure, assumes that the strength does not reduce during cyclic loading, and hence the strength after cyclic loading $P_c = P_s$ when the number of applied cycles of load N $< E_e$, and also that P_c approaches zero when $N = E_e$.

The assumption of a rectangular residual strength envelope, A-B-C in Fig. 3.1, can be considered to be accurate in many steel elements. This is because, as a visual simplification, it can be assumed that most of the number of cyclic loads to cause failure E_e is required to initiate a crack, and once the crack develops, it propagates rapidly, reducing the strength P_c rapidly. This is shown diagrammatically in Fig. 3.1, where N_{init} is the number of cycles required to initiate a crack, N_{prop} is the number of cycles to propagate the crack to such a size that will cause P_c to equal F_p and hence fracture. Therefore, $N_{init} + N_{prop} = E_e$, and $N_{prop} \ll E_e$.

As it is assumed that the strength of the component is unaltered when N $< E_e$, the prime object of this form of testing is to determine the endurance E_e, and the standard method of accomplishing this is with the use of what are referred to as S-N curves.

3.2.2   S-N CURVES AND STANDARD FATIGUE TERMINOLOGY

The standard procedure in quantifying the endurance of a component is the S-N curve shown in Fig. 3.2. The term S-N is somewhat of a misnomer, because S does not refer to the strength of a component after cyclic loading P_c, but either to the range of the cyclic load R that is applied to the component, or to some other variable such as the ratio of the peak load to the static strength F_p/P_s. Furthermore, N does not refer to the number of cycles applied to the component, but to the number of cycles to cause failure, that is the endurance E_e.

The variable N is usually large, and normally plotted as $\log_{10}E_e$ along the x-axis as shown in Fig. 3.2, and the variable S is normally plotted along the y-axis in log or non-log terms. This is contrary to most mathematical representations, where the independent variable is usually plotted along the horizontal axis, which in this case should be S. This may appear to be a trivial point, but in order to derive the best prediction equation from a set of results, it is necessary to minimise the scatter of the dependent variable about the prediction curve. In other words, we desire to minimise the distance x in Fig. 3.2, and not the distance y.

There is a tendency in statistical analyses to minimise the vertical distance y, and this has led to errors in predicting the endurance from S-N curves, and has led

to less accurate design endurance prediction equations. The loss in accuracy in minimising y in Fig. 3.2 depends on the scatter of results. For example, when all the points lie in a line, as in the results in Group A in Fig. 3.2, then the error is zero. However, when the scatter is large, as occurs in fatigue data, then minimising the wrong variable can lead to large differences between prediction equations, as can be seen in Group B. Therefore, S-N curves should really be referred to as N-S curves.
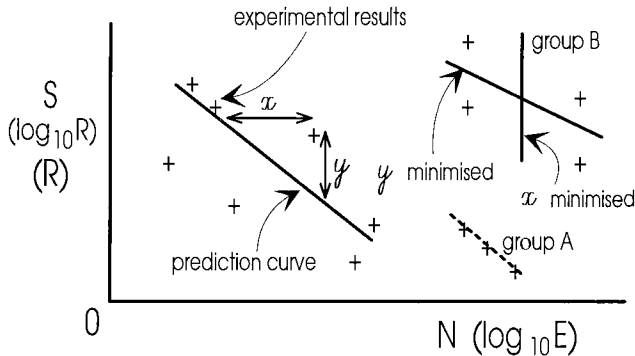

Fig. 3.2 S-N curves

The term *fatigue damage* that is often used in fatigue studies is also considered to be a misnomer. Fatigue damage is the ratio of the number of cycles applied to a component, N, as a proportion of the endurance E_e. Hence fatigue damage does not mean a loss of strength, but it is a measure of how much of the design life has been used, which is the used-life N/E_e. The term *accumulated damage* is simply the sum of the fatigue damage for each 'magnitude of range' of the cyclic load that has been applied to the component. The term *fatigue strength* is also not a strength, but rather is a range of load that will give a required endurance. *Fatigue life* is the total number of cycles for all the 'magnitudes of range' that will cause the component to fracture. When the number of cycles in a time interval is known, then the fatigue life can be converted to a *design life* that is normally measured in years. As an example, bridges are often designed for a fatigue design life of about 100 years. When the number of cycles of load induced by a vehicle crossing the bridge are known, then the fatigue life can be quoted as a number of vehicle traversals, and it is common practice to design a composite bridge for 200 x 10^6 vehicle traversals. Another term used is *fatigue limit*, and this refers to the range of load below which the endurance tends to infinity, and hence below which the component will never fracture through fatigue loading.

Because of the apparent ambiguity in standard fatigue terminology, S-N curves will be referred to as E_e-R curves herein, as described in the following section.

3.2.3 E_e-R CURVES

It was shown in Section 3.2.1 that the peak load F_p is not considered to affect the endurance E_e because of the presence of residual tensile stresses, and hence the only

variable that can be considered to affect the endurance is the range of load R. It is, therefore, standard experimental procedure to concentrate on determining the dependence of E_e on R by subjecting structural components to constant ranges of cyclic loads until they fracture. It is also common practice to assume that the dependence is related to the logarithm of the variables, as shown in Fig. 3.3. A linear regression analysis, in which the scatter of endurances is minimised, is then performed to determine the best prediction equation. The intercept H_e and slope m_e in Fig. 3.3 are used to define the prediction equation through the mean of the fatigue data. This will be referred to as the *mean endurance* $(E_e)_{mean}$, and is therefore defined by

$$\left(E_e\right)_{mean} = 10^{H_e} R^{-m_e} \tag{3.1}$$

The *characteristic endurance* $(E_c)_{ch}$ is the endurance at two standard deviations, $2D_e$, below the mean endurance, and is given by

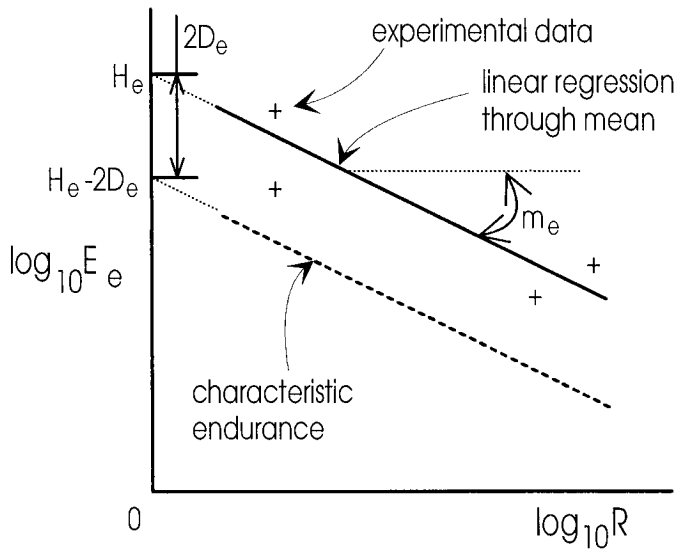$$\left(E_e\right)_{ch} = 10^{H_e - 2D_e} R^{-m_e} \tag{3.2}$$

Fig. 3.3 E-R curves

When a component is subjected to a range R_k, then the endurance, or fatigue life at this range $(E_e)_k$, can be determined from either Eqs. 3.1 or 3.2. If N_k applications of this range R_k are applied, then the proportion of the fatigue life that has been used is $N_k/(E_e)_k$. Similarly, if N_q applications of range R_q are applied, then the proportion of life used is $N_q/(E_e)_q$. It was proposed by Miner (1945) that if N_k applications of R_k are applied with N_q applications of R_q, then the proportion of the fatigue life that has been used is the sum of the individual components of the used life, which is $(N_k/(E_e)_k + (N_q/(E_e)_q)$. This summation is often referred to as the

accumulated damage but it is not a measure of a reduction in strength, rather it is a measure of the fatigue life that has been used. In order to prevent ambiguity in the nomenclature, and to allow the engineer to achieve a better feeling for fatigue analysis, the term accumulated damage will be referred to as the *accumulated used-life* in this book. The accumulated used-life is therefore the proportion of the fatigue life that has already been applied. Fracture of the component is assumed to occur when the accumulated used-life is equal to unity. Sometimes a value A_e is used instead of unity, but which is less than unity, to allow for experimental scatter. In this case, the accumulated used-life law can be written as

$$\sum_{k=1}^{k=z} \frac{N_k}{(E_e)_k} \leq A_e \tag{3.3}$$

where z is the total number of the 'magnitude of the ranges' of the cyclic load R, N_k is the number of cycles of load of range R_k that have been applied to the component, and $(E_e)_k$ is the endurance of a component that is subjected to the range R_k. One way of visualising Eq. 3.3 is that the left hand side is the proportion of the life that has been used, and the right hand side is the proportion that will cause fracture or some other limit state such as crack size.

3.2.4   ENDURANCES E_e

The exponent m_e of the endurance equations Eqs. 3.1 and 3.2, is the magnitude of the slope of the fatigue prediction line in Fig. 3.3, and is a function of the material properties. In welded steel components m_e is normally taken as equal to 3, for plain concrete m_e is about 20, and for stud shear connectors m_e is about 5. The magnitude of the exponent m_e defines the susceptibility of the material to changes in the cyclic range R. For example, for a concrete component with $m_e = 20$, halving the range will, from Eq. 3.1, increase the endurance by $2^{20} = 1,048,576$, that is, by a factor of just over one million. Conversely, doubling the range on a concrete component will reduce the endurance by a factor of approximately 10^{-6}. It can therefore be seen that in a concrete structure, most of the fatigue used-life, which is the left hand side of Eq. 3.3, will be due to high ranges of load. Conversely, small ranges have very little effect on the used-life of the components, as their endurances are very large compared with the endurances at high ranges. Hence, the fatigue life of a concrete component is governed by stresses that approach the static strength of the concrete which could be the compressive strength or the tensile strength, depending on the mode of failure. For a steel component with $m_e = 3$, halving the range R will increase the endurance by a factor of 8, that is 2^3. Hence, the accumulated used-life for steel components is not as susceptible to the range of load as compared with concrete components.

The intercept H_e in Fig. 3.3 defines the magnitude of the mean endurance in logarithmic terms that converts in non-logarithmic terms to 10^{H_e}, as shown in Eq. 3.1. The constant 10^{H_e} can be considered to define the susceptibility of the structural component detail to failure due to fatigue loads. It allows for the stress concentrations

induced by the geometric detail, the difference between non-welded, welded and bolted components, and the difference in magnitude of the endurances between materials. For example, for a steel flange plate with smoothly varying cross-sectional shape, 10^{H_e} is of the order of 2×10^{15} when the range of load is measured as a stress with units of N/mm^2. However, inserting a small hole in the flange can reduce the constant 10^{H_e} to about 4×10^{12}, and so reduce the endurance by a factor of $(2 \times 10^{15})/(4 \times 10^{12}) = 500$. It can be seen that the addition of a small hole in the plate will reduce the design life by a factor of 500 because of the stress concentrations induced by the hole. Welding a stud shear connector to the flange will not only induce stress concentrations, but will also cause minute cracks and residual stresses in the flange that can reduce the constant 10^{H_e} to about 2×10^{12}. The addition of the stud to the flange will therefore reduce the design life of the flange by a factor of 1000. One of the worst type of detail is to transfer the load between plates that are attached with fillet welds, and in this case the design life can reduce by a factor of about 4000.

It is standard practice in design to use the characteristic endurance which is given by the intercept H_e - $2D_e$ in Fig. 3.3, so that the constant in the endurance equation is now $10^{H_e - 2D_e}$, as shown in Eq. 3.2. The characteristic endurance as a proportion of the mean endurance is therefore given by $10^{H_e - 2D_e} / 10^{H_e}$ and has a value for steel components of about 0.4, depending on the type of detail. There is thus a 4.6% probability (the percentage of the population greater than two standard deviations from the mean) that a component designed for a mean design life of say 100 years will last less than 40 years or more than 250 years. It can therefore be seen that fatigue procedures that predict the correct order of magnitude of the endurance can be considered to be accurate, as compared with static flexural strength analyses of composite beams, where it is now possible to predict the strength to within an accuracy of about 15%.

3.3 Residual strength based procedures

3.3.1 GENERAL

In the previous section dealing with endurance based procedures, it was shown how the testing procedure was chosen so that the endurance was the dependent variable, that is, the endurance was the variable which was being determined. The aim of the residual strength approach in this section is to determine the strength after cyclic loading P_c, which will be referred to as the *residual* or *remaining strength*. In order to do this, the testing procedure has to be changed so that the strength is now the dependent variable.

3.3.2 METHOD OF TESTING

It was shown in Section 3.2.1 and in Fig. 3.1 that the standard method of fatigue testing is to apply a constant range of cyclic load R_1 to a specimen with an initial static strength P_s, until the component fractures at $(E_e)_1$ when the strength after cyclic

loading $(P_c)_1$ has reduced to the peak of the cyclic load $(F_p)_1$. These results are also shown in Fig. 3.4, where it can be seen that this form of testing only gives the strength at point A on the graph. However, point B can also be determined, as it is the static strength prior to cyclic loading at $N_b = 0$, where the residual strength P_c is P_s. What we do not know from endurance based testing procedures is how P_c reduces from point B to point A, and this path is referred to as the *failure envelope*. It is worth repeating that in this standard form of testing, the endurance E_e is the dependent variable.
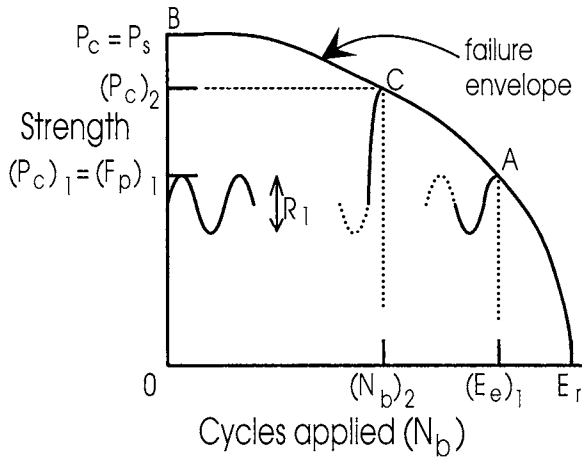

Fig. 3.4 Residual strength

In order to determine how this reduction in strength from $P_c = P_s$ at $N_b = 0$ to $(P_c)_1 = (F_p)_1$ at $N_b = (E_e)_1$ occurs, it is necessary to first apply blocks of cyclic loads $(N_b)_2$ of constant range R_1, and then to load the structure to failure at $(P_c)_2$, as shown in Fig. 3.4. We have therefore obtained another point C on the failure envelope of residual strengths. In comparison with the endurance based testing procedures, in this form of testing the block of cyclic loads N_b is the independent variable, and the residual strength P_c is the dependent variable. It is a simple procedure to determine the failure envelope of residual strengths by repeating the procedure for different values of N_b, but at the same range R_1. The residual strength curve will be referred to as the P-N curve, where P is the strength of a component P_c after N cycles of load N_b have been applied to it.

3.3.3   P-N CURVES

The failure envelope in Fig. 3.4 can be idealised into a trilinear shape (Oehlers 1992a) as shown in Fig. 3.5. During the first N_{init} cycles of load, the strength is virtually unchanged and, in a simplistic view, N_{init} can be associated with the crack initiation. At the transition point B, the crack is large enough to start to affect the strength of the structure. During the next N_{prop} cycles, the crack propagates and gradually reduces

the strength. At the transition point C, the strength of the component starts to reduce rapidly, and this is represented by the vertical path C-D at E_r. It must be emphasised that the visualisation of the failure envelope in terms of crack initiation and propagation is a very simplified model of what is normally a very complex problem.
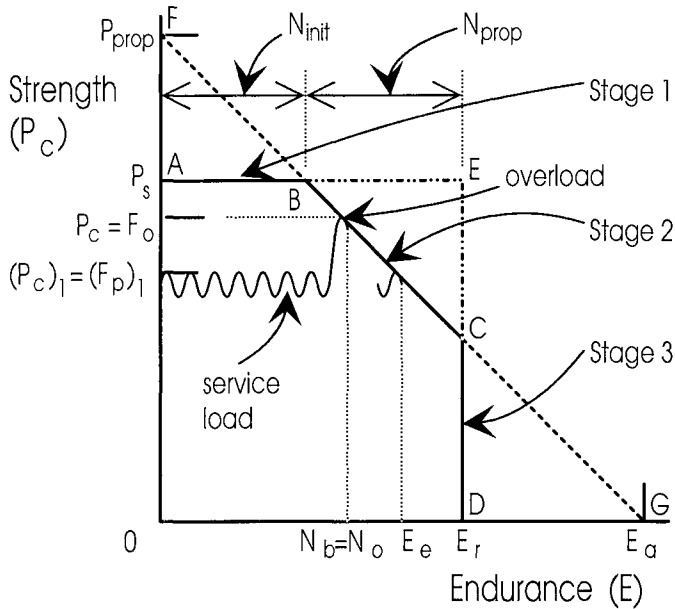

Fig. 3.5 Linearised residual strength envelope

This failure envelope can be used to predict the endurance of a component. For example, most structures are subjected to cyclic loads at working or service load levels, plus intermittent very large loads or overloads as shown in Fig. 3.5. The service load will cause the component to fracture when the strength of the component $(P_c)_1$ reduces to the peak of the service load $(F_p)_1$ at endurance E_e, as shown. However, the intermittent overload F_o will cause the structure to fail at the reduced number of cycles at $N_b = N_o$.

The second stage in the failure envelope, path B-C, is defined by P_{prop} and E_a in Fig. 3.5. The theoretical static strength prior to cyclic loading P_{prop} is simply the intercept of the extrapolated crack propagation part of the residual strength envelope. In linear elastic fracture mechanics, it would be the load to cause a component, that has not been subjected to cyclic loads but which does have an initial crack, to fracture. Often, and particularly when the initial crack is small, yielding of the material will prevent P_{prop} from being achieved. The theoretical endurance E_a will be referred to as the *asymptotic endurance* as it can never be achieved but only approached, as fracture will always occur when the strength of the component has reduced to the peak of the cyclic load, and hence N_b or E_e will always be less than E_a. The failure envelope for stage two is therefore given by

$$P_c = P_{prop} \left(1 - \frac{N_b}{E_a} \right) \tag{3.4}$$

where, for example, when the number of cycles of load that have been applied to the component $N_b = 0$ then $P_c = P_{prop}$, and when $N_b = E_a$ then $P_{prop} = 0$.

The first stage, path A-B in Fig. 3.5 is defined by the static strength P_s of the structure, and this is usually easy to determine. The third stage, path C-D is associated with both material failure and a rapid increase in the stress field in the vicinity of the failure zone.

The failure envelope A-B-C-D in Fig. 3.5 defines the general failure envelope of residual strengths. Experimental research has shown that this general shape has been found to occur in reinforced concrete structures subject to fatigue loads (Warner 1985), and also theoretical fracture mechanics can be used to derive this general shape for steel components (Wahab, Oehlers and Gosh 1993). It has been suggested in Section 3.2.1 that for many steel components the assumption of a rectangular strength envelope, such as A-E-D in Fig. 3.5, is accurate, and hence standard fatigue procedures, based on the endurances, can be used in the analysis or design of these components. This rectangular failure envelope can be considered to be an extreme case of the general shape, as it is completely defined by both stage 1, $P_c = P_s$, and by stage 3 where $E = E_r$. Experimental tests on stud shear connectors (Oehlers 1990a) clearly show that their strength reduces immediately cyclic loads are applied, and that the reduction in strength can be assumed to be linear. This is also another extreme case of the general failure envelope, as in this case $P_{prop} = P_s$ and both the first stage and the third stage do not exist so that the failure envelope is defined by F-B-C-G.

Having defined the general shape of the failure envelope of residual strengths, it is also necessary to determine both the asymptotic endurance and dependence of the asymptotic endurance on the range of load. This can be done using E_a-R curves, as follows.

3.3.4 E_a-R CURVES

Equation 3.4 can be used in the following forms to determine the asymptotic endurance E_a. When the endurance form of fatigue testing has been used, as illustrated in Fig. 3.1, and when the failure envelope is linear as in stage 2 in Fig. 3.5, then the asymptotic endurance $(E_a)_1$ at cyclic range R_1 with a peak load of $(F_p)_1$ is given by

$$(E_a)_1 = \frac{(E_e)_1}{1 - \frac{(F_p)_1}{P_{prop}}} \tag{3.5}$$

where $(E_e)_1$ is the number of cycles to cause fracture. When the residual strength form of fatigue testing is used and when the failure envelope is linear, as illustrated in Fig. 3.5, then the asymptotic endurance $(E_a)_2$ at a cyclic range R_2 is given by

$$(E_a)_2 = \frac{(N_b)_2}{1 - \dfrac{(P_c)_2}{P_{prop}}} \tag{3.6}$$

where $(N_b)_2$ applications of cyclic load were applied before testing to failure that occurred at a load $(P_c)_2$. Hence from each experimental test, the asymptotic endurance E_a can be determined for a given range of load R. It is noteworthy that the only variable which does not change in Eqs. 3.5 and 3.6 is the upper bound static strength P_{prop}.

The dependence of the asymptotic endurance E_a on R is determined in exactly the same way as the dependence of E_e on R, as described in Section 3.2.3. This procedure is illustrated in Fig. 3.3, where the subscript 'e' should be replaced by the subscript 'a', and this will lead to the prediction equation

$$(E_a)_{ch} = 10^{H_a - 2D_a} R^{-m_a} \tag{3.7}$$

where $(E_a)_{ch}$ is the characteristic asymptotic endurance, H_a is the intercept through the y-axis, D_a is the standard deviation of the asymptotic endurance about a regression line through the mean of the data, and m_a is the slope of the regression. The mean asymptotic endurance is given simply by substituting the exponent $H_a - 2D_a$ with H_a, as it occurs at a standard deviation of zero.

The failure envelope of residual strengths is given in Eq. 3.4. This can be rearranged and written in the form

$$\frac{N_b}{E_a} = 1 - \frac{P_c}{P_{prop}} \tag{3.8}$$

where the left hand side of the equation is the proportion of the asymptotic endurance that has been used, and the right hand side is the surplus strength as a proportion of the static strength, $(P_{prop} - P_c)/P_{prop}$, that is available for fatigue damage. Furthermore, when N_b/E_a is known, then the residual strength of the component P_c can be calculated whenever the maximum static strength P_{prop} is known.

Equation 3.8 can also be used for variable cyclic loads, in which case it can be written as

$$\sum_{k=1}^{k=z} \frac{N_k}{(E_a)_k} = 1 - \frac{P_c}{P_{prop}} \tag{3.9}$$

where z is the total number of R, that is the total number of the magnitudes of the ranges of load R, N_k is the number of cycles of load of range R_k that have been applied to the component, and $(E_a)_k$ is the asymptotic endurance of the component when subjected to the range R_k. When the used-life is known, which is the left hand side of Eq. 3.9, then the residual strength P_c can be calculated. If P_c is greater than the minimum strength required of the component, then the used-life to reduce the strength to the minimum requirement can be calculated, and this is termed the *residual* or *remaining life*. Methods of doing this are described in Chapter 19.

The strength after cycling P_c is also equal to the maximum overload F_o that can be applied after cyclic loading, and hence F_o can be substituted for P_c in Eq. 3.9, which can then be written as the following accumulated used-life equation

$$\sum_{k=1}^{k=z} \frac{N_k}{(E_a)_k} \leq 1 - \frac{F_o}{P_{prop}} \tag{3.10}$$

where F_o is the maximum overload that the component is subjected to.

3.4   Stud shear connectors

3.4.1   GENERAL

The behaviour of stud shear connectors under cyclic loading is determined from the same type of push test as is used to determine their static strengths, and these have already been described in Section 2.4.3.1. The behaviour under fatigue, described in the following sections, was derived from fatigue tests in which uni-directional cyclic loads were applied, as illustrated in Fig. 3.1. However, experimental research has also shown that the endurance under reverse cyclic loading (Oehlers 1995) is the same as the endurance under uni-directional cyclic loading, when the total range of the reverse cyclic load is used in the analysis, for example R_2 in Fig. 3.1.

The deformed shape of a stud shear connector is shown in Fig. 2.14(b). The resistance to the shear load induces tension at the front of the stud at zones A and B. The head of the stud prevents the top of the shank from rotating, so that secondary tensile stresses are induced behind the stud at zone C. Under static loads, the stud tends to fail in zone B, at the weld-collar/shank interface. When the height of the weld-collar is large, the failure zone is moved into position A at the weld-collar/flange interface. Rarely, if ever, does static failure cause cracking in zone C. However, fatigue loads tend to cause cracking in all three zones, although not simultaneously in zones A and B.

An example of fatigue cracking at the weld-collar/shank interface at zone B in Fig. 2.14(b) is shown in Fig. 3.6. The fatigue crack front can be seen as a horizontal almost straight line. The dull smooth region below the crack front is the fatigue crack zone. The bright irregular region above the fatigue crack front is the fracture zone. The fatigue crack started at the front of the stud, position B in Fig. 2.14(b), and at the lower edge of the shank perimeter in Fig. 3.6. Under fatigue loading, the crack front moved upwards, in Fig. 3.6, and remained horizontal. As the crack front moves upwards, the remaining uncracked area reduces and hence the strength reduces. Fracture occurs when the area of the uncracked region can no longer resist the maximum load applied to it. This maximum load can be an overload or the peak of the cyclic load. A good estimate of the size of the shear load that caused fracture is given by the area of the fracture zone. In Fig. 3.6, the fracture zone is about 40% of the total area of the shank, this would suggest that the load to cause fracture was about 40% of the dowel strength of the connector prior to cyclic loading D_{max}.

Fig. 3.6 Weld-collar/shank failure zone

Figure 3.7 shows an example of simultaneous fatigue cracking at both the weld-collar/flange interface and in the shank above the weld-collar. Simultaneous horizontal fatigue cracking in zone A and in zone C in Fig. 2.14(b) will allow the shank between A and C to rotate towards a horizontal position. Experimental fatigue tests have shown that this rotation increases the ductility of the stud shear connectors (Oehlers 1990a, 1992b). However, this increase in ductility through cyclic loading has not been quantified, so it would be conservative to assume that the connectors have the same ductility as given in Section 2.4.6.2. As well as the three possible fatigue failure zones in the stud, at A, B and C in Fig. 2.14, the concrete in the bearing zone in front of the stud can also fail in fatigue.

3.4.2   LOAD/SLIP PATH

3.4.2.1   *Change in path between initial loading and unloading*

The load/slip path for stud shear connectors under static loads has already been described in Section 2.4.6.2. Here, the behaviour under cyclic loads will be described,

as it affects both the mean and characteristic endurance of the connection in a composite beam.

Under working loads, the load/slip paths shown in Fig. 2.21 can be assumed to be linear, as shown in Fig. 3.8. When a load F_1 is first applied to a stud shear connector, the response is linear and the connector follows the path O-A. On unloading, the connector follows the path A-B-O, that has a permanent set O-B. On further application of the load F_1, the connector first displaces along O-B and then starts to resist the load until it reaches the same point A, as in the original application of load. When the load is increased from F_1 to F_2, the connector follows the original static path A-C, and will then unload to point D, with an increased permanent set.
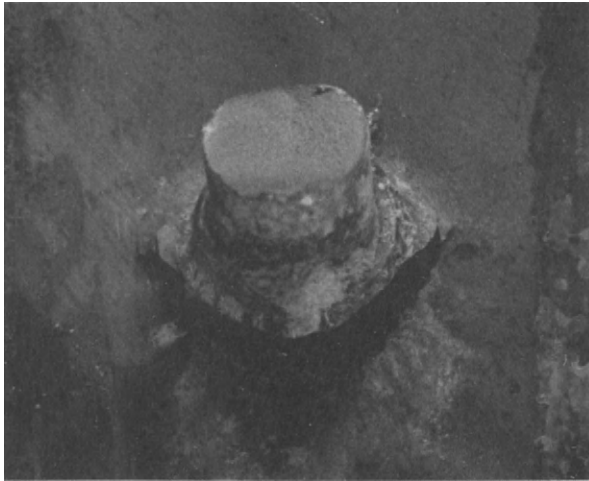

Fig. 3.7 Fatigue failure zone

In push tests, the connectors are loaded directly, and hence the load on the connectors is exactly the load that is applied to the push specimen. Thus the changes in the load path do not affect the actual forces on the connectors, as they have to be in equilibrium with the applied load.

It was shown in Section 1.2 and illustrated in Fig. 1.12 that the shear connectors in composite beams are not directly loaded by the forces applied to the beam, but are loaded indirectly through the flexural deformation of the beam. For example, when there are no connectors in a composite beam, then the composite beam can still resist a load through the flexural resistance of the steel section, but the force on the connectors is zero. Hence the force on the connectors in a composite beam depends on the stiffness of the connectors, and thus will change when the load/slip path changes.
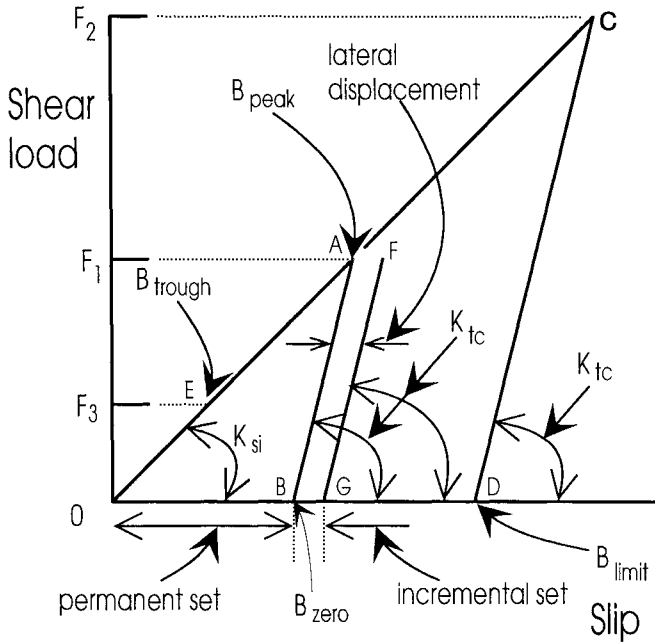
Fig. 3.8 Load/slip stud shear connectors

3.4.2.2 *Range of cyclic load in composite beams*

Consider a connector in a composite beam that is being subjected to cyclic loads. Let us assume that, on initial loading, the trough of the cycle of load on the beam B_{trough} causes a force on the connector F_3 in Fig. 3.8, and that the peak of the cycle of load on the beam, B_{peak}, causes a force F_1 on the connector. Therefore, on the initial application of the cyclic load on the beam, the connector follows the path E-A. On unloading the beam from B_{peak} to B_{trough}, the connector unloads along the path A-B-O.

In order to determine the range of load on the connector on unloading, and hence its endurance, it is necessary to determine the force on the connector when B_{trough} is being applied to the beam. This can be done by first removing the applied load on the beam, so that both the shear load on the connector and the displacement of the connector are now zero. On gradually reapplying the beam load, the connector first follows the path O-B in Fig. 3.8, and remains unloaded until the force on the beam is B_{zero} at slip B. On further loading, the force on the connector will reach F_1 at a beam load B_{peak}. When $B_{zero} = B_{trough}$, the range of load on the connectors is F_1, and it is greater than the range F_1-F_3 on the original loading path O-A. When $B_{zero} > B_{trough}$, the range of load on the connector remains at F_1. However, when $B_{zero} < B_{trough}$, the range will be less than F_1 but will always be greater than F_1-F_3. When $B_{trough} = 0$ and hence $F_3 = 0$, then the range of load on the connector is independent of the path, and remains at F_1.

It can therefore be seen that, for a given range of cyclic load on the beam (Oehlers and Singleton 1986), when the minimum cyclic load on a connector is greater than zero, the endurance will be less than in a connector where the minimum cyclic load is zero. The former case occurs in propped construction and the latter in unpropped construction, and these two forms of construction are described fully in Section 6.5. In addition, if fatigue analysis is based on a linear elastic analysis with the connectors at a stiffness K_{si} in Fig. 3.8, then this analysis will overestimate the endurance when $F_3 > 0$.

3.4.2.3 *Overloads, fatigue limit and load traversals in composite beams*

Let us assume that the connector load F_2 in Fig. 3.8 was induced by an overload on the beam and that the beam is now unloaded. We will also assume that on reloading, a beam load of B_{limit} has to be applied for the connector to slip to point D before it starts resisting shear load. It can therefore be seen that any beam load that is less than B_{limit} will not load the connector, thus beam loads less than B_{limit} will not reduce the endurance of the connector. Because of this, stud shear connectors in composite beams have a fatigue limit that is due to their change in load/slip path. This fatigue limit does not occur in shear connectors in push specimens where the shear connection is loaded directly.

Overloads, therefore, reduce the working forces on connectors, although it is worth bearing in mind that overloads have no effect on the maximum load applied to a connector. The reduction in the connector shear forces at serviceability loads reduces the composite action, which must be compensated for by an increase in the flexural forces in the steel and concrete elements. Hence, applying overloads to composite beams may increase the endurance of the shear connectors, but may reduce the endurance of the steel and concrete elements.

It was shown in Section 2.4.6.3 that the static dowel strength of connectors in push specimens is not the same as in composite beams, due to the different restraints between the two systems. It has been shown in this section that the endurance of connectors in push tests is different from those in beams, due to the different loading configurations. It is therefore worth re-emphasising the point that the results of push tests have to be applied with caution when used in composite beam analyses.

3.4.2.4 *Change in path during cyclic loading*

It has been shown in the previous section that a change in the path occurs between the initial loading and subsequent unloading. In this section, it will be shown that cyclic loads also cause a change in path that affects the endurance of the shear connectors.

(a) Incremental set

Experimental research (Oehlers and Foley 1985) has shown that each time a cycle of load is applied to a stud shear connector, the load/slip path is displaced by a

permanent set, such as B-G in Fig. 3.8. This permanent-set/cycle will be referred to as the *incremental set* S_{set}. It was also shown experimentally that the incremental set occurs as soon as cyclic loads are applied, that it does not change in magnitude for a given range, and that the slope K_{tc} of the load path G-F remains constant during most of the fatigue life.

(b) Loss of energy

The lateral displacement per cycle of the load/slip path from B-A to G-F in Fig. 3.8 represents a loss of energy, and because the incremental set S_{set} and the stiffness K_{tc} remain constant, the loss of energy per cycle is also constant. This loss of energy represents a degradation of the material of the stud connection, such as powdering or micro-cracking of the concrete element bearing against the stud, or crack propagation in the stud. Both of these forms of material degradation represent a loss in the dowel strength of the shear connection, and this was the first indication that the dowel strength of stud shear connectors reduces as soon as cyclic loads are applied to them.

Based on the energy released per cycle (Oehlers and Foley 1985), the following method for predicting the incremental set was developed from Paris' crack growth rate equation (Paris and Erdogan 1963), namely

$$\frac{dS_{set}}{dN} = K\left(\frac{R}{D_{max}}\right)^{m_a} \tag{3.11}$$

where D_{max} is the dowel strength of the stud connector and the units are in N and mm. It was shown theoretically, and confirmed experimentally, that the exponent m_a was also the exponent of the asymptotic endurance equation given in Eq. 3.7. Hence, there is a direct correlation between the incremental set and the endurance under cyclic loads. From the population of the fatigue data analysed in this research, the constant K may be taken as 1.70×10^{-5} and the exponent m_a as 4.5. These values can be used in computer simulations if required (Murray 1988).

(c) Redistribution of connector loads

It can be seen in Eq. 3.11 that the incremental set is proportional to the ratio $(R/D_{max})^{4.5}$. Let us suppose that there is a group of two connectors in a composite beam that is being subjected to the same range of load per connector R. Furthermore, let us assume that even though the connectors are of the same size and cast in the same concrete, they have a variation in static dowel strength ranging from the weaker, D_{weak}, to the stronger, D_{strong}, which is associated with the normal variation in strength which was discussed in Section 2.4.4.

On applying a cycle of load R to each connector , the incremental set of the weaker connector will be greater than that of the stronger connector because $\left(R / D_{weak}\right)^{4.5} > \left(R / D_{strong}\right)^{4.5}$. This implies that the reduction in the overall stiffness of the weaker connector will be greater than the reduction in the stronger

connector, so that the weaker connector will now be less stiff than the stronger connector. As the load on the connectors in beams depends on their stiffness (as explained in Section 1.2), during the subsequent cycle of load, the weaker connector will attract less load, R_{weak}, than the stronger connector, R_{strong}. An alternative method of visualising this behaviour is to assume that the total set of the weaker connector, such as O-G in Fig. 3.8, is greater than the total set of the stronger connector, such as O-B. Hence, and according to Section 3.4.2.1, during the next cycle of load the stronger connector will attract more load than the weaker connector. Shear connectors, therefore, have an ability to shed load from weaker connectors to stronger connectors during cyclic loading. This shedding of the load will continue until $\left(R_{strong} / D_{strong} \right) = \left(R_{weak} / D_{weak} \right)$. As R/D is now the same, the remaining endurance of both connectors will be the same (as explained in the following Section 3.4.3).

The same sequence of redistribution occurs in groups of n connectors. Hence, connectors can be assumed to fail at their mean endurance. This is analogous to the static failure of a group of n ductile connectors, where it was shown in Section 2.4.4 that because they fail as a group, their characteristic strength should be taken as the characteristic strength of the mean of the group, as given in Eq. 2.30. The form of Eq. 2.30 in which the $\sqrt{n}$ is included to allow for the characteristic strength of the mean (Walpole and Myers 1978), can therefore be applied to the endurances of stud shear connectors, not because they have a ductile plateau (which they do), but because of the redistribution due to the incremental set. The form of the characteristic asymptotic endurance of an individual connector is given in Eq. 3.7, and hence the characteristic asymptotic endurance of a group of n connectors is given by the equation

$$\left(E_a \right)_{ch} = 10^{H_a - 2\frac{D_a}{\sqrt{n}}} R^{-m_a} \tag{3.12}$$

in which n is the number of connectors in a group in which the connectors are subjected to similar displacements. This can be taken as the number of connectors in a shear span when the composite beam has been designed against fracture of the shear connection as described in Chapter 8, as in the static strength analyses as already described in Section 2.4.4.

(d) Redistribution in composite beams

It has been established in the previous section that the incremental set redistributes the shear load from weaker to stronger connectors. Exactly the same sequence of redistribution can occur in composite beams from overloaded connectors to underloaded connectors. The shear connection in composite beams under fatigue loading has therefore an unusual ability to 'mend' itself by redistributing the forces, although there is a limit to the amount of incremental set that can occur during a design life, and hence there is a limit to the amount of redistribution.

As the total permanent set in Fig. 3.8 increases because of the incremental set, the overall force on the connectors in the beam reduces, increasing the endurance of the connectors. It should be remembered, though, that the beneficial effect of the reduction in connector forces, and hence the increased connector design life, is offset by an increase in the forces in the steel and concrete elements of a composite beam, and hence there is a reduction in their design life.

Because of both the incremental set and the change in path, the shear flow in composite beams under fatigue loading is continually changing with time. However, nonlinear fatigue analyses of composite beams (Oehlers and Carroll 1987, Murray 1988) suggest that design based on shear flows derived from full interaction analyses would be adequate.

3.4.3 STRENGTH AND ENDURANCE

3.4.3.1 *Residual strength*

Unlike 'endurance based fatigue procedures' which assume that the strength and endurance are not dependent, 'residual strength based procedures' assume a high dependence, and hence the strength and endurance must be considered together.

It has been shown in Section 3.4.2.4 that the incremental set represents a loss of energy, and hence a reduction in the strength of the stud shear connectors. It was also shown that the incremental set occurred as soon as cyclic loads were applied, which suggested that the strength reduced as soon as these cyclic loads were applied. This reduction in strength was confirmed directly through experimental tests (Oehlers 1990a), in which push specimens were subjected to blocks of cyclic loads and then loaded to failure, as shown diagrammatically in Fig. 3.4. The failure envelope was found to have the bilinear shape F-C-D in Fig. 3.5, with P_{prop} equal to the static dowel strength of the connectors D_{max}. Hence, it was confirmed directly that the static strength of stud connections reduces as soon as cyclic loads are applied. The failure envelope for the crack propagation stage of the failure envelope is given by Eq. 3.4, and thus can be written for stud shear connectors in the form

$$D_c = D_{max}\left(1 - \frac{N_b}{E_a}\right)$$ (3.13)

where D_c is the dowel strength after fatigue loading, D_{max} is the dowel strength prior to fatigue loading, N_b is the number of cycles of load of range R, and E_a is the asymptotic endurance at the same range R.

It is necessary to be able to visualise the mechanism of fatigue failure in order to understand why the failure envelope is linear.

3.4.3.2 *Mechanism of fatigue failure*

Consider the forces on the shear connector in Fig. 2.14(a) that is subjected to a constant range of load R, with a peak load F and a trough load of zero. If we assume that the main cause of fatigue failure is crack propagation in the steel failure zone (Oehlers and Foley 1985) then Paris' equation (Paris 1963) shows that the fatigue crack growth rate, that is the increase in crack per cycle, is proportional to the stress intensity factor. This stress intensity factor is a function of the energy release rate, and will be referred to as G. A simplified way of visualising the problem is that the rate of crack propagation depends on the range of the cyclic stress around the crack tip.

Let us first assume that the connector acts as a cantilever, so that it is not encased in concrete, and that the force F in Fig. 2.14(a) remains at an eccentricity e as shown. Cyclic loading will cause the crack to start at the surface of the dowel and to propagate into the dowel, thereby reducing the uncracked area of the dowel. As the uncracked area reduces, the range of stress at the crack tip will increase, causing an increase in the rate of crack propagation. This is shown as the rapid increase in G in Fig. 3.9 for the 'cantilever' case. The rapid increase in the energy release rate signifies accelerated crack propagation, that suggests a very rapid reduction in strength as soon as significant cracking occurs. This failure mechanism is represented by the failure envelope A-B-C in Fig. 3.1 where $N_{prop} \ll E_e$, and hence does not explain the linear failure envelope that has been determined experimentally.
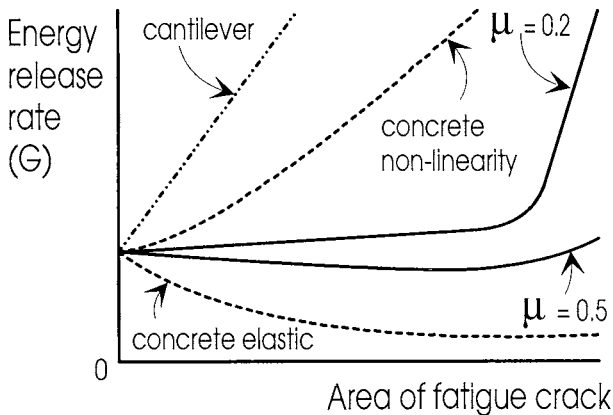

Fig. 3.9 Energy release rate

Now let us assume that the shear connector is acting as a steel beam supported by a concrete medium. This is the same analogy as was used in describing the static strength in Section 2.4.2, and is illustrated in Fig. 2.15. Let us also assume that the concrete remains elastic, and so can resist any stress. It was shown in Section 2.4.2 that propagation of the crack is equivalent to a reduction in dowel stiffness. This will cause the eccentricity e in Fig. 2.15 to reduce and so reduce the flexural stresses at the crack tip, which in turn will reduce G, for the 'concrete elastic' case in Fig. 3.9, with a consequent reduction in the rate of crack propagation. This is an ideal mechanism, but in reality as e reduces, the area of concrete resisting F reduces and so

the compressive stresses in the concrete increase. The peak of the cyclic load F, which is a serviceability load, is usually much less than the dowel strength of the connector D_{max}, which occurs with crushing of the concrete. Therefore the shear connection can accommodate some reduction in e, with its associated increase in the concrete stress before the concrete crushes. It can be seen in Fig. 3.9 that allowance for nonlinearity in the concrete increases G and hence the rate of crack propagation. Friction at the dowel/concrete interface, shown in Fig. 2.14(a), also resists the opening of the crack and hence reduces the cyclic stresses in the crack tip, and thereby reduces G as shown in Fig. 3.9 for a coefficient of friction $\mu = 0.2$ and $\mu = 0.5$.

It can be deduced from Fig. 3.9 that at a given rage of load R, the rate at which the fatigue crack propagates can be assumed to be constant over much of the fatigue life, both because of the friction across the shank/concrete interface and because the maximum stress in the concrete can increase as the crack propagates. Because of this, there is a mechanism of fatigue failure in steel dowels embedded in a concrete medium which allows a gradual reduction in strength, as signified by F-C-G in Fig. 3.5.

3.4.3.3   Asymptotic endurance

The exponents in Eq. 3.12 were derived from a statistical analysis of fatigue data (Oehlers 1990b) using the procedure described in Section 3.3.4. Hence

$$
\left(E_a\right)_{ch} = 10^{\left(3.12 - \frac{0.70}{\sqrt{n}}\right)} \left(\frac{R}{D_{max}}\right)^{-5.1}
\tag{3.14}
$$

The dependence of E_a with the non-dimensional parameter R/D_{max} was found to give a better fit than the dependence with just the range of shear load R, which is used in some national standards (Oehlers 1990b). Equation 3.14 can be used to determine the endurance of stud shear connectors in composite beams by simply substituting the strength of the stud shear connectors in beams $\left(D_{max}\right)_{beam}$ for D_{max}, where $\left(D_{max}\right)_{beam}$ can be derived from Eq. 2.37.

3.4.3.4   Accumulated used-life law

The accumulated used-life law for residual strength based on the procedures used to form Eq. 3.10 can be used for stud shear connectors in the form

$$
\sum_{k=1}^{k=z} \frac{N_k}{\left(E_a\right)_k} \leq 1 - \frac{F_o}{D_{max}}
\tag{3.15}
$$

The left hand side of the equation can be visualised as the area of fatigue cracking as a proportion of the area of the shank, such as the dull zone below the horizontal crack front in Fig. 3.6. The right hand side of the equation can be visualised as the area of fatigue cracking that can occur before fracture. For example, if the peak load F_o is

three-quarters of the dowel strength D_{max}, then the area of the shank that can crack through fatigue is one-quarter. Therefore, fracture will occur when the accumulated used-life is also one quarter.

It is worth bearing in mind that the peak load or an occasional overload does not affect the rate of crack propagation, but does affect the endurance by limiting the amount of fatigue cracking which can occur before the stud fractures.

3.4.3.5 *Endurance based fatigue properties*

Most design procedures assume that the strength of stud shear connectors does not reduce as soon as fatigue loads are applied. Hence, the endurances used in most design procedures are based on the Stage 3 failure envelope shown in Fig. 3.5 that assumes that the strength does not reduce during the design life, but that the strength then reduces very rapidly.

A statistical analysis of two hundred and eighty fatigue push tests (Oehlers 1990b) was used to derive the following endurance equations for stud shear connectors.

$$(E_e)_{ch} = 10^{\left(15.9 - \frac{0.7}{\sqrt{n}}\right)} \left(\frac{R}{A_{sh}}\right)^{-5.1} \tag{3.16}$$

where the units and in N and mm, and

$$(E_e)_{ch} = 10^{\left(2.27 - \frac{0.70}{\sqrt{n}}\right)} \left(\frac{R}{D_{max}}\right)^{-5.4} \tag{3.17}$$

3.5   References

Miner, M.A. (1945). "Cumulative damage in fatigue", Transactions, ASME, Vol. 67, A159-A164.

Murray, K.J. (1988). "The fatigue behaviour of composite bridge beams subjected to a spectrum of highway loading", M.Eng.Sc. Thesis, University College Cork, National University of Ireland.

Oehlers, D.J. (1990a). "Deterioration in strength of stud connectors in composite bridge beams", Journal of Structural Engineering, ASCE, Vol. 116, No. 12, 3417-3431.

Oehlers, D.J. (1990b). "Methods of estimating the fatigue endurances of stud shear connections", Proceedings, IABSE, P-145/90.

Oehlers, D.J. (1992a) "Residual strength of structural components subjected to cyclic loads", Journal of Structural Engineering, ASCE, Vol. 118, No. 10, 2645-2659.

Oehlers, D.J. (1995). "Design and assessment of shear connectors in composite bridge beams", Journal of Structural Engineering, ASCE, Vol. 121, No. 2, 214-224.

Oehlers, D.J. and Carroll, M.A. (1987). "Simulation of composite beams subjected to traffic loads", Proceedings of Engineering Foundation Conference on Composite Construction in Steel and Concrete, ASCE, Henniker, U.S.A, 450-459.

Oehlers, D.J. and Foley, L. (1985). "The fatigue strength of stud shear connectors in composite beams", Proceedings, Institution of Civil Engineers, London, Part 2, Vol. 79, 349-364.

Oehlers, D.J. and Singleton, W.M. (1986). "The simulation of simply supported composite beams tested under fatigue loads", Proceedings, Institution of Civil Engineers, London, Part 2, Vol. 81, 647-657.

Paris, P.C. and Erdogan, F. (1963). "A critical analysis of crack propagation laws", Journal of Basic Engineering, Transactions ASME, Vol. 85, No. 4, 528-539.

Wahab, M., Oehlers, D.J. and Gosh, A. (1993). "Residual strength approach for fatigue design of structural components", Australian Fracture Group Conference, Melbourne.

Walpole, R.E. and Myers, R.H. (1978). *Probability and Statistics for Engineers and Scientists*, McMillan, New York

Warner, R.F. (1985). "Design of concrete structures for fatigue reliability", Bulletin, Disaster Prevention Research Institute, Vol 35, 21-40.

4 Effective Size of Reinforced Concrete Elements

4.1 General

The idealised material properties that are required for the analysis of composite members have been identified and defined in Part 2. Before proceeding to analyse a composite member in the following parts of this book, it is necessary to define the geometric dimensions of the member for use in the ensuing analysis procedures. In the majority of cases, the actual physical dimensions of the member can be used. However, effective or idealised dimensions may have to be used to allow for the variation in slab membrane stress, changes in cross-section, shear lag, as well as local buckling of the steel. The effective size of the reinforced concrete element is dealt with in this chapter. Local buckling of the steel plate elements of the section is dealt with in Chapter 5. These two chapters will allow the design engineer to size the steel and concrete elements, so that an analysis of the composite members may be carried out.

4.2 Effective width

4.2.1 ANALYSIS

The design of a composite beam consisting of steel elements supporting a concrete slab attached by shear connection is simplified greatly by considering an isolated beam having such a width that the behaviour of the associated T-beam closely approximates that for the slab/steel element system. In the analysis of a composite beam, it is assumed that the composite action induces either a linear strain distribution, as shown in Fig. 1.23(b), or a bi-linear strain distribution, as shown in Fig. 1.23(c). It is also assumed that this strain distribution does not vary along the width of the cross-section. For example, at section A-A in Fig. 1.1(a), the strain distribution in the concrete element is assumed to occur over the full width w of the concrete element in (b). This does not occur in practice, owing to nonlinearities somewhat akin to post-local buckling in thin steel plates (Trahair and Bradford 1991) and to in-plane shear lag. Because of this, the stresses at the edges B in Fig. 1.1(c) will be less than those over the steel section at C, and this is illustrated by the curvilinear variation in stress σ_ℓ in (c) that varies from σ_B at the edges to a maximum of σ_C over the steel element.

In conventional bending theory, shear strains are neglected and so the usual engineering assumption for the concrete element in Fig. 1.23 is that plane sections remain plane after loading. Shear lag (Timoshenko and Goodier 1970) relates to some of the discrepancies between this approximate assumption in the theory of the bending of beams and the real behaviour observed in practice.

The phenomenon of shear lag is very important for steel beams with wide flanges, and a detailed explanation is given in Trahair and Bradford (1991). Shear lag is not quite so important for concrete elements in composite beams owing to their reasonable thicknesses h_{conc} when compared with the spacing of the I-section elements T_{adj} in Fig. 4.1, but nevertheless the effects of shear lag should be incorporated in design. It is thus necessary to proportion the concrete element to incorporate the nonlinear effects of shear lag.
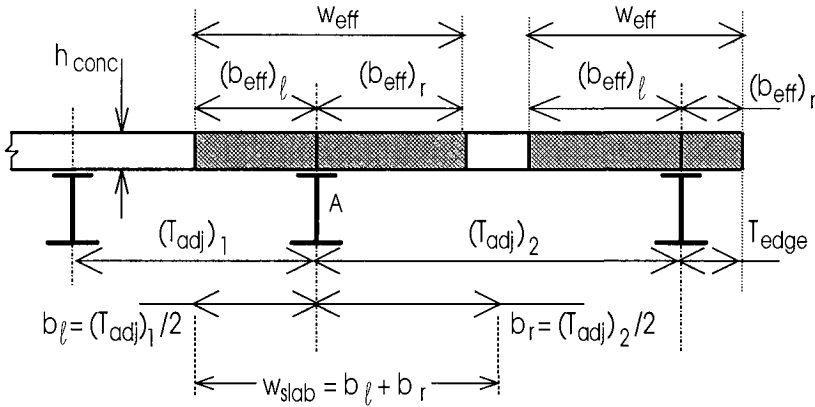
Fig. 4.1 Effective width

The engineer selects the dimensions of the slab in a composite beam using simple T-beam theory based primarily on the engineering assumption that plane sections remain plane after bending, so that $\sigma_B = \sigma_C$ in Fig. 1.1(c). The idealised T-beam consists of the steel element with a certain width of slab referred to as the *effective width* w_{eff} that is stressed uniformly.

Methods to calculate the effective width may proceed by rigorously solving the appropriate elasticity equations using series solutions for the flexural and membrane behaviour of the T-beam, as was done by Allen and Severn (1961), by the method of finite differences as used by Khan and Kemp (1970), or by the much simpler method of finite elements (Ansourian 1975). The results of Ansourian's finite element approach have been used in the following sub-section to quantify the effects of various parameters on the effective width, and to derive the subsequent recommendations for sizing the concrete element. Recommendations are also given in Section 4.2.3 based on the Eurocode 4 (1994).

4.2.2 BEHAVIOUR

4.2.2.1 *Range of parameters*

Ansourian (1975) analysed a large number of composite systems using his finite element method. The ratio T_{adj}/L_c of the distance T_{adj} between the webs of the steel elements in Fig. 4.1 to the span L_c between the points of contraflexure was studied,

and values of this ratio of 0.5, 0.3 and 0.1 were used. Also varied was the ratio γ of the flexural stiffness of the steel element to that of the concrete slab, given by

$$\gamma = \frac{(EI)_s}{D_c(b_\ell + b_r)} \tag{4.1}$$

where the breadths b_ℓ and b_r are defined for the central beam marked A in Fig. 4.1 and where

$$D_c = \frac{E_c h_{conc}^3}{12(1 - v_c^2)} \tag{4.2}$$

in which E_c and v_c are the short-term elastic modulus and Poisson's ratio of the concrete element respectively, h_{conc} is its thickness, and $(EI)_s$ is the flexural rigidity of the steel element. The values of γ were in the range 0.24 to 6.0. The loading considered was either a uniformly distributed load over the entire concrete element, or a line load along the centreline of the steel element, or a concentrated load at the beam midspan. The boundary conditions considered were either simple supports at both longitudinal ends, or built-in at both longitudinal ends.

4.2.2.2 *Definition of effective width*

The effective width may be defined in a number of ways (Brendel 1964, Heins and Fan 1976), but generally to allow for a nonuniform distribution of stress due to shear lag, we assume that the concrete element is narrower such that the rectangular stress block of area $w_{eff}\sigma_C$ in Fig. 1.1(c) is equal to the area under the curvilinear stress block σ_ℓ over the width w. This is equivalent to integrating the rigorously calculated longitudinal stress σ_ℓ in the concrete slab over the width w, and dividing by the peak value of the stress σ_C. Thus

$$w_{eff} = \frac{\int_{b_\ell}^{b_r} \sigma_\ell \, dx}{\sigma_C} \tag{4.3}$$

where the breadths b_ℓ and b_r are half of the transverse spans of the slab on the left and right of the steel element, as shown in Fig. 4.1 and x is the coordinate transverse to the centreline of the steel element

The problem is extremely complex, and even calculations of deflections using the effective width approach and simple bending theory on the idealised T-beam do not necessarily model the behaviour produced by the true stress distribution. The use of the effective width concept is only justified if the design is conservative, so that deflections and stresses derived from linear elastic analysis are greater than the values calculated rigorously. However, it will be seen in Chapter 7 that rigid plastic analyses are not sensitive to errors in the effective width.

4.2.2.3 *Effect of panel dimensions*

Under a given type of loading, Ansourian (1975) established that the parameter T_{adj}/L_c had the greatest influence on the effective width ratio w_{eff}/w_{slab} for continuous T-beams, where $w_{slab} = b_\ell + b_r$ as shown in Fig. 4.1 for steel element A and L_c is the distance between points of contraflexure. Additionally, as the panel became more elongated, that is L_c/w_{slab} increased, it was found that the effective width ratio was seen to increase. This is reflected in the sizing recommendations given in Section 4.2.3.

4.2.2.4 *Effect of stiffness ratio* γ

The effect of the relative stiffness ratio γ in Eq. 4.1 on the effective width ratio w_{eff}/w_{slab} was found to be only minor over the wide range of γ values considered. Ansourian found that the maximum effect occurred under concentrated loading. Furthermore, increasing either the depth of the concrete element or the steel element, whilst keeping the second moment of area of the composite section constant, had negligible effect on the effective width ratio.

4.2.2.5 *Effect of loading conditions*

The finite element parameter study ascertained that the effective width is virtually insensitive as to whether the distributed load exists over the entire concrete slab or over the axis of the steel element. However, the effect of concentrated loading is more marked, and can reduce the effective width w_{eff} by up to 40%.

4.2.3 SIZING FOR EFFECTIVE WIDTH

As has been noted in the previous sub-sections, the determination of the effective width is an extremely complex problem owing to the number of parameters that affect its value. National standards give a variety of guidelines to this complex problem in much the same way as those for reinforced concrete T-beams. For composite beams in buildings, the guidelines are based on the lateral spacing between adjacent composite beams, T_{adj} in Fig. 4.1, the distance to the free edge T_{edge} and the distance between points of contraflexure L_c in Fig. 4.2 or the length L between supports in continuous beams. Typical examples of simplified methods for calculating the effective widths w_{eff} (Ansourian 1975) are given in the following equations. We firstly define the effective width to be

$$w_{eff} = (b_{eff})_\ell + (b_{eff})_r \tag{4.4}$$

where $(b_{eff})_\ell$ is the effective breadth of slab on the left of the steel element and $(b_{eff})_r$ is the effective breadth on the right.
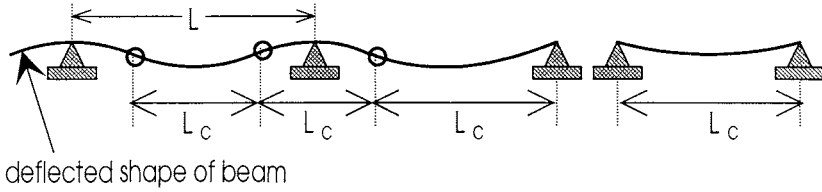
deflected shape of beam

Fig. 4.2 Effective span

For a continuous beam

$$\frac{b_{eff}}{T_{adj}/2} = 1.0 - 1.2\frac{T_{adj}}{L_c} \quad \text{when} \quad \frac{T_{adj}}{L_c} \leq 0.5 \tag{4.5}$$

$$b_{eff} = 0.1L_c \quad \text{when} \quad \frac{T_{adj}}{L_c} > 0.5 \tag{4.6}$$

where b_{eff} and T_{adj} refer to the same side of the steel element, such as $(b_{eff})_\ell$ and $(T_{adj})_1$ for the left side of steel element A in Fig. 4.1, or $(b_{eff})_r$ and $(T_{adj})_2$ for the right hand side of the same steel element. On the other hand, for a simply supported beam,

$$\frac{b_{eff}}{T_{adj}/2} = 1.0 - 0.6\frac{T_{adj}}{L_c} \quad \text{when} \quad \frac{T_{adj}}{L_c} \leq 1.0 \tag{4.7}$$

$$b_{eff} = 0.2L_c \quad \text{when} \quad \frac{T_{adj}}{L_c} > 1.0 \tag{4.8}$$

Note that in the provisions of Eqs. 4.5 to 4.8, the effective width w_{eff} tends to the full width of the slab w_{slab} as the ratio T_{adj}/L_c approaches zero. Of course, the above equations are subject to the geometric limitations

$$b_{eff} \leq \frac{T_{adj}}{2} \tag{4.9}$$

and

$$b_{eff} \leq T_{edge} \tag{4.10}$$

It is worth noting that the Eurocode 4 (1994) simplifies Eqs. 4.5 to 4.8 with the recommendation

$$b_{eff} = 0.125L_c \tag{4.11}$$

where L_c is defined as the maximum distance between points of contraflexure and recommended values are given as in Fig. 4.3. The geometric constraints of Eqs. 4.9 and 4.10 are also assumed to apply. The difference between Eqs. 4.5 to 4.8 and 4.11 is attributable to simplifying a difficult structural problem, and both are considered to be conservative.
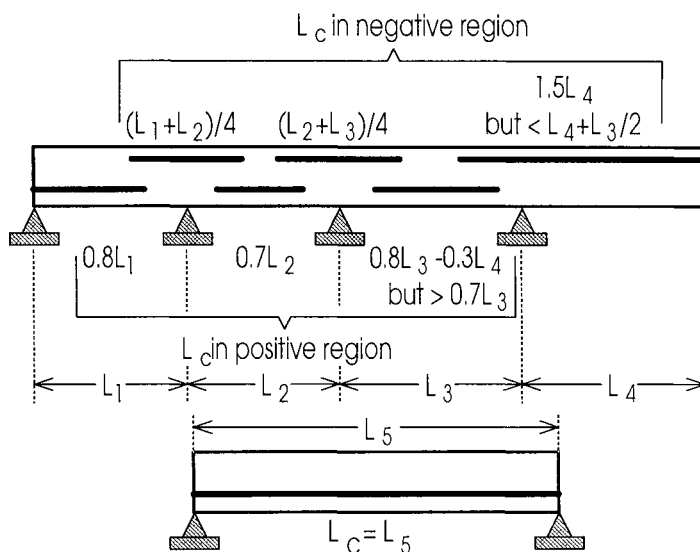

Fig. 4.3 Eurocode 4 approach

Example 4.1 Effective widths

The composite T-beam shown in Fig. 4.1 has $(T_{adj})_1 = (T_{adj})_2 = 1500$ mm and is continuous with a distance between points of contraflexure of $L_c = 5$ m. From Eq. 4.5, $b_{eff}/(1500/2) = 1.0 - 1.2 \times (1500/5000)$, so $b_{eff} = 480$ mm and from Eq. 4.4, $w_{eff} = 2 \times 480 = 960$ mm. This is more conservative than the prediction of $2 \times 0.125 \times 5000 = 1250$ mm of Eq. 4.11. More typically for this spacing T_{adj}, $L_c = 20$ m. From Eq. 4.5, $b_{eff} = 683$ mm so $w_{eff} = 1366$ mm. The Eurocode predicts $b_{eff} = 2500$ mm > 1500 mm, so $b_{eff} = 1500$ mm and the slab is fully effective.

4.3   Effective section of composite element

When a steel element acts compositely with a composite slab as shown in Fig. 1.11(b) and (c), then the cross-sectional shape of the composite slab to be used in the analysis depends on the relative direction of the span of the ribs in the concrete slab to the span of the steel element.

The cross-section of a composite member in which the profile ribs span in the same direction as the composite beam is shown in Fig. 4.4(a), where h_{solid} is the height of the solid part of the concrete element, h_{rib} is the height of the rib, A_{rib} is the area of an individual rib, A_{void} is the area of an individual void between the ribs, and $\theta = 0°$ where θ is the angle, in degrees, between the direction of span of the ribs and that of the composite beam as shown in Fig. 4.5. For simplicity, the cross-section can be analysed as shown in Fig. 4.4(b), where the area of the haunch is equal to the sum of the areas of the individual ribs over the effective width of the section. Therefore, the mean width of the haunch b_{haunch} can be calculated from the section proportions, and is given by

$$(b_{haunch})_{\theta=0} = \frac{A_{rib}}{A_{void} + A_{rib}}(b_1 + b_2) \tag{4.12}$$

where the dimensions b_1 and b_2 are shown in Fig. 4.3. Unless the haunch is very deep, it can be assumed to have vertical sides instead of the sloping sides shown.
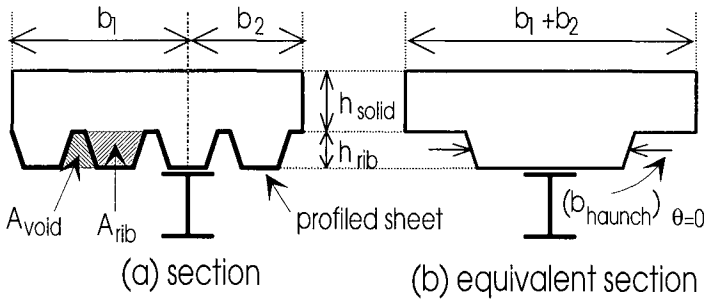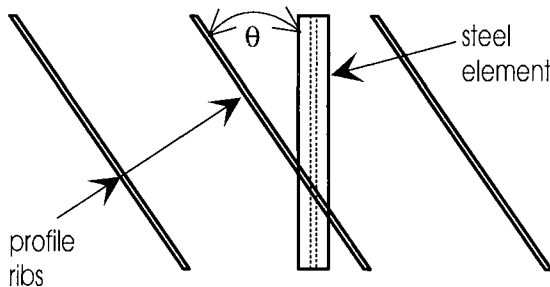

Fig. 4.4 Longitudinal ribs

Fig. 4.5 Oblique ribs

The cross-section of a composite member in which the ribs are transverse to the direction of span of the composite beam, that is $\theta = 90°$ in Fig. 4.5, is shown in Fig. 4.6. As is normal design practice, the weakest cross-section is used in the

analysis, and this occurs at a section through a void between the ribs. Hence $(b_{haunch})_{\theta=90} = 0$ when $\theta = 90^{\circ}$.
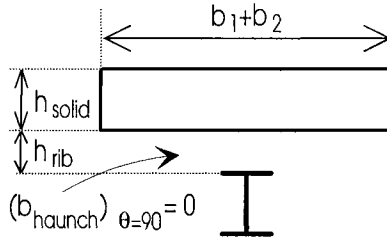

Fig. 4.6 Transverse ribs

When the rib is oblique to the span of the beam, as shown in Fig. 4.5, then the effective cross-sectional shape lies between that shown in Fig. 4.4(b) and that shown in Fig. 4.6. Hence, the width of the effective haunch lies between zero and $(b_{haunch})_{\theta=0}$. Any reasonable variation between these two extreme values can be used in design, because in general the area of the haunch has only a minor effect on the strength of the member. For example, when the neutral axis in the concrete element lies within the solid region of the slab, h_{solid} in both Figs. 4.4 (b) and 4.6, then the area of the flange does not contribute to the strength. Moreover, even if the neutral axis lies within the haunch, the difference in flexural strength using different values of haunch width will only be small, because the haunch lies close to the centroid of the section. It may be assumed that the width of the haunch varies linearly with θ or $\cos\theta$ or $\cos^2\theta$, with the latter recommendation being given in the Eurocode. If it is to assumed that the width varies linearly with θ, then the effective width is given by

$$(b_{haunch})_{\theta} = (b_{haunch})_{\theta=0} \left(\frac{\theta^{o}}{90} \right) \tag{4.13}$$

It is also worth noting at this stage that the strength of the mechanical shear connectors that are used to tie the concrete element to the steel element can also vary with θ, and this variation is dealt with in Chapter 11.

4.4   References

Allern, D.N. de G. and Severn, R.T. (1961). "Composite action between beams and slabs under transverse load", The Structural Engineer, Vol. 39, 149-154.

Ansourian, P. (1975). "An application of the method of finite elements to the analysis of composite floor systems", Proceedings of the Institution of Civil Engineers, London, Part 2, Vol. 59, 699-726.

Brendel, G. (1964). "Strength of the compression slab of T-beams subject to simple bending", ACI Journal, Vol. 61, No. 1.

Eurocode 4 (1994). *Part 1: Design of Composite Steel and Concrete Structures.* DDENV 1994 -1-1: 1994. Draft for development.

Heins, C.P. and Fan, H.H. (1976). "Effective composite beam width at ultimate load", Journal of the Structural Division, ASCE, Vol. 102, No. ST11, 2163-2179.

Khan, M.A. and Kemp, K.O. (1970). "Elastic full composite action in a slab and beam system", The Structural Engineer, Vol. 48, No. 9, 353-359.

Timoshenko, S.P. and Goodier, J.N. (1970). *Theory of Elasticity*, 3rd edn., McGraw Hill, New York.

Trahair, N.S. and Bradford, M.A. (1991). *The Behaviour and Design of Steel Structures*, revised 2nd edn., Chapman and Hall, London.

5 Local Buckling of Steel Elements

5.1 Introduction

The phenomenon of *local buckling* was introduced in Section 1.2.3.3. Basically, it occurs when thin steel elements are compressed in their planes, and the elements find a more stable equilibrium position by buckling or distorting out of their planes, as shown in Fig. 1.17. When this occurs, the buckles "ripple" over a short buckling half-wavelength of the order of the width of the plate element, which is either the flange width or the web depth. When local buckling occurs, the line junctions between the intersecting plates, such as the junction of the bottom compressive flange and web in Fig. 1.17, remain straight. The localised distortions of the plate elements, coupled with the line junctions remaining straight, characterise local buckling.

Local buckling is important in thin steel members, and particularly in cold formed steel members such as purlins and girts in industrial buildings, and wall studs in modern domestic construction. Because steel components are used in a composite member, it is instructive to firstly look at local buckling in steel web and flange elements, as most of the research into local buckling has focussed on these members. Steel members are considered firstly, followed by their extension to the components of composite members.

Unlike lateral-torsional buckling or the lateral-distortional buckling covered in Chapter 10 that requires the limitation of moments or axial loads below a level which causes failure, local buckling is usually designed against by limiting the geometric dimensions of the steel component. Steel elements such as flange outstands and webs in compression are likely to buckle locally when they are slender, that is when their width to thickness ratio is large. Local buckling can be eliminated by placing restrictions on the width to thickness ratio, and thus it is considered here in the Geometric Dimensions part of this book.

5.2 Steel web and flange members

5.2.1 THEORETICAL ANALYSIS OF PLATE ELEMENTS

The local buckling of thin steel flanges and webs can be illustrated by considering the flat rectangular plate shown in Fig. 5.1, which is simply supported along all four sides and subjected to uniform membrane compression. Initially, the plate is loaded by the uniform compressive stress σ and it remains flat. However, when the stress reaches its critical value σ_{cr} a more favourable equilibrium position is for the plate to buckle with a deformation u in the x-direction out of its plane.
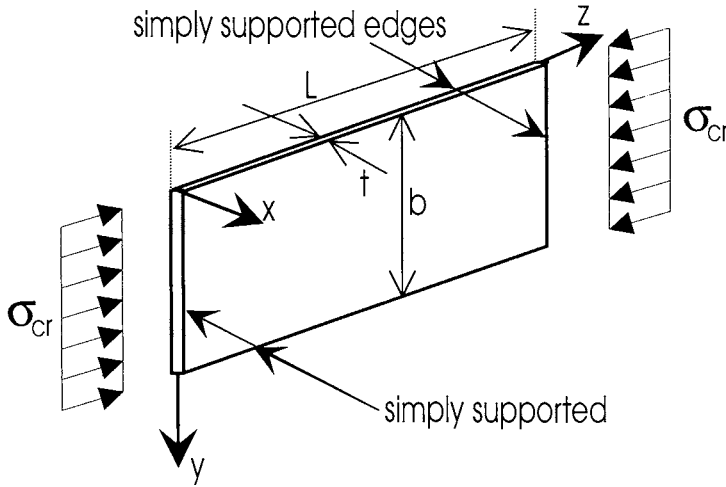
Fig. 5.1 Rectangular simply supported plate in uniform compression

It is shown in Trahair and Bradford (1991) that this buckled equilibrium position is given by the general equation

$$u = \delta \sin\frac{m\pi y}{b} \sin\frac{n\pi z}{L} \tag{5.1}$$

where n and m are the number of half-wavelengths in the longitudinal and transverse directions respectively into which the plate buckles (where m = 1 for the case of one transverse buckle), and δ is the magnitude of the central deflection. All critical buckling problems, such as the local buckling in this chapter, are really forms of eigenvalue problems. The critical stress σ_{cr} at which the plate buckles represents the eigenvalue, while the right hand side of Eq. 5.1 represents the eigenvector or buckled shape. The elastic local buckling stress σ_{cr} is of paramount importance in proportioning steel elements. Of course, the magnitude of the eigenvector in eigenvalue problems cannot be determined explicitly, and so δ represents the undetermined magnitude of the central deflection.

When the deflected shape u in Eq. 5.1 is substituted into the appropriate differential equation for buckling of a rectangular plate (Timoshenko and Woinowsky-Krieger 1959), the elastic critical or local buckling stress σ_{cr} can be expressed in the form

$$\sigma_{cr} = k\frac{\pi^2 E_s}{12(1-\nu_s^2)}\frac{1}{(b/t)^2} \tag{5.2}$$

in which E_s is the Young's modulus of the steel, ν_s is the Poisson's ratio of the steel, t is the plate thickness, b is the width of the plate transverse to the applied stress as

shown in Fig. 5.1, and k is the so-called *local buckling coefficient.* For the rectangular plate shown in Fig. 5.1, k may be written as (Trahair and Bradford 1991)

$$k = 2 + \left(\frac{nb}{L}\right)^2 + \left(\frac{L}{nb}\right)^2 \tag{5.3}$$

when m = 1, that is, when there is one transverse buckle. The variation of the local buckling coefficient k with the plate aspect ratio L/b, for integral values of n in Eq. 5.3, is shown in Fig. 5.2. It can be seen that the lowest value of the local buckling coefficient is

$$k = 4 \tag{5.4}$$

and this is the value usually quoted in design.
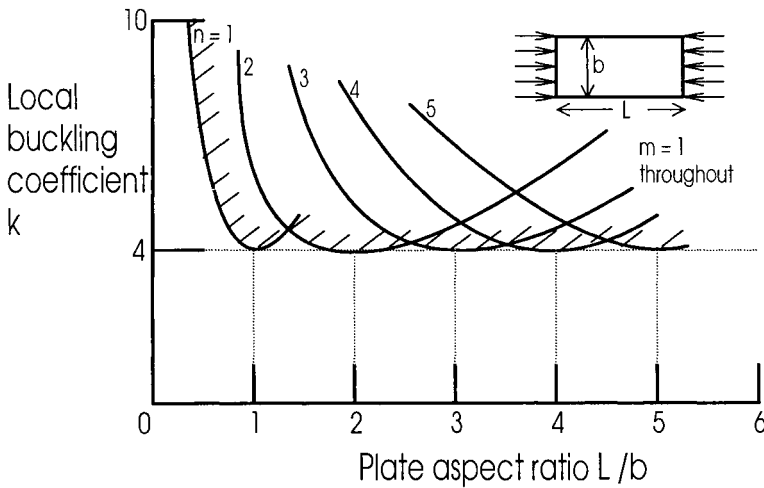
Fig. 5.2 Variation of k for a simply supported plate in uniform compression

The plate in Fig. 5.1 is typical of an idealised flange element in a steel box girder or box-section column which is supported along its unloaded longitudinal edges and loaded at the ends. Equation 5.2 is, however, quite general, and can be applied to other elements with different loading and restraint cases as well. Consider, for example, the flange outstand of width b which is loaded in uniform compression and has one edge simply supported and the other edge free, as shown in Fig. 5.3. The critical stress σ_{cr} is still given by Eq. 5.2, but the value of k is closely approximated by

$$k = 0.425 + \left(\frac{b}{L}\right)^2 \tag{5.5}$$

so that for long plates, k = 0.425. Another example is the web plate shown in Fig. 5.4, which is loaded in uniform bending (that is, with the neutral axis at mid-depth) but with its unloaded edges simply supported. Again, the local buckling stress σ_{cr} can be obtained from Eq. 5.2 with b replaced by the depth of the web d, for which it can be shown that the minimum value of the local buckling coefficient is
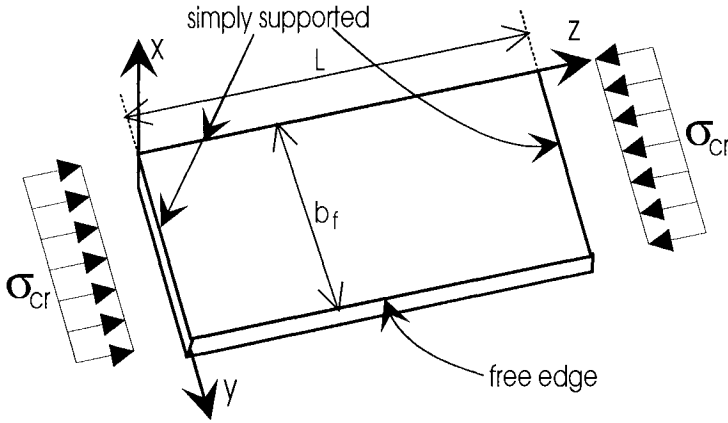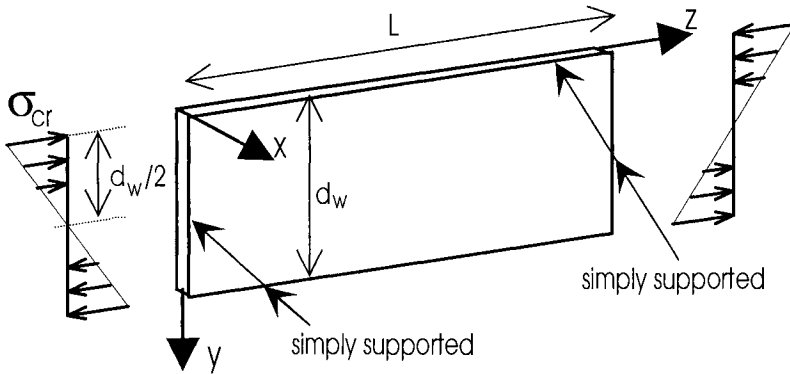
$$k \quad = \quad 23.9 \qquad\qquad (5.6)$$

Fig. 5.3 Flange outstand

Fig. 5.4 Web plate in uniform bending

Web plates usually have to resist shear if a moment gradient exists. Such a plate is illustrated in Fig. 5.5, and the critical shear stress τ_{cr} may be obtained similarly to Eq. 5.2 from

$$\tau_{cr} \quad = \quad k\frac{\pi^2 E_s}{12(1-v_s^2)(d/t)^2} \qquad\qquad (5.7)$$

The local buckling coefficient k in Eq. 5.7 is given to close accuracy by

$$k = 5.35 + 4\left(\frac{d}{L}\right)^2 \qquad (5.8)$$

when L > d, and by

$$k = 5.35\left(\frac{d}{L}\right)^2 + 4 \qquad (5.9)$$

when L ≤ d. Hence for a long web plate in shear, the value of the local buckling coefficient may be taken as

$$k = 5.35 \qquad (5.10)$$

If bending and shear stresses co-exist, which is the usual case for a web plate subjected to bending, then it has been shown (Bradford and Azhari 1992) that a close buckling interaction equation is

$$\left(\frac{\tau_{cr}}{\tau_{cro}}\right)^2 + \left(\frac{\sigma_{cr}}{\sigma_{cro}}\right)^2 = 1 \qquad (5.11)$$

where τ_{cr} and σ_{cr} are the combination of the shear and flexural stresses respectively to cause buckling, while τ_{cro} is the value of τ_{cr} in the absence of bending, and σ_{cro} is the value of σ_{cr} in the absence of shear.
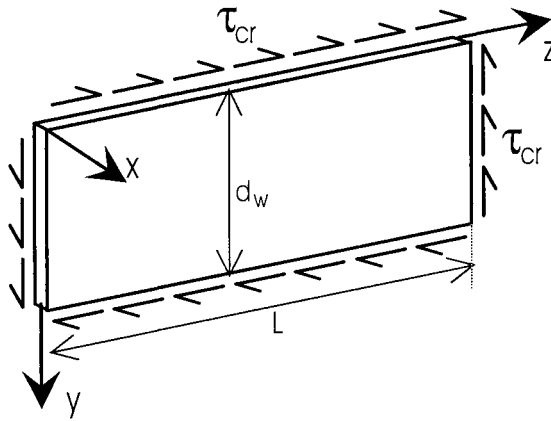

Fig. 5.5 Web plate in shear

5.2.2 POST-LOCAL BUCKLING OF STEEL PLATE ELEMENTS

For a thin elastic plate, the linear elastic assumptions from which Eq. 5.2 was derived lead to an underestimate of the plate's actual strength. Because of this, a thin elastic plate does not fail soon after it buckles, but can support stresses much larger than the critical stress σ_{cr} without deflecting excessively. This postbuckling reserve of strength in a plate structure may be substantial, and is utilised in design. Note that an Euler strut which undergoes flexural buckling, or a beam member which undergoes flexural-torsional buckling, possess negligible postbuckling strength reserve, unless the buckling deformations are excessive.

Figure 5.6 illustrates the elastic behaviour of a flat plate, and a geometric imperfect plate which has a small initial sinusoidal out-of-flatness of maximum magnitude δ_0 It can be seen from the figure that the perfectly flat plate does not deflect at stresses below the critical stress σ_{cr}, but the out-of-plane displacements increase rapidly when the applied stress exceeds σ_{cr}. On the other hand, an imperfect plate does not possess a critical point (σ_{cr}), but displaces out-of-plane in a smooth fashion from the outset of loading. When the applied stress is significantly large, the effect of the initial imperfection reduces, and the imperfect plate becomes close to a perfect plate. The nonlinear behaviour increases until the onset of plastification or yielding, when the postbuckling reserve of the plate is all but exhausted.
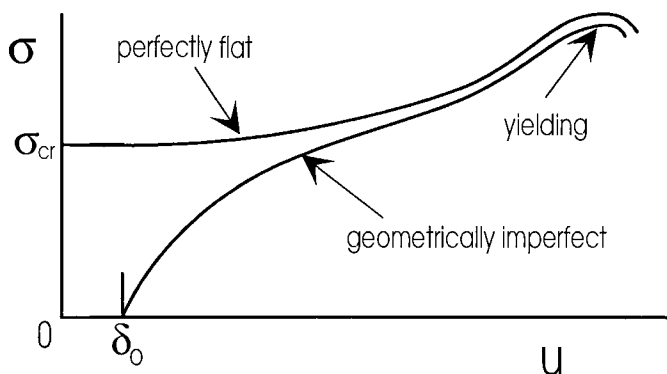

Fig. 5.6 Postbuckling deformations of elastic plates

The main reason for the postbuckling behaviour of a flat plate is that its deflected configuration cannot be developed from its prebuckled configuration without some redistribution of the in-plane stresses within the plate. This redistribution is ignored in the linear eigenvalue theory upon which Eq. 5.2 is based. The stress redistribution favours the less stiff portions of the plate, which is in the region near its centreline, with the redistribution causing larger stresses to develop along the stiffer supported edges.

The analytical modelling of postbuckling is very difficult, and for design purposes recourse is usually made to an effective width concept, which is in some

ways analogous to the effective widths treated in Chapter 4 which were based on shear lag. For this, the stress distribution at failure in Fig. 5.7(a) in which yielding occurs at the position of maximum stress is replaced by a simplified distribution, as in (b), for which the central portion of the plate is ignored and the remaining effective width b_e carries the yield stress f_y. Von Karman (1910) proposed that the effective width be could be calculated from

$$b_e = \frac{b}{\lambda_e} \tag{5.12}$$

in which

$$\lambda_e = \sqrt{\frac{\sigma_{max}}{\sigma_{cr}}} \tag{5.13}$$

where σ_{cr} is the elastic critical stress and $\sigma_{max} = f_y$ at ultimate load.

(a)
Stress distribution at failure
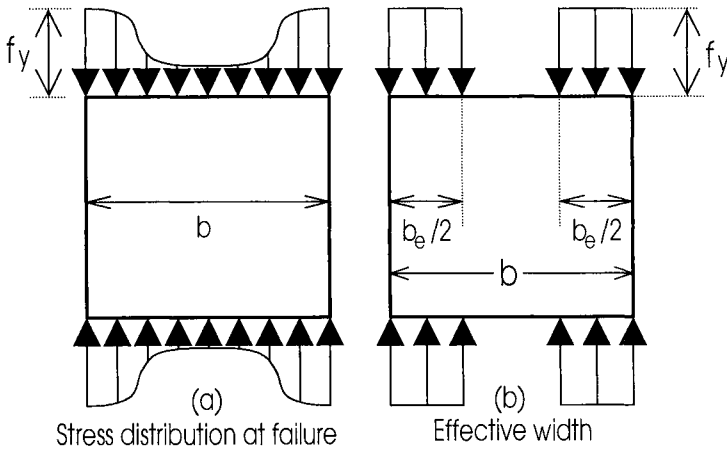
(b)
Effective width

Fig. 5.7 Effective width concept

The proposal of Eqs. 5.12 and 5.13 is equivalent to assuming that the ultimate load carrying capacity of the plate $b_e t f_y$ is equal to the elastic buckling load of a plate of width b_e. Another way of looking at this is to suppose that the average ultimate stress σ_{ult} acts over the full width b of the plate. Hence, Eqs. 5.12 and 5.13 can be written as

$$\sigma_{ult} = \frac{f_y}{\sqrt{f_y / \sigma_{cr}}} \tag{5.14}$$

Experiments on real plates which contain initial imperfections and residual stresses (Section 2.2) have confirmed the qualitative validity of the effective width

approach. By comparing a sophisticated numerical model of postbuckling with test results undertaken at Cambridge University, Bradford (1985) proposed that the effective width ratio b_e/b for hot-rolled and welded steel plates should be obtained from

$$\frac{b_e}{b} = \frac{\alpha}{\sqrt{f_y / \sigma_{cr}}} \tag{5.15}$$

where the coefficient α obtained from tests, reflects the influence of initial curvatures and residual stresses. For a perfectly flat plate free from residual stresses, $\alpha = 1$ in Eq. 5.15, and then this equation reduces to Eq. 5.14. Values for α for a number of realistic cases have been given by Bradford *et al.* (1987). The section classifications, as given in Section 5.2.4 following, deploy these values of α to account for geometric imperfections and inelasticity caused by residual stresses. Thus Eq. 5.15 is a semi-empirical prediction which may be used to convert the elastic buckling stress σ_{cr} into a buckling *strength*, in much the same way as the Perry curve for columns described in Section 1.3.4.2.

5.2.3   LOCAL BUCKLING OF PLATE ASSEMBLIES

Rarely is a steel structural member composed of one plate element. Instead, either hot-rolled shapes or members built-up by welding are formed when a number of plate elements are attached along one or more of their longitudinal edges. The most common examples are welded or hot-rolled I-sections, or welded box sections.

The local buckling analysis in the previous section was germane to isolated plates with idealised boundary conditions. When a plate assembly such as an I-section beam buckles locally, there is an interaction between the local buckling of the compression flange and the compressive portion of the web. The restraint of the flange on the web and vice versa must therefore be taken into account if an accurate buckling stress is to be obtained.

Such a study usually involves a computer analysis, and fortunately the results of these are now appearing in the literature in a useable form. For example, Fig. 5.8 shows the local buckling coefficient k for an I-section in pure bending, incorporating the interaction between the flanges and web, which was obtained by Hancock, Bradford and Trahair (1980). However, most design is usually still carried out on the basis that the edge to which the component plate is attached is simply supported, but it is shown in Section 5.3 how the results of recent research may be used to account for the interaction of intersecting plates in the local buckling of composite members.

5.2.4   SECTION CLASSIFICATIONS

5.2.4.1 *General*

As was mentioned previously, local buckling is designed against by proportioning the cross-section in such a way that the desired limit state such as full plastification or first yielding occurs before the onset of local buckling. The types of cross-section

which correspond to the various limit states are called *plastic, compact, semi-compact* and *slender.*
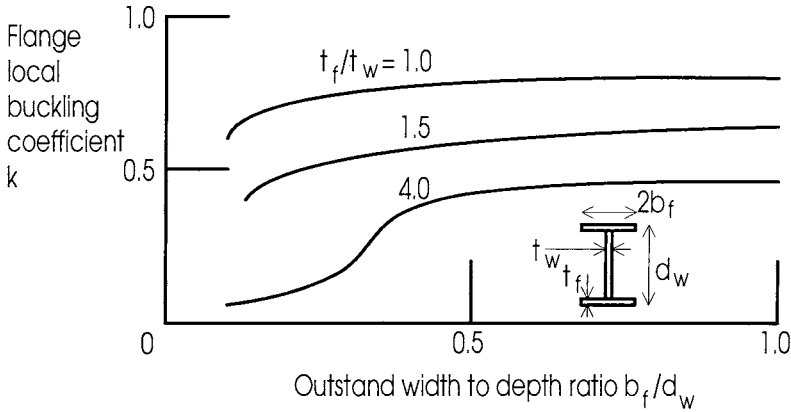

Fig. 5.8 Local buckling coefficient of I-beam

The rationale behind limiting the width to thickness ratio may be illustrated if we set the elastic local buckling stress σ_{cr} in Eq. 5.2 equal to the steel's yield stress f_y. The right hand side of Eq. 5.2 must be multiplied by a coefficient α less than unity (similar to that of Eq. 5.15) to account for residual stresses which affect the local buckling. By using $E_s = 200 \times 10^3$ N/mm^2 and $v_s = 0.3$ as the values typically adopted for structural steel (Section 2.2), then rearranging Eq. 5.2 produces

$$\frac{b}{t} = \frac{425.2}{\sqrt{f_y}}\sqrt{k\alpha} \qquad (5.16)$$

where k is the appropriate local buckling coefficient, and α is the empirically derived material imperfection coefficient.

5.2.4.2 *Plastic sections*

Plastic cross-sections allow a plastic hinge to develop. They also allow sufficient plastic rotation to occur and permit a plastic mechanism to form with the bending moments redistributing (Neal 1977), before the onset of local buckling. Thus, the width to thickness ratios must be limited to allow the plate structure to strain harden while permitting a redistribution of moments within the structure, without premature local buckling taking place. Hence by using the appropriate local buckling coefficient k in Eq. 5.16 for the type of plate, and the value of α that allows strain hardening to occur before buckling, the b/t limits may be found. For example, the b/t ratio for a flange outstand in a welded plastic section must be less than $124/\sqrt{f_y}$ while for a rolled section it should be less than $141/\sqrt{f_y}$, where f_y is in N/mm^2.

Correspondingly, the d/t ratio for a web in pure bending should be limited to $1310/\sqrt{f_y}$ where again f_y is expressed in N/mm^2.

5.2.4.3 *Compact sections*

Compact sections are similar to plastic sections, except that the requirement of the formation of a plastic mechanism is relaxed. Hence for a compact section, the full plastic moment M_P must be reached before local buckling. For a welded outstand, this limits its b/t ratio to $141/\sqrt{f_y}$ and for an outstand in a rolled section to $158/\sqrt{f_y}$, while the d/t ratio in a web in uniform bending is limited to $1550/\sqrt{f_y}$. These limits are, of course, more liberal than those for a plastic section.

5.2.4.4 *Semi-compact sections*

Semi-compact sections must be able to reach the yield moment M_y before local buckling, but will buckle locally before the full plastic moment M_P is attained. The semi-compact b/t limit for a welded outstand is $216/\sqrt{f_y}$, for the outstand of a hot-rolled section it is $249/\sqrt{f_y}$, and the d/t limit for a web in uniform bending is $1990/\sqrt{f_y}$. For b/t or d/t ratios between the previous semi-compact and compact section limits, it is suggested (Bradford *et al.* 1987) that linear interpolation be used between M_y and M_P, based on the relevant limits and the b/t or d/t ratio.

5.2.4.5 *Slender sections*

Slender sections buckle locally before the moment to cause first yield, M_y, is reached. They are best designed on the basis of the effective widths of their component plate elements, since they fail in the postbuckling range of structural response. The effective widths for an I-section in bending and a box section in bending are shown in Fig. 5.9. The effective widths b_e are obtained from the appropriate semi-compact limits, and regions of the plate element away from the supported edges are ignored in calculating the section strength as shown. Note that if the section is slender and subject to bending, then generally the effective cross-section will be monosymmetric.

5.3   Composite members

5.3.1   GENERAL

As was mentioned in Section 1.2.3, the steel elements which are a part of a composite member may buckle locally. The most important types of local instability occurring in composite members are the buckling of the bottom flange and web of a composite T-beam in negative bending, the buckling of the top flange of an I-section component of a composite T-beam in positive bending, and the buckling of the steel skin of a concrete-filled steel tubular column.
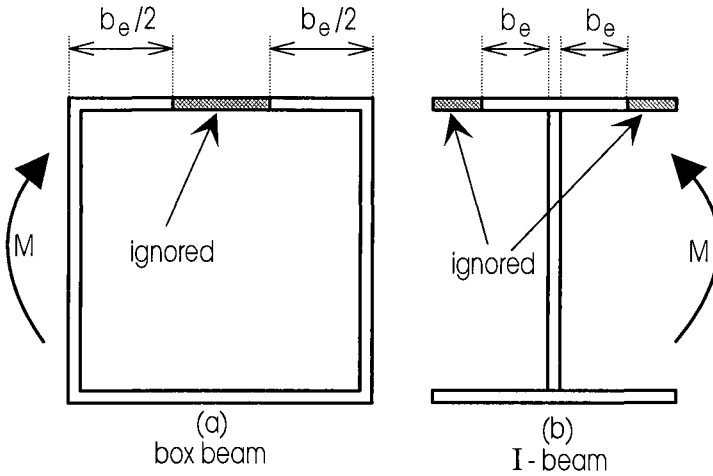
Fig. 5.9 Effective sections

The buckling behaviour may be treated in the same way as that for steel members, with local buckling being eliminated by placing geometric limits on the dimensions of the plate components. The main difference is that the restraint provided by the concrete component may delay the onset of local buckling owing to its retraining action, while in composite beams the presence of the concrete places the steel component in axial compression as well as bending, so that the neutral axis no longer lies at the steel web mid-depth.

5.3.2 BEAMS IN NEGATIVE BENDING

5.3.2.1 *Local buckling behaviour*

When an I-section such as that in Fig. 1.8(a), or a box section such as that in (g) are loaded in negative bending, the bottom flange and the lower portion of the web or webs are subjected to compression, and may buckle locally. Generally, a rule similar to that of Eq. 5.16 may be adopted to limit the flange width or web depth. Usual design practice is to use the appropriate value of the local buckling coefficient k for simple supports, but it is suggested in this book that the results of a rational local buckling analysis can be used to obtain a more accurate value of k that incorporates the interaction between flange and web local buckling.

The elastic local buckling of composite sections has been considered by Azhari and Bradford (1993a), and design recommendations have been made. This study was based on the now well-cited finite strip method of analysis (see Chapter 10), and incorporates the interaction between buckling of the flange and web. Also considered therein was the effect of placing a longitudinal stiffener on the web in its compressive zone, as shown in Fig. 5.10, as it was established that the local buckling coefficient may be enhanced significantly. The values in this study may be used to determine a rational value of the local buckling coefficient k.
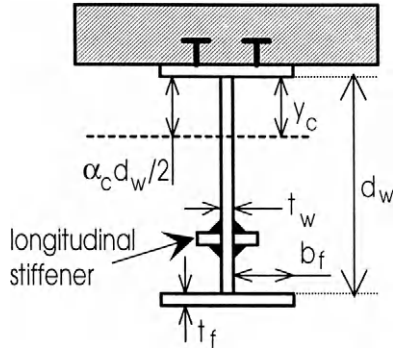
Fig. 5.10 T-beam in negative bending

5.3.2.2 *Plastic sections*

Plastic composite sections are used in continuous bridge girders where a plastic mechanism must be developed that has sufficient rotation capacity for a redistribution of moments to occur (Chapter 9). For an outstand, such as b_f in Fig. 5.10 built-up by welding, this will occur when

$$\frac{b_f}{t_f} \leq \frac{124}{\sqrt{f_y}} \sqrt{\frac{k}{0.425}} \tag{5.17}$$

or for a hot-rolled outstand when

$$\frac{b_f}{t_f} \leq \frac{141}{\sqrt{f_y}} \sqrt{\frac{k}{0.425}} \tag{5.18}$$

where k is the rationally determined local buckling coefficient as given in chart form by Azhari and Bradford (1993b), t_f is the thickness of the outstand, and f_y is expressed in N/mm^2. If the section is to proportioned in a simple way without using the enhanced limits in Eqs. 5.17 and 5.18, then k should be taken as 0.425 (Eq. 5.5) in lieu of the more accurate rational buckling analysis.

The corresponding flange limits for a supported flange, such as that in a rectangular box section where the bottom flange is subjected to compression, are

$$\frac{b_f}{t_f} \leq \frac{381}{\sqrt{f_y}} \sqrt{\frac{k}{4}} \tag{5.19}$$

for a flange built-up by welding, and

$$\frac{b_f}{t_f} \leq \frac{431}{\sqrt{f_y}}\sqrt{\frac{k}{4}} \tag{5.20}$$

for a hot-rolled flange as would occur in a rolled box profile. As a lower bound, a value of k = 4 can be used in lieu of a rational calculation of the local buckling coefficient in Eqs. 5.19 and 5.20.

The limits placed on the web depth depend on the amount of the web in compression. By denoting α_c as the plastic neutral axis parameter in Fig. 5.10, so that

$$\alpha_c = \frac{y_c}{d_w/2} \tag{5.21}$$

where y_c is the distance from the plastic neutral axis to the edge of the web connected to the compression flange, then it is suggested that d_w/t_w be limited to

$$\frac{d_w}{t_w} \leq \frac{1310}{(0.4+0.6\alpha_c)\sqrt{f_y}}\sqrt{\frac{k}{23.9}} \tag{5.22}$$

If the web local buckling cannot be determined accurately then it is suggested that k in Eq. 5.22 be taken as 23.9 (Eq. 5.6).

5.3.2.3 *Compact sections*

Compact composite sections permit a plastic hinge to form in the composite section, but the steel component will buckle locally before a plastic mechanism can develop. The b_f/t_f counterparts to Eqs. 5.17 and 5.18 are then

$$\frac{b_f}{t_f} \leq \frac{136}{\sqrt{f_y}}\sqrt{\frac{k}{0.425}} \tag{5.23}$$

for an outstand built-up by welding, and

$$\frac{b_f}{t_f} \leq \frac{158}{\sqrt{f_y}}\sqrt{\frac{k}{0.425}} \tag{5.24}$$

for a hot-rolled outstand. Similarly, the counterparts to Eqs. 5.19 and 5.20 for a welded supported flange plate are

$$\frac{b_f}{t_f} \leq \frac{415}{\sqrt{f_y}}\sqrt{\frac{k}{4}} \tag{5.25}$$

while

$$\frac{b_f}{t_f} \leq \frac{531}{\sqrt{f_y}} \sqrt{\frac{k}{4}} \tag{5.26}$$

for a rolled supported plate. Again if a rational buckling analysis is not performed, k should be taken as 0.425 in Eqs. 5.23 and 5.24, and as 4.0 in Eqs. 5.25 and 5.26.

The suggested web limit d_w/t_w corresponding to the plastic neutral axis parameter α_c in Eq. 5.21 and Fig. 5.10 is

$$\frac{d_w}{t_w} \leq \frac{1625}{\alpha_c \sqrt{f_y}} \sqrt{\frac{k}{23.9}} \tag{5.27}$$

where, as before, the web local buckling coefficient k is taken as 23.5 if a rational buckling analysis is not undertaken.

5.3.2.4 *Semi-compact sections*

Semi-compact composite sections allow the moment at first yield of the composite section M_y to develop before local buckling of the steel. However, they buckle locally before the section's plastic moment M_P is reached. Appropriate b_f/t_f limits suggested for the semi-compact classification for composite sections are

$$\frac{b_f}{t_f} \leq \frac{216}{\sqrt{f_y}} \sqrt{\frac{k}{0.425}} \tag{5.28}$$

for a welded flange outstand, and

$$\frac{b_f}{t_f} \leq \frac{249}{\sqrt{f_y}} \sqrt{\frac{k}{0.425}} \tag{5.29}$$

for a hot-rolled outstand. For a welded supported flange plate, the width to thickness ratio b_f/t_f should be limited to

$$\frac{b_f}{t_f} \leq \frac{464}{\sqrt{f_y}} \sqrt{\frac{k}{4}} \tag{5.30}$$

while it is

$$\frac{b_f}{t_f} \leq \frac{647}{\sqrt{f_y}} \sqrt{\frac{k}{4}} \tag{5.31}$$

for a supported flange in a rolled section. The web depth to thickness ratio d_w/t_w should be limited to

$$\frac{d_w}{t_w} \leq \frac{1818}{\alpha_c \sqrt{f_y}} \sqrt{\frac{k}{23.9}} \qquad\qquad (5.32)$$

In the absence of direct evidence, it is suggested that the elastic neutral axis parameter α_c given by Eq. 5.21, but calculated using transformed area theory for the steel and concrete (Hall 1984), be incorporated into the above Eq. 5.32. As before, in lieu of a rational buckling analysis that is used to determine exact values of the local buckling coefficients, k should be taken as 0.425 in Eqs. 5.28 and 5.29, as 4.0 in Eqs. 5.30 and 5.31, and as 23.9 in Eq. 5.32.

If the b_f/t_f or d_w/t_w limits lie between the above provisions for a semi-compact section and those of Eqs. 5.23 to 5.27 for a compact section, then linear interpolation can be used to obtain the section bending capacity between M_y and M_P. Thus for a given moment which is between M_y and M_P, an iterative procedure must be used to obtain the limiting b_f/t_f or d_w/t_w ratio. It is also suggested in this linear interpolation procedure that the appropriate elastic value of α_c be used for the web slenderness calculation.

5.3.2.5 *Slender sections*

Slender composite sections most often occur in deep T-section bridge girders in which the web may buckle locally before the first yield moment is reached, or in slender box sections where the flange and/or web may also buckle locally before M_y is attained. These sections should be treated in a similar way to the steel members discussed in Section 5.2.4.5, in which an effective width concept is deployed for the steel based on the semi-compact limits. Because the sections are elastic, their bending capacities are most conveniently calculated using transformed area theory (Hall 1984) described in Chapter 6.

5.3.3   BEAMS IN POSITIVE BENDING

Composite sections under positive bending may have the region adjacent to the concrete portion subjected to compression. The flanges of such sections may only buckle locally in one direction, as in Fig. 5.11, since the concrete restrains the steel. This behaviour has been investigated by Uy and Bradford (1994a) for profiled composite beam construction in Chapter 17, but research into the local buckling behaviour of compressive flanges connected by stud shear connectors to the slab is not extensive. It is suggested, though, that the longitudinal spacing of the shear connectors in the direction of the compression, s in Fig. 5.11, should not exceed

$$\frac{452t_f}{\sqrt{f_y}}$$

where t_f is the top flange thickness. The above limit on s is based on limited test results, and has been adopted in design codes. Further research is necessary to establish its validity, or to present an alternative proposal.
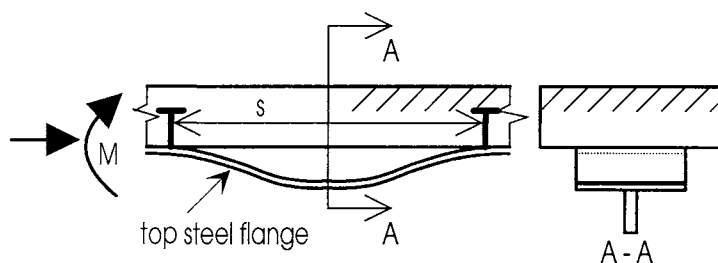

Fig. 5.11 Buckling of top flange in positive bending

Because the web is restrained at its top by the attachment of the compression flange to the concrete, and is restrained at its bottom by the tensile stresses under positive bending, it is much less prone to local buckling than is a web subjected to negative bending. Nevertheless, it is usual to conservatively proportion the web on the limits for negative bending. Depending on the section classification, the provisions of Eqs. 5.22 and 5.27 should thus be used to select the limiting value of d_w/t_w. Of course, if a rational elastic local buckling analysis which incorporates the top and bottom restraining actions on the web is used to obtain the accurate buckling coefficient k, then the provisions for a web in negative bending using this value of k will be quite accurate.

5.3.4 CONCRETE-FILLED STEEL TUBES

Concrete-filled rectangular or circular tubes are almost invariably used as compression members. The section classifications for compression members are only slender or semi-compact, since the yield and plastic moments are irrelevant in the absence of bending. Semi-compact composite sections allow the yield stress to be attained in the steel tube before the onset of local buckling, while slender sections buckle locally at a reduced stress before f_y is attained.

Unlike hollow steel rectangular sections, local buckling of concrete-filled steel tubes is retarded by the concrete core. Because of this, the buckling mode is of the form shown in Fig. 5.12 for a rectangular section, in which the steel may only buckle away from the concrete. The case of a plate with two clamped unloaded sides, such as an element of the steel in a concrete-filled rectangular tube, was first considered by Timoshenko and Gere (1961) using a double Fourier series representation for the buckled shape. The problem was also considered recently by Uy and Bradford (1994b) using the finite strip method. The latter analysis produced a minimum local buckling coefficient of k = 10.30, while the value derived by Timoshenko and Gere was 10.67.
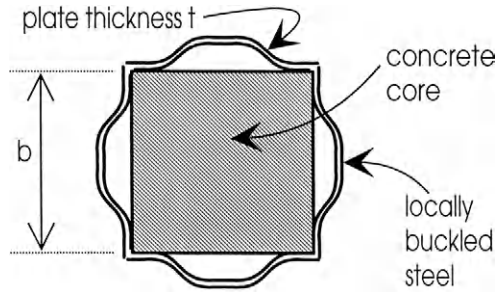
Fig. 5.12 Local buckling of concrete-filled tube

Hence, the limiting b/t ratio for the flat of a concrete-filled rectangular steel tube may be obtained from either Eq. 5.30 or 5.31 using a value of k of 10.30. The b/t limit for a rectangular tube built-up by welding is thus

$$\frac{b}{t} \leq \frac{745}{\sqrt{f_y}} \tag{5.33}$$

while for a rectangular tube formed by hot-rolling it is

$$\frac{b}{t} \leq \frac{1038}{\sqrt{f_y}} \tag{5.34}$$

Effective widths should be used for slender composite columns whose b/t limits exceed those of Eqs. 5.33 and 5.34 above, and transformed area theory may be adopted since the structural behaviour is elastic.

5.4 References

Azhari, M. and Bradford, M.A. (1993a). "Local buckling of composite tee-beams with longitudinal stiffeners", Canadian Journal of Civil Engineering, Vol. 20, No. 6, 923-930.

Azhari, M. and Bradford, M.A. (1993b). "Inelastic local buckling of plates with and without residual stresses", Engineering Structures, Vol. 15, No. 1, 31-39.

Bradford, M.A. (1985). "Local and post-local buckling of fabricated box members", Civil Engineering Transactions, Institution of Engineers, Australia, Vol. CE27, No. 4, 391-396.

Bradford, M.A. and Azhari, M. (1992). "Local buckling of I-section beams under shear and bending", First World Conference on Structural Steel Design, Acapulco, Mexico, 12-21.

Bradford, M.A., Bridge, R.Q., Hancock, G.J., Rotter, J.M. and Trahair, N.S. (1987). "Australian design rules for the stability of steel structures", International Conference on Steel and Aluminium Structures, Cardiff, U.K., 11-23.

Hall, A.S. (1984). *An Introduction to the Mechanics of Solids*, John Wiley, Sydney.

Hancock, G.J., Bradford, M.A. and Trahair, N.S. (1980). "Web distortion and flexural-torsional buckling", Journal of the Structural Division, ASCE, Vol. 106, No. ST7, 1557-1571.

Neal, B.G. (1977). *The Plastic Methods of Structural Analysis*, 3rd edn., Chapman and Hall, London.

Timoshenko, S.P and Gere, J.M. (1961). *Theory of Elastic Stability*, McGraw-Hill, New York.

Timoshenko, S.P. and Woinowsky-Krieger, S. (1959). *Theory of Plates and Shells*, McGraw-Hill, New York.

Trahair, N.S. and Bradford, M.A. (1991). *The Behaviour and Design of Steel Structures*, revised 2nd edn. Chapman and Hall, London.

Uy, B. and Bradford, M.A. (1994a). "Slenderness limits for thin steel plates when restrained by concrete", Australasian Structural Engineering Conference 1994, Sydney, 631-634.

Uy, B. and Bradford, M.A. (1994b). "Local buckling of composite steel-concrete rectangular columns", Fifth International Conference on Steel Structures, Jakarta, 313-322.

Von Karman, T. (1910). "Festigkeitsprobleme in Maschinebau", Encyk. der Math Wiss, Vol. 4, Part 4, art. 27, 349.

6   Behaviour under Serviceability Loads

6.1   Introduction

The general behaviour of composite members has been described in Part 1 of this book and the material and geometric properties in Parts 2 and 3. Part 4 of this book will deal with the analysis of standard composite steel and concrete beams of the type shown in Fig. 1.8, where the steel and concrete elements are at different levels and bonded together using mechanical shear connectors.

Service loads are the loads usually experienced by a composite member over a relatively long period of time. They include self-weight and sustained loads. Under such day to day loading, which is primarily what the structure is designed to resist, the composite member should not *deflect* excessively, it should not *vibrate* greatly, and *crack widths* within the reinforced concrete element should remain sufficiently small. Although design standards now give some guidance, it is usually left to the structural engineer to choose limiting values for use in these criteria which are appropriate to the composite structure, and to its intended use.

Behaviour under serviceability loads is the second requirement in limit states design. It should not be confused with strength design, where load factors are often used to increase the nominal loads and capacity reduction factors are used to decrease the structural strength. Rather, service load behaviour merely uses the nominal loads to calculate the response of the structure to its intended loading, and not to overload. It is also worth noting that service loads are used in fatigue design to ensure that a structure that is subjected to repetitive loads does not fail during its design life, as described in Chapter 19. Hence fatigue design is based on service loads, even though it is a failure criterion. Linear elastic analysis techniques are usually used to determine the behaviour under serviceability loads. However, they are also used in strength design at overloads to determine the onset of lateral-distortional buckling as described in Chapter 10.

Vibration of a composite structural member at low load levels is not considered explicitly in this book, and reference to well-known texts such as Clough and Penzien (1975) and Irvine (1986) is suggested to calculate the dynamic response of the member. This dynamic response differs, of course, from the fatigue behaviour presented in Chapters 3 and 19. There is little guidance in the literature on the calculation of crack widths in the concrete element of a composite beam, either due to shrinkage or tension caused by negative bending, and because of the limited research, discussion of this behaviour is omitted. Deflections under sustained loads represent the most important response to serviceability loads, and are treated in detail in the following sections. Linear elastic analysis is also used to determine the onset of yield, buckling and the forces that induce fatigue damage.

The behaviour of the three constituent materials of a composite member, that is the steel, reinforced concrete and the shear connectors, determine the type of linear

elastic analysis that can be applied. At serviceability loads, all three materials will be assumed to be linear elastic.

6.2   Material properties

6.2.1   STEEL AND CONCRETE

The deformation behaviour of a composite member under sustained loading may be either instantaneous or time-dependent. When the load is first applied at time $t = \tau$, after composite action has been achieved, the member deflects based on its elastic moduli E_s and E_c (see Section 2.3.2), but if the load is sustained, the concrete element creeps and shrinks with time $t > \tau$, so that the deformations may be much greater than those experienced at $t = \tau$ (see Section 2.3.2). It is important for the designer to be able to predict these deflections. The time-dependent deformations increase at a decreasing rate, and depending on the ambient conditions most of the deformation will have taken place after only five years or so.

6.2.2   SHEAR CONNECTORS

Typical load-slip characteristics of shear connectors are shown in Fig. 2.17. It can be seen that at low shear loads, the behaviour can be considered to be linear elastic, and hence can be represented as having a constant stiffness K.

In analysis, the stiffness of the shear connectors per unit length of beam, called the *shear connection stiffness*, is much more important than the stiffness of the individual connectors, called the *shear connector stiffness*, as defined by K in Fig. 2.17. If we change the vertical axes in Fig. 2.18 from D_{max} to D_{max}/L_s, where L_s is the longitudinal spacing of the connectors if they were placed in a single line, then K in Fig. 2.18 is the shear connection stiffness. The shear connection stiffness therefore depends on the shear connector stiffness and the spacing of the shear connectors. Analyses that allow for the connection stiffness K are referred to as *partial interaction* analyses. When there are few connectors in a beam, then K approaches zero and this is referred to as *no interaction*, as shown in Fig. 2.18. When there are a large number of connectors, then K approaches infinity and this is referred to as *full interaction* which is also shown in Fig. 2.18. It is also noteworthy that the size of the shear connector affects the shear connection stiffness. For example, the shear connection stiffness in a composite beam with 13 mm stud shear connectors is stiffer than in the same beam with 19 mm stud shear connectors that have the same total shear connection strength, as can be deduced from the shear connector stiffnesses in Section 2.4.6.2.

All composite beams with mechanical shear connectors exhibit partial interaction (as described in Section 1.2.5.3), since the mechanical shear connectors have to slip before they resist shear. The strain distribution associated with partial interaction is shown in Fig. 1.23 (c) and the stress distribution will have a similar shape as we are dealing with linear elastic analyses. Because the shear connection has a finite stiffness, the strain profile will always have a step change of ds/dx as shown,

and hence standard linear elastic methods of analysis, such as those applied to steel beams, cannot be used. Analyses based on partial interaction are described in Section 6.3.

When there are a large number of shear connectors in a shear span, as may be assumed to occur when there is full shear connection as described in Section 1.2.4.4, then even though there will be slip, it is often assumed that there is full interaction, as represented by the line $K = \infty$ in Fig. 2.18. It must be emphasised that full interaction does not mean full shear connection. However, when there is full shear connection, there is generally a large number of connectors so that their overall stiffness is large and hence full interaction analyses can be applied. Full interaction analysis is represented by the uni-linear strain profile in Fig. 1.23(b), which also represents the stress profile as we are dealing with linear elastic analyses. Since zero slip strain is assumed, as shown, standard techniques of linear elastic analysis can be applied, such as the well-known equations for shear stress $\tau = VA\bar{y}/Ib$ and flexural stress $\sigma = My/I$, and it is also worth bearing in mind that there will be only one neutral axis. Analyses based on full interaction are covered in Sections 6.4 to 6.7.

6.3   Partial interaction

6.3.1   GENERAL

Under partial interaction, the slip s must be taken into account in determining the service load deflections v. A general numerical scheme incorporating material nonlinearities was developed by Ansourian and Roderick (1978), however closed form solutions were developed under simplifying linear elastic assumptions much earlier by Newmark, Siess and Viest (1952), while a numerical analysis under these simplifying assumptions incorporating time-dependent effects was developed by Bradford and Gilbert (1992a).

Although Newmark, Siess and Viest's classical analysis has little direct applicability because of the complexity of the closed form solution, it does provide the basic groundwork for the development of this subject and hence is described in detail in Section 6.3.2. This is then followed in Section 6.3.3 with a practical method for allowing for the effect of slip on the deflection of a beam with fewer shear connectors, that is with partial shear connection.

6.3.2   LINEAR ELASTIC ANALYSIS

Consider the load-slip relationship for a stud shear connection as depicted in Fig. 2.21. We are concerned only with linear behaviour of the initial modulus K_{si} so the slip s is given by

$$s \;=\; \frac{D}{K_{si}} \tag{6.1}$$

where D is the shear force in the dowel. Hence under a uniform spacing L_s of the connectors

$$s = \frac{qL_s}{K_{si}} \tag{6.2}$$

in which q is the shear force transmitted per unit length of the beam, which is often referred to as the shear flow.

Consider the composite beam in Fig. 1.18(a) with the geometric and material properties shown. The axial forces F and moments M in each element of the composite beam and at any section of the composite beam are shown in (g). These actions act through the centroid of the concrete element at a distance h_c from the steel/concrete interface, as shown in (b), and at the centroid of the steel element at a distance h_s from the interface.

The elastic strain ε_c at the bottom of the concrete element given in Fig. 1.23(c) is given from elementary mechanics (Hall 1984) by

$$\varepsilon_c = \frac{M_{conc} h_c}{E_c I_c} - \frac{F_{conc}}{E_c A_{conc}} \tag{6.3}$$

while the elastic strain ε_s at the top of the steel element is, similarly

$$\varepsilon_s = \frac{F_{steel}}{E_s A_{steel}} - \frac{M_{steel} h_s}{E_s I_s} \tag{6.4}$$

where A_{conc} and A_{steel} are the areas of the concrete and steel elements respectively, while I_c and I_s are the second moments of area of the concrete and steel elements respectively about their centroidal axes.

From Fig. 1.19, it can be seen that $F_{conc} = F_{shear}$, where F_{conc} is the axial force in the concrete element at a distance $x = L_{sp}$ from a point of contraflexure or from the support of a simply supported beam, and F_{shear} is the total shear force on the shear connectors in this shear span of length x. Similarly, by considering the steel element by itself, $F_{steel} = F_{shear}$ and hence

$$F_{conc} = F_{steel} = F_{shear} \tag{6.5}$$

As the shear connection force $F_{shear} = qx$, it follows that

$$q = \frac{dF_{shear}}{dx} \tag{6.6}$$

The slip strain in the composite beam, ds/dx in Fig. 1.23(c), is given by Eq. 1.8 and hence substituting Eqs. 6.2 and 6.6 into this equation produces

$$\frac{L_s}{K_{si}} \frac{d^2 F_{shear}}{dx^2} = F_{shear} \left[\frac{1}{E_c A_{conc}} + \frac{1}{E_s A_{steel}} \right] - \left[\frac{M_{conc} h_c}{E_c I_c} + \frac{M_{steel} h_s}{E_s I_s} \right]$$

(6.7)

The total moment at the section being considered in Fig. 1.18(g) and hence the applied moment M is given by Eq. 1.2. Substituting F_{shear} for F_{conc} into this equation gives

$$M = M_{conc} + M_{steel} + F_{shear}(h_c + h_s)$$

(6.8)

Since the shear connection is required to prevent separation between the steel and concrete elements, the curvatures κ in the concrete and steel elements are the same, as shown in Fig. 1.22(d), so that

$$\kappa = \frac{M_{conc}}{E_c I_c} = \frac{M_{steel}}{E_s I_s}$$

(6.9)

which produces from Eqs. 6.8 and 6.9

$$\kappa = \frac{M - F_{shear}(h_c + h_s)}{\Sigma EI}$$

(6.10)

where $\Sigma EI = E_c I_c + E_s I_s$. Equating Eqs. 6.9 and 6.10 and substituting into Eq. 6.7 yields the following ordinary linear differential equation for F_{shear}

$$\frac{d^2 F_{shear}}{dx^2} - F_{shear} \frac{K_{si}}{L_s} \frac{\overline{EI}}{\overline{EA} \Sigma EI} = -\frac{K_{si}}{L_s} \frac{(h_c + h_s)}{\Sigma EI} M$$

(6.11)

which makes use of the notation

$$\frac{1}{\overline{EA}} = \frac{1}{E_c A_{conc}} + \frac{1}{E_s A_{steel}}$$

(6.12)

and

$$\overline{EI} = \Sigma EI + \overline{EA}(h_c + h_s)^2$$

(6.13)

Finally, noting that $\kappa = d^2 v/dx^2$ in Eq. 6.10 produces

$$\frac{d^2 v}{dx^2} = -\frac{M}{\Sigma EI} + C \frac{d^2 F_{shear}}{dx^2}$$

(6.14)

so that, on integrating twice with respect to x,

$$v_{part} = v_{full} + CF_{shear} \qquad (6.15)$$

where v_{part} is the deflection with partial interaction, v_{full} is the deflection of the beam with full interaction, and C is the flexibility coefficient given by

$$C = \frac{L_s}{K_{si}} (h_c + h_s) \frac{\overline{EA}}{\overline{EI}} \qquad (6.16)$$

Of course, for full interaction, K_{si} approaches infinity and so C approaches zero, producing $v_{part} = v_{full}$ as expected.

Some closed form solutions for F_{shear} in Eq. 6.11 have been derived which may be used to obtain the deflection v_{part}. For example, for a simply supported beam of length L subjected to a uniformly distributed load w per unit length, it can be shown that

$$F_{shear} = \frac{\overline{EA}\,(h_c + h_s)}{\overline{EI}}\, wL^2 \bullet$$

$$\left\{ \frac{x(L-x)}{2L^2} + \frac{C_I^2}{\pi^2} \left[\frac{1 - \cosh \pi / C_I}{\sinh \pi / C_I} \sinh\left(\frac{\pi x}{C_I L}\right) + \cosh\left(\frac{\pi x}{C_I L}\right) - 1 \right] \right\} \qquad (6.17)$$

where x is measured from the supports and where

$$C_I = \frac{\pi}{L} \sqrt{\frac{L_s}{K_{si}} \frac{\overline{EA}\,\Sigma EI}{\overline{EI}}} \qquad (6.18)$$

Once the distribution of F_{shear} is known, it can be differentiated to find q (Eq. 6.6), and once q is known it can be used to determine the slip s (Eq. 6.2). In general, however, a finite difference scheme may be used to solve the differential equation numerically for the deflection v_{part} of a beam with partial interaction. In the long-term for realistic beams, the deflections caused by the time-dependent deformation of the concrete element far outweigh those caused by partial interaction (Bradford and Gilbert 1992a) when there is full shear connection, so that a calculation such as that presented above would rarely be carried out for service load behaviour.

Example 6.1 Increase in deflection due to partial interaction

The composite beam shown in Fig. 6.1 is simply supported, spans 6 m and supports a uniformly distributed load of 45 kN/m. The beam is designed for full shear connection and has 16 mm diameter stud shear connectors at a longitudinal spacing of L_s = 110 mm. The strength of the concrete slab is f_c = 35 N/mm^2 and the dowel strength of each shear connector is 58 kN.

From Eq. 2.32, the shear connection stiffness K_{si} = 36 kN/mm and from the beam properties L = 6 m, $h_c + h_s$ = 227 mm, $\overline{EA}$ = 1.012x10^9 N, $\overline{EI}$ = 8.301x10^{13} Nmm^2 and Σ EI = 3.088x10^{13} Nmm^2. Substituting into Eq. 6.18 gives C_1 = 0.562, into Eq. 6.17 at x = L/2 gives F_{shear} = 435 kN at midspan, and into Eq. 6.16 gives C =8.454x10^{-6} mm/N. Hence CF_{shear} = 3.7 mm which is the increase in deflection due to partial interaction as shown in Eq. 6.15. It will be shown in Example 6.2 that the flexural rigidity EI of the composite section with full interaction is 8.308x10^{13} Nmm^2 and hence from elementary structural mechanics the deflection of the beam with full interaction is v_{full} = 9.1 mm. Hence partial interaction causes an increase in deflection of 3.7/9.1 = 40%.

E_c = 28.6 kN/mm^2

(units of mm unless specified)
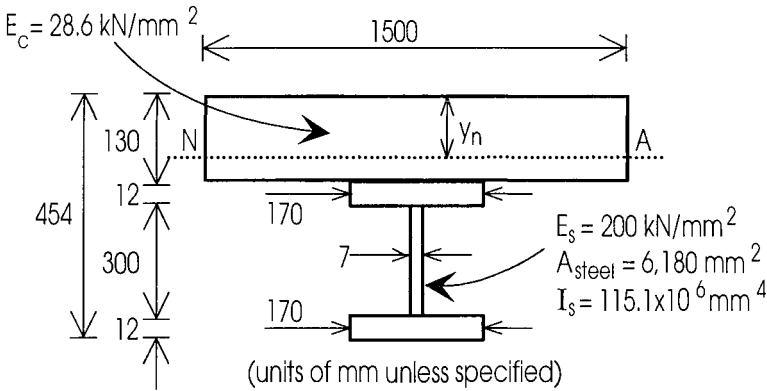
Fig. 6.1 Standard composite beam

6.3.3 BEAMS WITH PARTIAL SHEAR CONNECTION

Experience has shown that when there is full shear connection, the increase in deflection due to partial interaction can be ignored, as it is much less than that due to time-dependent deformations. However, when the maximum degree of shear connection η_{max} < 1, the increase in deflection due to slip should be allowed for, as the shear connection stiffness reduces in proportion to the degree of shear connection, and could in theory be zero when there are no shear connectors. It has been shown in Section 6.3.2 that partial interaction theory is complex, and therefore not suitable for practice in determining the deflection with partial interaction v_{part} as given by Eq. 6.15. Instead, design recommendations are often based on the deflection with full interaction v_{full} and the deflection with no shear connection v_{no}.

When there is full interaction, then standard techniques can be used to determine the flexural rigidity of the composite section $E_c I_{nc}$ as described in Section 6.4, and this can be used to determine the deflection with full interaction v_{full}. When there is no interaction, then we have a choice between ignoring or including the concrete element in the analysis.

If it is assumed that the tensile strength of the concrete is zero, that there are no longitudinal reinforcing bars in the concrete element and that the concrete element can separate vertically from the steel element, then the concrete element can be ignored so that $v_{no} = v_{steel}$, where v_{steel} is the deflection of the steel element acting by itself.

Alternatively, let us assume that the concrete has a tensile strength, that there are a few longitudinal reinforcing bars to restrict cracking, and that vertical separation of the concrete and steel elements is limited by the method of loading or the presence of a few connectors. Then combining Eqs. 6.8 and 6.9 with $F_{shear} = 0$, as we are dealing with no interaction, gives

$$\frac{M}{\kappa} = \Sigma EI = E_c I_c + E_s I_s = (EI)_{no} \tag{6.19}$$

so that the flexural rigidity of the composite beam with no interaction $(EI)_{no}$ is simply equal to the sum of the flexural rigidities of the individual elements, and this can be used to determine the deflection v_{no} using standard procedures based on full interaction.

Having determined v_{full} and v_{no} an interpolation procedure can be used to determine v_{part} between these two extremes. A simple approach when $\eta > 0.5$ (Johnson and May 1975) is to assume that the deflection v_{part} is proportional to the degree of shear connection η so that

$$v_{part} = v_{full} + \alpha \left(v_{steel} - v_{full} \right) (1 - \eta) \tag{6.20}$$

With $\alpha = 1$, $v_{part} = v_{full}$ when $\eta = 1$ as would be expected, and with $\alpha = 1$, $v_{part} = v_{steel}$ when $\eta = 0$. The parameter α is taken as less than unity to improve the correlation with experimental data, and values of around 0.4 are recommended (as used in Eurocode 4) depending on whether propped or unpropped construction is used.

6.4 Full interaction

6.4.1 TRANSFORMED CONCRETE SECTIONS

Partial interaction analyses are rarely used because of their complexity. Instead, composite beams with full shear connection are assumed to have full interaction, so that slip and hence slip strain are ignored. Furthermore, under service loading, the steel modulus E_s and the short and long-term concrete moduli E_c and E_e can be considered to be elastic, and for ease of analysis transformed area principles may be adopted. The basis of a general and more accurate analysis technique is described in Section 6.7.

Consider for example the T-beam shown in Fig. 6.2(a) in which the modular ratio of the constituent materials is defined as $n = E_s/E_c$ or $n = E_s/E_e$, depending on whether we are dealing with short or long-term behaviour. The composite section can

be transformed into a concrete section by increasing the area of reinforcement A_{rein} to nA_{rein} and the area of the steel element A_{steel} to nA_{steel} as shown. In order to ensure that the flexural stiffness of the transformed concrete section is the same as that of the composite section, the area of concrete nA_{rein} must act at the same level as A_{rein}. Similarly, the area of concrete nA_{steel} must act at the same level as A_{steel}, and this can be achieved by increasing the widths of the components of the steel element by a factor of n as shown. It should be noted that A_{conc} is the cross-sectional area of the concrete, or the area of the slab less the area A_{rein}. An alternative procedure is to assume that A_{conc} is the cross-sectional area of the whole slab, and that the area of the transformed reinforcement is either $(n-1)A_{reinf}$ when it lies in a region of uncracked concrete or nA_{rein} when it lies in a region of cracked concrete.
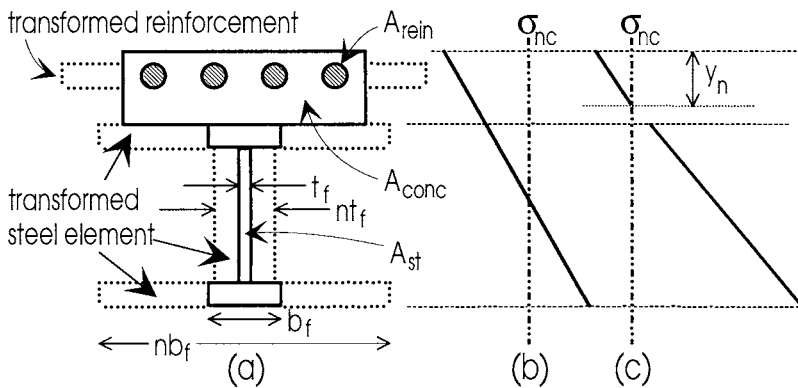
Fig. 6.2 Transformed concrete beam

The composite section in Fig. 6.2(a) has been transformed into a concrete section on the assumption that the concrete has not cracked in tension. Should the stress distribution be such that the concrete element can crack in tension, then it is necessary to determine the region of the concrete that has cracked, so that it can be removed from the transformed section, and this is done by determining the position of the neutral axis as outlined in the following.

6.4.2 POSITION OF NEUTRAL AXIS

6.4.2.1 *Sagging or positive region*

Consider the transformed section in Fig. 6.2(a) when it is subjected to positive bending so that the top fibre of the concrete is in compression. If the neutral axis is assumed to lie in the steel element as shown in (b), where σ_{nc} is the stress in the transformed concrete section, then all of the concrete element is in compression and none in tension, so that the shape of the transformed section remains as in (a). The size and position of all the elements in (a) are known, so that the position of the neutral axis lies at the centroid of the transformed section.

The calculation is more difficult if the neutral axis is found to lie in the concrete element as shown in Fig. 6.2(c), as the depth of the uncracked concrete element is now not known. In this case, the transformed stress σ_{nc} including that in the tensile reinforcement but excluding that in the cracked concrete below the neutral axis is integrated over the area of section, and the tensile force is equated to the compressive force. This then yields the location of the neutral axis y_n in (c). An alternative way of stating this is that the first moment of the area of the transformed section above the neutral axis, and taken about the neutral axis, is equal to the first moment of the transformed section below the neutral axis, and taken about the neutral axis.

Once the neutral axis has been located, the second moment of area of the transformed section I_{nc} about the neutral axis may be calculated easily. The flexural rigidity $E_c I_{nc}$ may thus be used to calculate the stresses and deformations in a simply supported beam, or in a sagging region between points of contraflexure. For the standard forms of composite beams shown in Fig. 1.8, the reduction in the flexural rigidity that can occur through cracking is very small, so that composite beams in positive regions are generally treated as being uncracked.

Example 6.2   Flexural rigidity in positive region

Consider the composite beam shown in Fig. 6.1 that is made from materials that have a short-term modular ratio of n = 200/28.6 = 7.0. The steel element can be transformed into a concrete element that has an area nA_{steel} = 43,260 mm^2, a second moment of area $nI_s = 806 \times 10^6$ mm^4 and the same depth 324 mm.

If the concrete is assumed to be uncracked, then the position of the neutral axis lies at the centroid of the section, and hence from the first moment of area the neutral axis is y_n = 106.2 mm from the top fibre, and this gives a second moment of area of the uncracked section of $I_{nc} = 2905 \times 10^6$ mm^4. This neutral axis lies in the concrete element, so that the concrete below the neutral axis is fully cracked if we assume that the tensile strength of the concrete is zero. The position of the neutral axis in the cracked section can be determined by equating the first moment of area about the neutral axis of the transformed sections above with that below the neutral axis. This gives $1500 y_n^2 /2 = 43260(292 - y_n)$ from which y_n = 104.1 mm and the second moment of area of the cracked section of $I'_{nc} = 2897 \times 10^6$ mm^4.

The flexural rigidity of the cracked section is only 0.3% less than that of the uncracked section and hence cracking can be ignored in standard composite sections in sagging or positive regions. Of course, the difference is even less if the tensile strength of the concrete is allowed for. Making the steel beam composite with the concrete slab has increased the flexural rigidity by $E_c I_{nc}/E_s I_s$ = 3.6, so that the deflection of the composite beam will be only 28% of that of the steel beam when acting by itself, and this will allow significant increases in span to depth ratios. It is also worth noting that if the concrete element in Fig. 6.1 was made from a transverse profiled slab, as shown in Fig. 1.11(c), then the voids between the ribs of the profiled

slab will have virtually no effect on the flexural rigidity as they occur in the region of cracked concrete and are very close to the neutral axis.

6.4.2.2 *Hogging or negative regions*

Consider the transformed section in Fig. 6.2(a) when it is subjected to a hogging or negative moment, so that the top fibre of the concrete slab is in tension. If the neutral axis is first assumed to be in the steel element, then the concrete will be fully cracked so that the area of concrete $A_{conc} = 0$ in (a). The beam will therefore comprise of two steel elements consisting of the reinforcing bars and the steel element. As the size and position of these elements is known, the neutral axis lies at the centroid of this composite steel section.

If the neutral axis is found to occur in the concrete element, then the area of concrete below the neutral axis is uncracked and the depth of this section is not known. The position of the neutral axis can now be determined by equating the first moment of area about the neutral axis of the transformed section above to that of the transformed section below, as described in Section 6.4.2.1. However, the likelihood of the neutral axis being in the concrete element in standard composite beams is remote, as it would require a very large area of reinforcement or a very deep slab. It is worth bearing in mind that the flexural rigidity of the fully cracked section is a lower bound to the flexural rigidity of a beam in negative regions, as it ignores the beneficial effect of tension stiffening between the cracked concrete sections.

Example 6.3 Flexural rigidity in negative region

Let us assume that the composite beam in Fig. 6.1 is subjected to negative moments. The concrete element has 0.6% reinforcement (1170 mm^2) that has the same elastic modulus as that of the steel element, and the centroid of the reinforcement is 35 mm below the top surface of the slab.

If we first assume that the neutral axis lies in the steel element, then the composite beam will only consist of the reinforcement element and the steel element. As both of these elements have the same elastic moduli, the section can be left as a steel section. The centroid of this composite steel section lies 203 mm from the bottom fibre of the steel element which is well within the steel element, and this gives a flexural rigidity which is 56% greater than that of the steel element by itself and 43% of that of the composite section in the positive region (Example 6.2).

6.4.3 CONTINUOUS COMPOSITE BEAMS

Continuous beams are deployed widely in composite construction, and because of the differing values of the flexural rigidities $E_c I_{nc}$ and $E_c I'_{nc}$ in sagging and hogging bending respectively, they must be treated as nonuniform beams. For example, consider the two-span continuous beam shown in Fig. 6.3 which is one-fold indeterminate and which has full interaction, with spans L_ℓ to the left and L_r to the

right. Under a given loading (a distributed load of w in this case), it can be assumed that the beam is subjected to sagging bending with transformed rigidity $E_c I_{nc}$ over the regions of a_ℓ and a_r, and to hogging bending with transformed rigidity $E_c I'_{nc}$ over the central support region covering a_c. If a hand calculation is being carried out, the principle of virtual forces may be invoked to determine the bending moment diagram, or more commonly recourse may be made to a computer stiffness package to determine this bending moment distribution, by assuming values for a_ℓ and a_r. If the moment is not zero at a_ℓ and a_r from the ends (the points of contraflexure), then new trial values of a_ℓ and a_r must be selected and the analysis repeated. When the iterative scheme, which can generally be performed by trial and error, has converged to acceptable accuracy the final bending moment diagram may be used to determine the deformations.
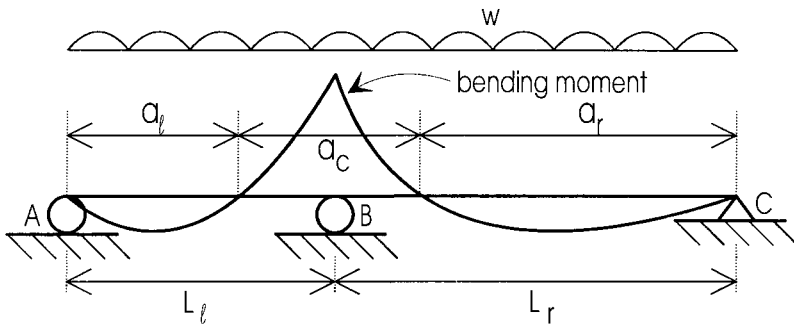
Fig. 6.3 Two-span continuous beam

An example of such a calculation for a fixed ended composite beam was given by Bradford and Gao (1992), where the position of the point of contraflexure was established by solving a cubic polynomial whose coefficients were quite complex and difficult to derive. Because of this, it is recommended that a trial and error method be used, and state of the art stiffness packages which are user-friendly are ideal for this. The designer can then merely adjust the positive bending region (a_ℓ and a_r) and the negative bending region of the nonuniform beam at the computer terminal until the correct points of contraflexure are obtained. Note that the problem as stated is linear elastic, as we have assumed throughout this chapter, and increasing the load factor on the applied loading merely changes the ordinate but not the shape of the bending moment diagram. Continuous beams are treated more fully in Chapter 9.

6.4.4 APPLICATION OF FULL INTERACTION

Transformed sections are used in Section 6.5 to determine the deformations and actions of composite beams that are subjected to short-term loading by using a modular ratio based on the short-term modulus of the concrete E_c. Similarly, transformed sections can be used to determine the behaviour under long-term loading using the long-term modulus E_e that allows for creep. Transformed sections are used in Section 6.6 to determine the effects of concrete shrinkage and thermal gradients.

As we are dealing with a linear elastic analysis, the effects of short-term loading, long-term loading, shrinkage and thermal gradients can be determined from separate analyses based on transformed sections and the results superposed. Alternatively, the general analysis technique described in Section 6.7 can be applied as this gives simple but accurate solutions.

6.5   Method of construction

6.5.1   GENERAL

Composite beam construction is generally termed *propped* or *unpropped*. Propped construction is usually deployed for building construction, where the weight of the wet concrete in a storey is transferred through the steel element into a number of closely spaced props. Once the concrete has cured and sufficient composite action is achieved, the props are removed and the behaviour of the composite beam can then be ascertained.

Because of their construction environment, bridges generally use unpropped construction. Under this condition, the steel element is required to support the weight of the wet concrete. As composite action is not realised at this stage, the deformations must be calculated from the flexural rigidity $E_s I_s$ of the steel element alone. The beam thus deflects based on the steel stiffness, but once the beam becomes composite the stiffness is increased and short-term behaviour due to any additional load is governed by the flexural rigidity of the entire composite beam. Analysis of beams using unpropped construction is a little more complex than for propped construction, and guidance is given in Sections 6.5.2 and 6.5.3 for both types of construction.

6.5.2   FLEXURAL STRESSES

The flexural analysis of composite beams made by propped construction is summarised in Fig. 6.4. The composite beam has to be transformed into a concrete section for both short-term and long-term loading, and hence the two neutral axes shown in (a). The transformed stress distributions σ_{nc} can then be determined from $\sigma_{nc} = My/I_{nc}$ for both short and long-term loadings, as in (b) and (c), and the stresses superposed and transformed back to their original constituents as in (d).

The analysis of an unpropped beam is shown in Fig. 6.5. In this typical analysis, it has been assumed that all the long-term load is resisted by the steel element as in (b), and all the short-term load by the composite section as in (c). If part of the long-term load were resisted by the composite section, then a third analysis would be required as depicted by Fig. 6.4(b). The flexural stresses can then be superposed and transformed, as in Fig. 6.5(d).

The difference between propped and unpropped construction can be seen by comparing Figs. 6.4 and 6.5. Let us assume that all of the long-term load is dead load, and the short-term load is live load. As (c) in both figures is the same, the stress distribution and deflection due to live loads is unaffected by the form of construction.

A comparison of (b) in both figures shows firstly that the stresses and hence deflections due to dead load are much greater in unpropped construction than in propped construction, and secondly that beams built by propped construction will gradually deflect due to creep as the dead load is acting on the composite section. A comparison of (c) in both figures shows that there are large variations in the stress distributions at service loads. However, this will not affect the rigid plastic strength as described in Chapter 7, but may affect lateral-distortional buckling as described in Chapter 10.
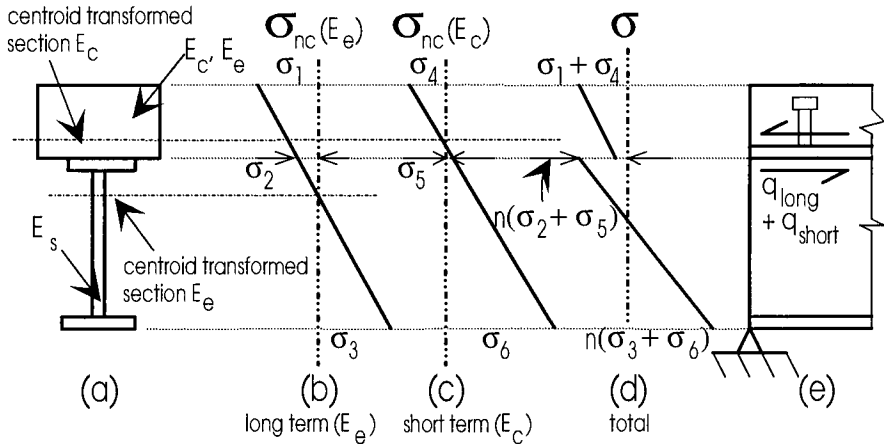
Fig. 6.4 Propped construction
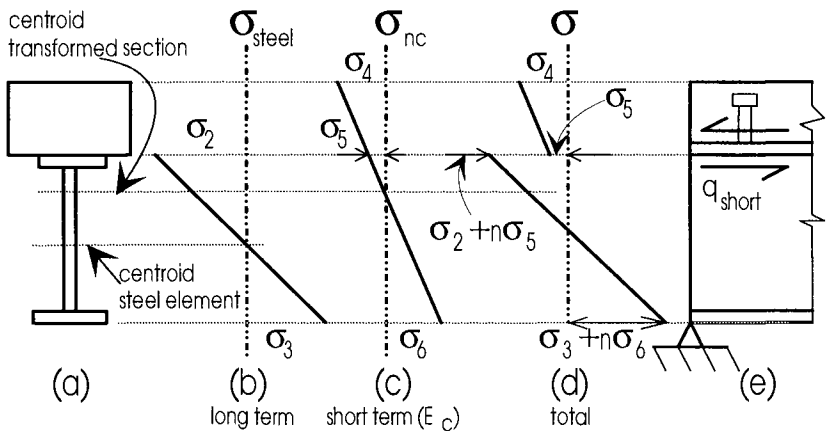
Fig. 6.5 Unpropped construction

It can thus be seen that linear elastic analyses are not only required to limit deflections, but they are also required to limit yield, buckling and fatigue stresses in the steel element.

6.5.3 SHEAR FLOW ON CONNECTORS

The shear flow in the shear connectors in a composite beam can be derived from the transformed section and using the well-known equation $q = VA_{conc} \bar{y} / I_{nc}$ which has been described in Section 1.3.1. In propped construction, the shear flows due to the short and long-term loads have to be determined separately from the short and long-term transformed sections, and then the flows added as in Fig. 6.4(e). However, in unpropped construction, only the composite behaviour induces shear forces in the connectors, so that most of this will be due to short-term loading as shown in Fig. 6.5(e).

Let us assume once again that the long-term load is the dead load, while the short-term load is the live load. In propped construction, the forces in the shear connectors will have a base level equal to the shear force induced by the dead load, q_{long} in Fig. 6.4 (e), and superposed on this base load will be cyclic forces due to the live loads of q_{short}. On the other hand, in unpropped construction, the base load due to dead load is zero and the connectors are only subjected to cyclic live loads q_{short}. Hence the form of construction will affect both the static and fatigue loads on the connectors.

If the ultimate strength of the composite beam is determined by rigid plastic analyses as described in Chapter 7, then the distribution of connectors is independent of the serviceability shear flows, and methods of determining the size and spacing of the connectors are described in detail in Section 7.5.2.

If the ultimate strength is governed by lateral-distortional buckling, as described in Chapter 10, then the connectors have to be distributed according to the linear elastic shear flow, such as q in Fig. 6.6. This would require a gradual change in the spacing of the connectors throughout the length of the beam that would be impractical. Instead, connectors are placed in blocks with uniform spacing, as shown, and guidelines are given in standards as to the maximum overstress permitted such as the 10% shown. It has been shown in Sections 2.4.6.2 and 3.4.2.4 that shear connectors are highly adaptable components, and have the ability to shed load from highly stressed regions to understressed regions through incremental set and the plastic plateau, and hence regions of overstress are not important whilst there are regions of understress. Once the shear flow in a block is known, the connectors can be designed according to Sections 7.5.2.2 and 7.5.2.3 and in Example 7.6, bearing in mind that n in Eq. 2.37 is the number of connectors (that can be assumed to fail as a group which could be the number of connectors) between the design point and the point of contraflexure.

Methods for the linear elastic static and fatigue design of shear connectors in bridge beams are described in detail in Chapter 19.
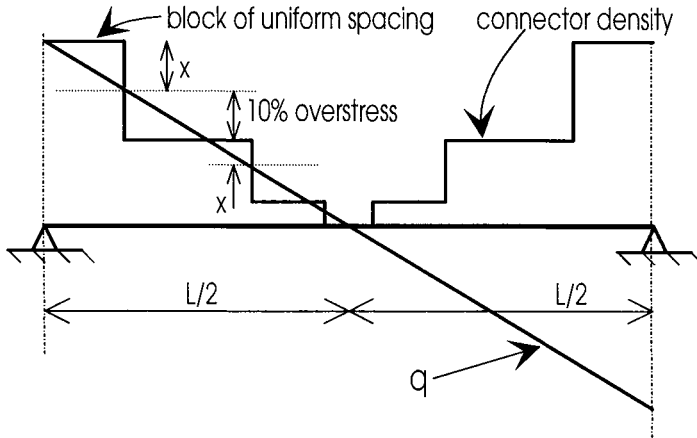
Fig. 6.6 Distribution of connectors

Example 6.4   Analysis of propped and unpropped beams

The composite beam shown in Fig. 6.1 is simply supported, spans 6 m, is subjected to a uniformly distributed long-term dead load w of 15 kN/m and a short-term live load of 30 kN/m. The concrete has a creep coefficient $\phi = 1.0$ so that the effective modulus from Eq. 2.23 is $E_e = 28.6/2 = 14.3$ kN/mm^2, and hence the modular ratio for long-term loading is n = 14.0.

The cross-sectional properties of the transformed concrete beam for short-term loading have been determined, in Example 6.2, as $y_n = 106$ mm from the top fibre and $I_{nc} = 2905 \times 10^6$ mm^4. Following a similar analysis with n = 14 for long-term loading yields $y_n' = 135$ mm and $I_{nc}' = 4974 \times 10^6$ mm^4.

For propped construction, the long-term stress distribution in Fig. 6.4(b) is $\sigma_1 = 1.8$ N/mm^2 (compressive stresses positive), $\sigma_3 = -4.3$ N/mm^2, and the short-term stress distribution in (c) is $\sigma_4 = 4.9$ N/mm^2 and $\sigma_6 = -16.2$ N/mm^2. Hence the total stress at the top fibre of the concrete in (d) is 6.7 N/mm^2 and at the bottom fibre of the steel element it is -174 N/mm^2. The midspan deflection due to long-term loads is 3.6 mm, and that due to short-term loads is 6.1 mm, which gives a total deflection of 9.7 mm.

For unpropped construction, the long-term stress distribution in Fig. 6.5(b) is $\sigma_2 = -\sigma_3 = 95$ N/mm^2 and the short-term stress distribution is the same as for propped construction. Hence the total stress in the top fibre of the concrete in (d) is 4.9 = N/mm^2 and at the bottom fibre of the steel element it is -208 N/mm^2. As the midspan deflection $\delta = 5wL^4/384EI$ for simply supported beams, the deflection due to long-term loading is 11.0 mm, that due to short-term loading is the same as in propped construction, producing a total deflection of 17.1 mm, as compared with only 9.7 mm for propped construction.

For propped construction, the shear flow on the shear connectors adjacent to the supports is q_{long} = 123 N/mm, q_{short} = 249 N/mm and hence a total shear flow of q_{total} = 372 N/mm. On the other hand, for unpropped construction only the short-term loads exert shear forces on the shear connectors, and this is the same as in propped construction of q_{short} = 249 N/mm. Let us assume that we will be designing the shear connectors for propped construction, that is a shear flow of 372 N/mm, so that the ultimate strength is not based on rigid plastic analysis.

A conservative approach would be to base the design on the characteristic strength of an individual connector such that n = 1 in Eq. 2.37 for stud shear connectors (design based on the characteristic strength, that is n > 1, is described in Example 7.6 and in Chapter 19). Let us assume that $(D_{max})_{beam}$ = 60 kN in Eq. 2.37, after inserting the geometric and material properties and assuming n = 1. Then the spacing required at the supports s = 60,000/372 = 161 mm, and that at midspan is zero as shown in Fig. 6.6 The connectors can be placed in blocks as shown in Fig. 6.6.

If we are willing to accept an understress of x = 25% in Fig. 6.6, then the length of the block adjacent to the supports is 750 mm, where the connectors will have a spacing of 161 mm. If we accept an overstress of 10%, then the length of the next block is 1050 mm, where the connectors will have a spacing of 248 mm. The next block will have a length of 1050 mm and a spacing of 538 mm, and the central portion will have nominal connectors as described in Section 7.5.2.3. The procedure outlined in Fig. 6.6 tends to be more conservative at the supports than between the supports, which is desirable as theoretical and experimental research has shown that the shear connectors at the support regions are more prone to failure.

6.6   Lack of fit

6.6.1   GENERAL

Because the concrete and steel elements in standard composite beams are at different levels as shown in Fig. 1.8, shrinkage of the concrete element and thermal gradients through the depth of the composite beam have a much greater effect than in either reinforced concrete or steel beams. The effect of shrinkage and thermal gradients in composite beams are dealt with in this section using simple lack of fit procedures that can be considered to be a precursor to a general analysis technique described in Section 6.7, that is based on a relaxation procedure.

6.6.2   SHRINKAGE

6.6.2.1 *Behaviour*

Shrinkage of the concrete element depends on the environment and the constituents of the concrete as described in Section 2.3.3.3 and shrinkage strains can reach values in excess of $\varepsilon_{sh} = 500$ microstrains (500×10^{-6}). Furthermore, shrinkage is time-dependent, and therefore the forces that are induced will cause creep. Because of this, the effective modulus E_e in Section 2.3.3.2 should be used in the analysis.

The effect of shrinkage in the sagging or positive region of a composite beam is illustrated in Fig. 6.7. In the absence of shear connectors, the concrete will contract as shown in (a). The shear connectors resist this contraction as shown in (b), so that the shear forces in the connectors due to shrinkage are in the opposite direction to those induced by gravity loads, as shown in Fig. 1.12(b). Hence shrinkage is beneficial to the connectors, although it should be remembered that expansion of the concrete would be detrimental. Contraction of the concrete through shrinkage will cause the deformation shown in Fig. 6.7(b), and hence induce deflections and flexural stresses in the steel that are in the same direction as those induced by gravity loads.

(a) unrestrained shrinkage

(b) restrained shrinkage
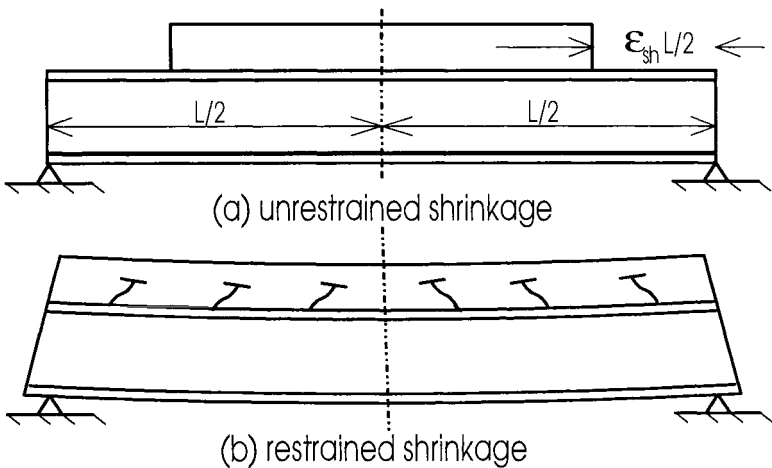
Fig. 6.7 Shrinkage deformations

6.6.2.2 *Analysis*

In order to determine the forces and deformations induced by shrinkage, let us consider the right hand side of the beam in Fig. 6.7(a) which does not have shear connectors and which is also shown in Fig. 6.8(a). The concrete element is allowed to contract due to shrinkage as shown, so that there is a lack of fit of $\varepsilon_{sh}L/2$ in Fig. 6.7(a). The connectors will resist this contraction as shown in (b). Although mechanical shear connectors have to slip to resist shear, we will assume that there is zero slip so we can apply a full interaction analysis based on transformed sections.
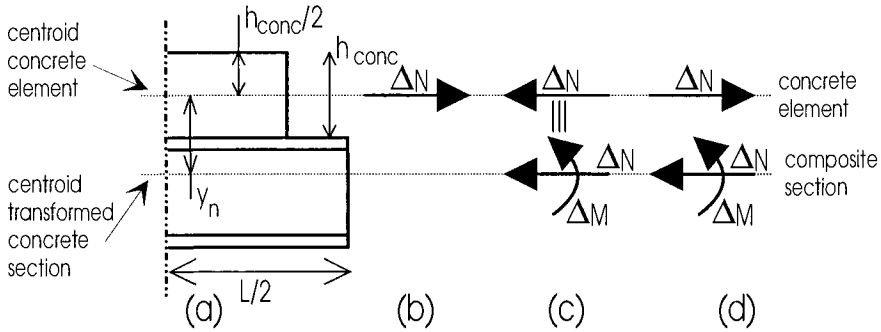
Fig. 6.8 Equivalent force system for shrinkage

In order to prevent slip and hence the lack of fit, shown in Fig. 6.8(a), an axial force ΔN in (b) has to be applied to the concrete element. This force has to induce a uniform strain in the concrete of ε_{sh} and so must be applied in line with the centroid of the concrete element and have a magnitude of

$$\Delta N = E_e \varepsilon_{sh} A_{conc} \tag{6.21}$$

Applying ΔN to the concrete element in (b) ensures compatibility, but the system is now not in equilibrium. To maintain equilibrium of the composite beam, an equal and opposite force ΔN has to be applied in line with the centroid of the concrete element, and this force has to be applied to the composite beam as shown in (c). This force ΔN is statically equivalent to an axial force ΔN and a moment ΔM acting on or through the centroid of the transformed composite section also shown in (c), where

$$\Delta M = \Delta N \, y_n \tag{6.22}$$

and where y_n is the distance between the centroids as shown in (a). In conclusion, the effect of shrinkage is equivalent to a tensile force ΔN acting on or through the centroid of the concrete element, as shown in (d), and a compressive force ΔN and moment ΔM acting on and through the centroid of the composite section.

From Fig. 6.8(d), it can be seen that the deflection due to shrinkage is equivalent to the deflection of a composite beam that is subjected to a constant moment ΔM throughout its length L. Furthermore, as the force in the shear connectors F_{shear} is always equal to the axial force in the concrete element F_{conc}, as shown in Fig. 1.19, the shear connector force induced by shrinkage F_{shear} can be determined by integrating the stress distribution produced by the actions in Fig. 6.8(d) over the cross-sectional area of the concrete element. Linear elastic partial interaction techniques such as those described in Section 6.3.2 can be applied to determine the distribution of F_{shear}. However in practice, the shear connectors are generally distributed uniformly over a length of about 0.2L adjacent to each support.

The analysis technique outlined above for sagging or positive regions can be applied to hogging or negative regions, but the effect of shrinkage is less pronounced in negative regions because tensile cracking of the concrete relieves or can even eliminate shrinkage forces.

Example 6.5   Concrete shrinkage in composite beams

The concrete element in the composite beam in Example 6.4 and shown in Fig. 6.1 is subjected to a shrinkage strain of 300×10^{-6}. Since we are dealing with time-dependent properties, E_e, y'_n and I'_{nc} in Example 6.4 should be used in this analysis to determine the effects of shrinkage. Hence from Eq. 6.21, $\Delta N = 837$ kN and from Eq. 6.22, $\Delta M = 190$ kNm.

  For a beam subjected to a uniform moment, the midspan deflection $\delta = ML^2/8EI = 12.0$ mm, which is slightly less than the deflection due to propped construction calculated in Example 6.4 of 17.1 mm. The stresses induced in the steel element due to shrinkage are caused by ΔM and ΔN in Fig. 6.8(d) acting on the composite beam at its centroid. These induce an increase in stress at the bottom fibre of the steel element of 129 N/mm^2 which could cause the beam in Example 6.4 to yield. The force in the shear connectors in each half of the beam, induced by shrinkage, is 318 kN. In this example, these shear forces are beneficial as they act in the opposite direction to those caused by gravity. If these forces were induced by thermal expansion of the concrete, then it may be necessary to add connectors of strength 318 kN to each half of the beam, and concentrate them near the supports over a distance of about $0.2L = 1.2$ m.

6.6.3   THERMAL GRADIENTS

Longitudinal strains can be induced in composite beams due to thermal gradients as shown in Fig. 6.9(a). The method of analysis is the same as for shrinkage. The changes in strains can be determined from the coefficient of thermal expansion in Section 2.3.3.4. Hence the forces required to prevent this change can be determined as shown in Fig. 6.9(b) and these are equivalent to the shrinkage forces in Fig. 6.8(b). As can be seen in Fig. 6.9, it is convenient to divide the section into small elements in which the position and magnitude of the resultant forces can be determined. The remainder of the procedure is the same as for shrinkage as shown in Fig. 6.9(c).

6.7   General analysis technique

6.7.1   GENERAL

A method for the accurate time-dependent analysis of propped composite beams was developed and modified by Gilbert (1988) and by Bradford and Gilbert (1989, 1992b), and is presented here. The method given allows the engineer to perform the calculation of the deformations of simply supported composite beams relatively easily by hand, or to develop a simple computer program. It is more accurate than using

simple modular ratio theory based on E_e, as in Section 6.4, but in most cases the differences in stresses and deflections calculated using the general analysis technique of this section and that of Section 6.4 are only minor.
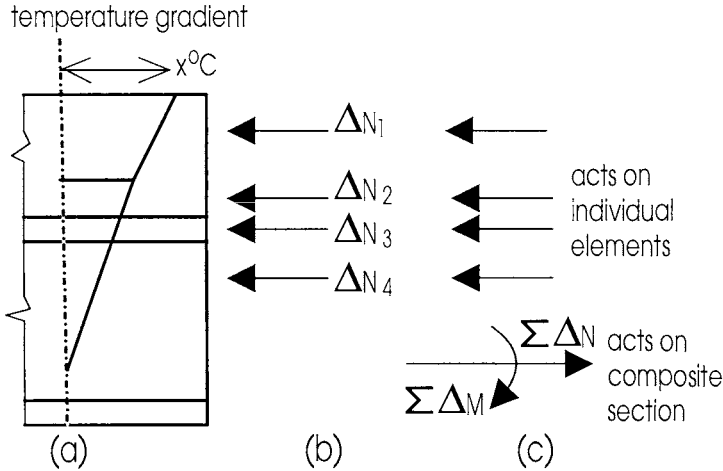

Fig. 6.9 Equivalent force system for thermal gradients

6.7.2   SIMPLY SUPPORTED BEAMS

6.7.2.1 *Short-term response*

Figure 6.10 shows a composite T-beam containing reinforcement in the concrete element subjected to an initial strain distribution causing positive or sagging bending. It is assumed that there is full interaction, so the slip s is negligible at service loads when compared to time-dependent deflections (Bradford and Gilbert 1992a), and the strains are linear over the full depth of the cross-section with one neutral axis. It is assumed further that the concrete remains uncracked, that the neutral axis lies in the steel element, and as we are dealing with short-term responses the concrete modulus is E_c. A convention is adopted where compressive stresses are positive, and a positive bending moment on the section results in tension in the bottom fibres of the steel element.

Consider firstly the transformed cross-section in Fig. 6.10(a), which is similar to that of Fig. 6.2. The area of the transformed section A in Fig. 6.10, and the first and second moments of area of the transformed section about the top fibre, B and I respectively, are

$$A = bh_{conc} + (n-1)A_{sr} + nA_s \tag{6.23}$$

$$B = \frac{bh_{conc}^2}{2} + (n-1)A_{sr}d_{sr} + nA_s d_s \tag{6.24}$$

$$I = \frac{bh_{conc}^{3}}{3} + (n-1)A_{sr}d_{sr}^{2} + n\left(I_{s} + A_{s}d_{s}^{2}\right) \qquad (6.25)$$

where $n = E_{s}/E_{c}$, A_{s} is the cross-sectional area of the steel element, I_{s} is the second moment of area of the steel element about its own centroidal axis, and the geometrical properties b, h_{conc}, h_{steel}, d_{sr} and d_{s} are given in Fig. 6.10. These properties are used subsequently in the analysis. Note that since we are considering here the gross concrete area, the modular ratio for the reinforcing steel embedded in the concrete element is n-1 and not n.

(a) Section   (b) Short-term strains   (c)
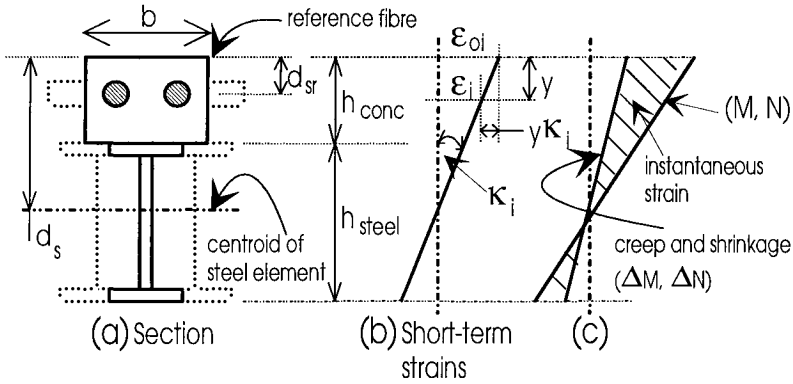
Fig. 6.10 Model of T-beam used for time dependent analysis

If ε_{oi} is the initial or short-term fibre strain in the section at the top of the concrete element (Fig. 6.10(b)) and κ_{i} is the initial curvature, the strain ε_{i} at any depth y below the top reference fibre may be written as

$$\varepsilon_{i} = \varepsilon_{oi} - y\kappa_{i} \qquad (6.26)$$

The short-term axial force N_{i} on the section (which is usually zero in a T-beam) may be obtained by integrating the short-term stresses as

$$N_{i} = \int E_{c}\varepsilon_{i}dA \qquad (6.27)$$

so that, from Eq. 6.26

$$N_{i} = E_{c}\varepsilon_{oi}A - E_{c}\kappa_{i}B \qquad (6.28)$$

where A and B are given by Eqs. 6.23 and 6.24 respectively. The short-term moment taken about the top reference surface may be obtained by integrating the first moment of the stress block about the top reference surface. Hence

$$M_{i} = -\int E_{c}\varepsilon_{i}ydA \qquad (6.29)$$

so that, from Eq. 6.26

$$M_i = -E_c \varepsilon_{oi} B + E_c \kappa_i I \tag{6.30}$$

where I is given by Eq. 6.25. Solving Eqs. 6.28 and 6.30 simultaneously for ε_{oi} and κ_i produces

$$\varepsilon_{oi} = \frac{BM_i + IN_i}{E_c\left(AI - B^2\right)} \tag{6.31}$$

and

$$\kappa_i = \frac{AM_i + BN_i}{E_c\left(AI - B^2\right)} \tag{6.32}$$

Of course, if $N_i = 0$ as in beams, the short-term flexural rigidity $E_c I_{nc}$ in Section 6.4.2 is merely M_i / κ_i .

It can be seen from Fig. 6.10(b) that the initial or short-term stresses σ_{ci} in the concrete element, σ_{si} in the steel element and σ_{sri} in the reinforcing steel are given by

$$\sigma_{ci} = E_c\left(\varepsilon_{oi} - y\kappa_i\right) \qquad y < h_{conc} \tag{6.33}$$

$$\sigma_{si} = E_s\left(\varepsilon_{oi} - y\kappa_i\right) \qquad y \geq h_{conc} \tag{6.34}$$

$$\sigma_{sri} = E_s\left(\varepsilon_{oi} - y\kappa_i\right) \tag{6.35}$$

6.7.2.2 *Long-term response*

For the time analysis applicable to a sustained moment M and axial force N, the relaxation procedure outlined by Gilbert (1988) is used. During any time interval, the strain state is frozen at (M,N) in Fig. 6.10(c) so that the strain distribution is assumed to remain unchanged. If the total strain is held constant, and the creep and shrinkage components change, then the instantaneous component of strain shown hatched in Fig. 6.10(c) must also change by an equal and opposite amount. As the instantaneous strain changes, so too does the concrete stress. The stress on the cross-section is therefore allowed to vary freely owing to relaxation. As a result, the internal actions change and equilibrium is not maintained. In order to restore equilibrium, an axial force ΔN and moment ΔM must be applied to the section. The change of strain due to creep and shrinkage may be considered to be artificially prevented by the restraining actions $-\Delta N$ and $-\Delta M$. When ΔN and ΔM are applied to the section, the restraining actions are removed and equilibrium is restored. It can thus be seen that the technique follows a similar procedure to that outlined in Section 6.6.

The restraining actions $-\Delta N$ and $-\Delta M$ are calculated easily in the following. If creep was not constrained in any way in Fig. 6.10, the top fibre strain and curvature would increase by $\phi\varepsilon_{oi}$ and $\phi\kappa_i$ respectively, where ϕ is the creep coefficient discussed in Section 2.3.3.2. The restraining forces required to prevent this deformation may be obtained, similarly to Eqs. 6.28 and 6.30, as

$$-\Delta N_{cr} \;=\; -\overline{E}_e\phi\left(A_{conc}\varepsilon_{oi} - B_{conc}\kappa_i\right) \tag{6.36}$$

and

$$-\Delta M_{cr} \;=\; -\overline{E}_e\phi\left(-B_{conc}\varepsilon_{oi} - I_{conc}\kappa_i\right) \tag{6.37}$$

where A_{conc}, B_{conc} and I_{conc} are the counterparts of Eqs. 6.23 and 6.25 for the concrete element only, as only the concrete is creeping, and $\overline{E}_e$ is the age-adjusted effective modulus given by Eq. 2.25.

If shrinkage is now uniform over the depth of the concrete element and is completely unrestrained, the shrinkage-induced top fibre strain which develops is simply the shrinkage strain ε_{sh}, and the curvature is zero. The restraining forces required to prevent this uniform deformation are again, similarly to Eqs. 6.28 and 6.30

$$-\Delta N_{sh} \;=\; -\overline{E}_e\varepsilon_{sh}A_{conc} \tag{6.38}$$

and

$$-\Delta M_{sh} \;=\; \overline{E}_e\varepsilon_{sh}B_{conc} \tag{6.39}$$

Hence summing Eqs. 6.36 and 6.38, and Eqs. 6.37 and 6.39, the restraining axial force and bending moment $-\Delta N$ and $-\Delta M$ respectively, that are required to prevent the free development of creep and shrinkage in the concrete element, are

$$-\Delta N \;=\; -\overline{E}_e\left\{\phi(A_{conc}\varepsilon_{oi} - B_{conc}\kappa_i) + \varepsilon_{sh}A_{conc}\right\} \tag{6.40}$$

and

$$-\Delta M \;=\; -\overline{E}_e\left\{\phi(-B_{conc}\varepsilon_{oi} + I_{conc}\kappa_i) - \varepsilon_{sh}B_{conc}\right\} \tag{6.41}$$

By using the transformed section properties $\overline{A}_e$, $\overline{B}_e$ and $\overline{I}_e$ corresponding to A, B and I in Eqs. 6.23 to 6.25 but using a modular ratio of $\overline{n} = E_s/\overline{E}_e$, the time-dependent change of top fibre strain $\Delta\varepsilon_o$ and curvature $\Delta\kappa$ may be obtained, similarly to Eqs. 6.31 and 6.32, as

$$\Delta\varepsilon_o \;=\; \frac{\overline{B}_e\Delta M + \overline{I}_e\Delta N}{\overline{E}_e\left(\overline{A}_e\overline{I}_e - \overline{B}_e^{\,2}\right)} \tag{6.42}$$

and

$$\Delta\kappa = \frac{\overline{A}_e \Delta M + \overline{B}_e \Delta N}{E_e\left(\overline{A}_e\overline{I}_e - \overline{B}_e^{\,2}\right)} \tag{6.43}$$

The final long-term top fibre strain ε is $\varepsilon_{oi} + \Delta\varepsilon_o$ and the long-term time-dependent curvature κ is $\kappa_i + \Delta\kappa$ under sustained service loading.

6.7.2.3 *Stresses*

Addition of the stress loss that occurs during the relaxation procedure and the gain in stress that occurs when ΔN and ΔM are applied to the cross-section gives the change in stress $\Delta\sigma_c$ in the concrete element at any point y below the top fibre. The loss of stress in the concrete distant y below the top fibre as a result of relaxation (when the strain state is initially frozen) is given by

$$\Delta\sigma_{relax} = -\overline{E}_e\{\phi(\varepsilon_{oi} - y\kappa_i) + \varepsilon_{sh}\} \tag{6.44}$$

and the change of stress which occurs when the actions ΔN and ΔM are applied to the section to restore equilibrium is

$$\Delta\sigma_{restore} = \overline{E}_e(\Delta\varepsilon_o - y\Delta\kappa) \tag{6.45}$$

Hence, the actual change in concrete stress $\Delta\sigma_c$ owing to the effects of creep and shrinkage caused by sustained service actions is

$$\Delta\sigma_c = \Delta\sigma_{relax} + \Delta\sigma_{restore}$$

$$= -\overline{E}_e\{\phi(\varepsilon_{oi} - y\kappa_i) + \varepsilon_{sh} - (\Delta\varepsilon_o - y\Delta\kappa)\} \tag{6.46}$$

while in the reinforcement, the stress change $\Delta\sigma_{sr}$ is

$$\Delta\sigma_{sr} = E_s(\Delta\varepsilon_o - d_{sr}\Delta\kappa) \tag{6.47}$$

and the stress change in the steel element $\Delta\sigma_s$, for $y \geq h_{conc}$ is

$$\Delta\sigma_s = E_s(\Delta\varepsilon_o - y\Delta\kappa) \tag{6.48}$$

6.7.2.4 *Deflections*

The curvature $\kappa = \kappa_i + \Delta\kappa$ may be integrated twice to obtain the deflection v of the beam under a sustained service moment M_i (or including the axial force N_i if it is nonzero) as

$$v = \int\int \kappa(x)dxdx \qquad (6.49)$$

subject to the appropriate boundary conditions, which for a simply supported beam is that $M_i = 0$ at the ends. In order to circumvent the rather tedious hand calculation of the curvature κ from the theory presented in Section 6.7.2.2, Bradford (1991) studied parametrically a large number of cross-sections with different creep coefficients and different shrinkage strains. Because of the linearity of the equations in Section 6.7.2.2 above, Bradford (1991) proposed that the curvature κ under sustained service loading be given by the simplified equation

$$\kappa = \alpha + \beta M \qquad (6.50)$$

where the shrinkage-induced coefficient α is

$$\alpha = \varepsilon_{sh}\left(\frac{1 + 0.2/(1+\phi)}{h_{conc} + h_{steel}}\right) \qquad (6.51)$$

in which ϕ is the creep coefficient, and in which

$$\beta = \frac{1}{E_c I_{nc}} \qquad (6.52)$$

where, as before, I_{nc} is the second moment of area of the transformed section relative to the concrete about the neutral axis of the transformed area. The validity of the curvature-moment relationship of Eq. 6.50 has been established by Bradford and Gilbert (1991).

Example 6.6   Time-dependent behaviour under sustained load

In order to demonstrate the time-dependent behaviour under sustained load, a simply supported T-beam was investigated both experimentally and theoretically by Bradford and Gilbert (1991). The composite beam had the following properties: L = 5.9 m, b_c = 1000 mm, h_{conc} = 70 mm, b_f = 133 mm, t_f = 7.8 mm, t_w = 5.8 mm, E_c = 25.2 kN/mm^2, and the slab was lightly reinforced. One of the beams was loaded with a superposed uniformly distributed service load of 7.52 kN/m, while the other beam was subjected to self-weight shrinkage deformations alone. The results of the measured shrinkage strains ε_{sh} in companion concrete specimens are given in Fig. 6.11, while the computed creep coefficient $\phi(t,10)$ from the test measurements is given in Fig. 6.12 for specimens loaded after 10 days.

Figure 6.13 shows the measured central deflection $v_{L/2}$ for both beams as a function of time. Using the design rule of Eq. 6.50 with the measured material properties, the midspan deflection was obtained, using Eq. 6.49, as

$$v_{L/2} = \int_0^{L/2}\int_0^x (\alpha + \beta M)dxdx \qquad (6.53)$$

so that, if $M_m = wL^2/8$ is the midspan moment for a uniformly distributed load w over a simply supported span of length L, then

$$v_{L/2} = \frac{\alpha L^2}{8} + \frac{5}{48} \frac{M_m L^2}{E_c I_{nc}} \tag{6.54}$$

where the parameter $\alpha L^2 / 8$ is the additional deflection due to the time-dependent response and the second parameter on the right is the short-term deflection. Values of the midspan deflection using the measured material properties were calculated from Eq. 6.54, and these are also given in Fig. 6.13. The agreement between theory and experiment is shown in the figure to be good.

For the beam subjected to self-weight load only, the deflection at $\tau = 10$ days when the props were removed was about 3 mm, and this increased more than fourfold to about 13 mm after t = 250 days. A similar increase from about 11 mm to 23 mm occurred for the beam subjected to superimposed sustained load. It is therefore important for the designer to be able to predict this time-dependent increase in deformation due a sustained service load, and the formulation of Eq. 6.50 permits this to be achieved rapidly.

In addition, Bradford and Gilbert (1992b) used the theory of Section 6.7.2.3 to determine the stresses σ_c in the concrete element. Under positive bending and with reduced superimposed loads, tensile stresses of the order of 1 N/mm^2 were calculated for high-shrinkage concretes. With large reinforcement ratios and small sustained loads, the tensile stresses increased so that tensile cracking under sagging bending due to shrinkage may be a problem. Measurements made by Roll (1971) on a real composite building also confirm this observation.

The assumption of negligible slip was investigated both experimentally and theoretically (Bradford and Gilbert 1992a). The theoretical study, which correlated closely with tests, ascertained that long-term deformations at service load levels are much greater than those caused by slip, so that at service loads the slip-induced deflections may be neglected for all but the most flexible connection. This is, of course, not the case as ultimate conditions are reached where the ramifications of slip are very important.
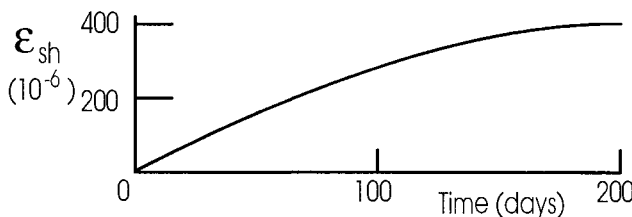
Fig. 6.11 Measured shrinkage strains
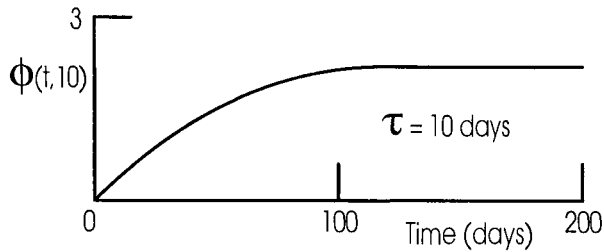
Fig. 6.12 Measured creep coefficient
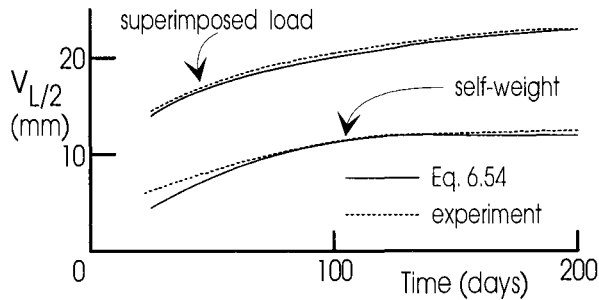
Fig. 6.13 Measured central deflection

6.7.3   CONTINUOUS BEAMS

The response of continuous beams under service loads is not nearly as straightforward as that for simply supported beams, since the prediction of behaviour under these sustained service loads is complicated by the time-dependent deformations in the concrete element due to creep and shrinkage, and the additional nonlinearity caused by cracking of the concrete over each internal support. Gilbert and Bradford (1995) addressed this problem, but could find virtually no research carried out on the time-varying behaviour of continuous composite beams subject to sustained service loads.

In a statically indeterminate beam, Gilbert and Bradford showed that the relationship between curvature κ and moment M in positive or sagging bending can be written, similarly to Eq. 6.50 as

$$\kappa \quad = \quad \alpha_1 + \beta_1 M + \gamma_1 \delta M \tag{6.55}$$

where in addition to the initial applied moment M, each cross-section is subjected to a time-dependent increment of applied moment δM that is caused by changes in the restraining moments induced by the time-dependent effects (not to be confused with ΔM), in which the increment of curvature $\delta \kappa$ caused by δM is expressed as $\gamma_1 \delta M$, and where the constants α_1, β_1 and γ_1 in Eq. 6.55 are given by

$$\alpha_1 = \frac{\varepsilon_{sh}\left(\overline{B}_e A_{conc} - \overline{A}_e B_{conc}\right)}{\overline{A}_e \overline{I}_e - \overline{B}_e^2} \tag{6.56}$$

$$\beta_1 = \frac{1}{E_c\left(AI - B^2\right)}\left[A + \frac{\phi\left(A_{conc}B\overline{B}_e - B_{conc}A\overline{B}_e - B_{conc}B\overline{A}_e + I_{conc}A\overline{A}_e\right)}{\overline{A}_e \overline{I}_e - \overline{B}_e^2}\right] \tag{6.57}$$

and

$$\gamma_1 = \frac{\overline{A}_e}{\overline{E}_e\left(\overline{A}_e \overline{I}_e - \overline{B}_e^2\right)} \tag{6.58}$$

A similar relationship to Eq. 6.55 holds for a cracked cross-section in negative bending, but where the tensile portion of the concrete is ignored.

During a period of sustained service load, cracking of the slab may occur on previously uncracked cross-sections, since the hogging moments at interior supports tend to increase with time in a continuous beam. This further reduction in stiffness is handled numerically in the analysis of Gilbert and Bradford (1995) at the end of each time period by checking the concrete stress levels on previously uncracked cross-sections and re-analysing the sections on which time-dependent cracking is detected. The procedure is ideal for computer application.

The bending moment diagram, and hence the distribution of deflections, may be obtained from an analysis of the continuous beam in the x-direction by invoking the principle of virtual forces. This was performed by Gilbert and Bradford, where the predicted deflections for a two-span beam agreed very well with their test results. In their study, they found that with increasing time, the sagging moment is reduced, but the hogging moment over the internal support increases substantially. The hogging moment region of the beam also increases, so that time-dependent cracking of the concrete element would be expected to move from the internal support toward the end supports as the duration of the sustained load increased. This behaviour of continuous beams subjected to sustained loads in the time domain should therefore be borne in mind by the structural designer.

6.8 References

Ansourian, P. and Roderick, J.W. (1978). "Analysis of composite beams", Journal of the Structural Division, ASCE, Vol. 104, No. ST10, 1631-1645.

Bradford, M.A. (1991). "Deflections of composite beams subjected to creep and shrinkage", ACI Structural Journal, Vol 88, No. 5, 610-615.

Bradford, M.A. and Gilbert, R.I. (1989). "Nonlinear behaviour of composite beams at service loads", The Structural Engineer, Vol. 67, No. 14, 263-268.

Bradford, M.A. and Gao, Z. (1992). "Distortional buckling solutions for continuous composite beams", Journal of Structural Engineering, ASCE, Vol. 118, No. 1, 73-89.

Bradford, M.A. and Gilbert, R.I. (1991) "Experiments on composite T-beams at service loads", Civil Engineering Transactions, Institution of Engineers, Australia, Vol. CE33, No. 4, 285-291.

Bradford, M.A. and Gilbert, R.I. (1992a) "Composite beams with partial interaction under sustained loads", Journal of Structural Engineering, ASCE, Vol. 118, No. 7, 1871-1883.

Bradford, M.A. and Gilbert, R.I (1992b) "Time-dependent stresses and deformations in propped composite beams", Proceedings, Institution of Civil Engineers Structures and Buildings, London, Vol. 94, 315-322.

Eurocode 4 (1994). *Design of Composite Steel and Concrete Structures*, DDENV 1994-1-1:1994. Draft for development.

Clough, R.W. and Penzien, J. (1975). *Dynamics of Structures*, McGraw-Hill, New York.

Gilbert, R.I. (1988). *Time Effects in Concrete Structures*, Elsevier, Amsterdam.

Gilbert, R.I. and Bradford, M.A. (1995). "Time-dependent behaviour of continuous composite beams at service loads", Journal of Structural Engineering, ASCE, Vol. 121, No. 2, 319-327.

Hall, A.S. (1984). *An Introduction to the Mechanics of Solids*, John Wiley, Sydney.

Irvine, H.M. (1986). *Structural Dynamics for the Practising Engineer*, Allen and Unwin, London.

Johnson, R.P. and May, I.M. (1975). "Partial interaction design of composite beams", The Structural Engineer, Vol. 53, 305-311.

Newmark, N.M., Siess, C.P. and Viest, I.M. (1952). "Studies of slab and beam highway bridges, Part III- Small scale tests of shear connectors and composite T-beams", Bulletin 396, University of Illinios, Urbana, Illinios.

Roll, F. (1971) "The effects of differential creep and shrinkage on a composite steel-concrete structure", ACI Special Publication SP-9, No. 5, 115-128.

7   Ultimate Strength Rigid Plastic Analysis

7.1   Introduction

The behaviour of composite beams in which the materials remain essentially linear elastic has been described in Chapter 6. It has been shown that linear elastic analysis can be applied at working or service loads to control both serviceability limit states such as deflections and crack widths and the ultimate limit state of fatigue. Linear elastic analysis can also be applied at ultimate loads to determine the onset of buckling, or when yield first occurs. However, in order to determine the maximum possible strength of a composite beam, we have to revert to nonlinear techniques such as rigid plastic analysis. In this chapter, we will determine the maximum possible strength of standard composite steel and concrete beams, of the type shown in Fig. 1.8, where neither the steel nor the concrete elements are encased by the other.

The maximum attainable strength of a composite steel and concrete beam can be determined using a *rigid plastic analysis*, which assumes that the materials are either not stressed at all or are fully yielded with an infinite deformation capacity at the yield stress or plastic plateau, as shown in Fig. 7.1. The rigid plastic strength is therefore an upper bound to the strength of the composite beam and requires that all other modes of failure do not occur prior to this strength being achieved. It is therefore necessary to ensure that premature failure through the following modes does not occur: local buckling of the steel elements as described in Chapter 5; lateral-distortional buckling of the steel as described in Chapter 10; fracture of the shear connectors because of their limited slip capacity which is dealt with in Chapter 8; and failure of the concrete element due to the concentrated dowel loads imposed on it by the shear connectors, and this is covered in Chapters 11 to 14. Furthermore, it may also be necessary to ensure that the composite beam has sufficient rotational capacity to attain these ultimate strengths, and this is covered in Chapter 9.
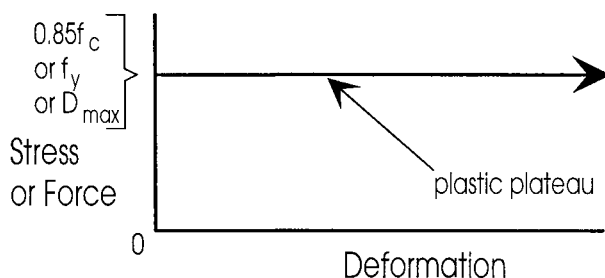
Fig. 7.1 Idealised material properties

168

7.2   Rigid plastic material properties

Before a section can be analysed, it is necessary to define the idealised material properties, represented in Fig. 7.1, for the concrete element, for the steel element and for the mechanical shear connectors.

The material behaviour of concrete has been described in Section 2.3, and the idealised properties have been defined in Section 2.3.2 and summarised in Fig. 2.8. As we are assuming that all the materials have yielded, we will be dealing with very large curvatures κ as shown in Fig. 7.2(b) and hence a typical example of the stress distribution near the maximum load resembles (c). The concrete is in compression in region A, is in tension in region B and cracked through tension in region C. Because the curvature and hence the strain gradient are assumed to be large, region B can be assumed to be very small compared with region A, and therefore it will have an insignificant effect on the flexural strength of the beam. It is therefore normal practice to assume that the tensile strength of the concrete is zero.
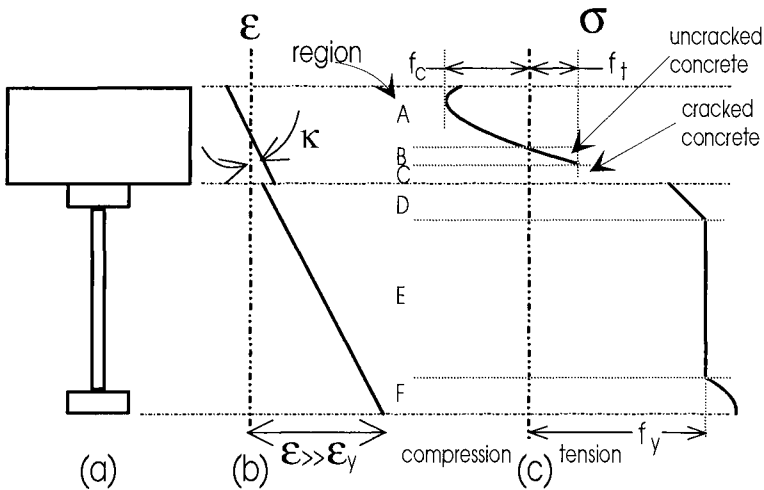
Fig. 7.2 Real behaviour of composite beams

We will allow for the nonlinearity in the concrete in compression in region A in Fig. 7.2(c) by following the currently accepted procedures, as shown in Fig. 2.8, that assume an effective yield strength of $0.85f_c$. Furthermore, as we are dealing with standard composite beams where one element does not encase the other, it will not be necessary to ensure that the steel element has fully yielded when the concrete crushes at a strain of 0.003, and so there will be no need to define the real neutral axis using the γ factor as suggested in Section 2.3.2 and applied to reinforced concrete beams. Hence the concrete in compression will be assumed to be fully yielded with an unlimited plastic plateau, as shown in Fig. 7.1. Furthermore, as the tensile strength is assumed to be zero, any neutral axis in the concrete element will occur at a step change in stress from $0.85f_c$ to zero.

The steel element of a composite beam will have the material properties shown in Fig. 2.2, and hence at large curvatures in the beam, the steel element will have the stress distribution shown in regions D, E and F in Fig. 7.2(c). As the strains at fracture, ε_{fr} in Fig. 2.2, can be orders of magnitude times the strain at first yield ε_y it is very unlikely that the steel will fracture before the concrete crushes, and so the assumption of an infinite plastic plateau as depicted in Fig. 7.1 is adequate. Moreover, the linear elastic zone in region D in Fig. 7.2(c) will be very small or non-existent because of the high curvatures, and for ease of calculation this region will be assumed to be fully yielded. This may appear to give a slightly unconservative result, but this is compensated for by the increase in strength through strain hardening of the steel which is usually ignored in practice. Hence the steel element in both the tensile and compressive regions will be assumed to be fully yielded at f_y and to have an unlimited strain capacity.

It was explained in Section 2.4.5 that the load/slip characteristics of mechanical shear connectors range from the brittle to the ductile, as shown in Fig. 2.17. Rigid plastic analyses can only be applied to structures made from materials with large plastic plateaux and hence can only be applied to composite beams made with ductile connectors, such as the stud shear connectors described in Section 2.4.6. It will therefore be assumed when dealing with the forces in the connectors that they are always fully loaded at an effective yield load of D_{max} as shown in Fig. 7.1, and that they have an unlimited slip capacity. Techniques for ensuring that the ultimate slip capacity S_{ult} shown in Fig. 2.18 is not exceeded are described in Chapter 8.

In the following sections, the positive or sagging region of the composite beam, as shown in Figs. 1.12(b) and (c), is dealt with separately from the negative or hogging region of the beam, as in Figs. 1.12(d) and (e), even though it will be seen that the analysis procedures used in both regions are similar.

7.3   Flexural strength of positive or sagging regions

7.3.1   GENERAL

Having now defined the idealised material properties, the next step is to define the dimensions of the cross-section of the beam to be used in the analysis. Consider the cross-section of the composite T-beam shown in Fig. 7.3(a). The effective dimensions of the concrete element for use in the analysis can be determined from Chapter 4. Chapter 5 can be used to determine whether local buckling of the web and flange components of the steel element occurs prior to the rigid plastic strength being achieved. If local buckling does occur prematurely, then Chapter 5 can be used to determine effective sizes to be used in the analysis procedure.

The rigid plastic analysis of the sagging region of a continuous composite beam between points of contraflexure, as shown in Fig. 1.12(a), is the same as the analysis of a simply supported beam between supports. This is because at both the supports of the simply supported beam and the points of contraflexure in the

continuous beam, the flexural force in the concrete and steel elements is zero. Hence the following analyses on simply supported beams can also be applied directly to the sagging region of a continuous beam. It is also worth re-emphasising the point that that the forces in the concrete element in the sagging region vary, as shown in Fig. 1.19, from $F = 0$ to $F = F_{conc}$ over the length L_{sp}.
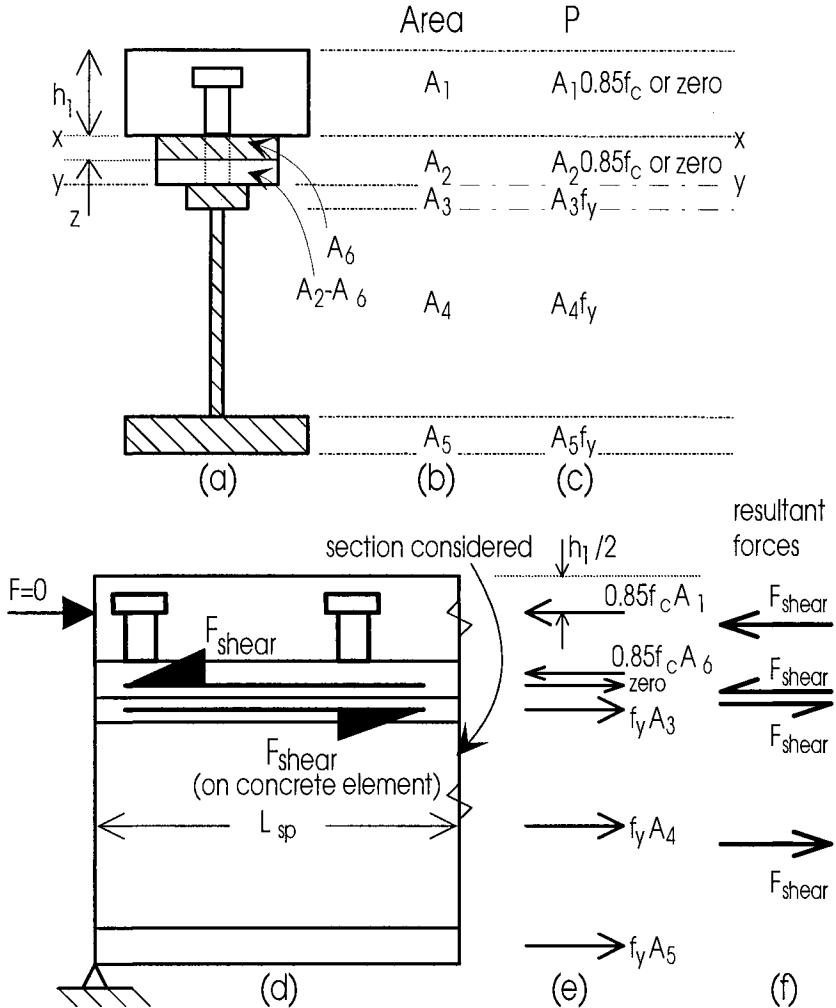

Fig. 7.3 Rigid plastic analysis

As the magnitudes of the 'yield stresses' or 'yield loads' are fixed at $0.85f_c$, f_y or D_{max}, the rigid plastic flexural strengths of composite beams can be determined directly from equilibrium of the forces, and there is no need to consider compatibility or deformation of the section. The distribution of the flexural forces and the terminology used in describing them are explained in qualitative terms in Section 1.2.4, and it is suggested that the reader glance through this section before proceeding.

The method of analysis that is used to determine the flexural strengths depends on whether there is full shear connection, as shown in Cases 1 and 2 in Fig. 1.20, or whether there is partial shear connection, as shown in Case 3.

7.3.2 FULL SHEAR CONNECTION

7.3.2.1 *Position of neutral axis*

Having now defined the material and geometric properties of the beam in the previous sections, the next step is to find the position of the neutral axis. The possible distributions of the strain profile for beams with full shear connection are shown in Figs. 1.20(c) and (f). It can be seen that beams with full shear connection only have one neutral axis which can occur in either the steel element or concrete element.

The neutral axis can be determined by considering the distribution of the axial strengths of each of the elements of the composite beam in Fig. 7.3(a). In this example, the steel and concrete elements have been subdivided into their rectangular parts and the cross-sectional areas of these parts are listed in (b). The axial strengths of these parts are listed in (c), where it can be seen that the concrete components can have either a zero tensile strength or a compressive strength depending on the position of the neutral axis. However, the tensile and compressive strengths of the steel component are the same.

The neutral axis can simply be found by determining the level at which the sum of the compressive strengths above the neutral axis is equal to the sum of the tensile strengths below, as there is no externally applied axial load. As an example, at level x-x in Fig. 7.3(c) the compressive strength above x-x is $A_1 0.85 f_c$, while the tensile strength below x-x is $(A_3+A_4+A_5)f_y$, because the tensile strength of the concrete area A_2 is zero. If at level x-x the compressive strength above this level is less than the tensile strength below this level, that is

$$A_1 0.85 f_c \quad < \quad \left(A_3 + A_4 + A_5\right)f_y \tag{7.1}$$

but at level y-y the compressive strength above is greater than the tensile strength below, that is

$$\left(A_1 + A_2\right)0.85 f_c \quad > \quad \left(A_3 + A_4 + A_5\right)f_y \tag{7.2}$$

then the neutral axis must lie between these two levels. It is now a simple algebraic procedure to find its exact position between these two levels by equating strengths. For example, if we assume that the neutral axis divides area A_2 into areas A_6 and A_2-A_6, then

$$\left(A_1 + A_6\right)0.85 f_c \quad = \quad \left(A_3 + A_4 + A_5\right)f_y \tag{7.3}$$

which will allow us to calculate the area A_6 and hence the depth z of area A_6 which defines the position of the neutral axis.

7.3.2.2 Distribution of flexural forces

Having determined the position of the neutral axis, we know the distribution of the flexural forces across the section, and these are shown in Fig. 7.3(e). These are the forces at a distance L_{sp} from the support (or from the point of contraflexure if it is a continuous beam) as shown in (d). The zero force in (e) is there to remind the reader that the concrete below the neutral axis is in tension and is therefore assumed to have no strength. Because the section was subdivided into rectangular parts, the forces shown in (e) act at the mid-depth of their rectangular part of the cross-section. For example, the force in area A_1 of depth h_1 in (a) acts at a depth $h_1/2$ from the top surface, as shown in (e).

At this stage of the analysis, we have to check that the initial assumption of full shear connection is correct. We have to ensure that the connectors are sufficiently strong so that they do not affect the force distribution shown in Fig. 7.3(e). This can be achieved by considering the equilibrium of forces in the concrete element in (d), between the section being considered and the support. The concrete element is subjected to the flexural forces in the concrete of

$$F_{conc} = 0.85 f_c \left(A_1 + A_6 \right) \tag{7.4}$$

when the neutral axis is in the concrete element, or to

$$F_{conc} = 0.85 f_c \left(A_1 + A_2 \right) \tag{7.5}$$

when the neutral axis is in the steel element. As the force in the concrete at the supports in (d) is zero, the flexural force in the concrete F_{conc} must be resisted by the shear force F_{shear} that the shear connectors impose on the concrete element and which acts towards the right as shown, so that from statics

$$F_{conc} = F_{shear} \tag{7.6}$$

Hence the total strength of the shear connectors over the span L_{sp}, which we will call P_{shear}, has to be greater than or equal to the shear force F_{shear}, that is

$$P_{shear} \geq F_{shear} = F_{conc} \tag{7.7}$$

where F_{conc} is given by either Eqs. 7.4 or 7.5. Simply stated, the strength of the shear connectors in the shear span must be greater than or equal to the force in the concrete for there to be full shear connection. If this is not the case, then there is partial shear connection and the analysis procedure for this is described in Section 7.3.3.

It is worth noting at this stage of the analysis that for both full or partial shear connection, the force on the shear connectors in a shear span is equal to the axial force in the concrete element, and that a rigid plastic analysis is not affected by the position of these connectors within a shear span. Methods for distributing these shear

connectors are given in Section 7.5.2. Note also in Fig. 7.3(d) that the shear force at the steel/concrete interface has been depicted as a parallel system of forces of equal but opposite magnitude of F_{shear}. Hence a force of F_{shear} acts on the concrete element, but the resultant force across the steel/concrete interface is zero and so does not directly contribute to the force system in (e).

7.3.2.3 Neutral axis in concrete element

In the majority of composite beams in buildings, the axial compressive strength of the concrete element, P_{conc} in Fig. 7.4(b), is greater than the axial tensile strength of the steel element, P_{steel} in (b). Therefore, in order to maintain equilibrium, the whole steel element must yield in tension, only part of the concrete element will be fully yielded in compression and the remainder of the concrete will have cracked under tensile stress. The neutral axis will then lie in the concrete element as shown in (c), and the stress profile will have the shape shown in (d).
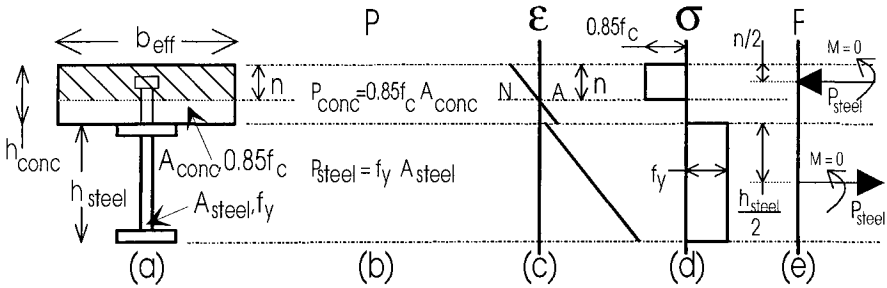
Fig. 7.4 Neutral axis in concrete element

The position of the neutral axis and then the distribution of flexural forces can now be determined as described in Sections 7.3.2.1 and 7.3.2.2. For the example shown in Fig. 7.3, the flexural force distribution is given in (e). The ultimate flexural capacity of the section can be derived by taking the moments of the flexural forces in (e) about any level of the beam.

For most composite beams with rectangular slabs and symmetrical I-sections, the solution is simple. For example, for the section in Fig. 7.4(a) and assuming that the I-section is symmetrical, then the tensile force in the steel element, P_{steel} in (e), acts at the mid-depth of the steel element as shown. The same force P_{steel} acts in the concrete element. This force acts over an area of concrete of width b_{eff} and depth n as shown in (a), and hence the neutral axis depth n can be derived from

$$P_{steel} = f_y A_{steel} = 0.85 f_c b_{eff} n \qquad (7.8)$$

As the cross-section over which the compressive stress acts is rectangular, the resultant force in the concrete, P_{steel}, acts at a distance n/2 from the top fibre of the beam, as shown in (e). The magnitude and position of the resultant axial forces in the

section are now known, so that the ultimate flexural capacity M_{fsc} can be derived by taking moments about any level. For example, taking moments about the top fibre of the beam produces

$$M_{fsc} = P_{steel}\left(\frac{h_{steel}}{2} + h_{conc}\right) - P_{steel}\frac{n}{2} \qquad (7.9)$$

In rigid plastic analysis, the stress distribution in the concrete element, as shown in Fig. 7.4(d), will always be compressive as we are treating the tensile strength of the concrete as zero. Hence there will not be a moment in the concrete element as depicted by $M = 0$ in the concrete element in (e). When the neutral axis is in the concrete element, the steel will be uniformly stressed in tension as shown in (d), and hence the moment in this element will also be zero as shown in (e). Because of this, when the neutral axis is in the concrete element, the ultimate strength is developed solely from the internal resistance due to the composite action as described in Section 1.2.4.2.

Example 7.1 Full shear connection flexural strength with neutral axis in concrete

Consider the composite beam shown in Fig. 7.5(a) in which the concrete has a compressive cylinder strength of 30 N/mm^2 and the steel has a yield strength of 250 N/mm^2. The concrete element consists of a composite slab whose soffit has transverse ribs of depth 40 mm, and so according to Section 4.3 the region of the ribs should be ignored in the analysis and hence the effective section has a void of depth 40 mm, as shown in (a).

The axial strength of the concrete element P_{conc} is greater than that of the steel element P_{steel} as shown in Fig. 7.5(b). Hence the concrete element is only partly stressed and the steel element is fully stressed as in (c), and the neutral axis lies in the concrete element as in (d). Because the steel element is fully stressed and symmetrical, the axial force in the steel element is equal to its strength and acts at mid-depth as in (e). For equilibrium, the force in the concrete must also equal 1545 kN and this acts over the shaded region in (a) of width 1500 mm and depth n and at a stress of $0.85f_c$ Solving for n gives the depth of the neutral axis from the top fibre as n = 40 mm. The magnitudes and positions of all the resultant forces in the section are now known as shown in (e), so the full shear connection moment capacity can now be determined by taking the moments of the forces in (e), giving M_{fsc} = 420 kNm. In order to achieve this moment capacity, the strength of the shear connectors in each shear span of the beam must be greater than or equal to the force in the concrete element of 1545 kN, so that the total strength of the shear connectors in the beam must be at least 3090 kN.

Rigid plastic analysis can also be used to determine the flexural strength of the steel element acting by itself. In this case, the axial forces induced are shown in Fig. 7.5(f) and this leads to a moment capacity of 199 kNm Hence tying the concrete slab to the steel beam using shear connectors increases the flexural strength by a factor of 2.1 (that is, 420/199). It may be worth noting, as shown in Chapter 6, that the flexural rigidity also increases by about the same amount, so that making the steel beam

composite with the existing concrete slab can double both the strength and stiffness, and lead to large increases in span to depth ratios.

The top flange of the steel element only plays a minor role in resisting flexure, and its main purpose is to support the shear connectors which tie the steel element to the concrete element. For example, if the top flange in Fig. 7.5(a) is removed, then the flexural strength reduces by 12%, even though the top flange contains 33% of the area of the steel in the original section. Hence the efficiency of hybrid beams of the type shown in Fig. 1.8(c) can be seen. Alternatively, if the bottom flange in Fig. 7.5(a) is doubled in width, then the flexural strength increases by 49%. This is why plated beams of the type shown in Fig. 1.8(b) can be very efficient forms of construction.
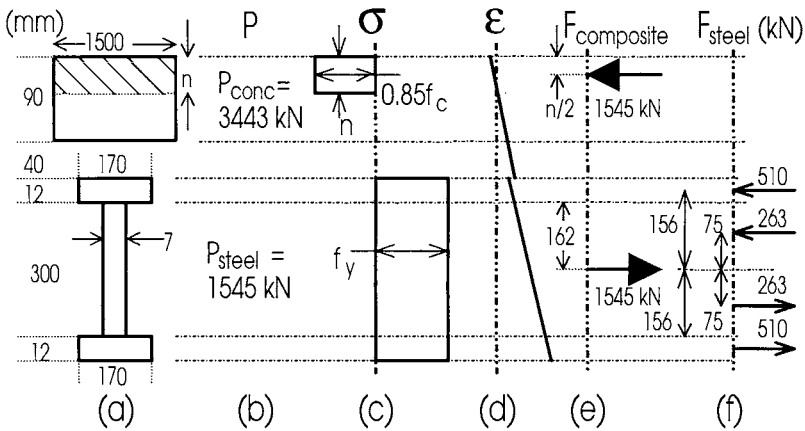
Fig. 7.5 Example 7.1 on full shear connection

7.3.2.4 *Neutral axis in steel element*

Occasionally composite beams have large steel elements, so that the axial strength of the steel element, P_{steel} in Fig. 7.6 (b), is greater than the axial strength of the concrete element P_{conc}. Therefore, the concrete element will have fully 'yielded' at $0.85f_c$ as in (d), and the resultant force in the concrete element will be the strength of the concrete element P_{conc} as in (e). The strength of the shear connectors in each shear span must be at least equal to P_{conc} in order to attain full shear connection.

As $P_{steel} > P_{conc}$, the neutral axis will lie in the steel element, as shown in Fig. 7.6(c), so that the upper part of the steel element will be in compression and the lower part in tension, as shown in (d). The resultant axial force in the steel element will be P_{conc}, as in (e), in order to be in equilibrium with the axial force in the concrete element.
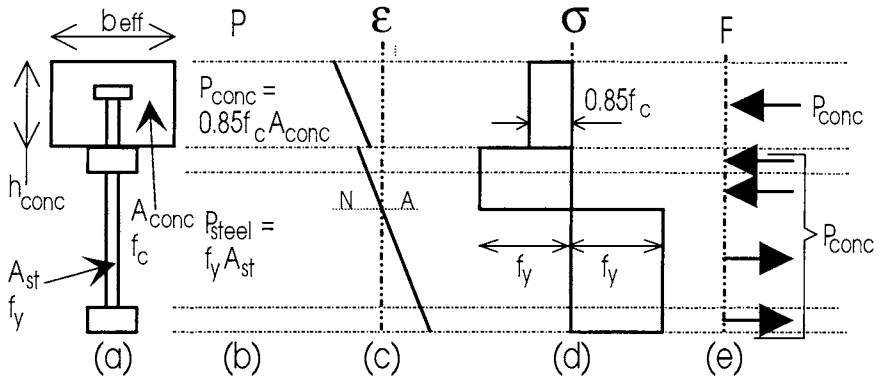
Fig. 7.6 Neutral axis in steel element

In deriving the flexural capacity, the position of the neutral axis must firstly be determined using the procedure described in Section 7.3.2.1 and illustrated in Fig. 7.3. It is necessary to determine the strength of each component of the steel element, as shown in (c), as the neutral axis could lie in either the web or the flange. Once the neutral axis is located, then the magnitude and distribution of the axial forces in the composite section, as shown in Fig. 7.6(e), are known and the flexural capacity can be determined by taking the moments of the axial forces. The applied load is now resisted by the moment M_{steel} in the steel section, as shown in Fig. 1.20(d), and the moment induced by the composite action $P_{conc}h_3$.

A slightly different calculation approach, that is more rapid when the I-section is symmetrical, is to use the equivalent stress system shown in Fig. 7.7(b) instead of the actual stress distribution shown in Fig. 7.6(d). It can be seen that the resultant of these two systems is identical. There is a slight saving in computational time because the centroid of the steel section is now known, assuming the section is symmetrical, and so the position of P_{steel} in the steel element in Fig. 7.7(c) is known. The position of the neutral axis still has to be determined using the procedure described previously in Section 7.3.2.1, and once this is established the magnitude and position of the resultant forces due to the stresses at $2f_y$ are known and hence the flexural capacity can be determined by taking the moments of the force system in (c).

Example 7.2 Equivalent stress block method with neutral axis in steel element

Consider the composite beam in Fig 7.8(a) in which the concrete has a compressive cylinder strength of 25 N/mm^2 and the steel has a yield strength of 450 N/mm^2. The concrete element consists of a composite slab with longitudinal ribs of depth 50 mm. The ribs and voids of this slab have an equal cross-sectional area as shown in Fig. 1.11(b), so that the total width of all the ribs will be equal to half the effective width of the slab, and this can be represented by a single haunch as shown in Fig. 7.8(a). The slope of the ribs should be allowed for in the analysis, as indicated by the dashed lines adjacent to the haunch in (a), however the error in assuming that the sides are vertical, as is done in this analysis, can be shown to be insignificant.

The axial strengths of each of the rectangular elements are listed in Fig. 7.8(b). The level of the neutral axis can be found by balancing the force above the neutral axis with the force below, and occurs in the top flange of the steel element and at a distance of 10.6 mm from the steel-flange/concrete-haunch interface. The shape and magnitude of the equivalent stress system in (c) is now known, and hence the positions and magnitudes of the resultant force distribution in (d). The flexural capacity can be determined by taking the moments of the forces in (d), and this produces M_{fsc} = 1322 kNm. The analysis assumes of course that there is full shear connection, and so the strength of the shear connectors in a shear span must at least equal the axial strength of the concrete element, which is 3124 kN. Therefore, the total shear strength of the shear connectors required in this simply supported beam or between points of contraflexure if the beam is continuous is 6248 kN.
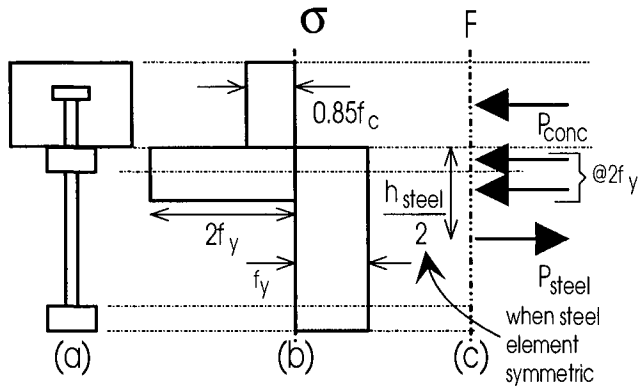
Fig. 7.7 Equivalent stress block
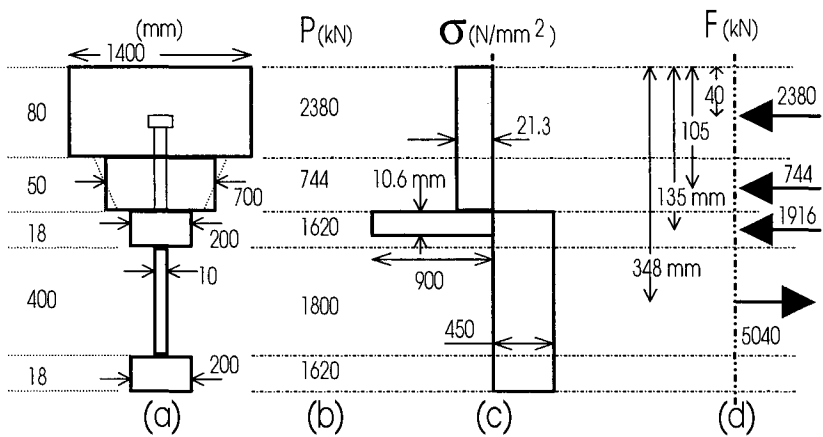
Fig. 7.8 Example 7.2 on equivalent stress system

7.3.3   PARTIAL SHEAR CONNECTION

7.3.3.1 *Distribution of forces*

When there is full shear connection, the resultant axial force in both the steel and concrete elements is equal to either the axial strength of the steel element, or the axial strength of the concrete element. For example, when the axial strength of the steel element P_{steel} is less than the axial strength of the concrete element P_{conc}, then the resultant force in both the steel element and the concrete element is P_{steel}, that is, the weaker of the two elements as shown in Fig. 1.20(a). Similarly, when $P_{conc} < P_{steel}$, the resultant axial strength in both elements must equal P_{conc}, that is, the weaker of the two elements as shown in Fig. 1.20(d). Hence, when there is full shear connection, the resultant axial force in both elements is equal to the axial strength of the weaker of the two elements. The axial strength of the weaker of the two elements in Fig. 7.9(a), that is the lesser of P_{steel} and P_{conc}, is referred to as P_{weak} in (b).
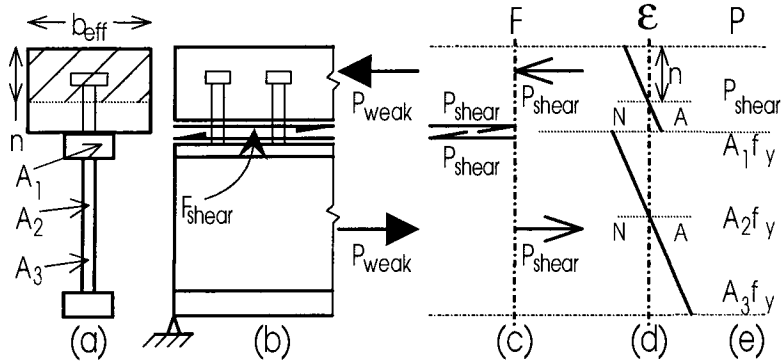
Fig. 7.9 Resultant axial force in each element

The whole beam in Fig. 7.9(b) must be in equilibrium, so that P_{weak} in the concrete element must be equal and opposite to P_{weak} in the steel element. Moreover, the individual elements of the composite beam must be in equilibrium, so that the force in the shear connectors F_{shear} must equal P_{weak}. When the strength of the shear connectors P_{shear} is not strong enough to resist P_{weak}, then the resultant force in all of the components of the composite beam is equal to the strength of the shear connectors as in (c). When the strength of the shear connectors governs the distribution of forces within a composite beam, then this is referred to as *partial shear connection* and occurs when

$$P_{shear} \quad < \quad P_{weak} \tag{7.10}$$

The force in the shear connectors at the steel/concrete interface has been represented by the shear forces on the left of the vertical line in (c), while the axial forces across the depth of the composite beam are shown on the right of the vertical line. The

diagram has been drawn this way to remind the reader, once again, that the shear forces do not contribute directly to equilibrium of the whole composite section, but they can control the axial forces in the composite section.

7.3.3.2 *Position of neutral axes*

Having now determined the magnitude of the axial forces in both the steel and concrete elements, the next step is to determine the strain distribution. When we were dealing with full shear connection, at least one of the elements was fully stressed in one direction as shown in Figs. 1.20(b) and (e) and so there was always one neutral axis within the other element. When there is partial shear connection, neither the steel nor concrete elements are fully stressed in one direction, as P_{shear} in Fig. 7.9(c) is less than P_{weak} in (b), so that both elements will have a neutral axis as shown in Fig. 1.20(i) and in Fig. 7.9(d).

The position of the upper neutral axis in the concrete element in Fig. 7.9(d) is easily determined by equating the axial force in the concrete element, P_{shear} in (c), with the strength of the area over which it acts, $0.85f_c b_{eff} n$, so that the depth of the rectangular stress block in compression, n in (a), can be determined. The position of the neutral axis in the steel element can be determined using the procedure outlined in Section 7.3.2.1. However in this case of partial shear connection, the equivalent strength of the concrete element is P_{shear} in Fig. 7.9(e), as this is the maximum force that can be applied to the concrete element. The position of the neutral axis in the steel element can now be found from (e), by determining the level at which the compressive force above is balanced by the tensile force below.

7.3.3.3 *Flexural capacity*

The distribution of flexural stresses within the composite beam can now be plotted as shown in Fig. 7.10(b), as the positions of the neutral axes are now known. From the stress distribution in (b), the distribution of the resultant forces in rectangular sections of the beam can be derived, as in (c). The stresses are uniform over the five rectangular elements in (a), and hence the magnitude of the resultant force in each rectangular element can be determined. Moreover, as the elements are rectangular, these forces act at the mid-depth of the rectangles, as shown in (c). The flexural capacity can be derived by taking the moments of these five forces. Alternatively, the equivalent stress block in (d) can be used, leading to the distribution of forces in (e) that consists of four forces instead of the five forces in (c).

It is now possible to determine the change in the flexural capacity of a composite beam with varying degrees of shear connection, as discussed in Section 1.2.5.5 and illustrated in Fig. 1.21. The flexural capacity varies from that of the steel section acting alone M_{steel} where the degree of shear connection is zero, to that of the composite section with full shear connection M_{fsc}. It is therefore necessary to construct at least part of the curve to determine the flexural capacity of a section with partial shear connection. An alternative simple but conservative method for determining the flexural capacity is to assume a linear interpolation between the two extreme values of M_{steel} and M_{fsc}, shown as M_{linear} in Fig. 1.21.
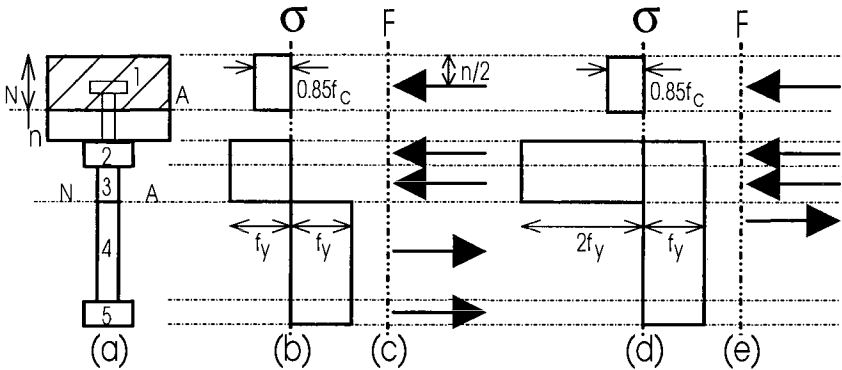
Fig. 7.10 Partial shear connection analysis

Example 7.3 Partial shear connection flexural strength of sagging region

Consider the beam analysed previously in Example 7.1 and shown in Fig. 7.5, in which the concrete strength is 30 N/mm^2 and the steel yield strength is 250 N/mm^2. The strength of the shear connection required for full shear connection is 1545 kN, which is the weaker of the axial strengths shown in (b). We will assume that the strength of the shear connection in a shear span is 75% of that required for full shear connection, that is 1159 kN. As defined in Section 1.2.4.4, the composite beam has a degree of shear connection $\eta = 0.75$.

The distribution of axial strengths is shown in Fig. 7.11(b), where the axial strength of the concrete element is shown as equal to the strength of the shear connectors in the shear span. Equating the force in the concrete element of 1159 kN with the strength of the rectangular block over which it acts, shown shaded in (a), gives the depth of the upper neutral axis n = 30 mm. The level of the neutral axis in the steel element can be derived from (b) by balancing the compressive force above with the tensile force below, giving the position of the neutral axis as 5 mm from the top surface of the upper steel flange. Using the equivalent stress system, represented in Fig. 7.10(d), gives the distribution and magnitude of forces shown in Fig. 7.11(c). Taking the moments of these forces produces a flexural strength of $M_{75\%} = 383$ kNm. If we now apply the linear interpolation technique shown in Fig. 1.21 to design a beam with a moment capacity of $M_{linear} = 383$ kNm, then the degree of shear connection required is 83% instead of the 75% that is required by the more accurate partial shear connection analysis.

It is worth noting that the flexural strength with full shear connection, which was derived in Example 7.1, is 420 kNm. The flexural strength of the same beam but with a degree of shear connection of 75% was found to be 383 kNm. Hence a 25% reduction in the degree of shear connection has only reduced the flexural strength by 9%. This example illustrates the point that the flexural strength of composite beams is not greatly sensitive to the degree of shear connection. Composite beams can

withstand a relatively large reduction in shear connector capacity without undue loss of flexural capacity.
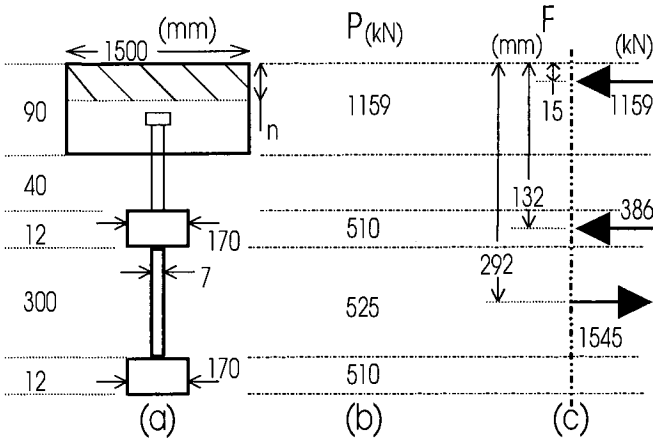
Fig. 7.11 Example 7.3 on partial shear connection

7.4 Flexural strength of negative or hogging regions

All of the procedures that have been developed in the preceding sections to determine the flexural strength of positive regions can be applied directly to determining the flexural strength of negative regions. Some of these procedures are illustrated in this section.

A composite beam under negative or hogging moments is shown in Fig. 7.12(a). The section being considered in the analysis is at B-B, which could be the position of the maximum negative moment. Section A-A represents the point of contraflexure in the beam when the member is continuous, and it could also represent the free end of a cantilevered beam. At A-A the axial load in both elements is zero, so that the force in the shear connectors over the shear span L_{sp} is equal to the force in the concrete element as well as the force in the steel element. The connectors are applying a tensile load to the concrete element, as shown in (a), and as the concrete is assumed to have zero tensile strength it will be fully cracked. Therefore, the effective cross-section for analysis will consist of the reinforcing bars and the steel element as in (c). The concrete element will not directly resist flexure, but is required to transfer the shear connector loads to the reinforcing bars. In order to allow for shear lag, the total area of the reinforcing bars to be used in the analysis, A_l in (c), will be the area of the reinforcing bars encompassed by the effective width w_{eff} of the section as shown, where w_{eff} can be derived from Section 4.2.
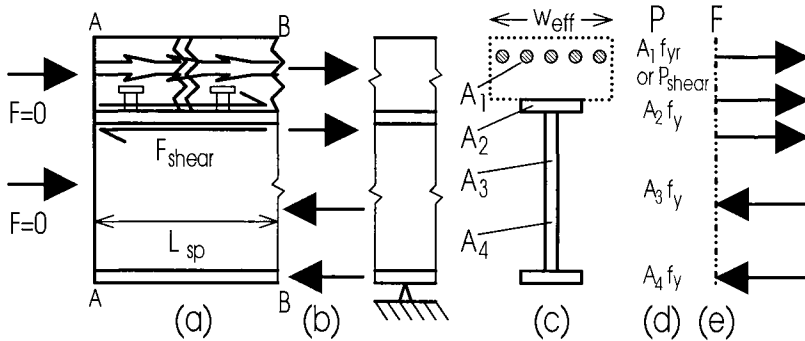
Fig. 7.12 Negative or hogging regions

Having defined the shape of the cross-section, the next step is to determine the position of the neutral axis from the axial strengths listed in Fig. 7.12(d). Let us assume in this example that the axial strength of the reinforcing bars $A_1 f_{yr}$ is less than the axial strength of the steel element $(A_2 + A_3 + A_4)f_y$ which is usually the case. When the strength of the shear connectors in the shear span P_{shear} is greater than the axial strength of the reinforcing bars $A_1 f_{yr}$, then the force in the concrete element is the strength of the reinforcement $A_1 f_{yr}$ in (d). This is the case for full shear connection, otherwise the force in (d) would be P_{shear}. The neutral axis can now be found by determining the level at which the tensile force above equals the compressive force below. Having found the position of the neutral axis, the magnitude and position of the axial forces in the steel element can be determined as in (e). The axial force in the concrete element acts in line with the centroid of the reinforcing bars. The flexural capacity can now be determined by taking the moments of the axial forces.

When the strength of the shear connectors in a shear span is less than the axial strength of the reinforcing bars, we have a case of partial shear connection, so that the reinforcing bars are only partly stressed and have a force in them of P_{shear} in Fig. 7.12(d). As this is a case of partial shear connection, there is a neutral axis in both the steel element and in the reinforcing bar element. The reinforcing bars are therefore subject to a moment, but as the depth of these bars is very small, this moment can be ignored. The remainder of the analysis is as described in the previous paragraph, bearing in mind that the axial force in the reinforcing bars is now P_{shear}.

Example 7.4 Flexural strength of negative region

Consider the composite beam in Example 7.1 and as shown in Fig. 7.5. It will be assumed that this beam is subjected to negative bending and that the strength of the reinforcement within the effective area of the slab is 468 kN, which is equivalent to an area of reinforcement of 0.6% of the area of the slab. We will consider a section of the beam in which there is full shear connection, so that the reinforcement is fully yielded.

The effective dimensions of the beam are shown in Fig. 7.13(a). The strengths of the elements are shown in (b), and by inspection it can be seen that the neutral axis lies in the web. Ensuring equilibrium of the compressive and tensile forces gives the neutral axis position as being 16 mm from the top of the web. The force distribution is shown in (c) and this is based on the equivalent stress system, such as that illustrated in Fig. 7.10(d). These forces give a flexural capacity of 292 kNm, which is 47% larger than the flexural capacity of the steel element as determined in Example 7.1, but 30% less than the flexural capacity of the composite section in the positive or sagging region.

7.5   Variations along the shear spans of composite beams

7.5.1   FLEXURAL STRENGTH

Figure 7.14(b) shows a simply supported composite beam in which the applied loads in (a) cause the maximum applied moment M_{max} to occur at section A-A, as shown in (e). Let us assume that the composite beam has been designed so that at section A-A the flexural strength of the beam is just sufficient to resist the maximum applied moment M_{max}, and let us also assume that the design was based on full shear connection so that the flexural capacity is M_{fsc} at A-A, and the strength of the shear connectors in each shear span is P_{fsc} as shown in (c).
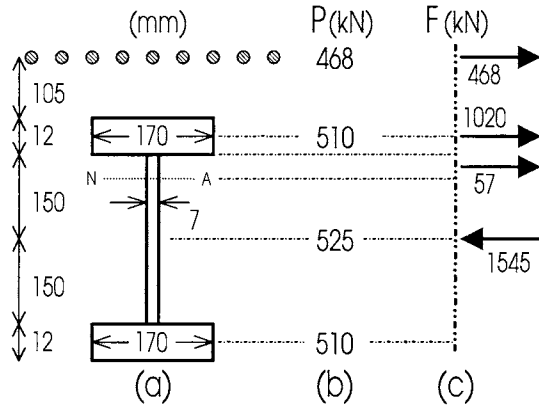
Fig. 7.13 Example 7.4 on the negative region

From rigid plastic analysis, the strength of the shear connection in the left hand shear span A-B in Fig. 7.14(b) must equal the strength of the shear connectors over the right hand shear span A-C, so that the number of connectors in each shear span will be the same. As rigid plastic analysis is based purely on an equilibrium approach, it cannot be used to determine the optimum distribution for these connectors. Techniques for determining the distribution of the connectors are covered in Section 7.5.2 and in Chapter 8. However for this analysis, we will assume that the connectors

are uniformly distributed within each shear span, so that the longitudinal spacing of the shear connectors in A-B in Fig. 7.14(b) will be greater than in A-C. Because the thrust of the connectors is of the same magnitude but of opposite direction in each shear span, as shown in (c), the slip of the connectors at section A-A will be zero. This is of fundamental importance for the analysis in Chapter 8.
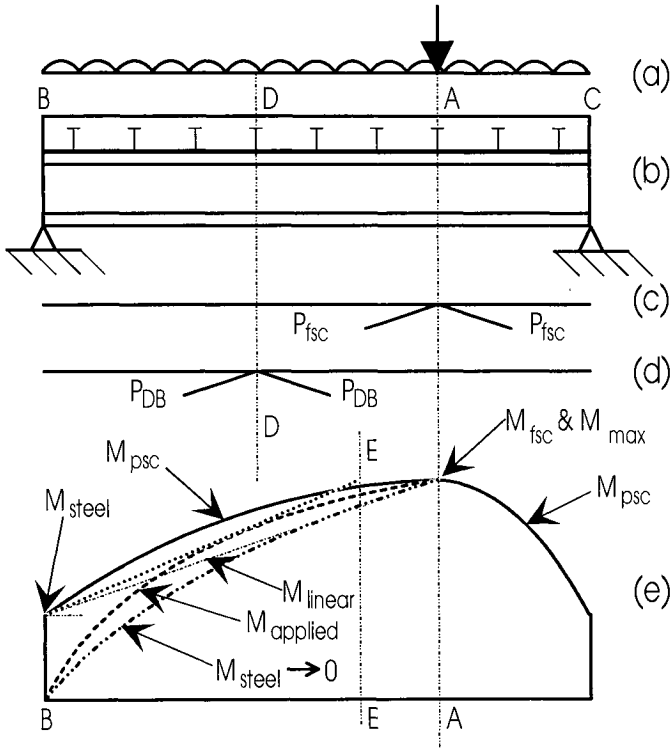
Fig. 7.14 Variation in strength along a beam

Let us now consider the beam at section D-D in Fig. 7.14(b) at a distance B-D from the left hand support. The maximum thrust that the connectors can apply to this section is governed by the weaker of the strengths of the shear connectors in each shear span. As the strength of the shear connectors in shear span D-B is less than the strength in shear span D-C, the strength of the shear connectors in shear span D-B, denoted P_{DB}, controls design as shown in (d), where the connectors to the left of D are fully stressed in the same direction, but those to the right are fully stressed but in both directions with a resultant force of P_{DB}. As P_{DB} is less than P_{fsc}, there is partial shear connection at section D-D and hence the strength at D-D must be less than the strength at A-A where there is full shear connection. The further the section is from A-A, the weaker is the composite beam, and at section B-B the degree of shear connection is zero, so that the flexural capacity is that of the steel element M_{steel}, as shown in (e). Therefore, the degree of shear connection in a composite beam varies throughout the beam. It is worth noting, however, that composite beams are often categorised with regard to the maximum degree of shear connection which will be

referred to as η_{max}, and that this parameter is of fundamental importance in preventing fracture of the shear connection, as described in Chapter 8.

The flexural capacity of the composite beam in Fig. 7.14(b) varies along its length from M_{steel} at the supports to M_{fsc} at the position of maximum moment as shown in (e). As in this illustration we are assuming that there is a uniform distribution of connectors, the variation in strength from B to A and from C to A will be the same as that derived from a partial shear connection analysis as for M_{psc} in Fig. 1.21. Because the flexural strength varies along its length, it is necessary to ensure that the flexural capacity exceeds the applied moment over the full length of the beam, and not just at the position of maximum moment. For example, if the flexural capacity envelope exceeds the applied moment envelope throughout the beam then the design is satisfactory.

It can be seen in Fig. 7.14(e) that for a given M_{fsc}, the probability of the flexural capacity M_{psc} being exceeded by the applied moment $M_{applied}$ within the shear span increases as M_{steel} reduces. When M_{steel} approaches zero in (e), as occurs when the steel element consists of a plate or a profiled sheet, then there is a high probability that the flexural capacity M_{psc} is exceeded by the applied moment $M_{applied}$ within the span. Also shown in (e) is the flexural capacity based on the linear interpolation procedure M_{linear}, and in this example M_{linear} is exceeded over much of the span. This problem can be overcome by simply adding more connectors, so that full shear connection is achieved at the section E-E, such that the M_{linear} line is now tangential to the applied moment envelope $M_{applied}$. Alternatively, all the connectors can be moved into the region B-E as, theoretically, connectors are not required in the region E-A.

Example 7.5 Variation in flexural strength along the length of a beam

Consider the beam in Fig. 7.5 that has already been analysed in Examples 7.1 and 7.3 Let us assume that the beam is simply supported, has a uniform distribution of shear connectors, has a maximum degree of shear connection of $\eta_{max} = 1$, is supporting a uniformly distributed load and that the maximum applied moment is equal to the maximum flexural capacity of the beam.

From the full and partial shear connection analyses illustrated in Examples 7.1 and 7.3, the variation in the flexural capacity of the beam with the degree of shear connection can be derived as curve 1 in Fig. 7.15. As the beam has a uniform distribution of shear connectors, the abscissa in the figure is also a measure of the distance from a support as shown in the brackets. Therefore, curve 1 is also the variation in the strength of the beam over the half span L/2. Curve 2 is the variation of applied moment. The flexural capacity envelope, curve 1, exceeds the applied moment envelope, curve 2, over most of the shear span except in region B, however the difference is small and could be ignored in design.

Curve 3 in Fig. 7.15 has been derived from a linear interpolation between M_{steel} and M_{fsc}. If design were based on M_{linear}, then the flexural capacity, curve 3,

would be exceeded by the applied moment, curve 2, by a large amount within region C. In this case it may be necessary to add more shear connectors to the beam or to redistribute the connectors, to raise the M_{linear} line above the applied moment $M_{applied}$. A simple solution is to first draw curve 4 as a linear variation tangential to curve 2 as shown. In order for the failure envelope that is represented by curve 4 to be achieved but not exceeded, the beam has to reach its maximum flexural capacity at a distance A from midspan as shown. Therefore, all the connectors required for full shear connection should be distributed within region D and an extra nominal amount placed in region A to ensure that the curvature between the steel and concrete elements is the same.
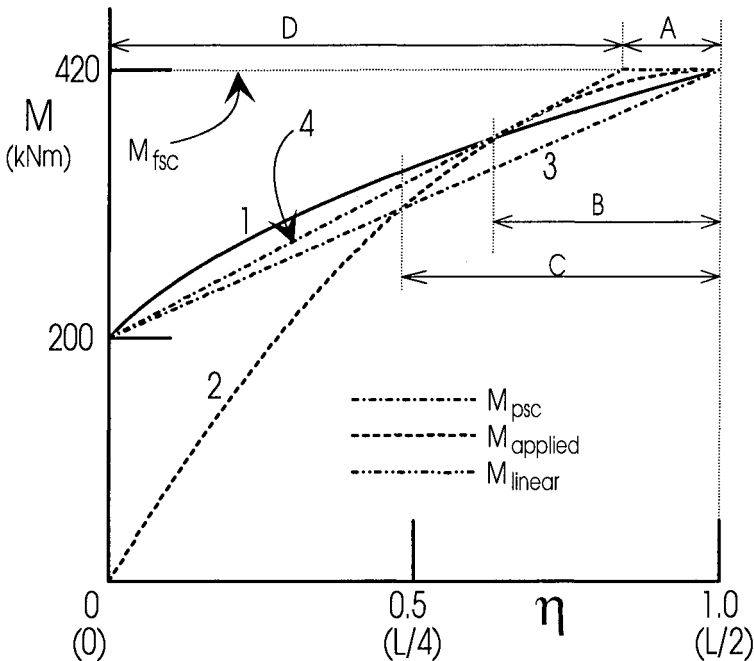
Fig. 7.15 Example 7.5 on variation in strength along beam

7.5.2   DISTRIBUTION OF SHEAR CONNECTORS

7.5.2.1 *General*

The connectors in a composite beam have to be carefully positioned within a shear span in order to ensure that the flexural capacity of the beam is never exceeded by the applied moment envelope, and also to ensure that the connectors do not fracture prior to the applied moment being achieved. This subject is covered in the following sub-section on global distribution. It is also necessary to ensure that the connectors do not damage the flange of the steel element, can achieve their dowel strength, and that they prevent the concrete element from separating from the steel element. This is discussed in the sub-section on local distribution.

7.5.2.2 *Global distribution*

It is normal practice for the engineer to design the composite beam at the position of the maximum applied moment, and hence determine the number of shear connectors in the shear spans on either side of the position of maximum moment. In most design cases, it would be impractical to ensure that the moment capacity exceeds the applied moment along the shear spans by using the analysis techniques described in Section 7.5.1 and which are based on first principles. Instead, rules of thumb or guidelines are often used by designers to decide on the distribution of the shear connectors.

One such guideline is to concentrate the connectors according to the distribution of the vertical shear force V, as the linear elastic shear flow q is directly proportional to V, as shown in Eq. 1.9. Take for example the beam shown in Fig. 7.16(a). The maximum moment occurs at midspan, and hence the number of connectors required in each half span can be determined from a rigid plastic analysis. These connectors should then be distributed according to the area of the vertical shear force diagram in (b), so that two-thirds of the connectors should be placed within the outer quarter spans and the remaining third within the middle quarter spans. The connectors should be uniformly distributed within each quarter span, as the distribution of the vertical shear force within these spans is also uniform. Even though this guideline for plastic strengths is based on the assumption of linear elastic shear flows, it does tend to prevent fracture of the shear connectors as will be described in Chapter 8.
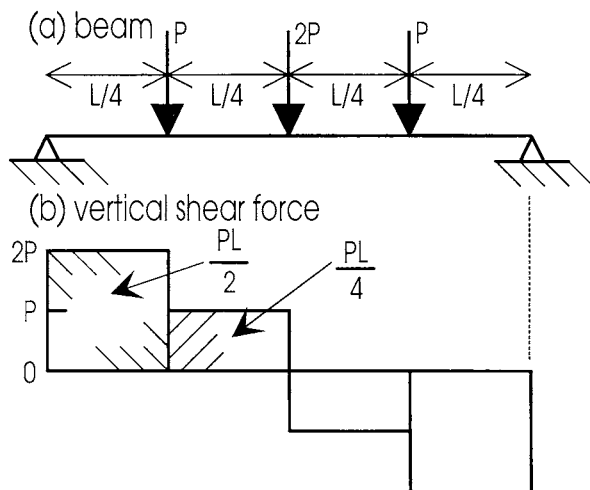
Fig. 7.16 Distribution of connectors in beam with concentrated loads

Consider the beam in Fig. 7.17(a) which has uniformly distributed loads as well as point loads. The connectors are once again distributed according to the areas of the shear force diagram in (b), so that the left quarter will have $A_1/(A_1+A_2)$ of the connectors in the left shear span, that is the left half of the beam. It is also standard

convention to distribute the connectors uniformly within each of the zones A-B, B-C and C-D, as indicated by the dashed line. A zone is defined as the length of beam between either concentrated loads, reactions, the position of maximum moment, or changes in geometry such as at a service opening in the web of the steel element.
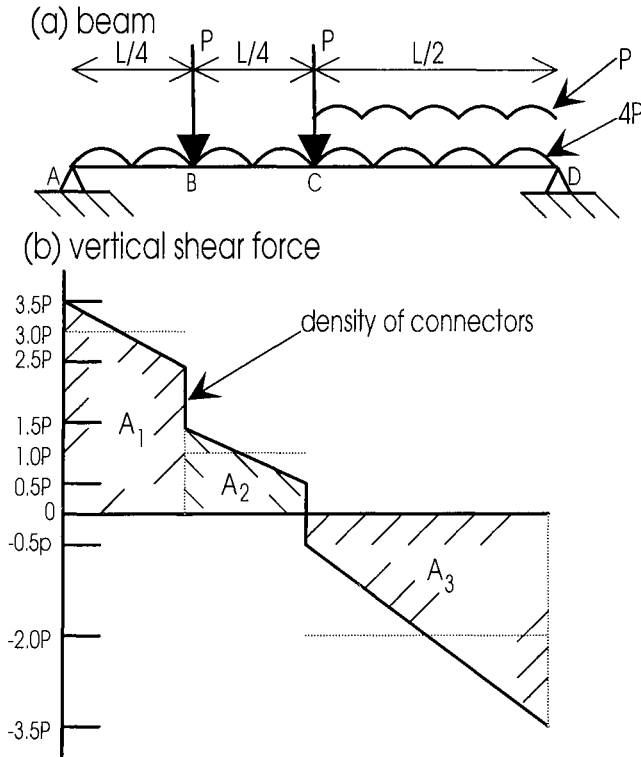
Fig. 7.17 Distribution of connectors in beam with uniformly distributed loads

7.5.2.3 *Local distribution*

Having now determined the number and distribution of connectors within a zone, it is necessary to determine the local position of the shear connectors to ensure that the full potential of the shear connection is achieved. This is done by using detailing rules which are often based on a limited amount of experimental data, and are seldom based on a theoretical understanding. For example, design standards often state that the longitudinal spacing of the shear connectors must not exceed 800 mm or six times the slab depth. This is required to ensure that the curvature in both the steel and concrete elements is the same, and by doing so it also restricts the vertical separation between the two elements and thus helps to prevent embedment failure which is described in Chapter 14.

Most detailing rules apply directly to stud shear connectors, as these are the most common form of shear connection. It has already been shown in Section 2.4.6.1

that the longitudinal spacing of stud shear connectors, of shank diameter d_{sh}, must be greater than $5d_{sh}$ and that the lateral spacing must exceed $4d_{sh}$ as shown in Fig. 7.18(a), in order to ensure that the dowel strength can be achieved. Furthermore, to ensure that the flange to which the stud is welded does not fail due to the forces imposed on it by the shear connectors, design standards often require that the flange thickness t_f is greater than about $0.4d_{sh}$ and that the distance from the side of the stud to the free edge of the flange is at least 25 mm, as shown in Fig. 7.18(b). It is felt that requiring a 25 mm edge distance for both large and small diameters is somewhat absurd, and it is suggested that this guideline should be changed to $1.3d_{sh}$.
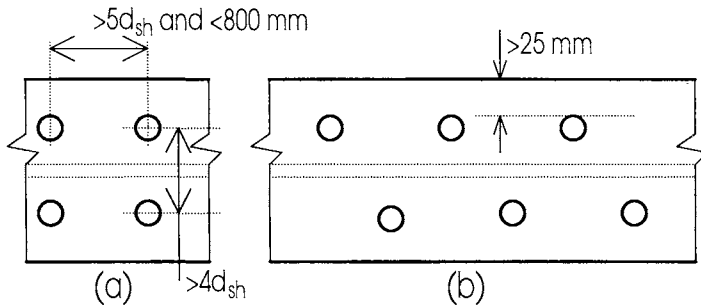
Fig. 7.18 Local position of stud shear connectors

Example 7.6 Distribution and detailing of shear connectors

A simply supported composite beam spans 6 m and has the load and shear force configuration shown in Fig. 7.17. The beam has the cross-sectional dimensions shown in Fig. 7.5, except that the slab is solid. This proviso does not change the flexural strength of the beam, as calculated in Example 7.1, but allows the shear connectors to be placed at any position along the length of the beam, otherwise the connectors would have to be placed in the troughs between the ribs. The slab is made from lightweight concrete with a density ρ of 2000 kg/m^3 and a cylinder compressive strength f_c of 30 N/mm^2. The slab is tied to the steel element with stud shear connectors which have a shank diameter d_{sh} of 16 mm, an ultimate tensile strength f_u of 500 N/mm^2, and the welding technique used creates a mean height of the weld collar h_{wc} of 2 mm.

From Example 7.1, the strength of the shear connection required in each span, A-C and C-D in Fig. 7.17(a), is 1545 kN. The characteristic strength of an individual connector in a group of n connectors can be derived from Eq. 2.37, and this produces

$$\left(D_{max}\right)_{beam} = \left(4.3 - \frac{1.1}{\sqrt{n}}\right)13365 \qquad (7.11)$$

where it has been assumed that E_s = 200 kN/mm^2 (Section 2.2), E_c = 21.1 kN/mm^2 (Eq. 2.14) and R_{WC} = 0.88 (Eq. 2.38). The number of connectors required can be

determined using the iterative procedure described in Section 2.4.6.3 (d). Starting the analysis with n = ∞, the bracketed term in Eq. 7.11 becomes $K_{ch} = 4.3$, which gives a characteristic strength of an individual connector of $D_{max} = 57.5$ kN and hence the number of connectors in the shear span N is 1545/57.5 = 26.9. This is the number of connectors that are required when the analysis is based on the mean strength. Substituting N = 26.9 for n in Eq. 7.11 and repeating the analysis produces D_{max} = 54.6 kN and N = 28.3, and a further iteration gives virtually the same result. It can be seen that the iterative procedure converges rapidly and because we assume that the connectors can fail as a group, we only require 28.3 - 26.9 = 1.4 more connectors than the requirement based on the mean strength. The number of shear connectors required in a shear span is therefore 29.

Consider the shear span A-C in Fig. 7.17(a). The connectors should be distributed in proportion to the areas A_1 and A_2 of the shear force diagram in (b). Hence the number of connectors required in zone A-B is 21.8. It has been shown that in rigid plastic analysis that it is better to concentrate the connectors towards the supports than at midspan, as this increases the flexural capacity within the shear span, although it does not affect the strength at the supports nor at midspan. Therefore, it would be preferable to increase the proportion of the connectors in zone A-B than in zone B-C, and so there should be 22 connectors in zone A-B and the remaining 7 connectors in zone B-C. Zone C-D will require the total number of 29. The connectors should be uniformly distributed within each zone.

Having defined the global distribution of the shear connectors, the local distribution of the connectors must now be determined. Zone A-B in Fig. 7.17(a) is 1.5 m long, therefore the longitudinal spacing for one line of connectors is 1500/22 = 68 mm, which is less than the permissible value of $5d_{sh} = 90$ mm. Two longitudinal lines of connectors are therefore necessary, and their lateral spacing should be greater than $4d_{sh} = 84$ mm. A lateral spacing of 100 mm will give a clearance between the side of the stud and the edge of the flange in Fig. 7.5(a) of 27 mm, which is greater than the suggested minimum requirement of $1.3d_{sh}$. Furthermore, as the flange thickness of 12 mm exceeds $0.4d_{sh} = 8.4$ mm, the flange should not be damaged by the connectors. In zone B-C in Fig. 7.17, the connectors can be placed in a single line at a spacing of 1500/7 = 214 mm, as this is greater than the minimum requirement of $5d_{sh}$ and is less than the maximum requirement of 800 mm. In zone C-D, the connectors could also be placed in a single line at a spacing of 1500/29 = 103 mm, which is close to the minimum allowable spacing of 90 mm. It will be shown in Chapter 11 that a single line of closely spaced connectors can cause the concrete element to split, and hence it would be better to stagger the connectors as shown in Fig. 7.18(b).

7.5.3 EFFECT OF SHEAR ON THE FLEXURAL CAPACITY

7.5.3.1 *General*

In positive or sagging regions, as shown in Fig. 1.12(b), the maximum moment occurs in a region of zero shear, so that the maximum flexural capacity of the composite

beam, such as M_{fsc} in Fig. 7.14(e), remains unchanged. At the other end of the shear span, such as at the left hand side of (e), the moment capacity is always greater than the applied moment which tends to be zero, so that any reduction in the moment capacity of this region due to shear can be ignored. There is therefore a general tendency to ignore the interaction between shear and flexure in positive moment regions.

In negative or hogging regions of a beam, as shown in Fig. 1.12(d), the regions of maximum shear and maximum flexure coincide, so that the flexural strength is reduced throughout this region by the interaction of these two actions. Hence vertical shear forces have a much greater effect in negative regions than in positive regions, and so procedures that allow for this interaction have been applied in the following sections to the negative regions, although it is worth noting that the same procedures can be applied to the positive region.

7.5.3.2 Material failure

The vertical shear force V in the composite beam is resisted by both the concrete element and the steel element, as shown in Fig. 1.18(b). However, it is difficult to quantify the shear resisted by the slab, and so most procedures assume that the shear is resisted only by the web of the steel element. As we are dealing with rigid plastic analysis where the stresses are all at yield, it is assumed that the shear stress is distributed uniformly throughout the web (Trahair and Bradford 1991). For rolled steel sections, the shear is assumed to be resisted by the full depth of the section D so that the uniform shear stress in the web τ_w is $V/(Dt_w)$, where t_w is the web thickness. For plate girders, the shear is assumed to be resisted by the web plate of depth d_w, so that $\tau_w = V/(d_w t_w)$.

The effect of shear stresses on the yield strength of steel plates can be determined from the von Mises yield criterion for biaxial stresses that is given in Eq. 2.2. We will assume that an element of the web, as shown in Fig. 2.3, is subjected only to a flexural stress $f_{1'}$ and a shear stress $f_{1'2'} = \tau_w$, so that the stress $f_{2'} = 0$. Substituting these values into Eq. 2.2 and rearranging gives

$$f_{1'} = \sqrt{f_y^2 - 3\tau_w^2} = f_{fy} \tag{7.12}$$

so that f_{fy} is the flexural stress to cause yielding in the presence of shear stresses τ_w.

7.5.3.3 Analysis technique

The composite beam can be considered to consist of three materials. The materials in the positive region have yield strengths of $0.85f_c$, f_y and f_{fy}, and the materials in the negative region have yield strengths of f_{yr}, f_y and f_{fy}. Consider the beam in Fig. 7.19(a) which represents a cross-section in the negative region of a composite beam with a rolled steel section. The axial strength at each level is shown in (b). Once

these strengths have been determined, the same procedure as outlined in Section 7.3 can be followed to determine the neutral axis and hence the flexural strength.
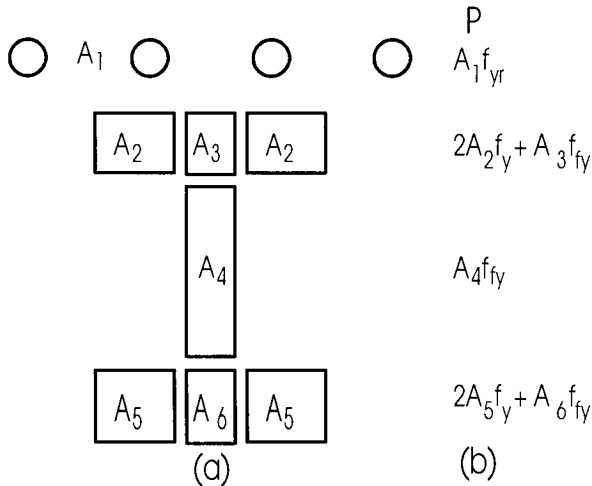
Fig. 7.19 Interaction between shear and flexure

Example 7.7 Reduction in flexural capacity due to vertical shear forces

The continuous composite beam in Fig. 1.12(a) has a span of L = 8 m and is made from a rolled steel section. The equivalent cross-section of the beam in the positive region (c) has the dimensions in Fig. 7.5(a), and that in the negative region in Fig. 1.12(e) has the dimensions in Fig. 7.13(a). The restraints at the supports of the beam in Fig. 1.12(a) are symmetrical and the beam is subjected to a uniformly distributed load with a total value of W kN. Hence the behaviour of the beam is symmetrical about midspan. The negative region of the beam has a flexural capacity of 292 kNm, from Example 7.4, while the positive region has a flexural capacity of 420 kNm, from Example 7.1.

While the beam remains elastic, the maximum applied negative moment is twice the maximum positive moment, and as the moment capacity of the negative moment region is much less than that of the positive moment region, plastic hinges will first form at the supports. From simple statics, the applied load to cause the negative moment capacity of 292 kNm to be reached is W = 438 kN. Therefore at this load, the shear load at the supports is 219 kN and that at the points of contraflexure is 127 kN.

At the supports, the degree of shear connection $\eta = 1$, so that the strength of the shear connection does not affect the axial forces in the member when calculating the flexural capacity. The shear stress in the web is $219 \times 10^3/(324 \times 7) = 97$ N/mm^2, and substituting this into Eq. 7.12 gives an effective yield stress of the web $f_{fy} = 186$ N/mm^2. The rigid plastic calculation follows the same sequence as has already been described several times in this chapter. The results of the analysis are shown in Fig.

7.20, and this can be compared with the same calculation for the section without shear which is shown in Fig. 7.13. In this case, the composite section consists of three materials as shown in Fig. 7.20(a), which gives the strength distribution in (b), leading to the force distribution in (c) and a flexural capacity of 270 kNm. It can thus be seen that the shear forces have reduced the flexural capacity by 8% from 292 kNm from Example 7.4 to 270 kNm in this example.

A similar calculation can be followed for the composite beam at the point of contraflexure where the shear force is 127 kN. As the degree of shear connection at this position is zero, the axial force in the reinforcement is zero, so we are dealing with the steel section acting by itself. The flexural capacity of the steel section without shear is 199 kNm, from Example 7.1, and the shear force of 127 kN reduces this value to 195 kNm, which is a reduction of 2%.

Let us suppose that the composite beam has sufficient rotational capacity to resist a greater load by redistributing the moments, as will be treated more fully in Chapter 9. The maximum shear stress that can be applied to the web is $f_y / \sqrt{3}$, which can be derived from Eq. 7.12 by substituting $f_{fy} = 0$. Therefore the maximum shear load in the web is $324 \times 7 \times 250 / \sqrt{3} = 327$ kN. At this shear load $f_{fy} = 0$ in Figs. 7.20(a) and (b), and the flexural capacity at the supports has reduced to 206 kNm, which is a reduction of 29% from the strength without shear. This is the maximum reduction in the flexural strength that can occur through shear. However, in this continuous composite beam the maximum positive moment capacity is reached at a maximum shear load of about 315 kN, which occurs just before the shear capacity of the web is reached.
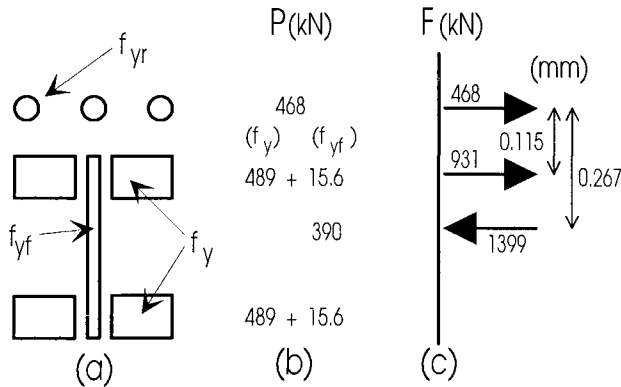
Fig. 7.20 Example 7.7 on shear in negative region

7.6   Reference

Trahair, N.S. and Bradford, M.A. (1991). *The Behaviour and Design of Steel Structures*, revised 2nd edn., Chapman and Hall, London.

8   Limited slip capacity of shear connectors

8.1   Introduction

It was shown in Section 2.4 that all types of mechanical shear connectors have a finite slip capacity because of the mechanism by which they transfer the shear. It is therefore necessary in the design procedure to ensure that the connectors do not fracture through excessive slip before one of the required limit states, described in Chapters 6 and 7, is reached. Furthermore, it was shown in Section 2.4.4 that the characteristic strength of mechanical shear connectors, that is the strength used in design, is a function of the number of connectors that can be assumed to fail as a group, and this depends on the connectors in the group not fracturing prematurely through excessive slip.

Endeavouring to ensure that mechanical shear connectors do not fracture prematurely has been one of the most intractable problems in composite construction. This is because we have to deal with the behaviour of the whole length of composite beam, and have to allow for variations in the connector density and distribution, time-dependent effects of creep and shrinkage, variations in restraint from simply supported to continuous beams, and variations in the distribution of applied loads. Unlike both rigid plastic analysis in Chapter 7 and linear elastic analysis in Chapter 6 that deal primarily with the behaviour at a section of a beam, connector fracture deals with the whole length of the beam where the section properties could range from fully plastic to fully elastic.

Consider the simply supported composite beam in Fig. 8.1(b) that comprises the three constituent materials shown in (a) of concrete, steel and shear connectors. When the beam is first loaded, the three materials have linear elastic properties and hence linear elastic partial interaction theory, as described in Section 6.3.2, can be applied to determine the slip distribution, and this is dealt with in Section 8.2. On further loading and particularly with low degrees of shear connection, the slips tend to uniformity as shown in Fig. 8.1(c). Hence the connectors tend to be fully loaded, that is plastic, over most of the beam as shown in (c) even though the steel and concrete elements remain linear elastic, and this situation is covered in Section 8.3. When the applied moment approaches the rigid plastic strength, the steel and concrete become plastic in a small region near midspan in Fig. 8.1(b) where the flexural forces are greatest, and remain elastic throughout the rest of the beam where tensile cracking of the concrete element may occur. Non-linear analysis techniques are now required to simulate this behaviour and these are described in Section 8.4.

It is certainly worth remembering that the basis for all of these techniques for determining the fracture load is the classical linear elastic analysis of Newmark, Siess and Viest (1951) that is described in Section 6.3.2. It is also worth noting that most standards try to ensure that connectors do not fracture due to excessive slip. However, the designer should be aware that in a small number of circumstances when dealing with a few flexible connectors, it may be necessary to ensure that the slip

throughout the beam is sufficient for the connectors to reach their maximum strength in order for the composite beam to attain its design flexural capacity. Although the problem of flexible shear connection is not covered in this book, the analysis procedures are similar to those described in this chapter.
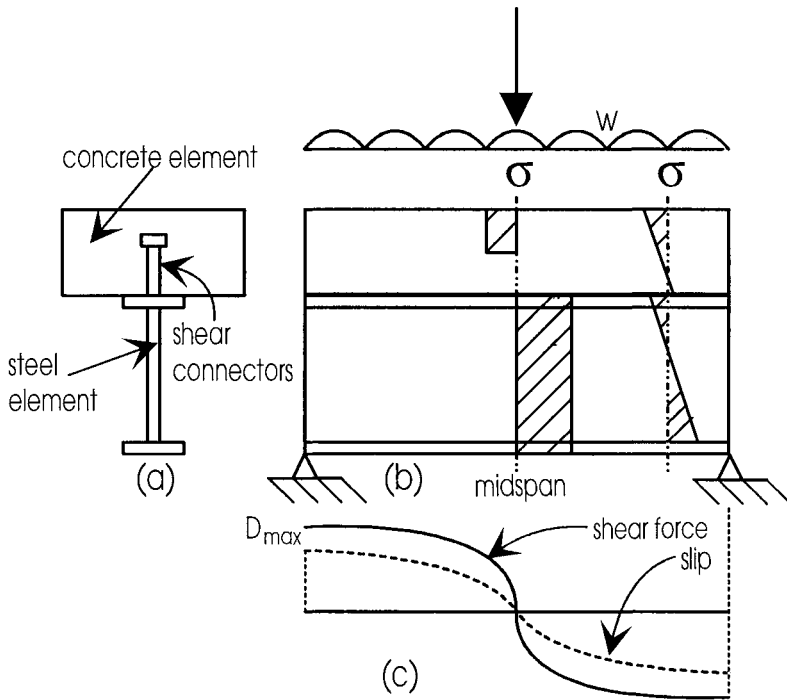
Fig. 8.1 Material properties in composite beam

The analyses in this chapter are a continuation of the partial interaction analyses of Section 6.3 and use the notation already defined in that section.

8.2   Linear elastic analysis

8.2.1   PARTIAL INTERACTION

When plasticity in the steel and concrete elements is either negligible or non existent, and when brittle connectors are used (such as the block connectors in Fig. 1.5(e) that have the brittle load/slip relationship shown in Fig. 2.17), then the classical linear elastic procedure (developed by Newmark, Siess and Viest (1951), and described in Section 6.3.2) can be used to determine the onset of fracture. As an example, consider a simply supported composite beam with a uniformly distributed load. A closed form solution for this problem has been developed in Section 6.3.2 and is given by Eq. 6.17. Differentiating Eq. 6.17 gives the shear flow as shown in Eq. 6.6, substituting $x = 0$ gives the shear flow at the supports which is also the maximum shear flow, and substituting this into Eq. 6.2 gives the maximum slip s_{max}. In order to prevent fracture,

it is necessary to ensure that s_{max} is less than the slip to cause the brittle connector to fracture.

Closed form solutions can only be found for simple loading conditions and simple distributions of the shear connectors, and even these solutions are too complex for general use. Hence this form of analysis is rarely used in practice.

Example 8.1 Slip at serviceability loads

The composite beam in Fig. 6.1 has already been analysed in Example 6.1 to determine the deflection at serviceability loads. We will continue this analysis to determine the shear connection slip at the supports.

From Eq. 6.6, it can be seen that the derivative of Eq. 6.17 gives the distribution of the shear flow q along the length of the beam. The maximum slip occurs at the supports so substituting x = 0 into the derivative of Eq. 6.17 gives the shear flow at the supports of 241 N/mm. Substituting this shear flow into Eq. 6.2 gives a slip of 0.73 mm. Substituting this slip into Eq. 6.1 gives the load D on the connector of 26 kN which is 45% of the dowel strength of 58 kN. From Eq. 2.33, the slip capacity of this 16 mm stud shear connection is 5.3 mm. Hence the slip at the serviceability load is only 14% of the slip capacity of the shear connection so that the connector is unlikely to fracture at these loads.

8.2.2   NO INTERACTION

The maximum slip in a composite beam with no shear connectors may not be of any direct practical value, but it is a fundamental component of many analysis procedures and hence is worth considering.

When there are no shear connectors, then F_{conc} in Eq. 6.3, F_{steel} in Eq. 6.4 and F_{shear} in Eq. 6.8 are all zero. Equation 6.9 still applies, as we will assume that there is no vertical separation between the steel and concrete elements so that they have the same curvature. Substituting these equations into Eq. 1.8 gives

$$\frac{ds}{dx} = -\frac{M}{\sum EI}(h_c + h_s) \tag{8.1}$$

where

$$\sum EI = E_c I_c + E_s I_s \tag{8.2}$$

Integrating Eq. 8.1 then produces

$$\Delta s = \frac{h_c + h_s}{\sum EI}\int_{\Delta L} M dx \tag{8.3}$$

Equation 8.3 defines the following important parameters that affect the slip in a composite beam. The change in slip Δs between two points ΔL apart is inversely proportional to the sum of the flexural rigidities of the steel and concrete elements $\sum EI$. The slip is directly proportional to the depth of the section D, as D is a function of $(h_c + h_s)$. Furthermore, Δs is directly proportional to the area of the applied moment envelope $\int M dx$ along the length ΔL of the beam, and hence uniformly distributed loads will cause a greater slip than concentrated loads and the slip will increase with the length of the beam.

For a simply supported beam with a concentrated load at midspan (Fig. 1.24(a)), the slip at midspan is zero as in (c) because of symmetry. Hence from Eq. 8.3, integrating the applied moment between the support and midspan gives the maximum slip s_{max} in (c) as

$$s_{max} = M_{max} \frac{L(h_s + h_c)}{4 \sum EI} = \frac{M_{max} L}{4} K_1 \tag{8.4}$$

where M_{max} is the maximum applied moment and

$$K_1 = \frac{h_c + h_s}{\sum EI} \tag{8.5}$$

Similarly for a uniformly distributed load, the maximum slip is

$$s_{max} = \frac{M_{max} L}{3} K_1 \tag{8.6}$$

where K_1 is given by Eq. 8.5. It can be seen in Eqs. 8.4 and 8.5 that the maximum slip is directly proportional to the length of the beam L and that the uniformly distributed load induces more slip than the point load when the same maximum moment is applied.

Example 8.2 Slip in a composite beam without shear connectors

Consider the composite beam in Example 6.1 and in Fig. 6.1 and which has already been analysed with partial interaction in Example 8.1. Let us assume that there are no shear connectors and hence no interaction and that the concrete has a creep coefficient $\phi = 1$ so that $E_e = 14.3$ kN/mm^2.

From Eq. 8.6, the maximum slip is 2.98 mm when the load is first applied and hence E_c is used in the analysis. This increases to 3.41 mm if the load is maintained and E_e used in the calculations. The difference in slip between the 0.73 mm in Example 8.1 and the 2.98 mm in this example is the reduction in slip due to the shear connectors.

8.3 Linear elastic and rigid plastic analysis

8.3.1 GENERAL ANALYSIS

Plasticity in the steel and concrete elements only occurs in a small volume of the composite beam, and hence a feasible solution is to assume that the steel and concrete elements remain linear elastic whereas the shear connectors are fully loaded, that is plastic. This idealisation has been found to give good correlation with experimental and non-linear computer models (Oehlers and Sved 1995) even though the composite beam would have been designed using rigid plastic analysis.

Referring once again to the linear elastic analysis in Section 6.3.2, F_{conc} in Eq. 6.3 is now equal to P_{shear}, where P_{shear} is the strength of the shear connection in the shear span, as we are assuming that all the connectors are fully loaded. For a simply supported beam this would be the strength of the shear connectors between the section being considered and the support. The parameter P_{shear} is therefore a function of the distance along the span. Similarly, P_{shear} should be substituted for F_{steel} in Eq. 6.4, and for F_{shear} in Eq. 6.8. Equation 6.9 is still applicable. Substituting these equations into Eq. 1.8 gives the following variation of slip strain along the length of the beam

$$\frac{ds}{dx} = P_{shear}\left(\frac{1}{\overline{EA}} + \frac{(h_c + h_s)^2}{\sum EI}\right) - \frac{M(h_c + h_s)}{\sum EI} \tag{8.7}$$

where $\overline{EA}$ is defined in Eq. 6.12 and $\sum EI$ in Eq. 8.2. Integrating Eq. 8.7 gives

$$\Delta s = K_1 \int_{\Delta L} M dx - K_2 \int_{\Delta L} P_{shear} dx \tag{8.8}$$

in which

$$K_2 = \frac{1}{\overline{EA}} + \frac{(h_c + h_s)^2}{\sum EI} \tag{8.9}$$

The change in slip between two points Δs can now be determined from Eq. 8.8. In order to determine the maximum slip s_{max}, we need to be able to determine the change in slip from a position of zero slip.

We are assuming that the composite beam has been designed using rigid plastic analysis so that all the connectors are fully loaded. It was shown in Chapter 7 that in rigid plastic analysis, the composite beam is first designed at the position of maximum moment to ensure that the maximum flexural capacity can withstand this maximum moment, as shown in Fig. 7.14(e). The rigid plastic design procedure requires that the connectors in both shear spans on either side of the position of maximum moment, that is spans A-B and A-C in (a), have the same strength and are applying a thrust that is directed at A, as shown in (c). As the connector thrusts in each shear span are in opposite directions, the direction of slip in each shear span must also be in opposite directions. Hence, the reversal in the slip direction must occur at the position of

maximum moment where the slip must be zero. Therefore, integrating the slip from the position of maximum moment to a support, for a beam designed using rigid plastic analysis, will give the maximum slip in that shear span.

The general method of analysis is illustrated in Fig. 8.2. Consider the simply supported beam in (a) that is subjected to a non-uniform load. The maximum moment in the beam is M_{max} and the moment is distributed as shown in (b). The shear connectors are fully loaded so that the axial force they exert on the concrete element can be determined easily from their strength and position. For example, in the right hand shear span in (c) a group of n connectors applies a thrust of $P_1 = nD_{max}$ at position (1), another group at (2) applies a thrust of P_2, and another group at (3) a thrust of P_3. Hence from Eq. 8.7 and for the right hand shear span in Fig. 8.2, the maximum slip which occurs at the right hand support is given by

$$s_{max} = A_m K_1 - A_{shear} K_2 \qquad (8.10)$$

where A_m is the area of the moment diagram between the position of maximum moment and the support as shown in (b) and A_{shear} is the area of the axial force diagram over the same region as shown in (c). It can be seen that a simple graphical solution can be used to determine the maximum slip for complex distributions of applied load and connector distributions. Furthermore, the same technique can be used to determine the distribution of slip throughout the length of the beam.

In general, the maximum slip occurs at the support adjacent to the longest shear span since we are integrating over a longer length. In addition, the maximum slip can be reduced by placing more connectors nearer the supports and hence increasing the area A_{shear} in Fig. 8.2(c) for the same value of connector strength P_{max}.

8.3.2 SYMMETRICAL SIMPLY SUPPORTED BEAMS

For a simply supported beam of span L with a concentrated load at mid-span and with a uniform distribution of shear connectors, the maximum slip can be derived from Eq. 8.10 and is given by

$$s_{max} = \frac{M_{max} L}{4} K_1 - \frac{P_{max} L}{4} K_2 \qquad (8.11)$$

Similarly, for the same beam but with a uniformly applied distributed load

$$s_{max} = \frac{M_{max} L}{3} K_1 - \frac{P_{max} L}{4} K_2 \qquad (8.12)$$

From a comparison between Eqs. 8.4 and 8.11 and between Eqs. 8.6 and 8.12, it can be seen that the first parameter on the right hand side of Eqs. 8.11 and 8.12 is the maximum slip without connectors. Hence the second parameter, $P_{max}LK_2/4$, is the reduction in slip due to the shear connectors. It is worth noting that if all the connectors in a shear span are placed adjacent to the supports, which is theoretically possible but practically impossible, then the second parameter doubles in size reducing

the maximum slip. Concentrating connectors towards the supports thus helps to reduce the maximum slip in a beam and hence the possibility of fracture.
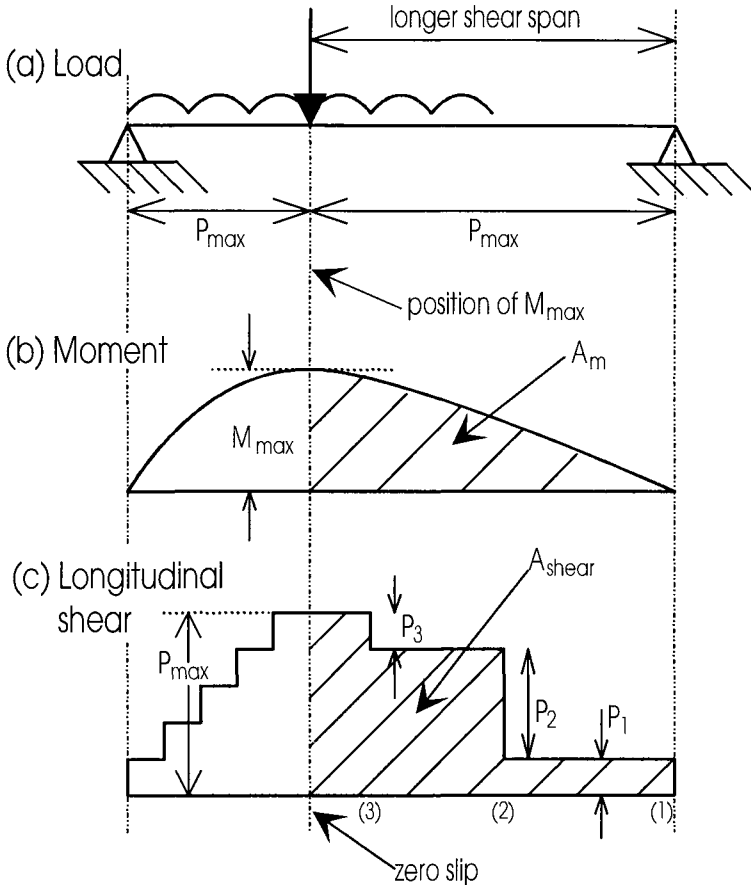
Fig. 8.2 General analysis procedure for fracture

Example 8.3 Connector fracture in a beam with partial shear connection

A simply supported composite beam has the cross-section in Fig. 6.1, spans 10 m, has a uniform distribution of shear connectors and is subjected to a uniformly distributed load. The concrete element has a strength of $f_c = 30$ N/mm^2 and 16 mm diameter stud shear connectors are used. The composite beam is designed with a degree of shear connection of $\eta_{max} = 0.40$. Following a similar analysis to that in Example 7.3, the partial shear connection flexural capacity can be determined as $M_{max} = 320$ kNm and P_{max} as 618 kN.

The maximum slip in the composite beam at the ultimate strength can be determined from Eq. 8.12. The first parameter on the right hand side comes to 7.84 mm which is the slip without shear connectors. The second parameter comes to 4.11

mm which is the reduction in slip due to the shear connectors. The difference of 3.73 mm is the maximum slip s_{max} that occurs. The maximum slip that the 16 mm diameter stud shear connector can withstand is given by S_{ult} in Eq. 2.33, and this comes 5.66 mm. As $s_{max} < S_{ult}$ the beam can reach its ultimate strength capacity without fracture of the shear connectors.

8.3.3 DEGREE OF INTERACTION

An interesting phenomenon occurs at a theoretical zero maximum slip, $s_{max} = 0$, when the two parameters on the right hand side of Eq. 8.10 are equal. This can be defined as a condition for full interaction and can be considered to be analogous to full shear connection. From Eq. 8.10, full shear connection is defined as

$$A_{shear} = A_m \frac{K_1}{K_2} \tag{8.13}$$

where A_{shear} is shown in Fig. 8.2(c). The shear connection strength required for full interaction P_{fi} is the value of P_{max} in (c) which satisfies Eq. 8.13. Therefore the degree of interaction ψ is given by

$$\psi = \frac{P_{shear}}{P_{fi}} \tag{8.14}$$

where P_{shear} is the strength of the shear connection in a shear span. The degree of interaction ψ in Eq. 8.14 is analogous to the degree of shear connection η in Eq. 1.7.

Zero slip can only be achieved in theory, as it is assumed that the connectors are fully loaded even at zero slip, as shown by the idealised model for D_{max} in Fig. 7.1. However, the degree of interaction ψ is a useful gauge for estimating the probability of connector fracture, in the same way as the degree of shear connection η_{max} is a useful gauge for estimating the flexural strength of a composite beam.

Consider, for example, a simply supported beam with a uniform distribution of applied load and shear connectors. The maximum slip in this beam is given in Eq. 8.12. Hence the strength of the shear connectors in a shear span required for full interaction P_{fi}, when the maximum applied moment is M_{max}, is the strength required for $s_{max} = 0$ and is given by

$$P_{fi} = \frac{4 M_{max} K_1}{3 K_2} \tag{8.15}$$

Example 8.4 Degree of interaction

Consider the beam in Example 8.3 in which $\eta_{max} = 0.4$ and $P_{max} = 619$ kN. Applying Eq. 8.15 gives $P_{fi} = 1180$ kN and hence $\psi = 0.52$.

For the same beam with full interaction ($\eta_{max} = 1$), $P_{max} = 1545$ kN, as derived in Example 7.1, hence $\psi = 1.31$. Fewer shear connectors are thus required for full interaction than for full shear connection and hence the connectors are unlikely to fracture. It is for this reason that design procedures do not require a check for connector fracture when the beam has full shear connection.

8.3.4 FRACTURE STRENGTH ANALYSIS

In design, it is necessary to ensure that the applied moment is less than the moment required to cause a connector to fracture M_{frac} at its maximum slip capacity S_{ult}. This requirement can be determined directly from Eq. 8.10, for any distribution of load and connectors, by substituting S_{ult} for s_{max} in Eq. 8.10 and M_{frac} for the maximum applied moment M_{max} in Fig. 8.2(b).

Let us consider the case of a simply supported composite beam with a uniform distribution of connectors and loads. The maximum slip is given by Eq. 8.12. We will assume that the concrete element is rectangular and that the I-section is symmetrical so that the depth of the composite beam $D = 2(h_c + h_s)$. Substituting $s_{max} = S_{ult}$, $M_{max} = M_{frac}$ and $P_{max} = \eta_{max}(P_{shear})_{fsc}$, where $(P_{shear})_{fsc}$ is the strength of the shear connection required for full shear connection, produces the moment to cause a connector to fracture M_{frac} as

$$M_{frac} = \frac{6S_{ult}\sum EI}{LD} + \frac{3\eta_{max}\left(P_{shear}\right)_{fsc}\sum EI}{2D}\left(\frac{1}{E_cA_{conc}} + \frac{1}{E_sA_{steel}} + \frac{D^2}{4\sum EI}\right) \quad (8.16)$$

It can be seen from Eq. 8.16 that the moment capacity at which fracture occurs is clearly a function of the following parameters

$$M_{frac} = f\left(\frac{S_{ult}}{L}, \eta_{max}\left(P_{shear}\right)_{fsc}, \left(\frac{1}{E_cA_{conc}} + \frac{1}{E_sA_{steel}}\right)\right) \quad (8.17)$$

Hence the moment to cause fracture is directly dependent on the connector slip capacity as a proportion of the span of the beam, the strength of the shear connection and hence the degree of shear connection, and inversely dependent on the axial stiffness of the steel and concrete elements. The effect of the depth of the beam D and the flexural rigidity $\sum EI$ is variable. It can also be seen in Eq. 8.16 that the variation of the fracture strength with the degree of shear connection is linear.

Example 8.5 Variation of fracture strength with degree of shear connection

The composite beam shown in both Figs. 6.1 and 7.5 is simply supported and has a uniformly distributed applied load and a uniform connector distribution. From rigid plastic analysis, the variation in the flexural capacity of the beam M_{psc} with the degree of shear connection was determined in Example 7.5. The results are shown in Fig. 8.3 for the equilibrium approach M_{psc} and for the linear interpolation technique M_{linear}, both of which assume that the connectors have unlimited ductility.

Inserting the material properties into Eq. 8.16 and using units of N and mm gives

$$M_{frac} = 4.08 \times 10^{11} \frac{S_{ult}}{L} + 4.19 \times 10^8 \eta_{max} \qquad (8.18)$$

The same composite beam was analysed in Example 8.3, with a span of L = 10 m and with 16 mm diameter stud shear connectors that had a maximum slip capacity of S_{ult} = 5.7 mm. The variation of the fracture strength of this composite beam with the degree of shear connection is shown as line A in Fig. 8.3. Both the equilibrium and interpolation partial interaction strengths lie below the fracture strength of line A, so the connectors are unlikely to fracture before their partial interaction flexural capacities are reached, even at very low degrees of shear connection.

If we now increase the span of the beam to 12 m and use 13 mm stud shear connectors (S_{ult} = 4.6 mm from Eq. 2.33) instead of 16 mm stud shear connectors, then the fracture strength is line B in Fig. 8.3. Consider the partial shear connection moment capacity M_{psc} that was derived from the equilibrium approach. There is a transition point at $\eta_{max} = (\eta_t)_1$. For beams with $\eta_{max} > (\eta_t)_1$, M_{psc} will be attained before fracture. For beams with $\eta_{max} < (\eta_t)_1$, the connectors will fracture before M_{psc} is attained and hence M_{frac} will govern design down to $\eta_{max} = \eta_3$. The change in slope between M_{psc} and M_{frac} at the transition point $(\eta_t)_1$ is fairly gentle so that there is no need to restrict design to $\eta_{max} > (\eta_t)_1$. Below η_3, the connectors will fracture at a moment less than the capacity of the steel section M_{steel} but this will not prevent M_{steel} from being achieved. If the interpolation technique M_{linear} is being used, then the transition point $(\eta_t)_2$ occurs at a lower degree of shear connection as shown.
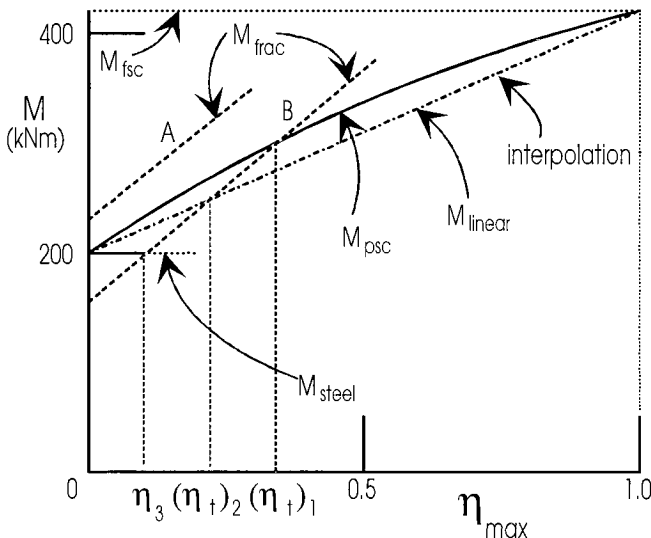
Fig. 8.3 Example 8.5 on connector fracture

8.4   Non-linear procedure

8.4.1   GENERAL

The technique described in Section 8.3 can be applied when there is a low degree of shear connection (Oehlers and Sved 1995). At high degrees of shear connection, non-linear techniques are required to allow for plasticity in the steel and concrete elements as well as tensile cracking in the concrete element. However, as with all non-linear problems, a closed form solution is difficult to find and researchers have resorted to developing guidelines based on parametric studies of experimental and non-linear computer models.

The ground rules for non-linear analysis procedures of the type used in computer simulations that allow for slip strain and hence slip are described in the following section. This is followed by the results of a parametric study based on such computer simulations from which design guidelines are derived.

8.4.2   NON-LINEAR ANALYSIS TECHNIQUES

In the analysis of concrete structures, it is a simple procedure to develop the moment-curvature relationship for a a particular shape of section when the material properties are non-linear, just as long as the stress-strain relationships of the three constituent materials, that is the steel, concrete and shear connection, are known. For example, let us assume that the strain profile in Fig. 1.23(b) is the strain profile in a reinforced concrete section. Then for a given curvature κ, the position of the neutral axis y_n can be varied until the axial compressive force above the neutral axis is equal to the axial tensile force below the neutral axis. Once this situation is reached, the moment M for the curvature κ can be derived from the axial forces. The procedure can be repeated for other curvatures to generate a moment curvature relationship that is applicable throughout the length of the beam. An equivalent analysis in composite beams would be to fix the slip strain as in Fig. 1.23(c) and develop a moment curvature relationship for this slip strain, but this would be of little use as the slip strain in a composite beam varies along the length of the beam and the variation is not known. Instead an iterative segmental procedure has to be applied.

Consider the composite beam in Fig. 8.4 in which it is assumed that we know all the material properties. The beam is divided into small segments of length x as shown, where the length of the segment is much less than the length of the beam, so that it can be assumed that the forces and displacements within each segment are constant.

The analysis is started at the support at section 1 where the axial force in the concrete and steel elements P_0 and the applied moment M_1 are zero. Furthermore, as the applied moment at this section is zero, the slip strain $(ds/dx)_1 = s'_1 = 0$. The only unknown variable at this section is the slip s_1, so to start the analysis we have to make

an initial guess for s_1 say s_{ig}. From the slip s_{ig}, the average force P_1 in the connectors in the region x_1 can be determined.
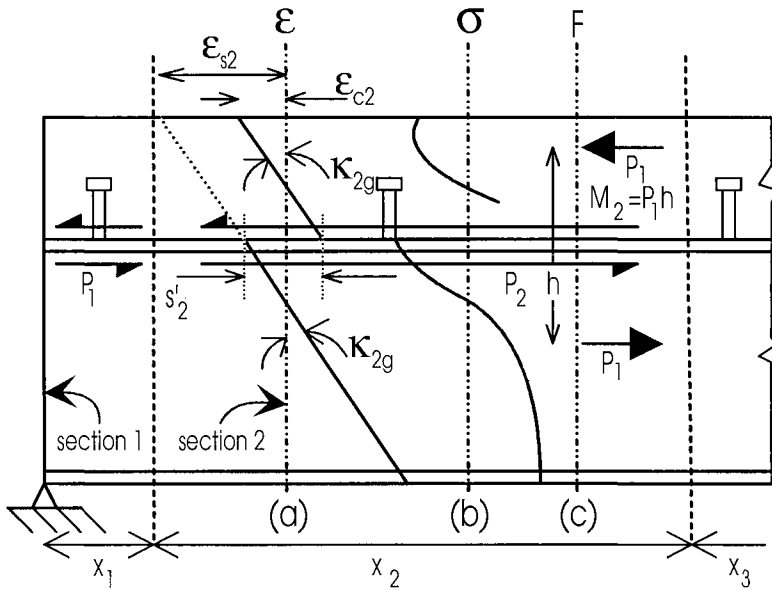
Fig. 8.4 Non-linear analysis

Now consider the adjacent element at section 2. The applied moment M_2 is known. The axial force in the concrete and steel elements is the force in the shear connectors to the left of this section. As we are assuming that $x \ll L$, the axial force is P_1, as derived in the previous analysis. Therefore, it is necessary to find a strain distribution as in Fig. 8.4(a) and hence from the material properties a stress distribution (b) which is in equilibrium with both M_2 and P_1 as shown in (c). We therefore have to determine both the slope of the strain profiles κ_2 and the position of the strain profiles ε_{c2} and ε_{s2}, as shown in (a), that results in a section that is in equilibrium with the stress resultants M_2 and P_1.

In order to do this, it is necessary to first guess a curvature at section 2, κ_{2g} as shown in Fig. 8.4(a). Starting with the concrete element, the position of the strain profile is moved by changing ε_{c2} until the resultant force in the concrete element is compressive and equal to P_1. Similarly for the steel element, the position of the strain profile is changed by altering ε_{s2} until in the equivalent stress profile (b) there is a resultant tensile force P_1 in the steel element as shown in (c). The section is now in equilibrium with the axially applied loads at the strain profile defined by κ_{2g}, ε_{c2} and ε_{s2}. Moments of the axial forces in (c) can now be taken to determine the internal moment. If this is not equal to the applied moment M_2 it will be necessary to try a new curvature κ_{g2} and keep repeating the analysis until equilibrium is attained at a strain profile κ_2, ε_{c2} and ε_{s2}. Once the strain profile is known, the slip strain s'_2 can be determined as shown in (a). Integrating the slip strain over the length x_2 gives the

increase in slip Δs in segment 2 over that in segment 1 of s_1 and hence the slip in segment 2, s_2. From the slip s_2 can be determined the force in the connectors within region x_2.

The axial force in the concrete and steel elements in the next section x_3 will be the force in the shear connectors in the shear span to the left of this section and hence equal to $P_1 + P_2$. It will be necessary to find a strain distribution which is now in equilibrium with the applied moment M_3 and axial force $P_1 + P_2$, and this can be achieved using the procedure described in the previous paragraph. The analysis proceeds along the beam until a section is reached where a boundary condition is known. For example, if we were analysing a simply supported composite beam with a uniform distribution of both the applied load and the shear connectors then the slip at midspan is zero, otherwise we would have to continue the analysis to the other support where the slip strain is zero. Having reached a section where a boundary condition is known, the known and computed values can be compared and if they do not agree the whole procedure has to be repeated with a new value for the initial slip s_{ig}. Once the boundary conditions are attained, the slip distribution is known and this can be compared with the maximum slip capacity S_{ult} to ascertain whether fracture occurs.

The procedure described above represents a particular solution technique to what is referred to as a boundary value problem (Hornbeck 1975). This procedure is called a 'shooting method' technique. It can be seen that this non-linear procedure is ideally suited for computer modelling as the main task is to repeat simple routines.

8.4.3   DEGREE OF SHEAR CONNECTION APPROACH

Whenever there is a lack of understanding of the behaviour of a structural response, national standards tend to place limits on the range of applicability of design rules. These limits are characterised by step changes, and this has occurred in the development of design rules for the prevention of fracture.

The approach that is used to prevent fracture of mechanical shear connectors is simply to place limits on the use of rigid plastic partial interaction analyses of the type described in Section 7.3.3. As an example, rigid plastic analysis can be used to determine the variation in the flexural capacity of a composite beam with the degree of shear connection, that is shown as M_{psc} in Fig. 8.5. In order to prevent fracture, limits are usually placed on the minimum degree of shear connection for which M_{psc} can be applied, that is shown as η_t. Above this transition point, for $\eta_{max} > \eta_t$, M_{psc} can be used in design, while below this transition point, $\eta_{max} < \eta_t$, the strength is assumed to be that of the steel element acting by itself M_{steel}. The transition point at η_t therefore represents a sudden step change in the strength from M_t to M_{steel} which is really unsatisfactory for design purposes since it places the designer in a dilemma when the degree of shear connection falls just below this limit.

Design rules for fracture generally assume that when the degree of shear connection $\eta_{max} \geq 1$, fracture of the shear connection never occurs and this is a reasonable assumption as the degree of interaction as defined in Section 8.3.3 is large. Hence, design rules assume that it is only necessary to check for connector fracture

when there is partial shear connection. The design rules are often based on parameters that can be determined from partial interaction analysis. For example, it can be seen in Eq. 8.16 that the applied moment to cause fracture is directly proportional to both the slip capacity of the shear connectors S_{ult}, and the strength of the shear connectors $\eta_{max}(P_{shear})_{fsc}$ and inversely proportional to the span of the beam L.
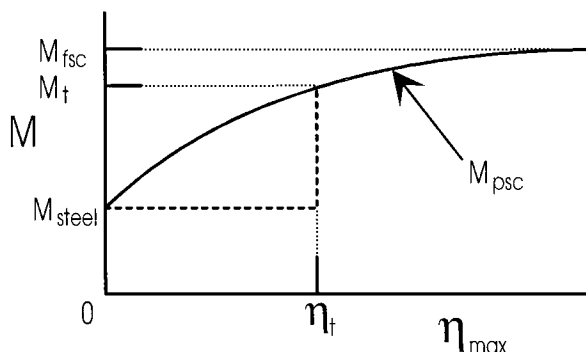
Fig. 8.5 Standard design procedure for fracture

The first attempts in national standards to prevent fracture of the connectors placed limits on the maximum span of the beam of around 20 m, and also placed limits on the minimum value of the degree of shear connection η_t that could be used which was around 0.4 to 0.5. Furthermore, these standards required that ductile connectors were used such as stud shear connectors in medium or low strength concrete. Hence, these first attempts ignored the slip capacity of the connectors S_{ult}, and relied on the plastic properties of the beam by completely ignoring the elastic properties of the composite beam.

The technique was improved (Johnson and Molenstra 1991) by including the slip capacity of the shear connectors S_{ult} and the length of the beam L with the degree of shear connection η_t. Examples of these design recommendations are shown in Fig. 8.6 which gives the transition point η_t for use in Fig. 8.5. This procedure still does not allow for the elastic properties of the composite beam so design procedures tend to be conservative. It is worth noting that the transition point η_t can also be determined from the intercept of M_{psc} and M_{frac}, in Eq. 8.16. This is shown as $(\eta_t)_1$ in Fig. 8.3 and the results from such studies (Oehlers and Sved 1995) are also shown in Fig. 8.6.

More advanced techniques were derived from parametric studies of the results of non-linear computer simulations (Johnson and Molenstra 1991) based on multi-variable regression analyses of non-dimensional parameters which were considered to affect the slip capacity. Even though this is not a rigorous mathematical model of the behaviour of composite beams, the procedure at least included all the parameters that affect slip. Johnson and Molenstra (1991) proposed the following prediction equation when design is based on rigid plastic partial interaction analysis.

$$S_{ult} \geq \left(\frac{M_{steel} L h_{steel}}{6 E_s I_s} \right) \left(\frac{L}{D} \right)^{\alpha} \left(\frac{M_{psc} - M_{steel}}{M_{steel}} \right)^{\beta} \tag{8.19}$$

where D is the depth of the composite section, and for $\eta_{max} = 0.5$, $\alpha = -0.13$ and $\beta = 1.03$, while when $\eta_{max} = 0.75$, $\alpha = -0.24$ and $\beta = 1.70$.
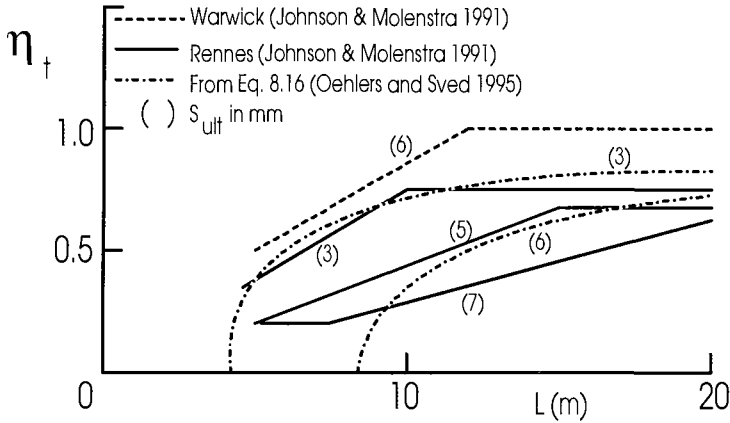
Fig. 8.6 Design rules for transition point

The maximum slip in a linear elastic composite beam without shear connectors is given by Eq. 8.6. If it is assumed that the concrete element does not exist then $h_c = E_c = I_c = 0$ in Eq. 8.6 which becomes

$$s_{max} = \frac{M_{max} L h_{steel}}{6 E_s I_s} \tag{8.20}$$

which is virtually the same as the first term on the right hand side of Eq. 8.19, except that the plastic moment capacity of steel element M_{steel} has been substituted for M_{max} which is a reasonable approach to allow for some plasticity in the beam. The first term in Eq. 8.19 therefore allows for elasticity in the beam, the second term for the span and the third term for the degree of shear connection and plasticity, and hence all the main parameters that affect slip are included in this prediction equation.

It can be seen in Fig. 8.3 that when a linear interpolation technique is used with M_{linear} instead of the rigid plastic approach M_{psc}, the transition point reduces from $(\eta_t)_1$ to $(\eta_t)_2$. This means that a lower degree of shear connection or a smaller slip capacity can be used when design is based on the linear interpolation technique M_{linear}. When Johnson's beams were designed using the linear interpolation procedure (Johnson and Molenstra 1991), the slip requirement was two-thirds that given in Eq. 8.19.

8.5   References

Hornbeck, R. (1975). *Numerical Methods.* Quantum Publishers, New York.

Johnson, R.P. and Molenstra, N. (1991). "Partial shear connection in composite beams for buildings." Proceedings, Institution of Civil Engineers, London, Part 2, Vol.91, 679-704.

Newmark, N.M., Siess C.P. and Viest I.M. (1951). "Tests and analysis of composite beams with incomplete interaction." Proceedings Society for Experimental Stress Analysis, 9, No.1, 75-92.

Oehlers, D.J. and Sved, G. (1995). "Flexural strength of composite beams with limited slip capacity shear connectors." Journal of Structural Engineering ASCE, June.

9   Moment Redistribution within Continuous Composite Beams

9.1   Introduction

It is well-known that under certain conditions, statically indeterminate steel frame structures can be analysed and designed *plastically*. Beams continuous over one or more internal supports represent a particular example of such an indeterminate structure. The main requirement for plastic analysis and design of continuous steel beams is that the moment versus curvature response is *ductile*. In addition, the phenomenon that permits the plastic analysis and design of continuous beams is that of *moment redistribution*. This occurs because, under a monotonic or proportional loading regime, the maximum moment is first attained at the most highly strained section of the beam, say A. While this maximum moment may reach the maximum attainable at section A, collapse of a continuous beam does not occur, and we shall see that under further loading the bending moments redistribute, with the moment remaining constant at A, until the maximum attainable moment is reached at the next most highly strained cross-section, say B. With the moments remaining constant at sections A and B, further likewise moment redistribution occurs under increasing load until collapse eventually occurs. The load at collapse may be much higher than that to reach the section capacity at A, and cannot be ignored in design.

Plastic analysis and design may be used for composite continuous beams as well as steel beams, for which the theory was originally formulated. Again, the major requirement is a ductile moment-curvature relationship. While prediction of the plastic behaviour of steel beams is relatively straightforward, that of composite beams is somewhat more difficult because there are two ultimate or plastic moments corresponding to sagging and hogging bending, as we saw in Chapter 7. In addition, the ductility requirement that allows the moments to redistribute is much harder to quantify for sagging composite cross-sections than for a steel cross-section. As for steel beams, instability or buckling effects are not allowed to occur before the collapse load is reached. Hence, for continuous composite beams, lateral-distortional buckling and local buckling must be prevented. The occurrence of overall buckling can be checked by the methods of Chapter 10, and eliminated by bracing the cross-section, while local buckling can be prevented by limiting the width to thickness ratio of the component plates of the section to satisfy the plastic section classification of Section 5.3.2.2. As with steel beams, plastic analysis and design of composite continuous beams can therefore only be used when the steel element is a plastic hot-rolled universal or I-section that exhibits substantial ductility.

The methods of plastic analysis and design are very well documented for steel members, but the concept is introduced in this chapter for steel beams for the reader who in unfamiliar with the all-important ductility requirements that are often treated superficially in a first course on the plastic behaviour of steel beams. This is done because the ductility requirements, which determine rotation capacity, are then applied

to composite beams, and a background understanding of more simple steel beams is therefore needed. It should be noted that while much research has been undertaken on composite continuous beams, there still remain some grey areas related to rotation requirements, and the guidelines that are suggested could be significantly refined.

9.2　Continuous steel beams

9.2.1　GENERAL

The phenomenon of moment redistribution in continuous beams is attributable to the ductility of the cross-section of the beam, and can result in ultimate loads substantially higher than those predicted by an elastic analysis. Moment redistribution, which is governed by the inelastic response of structural members, was first utilised in steel beams, and the methods of plastic analysis and design of continuous steel beams originated from the work of Lord Baker and his colleagues during the 1940's. There has been a wealth of published work on the plastic analysis and design of steel beams, and the reader is referred to standard texts such as Beedle (1958), Baker and Heyman (1969), Neal (1977) and Horne (1978) for a full treatment of plasticity and moment redistribution.

　　The structural concepts germane to moment redistribution in continuous beams are most easily explained by considering steel beams first. We may then extend the principles to continuous composite T-beams, but it should be borne in mind there are more restrictions on the ability of the moments to redistribute in composite beams due to the different rotation capacities of steel and composite cross-sections. This section will therefore consider the basic concepts of plastic behaviour and moment redistribution in continuous steel beams.

9.2.2　INELASTIC STEEL CROSS-SECTIONS

9.2.2.1　*Moment-curvature response*

Consider the steel I-section shown in Fig. 9.1(a) that is subjected to a monotonically increasing curvature κ, as in (b). The assumption of plane sections remaining plane will be adopted, so that the strain distribution remains linear. We will also assume that the material is mild steel with the stress versus strain constitutive relationship shown in Fig. 2.2. It is usual to assume that the strain hardening modulus, E_{st}, in Fig. 2.2, is in the range of $E_s/30$ to $E_s/100$.

　　When the curvature κ in Fig. 9.1(b) is less than the curvature to cause first yield in the extreme fibres κ_y, which is given by

$$\kappa_y = \frac{2f_y}{E_s D} \qquad\qquad (9.1)$$

then the stress distribution is linear throughout the section, so that $\sigma = E_s\, y\kappa$, and the moment M produced by the stresses is

$$M = E_s\, I_s\, \kappa \tag{9.2}$$

and so the moment-curvature response is linearly elastic. However, once the curvature exceeds κ_y, the strains toward the extremities of the section will exceed the yield strain $\varepsilon_y = f_y\,/\,E_s$, and from Fig. 2.2 the stresses in these yielded regions will remain constant at f_y, as shown in Fig. 9.1(c). Yielding thus progresses through the depth of the cross-section until strain hardening occurs in the extreme fibres at a curvature κ_{st} given by

$$\kappa_{st} = \frac{2\,\varepsilon_{st}}{D} \tag{9.3}$$

where ε_{st} is the strain to cause strain hardening given in Fig. 2.2 Strain hardening will then progress through the depth of the section, and the moment of the stresses in Fig. 9.1(d) will increase.
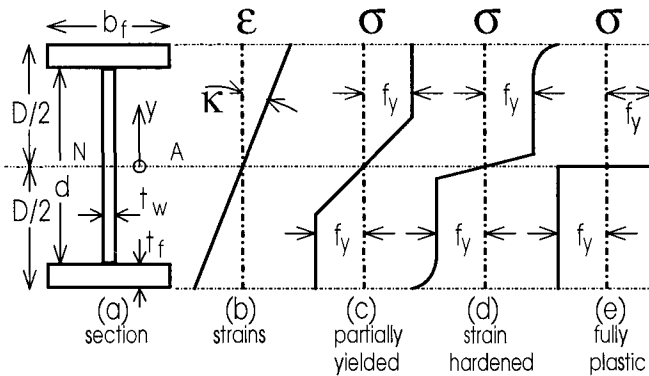
Fig. 9.1 Stresses and strains on steel cross-section

This moment versus curvature response can be represented by the curve in Fig. 9.2(a). The curve is linear below the first yield moment M_y in Eq. 9.2 with $\kappa = \kappa_y$, and becomes rounded following the elastic-plastic portion shown until strain hardening commences. The moment at which strain hardening starts is very close to the fully plastic moment, as discussed for a composite cross-section in Section 7.3, obtained by integrating the moments of the idealised stress block shown in Fig. 9.1(e).

It can be seen that the moment-curvature relationship in Fig. 9.2(a) is of a similar shape to the stress-strain curve of the steel, except for the rounding of the curve after M_y has been reached when yielding progresses through the flanges into the web. The main point worth noting is that the cross-section is *ductile*, except if premature local buckling takes place as discussed in Section 9.2.3. Hence the full

plastic moment M_P can be developed with large curvatures being attainable. This leads us to the concept of the *plastic hinge*, as discussed in the following Section.
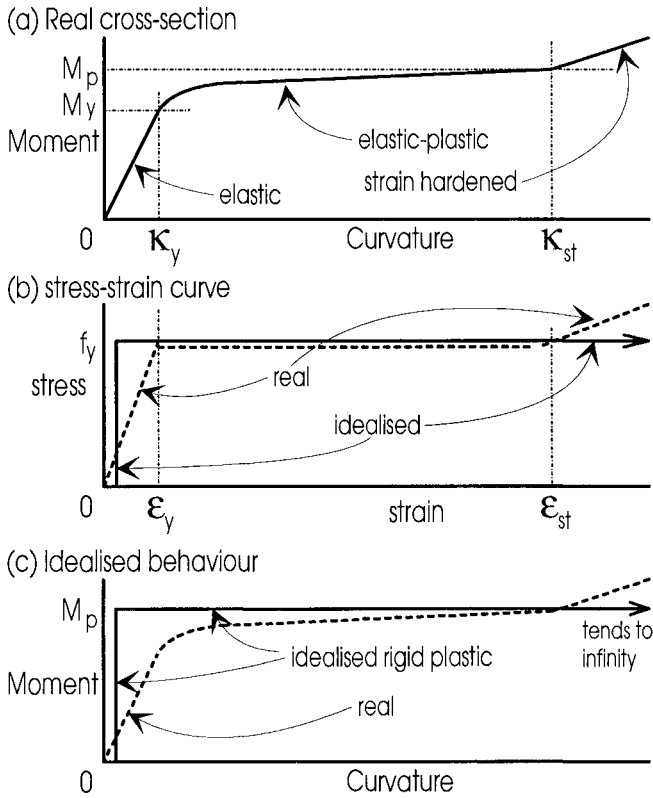
Fig. 9.2 Moment-curvature response of a steel beam

Example 9.1 Moment-curvature relationship of steel beam

The universal steel section in Fig. 9.1(a) with D = 607 mm, b_f = 228 mm, t_f = 17.3 mm and t_w = 11.2 mm has a yield stress f_y = 250 N/mm^2, a strain hardening strain ε_{st} = $10\varepsilon_y$ and elastic and strain hardening moduli E_s = 200 kN/mm^2 and E_{st} = 6 kN/mm^2 respectively.

The second moment of area I_s = 860 x 10^6 mm^4 and the curvature at first yield is κ_y = 4.119 x 10^{-6} mm^{-1} so the first yield moment M_y = 708.4 kNm. At strain hardening, ε_{st} = 10 x 250/200,000 = 12.5 x 10^{-3} at the extreme fibre, corresponding to a curvature κ_{st} = 41.19 x 10^{-6} mm^{-1}. At κ_{st}, the region at the centre of the web 30.35 mm from the centroid is elastic, with the remainder of the section being at yield. The moment at the onset of strain hardening is then M_{st} = 809.5 kNm. At a curvature κ = 1.5 κ_{st} = 61.79 x 10^{-6} mm^{-1}, the central region 20.33 mm each side of the centroid of the web is elastic, while strain hardening has progressed throughout each flange and

83.9 mm into the web. The moment is then M = 897.9 kNm. The fully plastic moment, obtained from the stress distribution in Fig. 9.1(e), is M_p = 810.8 kNm. Hence the moment at the onset of strain hardening is 809.5/810.8 or 0.998 M_p, and at 1.5 times the strain hardening curvature is 897.9/810.8 or 1.11 M_p. Note also that the well-documented shape factor μ, which is the ratio of the fully plastic moment to the moment at first yield, that is $\mu = M_p/M_y$, is 810.8/708.4 = 1.14.

9.2.2.2 *The plastic hinge*

An approximation to the construction of the moment-curvature relationship in Fig. 9.2(a) using the method of Section 9.2.2.1 is to assume that the constitutive curve for steel is given by the idealised rectangular stress block shown by the solid line in Fig. 9.2(b). This approximation ignores elastic strains as well as strain hardening strains. Hence the idealised moment-curvature relationship, as shown in (c), ignores the curvature of any elastic or elastic-plastic region when M < M_p, and assumes that infinite curvatures are attainable where M = M_p.

Consider the simply supported steel beam in Fig. 9.3(a) which has a central concentrated load P. The bending moment distribution in (b) is known from statics, so for the real beam the moment-curvature relationship such as that in Fig. 9.2(a) allows us to construct the curvature diagram, such as in Fig. 9.3(c). When the beam is loaded beyond yield, some of the beam near the load point will be in the elastic-plastic and strain hardened regions, so that the curvature will be as in (c). The rotation θ at point A on the beam in (a) measured x from midspan is given by the area under the curvature diagram in (c) from midspan to A, and is shown in (d). Because there is a finite length of beam that is elastic-plastic or strain hardened for which the curvatures are large, and a remaining elastic portion with much smaller curvatures, most of the slope change in θ in (d) occurs adjacent to the loaded midspan to give the deflected shape shown in (e).

Suppose now that the same beam is analysed by the idealised rigid plastic assumption of Fig. 9.2(c). If the beam is to become inelastic, then the maximum moment at midspan is M_p where the curvature becomes infinite from Fig. 9.2(c). Away from midspan, the moments are less than M_p, so that the curvatures are zero from (c), and therefore the distribution of curvatures is as shown in Fig. 9.3(g). Because of this, the infinite curvature at midspan causes a finite step change in the beam slope θ in (h). Hence the two halves of the beam remain straight, as in (i), with the beam reaching an ultimate load of P_u = 4 M_p/L. It can be seen that although the curvature distributions in (c) and (g) are quite dissimilar, the behaviour of the idealised *rigid-plastic* beam is similar to that of the real beam.

The infinite curvature that is assumed to occur at the point of full plasticity in Fig. 9.3(g) and the associated finite slope change θ in (i) predicted by the rigid-plastic assumption is the basis of the *plastic hinge* concept. The plastic hinge can assume any slope change θ once the fully plastic moment M_p has been reached. At M_p, the rigid-plastic assumption predicts a two bar mechanism will be formed by the plastic hinge
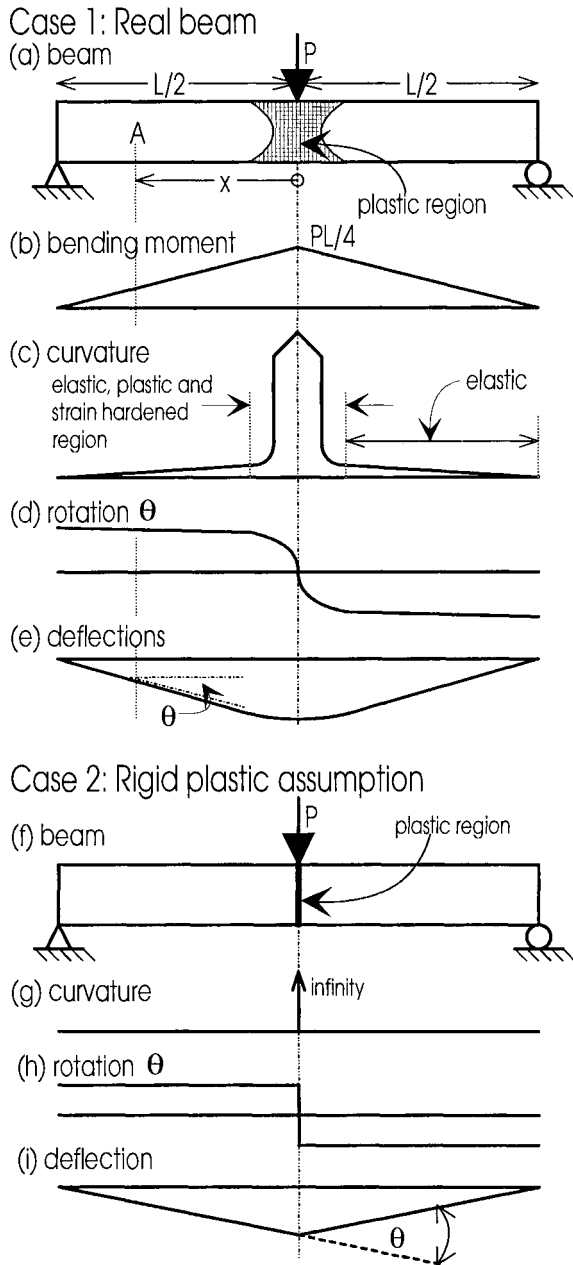
Fig. 9.3 Plastic hinge concept

and the two frictionless support hinges, as shown in Fig. 9.3(i), and the beam will deform freely without any further increase in load. It is worth noting that we cannot calculate explicitly the step change in the slope θ in (h) at the plastic hinge that results from the rigid-plastic assumption. However, the variation of slope in the elastic region along the real beam in (a) can be determined by integrating the known curvature distribution in the elastic region in (c), as shown in (d).

9.2.3   INELASTIC LOCAL BUCKLING

We have seen that the validity of the plastic hinge concept is dependent on large curvatures being realised near the plastic moment, that is on the ductility of the steel. The ductility of the moment-curvature relationship is, of course, attributable to the large plastic plateau and strain hardening nature of the stress-strain curve of Fig. 2.2.

When a steel I-section is subjected to bending, the compression flange and compressive portions of the web may buckle locally, as shown in Fig. 1.17. As was discussed in Section 5.2.4, if the flange or web are slender, they may buckle locally before the plastic moment M_p or even the first yield moment M_y are reached, as shown at A and B in Fig. 9.4. Unloading then takes place rapidly, and only very small curvatures can develop before failure. Slender sections are not ductile, and are unsuitable for plastic design. Similarly, semi-compact sections buckle locally before M_p is developed, but after the first yield moment M_y has been reached. Again, these sections fail by buckling at relatively small curvatures, and are also unsuitable for plastic design for which the moments must redistribute.
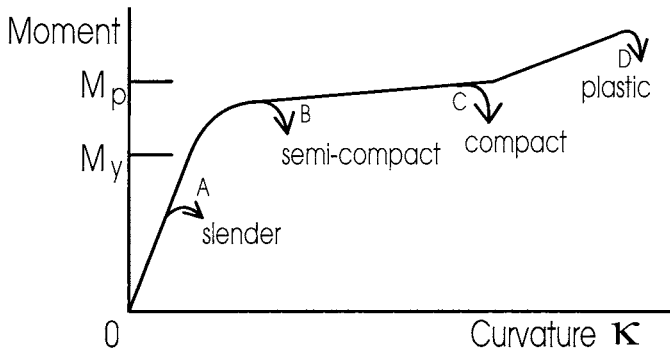
Fig. 9.4 Locally-buckling steel cross-section

Compact sections as at C in Fig. 9.4 buckle locally well into the elastic-plastic range, and they allow curvatures of more than five times the "elastic" curvature at M_p (that is $M_p/E_s I_s$) to develop (Azhari and Bradford 1993). They are therefore ductile, but in some cases may not be ductile enough to allow the large rotations required for moment redistribution, as discussed in Section 9.2.4, to occur. Plastic sections, as defined in Section 5.2.4, buckle locally at very large curvatures as at D in Fig. 9.4 when the strains have entered the strain hardening region. The rigid-plastic assumption of Fig. 9.2(c) is valid for plastic sections, and any slope change θ at a

plastic hinge can be assumed to be developed in a cross-section that is classified as plastic.

In summary, while a prerequisite for a plastic hinge to form is that the stress-strain curve for the steel is ductile, geometric constraints are placed on the section by its susceptibility to local buckling. We shall see in Section 9.3 that there are other constraints that must be placed on a composite cross-section if a plastic hinge is to form.

9.2.4   MOMENT REDISTRIBUTION IN STEEL BEAMS

9.2.4.1   *Encastered beam*

The feature of plastic design that distinguishes it from elastic design is the favourable redistribution of bending moments which it allows. If a continuous beam is analysed elastically and the maximum load taken as that when the largest moment equals M_p, then we have what is termed a *first hinge* analysis. However, once this first hinge forms, its capacity remains at M_p while additional loading may be supported until the moment at the next most highly strained section reaches M_p. Loading may continue, with the moments being redistributed, until enough hinges form to convert the continuous beam into a mechanism. The moment redistribution may be considerable, and the final load at which this collapse mechanism forms may be significantly higher than that at which the first hinge is developed.

To illustrate this, consider the encastered beam shown in Fig. 9.5(a) with a concentrated load at its third point. The beam is twice redundant, so three plastic hinges are needed to form to produce a collapse mechanism. If the beam is analysed elastically, all moments are proportional to the load until the first hinge forms at the support A, which is the most highly strained section, as shown in (b). The load for this first hinge to develop is $P = 6.75 \ M_p/L$. With further increases of load, the moment at A remains constant at M_p, but the moments at B and C increase. The next most highly strained section is under the concentrated load at B, which reaches M_p at $P = 8.68 \ M_p/L$, as shown in (c). The redistribution of moment from that at the formation of the first hinge in (b) is shown in (c). The moment at B then remains at M_p, while further load can be carried until a hinge forms at C when $P = 9 \ M_p/L$, and the bending moment distribution becomes as shown in (d). The second hinge load is 8.68/6.75 or 29% higher than the first hinge load, while the ultimate load when a collapse mechanism forms if 9/6.75 or 33% higher than the first hinge load. It is thus clear that moment redistribution takes place after the onset of yielding, and deploying this phenomenon in design may greatly increase the load carrying capacity of a continuous beam. It is important to note that moment redistribution only takes place in indeterminate beams. Once a first hinge formed in the determinate beam considered in Section 9.2.2.2, a mechanism was developed and the beam could carry no more load.

While successive intermediate hinge development requires an elastic or elastic-plastic analysis, it is very easy to calculate the ultimate load at which a mechanism forms. For the encastered beam considered in Fig. 9.5(a), the final

bending moment distribution in (d) is made up of the free moment distribution shown in (e) and the reactant moment distribution in (d) resulting from the plastic moments that produces a mechanism. The free moment at B is, from statics, $2PL/9$, so that in (d) $M_p + M_p = 2PL/9$, producing the collapse load $P = 9M_p/L$. It is therefore not necessary to consider intermediate hinge formation, as we are only interested in the final distribution of plastic hinges at collapse.
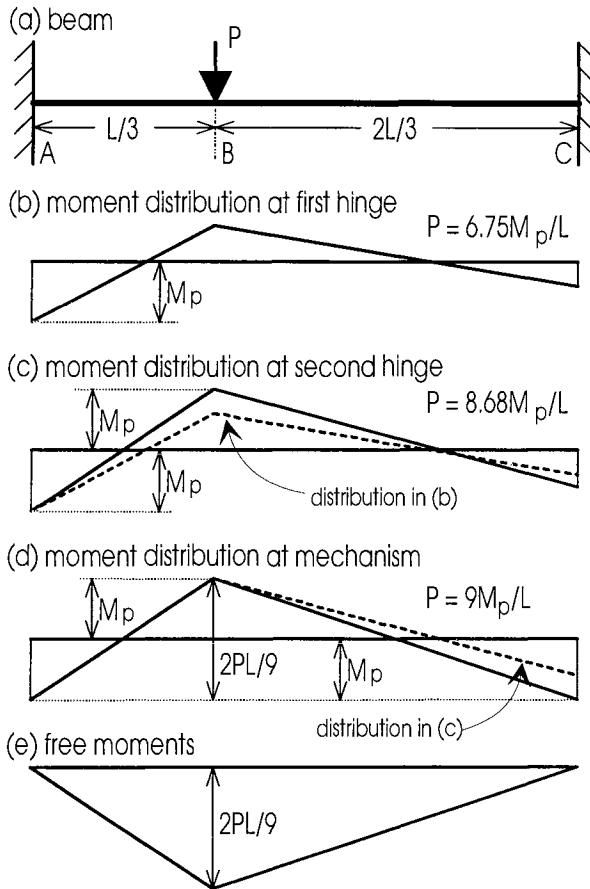
Fig. 9.5 Encastered beam

9.2.4.2   *Two internal supports*

Consider the continuous beam shown in Fig. 9.6(a) with three spans of length L, carrying a central concentrated load P in the middle span. The elastic bending moment diagram is shown in (b), and it can be established by standard analysis techniques (Hall and Kabaila 1986) that $M_B = M_D = -0.075PL$ and $M_C = 0.175PL$. Hence a first (sagging) hinge will form at midspan at a load $P = 5.71 \ M_p/L$. Upon further loading, two more hinges will form at B and D to make span BD a mechanism as shown in (c). From the free and reactant bending moment diagrams, $PL/4 = M_p +$

M_p, so at collapse $P = 8M_p/L$. This represents a 40% increase in the load carrying capacity when the moment redistribution, shown in (c), is utilised.

Case 1: Central concentrated load

(a) beam

(b) elastic bending moment

0.075PL

0.175PL

$P = 5.71M_p/L$

(c) mechanism

M_p M_p distribution in (b)

PL/4

M_p $P = 8M_p/L$

Case 2: Distributed load

(d) beam

(e) elastic bending moment

$0.05wL^2$

$0.075wL^2$

$w = 13.33M_p/L^2$

(f) mechanism

M_p M_p distribution in (e)

$wL^2/8$

M_p $w = 16M_p/L^2$
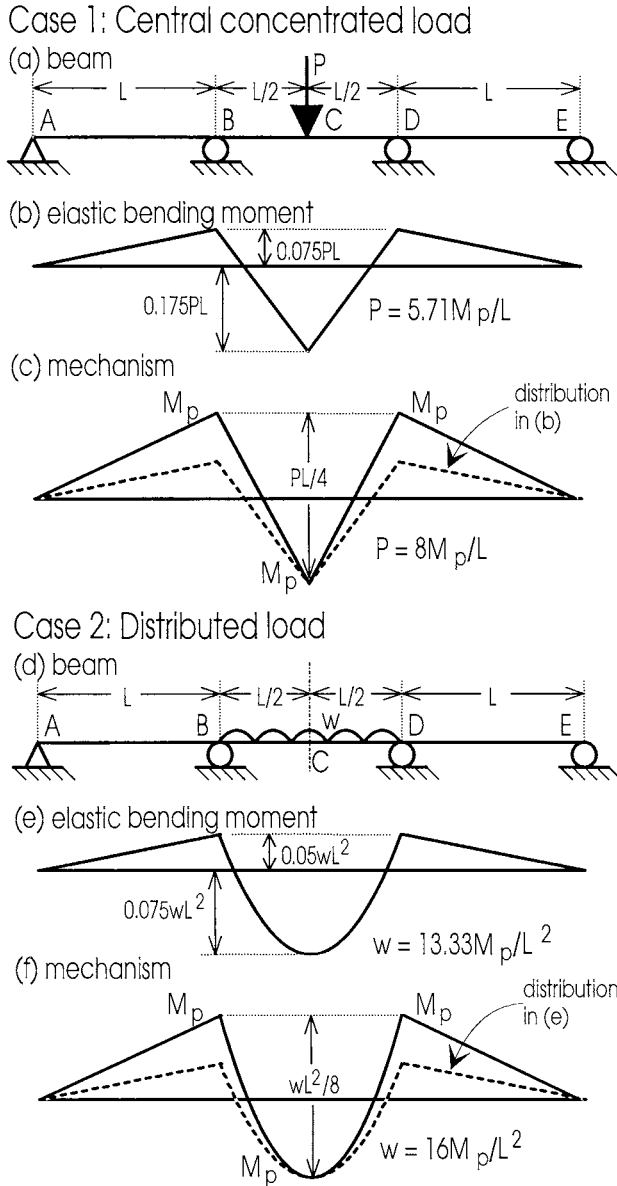
Fig. 9.6 Three-span continuous beam

Similarly, a three-span continuous beam carrying a uniformly distributed load w in the central span is shown in Fig. 9.6(d). The elastic bending moment diagram is shown in (e), with $M_B = M_D = -0.05wL^2$ and $M_C = 0.075wL^2$ The sagging region of

the central span carries the highest moment, so that $w = 13.33\ M_p/L^2$ at the formation of the first hinge. When plastic hinges form at B and D, rendering the span BD a mechanism as shown in (f), the bending moment diagram requires that $wL^2/8 = M_p + M_p$, producing a collapse load of $w = 16\ M_p/L^2$. This represents a 20% increase in the load carrying capacity due to the bending moment redistribution shown in (f).

9.2.4.3   *One internal support*

A two-span continuous beam supporting a central concentrated load in the span AB is shown in Fig. 9.7(a). The elastic moments at B and C are -0.094PL and 0.203PL respectively. The first (sagging) hinge therefore forms at C at a load $P = 4.93\ M_p/L$. When an additional plastic hinge forms at B as shown in (c) the span is reduced to a collapse mechanism because the support A is a physical hinge with zero moment. Hence from the bending moment diagram in span AB in (c), $PL/4 = M_p + M_p/2$, that is $P = 6M_p/L$. The collapse load is thus 22% greater than the first hinge load.

A slightly more difficult case occurs with the two-span beam shown in Fig. 9.7(d), which carries a uniformly distributed load w on the span AB. The sagging and hogging moments from an elastic analysis are $0.096wL^2$ and $-0.063wL^2$ respectively. The first hinge load is thus $w = 10.42\ M_p/L^2$.

When first yielding of the beams starts at the most highly strained region, C which occurs 0.543L to the left of B in Fig. 9.7(f), then the moment increases at B and we get redistribution of the bending moments. When this redistribution occurs, a region very slightly to the left of the original position of first yield within the span increases in its bending moment above M_p. Since the idealised rigid plastic behaviour in Fig. 9 2(c) shows that the maximum attainable bending moment is M_p, the original point of plastification, C in Fig. 9.7(f), "unloads" and the position of the plastic hinge moves slightly towards the left as w increases. Finally, when the moment at the support B is large enough for a plastic hinge to form at that position, the condition of a "propped cantilever" is reached, for which it is shown in Trahair and Bradford (1991) that the plastic moment within the span lies 0.586L to the left of the support B. The free moment at this location is $0.121\ wL^2$, so that $0.121wL^2 = M_p + 0.414M_p$, or $w = 11.66M_p/L^2$. This is an increase of 12% over the first hinge load.

9.3   Continuous composite beams

9.3.1   GENERAL

In Section 9.2 the concept of the plastic analysis of continuous steel beams was introduced, and it was demonstrated that the rotation capacity of a plastic hinge permitted substantial redistribution of the bending moments, with a consequent increase in the ultimate load to cause collapse above that calculated elastically to form a first hinge. Further, the examples considered in Section 9.2.4 illustrated that plastic analysis can be an elegant way of calculating the collapse load, and for hand

calculation it is usually considerably simpler than the elastic analysis of indeterminate structures.

Case 1: Concentrated load

(a) beam

(b) linear elastic bending moment

0.094PL

0.203PL $P = 4.93M_p/L$

(c) mechanism

$M_p/2$

M_p

M_p

$P = 6M_p/L$

distribution in (b)

Case 2: Distributed load

(d) beam

(e) linear elastic bending moment

$0.063wL^2$

$0.096wL^2$ $w = 10.42M_p/L^2$

(f) mechanism

$0.414M_p$

M_p

M_p

$0.586L$

$w = 11.66M_p/L^2$

distribution in (e)
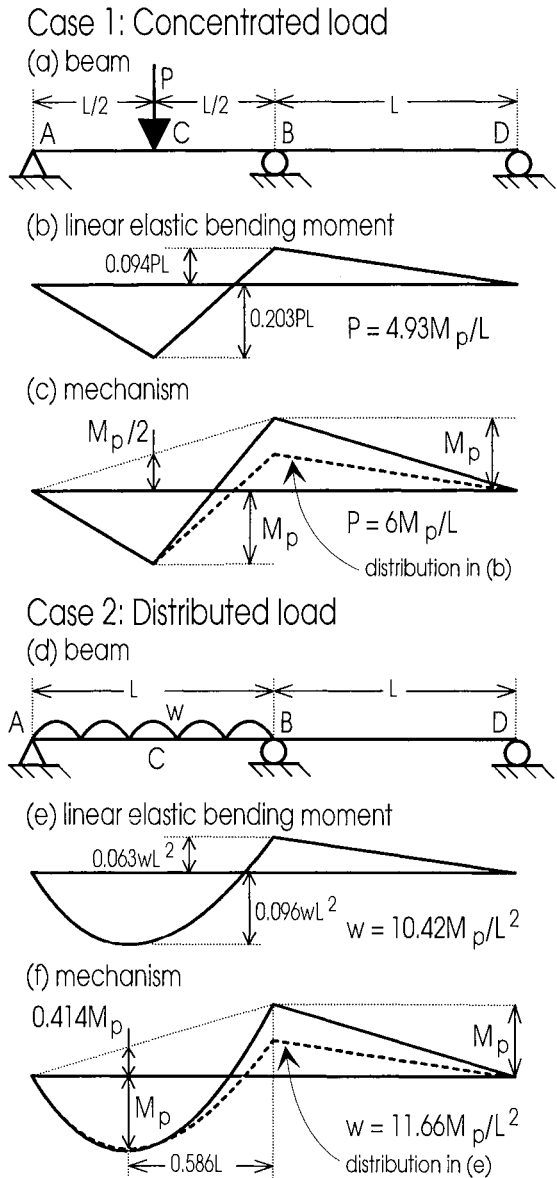
Fig. 9.7 Two-span continuous beam

Also in Section 9.2, it was stressed that the underlying concept in the plastic analysis and design of continuous beams is that of the plastic hinge. The plastic hinge concept was based on the ductility of the moment-curvature response which is a direct result of the ductile stress versus strain curve in Fig. 2.2. Ductility may be limited, as

was explained in Section 9.2.3, by local buckling so that only sections whose width to thickness ratios satisfied the plastic classification of Section 5.3.2.2 could be deployed for plastic analysis and design.

Plastic analysis may also be used for continuous composite T-beams. This again requires that the moment versus curvature response is ductile enough to permit the development of the required rotation capacity for a plastic collapse mechanism. We shall see in this section that there are much more stringent requirements on the geometrical and material properties of a composite cross-section to allow a plastic hinge to form in the sagging region. In addition, a composite T-beam is monosymmetric, so that there are different values for the plastic sagging moment $(M_p)_{sag}$ and the plastic hogging moment $(M_p)_{hog}$.

9.3.2 MOMENT-CURVATURE RESPONSE

9.3.2.1 *Hogging bending*

It was shown in Section 7.4 that the concrete element of a T-beam is wholly or partially in tension under hogging or negative bending, and that composite action between the steel element and slab reinforcement can be attained with adequate shear connection. The behaviour of a T-beam under hogging bending resembles closely that of a steel beam, as discussed in Section 9.2. Because of this, composite beams subjected to hogging bending may be termed "strain-hardening" (Barnard and Johnson 1965), and ductility is limited by local buckling or secondary failures. Local buckling under hogging bending has been considered by Climenhaga and Johnson (1972), Bradford (1986), Bradford and Johnson (1987) and Azhari and Bradford (1993), and it was found that sufficient rotation capacity at hogging regions can be achieved in continuous composite beams whose cross-sections satisfy the plastic classification of Section 5.3.2.2. We will therefore restrict the discussion here to composite beams with plastic cross-sections.

Generally, the neutral axis lies in the steel element, so that the cross-section comprises of a steel section consisting of the steel element plus the reinforcement, when the concrete is assumed cracked and tension field action is ignored, as shown in Fig. 9.8. The depth of the elastic neutral axis below the top surface, d_n, is then

$$d_n = \frac{d_r A_{reinf} + (h_{conc} + h_{steel}/2) A_{steel}}{A_{reinf} + A_{steel}} \tag{9.4}$$

and the second moment of area of this effective steel section about the neutral axis is

$$I = I_{steel} + A_{steel}(h_{conc} - d_n + h_{steel}/2)^2 + A_{reinf}(d_n - d_r)^2 \tag{9.5}$$

where A_{steel} is the area of the steel element, A_{reinf} is the area of the longitudinal reinforcement positioned d_r below the top surface, I_{steel} is the second moment of area of the steel element about its centroid, and h_{conc} and h_{steel} are the depths of the

concrete and steel elements respectively and the steel element is symmetrical about both axes as shown in Fig. 9.8.
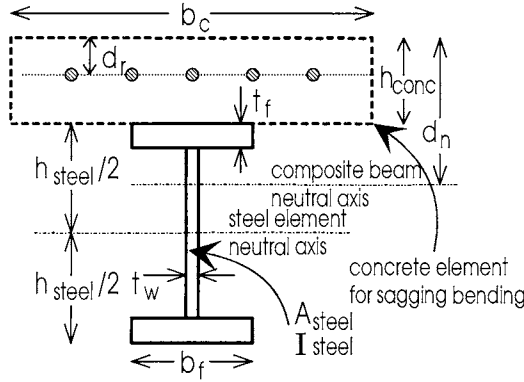
Fig. 9.8 Hogging bending for symmetric I-section

The moment-curvature relationship may be approximated by the idealised curve shown in Fig. 9.9(a), consisting of an elastic portion of stiffness E_sI, where I is given by Eq. 9.5, up to the hogging plastic moment $(M_p)_{hog}$. This may be determined by the methods set out in Section 7.4. When the plastic neutral axis is in the top flange of the steel element, then

$$d_n = h_{conc} + \frac{A_{steel}}{2b_f} - \frac{A_{reinf}\,f_{yr}}{2b_f\,f_y} \qquad (9.6)$$

and

$$(M_P)_{hog} = A_{steel}f_y\left(h_{conc} - \frac{h_{steel}}{2}\right) - A_{reinf}\,f_{yr}d_r - b_f f_y(d_n^2 - h_{conc}^2) \quad (9.7)$$

where b_f is the width of the flange, while if it is in the web of the steel element then

$$d_n = h_{conc} + h_{steel}/2 - \frac{A_{reinf}\,f_{yr}}{2\,t_w\,f_y} \qquad (9.8)$$

and

$$(M_P)_{hog} = A_{steel}f_y\left(h_{conc} + \frac{h_{steel}}{2}\right) - A_{reinf}\,f_{yr}d_r - 2b_f t_f f_y\left(h_{conc} + \frac{t_f}{2}\right)$$

$$-t_w f_y[d_n^2 - (h_{conc} + t_f)^2] \qquad (9.9)$$

where t_f is the flange thickness and t_w is the width of the web.
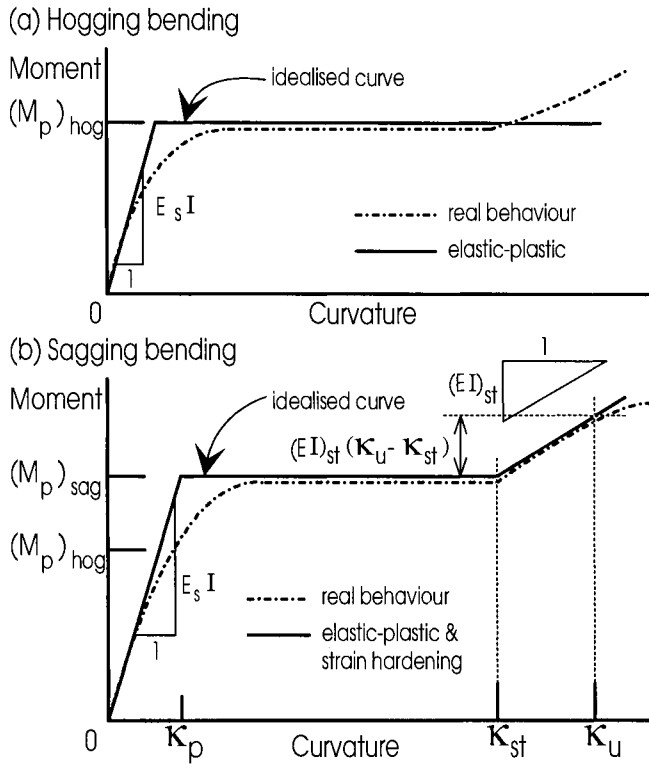
Fig. 9.9 Moment-curvature response of a composite cross-section

Ansourian (1980) and Bradford (1986) showed that strain hardening of the steel element may allow moments of up to 40% more than the plastic moment $(M_p)_{hog}$ to be attainable before unloading due to local buckling. However, negative regions in continuous beams usually have high coincident shear forces which may reduce the section capacity as described in Section 7.5.3. Because of this, the value of $(M_p)_{hog}$ given by either of Eqs. 9.7 or 9.9 is a satisfactory approximation to the plastic hinge moment in hogging bending.

9.3.2.2   Sagging bending

When a composite T-beam has full shear connection, as was discussed in Section 7.3, the resistance of its cross-section to sagging bending is governed by the strength of the concrete element in compression and the steel element in both bending and axial tension. We have seen in Section 9.2 that the deeper steel element is ductile and can sustain large curvatures. However, when the compressive strains in the concrete element are sufficiently large, the concrete crushes and the stress reduces, as indicated by its softening stress-strain curve in Fig. 2.7. The maximum curvature before unloading is therefore governed by the material and geometric properties of the

concrete element. Sagging hinges have thus been classified as "strain-softening" (Barnard and Johnson 1965).

The moment-curvature relationship may be conveniently generated by using elementary mechanics of materials deploying the relevant constitutive relationships for the concrete, reinforcement and structural steel. Such a study was performed by Rotter and Ansourian (1979) and Uy and Bradford (1993). At a given curvature, a trial position for the neutral axis depth d_n is chosen and thus the strains in the composite section are established. The strains define the stresses in terms of the relevant material constitutive curves, so that the stresses can be integrated over the area of the concrete, reinforcement and steel to produce an axial force N. Since the cross-section is in pure bending, the axial force N must vanish, so the trial position of d_n is altered until N = 0, thereby defining uniquely the stresses through the depth of the section. Integration of the first moment of the stresses over their areas thus produces the moment resisted by the section at the given curvature. The curvature may then be incremented and the moment calculated, thus defining the moment-curvature curve, until the moment starts to decrease due to crushing of the concrete. A typical ductile curve derived in this way is shown in Fig. 9.9(b).

The moment versus curvature response may be approximated by a linear elastic portion up to the sagging plastic moment $(M_p)_{sag}$, then by a plastic plateau, and then by a strain hardening region as shown by the solid curve in Fig. 9.9(b). For example, if the neutral axis lies in the steel element at a depth d_n below the top fibre, then from linear elastic analysis

$$d_n = \frac{b_c\, h_{conc}^2 / 2n + A_{steel}\left(h_{conc} + h_{steel}/2\right)}{b_c\, h_{conc}/n + A_{steel}} \tag{9.10}$$

where b_c is the width of the concrete element and

$$I = I_{steel} + \left(\frac{b_c h_{conc}^3}{12n}\right) + b_c\, h_{conc}\left(d_n - \frac{h_{conc}}{2}\right)^2 / n$$

$$+ A_{steel}\left(h_{conc} + \frac{h_{steel}}{2} - d_n\right)^2 \tag{9.11}$$

so that the flexural rigidity $E_s I$ in Fig. 9.9(b) can be determined, where n in Eqs. 9.10 and 9.11 is the modular ratio E_s/E_c. The curvature κ_{st} in Fig. 9.9(b) at strain hardening of the bottom fibre of the steel element is

$$\kappa_{st} = \frac{\varepsilon_{st}}{h_{conc} + h_{steel} - d_n} \tag{9.12}$$

where ε_{st} is the strain hardening strain in the steel element (Fig. 2.2) and d_n is now the depth of the plastic neutral axis below the top fibre, given from Section 7.3.2.3 as

$$d_n \quad = \quad \frac{A_{steel} \, f_y}{0.85 \, f_c \, b_c} \tag{9.13}$$

where the plastic neutral axis lies in the concrete element. The strain hardening flexural rigidity $(EI)_{st}$ in Fig. 9.9(b) may then be closely approximated by (Rotter and Ansourian 1979)

$$(EI)_{st} \quad = \quad E_{st} \, A_f \left(h_{conc} + h_{steel} \right)^2 \tag{9.14}$$

where A_f is the area of the bottom flange of the steel I-section element and E_{st} is the modulus value at strain hardening shown in Fig. 2.2. The concrete strain at crushing ε_u is often expressed as

$$\varepsilon_u \quad = \quad 0.0041 - 0.000,026 \, f_c \tag{9.15}$$

from which the curvature κ_u in Fig. 9.9 at crushing can be determined from

$$\kappa_u \quad = \quad \varepsilon_u / d_n \tag{9.16}$$

where d_n is given by Eq. 9.13. The moment at crushing M_u is then

$$M_u \quad = \quad \left(M_p \right)_{sag} + (EI)_{st} \left(\kappa_u - \kappa_{st} \right) \tag{9.17}$$

where $(M_P)_{sag}$ is the sagging plastic moment capacity that can be derived from Section 7.3 and $(EI)_{st}(\kappa_u - \kappa_{st})$ is the increase in the moment capacity due to strain hardening as shown in Fig. 9.9.

9.3.2.3 *Ductility parameter* χ

Ductility in a reinforced concrete beam is considered to be inversely proportional to the depth to the plastic neutral axis from the top fibre of the concrete in compression. In reinforced concrete design, under-reinforced beams yield before crushing because the neutral axis depth is shallow, and these beams are ductile, while over-reinforced beams are brittle since the concrete crushes before the tensile steel yields because the neutral axis is deep. In an analogous manner, we can define composite T-beams in bending to be ductile if strain hardening of the bottom flange of the steel element occurs before crushing of the concrete element. Therefore, for ductile behaviour

$$\kappa_{st} \quad < \quad \kappa_u \tag{9.18}$$

in Fig. 9.9, so that on substituting Eqs. 9.12 and 9.16

$$d_n \quad < \quad \frac{\varepsilon_u \left(h_{conc} + h_{steel} \right)}{\varepsilon_u + \varepsilon_{st}} \tag{9.19}$$

Typically, ε_u can be taken as 0.0035 and ε_{st} as $10\varepsilon_y$, so that for $f_y = 350$ N/mm^2, $\varepsilon_{st} = 0.0192$. Then d_n must be less than 0.15 ($h_{conc} + h_{steel}$) for ductility. For yielding before crushing of a reinforced concrete beam with the same material properties as the composite beam, the neutral axis d_n must lie above 0.67 times the depth of the section. The neutral axis requirement is thus very different for ductile reinforced concrete and composite beams.

If it is required that $d_n < 0.15$ ($h_{conc} + h_{steel}$), then the neutral axis will lie typically in the concrete element. Equation 9.13 can then be used for d_n, and substitution in Eq. 9.19 produces, for ductility

$$\chi \quad > \quad 1 \tag{9.20}$$

where the ductility parameter χ is given by

$$\chi \quad = \quad \frac{0.85 \, f_c \, b_c \, \varepsilon_u \left(h_{conc} + h_{steel} \right)}{A_{steel} \, f_y \left(\varepsilon_u + \varepsilon_{st} \right)} \tag{9.21}$$

The ductility parameter was introduced by Rotter and Ansourian (1979). That given in Eq. 9.21 differs from Rotter and Ansourian's parameter because the latter researchers used the γ-concept for the depth of the concrete stress block shown in Fig. 2.8. Hence the idealised plastic assumption in this book results in the 0.85 factor in Eq. 9.21, while the γ-concept replaces this with $0.85\gamma \approx 0.72$.

Ansourian (1982a) analysed a number of simply supported composite T-beams of the type shown in Fig. 9.3(a) to determine the rotation capacity. A lower bound expression for the ultimate plastic rotation θ_p was proposed as

$$\frac{\theta_p}{\theta_e} \quad = \quad 1.9 \, \chi \quad - \quad 1.85 \tag{9.22}$$

where θ_e is the "elastic" beam rotation at the sagging hinge at the collapse load (that is, $(M_P)_{sag}/(E_s I)$) and the concrete stress block is assumed here as idealised plastic, so that the γ-factor concept is not assumed. The prediction of Eq. 9.22 was found to be conservative when the beam was subjected to a uniformly distributed load, since the bending moment is approximately uniform over a significant portion of the length. The rotation capacity θ_p for simply supported beams under a uniformly distributed load was found by Ansourian to be from 1.6 to 2.5 times greater than that predicted by Eq. 9.22.

Example 9.2   Rotation capacity

The steel element whose dimensions and properties are given in Example 9.1 is composite with a concrete slab 750 mm wide and 75 mm deep of strength $f_c = 30$ N/mm^2.

   The crushing strain from Eq. 9.15 is $\varepsilon_u = 0.0033$ and so the ductility parameter in Eq. 9.21 is $\chi = 2.0$.   Hence from Eq. 9.22, $\theta_p = 2.0\theta_e$ so that this section conservatively allows plastic sagging rotations which are 200% of the elastic rotations.

   If now the slab is only 375 mm wide, then $\chi = 1.0$ and $\theta_p = 0.05\ \theta_e$. There is thus insufficient rotation capacity to develop and maintain the fully plastic moment.

9.3.2.4   *Composite plastic hinges*

The ductile nature of a hogging composite region, as discussed in Section 9.3.2.1, means that curvatures past the onset of strain hardening of the steel element can be developed. Because of this, the elastic curvatures can be ignored, and rigid-plastic theory, as in Section 9.2.2.2, may be applied. The plastic moment for hogging bending $(M_p)_{hog}$ is then given by either Eq. 9.7 or 9.9.

   Similarly, a rigid-plastic assumption may be adopted for a sagging hinge, provided the ductility condition is satisfied. The plastic moment $(M_p)_{sag}$ may thus be as in Section 7.3, and we shall see that in Section 9.3.3 that a requirement for a sagging hinge to form and allow redistribution is that $\chi \geq 1.6$.

9.3.3   MOMENT REDISTRIBUTION

It is evident from the discussion of the ductility of hogging and sagging hinges in the previous sub-section that plastic analysis of continuous composite beams may be used for sections for which the sagging hinge is the last to form. This is because the development of earlier hogging hinges allows sufficient rotation capacity for the bending moments to redistribute, with sufficient rotations not being needed at the final hinge location which is loaded to $(M_p)_{sag}$.

   Because the values of the elastic flexural rigidities in sagging bending and hogging bending are different, it is not always obvious which hinge will form first, unlike the steel beams analysed in Figs. 9.6 and 9.7 where the hogging and sagging elastic stiffnesses were identical. A first hinge elastic analysis of a continuous composite beam is also made difficult because the stiffness is that of the hogging section on the negative bending side of the point of contraflexure, and that of the sagging section on the positive bending side of the point of contraflexure, and the location of this point is unknown. An analysis such as that described in Section 6.4.3 will determine whether or not the sagging hinge is the last plastic hinge to form,

although tabulated bending moments for uniform continuous beams can be used with some engineering judgement to establish which hinge will form last.

The continuous composite beam shown in Fig. 9.7 is one for which the sagging hinge forms first, and sufficient rotation capacity is needed at this hinge for the sagging plastic moment to develop and be maintained while a plastic mechanism forms. From the geometry of the free moments and the reactant bending moment diagram produced by $(M_p)_{sag}$ and $(M_p)_{hog}$, a plastic mechanism will form when $P_pL/4$ = $(M_p)_{sag} + (M_p)_{hog}/2$, so that

$$P_p = \frac{4}{L}\left[\left(M_p\right)_{sag} + \left(M_p\right)_{hog}/2\right] \tag{9.23}$$

Continuous beams of this type were tested by Ansourian (1982b) in order to more accurately quantify the degree of moment redistribution which the positive hinge allowed in order for the fully plastic failure load P_p in Eq. 9.23 to develop. A two-span beam with a central concentrated load in only one span requires severe rotation capacity for a plastic mechanism to form. For a beam with a ductility parameter of χ = 1.8, theoretical studies predicted that the moments redistributed at failure so at the sagging hinge $M_{max} = 1.09(M_p)_{sag}$, while in the negative region at the internal support M_{max} was $0.7(M_p)_{hog}$. Thus although the sagging hinge had just entered the strain hardening region, there was still insufficient sagging rotation capacity to allow the hogging plastic moment to form. When self-weight of the beam is included as a uniformly distributed load over the length of the beam, then it can be shown that a collapse mechanism is achievable with χ = 1.8 in which both sagging and hogging hinges form.

Tests were also undertaken by Ansourian (1982b) on continuous composite beams with χ = 1.5, 2.4 and 3.5. The beam with the least ductility unloaded before a plastic mechanism was developed, while those with χ = 2.4 and 3.5 permitted enough moment redistribution for both sagging and hogging hinges to extend into the strain hardening region.

It may thus be concluded that simple rigid-plastic design may be used for continuous composite beams with adequate shear connection for which the parameter χ in Eq. 9.21 exceeds 1.6 and for which the cross-section is plastic in accordance with the requirements of Section 5.3.2.2 if a severe sagging rotation requirement is needed to form a plastic mechanism.. The bending moments will then redistribute to form a fully ductile plastic collapse mechanism.

9.4 References

Ansourian, P. (1980). "Rigid frame connections in composite structures", Civil Engineering Transactions, Institution of Engineers, Australia, Vol. CE22, No 2, 85-92.

Ansourian, P. (1982a). "Plastic rotation of composite beams", Journal of the Structural Division, ASCE, Vol. 108, No. ST3, 643-659.

Ansourian, P. (1982b). "Experiments on continuous composite beams ", Proceedings, Institution of Civil Engineers, London, Vol. 73, Part 2, 25-51.

Azhari, M. and Bradford, M.A. (1993). "Inelastic local buckling of plates with and without residual stresses", Engineering Structures, Vol. 15, No. 1, 31-39.

Baker, J.F. and Heyman, J. (1969). *Plastic Design of Frames - 1. Fundamentals*, Cambridge University Press, Cambridge.

Barnard, P.R. and Johnson, R.P. (1965). "Plastic behaviour of continuous composite beams", Proceedings, Institution of Civil Engineers, London, Vol. 32, 180-197.

Beedle, L.S. (1958). *Plastic Design of Steel Frames*, John Wiley, New York.

Bradford, M.A. (1986). "Local buckling analysis of composite beams", Civil Engineering Transactions, Institution of Engineers, Australia, Vol. CE28, No. 4, 312-317.

Bradford, M.A. and Johnson, R.P. (1987). "Inelastic buckling of composite bridge girders near internal supports", Proceedings, Institution of Civil Engineers, London, Vol. 83, Part 2, 143-159.

Climenhaga, J.J., and Johnson, R.P. (1972). "Local buckling in continuous composite beams", The Structural Engineer, Vol. 50, No. 9, 367-375.

Hall, A.S. and Kabaila, A.P. (1986). *Basic Concepts of Structural Analysis*, GreenwichSoft, Sydney.

Horne, M.R. (1978). *Plastic Theory of Structures*, 2nd edn., Pergamon Press, Oxford.

Neal, B.G. (1977). *The Plastic Methods of Structural Analysis*, 3rd edn., Chapman and Hall, London.

Rotter, J.M. and Ansourian, P. (1979). Cross-section behaviour and ductility in composite beams", Proceedings, Institution of Civil Engineers, London, Vol. 67, Part 2, 453-474.

Trahair, N.S. and Bradford, M.A. (1991). *The Behaviour and Design of Steel Structures*, revised 2nd edn. Chapman and Hall, London.

Uy, B. and Bradford, M.A. (1993). "Cross-sectional deformation of prestressed composite beams", Structural Engineering Review, Vol. 5, No. 1, 63-70.

10   Lateral - Distortional Buckling

10.1   Introduction

It was explained in Section 1.2.3.2 that when a composite beam is subjected to
negative or hogging bending, as is experienced over an internal support as shown in
Figs. 10.1(a) and (b), then the steel element may be subjected to *lateral-distortional
buckling*. Lateral-distortional buckling in a continuous composite T-beam is shown in
Fig. 10.1(c). This mode of buckling, which is shown in Fig. 1.16, is characterised by
distortion of the web of the steel element in the plane of its cross-section. In a beam
whose cross-section is plastic or compact in accordance with Section 5.3.2, premature
lateral-distortional buckling will prevent the full plastic moment of the composite
cross-section M_p from being achieved.
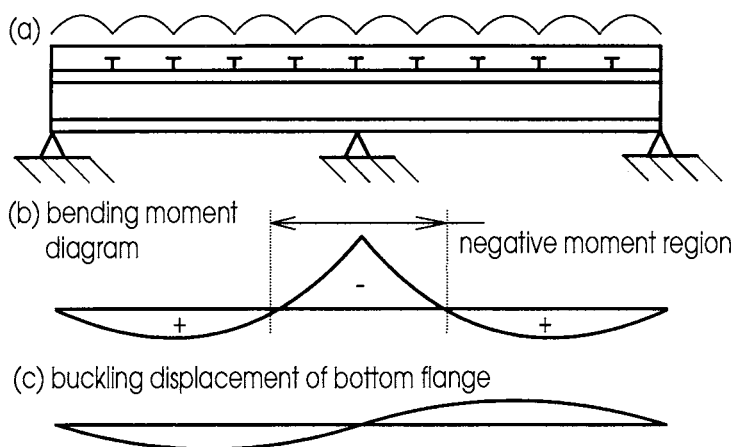
Fig. 10.1 Lateral-distortional buckling

In Section 1.2.3.2, it was also demonstrated that lateral-torsional buckling, as
shown in Fig. 1.15(a), cannot occur in the negative region of a composite beam
because this buckling mode is characterised by the beam cross-sections buckling out-
of-plane and twisting as rigid bodies in accordance with the Vlazov theory of thin-
walled structures (Vlazov 1961). Therefore, in order for the beam to buckle sideways
in an overall mode, the buckle must necessarily be lateral-distortional, as the cross-
sections of the steel element cannot remain rigid as in Vlazov's theory.

Research work on the lateral-distortional buckling of steel I-sections was
summarised in a state of the art paper by Bradford (1992), which highlighted the fact
that much less attention had been devoted to the phenomenon than to either lateral-
torsional buckling or local buckling which form the basis of design rules in steel
standards. In particular, the treatment of lateral-distortional buckling in composite
beams has received very little attention, and approximations have been made in design

standards which have been shown to be very conservative. Because of the importance of lateral-distortional buckling in composite construction, its development in steel I-section beams is considered in the following section as an introduction to its occurrence in composite T-beams, which is described in Section 10.3.

10.2   Lateral-distortional buckling of steel beams

10.2.1   ELASTIC BUCKLING

10.2.1.1 *General*

Elastic lateral-torsional buckling theory is now well established, and state of the art texts such as that by Trahair (1993) direct the designer to a proliferation of publications and design aids that present accurate solutions. However, even when the steel behaves in a linear elastic fashion, the lateral-distortional buckling analysis of a steel I-beam is quite difficult, and recourse must generally be made to a computer program. Such programs are generally only research tools. It is for this reason that the phenomenon was not treated in any depth until the late 1960's, and even then certain simplifying assumptions had to be made.

The most common computer-based methods for analysing lateral-distortional buckling are the finite element method and the finite strip method, and these are discussed in Sections 10.2.1.2 and 10.2.1.3 respectively. Both of these approaches are based on the stiffness method of structural analysis (Hall and Kabaila 1986). These numerical methods have been able to give a valuable insight into the parameters that influence distortion of the cross-section during overall buckling.

10.2.1.2 *Finite element method*

The finite element method is used extensively for analysing structures, and the reader can find a large number of textbooks describing the procedure. Its application to lateral-distortional buckling has been far less widespread, due mainly to the large computing times required when standard meshing of the beam is adopted.

Elastic finite element buckling analyses differ in their formulation to the stiffness analyses used in many commercially available packages. The elastic stiffness matrix [K] for buckling is the same as that for a stiffness analysis, and is assembled from the element elastic stiffness matrices $[K^e]$ using equilibrium and compatibility, as set out in texts such as Zienkiewicz's well-known book (1971). Buckling analyses, however, require the assembly of what is termed a geometric stiffness matrix or stability matrix. Consider a steel member subjected to the stress resultants λM, λV and λN, where M is the initial bending moment distribution, V represents the shear force distribution and N the axial loads. Under linear elastic assumptions, these stress resultants are all increased monotonically by the same load factor λ up to the value λ_{cr} at which buckling occurs. The stresses produced by the stress resultants move when the member buckles, and as the member shortens infinitesimally when it buckles the stresses do positive work, and the potential energy stored in the steel member is thus

reduced during the buckling. This loss of potential is sometimes referred to as the geometric stiffness of the member. The stresses thus serve to destabilise the member, and the destabilising effect of these stresses is quantified by the stability or geometric stiffness matrix $\lambda[G]$. The stability matrix $\lambda[G]$ is assembled from the stability matrices $\lambda[G^e]$ of each element in the same way as is the stiffness matrix $[K]$. It can readily be shown that because the problem is linear elastic, the matrix $[G]$ can be developed from the initial stress resultants M, V and N, and then each term in $[G]$ is multiplied by the load factor λ to produce the stability or geometric stiffness matrix $\lambda[G]$.

Buckling solutions are based on minimising the total potential energy stored, as set out in Zienkiewicz (1971). When this is done, the resulting equation is

$$([K] - \lambda_{cr}[G])\{Q\} = \{0\} \tag{10.1}$$

where $\{Q\}$ is the vector of global buckling degrees of freedom. Equation 10.1 has two solutions. The trivial solution is

$$\{Q\} = \{0\} \tag{10.2}$$

which of course means that the member does not buckle since there are no buckling displacements. If the member buckles, then $\{Q\}$ must be nonzero, and so the other solution to Eq. 10.1 is that

$$\left| [K] - \lambda_{cr}[G] \right| = 0 \tag{10.3}$$

which is called an *eigenvalue problem* (Hornbeck 1975). The critical load factor λ_{cr} that makes the determinant in Eq. 10.3 vanish is called the eigenvalue. If this value of λ_{cr} is substituted into Eq. 10.1, then the equation can be solved for the buckling shape or *eigenvector* $\{Q\}$. Because the determinant of the bracketed term in Eq. 10.1 vanishes, the terms in $\{Q\}$ are what is known as linearly dependent (Hornbeck 1975). This means that the terms in $\{Q\}$ cannot be determined explicitly, but rather only their ratios can be found. Hence only the buckling *shape* can be ascertained, rather than a unique definitive value for $\{Q\}$.

There are several computer subroutines available for determining the critical value λ_{cr} in Eq. 10.3. One of the most useful is the method set out by Hancock (1984) for banded matrices, that results in rapid solutions for both the eigenvalue and eigenvector. It is based on Householder's tridiagonalisation and the Sturm sequence property (Hornbeck 1975).

A few finite element distortional buckling studies have been performed by meshing the flanges and web into a large number of rectangular elements. An early and frequently cited study is that of Johnson and Will (1974), who subdivided the web and flanges into 96 elements. Even with this relatively coarse meshing, the amount of computer time required to calculate the buckling load was large using the computers

of the time. The method has been extended by Ronagh and Bradford (1994) to handle tapered and redundant structures by using triangular finite elements.

The flanges of I-section members are generally stocky, so that it is the web rather than the flanges which distorts during buckling. By assuming rigid flanges but using a web which may distort as a cubic curve during buckling, Bradford and Trahair (1981) developed a powerful "beam" or "line" type of finite element, which is similar to the line elements used in frame analysis programs, in that the degrees of freedom are lumped at the end of each line element. This element, which is shown in Fig. 10.2, can handle unequal end moments, loads remote from the shear centre and arbitrary conditions of restraint. By using the discretisation of Fig. 10.2(a) and (b), the stiffness and stability matrices [K] and [G] in Eq. 10.1 are not large, rendering the extraction of the buckling load factor λ_{cr} very much more rapid than in the conventional finite element modelling using many rectangular elements. The buckled cross-section with a flexible web and rigid flanges, is shown in Fig. 10.3.

(a) discretisation into "line" elements   (b) typical line element
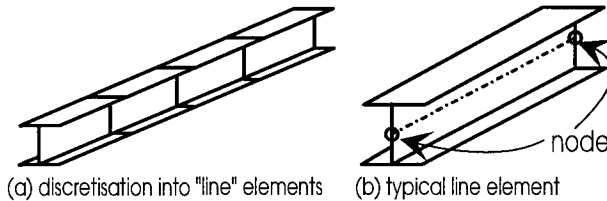
Fig. 10.2 Line-element model
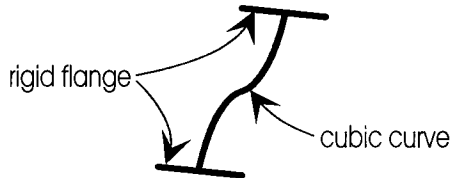
Fig. 10.3 Typical distortional buckling mode

10.2.1.3 *Finite strip method*

The finite strip method is another form of matrix stiffness analysis that has become reasonably popular in recent times. The basis of the method is presented in Cheung's book (1976). It differs from the finite element method in Fig. 10.4(a) in that the member is discretised into a number of longitudinal strips, as shown in Fig. 10.4(b).

In the finite element method, the buckled shape of each element is represented as a polynomial function, whereas in the finite strip method the longitudinal variation of buckling displacements is represented by harmonic functions. The advantage of the finite strip method is that it results in the same buckling formulation as Eqs. 10.1 and 10.3, but with the stiffness and stability matrices being very much smaller than those of the finite element method. Because of this, the

extraction of the elastic buckling load factor λ_{cr} by computer is much more rapid by the finite strip method than by the finite element method.

(a) Finite element discretisation   (b) Finite strip discretisation
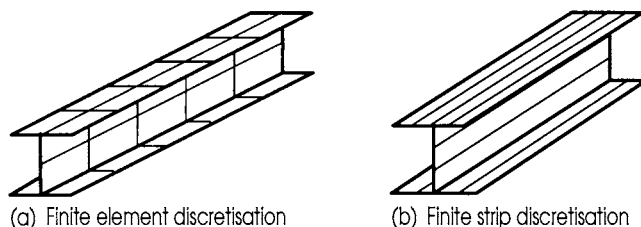
Fig. 10.4 Discretisation of steel I-section

The main disadvantage of using the finite strip method to model lateral-distortional buckling is that it can generally only be used for a simply supported member in uniform bending with equal and opposite end moments. While the latter restriction can be removed by deploying complex arithmetic while still maintaining high computational efficiency (Plank and Wittrick 1974, Bradford and Azhari 1994), general loading and restraint conditions can only be handled by recourse to the spline-based finite strip method (Lau and Hancock 1986) or using multiple harmonics (Graves Smith and Sridharan 1978, Bradford and Azhari 1995). Unfortunately, the latter two formulations lose much of the computational efficiency of the finite strip method that uses a single harmonic.

10.2.1.4 *Behaviour*

The finite strip method was used by Hancock (1978) to investigate the elastic buckling modes of an I-beam discretised as shown in Fig. 10.4(b) with simple supports and in uniform bending. The study showed that short or stocky elastic beams which are unrestrained along their length buckle in a local mode, long or slender beams in a lateral-torsional mode, while beams of intermediate length may buckle in a lateral-distortional mode which is a coupling of the local and lateral-torsional modes. In the finite strip meshing, both the flanges and web were modelled using several strips, and it was observed that during lateral-distortional buckling the flanges displace as rigid bodies while the web adopts a near cubic curve profile, as noted earlier.

Hancock's study, as well as a more detailed one by Hancock, Bradford and Trahair (1980), gave significant insight into the factors affecting distortion during the buckling of thin-walled I-section beams. In particular, beams with high values of the web slenderness ratio d_w/t_w and with stocky flanges (that is low values of b_f/t_f) tend to be influenced the most by distortion during buckling, in that the lateral-distortional buckling moment for these beams was reduced greatest below the lateral-torsional buckling moment. In addition, for all beams which are unrestrained along their lengths, lateral-distortional buckling takes place at a lower load than lateral-torsional buckling. The reduction in the buckling moment is illustrated by a typical graph in Fig. 10.5, where it can be seen that the effects of distortion increase as the beam becomes shorter. However, such short or stocky beams are likely to buckle locally or yield rather than buckle in a lateral-distortional mode.
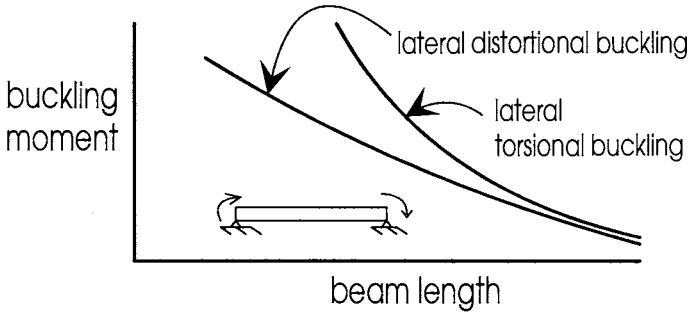
Fig. 10.5 Elastic buckling response

Because shorter or stocky beams buckle locally or yield, the effect of distortion in producing a lateral-distortional buckling load which is far below the lateral-torsional buckling load is not of great significance for beams which are simply supported, except if the flanges are very stocky and the web is very slender. For beams with thicker webs or more slender flanges, overall buckling predictions based on the lateral-torsional assumption of a rigid cross-section which are given in steel design standards are generally a satisfactory approximation.

The conclusion in the previous paragraph does not, however, apply for beams with partial restraint, such as a beam on a seat support as in Fig. 10.6 whose tension flange is fully restrained but whose compression flange is restrained only by the stiffness of the web, or by a beam with continuous tension flange restraint along its length. The line-type finite element of Section 10.2.1.2 was used by Bradford (1989a) to investigate the elastic lateral-distortional buckling of beams on seat supports, and it was shown that distortion of the web, even when quite stocky, results in the beam buckling in a lateral-distortional mode at a much lower load than that predicted by assuming lateral-torsional theory. This reduction in the buckling load is accounted for in many steel standards. I-section steel elements in composite beams are somewhat akin to partially restrained beams, so that lateral-distortional buckling results for this restraint condition are relevant to continuous composite beams as the concrete element continuously restrains the tension flange of the steel I-section element.
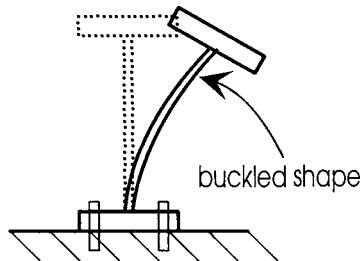
Fig. 10.6 Lateral-distortional buckling of a beam on a seat element

10.2.2 INELASTIC BUCKLING

The lateral-distortional buckling treatment considered in Section 10.2.1 assumed that the steel beam was elastic. However, real steel beams behave in an inelastic fashion, since they have residual stresses as in Figs. 2.5 and 2.6, and exhibit a stress-strain curve with yielding as shown in Fig. 2.2.

Local, lateral-distortional and lateral-torsional buckling of steel beams in the inelastic domain is quite difficult to predict, and there have been many approaches suggested for modelling the phenomenon. Rigorous analyses are based on either the so-called flow theory or deformation theory of plasticity, and as such treatments are beyond the scope of this book, the reader is referred to any one of a number of texts on the mathematical theory of plasticity. A simple method for treating overall buckling in the inelastic domain was set out by Bradford et al. (1987). It used the finite element method with line elements, and treated the steel beam as an elastic monosymmetric beam where the thicknesses of the yielded portion of the member were transformed according to the modular ratio E_{st}/E_s in accordance with dislocation theory of yielding, where E_s is the elastic modulus of the steel and E_{st} is its strain hardening modulus (Fig. 2.2).

The simplified method of transforming thicknesses in accordance with the strain hardening modulus was used by Bradford (1986) for studying inelastic lateral-distortional buckling. The finite element formulation was expressed as

$$\left| \left[K\left(\lambda_{cr}\right)\right] - \left[G\left(\lambda_{cr}\right)\right] \right| \;=\; 0 \tag{10.4}$$

which again has its basis on minimising the total potential. Equation 10.4 is similar to Eq. 10.3, but the stiffness and stability matrices [K] and [G] in Eq. 10.4 are not constants, as in the elastic formulation in Eq. 10.3, but depend nonlinearly on the load factor λ. This is because the transformed thicknesses used to determine [K] and the stress distribution used to determine [G] depend on the degree and extent of yielding, which is a function of the load factor λ. In order to solve Eq. 10.4, the method of bisections (Hornbeck 1975) was deployed whereby the determinant was calculated for small step increments of λ until it was found to change sign, bracketing λ_{cr} between positive and negative values of the determinant. Using the bisections method to then converge on λ_{cr} was found to alleviate the numerical problems that can develop using other solution strategies, owing to the poor behaviour of the determinant function. The determinant is not calculated explicitly as this is very inefficient. Rather, the method of Wittrick and Williams (1973) was modified, in which [K] - [G] is reduced to upper triangular form by simple Gaussian elimination (Hornbeck 1975), and the determinant calculated by multiplying the elements on the diagonal.

For partially restrained beams, either on seat supports as shown in Fig. 10.6 or where only the tension flange is continuously and fully restrained as would occur in a composite T-beam subjected to hogging bending, the inelastic study showed that as the beam became shorter distortion was significant during buckling. This behaviour, which is shown schematically in Fig. 10.7(a), differs from that for a simply supported

beam whose flanges are unrestrained throughout its span, where as the beam becomes shorter inelastic behaviour dominates distortional buckling and the inelastic buckling load approaches the plastic moment M$_P$, as in (b).

(a)

buckling moment

lateral distortional buckling

lateral torsional buckling

beam length

(b) M$_p$

strain-hardening buckling

elastic lateral-distortional buckling

Buckling moment

inelastic lateral-distortional buckling

Beam length
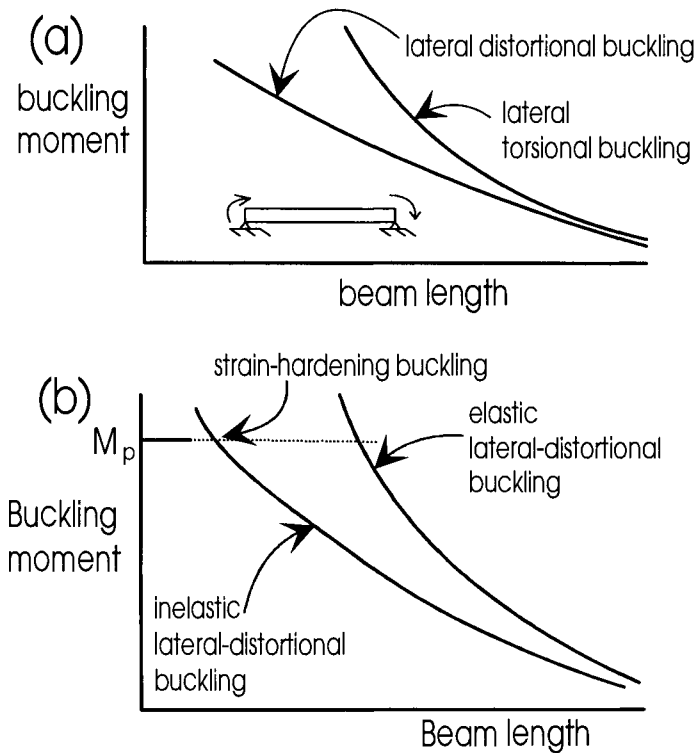
Fig. 10.7 Inelastic lateral distortional buckling

10.3   Lateral-distortional buckling of composite beams

10.3.1   ELASTIC BUCKLING

When a composite beam is subjected to load, some of the load is resisted by the concrete element, including the reinforcing, while some of the load is resisted by the steel element. Statics requires that the moments produced by these forces in the elements, as shown in Fig. 1.18(g) and in Eq. 1.2, be in equilibrium with the applied bending moments, while the net axial force should be zero. In addition, shear forces will generally be present, and as indicated in Section 7.5.3, it is sufficiently accurate to assume that the shear force is resisted by the web of the steel element. Therefore, in a lateral-distortional buckling analysis of the steel element of a composite beam, the destabilising effects caused by bending moment, axial force and shear force must be included.

In considering the overall buckling of beams or columns, the designer usually calculates the slenderness ratio λ as L/r_y and uses this as a basis for the buckling strength, where r_y is the radius of gyration about the minor axis of the beam or column and L is its effective length. More rational studies of the buckling of steel beams use the *modified slenderness* λ (not to be confused with the load factor in Section 10.2) given by (Trahair and Bradford 1991)

$$\lambda = \sqrt{\frac{M_p}{M_{cr}}} \qquad\qquad (10.5)$$

where M_p is the plastic moment of the beam and M_{cr} is its overall elastic buckling moment (either lateral-torsional or lateral-distortional).

For a composite T-beam subjected to negative bending, the buckling strength prediction of the steel element of the composite beam, given in Section 10.3.2 following is based on the modified slenderness λ_d for distortional buckling given by

$$\lambda_d = \sqrt{\frac{M_{ps}}{M_{od}}} \qquad\qquad (10.6)$$

where M_{ps} is the full plastic moment of the steel element and M_{od} is the elastic lateral-distortional buckling moment of the steel element which is partially restrained along its length by the concrete slab of the concrete element. It is therefore important to realise that in this design technique we are treating the steel element of the composite beam as a steel beam that is partially restrained by the concrete slab of the composite beam. It is therefore the properties of the steel element that control the design and not those of the composite section.

The difficulty in calculating the modified slenderness λ_d in Eq. 10.6 is that the lateral-distortional buckling moment M_{od} must be determined. As discussed in Section 10.2.1.2, this generally requires recourse to a computer program, and the line-type finite element of Bradford and Trahair (1981) described in Section 10.2.1.2 is ideal for this. Based on studies by Weston and Nethercot (1987), a suggested design approximation for λ_d is

$$\lambda_d = 0.018 \left(\frac{L_b}{r_y}\right)^{1/2} \left(\frac{d_w}{t_w}\right)^{1/3} - 0.40 \qquad\qquad (10.7)$$

where L_b is the length of the beam between supports, r_y is the radius of gyration of the bottom flange of the steel element about the web, while the web has a depth d_w and a thickness t_w. There are two points worth noting in Eq. 10.7. Firstly, λ_d is independent of the yield stress f_y which appears in Eq. 10.6 by the introduction of the plastic moment of the steel element M_{ps}. This is because Eq. 10.7 best predicted the computer solutions over a range of f_y of 250 N/mm^2 to 350 N/mm^2 which are the

yield stresses most commonly met in practice, and implicit in the formulation of Eq. 10.7 is that λ_d may be calculated from this equation regardless of whether the steel element is plastic, compact, semi-compact or slender (Section 5.3.2). The second point is that λ_d is independent of the moment gradient, and this independence was demonstrated by Bradford (1989b) using an inelastic finite element program.

An alternate approach is to calculate λ_d directly from Eq. 10.6 using the tabulations of M_{od} for a variety of geometries given by Bradford and Gao (1992). These solutions were only for compact steel elements typical of hot-rolled sections.

10.3.2 BUCKLING STRENGTH

Elastic buckling solutions only predict the strength of extremely slender members, as in general there will be an interaction between yielding and buckling, as outlined in Section 10.2.2. For example, if the well-known Euler buckling load for a pin-ended column N_{cr} in Eq. 1.14 which can be written as

$$N_{cr} = \frac{\pi^2 E A}{\left(L / r_y\right)^2}$$

(10.8)

is used where A is the cross-sectional area of the column, then clearly for very short columns N_{cr} would approach infinity, when in fact the maximum strength of the column is its squash load $A f_y$. This is taken account of by modifying the elastic buckling theories to produce semi-empirical design proposals for strength that incorporate yielding, residual stresses and initial crookedness. Hence, the column strength in many steel design standards is based on the well-known Perry-Robertson curve described in Section 1.3.4.2, so that short members will fail by yielding, long slender members by elastic buckling and intermediate length members by a combination of yielding and buckling.

The buckling strength of the steel element of a composite beam in a negative bending region may also be predicted by an interaction between yielding and elastic buckling. In one suggested interaction (Bradford 1989b), the buckling strength M_{bs} of the steel element in a composite T-beam may be obtained from

$$M_{bs} = 0.8 \left\{ \sqrt{\lambda_d^4 + 3} - \lambda_d^2 \right\} M_{ps} \leq M_{ps}$$

(10.9)

where λ_d is the modified slenderness given by Eq. 10.7 and M_{ps} is the full plastic moment of the steel section. Although the strength in Eq. 10.9 was determined for compact sections, it is suggested that it may also be used for semi-compact and slender sections by replacing M_{ps} by the actual section strength of the cross-section as influenced by local buckling. Note also that Eq. 10.9 is approximate, in that it ignores the axial force in the steel element, F_{steel}, in Fig. 1.18(g).

The relationship between M_{bs} and λ_d is plotted in Fig. 10.8. It can be seen that when λ_d is less than 0.76, the beam is stocky and the full plastic moment of the steel element is reached, while as the slenderness becomes large the design strength of the steel element approaches the elastic buckling curve (given in Fig. 10.8 and in Eq. 10.6 as M_{ps} / λ_d^2) which in turn approaches zero. For intermediate values of λ_d between 0.76 and around 1.3, the design curve falls below the plastic moment M_{ps} and the elastic lateral-distortional buckling moment of the steel element M_{od} owing to the interaction between buckling and yielding. The design curve is slightly unconservative for values of λ_d greater than 1.4, but such slendernesses are not typical of most composite T-beams. In calculating the strength of the composite beam in negative bending, the beam capacity of the steel element M_{bs} forms the basis of the design method, as is illustrated in the following examples.
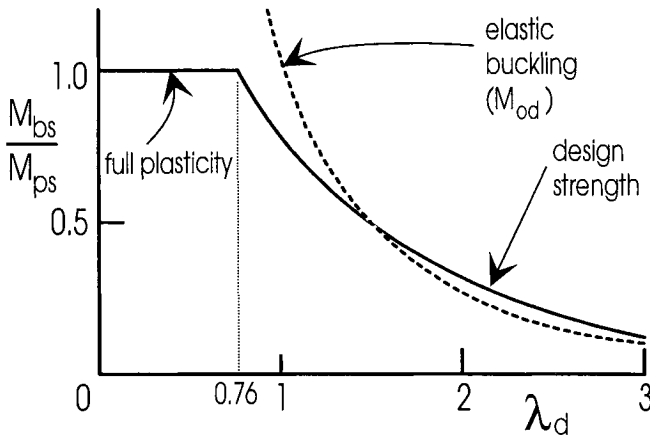
Fig. 10.8 Strength prediction of Eq. 10.7

Example 10.1 Buckling resistance of hot rolled element in composite beam

A hot-rolled steel I-section element used typically in a continuous composite T-beam has $h_{steel} = 612$ mm, $b_f = 229$ mm, $t_f = 19.6$ mm, $t_w = 11.9$ mm and so $d_w = 573$ mm. Its plastic section modulus is $S = 3680 \times 10^3$ mm^3 and the radius of gyration of its bottom flange is $r_y = 66.1$ mm. The yield stress is $f_y = 350$ N/mm^2, so that $M_{ps} = 1288$ kNm.

In Eq. 10.7 $\lambda_d = 0.00806 \sqrt{L_b} - 0.40$ (L_b in mm), so that in Eq. 10.9 the full plastic moment of the steel element will be reached for lengths between the supports L_b of less than 20.71 m. If the slab was typically 200 mm thick, then this represents a span to depth ratio of the composite beam of 26. This value is quite high, so a typical span length for this beam would be less than 20.71m, and the strength of the steel element of the composite beam would be its plastic moment of 1288 kNm. Hence it can be assumed that the steel element of the composite beam is fully yielded.

By knowing the properties of the slab, the section capacity of the composite beam may be calculated as in Sections 7.3 and 7.4.

It can thus be concluded that lateral-distortional instability of this steel element in this case is unlikely, and this conclusion can be extended to other typical hot-rolled sections. Because of this, most composite T-beams using hot-rolled sections for the steel element will reach the plastic moment capacity in negative or hogging bending as calculated in Section 7.4.

Example 10.2 Buckling resistance of welded plate girder in composite beam

Consider now a welded plate girder in a continuous composite T-beam bridge girder having $b_f = 350$ mm, $t_f = 30$ mm, $d_w = 1300$ mm and $t_w = 12$ mm. If $f_y = 350$ N/mm^2 then $(b/t)\sqrt{f_y} = 109$ and $(d/t)\sqrt{f_y} = 2027$, so from Section 5.2.4 the section is nearly compact and $M_{ps} = 6662$ kNm. The slenderness λ_d in Eq. 10.7 is $0.00854\sqrt{L_b} - 0.40$ (L_b in mm), so that from Eq. 10.9 M_{ps} will be reached for spans of less than 18.45 m. If the slab depth h_{conc} is 300 mm, then this corresponds to a span to depth ratio of 11.1 which for a bridge girder would be quite low. For a span to depth ratio of 20, then $L_b = 33.2$m, $\lambda_d = 1.16$ and $M_{bs} = 4540$ kNm from Eq. 10.9. This reduction of 32% below the full plastic moment of the steel element is a result of lateral-distortional buckling, and this reduced bending capacity must be used in calculating the section capacity of the composite member.

Unlike the hot-rolled steel element in Example 10.1, lateral-distortional buckling can take place when plate girders are used in composite T-beams. Most plate girders have cross-sections that are not plastic or compact, so plastic analysis cannot be used. Even if the plate girder is compact, as in this example, then lateral bracing must be provided to decrease L_b so that the full plastic moment of the steel element can be attained. Hence if the full plastic moment capacity of the composite section is required then bracing is needed at 18.45m centres. Alternatively, a reduced moment capacity can be used.

In order to calculate the reduced hogging moment capacity of the composite section M_{hog} with full shear connection when lateral-distortional buckling prevents full plasticity of the steel element, consider the stress distribution shown in Fig. 10.9(a). As $M_{bs} < M_{ps}$ in the steel element for lateral-distortional buckling, then the stress distribution may be considered conveniently as elastic as this will reduce the axial force F_{steel} in Fig. 1.18(g). The curvature in the steel element κ is therefore given by

$$\kappa = \frac{M_{bs}}{E_s \, I_s} \tag{10.10}$$

where I_s is the second moment of area of the steel element, and as there is full interaction this is also the curvature in the composite section as shown in Fig. 10.9(b). The axial force N_s in the steel element is obtained from the volume of the stress block over the area of the steel element. Then, upon some simplification

$$N_s = \frac{M_{bs}}{I_s}\left\{(2b_f t_f + t_w d_{steel})d_n - b_f t_f d_{steel} - \frac{t_w d^2_{steel}}{2}\right\} \qquad (10.11)$$

and this acts through the centroid of the steel element as shown in Fig. 10.9.
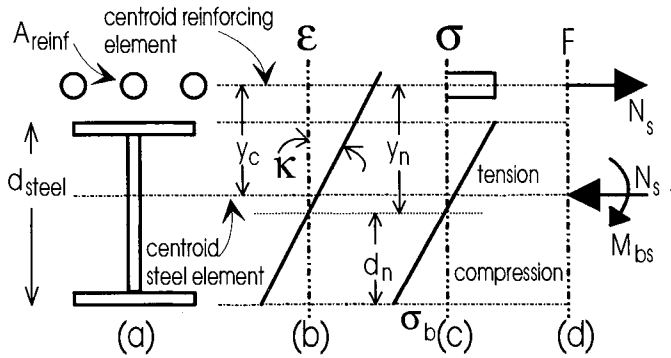
Fig. 10.9 Steel stresses for non-compact and slender beams

Equilibrium of axial forces requires that the force N_s in the steel element is equal and opposite to that in the slab reinforcement. If the reinforcement is assumed to have reached yield, then

$$N_s = A_{reinf} f_{yr} \qquad (10.12)$$

so that Eqs. 10.11 and 10.12 may be solved readily for d_n. The stress in the reinforcing bars is thus $y_n M_{bs}/I_s$. If this stress is found to be less than f_{yr}, then a revised value of d_n must be obtained by equating N_s in Eq. 10.11 to $y_n A_{reinf} M_{bs}/I_s$ where y_n is a function of d_n as shown in Fig. 10.9(c). Finally, if the reinforcement is at yield then the hogging capacity of the composite beam M_{hog} is

$$M_{hog} = M_{bs} + y_c A_{reinf} f_{yr} \qquad (10.13)$$

where y_c is the distance between the centroid of the steel element and the centroid of the reinforcing bars as shown in Fig. 10.9(a) if the stress in the reinforcing is below yield then

$$M_{hog} = M_{bs} + \frac{y_n M_{bs} A_{reinf} y_c}{I_s} \qquad (10.14)$$

Example 10.3 Moment capacity of composite beam with lateral-distortional buckling

Consider now the beam in Example 10.2 with $L = 33.2$ m for which it was found that $M_{bs} = 4540$ kNm. Assume the slab is 2000 mm wide with $h_{conc} = 300$ mm, and has 0.5% of longitudinal reinforcing bars at its midheight with $f_{yr} = 400$ N/mm^2. Then $I_s = 11.5 \times 10^9$ mm^4 and $A_{reinf} = 3000$ mm^2.

If it is assumed that the reinforcement is at yield, then $N_s = 1200$ kN from Eq. 10.12 and $d_n = 751.5$ mm from Eq. 10.11. The stress in the reinforcing from this value of d_n is $y_n M_{bs}/I_s = 87.5$ N/mm^2 which is less than f_{yr}. The reinforcement is thus below yield, giving a revised value of d_n of 702 mm, and so $y_n = 658$ mm. The hogging moment capacity for this beam is thus $M_{hog} = 4690$ kNm (Eq. 10.14). The hogging rigid plastic capacity M_p calculated from Section 7.4 is 6811 kNm, so that lateral-distortional buckling results in a reduction of 31% in the composite section capacity. This is very close to the 32% reduction in the capacity of the steel element above calculated in Example 10.2.

10.4   Inverted U-frame approach

10.4.1   ANALYSIS CONCEPT

The finite element approach of Section 10.3 assumed that the concrete element provided rigid restraint to the top of the steel element in regions of hogging bending. When a composite beam consists of a number of steel I-section elements acting compositely with a concrete slab, an alternative and widely used approach for analysing the lateral-distortional instability is the *inverted U-frame approach*, based on the design approach for steel through-girder bridges (Johnson and Buckby 1986). This method considers the flexibility of the steel web and slab in the transverse direction.

An inverted U-frame is shown in Fig. 10.10, and consists of two I-section elements at a transverse spacing B. The web is assumed to restrain the bottom flange elastically by its own flexibility, the flexibility of the shear connection and the flexibility of the slab. The restraint stiffness α_t per unit length of beam can be obtained by applying a pair of unit forces F = 1 at the centroid of each bottom flange and calculating the deflection δ, whence

$$\alpha_t = 1/\delta \tag{10.15}$$

which has units of N/mm^2.

When the webs are stiffened by vertical stiffeners, as may be required to prevent local buckling in shear by subdividing the web into a number of rectangular

panels (Trahair and Bradford 1991), then the beam consists of a number of discrete U-frames. While the flexibility of the shear connection can be ignored in regions where the web is unstiffened, it should be taken into account at the positions of discrete U-frames (Johnson and Buckby 1986).
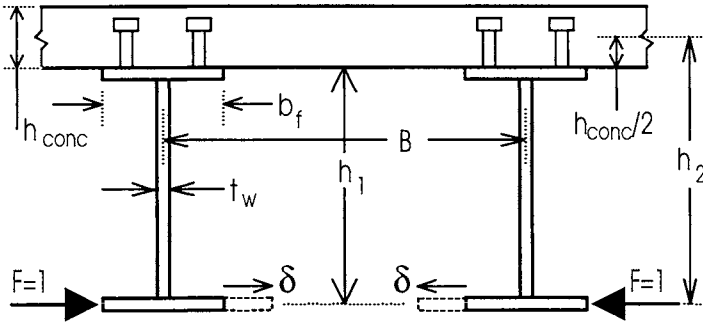
Fig. 10.10 Inverted U-frame concept

The inverted U-frame approach treats the bottom flange as a strut in the hogging region with a continuous translational restraint per unit length α_t. The elastic buckling load of the strut can be ascertained, as shown in Section 10.4.2, and this elastic buckling load can be used in a strength prediction of the type outlined in Section 10.3.2. Because the moment gradient is usually quite high in regions adjacent to internal supports, the compressive force in the flange decreases away from the support. The inverted U-frame approach treats the axial force as constant along a substantial length of flange, and is therefore conservative.

10.4.2 STRUT BUCKLING MODEL

Consider the bottom flange of the steel element shown in Fig. 10.10 that is restrained continuously by the web from buckling vertically, and restrained elastically in the plane of the flange by a continuous restraint of stiffness α_t per unit length of flange as shown in Fig. 10.11. As with the theory of Euler strut buckling (Trahair and Bradford 1991), the flanges remain straight under the axial force N until N reaches its critical value N_{cr}, and the strut undergoes infinitesimal buckling displacements u.
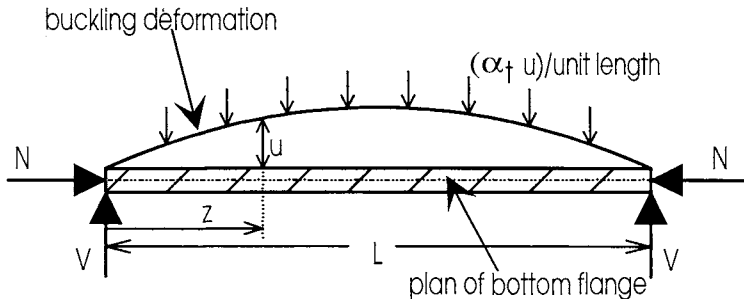
Fig. 10.11 Strut model

The buckling displacements are assumed to be represented by the curve

$$u = A \sin \pi z / L \tag{10.16}$$

where A is the undetermined magnitude of the central buckling displacement, and which satisfies the displacement end conditions that $u(o) = u(L) = 0$, and the pin-ended curvature conditions that $u''(o) = u''(L) = 0$. When the strut displaces u, the buckle is opposed by forces $\alpha_t u$ per unit length, and these forces are in equilibrium with the end shears V in Fig. 10.11. Following the theory given in Bleich (1952), it can be shown quite readily that the elastic critical load of the flange strut is

$$N_{cr} = \frac{\pi^2 E_s I_F}{L^2} + \frac{\alpha_t L^2}{\pi^2} \tag{10.17}$$

where I_F is the second moment of area of the flange about the axis through the web. The beam length L_{cr} that minimises N_{cr} is obtained by setting $dN_{cr}/dL = 0$. Hence

$$\frac{dN_{cr}}{dL} = -\frac{2\pi^2 E_s I_F}{L_{cr}^3} + \frac{2\alpha_t L_{cr}}{\pi^2} = 0 \tag{10.18}$$

so that

$$L_{cr} = \pi \left(\frac{E_s I_F}{\alpha_t} \right)^{1/4} \tag{10.19}$$

and substituting Eq. 10.19 into Eq. 10.17 produces

$$\left(N_{cr} \right)_{min} = 2\sqrt{E_s I_F \alpha_t} \tag{10.20}$$

Note that for an unrestrained strut, the second term in Eq. 10.17 vanishes and we have a standard Euler strut for which $(N_{cr})_{min} = 0$ at $L = \infty$.

It is worth noting that in strut theory, it is common to write the buckling load $(N_{cr})_{min}$ in terms of the effective length L_E by the equation (Trahair and Bradford 1991).

$$\left(N_{cr} \right)_{min} = \frac{\pi^2 EI}{L_E^2} \tag{10.21}$$

where EI is the flexural rigidity of the strut. Hence by equating Eqs. 10.20 and 10.21,

$$L_E = \frac{\pi}{\sqrt{2}} \left(\frac{E_s I_F}{\alpha_t} \right)^{1/4} \tag{10.22}$$

In some national codes of practice, the coefficient $\pi / \sqrt{2} \approx 2.221$ is taken as 2.5.

10.4.3   DESIGN APPROACH

When the inverted U-frame shown in Fig. 10.10 is subjected to the pair of unit forces $F = 1$, the deflection δ per unit length is the sum of that due to the flexibility of the web as a cantilever, $1 \times h_1^3 / 3 E_s I_{web}$, that due to the slab acted upon by a pair of equal and opposite moments $1 \times h_2$ which produce rotations $(1 \times h_2) B / 2 E_s I_{conc}$ and hence a deflection given by $h_2 (1 \times h_2) B / 2 E_s I_{conc}$, and that due to the flexibility of the shear connection which is ignored. Hence

$$\delta = \frac{h_1^3}{3 E_s I_{web}} + \frac{B h_2^2}{2 E_s I_{conc}} \tag{10.23}$$

where the second moment of area per unit length of the web is

$$I_{web} = \frac{t_w^3}{12} \tag{10.24}$$

and

$$I_{conc} = \frac{h_{conc}^3}{12n} \tag{10.25}$$

in which n is the modular ratio E_s/E_c. The elastic restraint stiffness may thus be found from Eq. 10.15 and the elastic critical load $(N_{cr})_{min}$ in the bottom flange from Eq. 10.20.

The elastic buckling stress in the bottom flange is $\sigma_{od} = (N_{cr})_{min} / A_F$, in which A_F is the area of the flange. This stress produces an elastic distortional buckling moment

$$M_{od} = \frac{(N_{cr})_{min} I_s}{A_F d_n} \tag{10.26}$$

where d_n is the neutral axis depth defined in Fig. 10.9 and I_s is the second moment of area of the steel element. The distortional buckling slenderness λ_d is then as in Eq. 10.6, and the buckling strength of the steel element is given by Eq. 10.9. The hogging section capacity is then obtained directly from either Eq. 10.13 or Eq. 10.14.

Example 10.4   Moment capacity using Inverted U-Frame approach

The beam in Examples 10.2 and 10.3 is assumed to have a modular ratio n = 12. The I-sections are spaced B = 5m and E_s = 200 kN/mm^2.

From Eqs. 10.24 and 10.25, I_{web} = 144 mm^4/mm and I_{conc} = 187.5 x 10^3 mm^4/mm. Noting that h_1 = 1300 + 30 + 30/2 = 1345 mm and h_2 = 1345 + 300/2 = 1495 mm, the first term of Eq. 10.23 is 28.16 mm per N/mm and the second term of Eq. 10.23 is 0.15 mm per N/mm, which is only 0.15/28.16 or less than 1% of the flexibility of the web. Hence α_t = (28.16 + 0.15)$^{-1}$ = 0.0353 N/mm^2 (Eq. 10.15).

Noting I_F = 350^3 x 30/12 = 107 x 10^6 mm^4 and A_F = 350 x 30 = 10,500 mm^2 produces an elastic buckling force of $(N_{cr})_{min}$ = 1738 kN (Eq. 10.20) and an elastic bottom flange buckling stress of σ_{od} = 1738 x 10^3/10,500 = 165.6 N/mm^2. From Example 10.3, d_n = 702 mm and so in Eq. 10.26 M_{od} = 4899 kNm giving a slenderness $\lambda_d = \sqrt{6662 / 4899}$ = 1.17 (Eq. 10.7) and a hogging steel capacity M_{bs} = 4470 kNm (Eq. 10.9); giving a composite beam capacity of M_{hog} = 4892 kNm. This result is only 4892/4968 or 1.5% conservative when compared with the finite element approach. This may be because the critical compressive span L_{cr} predicted by the inverted U-frame approach is L_{cr} = 8.77 m (Eq. 10.19) which is much less than the beam length of L = 33.2 mm, so that only 26% of the beam length adjacent to the internal support is assumed to be in uniform compression. The conservatism of the inverted U-frame approach is thus minimised in this case.

10.5   References

Bleich, F. (1952). *Buckling Strength of Metal Structures*, McGraw-Hill, New York.

Bradford, M.A. (1986). "Inelastic distortional buckling of I-beams", Computers and Structures, Vol. 24, No. 6, 923-933.

Bradford, M.A. (1989a). "Buckling of beams supported on seats", The Structural Engineer, Vol. 67, No. 23, 411-414.

Bradford, M.A. (1989b). "Buckling strength of partially restrained I-beams", Journal of Structural Engineering, ASCE, Vol. 115, No. 5, 1272-1276.

Bradford, M.A. (1992). "Lateral-distortional buckling of steel I-section members", Journal of Constructional Steel Research, Vol. 23, 97-116.

Bradford, M.A. and Trahair, N.S. (1981). "Distortional buckling of I-beams", Journal of the Structural Division, ASCE, Vol. 107, No. ST2, 355-370.

Bradford, M.A., Cuk, P.E., Gizejowski, M.A. and Trahair, N.S. (1987). "Inelastic lateral buckling of beam-columns", Journal of Structural Engineering, ASCE, Vol. 113, No. 11, 2259-2277.

Bradford, M.A. and Gao, Z. (1992). "Distortional buckling solutions for continuous composite beams", Journal of Structural Engineering, ASCE, Vol. 118, No. 1, 73-89.

Bradford, M.A. and Azhari, M. (1994). "Buckling modes in I-beams by a complex finite strip method", Civil Engineering Transactions, Institution of Engineers, Australia, Vol. CE36, No. 3, 219-226.

Bradford, M.A. and Azhari, M. (1995). "Buckling of plates with different end conditions using the finite strip method", Computers and Structures, to appear.

Cheung, Y.K. (1976). *Finite Strip Method in Structural Analysis*, Pergamon Press, Oxford, U.K.

Graves Smith, T.R. and Sridharan, S. (1978). "A finite strip method for the buckling of plate structures under arbitrary loading", International Journal of Mechanical Sciences, Vol. 20, 833-838.

Hall, A.S. and Kabaila, A.P. (1986). *Basic Principles of Structural Analysis*, GreenwichSoft, Sydney.

Hancock, G.J. (1978). "Local, distortional and lateral buckling of I-beams", Journal of the Structural Division, ASCE, Vol. 104, No. ST11, 1787-1799.

Hancock, G.J. (1984). "Structural buckling and vibration analyses on microcomputers", Civil Engineering Transactions, Institution of Engineers, Australia, Vol. CE26, No. 4, 327-332.

Hancock, G.J., Bradford, M.A. and Trahair, N.S. (1980). "Web distortion and flexural-torsional buckling", Journal of the Structural Division, ASCE, Vol. 106, No. ST7, 1557-1571.

Hornbeck, R.W. (1975). *Numerical Methods*. Quantum Publishers, New York.

Johnson, C.P. and Will, K.M. (1974). "Beam buckling by finite element procedure", Journal of the Structural Division, ASCE, Vol. 100, No. ST3, 669-680.

Johnson, R.P. and Buckby, R.J. (1986). *Composite Structures of Steel and Concrete. Vol. 2: Bridges*, 2nd edn., Collins Professional and Technical Books, London.

Lau, S.C.W. and Hancock, G.J. (1986). "Buckling of thin, flat-walled structures by a spline finite strip method", Thin-Walled Structures, Vol. 4, 269-294.

Plank, R.J. and Wittrick, W.H. (1974). "Buckling of thin, flat walled structures by a complex finite strip method", International Journal of Numerical Methods in Engineering, Vol. 8, No. 2, 323-339.

Ronagh, H.R. and Bradford, M.A. (1994). "Distortional instability of a tapered fabricated rafter in a portal frame building", Australian Structural Engineering Conference 1994, Sydney, 271-276.

Trahair, N.S. (1993). *Flexural-Torsional Buckling of Structures*, Chapman and Hall, London.

Trahair, N.S. and Bradford, M.A. (1991). *The Behaviour and Design of Steel Structures*, revised 2nd edn., Chapman and Hall, London.

Vlasov, V.Z. (1961). *Thin-Walled Elastic Beams*, 2nd edn., Israel Program for Scientific Translation, Jerusalem.

Weston, G. and Nethercot, D.A. (1987). "Continuous composite bridge beams - stability of the steel compression flange in hogging bending", Proceedings, Stability of Plates and Shell Structures, ECCS, Vandepitte, 47-52.

Wittrick, W.H. and Williams, F.W. (1973). "An algorithm for computing critical buckling loads of elastic structures", Journal of Structural Mechanics, Vol. 1, No. 4, 479-518.

Zienkiewicz, O.C. (1971) *The Finite Element Method in Engineering Science*, McGraw-Hill, London.

11   Splitting forces

11.1   Introduction

Part 4 of this book dealt with the elastic and rigid plastic behaviour of standard forms of composite beams, and in all cases it was assumed that the maximum dowel strength of the mechanical shear connectors, D_{max} in Section 2.4, could be achieved. It has also been shown in Chapter 2 that mechanical shear connectors transfer the longitudinal shear between the steel and concrete elements by imposing concentrated loads on the concrete element, and that the transfer of this concentrated load into the concrete element can cause the concrete to fail in tension by embedment cracking, ripping, shear and splitting as illustrated in Fig. 1.14. Part 5 of this book will look at ways of determining when these forms of tensile failure occur and the effect that tensile failure has on the maximum dowel strength D_{max}.

Tensile cracking of the concrete due to ripping, as shown in Fig. 1.14(b), does not affect the ability of the shear connection to transfer the shear, as it does not occur in a zone of high shear forces nor does it propagate into the bearing zone, shown in Fig. 2.14(a), that is in front of the connector. Hence, methods of predicting ripping failure (O'Brien 1986) are not covered. In this chapter, we will look at ways of determining when longitudinal splitting occurs in composite beams of all shapes and sizes and with shear connectors of variable geometry. The load to cause longitudinal splitting is a function of the transformed concrete area of the splitting zone (Oehlers and Johnson 1981). As the area of transverse reinforcement crossing this zone is relatively small, the splitting load can be considered to be independent of the transverse reinforcement, in the same way as the onset of flexural tensile cracking in reinforced concrete beams can be assumed to be independent of the longitudinal reinforcement. However, after longitudinal cracking has occurred, the dowel strength of the shear connectors depends on the amount of transverse reinforcement, and this subject is covered in Chapter 12. The transverse reinforcement is also required to transfer the shear across longitudinal cracks and this is covered in Chapter 13, and finally Chapter 14 deals with embedment failure and the ability of the shear connection to resist tensile forces that are normal to the steel/concrete interface of the composite beam.

11.2   Splitting

11.2.1 BEHAVIOUR

Consider a 20 mm diameter stud shear connector of tensile strength $f_u = 600$ N/mm^2 and $E_s = 200$ kN/mm^2, that is embedded in normal density concrete with a cylinder strength of $f_c = 30$ N/mm^2 (from Eq. 2.15, $E_c = 27.6$ kN/mm^2). Substituting these material properties and $n = \infty$ into Eq. 2.37 gives a mean dowel strength of $(D_{max})_{beam}$ = 129 kN. This force is transmitted into the concrete element by the bearing of the stud onto the concrete, in a region shown in Fig. 2.14(a) that is adjacent to the base of the stud. If we assume that stud bears onto the concrete over an area equal to the

252

width of the stud d_{sh} and a depth of equal length, that is over an area of $d_{sh}^2 = 400$ mm^2, then the bearing pressure is 322 N/mm^2 = 11f_c. It can be seen that the bearing pressure required to transmit the dowel force is an order of magnitude greater than the cylinder compressive strength of the concrete, and this can only be achieved if the concrete in the bearing zone is triaxially restrained. This is akin to the bearing stresses induced in a steel beam at the reaction points (Trahair and Bradford 1991).

The highly concentrated dowel force exerted by the shear connector is dispersed laterally into the concrete element, as represented by the arrows marked C in Fig. 1.14(b). Therefore, in order to maintain equilibrium, transverse tensile stresses are induced in the concrete that have a resultant force shown as T. If these transverse tensile stresses exceed the splitting tensile strength of the concrete f_{cb}, a longitudinal crack will occur in the concrete element that is in line with the shear connector. This crack will propagate through the bearing zone of the shear connection and hence release the triaxial restraint, so that the concrete will crush at a reduced bearing pressure. This means that the dowel strength will be reduced, unless there is an alternative form of lateral restraint such as that imposed by transverse reinforcement as described in Chapter 12.

Apart from flexural cracking, splitting is probably the most common form of tensile failure of the concrete element of the composite beam. Longitudinal cracking, through splitting, frequently occurs in composite beams that have limited side cover to the shear connector, such as L-beams in Fig. 1.8(e) (Johnson and Oehlers 1982); hybrid beams in (c) (Toprac and Dale 1967); haunched beams in (d) (Teraszkiewicz 1968); and in particular, composite beams with composite slabs with the ribs parallel to the steel element, as in Fig. 1.11(b) (Jayas and Hosain 1988). However, splitting can also occur in composite T-beams in which the side cover to the connectors is large, and can spread throughout the length of the beam, particularly when it is subjected to longitudinal moving loads as in bridges (Johnson and Oehlers 1981).

An example of splitting in a composite L-beam (Johnson and Oehlers 1982) is shown in Fig. 11.1, where the split has propagated throughout the length of the beam due to the absence of transverse reinforcement crossing the splitting plane. Figure 11.2 shows an example of splitting in a composite T-beam in which transverse reinforcement crosses the splitting plane. In this case a concentrated load was moved along the length of the beam (Johnson and Oehlers 1981) to simulate a moving wheel load on a bridge, and the movement of the load caused the split to propagate along the length of the beam. Splitting is also very common in push-tests, as shown in Fig. 11.3 for a single line of connectors (Johnson and Oehlers 1982) and in Fig. 11.4 for a slab with double connectors, and is the reason why shear connectors in push-tests sometimes appear weaker than the same shear connectors in T-beams.

In many forms of composite structures it may be necessary to prevent or restrict the occurrence of splitting at either serviceability or ultimate limit states, and methods for doing this are described in this Chapter. General analysis techniques are developed in Section 11.3 for a wide range of connector sizes and shapes of the concrete element, and application of these rules is described in Section 11.4. In Section 11.5, the general rules are applied to stud shear connections and it is shown how they can be simplified into detailing requirements.
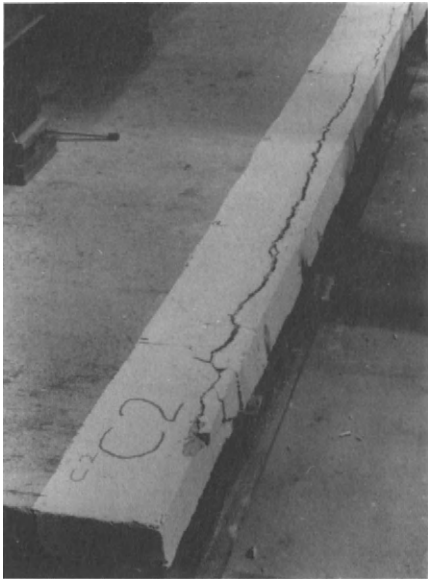
Fig. 11.1 Splitting of L-beam
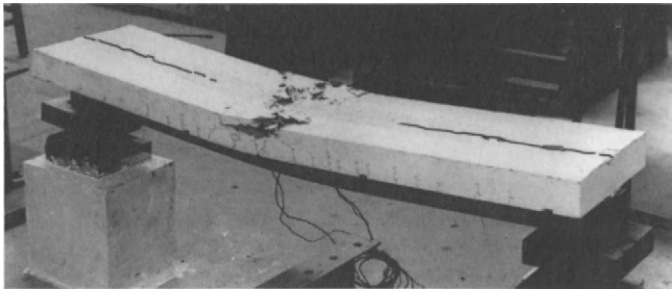
Fig. 11.2 Splitting in a T-beam
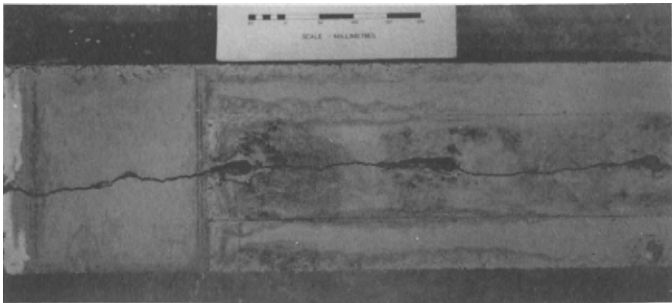
Fig. 11.3 Split push specimen with one line of connectors
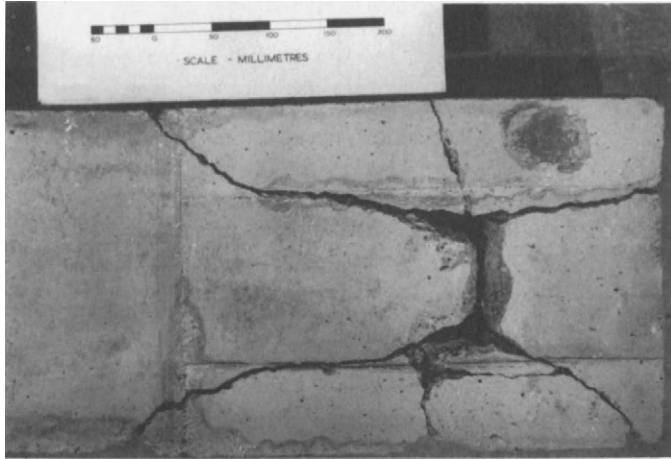
Fig. 11.4 Split push specimen with two lines of connectors

11.2.2 DESIGN PHILOSOPHY

Many of the concepts that have been developed for the design of the anchorage zone of post-tensioned concrete members (Leonhardt 1964) have been used in the following analyses of splitting by mechanical shear connectors. However, it should be remembered that anchorage zone design of post-tensioned members should not be applied directly to the design of mechanical shear connectors, as the procedures are based on differing design philosophies.

A procedure that is often used in anchorage zone design is to assume that splitting has occurred, and then place transverse reinforcement across the splitting zone that is of sufficient strength so that equilibrium can be maintained. Hence, the transverse reinforcement is now resisting the lateral tensile forces that are induced by the dispersal of the load. This equilibrium approach will work just as long as the concrete does not crush in the bearing zone due to the release of the triaxial restraint through splitting. Crushing of the concrete in the bearing zone can be prevented by either placing limits on the bearing pressure, or by confining the concrete in the vicinity of the bearing zone by surrounding it with reinforcement of sufficient stiffness.

It is difficult, if not impossible, to apply the anchorage zone approach to mechanical connectors as we are dealing with a large number of concentrated loads, and the bearing pressure in mechanical shear connectors tends to be much higher than in anchorage zones. Experimental research (Oehlers and Johnson 1981; Oehlers 1989) has shown that applying the equilibrium approach of anchorage zone design to mechanical shear connectors does not work, as the concrete in the bearing area crushes immediately splitting occurs. Hence even though the force system is in equilibrium after splitting, the dowel strength reduces through concrete crushing. Instead of applying the anchorage zone approach to the design of mechanical shear connectors, the post-splitting strength is based on the confining effect of the transverse reinforcement, that is on the stiffness and not on the strength.

In general, a two-pronged approach is recommended in the design of mechanical shear connectors against splitting: the concrete element is first designed so that splitting does not occur before the dowel strength is achieved; and then transverse reinforcement of sufficient stiffness is distributed so that the post splitting strength is the same as the splitting strength. Of course several approaches could be used. For example, it may be necessary to prevent the formation of splitting cracks at serviceability loads but allow them to occur before the dowel strength is reached, so that the post splitting strength is equal to the dowel strength. On the other hand, it may be impractical to try to achieve the maximum dowel strength and instead design for the reduced dowel strength after splitting.

11.3 General analysis

11.3.1 GENERAL

The general rules for splitting will first be developed in Sections 11.3.2 and 11.3.3, for the simplest case of a concentric strip load of width b_a that is applied to a prism of width b_c as shown in Figs. 11.5(a) and (b). Because the strip load is applied over the full depth of the prism h_c, the concentrated load is only dispersed in the x-y plane, that is in two dimensions. The effect of three-dimensional dispersal of the concentrated load is determined in Section 11.3.7 by considering the effect of concentric patch loads, as shown in Fig. 11.5(c). Sections 11.3.4 and 11.3.8 deal with splitting in non-symmetrical beams such as L-beams in Fig. 1.8(e), by considering eccentrically loaded prisms as in Fig. 11.5(d) and beams with sloping sides or haunches.

Consider the case of a connector acting in a composite T-beam as shown in Fig. 11.6(a). The centre line of the connector is in line with the centre line of the concrete element as shown, so that the concrete element is symmetrically loaded about the z axis. The connector is a bar connector (of the type shown in Fig. 1.5(e)) with a width b_a and height h_a. This is a stiff type of connector, so that we can assume that the bearing pressure between the connector and the concrete, over the area $b_a h_a$, is fairly uniformly distributed; as compared with the flexible type of connector (such as the stud shear connector and angle connector in Fig. 1.5(a) and (f)) where the bearing pressure is greatest adjacent to the base of the connector. The cross-section of the concrete element is rectangular with vertical sides and has a width b_c and depth h_c.

The dowel force exerted on the concrete element in Fig. 11.6(a) acts as a concentrated patch load and is dispersed both horizontally in the x-y plane and vertically in the z-x plane. In order to simplify the problem, the dispersal in the vertical direction can be eliminated by considering a connection in which the depth of the concrete element h_c is equal to the depth of the connector h_a; vertical dispersal will be considered in Section 11.3.7. Therefore, the problem has been simplified to that of a concentric rectangular strip load, of bearing area $b_a h_a$, acting on a rectangular prism, of cross-sectional area $b_c h_a$, that is shown as Prism 1 in Fig. 11.6(a).
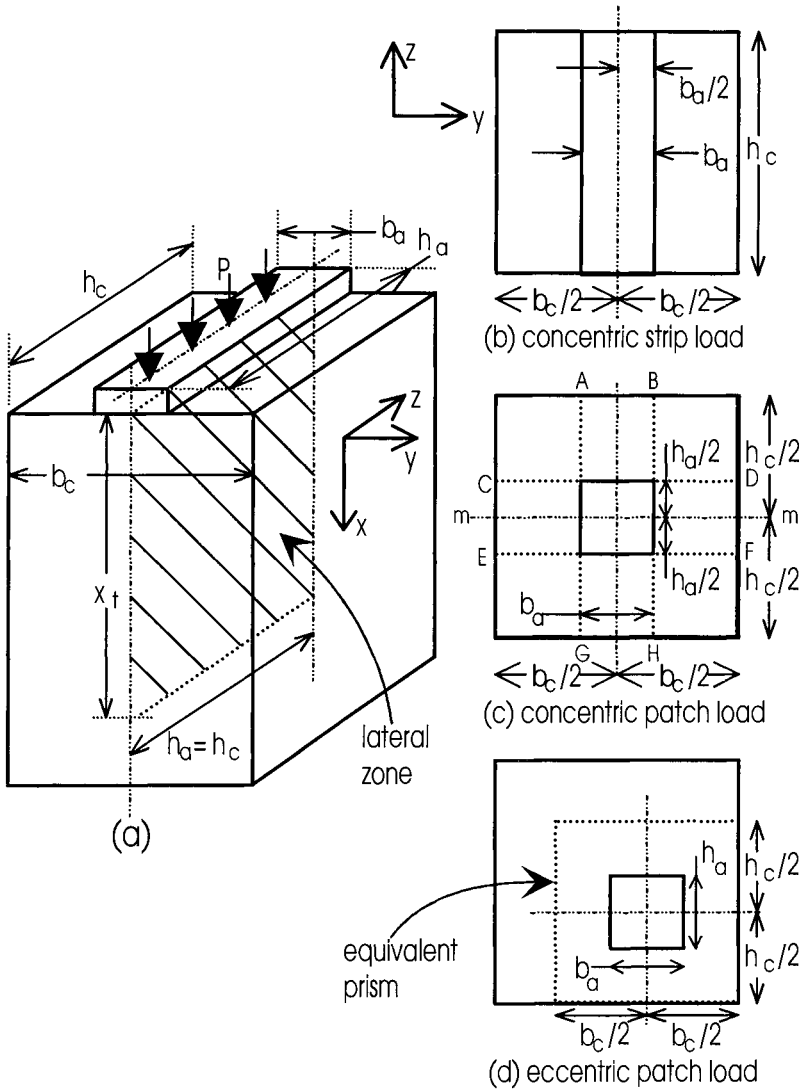
Fig. 11.5 Patch loads on prisms

We will first look at the lateral stresses induced by a single concentrated strip load, and this will be referred to as two-dimensional *local splitting*, and then we will look at the interaction between these lateral stresses when there is a longitudinal line of connectors and this will be referred to as two-dimensional *global splitting*. Section 11.3.7 will then describe procedures for adapting these two dimensional analyses to allow for the three-dimensional dispersal of the concentrated load.
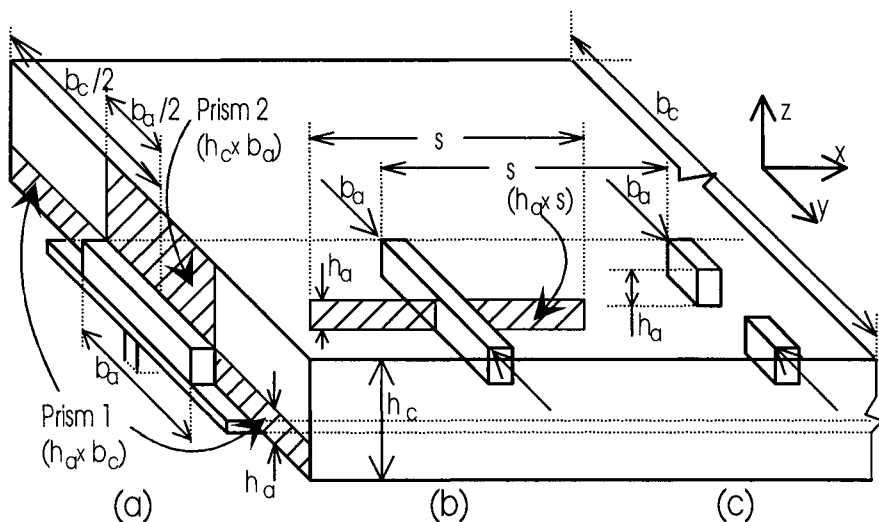
Fig. 11.6 Composite T-beam

11.3.2 LOCAL SPLITTING IN TWO DIMENSIONS

The stresses induced by individual connectors depends on the position of the connector relative to the ends of the beam. Where the connector is close to ends of the concrete element, such as at the supports of a simply supported beam at C in Fig. 1.12(b), then the behaviour is the same as that of a strip load P_{strip} on the surface of a concrete prism as shown in Fig. 11.7(a). This is a familiar problem to the anchorage zone design of post-tensioned reinforced concrete members (Leonhardt 1964, Gilbert and Mickleborough 1990).

The lateral stress distribution induced by the surface strip load has been determined from finite element elastic analyses (Oehlers and Johnson 1981) and is shown in Fig. 11.7(a). The distribution is characterised by a high compression zone over a short length adjacent to the strip load, that is in equilibrium with a tensile zone that is spread over a much greater length. The lateral compression zone helps to confine the concrete adjacent to the bearing area. The length of the transverse or lateral zone on one side of the connector, x_t in (a) was found to be dependent of the width of the element b_c and independent of the width of the concentrated load b_a and $x_t \approx 1.75b_c$. The zone in which the lateral stresses occur will be referred to as the *lateral zone* and has an area $x_t h_a$ as shown in Fig. 11.5(a).

When the connector is a long way from the ends of the concrete element, such as D in Fig. 1.12(b), then the lateral stress distribution is anti-symmetrical (Johnson and Oehlers 1981) as shown in Fig. 11.7(c). In this case, the shape of the lateral compressive stress distribution is identical to that of the lateral tensile stress distribution, and each extends over a distance of $x_t \approx 1.4b_c$ from the strip load. The length of the lateral zone is therefore $2x_t = 2.8b_c$. Therefore when the connectors have a longitudinal spacing of $s > 2.8b_c$, the lateral zones from each connector do not

overlap or interact. The stress distributions shown in Figs. 11.7(a) and 11.7(c) were derived from finite element analyses in which the distance $\ell_c \gg b_c$, so that the end restraints on the prisms did not affect the lateral stress distribution.
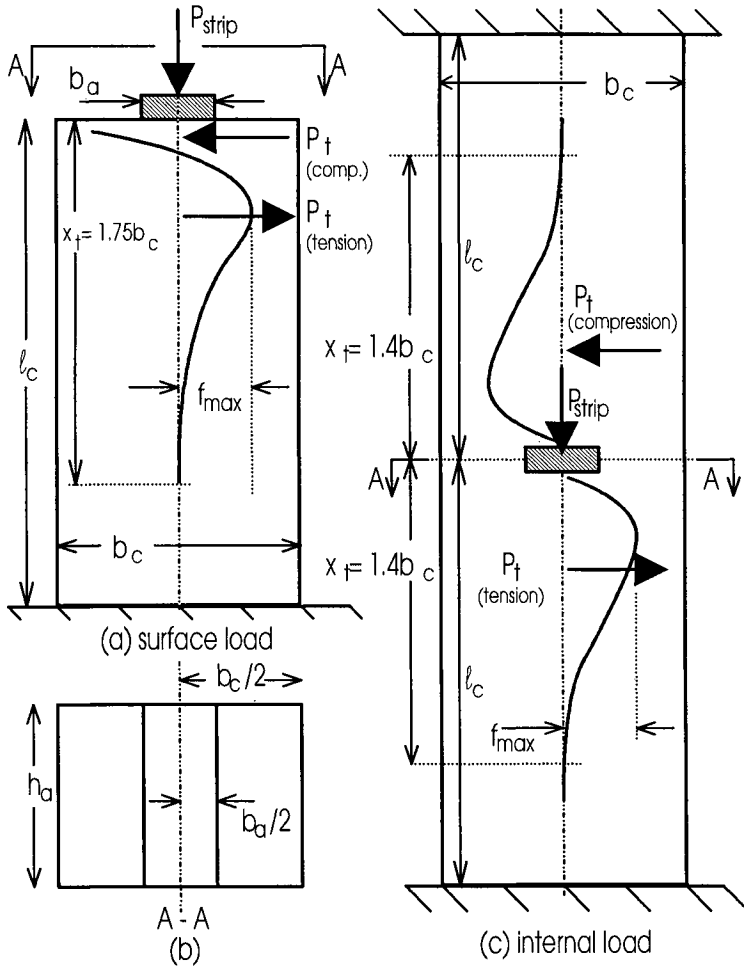
Fig. 11.7 Lateral stress zones

For convenience, let us define the ratio of the transverse tensile or compressive force P_t in Figs. 11.7(a) and (c) to that of the applied strip load P_{strip} as

$$K_d = \frac{P_t}{P_{strip}} \tag{11.1}$$

The mean lateral tensile stress over the lateral zone in which it acts is $f_{mean} = P_t / x_t h_a$. Let us also define the shape of the lateral tensile stress distribution K_{sh} as the ratio of

the mean stress f_{mean} to the peak stress f_{max} that is shown in Figs. 11.7(a) and (c), that is

$$K_{sh} = \frac{f_{mean}}{f_{max}} = \frac{P_t}{h_a x_t f_{max}} \tag{11.2}$$

Eliminating P_t from Eqs. 11.1 and 11.2 gives

$$P_{strip} = (x_t K_{sh}) \left(\frac{h_a f_{max}}{K_d} \right) \tag{11.3}$$

Finite element analyses of the structure shown in Figs. 11.7(a) and (b) (Oehlers and Johnson 1981) found that the lateral zone x_t varied in length when $\ell_c \leq 3b_c$ and that the length of x_t also depended on the form of restraint that was applied to the ends of the prisms. However, for a constant value of f_{max}, the force P_{strip} to cause this maximum stress was found to be constant even though x_t was varying. The only exception is when $\ell_c \leq b_c$, and as the length of the concrete element is unlikely to be less than its width in a composite beam, this condition can be ignored in practice. Hence the parameter $x_t K_{sh}$ in Eq. 11.3 is constant, as it will be shown in Section 11.3.3.4 that K_d is not a function of x_t. An analysis of the externally applied strip load in Fig. 11.7(a) (Oehlers and Johnson 1981) showed that $K_{sh} = 0.34$ and $x_t = 1.75b_c$, so that $x_t K_{sh} = 0.60b_c$. Therefore, Eq. 11.3 can be written as

$$P_{strip} = 0.6b_c \left(\frac{h_a f_{max}}{K_d} \right) \tag{11.4}$$

The load to cause the prism to split, P_{strip} in Eq. 11.4, depends on the ratio between the lateral force and the applied load K_d. When $b_c \rightarrow \infty$ in Fig. 11.7(a), we have a concentrated strip load that is being applied to the surface of an infinitely large plate. Flamant's original elastic solution of this problem (Timoshenko and Goodier 1970) showed that

$$(K_d)_{b_a=0} = \frac{P_t}{P_{strip}} = \frac{1}{\pi} \tag{11.5}$$

and this is also the solution for the case of $b_a/b_c \rightarrow 0$, and was found to be in good agreement with finite element simulations (Oehlers 1989). It is worth noting that Flamant's original solution for an infinitely wide plate showed that the lateral tensile stress f_{max} is zero, even though the lateral tensile force P_t is not zero and is given by Eq. 11.5 as $P_t = P_{strip}/\pi$. This can be explained by the fact that the length of the lateral zone is also a function of b_c ($x_t = 1.75b_c$ in Fig. 11.7(a)), and as $b_c \rightarrow \infty$ in Flamant's analysis then $x_t \rightarrow \infty$, so that the lateral tensile force is distributed over an infinite area and hence $f_{max} = 0$.

The lateral force parameter K_d in Eq. 11.5 only applies to a point load such that $b_a = 0$ on a prism of width b_c. In real structures b_a is always greater than zero. The

reliance of K_d on b_a is theoretically determined in Section 11.3.3.4 and is restated as follows to complete this section on local splitting:

$$K_d = \frac{P_t}{P_{strip}} = \frac{1}{\pi}\left(1 - \frac{b_a}{b_c}\right)^2 \tag{11.6}$$

This variation is in close agreement with finite element analyses (Johnson and Oehlers 1981) and Iyengar's analysis (Leonhardt 1964). It is worth noting that when $b_a = b_c$ in Eq. 11.6, $P_t = 0$ as there is no lateral dispersal of the load, and that the maximum lateral force P_t and hence the maximum lateral tensile stress f_{max} occurs when $b_a \to 0$.

When f_{max} in Eq. 11.4 is equal to the splitting tensile strength of concrete f_{cb}, that can be derived from Eq. 2.7, then P_{strip} is the applied load to cause the concrete element to split P_{split}, and hence incorporating K_d in Eq. 11.6 gives the following general equation for local splitting.

$$P_{split} = \frac{0.6 b_c h_a f_{cb}}{K_d} = \frac{0.6 b_c h_a f_{cb} \pi}{\left(1 - \frac{b_a}{b_c}\right)^2} \tag{11.7}$$

Equation 11.7 was found to be in good agreement with over 200 experimental tests by Williams (1979) (Oehlers and Johnson 1981), confirming that f_{cb} is the correct concrete tensile strength to be used in the analysis.

It can be seen in Eq. 11.7 that when the width of the patch b_a is equal to the width of the prism b_c, the splitting strength is infinite. This is because there is no lateral dispersal of the applied load and hence no lateral tensile stresses to cause splitting. This situation is analogous to a concrete cylinder or cube compression test. Furthermore when $b_c \to \infty$, $P_{split} \to \infty$ as the tensile zone tends to infinity. It should be remembered that Eq. 11.7 only gives the load at which splitting occurs and not the load at which the concrete crushes, although crushing often follows immediately after splitting when the bearing pressures are high.

Example 11.1 Two-dimensional local resistance to block shear connection

A composite T-beam uses bar connectors of the type shown in Fig. 1.5(e). The connectors have a width $b_a = 180$ mm, the concrete element an effective width of $b_c = 4000$ mm, and the remaining dimensions and properties of the shear connector are shown in Fig. 11.8. Experimental tests, or reference to codes, has shown that the connector has a maximum dowel strength of $D_{max} = 1300$ kN.

It has been shown in Section 2.4.2 and illustrated in Figs. 2.15 and 11.8 that the interface compressive pressure tends to be largest towards the base of the dowel. Hence the resultant compressive load tends to be closer to the base of the dowel than the top of the dowel. Therefore, a conservative approach to designing the fillet welds in Fig. 11.8 would be to assume that the resultant shear load D_{max} acts at a distance

$h_a/2$ from the base, so that the fillet welds would have to be designed for a shear force of D_{max} and a moment of $D_{max}h_a/2$.

From Eq. 2.7, $f_{cb} = 3.0$ N/mm^2 and hence from Eq. 11.7 the shear load to cause splitting is $P_{split} = 1984$ kN. This is a conservative estimate of the splitting resistance of the slab as vertical dispersal of the load has been ignored. As $D_{max} <$ P_{split}, the dowel strength can be achieved before splitting, so that splitting will not reduce the dowel strength. If D_{max} had been found to be greater than P_{split}, then the simplest solution would be to use a greater number of weaker connectors. It can be seen that local splitting can be prevented by increasing the number of connectors.

It is worth noting that from Eq. 11.6 $K_d = 0.912/\pi = 0.29$ so that the lateral tensile force $P_t = 0.29 \times 1300 = 377$ kN. Furthermore, as $b_a << b_c$ in this example, $K_d = 0.912/\pi \approx 1/\pi$ and so a conservative approach would be to assume in Eq. 11.6 that $(1-b_a/b_c)^2 = 1$. Therefore, a conservative estimate of the minimum width of the concrete element that is required to prevent splitting would be to substitute into Eq. 11.7 $P_{split} = D_{max}$ and $(1-b_a/b_c)^2 = 1$ which gives $b_c = 2874$ mm.
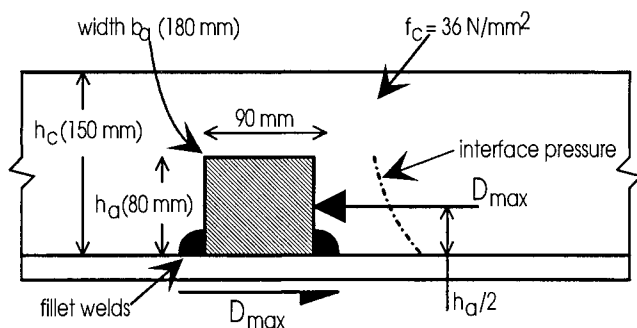
Fig. 11.8 Block shear connectors

11.3.3 GLOBAL SPLITTING IN TWO DIMENSIONS

11.3.3.1 *General*

Consider a single line of connectors of spacing s in a composite beam as shown in Fig. 11.9. The connectors are applying a thrust to the concrete element that is directed to the left as shown. Each connector induces a lateral tensile zone in front of the connector, such as A, and a compressive zone behind it of equal magnitude, such as B. Most of the lateral force occurs within a distance b_c from the connector. When the lateral zones of individual connectors overlap with the zones of other connectors, such as the overlap of zones B and C, then this interaction affects the splitting loads. This form of splitting will be referred to as global splitting, as it allows for the interaction of the lateral zones of all the shear connectors.
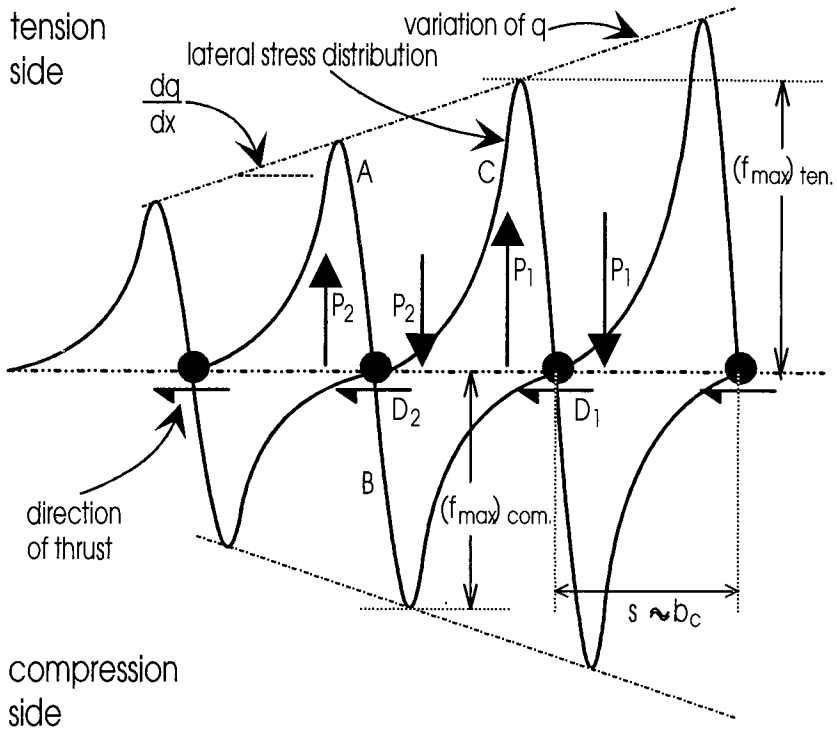
Fig. 11.9 Interaction of lateral stress zones

The lateral stress field for each connector is shown in Fig. 11.7(c). When the longitudinal spacing between connectors $s > 2x_t \approx 2b_c$, then the lateral stress fields are unaffected by adjacent connectors so they have the shape shown in (c) that has a highly non-uniform stress distribution. When $s \approx b_c$, then the lateral tensile and compressive zones overlap as shown in Fig. 11.9 for stress profiles C and B. The algebraic summation of these stresses reduces the magnitude of the maximum lateral stresses and tends to make the distribution of stress between connectors more uniform. When $s \ll b_c$, as is often the case in composite T-beams, then the lateral stresses between connectors can be assumed to vary uniformly, and it is this condition which will be dealt with in global splitting.

11.3.3.2 *Shear flow sign convention*

The lateral tensile stresses that induce splitting at a design point depend on the magnitude, variation and direction of the shear flow, as well as step changes in the shear flow. Let us first define a sign convention for describing these components of the shear flow, before defining the splitting stresses that they induce. It will be assumed that the shear flow in a composite beam can be idealised as linear variations with step changes at concentrated loads. When we are dealing with rigid plastic analysis, the magnitude and distribution of the shear flow will depend on the strength

and distribution of the shear connectors. However, when we are dealing with full interaction linear elastic analysis, it will depend on the vertical shear force.

Let us consider the shear flow on both sides of a section in a composite beam as shown in Fig. 11.10(a). The section being considered will be referred to as the design point. The shear flows on both sides of the design point have been drawn as positive in this example, so that the shear flows on either side of the design point are acting in the same direction. We will assume that these positive shear flows represent shear connectors applying a thrust to the concrete element that is directed to the right, as signified by the arrow; in other words, we are dealing with the connectors on the left hand side of the beam in Fig. 1.12(a). On the left hand side of the design point in Fig. 11.10(a), the shear flow can be represented by a constant component of magnitude q_L, as shown in (b), and *a varying component that is always zero at the design point* and which has a rate of variation along the length of the composite beam of $(dq/dx)_L$. Similarly on the right hand side, the shear flow can be represented by q_R and $(dq/dx)_R$. Hence any shear flow distribution at a design point can be represented by the four components.
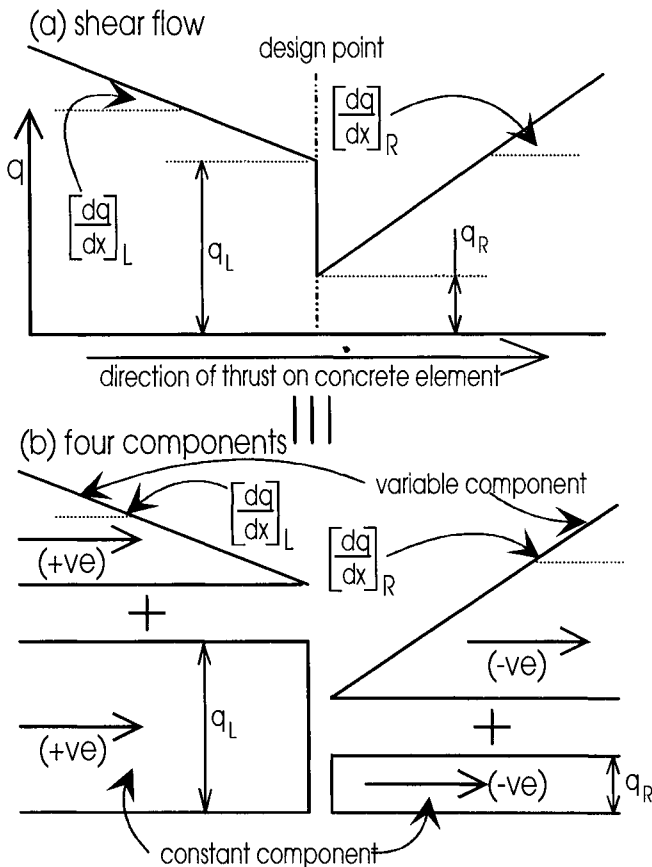
Fig. 11.10 Four components of shear flow

It is necessary to define a different sign convention for the shear flow when dealing with splitting analyses in order to distinguish between lateral tensile and lateral compressive zones. *We will define the constant component of the shear flow as positive when the connectors are applying a thrust to the concrete element that is directed towards the design point*, that is the shear flow is directed towards the design point. Hence q_L in Fig. 11.10(b) is positive as the thrust is towards the design point, whereas q_R is negative as the thrust is away from the design point. *We will also define the varying component of the shear flow as positive when the shear flow in the varying component is acting towards the design point.* Hence $(dq/dx)_L$ is positive as the shear flow in the varying component acts towards the design point, whereas $(dq/dx)_R$ is negative as the variable component of the shear flow is acting away from the design point. It will be shown in the following sections that *positive shear flows represent tensile lateral stresses at the design point, whereas negative shear flows represent compressive lateral stresses at the design point.*

Consider the beam shown in Fig. 11.11(a) where the distribution of shear flow and the direction of thrust is shown in (b). The four components of the shear flow for each of the design points A to G are shown in (c). At the design point A, $q_L = (dq/dx)_L = 0$, as the shear flow on the left hand side of the design point is zero. On the right hand side, the constant component of the shear flow is negative, that is $q_R = -q_1$, as the shear forces are acting away from the design point. The variable component of the shear flow must act towards the left, so that the sum of the variable component and the constant component is equal to the actual shear flow that reduces to the right. Further examples of the four components are given for the remaining design points in (c).

11.3.3.3 *Uniform component of shear flow*

A composite T-beam is subjected to a uniform shear flow of magnitude q over a length d_f as shown in Fig. 11.12(a). Half of the plan view of the concrete element of the composite beam is shown in (b) (Oehlers 1989). The shear flow q is induced by a uniform spread of shear connectors over a width b_a of the concrete element as shown by the hatched region in (b). This situation resembles a stub girder, as shown in Fig. 1.9(b), in which the shear flow along the stub is uniform.

Consider the connectors in the mid region of the shear flow, such as at G in Fig. 11.12(b), that is further than b_c from the ends E and H of the shear flow region. As we are dealing with a region of uniform shear flow, the lateral tensile and compressive stress zones will be the same magnitude for all of the connectors. Hence the tensile stress profile, such as C in Fig. 11.9, will be the same shape and magnitude as the compressive stress profile B from the adjacent connector as $dq/dx = 0$, so that the resultant lateral force will be zero. As we are assuming that $s \ll b_c$ in this global analysis, the lateral stress in this region will also be zero. The lateral stress zone that causes splitting occurs along the edge of the shear connectors, that is along the line C-D in Fig. 11.12(b). At a distance greater than b_c from the ends E and H, the lateral stresses as zero as shown (Oehlers 1989).
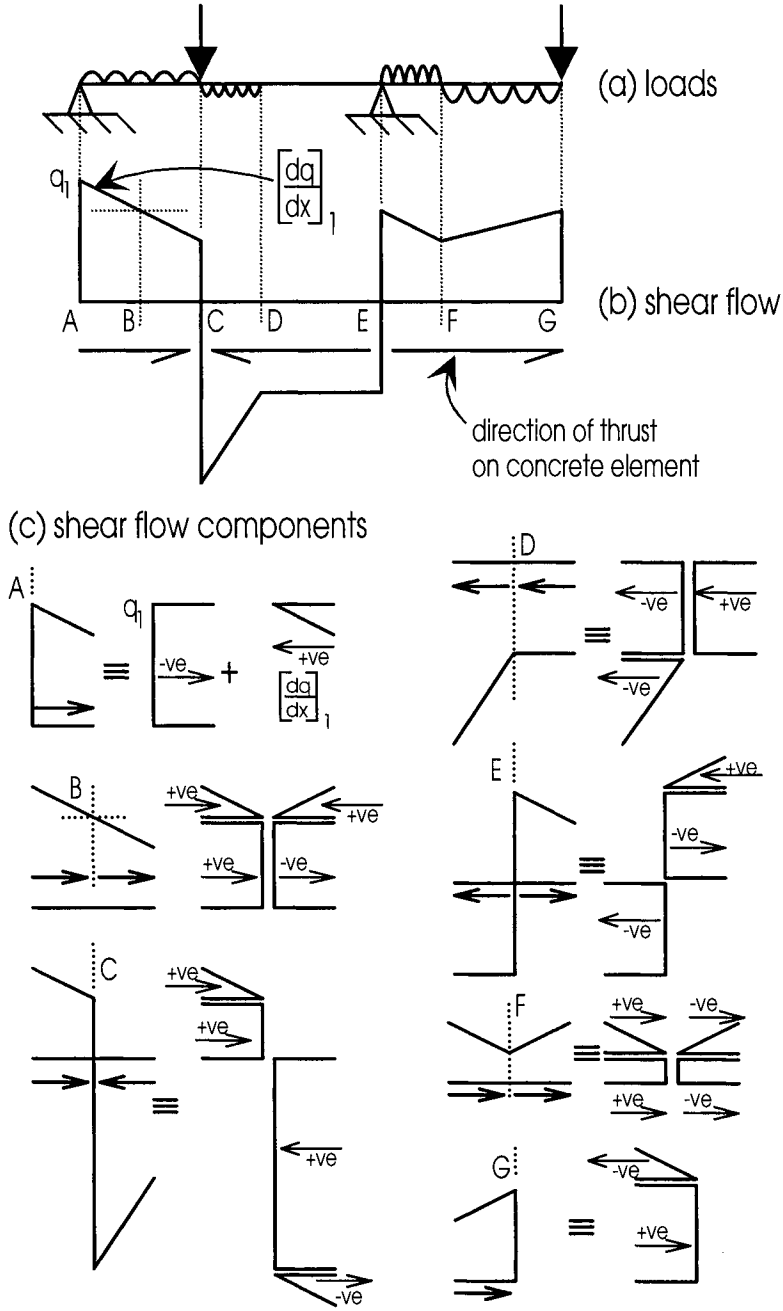
Fig. 11.11 Shear flow components
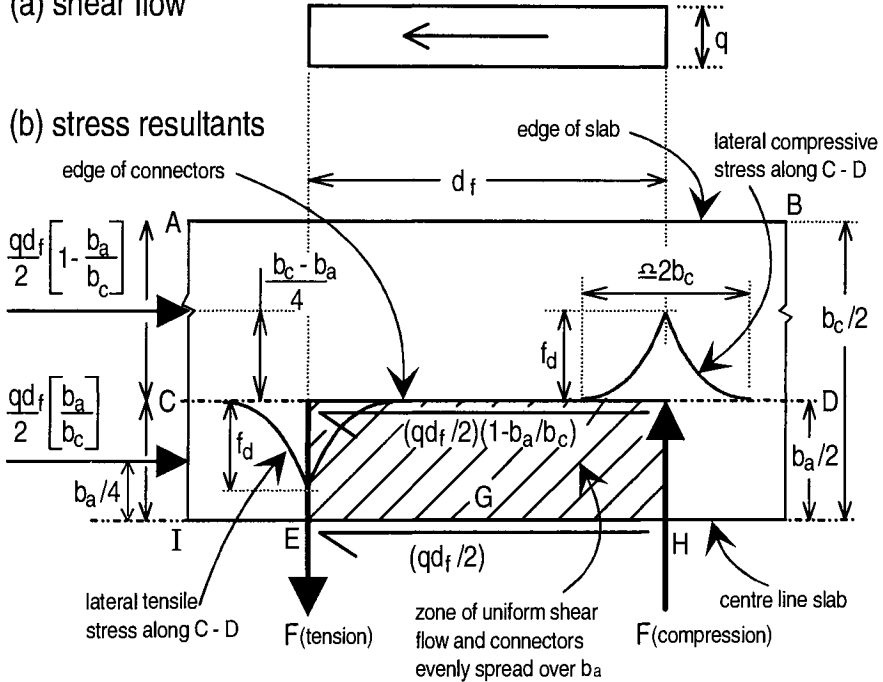
Fig. 11.12 Concrete element subjected to uniform shear flow

The tensile stresses at E in Fig. 11.12(b) and the compressive stresses at H are due to the discontinuity of the shear flow at these positions (Oehlers 1989). The magnitude of these stresses can be determined by considering the lateral tensile stress zones, induced by each of the connectors, separately from their lateral compressive stress zones. As an example, consider the lateral tensile stresses only. From Eq. 11.1, the lateral tensile force per connector $(P_t)_{tens}$ is given by

$$\left(P_t\right)_{tens} = K_d P_{strip} \tag{11.8}$$

As s is the longitudinal spacing of the connectors and h_a is the height of the tensile zone, as we are only dealing with two-dimensional splitting, then the cross-sectional area of the tensile zone per connector is $h_a s$, as shown in Fig. 11.6(b). Therefore, dividing the lateral tensile force in Eq. 11.8 by this area gives the mean lateral tensile stress f_d as follows

$$f_d = \frac{\left(P_t\right)_{tens}}{h_a s} = \frac{K_d P_{strip}}{h_a s} = \frac{K_d q}{h_a} \tag{11.9}$$

as P_{strip}/s is equal to the shear flow q.

The stress f_d in Eq. 11.9 is the maximum tensile stress that can occur as the beneficial effect of the lateral compressive stresses have been ignored in this analysis.

Position E in Fig. 11.12(b), at the very end of the shear flow, is a unique position in the beam because it is the only position where all the tensile stress zones from the uniformly distributed connectors and none of the compressive stress zones act (Johnson and Oehlers 1981). To the right of E, the lateral compressive stress zones gradually reduce the tensile stress to zero as shown, and to the left of E the tensile stresses gradually reduce due to the absence of tensile stress zones. Exactly the same argument can be applied to determining the lateral compressive stress f_d at H.

The lateral stress f_d at a discontinuity of a uniform shear flow is therefore given by

$$f_d = \frac{K_d q}{h_a} \qquad (11.10)$$

where q is the magnitude of the shear flow at the discontinuity. As can be seen in Fig. 11.12(b), the stresses at E are tensile as the thrust from the connectors is directed towards the design point E. From the notation in Section 11.3.3.2, q is defined as positive when determining the lateral stress at design point E as the lateral stress is tensile. Conversely, q is defined as negative when determining the lateral stresses at design point H, as the thrust imposed by the connectors is directed away from this design point so that the lateral stress is compressive.

The lateral stress at a design point that causes splitting is due to the shear flow on either side of the design point and is therefore equal to the step change Δq, that under the new sign convention is equal to the sum of the shear flows on either side of the design point, that is $\Delta q = q_L + q_R$. Consider the beam in Fig. 11.11 and let us ignore for the time being the variable component of the shear flow. At design point A, $\Delta q = 0 - q_R$ and hence splitting will not occur as the design point is only subjected to lateral compressive stresses. At design point B, $\Delta q = q_L - q_R = 0$ as the constant component of the shear flow on either side of the design point is of equal magnitude but opposite direction, and hence the constant component of the shear flow will not cause splitting. At design point C, $\Delta q = q_L + q_R$, that is the sum of the magnitudes of the shear flow, so that the splitting stresses could be large. However, at design point E $\Delta q = -q_L - q_R$ so that splitting would not occur.

Splitting will occur when $f_d = f_{cb}$ in Eq. 11.10, so that the step change in the shear flow to cause splitting Δq_{split} is given by

$$\Delta q_{split} = \frac{h_a f_{cb}}{K_d} \qquad (11.11)$$

It is worth noting that global splitting is a function of the shear flow and not the force per connector so that, unlike local splitting, increasing the number of connectors will not prevent global splitting. Furthermore as K_d is a function of the inverse of b_c, Δq_{split} reduces as b_c increases, so that wide slabs are more likely to split due to step changes in the shear flow. It is also worth noting that the analysis used to derive Eq. 11.11 is based on a sudden step change in the shear flow Δq, that may occur

theoretically when there is a point load. However, this sudden change rarely occurs in practice where the change in shear may be rapid but not sudden, and hence Eq. 11.11 tends to underestimate the resistance to splitting.

Example 11.2 Two-dimensional global resistance to step change in shear flow

The composite beam in Example 11.1 is part of a bridge and is subjected to a moving point load such as a group of wheels on an axle. From Example 11.1: $h_a = 80$ mm; f_{cb} = 3.0 N/mm²; and $K_d = 0.912/\pi$. Substituting these values into Eq. 11.11 gives Δq_{split} = 827 N/mm.

If we assume that the composite beam is behaving in a linear elastic fashion, then the shear flow can be derived from Eq. 1.9. The point load F_{point} to cause a step change in the shear flow of Δq_{split} can therefore be determined from Eq. 1.9 as

$$F_{point} = \Delta q_{split} \frac{I}{A \bar{y}} \tag{11.12}$$

It will be shown in Chapter 12 and discussed in Section 11.4 that transverse reinforcement crossing the lateral splitting zone will restrict the extent of the split, although it must be remembered that transverse reinforcement does not affect the onset of splitting. When the point load is stationary, the split will be restricted to a region adjacent to the point load and only affect a few connectors within this region, and hence the effect of splitting on the total strength of the shear connection may be negligible and could be ignored in practice. However, when the point load is moving along the length of the beam, then the split will move with the point load and hence extend over the full length of the beam. In this case, the strength of all the shear connectors may be affected; the strength after splitting will be determined in Chapter 12.

11.3.3.4 *Lateral force parameter K_d*

The parameter K_d in Eq. 11.11, and which was stated in Eq. 11.6, can be derived by considering the equilibrium of the slab A-B-C-D in Fig. 11.12(b) (Johnson and Oehlers 1981). The shear flow acting on this half of the slab is $q/2$, and therefore the longitudinal shear force is $qd_f/2$ along the edge E-H. This longitudinal shear force is resisted by a longitudinal in-plane compressive force in the concrete element as shown. Consider a section of the slab A-C-I that is far enough from the shear flow that the compressive force is uniformly distributed along the section so that there is no shear lag. The resultant force on the cross-section A-C is shown and acts mid-way between A and C and this is also the longitudinal shear force along C-D. Hence the lever arm between the longitudinal forces acting on the element of the slab A-B-C-D is $(b_c-b_a)/4$ as shown. The lateral forces F, due to the lateral stresses shown, act on the element A-B-C-D and have a lever arm of d_f.

Taking moments of all the forces acting on the element A-B-C-D gives

$$F = \frac{qb_c}{8}\left(1 - \frac{b_a}{b_c}\right)^2 \tag{11.13}$$

The same analysis can be applied to the condition of $b_a = 0$ in Fig. 11.12. In this case

$$F_{b_a=0} = \frac{qb_c}{8} \tag{11.14}$$

Dividing Eq. 11.13 by 11.14, and bearing in mind that the lateral forces are proportional to the lateral stresses which in turn are proportional to the lateral force per connector as shown in Eq. 11.9, gives

$$\frac{F}{F_{b_a=0}} = \left(1 - \frac{b_a}{b_c}\right)^2 = \frac{f_d}{(f_d)_{b_a=0}} = \frac{P_t}{(P_t)_{b_a=0}} \tag{11.15}$$

From Eq. 11.1,

$$P_t = P_{strip} K_d \tag{11.16}$$

and from Eq. 11.5,

$$(P_t)_{b_a=0} = \frac{P_{strip}}{\pi} \tag{11.17}$$

Hence dividing Eq. 11.16 by Eq. 11.17 and comparing with Eq. 11.15 gives

$$\frac{P_t}{(P_t)_{b_a=o}} = \frac{F}{F_{b_a=0}} = K_d\pi = \left(1 - \frac{b_a}{b_c}\right)^2 \tag{11.18}$$

Hence

$$K_d = \frac{1}{\pi}\left(1 - \frac{b_a}{b_c}\right)^2 \tag{11.19}$$

as previously stated in Eq. 11.6.

11.3.3.5 *Varying component of shear flow*

The analysis for the varying component of the shear flow (Oehlers 1989) is shown in Fig. 11.13 and follows a similar line to the previous analysis for the constant component of the shear flow in Fig. 11.12. The composite beam in Fig. 11.13(b) is subjected to a gradually reducing shear flow of magnitude q at H and zero at E as shown in (a).

(a) shear flow
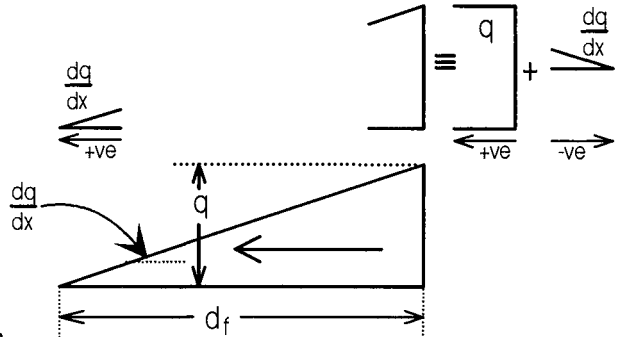
(b) stress resultants
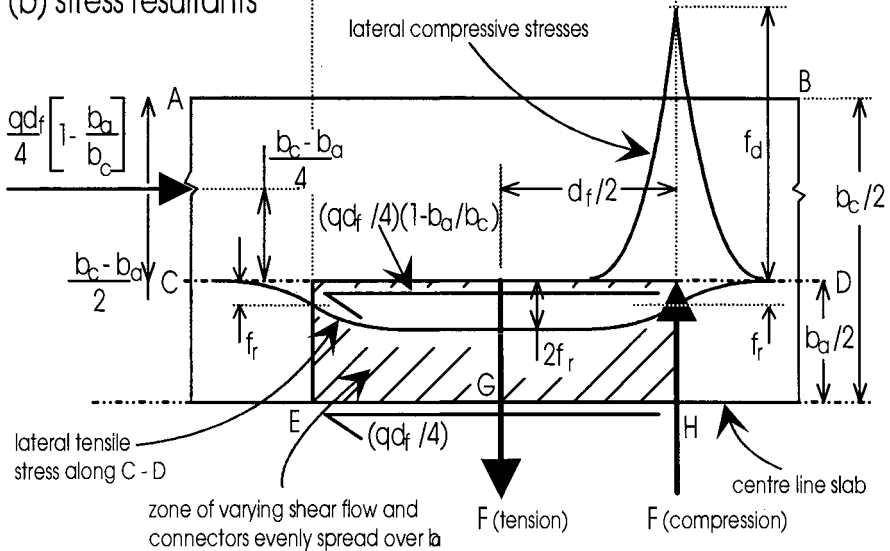
Fig. 11.13 Concrete element subjected to varying shear flow

Consider a group of connectors at G in Fig. 11.13(b) that is mid-way between the ends of the shear flow at E and H. Point G has been chosen as the lateral stress distributions at this point are not affected by the end effects at E and H, that is the sudden changes in the shear flows at E and H, and hence the local lateral stress distributions have the shapes shown in Fig. 11.9. The connector load D_1 induces a lateral tensile force P_1 in front of the connector and lateral compressive forces P_1 behind the connector. The connector load D_2 is less than D_1, because the shear flow is reducing to the left, so that the lateral forces P_2 will be less than P_1. The resultant lateral force between these connectors is therefore $\Delta P = P_1 - P_2$. Hence there is a resultant tensile load ΔP across the lateral zone between the connectors because the shear flow is reducing to the left.

In this global analysis, we are assuming that $s \ll b_c$, so that there are no local variations in the stress field. We are also assuming that dq/dx is constant, so that ΔP is also constant along the varying shear flow. Hence, we would expect a uniform

lateral tensile stress zone around point G in Fig. 11.13(b) and this has been confirmed through finite element analyses (Johnson and Oehlers 1981). The uniform lateral stress has been shown as $2f_r$ in Fig. 11.13(b). The lateral stress around the end of the shear flow at E is affected by the discontinuity in the shear flow. Finite element analyses or simply the summation of the local stress distributions of the individual connectors (Oehlers 1989) shows that the lateral stress reduces from $2f_r$ to f_r at E as shown. The variable component of the shear flow is applying a thrust towards the design point E and this causes a tensile stress at E, and hence this direction of shear flow has been defined as positive in the new shear flow sign convention.

At the other end H of the shear flow in Fig. 11.13(b), we are dealing with a uniform component of shear flow of magnitude q and a varying component of shear flow as shown in (a). The uniform component of the shear flow induces the compressive stress distribution at H in (b), as explained in Section 11.3.3.3. The variable component of the shear flow is applying a thrust towards the design point H and hence is the same as that at E, so that the lateral stress at H due to the variable component of the shear flow is also tensile and of magnitude f_r.

Because of the symmetry of the lateral tensile stress distribution, the resultant lateral tensile force F in Fig. 11.13(b) acts mid-way along the shear flow at $d_f/2$ from H. The longitudinal forces on element A-B-C-D are determined in an identical fashion to those in Fig. 11.12, as previously described, although it is worth noting that the total longitudinal shear load in Fig. 11.13(b) is half that in Fig. 11.12(b). Taking moments of the forces acting on element A-B-C-D in Fig. 11.13(b) gives the same value of lateral force F as in Eq. 11.13 for the uniform shear flow. This is to be expected since from equilibrium this is also the compressive force at H in Fig. 11.13(b). Dividing the lateral tensile force F by the area over which it acts $h_a d_f$ gives the lateral stress as

$$f_r = \frac{dq}{dx}\left(\frac{b_c \pi K_d}{16 h_a}\right) \qquad (11.20)$$

as q/d_f in the equation is dq/dx.

The lateral stress f_r in Fig. 11.13(b) is tensile since the varying component of the shear flow is acting towards the design point, so we will refer to this varying component as positive. If we reversed the direction of the varying component of the shear flow while maintaining the magnitude of the shear flow as zero at E and q at H, then the shape of the lateral stress distribution in (b) stays the same but stress directions reverse so that the lateral stress at E is now compressive. Therefore, when the varying component of the shear flow is applying a thrust away from the design point, this will be referred to as negative as it induces a compressive stress at the design point.

Consider design point B in Fig. 11.11. It has already been shown in Section 11.3.3.3 that the constant component of the shear flow produces zero lateral stress. The variable component of the shear flow to the left of the design point is acting towards the design point and hence induces a lateral tensile stress f_r at the design point. To the right of the design point the variable component must act to the left, in the

opposite direction to the constant component, so that the resultant shear flow reduces to the right. Hence the variable shear flow on the right of the design point is also acting towards the design point and induces a lateral tensile stress of f_r. Because of this, the resultant lateral tensile stress at the design point is $2f_r$, as would be expected, since we are dealing with a region without end effects, such as G in Fig. 11.13(b) where the lateral stress is shown to be $2f_r$.

Further examples that define the direction of the variable component of the shear flow are given in Fig. 11.11(c). Design point F is an interesting case, as the lateral stress is zero when dq/dx is the same on either side of the design point. *The lateral stress at any position along the beam can now be determined from Eqs 11.10 and 11.20, by summing the lateral stresses induced by the four components of the shear flow that are defined in Fig. 11.10.*

Splitting will occur when the sum of the four components of the lateral stresses reaches the tensile strength of the concrete f_{cb}. Where we are dealing only with the variable component of the shear flow, then the mean of the two variable components of the shear flow, $(dq/dx)_{mean} = ((dq/dx)_L+(dq/dx)_R)/2$, to cause splitting can be derived from Eq. 11.20 and is given by

$$\left(\left(\frac{dq}{dx} \right)_{mean} \right)_{split} = \frac{8h_a f_{cb}}{\pi K_d b_c} \tag{11.21}$$

Example 11.3 Two-dimensional global resistance to variable shear flow

The composite beam in Example 11.1 is subjected to a uniformly distributed load w. From Example 11.1: $h_a = 80$ mm; $f_{cb} = 3.0$ N/mm^2; $K_d = 0.912/\pi$; and $b_c = 4$ m. Substituting these values into Eq. 11.21 gives $(dq/dx)_{split} = 0.526$ N/mm^2.

For linear elastic behaviour, Eq. 1.9 can be differentiated with respect to the distance along the beam x, and substituting w = dV/dx gives the uniformly distributed load to cause splitting w_{split} as

$$w_{split} = \left(\frac{dq}{dx} \right)_{split} \frac{I}{A\bar{y}} \tag{11.22}$$

It was shown that the lateral tensile force F to cause splitting at a discontinuity of the uniform shear flow, at E in Fig. 11.12(b), is the same as the lateral tensile force F that is induced by the variable component of the shear flow at G in Fig. 11.13(b). However, the former is highly non-uniform and spread over a distance $2b_c$, at E in Fig. 11.12(b), whereas the latter is spread uniformly over what is normally a larger distance d_f as shown in Fig. 11.13(b). This can be confirmed by a numerical comparison of Eqs. 11.12 and 11.22 that will show that point loads are more likely to cause splitting than uniformly distributed loads.

11.3.4 EFFECTIVE WIDTHS

The splitting strengths derived in Sections 11.3.2 and 11.3.3 for both local and global splitting were developed from an analysis of concentrically loaded rectangular prisms, and therefore can only be applied directly to the analysis of symmetrical T-beams with rectangular concrete elements as shown in Figs. 1.8(a) and (b) where the cover to both sides of the connector is the same. This is not the case in most composite beams where the side covers are not the same, as shown in Figs. 1.8(e), (f), (g) and 1.11(a).

The problem of eccentrically loaded prisms occurs in the anchorage zone design of post-tensioned members where an equivalent prism concept (Leonhardt 1964) is used to convert eccentrically loaded prisms to concentrically loaded prisms, and is also used to allow for the interaction between adjacent anchorage zones. This concept has been adopted for mechanical shear connectors (Oehlers 1989).

Consider the composite beams in Figs. 11.14(a) and (b). The normal philosophy of design is to assume that the two beams are acting separately. Hence connectors A and B disperse their concentrated load into rectangular element 1, whereas connectors C and D disperse theirs into element 2, so that the stress fields in the effective elements do not overlap. The widths of these concrete elements are referred to as effective widths and methods for determining their magnitude and position are given in national standards, as described in Section 4.2.
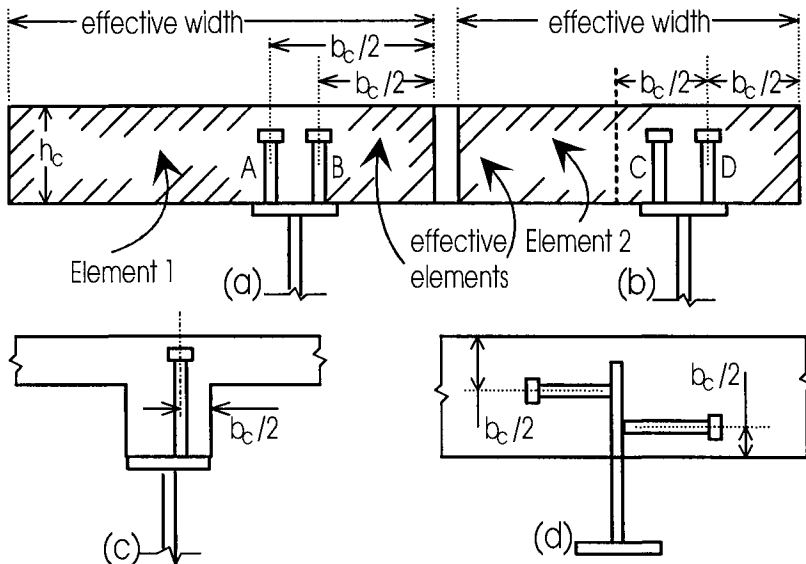
Fig. 11.14 Effective widths

Elements 1 and 2 in Fig. 11.14 are therefore effective elements that primarily allow for shear lag and the interaction between adjacent beams, and are analogous to the equivalent prism concept in anchorage zone design. Connector D in Fig. 11.14(b) is applying an eccentric load to element 2, and to allow for this eccentricity the

equivalent prism concept can be taken one stage further by assuming that connector D is applying a concentric load to the prism of width b_c and height h_c as shown. The effective width for the equivalent prism for splitting analyses is therefore twice the distance from the centre-line of the connector to the nearer side of the effective element as shown.

Further examples of the effective widths of equivalent prisms are shown in Fig. 11.14. In deep haunches as in (c), the effective width is the lateral dimension to the side of the haunch as shown, and not to the side of the slab. This is because the splitting stresses are concentrated at the base of the connector, so that dimensions relative to this position control the splitting strength. It is worth noting that splitting always starts near the base of the connector and hence generally near the soffit of the slab, and may eventually propagate to the top surface of the slab, particularly if the amount of transverse reinforcement is low. It is also worth noting that the effective width is the lateral dimension from the side of the connector, and so it is the vertical distance in the hybrid beam shown in (d). In the beam in (a), the effective width for connector A is different to that of connector B, and so it can be seen that the effective width varies for each connector. In theory, each connector or group of connectors within a composite beam should be checked for splitting, and techniques for doing this are discussed in Section 11.4.

Example 11.4 Effective widths: 2-dimensional local resistances

It was determined in Example 11.1 from Eq. 11.7, that a lower bound to the splitting strength of a 4 m wide concentrically loaded slab with the mechanical shear connector in Fig. 11.8 was 1984 kN.

If the connector in Example 11.1 was part of a L-beam, such as that in Fig. 11.14(b), with a minimum lateral distance from the centre line of the connector to the side of 1 m, then the effective width would be 2 m. Applying Eq. 11.7 gives a lower bound to the splitting strength of 1093 kN. If the connector was part of a haunched beam as in (c) with an effective width of 1 m, then the splitting strength reduces to 673 kN.

It can be seen in Eq. 11.7 that the splitting strength is proportional to b_c and inversely proportional to $(1-b_a/b_c)^2$. For example, when the width of the slab is halved, the strength will not be reduced by one half but will be reduced by a smaller amount because of the reduction in the factor $(1-b_a/b_c)^2$.

11.3.5 TWO LINES OF CONNECTORS

Sections 11.3.2 and 11.3.3 on two-dimensional splitting were based on single strip loads where the concentrated load was applied over a width b_a, as shown in Fig. 11.6(a). Analyses have shown that when the load is applied as two strip loads over the same width b_a, as shown in Fig. 11.6(c), so that the applied load is now concentrated at the edges of b_a instead of distributed over the width b_a, then the resistance to

splitting is reduced for both local (Oehlers 1989) and global splitting (Johnson and Oehlers 1981).

It was shown in Section 11.3.2 and in Fig. 11.7(a) and (c) that when a strip load is applied to a prism, the length of the lateral zone x_t is a function of the width of the prism b_c. Let us consider the case when $b_a \ll b_c$, as shown in Fig. 11.15(a). As we are dealing with a point load P_{strip}, the lateral force $P_t = P_{strip}/\pi$, as given by Eq. 11.5. The length of the splitting zone in Fig. 11.15(a), along the centre line of the prism at $b_c/2$ from the edges, is a function of b_c. Let us now divide the load into two, at a distance b_a apart as shown in (b). As a conservative estimate of the strength, we will assume that the lateral force P_t, along the splitting zone along the centre-line of the prism, is still equal to P_{strip}/π, as shown. Finite element analyses show that the length of the splitting zone is now a function of the side cover to the connectors of length $b_c - b_a$ (Johnson and Oehlers 1981), and this is in agreement with the equivalent prism concept of Section 11.3.4 that is used in anchorage zone design (Leonhardt 1964).
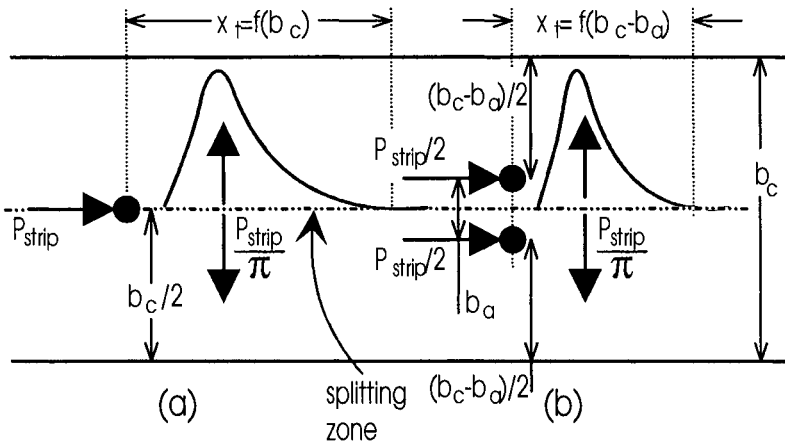
Fig. 11.15 Two lines of connectors

The splitting load P_{strip}/π in Fig. 11.15(a) is spread over a distance $x_t \approx 1.4b_c$ and the same splitting load in (b) is spread over a shorter distance $x_t \approx 1.4(b_c-b_a)$. Therefore, the splitting strength of (b) will be less than the splitting strength of (a) in proportion to the lengths of the splitting zones, that is in proportion to $(b_c-b_a)/b_c = (1-b_a/b_c) = R_{two}$. The load at which splitting occurs with two lines of connectors $(P_{split})_{two}$ can therefore be determined by multiplying Eq. 11.7 by the reduction in strength $R_{two} = (1-b_a/b_c)$ to give

$$\left(P_{split}\right)_{two} = 0.6b_c h_a f_{bc} \frac{R_{two}}{K_d} \tag{11.23}$$

It must be emphasised that this analysis is only an approximate method of allowing for the reduction in strength when there are two lines of connectors. It is also worth noting that it is not good practice to have two lines of connectors, and this form of

construction should be avoided if possible by distributing the connectors over the width b_a in Fig. 11.15(b) and staggering the longitudinal spread, as shown in Fig, 7.18(b), in order to minimise the overlap of the lateral tensile stress zones.

For convenience in the splitting analyses, we will define the lateral force factor for two lines of connectors $(K_d)_{two}$ as

$$\left(K_d\right)_{two} \quad = \quad \frac{K_d}{R_{two}} \quad = \quad \left(1-\frac{b_a}{b_c}\right)\frac{1}{\pi} \tag{11.24}$$

so that when there are two lines of connectors this value should be substituted for K_d.

The parameter $(K_d)_{two}$ can also be derived from a global analysis of splitting. Let us assume that one line of the connectors of strength $qd_f/2$ is placed along the line C-D in Fig. 11.12(b) and, as a conservative estimate, it will be assumed that the longitudinal reaction to this longitudinal force $qd_f/2$ is uniformly distributed only over the section A-C. Therefore, the reaction $qd_f/2$ acts at $(b_c-b_a)/4$ from the line C-D. Following the procedure used to determine K_d in Section 11.3.3.4 produces the same value of $(K_d)_{two}$ as in Eq. 11.24.

Example 11.5 Two lines of connectors: 2-dimensional local resistances

Consider the composite beam in Example 11.1. Let us assume that instead of one connector of width b_a =180 mm, that is concentric to the slab as shown in Fig. 11.6(b), we have two lines of connectors spread over the same overall width b_a = 180 mm as shown in (c).

From the analysis in Example 11.1, K_d = 0.912/π whereas from Eq. 11.24 $(K_d)_{two}$ = 0.955/π. Hence the lateral force parameter has increased by (0.955 - 0.912)/0.912 = 4.7%. As the local splitting strength of Eq. 11.7 and the global splitting strengths of Eqs. 11.11 and 11.21 are inversely proportional to K_d, the strength in all cases will reduce by 4.7%. It can be seen that the effect of two lines of connectors in wide slabs is insignificant, however the effect increases as the width of the slab reduces.

11.3.6 MINIMUM SPLITTING STRENGTH

The two-dimensional splitting strength of a concrete element that is subjected to a single strip load is given by Eq. 11.7 and can be written in the following form

$$P_{split} \quad = \quad 0.6b_a h_a f_{cb} \pi P^* \tag{11.25}$$

where the parameter P* is a non-dimensional 'splitting' strength given by

$$P^* = \frac{b_c}{b_a \left(1 - \dfrac{b_a}{b_c}\right)^2} \tag{11.26}$$

When the applied load is uniformly distributed over the whole cross-sectional area of the prism, there is no need for lateral dispersal of the applied load and so lateral tensile forces are not induced, and hence the prism has an infinite splitting strength. This situation occurs when $b_c \rightarrow b_a$ in Eq. 11.26, so that the splitting strength $P^* \rightarrow \infty$. The splitting strength is therefore asymptotic to the vertical asymptote at $b_c/b_a = 1$ in Fig. 11.16. Furthermore when $b_c \rightarrow \infty$, the length of the lateral splitting zone $x_t \rightarrow \infty$ and the lateral tensile stress tends to zero, as discussed in Section 11.3.2, so the strength of the prism tend to infinity. This situation is also predicted by Eq. 11.26, as when $b_c \gg b_a$, $P^* \rightarrow b_c/b_a$ which is the sloping asymptote in Fig. 11.16.
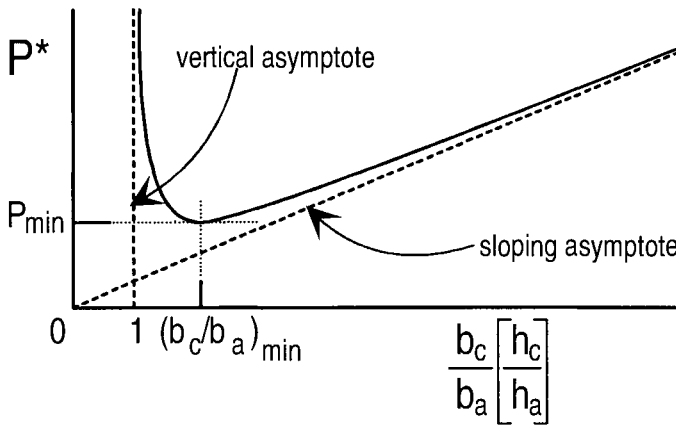
Fig. 11.16 Variation in splitting strength

The splitting strength of a prism tends to infinity at the two extremes of b_c as shown in Fig. 11.16. The minimum splitting strength P_{min} can be derived from the derivative of Eq. 11.26, and occurs when

$$b_c = 3b_a \tag{11.27}$$

and hence the minimum splitting strength occurs when the side cover to the connector is equal to the width of the connector b_a. Substituting b_c in Eq. 11.27 into Eq. 11.25 gives the minimum splitting strength as

$$P_{min} = 0.6b_a h_a f_{cb} \pi \frac{27}{4} = 12.7 b_a h_a f_{cb} \tag{11.28}$$

The same procedure can be applied when there are two lines of connectors. In this case $(K_d)_{two}$ in Eq. 11.24 has to be substituted for K_d in Eq. 11.7, so that the non-dimensional splitting strength P^*_{two} is now given by

$$P_{two}^* = \frac{b_c}{b_a\left(1-\dfrac{b_a}{b_c}\right)} \tag{11.29}$$

From the derivative of Eq. 11.29, it can be shown that the minimum splitting strength $(P_{min})_{two}$ occurs when the effective width $(b_c)_{two}$ is given by

$$\left(b_c\right)_{two} = 2b_a \tag{11.30}$$

and has a value of

$$\left(P_{min}\right)_{two} = 7.5 b_a h_a f_{cb} \tag{11.31}$$

Example 11.6 Minimum 2-dimensional local resistance

Consider the connector in Fig. 11.8 that was analysed in Examples 11.1 and 11.4 for the lower bound two-dimensional splitting strength. From Eq. 11.27, the minimum splitting strength occurs when the effective width of the slab is 540 mm; at this effective width the cover to the side of the connector is only 180 mm. From Eq. 11.28, the splitting strength with this cover is 550 kN.

It is worth noting that we have been looking at the minimum cover required to develop the minimum splitting strength. As the cover reduces below this minimum, the load to cause splitting increases. However, as the cover reduces, the triaxial restraint to the concrete in front of the connector reduces and so the dowel strength may reduce. Hence the mode of failure will change from dowel failure induced by relief of the tri-axial restraint through splitting, to simply dowel failure induced by relief of the tri-axial restraint through lack of cover. Therefore, it is worth bearing in mind that these analyses will help the engineer to determine the minimum cover that is required to prevent splitting, but the engineer also has to ensure that the dowel strength can be achieved with that cover, particularly when the side cover is very small. Guidelines for ensuring that the dowel strength of flexible stud shear connections can be achieved are given in Section 11.5. For stiff connectors, sufficient triaxial restraint is often ensured in national standards by limiting the bearing pressure.

11.3.7 THREE DIMENSIONAL SPLITTING

11.3.7.1 *General*

The two-dimensional analyses in Sections 11.3.2 and 11.3.3 underestimate the resistance to splitting, as it is assumed that the concentrated load is only dispersed in two dimensions. Hence the connector in Fig. 11.6(a) is assumed to be acting on Prism 1 of cross-sectional area $h_a b_c$, so that the concentrated load is only dispersed in the x-y plane. In reality, the dispersal of the concentrated load has a vertical component as well, that distributes the concentrated load to the remaining volume of the slab. This

vertical component will relieve the lateral stresses in the x-y plane and hence increase the concentrated load to cause splitting. A theoretical solution to this three-dimensional problem is difficult to find, so recourse is made to adapting two dimensional solutions for use in this three-dimensional problem.

11.3.7.2 Reciprocal relationship

Firstly, consider a concentric patch load acting on a prism as shown in Fig. 11.5(c), since this is the simplest form of three-dimensional splitting. Experimental research (Oehlers and Johnson 1981) has shown that the splitting resistance of this concentric patch loaded prism, in which the load is dispersed in three dimensions, can be predicted from the splitting resistance of the prism to strip loads in which only two-dimensional dispersal of the load occurs.

Let P_y be the strip load to cause the prism in Fig. 11.5(c) to split when subjected to a strip load over area A-B-H-G. The strength P_y can be derived from Eq. 11.7 where b_a is the width of the strip measured in the y-direction, b_c is the width of the prism measured in the y-direction, and h_a is the height of both the strip load and the prism measured in the z-direction which in this case is equal to h_c. Similarly, let P_z be the strip load to cause the prism to split when subjected to a strip load over the area C-D-F-E. The strength P_z can also be determined from Eq. 11.7. In this case b_a and b_c in Eq. 11.7 are the width of the strip load and prism measured in the z direction, which in this case is equal to h_a and h_c, and h_a in Eq. 11.7 is the height of both the strip load and prism measured in the y direction, that is h_c. Then the splitting strength of the prism P_{patch} under the patch load of area $b_a h_a$ in Fig. 11.5(c) is given by the following reciprocal relationship

$$\frac{1}{P_{patch}} = \frac{1}{P_y} + \frac{1}{P_z} \tag{11.32}$$

This reciprocal relationship was found to be in good agreement with experimental tests on patch loads on concrete prisms (Oehlers and Johnson 1981) for the range

$$0.04 \leq \frac{A_{patch}}{A_{prism}} \leq 0.36 \tag{11.33}$$

The reciprocal relationship of Eq. 11.32 gives a reasonable correlation with experimental research because it is correct at the extreme values. For example, when the prism in Fig. 11.5(c) is subjected to a strip load over the area C-D-F-E, then from Eq. 11.7 $P_y \rightarrow \infty$ so that $P_{patch} = P_z$ in Eq. 11.32 which is the correct result. Interpolating between known results, in this case the extremities, is always safer than extrapolation.

The composite slab in Fig. 11.6(a) can be assumed to be the upper half or the lower half of the prism in Fig. 11.5(c), where h_a in Fig. 11.6(a) is equal to $h_a/2$ in Fig. 11.5(c). The splitting strength of the prism in Fig. 11.6(a) is equal to the combined splitting strength of the upper and lower halves, and is therefore equal to twice the splitting strength of the composite slab in Fig. 11.6(a). This is correct when the

boundary between the prism halves along the line m-m in Fig. 11.5(c) is fully restrained. A better comparison is to assume that only the two halves of the patch on either side of m-m are fully restrained as the connector is welded to the steel flange, and that the slabs are free to separate along the remainder of the boundary m-m. *Hence this reciprocal relationship would be expected to overestimate the resistance to splitting and could therefore be used as an upper bound to the resistance to splitting. It will be shown in Section 11.3.7.4 that the reciprocal relationship does form an upper bound for most situations, but can be over conservative in the analysis of members with limited cover.* However, it has been included in this Chapter to complete the understanding of splitting.

Example 11.7 Upper bound to local resistance using reciprocal relationship

In Example 11.1, a lower bound to the splitting strength of a slab encasing the connector in Fig. 11.8 was determined by considering two-dimensional dispersal and ignoring dispersal in the vertical direction. It was shown that when the slab is 4 m wide the splitting strength is 1984 kN. Equation 11.32 can be used to determine an upper bound to the splitting resistance of the slab.

The composite beam is equivalent to either the upper or the lower half of the prism shown in Fig. 11.5(c) and hence the splitting resistance of this prism will be twice the splitting resistance of the slab. The dimensions of the prism are therefore: b_a = 180 mm; h_a = 160 mm; b_c = 4000 mm; and h_c = 300 mm.

Consider the strip load A-B-H-G in Fig. 11.5(c). The splitting resistance to this strip load is given by Eq. 11.7 that can be written in the following form

$$P_{strip} = \frac{5.65 A_{prism}}{\left(1 - \dfrac{b_a}{b_c}\right)^2} \qquad (11.34)$$

where A_{prism} = cross-sectional area of the prism, b_a = width of strip load and b_c = width of prism relative to the width of the strip load. For the strip load A-B-H-G, b_a = 180 mm, b_c = 4000 mm, and A_{prism} = 4000 x 300 mm^2 in Eq. 11.34. Hence the splitting resistance to this strip is P_y = 7440 kN. For the strip load C-D-F-E: b_a = 160 mm; b_c = 300 mm; and A_{prism} is unchanged in Eq. 11.34. Hence the splitting resistance to this strip is P_z = 31,159 kN. From the reciprocal relationship of Eq. 11.32, P_{patch} = 6005 kN. Hence an upper bound to the splitting resistance of the slab is $P_{patch}/2$ = 3002 kN, compared with the lower bound estimate of 1984 kN.

As a further comparison when b_c = 2m, the lower bound strength was 1093 kN (Example 11.4) whereas the upper bound strength from Eq. 11.32 is 1621 kN. When b_c = 1 m, the strengths are 673 kN (Example 11.4) and 952 kN from Eq. 11.32, and when b_c = 0.54 m (Example 11.6) the strengths are 550 kN and 691 kN.

11.3.7.3 Additive relationship

(a) General analysis for patch load

The composite beam in Fig. 11.6(a) can be viewed as the upper half of the prism in Fig. 11.5(c), above the line m-m. If the soffit of the slab in Fig. 11.6(a) were fully restrained as along m-m in Fig. 11.5(c), then the reciprocal relationship of Eq. 11.32 could be applied to allow for vertical dispersal. Unfortunately this is not the case for the composite beam in Fig. 11.6(a), as the slab is only restrained in the vertical direction by the axial stiffness, of the shear connectors, normal to the steel-flange/concrete-slab interface. For example, if the shear connectors had no axial stiffness, then none of the concentrated load could be dispersed vertically.

One way of allowing for three-dimensional dispersal is to follow the technique that is often used in the anchorage zone design of post-tensioned members (Leonhardt 1964). The anchorage zone or patch load of area $b_a h_a$ in Fig. 11.5(c) is assumed to be supported by both prisms A-B-H-G and C-D-F-E, so that the resistance to the patch is the sum of the resistances of each of these prisms. A similar approach can be applied to the splitting resistance of the prism, so that the load to cause the prism to split is the sum of the splitting resistances of the patch on C-D-F-E and on A-B-H-G, both of which can be determined from Eq. 11.7. It is important to note that we are assuming that the splitting resistance of both prisms can be achieved simultaneously before failure. This is not a bad assumption, as in reality the vertical splitting forces in the prism A-B-H-G in Fig. 11.5(c) are resisted in a composite beam by axial forces across the connector that are unlikely to cause the connector to fail in tension, and so failure will be governed by vertical splitting of the other prism.

As shown previously, the composite slab in Fig. 11.6(a) is equivalent to half the prism above line m-m in Fig. 11.5(c). Hence, the load to cause the prism above m-m to split P_{split} is half the load to cause the whole prism to split, and is given by

$$P_{split} \;=\; \frac{0.6 b_c h_a f_{cb}}{K_d} + \frac{0.6 b_a h_a f_{cb} \pi}{\left(1 - \dfrac{h_a}{h_c}\right)^2 \left(\dfrac{h_a}{h_c}\right)} \qquad (11.35)$$

where h_a and h_c are defined in Fig. 11.6(a).

The first term on the right hand side of Eq. 11.35 is the splitting strength of Prism 1 in Fig. 11.6(a). Hence dividing Eq. 11.35 by this first term gives the proportional increase in strength due to vertical dispersal Q as

$$Q \;=\; 1 + V \qquad (11.36)$$

where V is the percentage increase of the two-dimensional strength due to the vertical dispersal of the load, and is given by

$$V \;=\; K_d \pi \frac{b_a}{b_c} K_s \qquad (11.37)$$

where K_s is given by

$$\left(K_s\right)_{3h_a \le h_c \le 4.5h_a} = \left(\left(1 - \frac{h_a}{h_c}\right)^2 \frac{h_a}{h_c}\right)^{-1} \tag{11.38}$$

The parameter K_s in Eq. 11.38 is a geometric property of the vertical dimensions of the slab and assumes that prism A-B-H-G in Fig. 11.5(c) is fully restrained along the boundary m-m. A comparison with the results of push tests with stud shear connectors, as described in Section 11.5, has shown that it is on the conservative side.

The simplest method of allowing for the beneficial effects of vertical dispersal is to use an effective height of the shear connector h_v instead of the actual height h_a in all the two-dimensional splitting equations in Sections 11.3.2 to 11.3.6 for both local and global splitting, where

$$h_v = h_a Q \tag{11.39}$$

(b) Bounds of patch load analysis

The splitting analyses must be used within the bounds of both the theory and the experimental data that was used to confirm it. The first parameter on the right hand side of Eq. 11.35 is the splitting resistance of Prism 1 in Fig. 11.6(a) and is derived from Eq. 11.7. The variation in this splitting strength was derived in Section 11.3.6 and is shown in Fig. 11.16. The minimum splitting strength P_{min} was shown to occur at $b_c = 3b_a$ (Eq. 11.27). The rapid increase in the splitting strength to the left of P_{min} in Fig. 11.16 is academic, as compressive failure will precede splitting failure and so this part of the curve should be ignored in practice. To the right of P_{min}, $b_c > 3b_a$ which applies to the vast majority of composite structures, and it is this part of the curve that has been validated experimentally (Oehlers and Johnson 1981). Hence for design purposes, it is necessary to ensure that

$$b_c \ge 3b_a \tag{11.40}$$

It is necessary for the vertical dispersal factor V in Eqs. 11.36 and 11.37, and hence K_s, to reduce to zero as $h_c \rightarrow h_a$. This is because when $h_a = h_c$ in Fig. 11.6(a), the connector is acting as a strip load over the full depth of the slab and so none of the concentrated load is dispersed vertically. The variation in the strength of Prism 2 in (a) is also given by Fig. 11.16, with the parameter b_c/b_a replaced by h_c/h_a as shown in brackets. It can be seen that to the right of the minimum strength point P_{min}, the splitting strength reduces as h_c/h_a reduces, as required in this analysis, and hence this procedure can be applied when

$$h_c \ge 3h_a \tag{11.41}$$

As discussed previously, the theoretical splitting strengths represented by the curve to the left of P_{min} in Fig. 11.16 should not be used. From Eq. 11.38, $K_s = 6.75$

when $h_c = 3h_a$. Furthermore, $K_s = 0$ when $h_c = h_a$ as vertical dispersal is eliminated. We therefore know the value of K_s at the two extremities, and therefore a linear interpolation between these points will give

$$\left(K_s\right)_{h_a \leq h_c \leq 3h_a} = 10.1\left(1 - \frac{h_a}{h_c}\right) \tag{11.42}$$

As $h_c \to \infty$ in Fig. 11.6(a), the strength of Prism 2 also tends to infinity, so that splitting will occur in Prism 1 at a much lower applied load than the applied load to cause Prism 2 to split. Therefore, a limit has to be placed on h_c. It was found from the analysis of experimental tests (Oehlers 1993), described in Section 11.4, that Eq. 11.35 can be applied when h_c is less than $4.5h_a$, and when h_c is greater than this value then $h_c = 4.5h_a$ should be used in the analysis. Hence the design procedure can be applied when

$$h_c \leq 4.5h_a \tag{11.43}$$

as indicated by the subscript of K_s in Eq. 11.38.

(c) Two lines of connectors

The same sequence of analysis, from Eqs. 11.35 to 11.43, that was developed for patch loads in the previous section can be applied when there are two lines of connectors. The only difference is that K_d for Prism 1 in Fig. 11.6(a) should be replaced by $(K_d)_{two}$ as given in Eq. 11.24.

Following the sequence of analyses depicted by Eqs. 11.35 to 11.43, the parameter K_d in Eq. 11.35 and 11.37 should be replaced by $(K_d)_{two}$, and Eq. 11.40 should be replaced by

$$\left(b_c\right)_{two} \geq 2b_a \tag{11.44}$$

which is derived from Eq. 11.30, and the remaining equations are the same.

11.3.7.4 *Comparison of semi-empirical relationships*

As with all semi-empirical relationships, the *reciprocal* rule and the *additive* rule should be applied with care and within the bounds of the theoretical assumptions and experimental validation. This type of design rule is always open to improvement.

Consider the concentrically loaded square prism in Fig. 11.17 of area $b_c \times b_c$, that is subjected to a square patch load of area $b_a \times b_a$. Let the splitting resistance of Prism 1, of cross-sectional area $b_c \times b_a$ be P_{rect}. As Prism 2 is the same shape and size as Prism 1 and subjected to the same shape of load, the splitting resistance of Prism 2 is also P_{rect}. Therefore, applying the additive relationship of Eq. 11.35, the resistance to the patch load P_{patch} is given by

$$P_{patch} = 2P_{rect} \qquad (11.45)$$

Now consider the strip load of dimensions $b_a \times b_c$, of the same cross-section as Prism 2, acting on Prism 3 of dimensions $b_c \times b_c$. Let the splitting resistance to this strip load be P_{strip}. As the depth of Prism 1 in proportion to Prism 3 is b_a/b_c, the relative strengths of these prisms are in the same proportion, so that

$$\frac{P_{rect}}{P_{strip}} = \frac{b_a}{b_c} \qquad (11.46)$$

Eliminating P_{rect} from Eqs. 11.45 and 11.46 gives

$$P_{patch} = 2P_{strip}\frac{b_a}{b_c} \qquad (11.47)$$
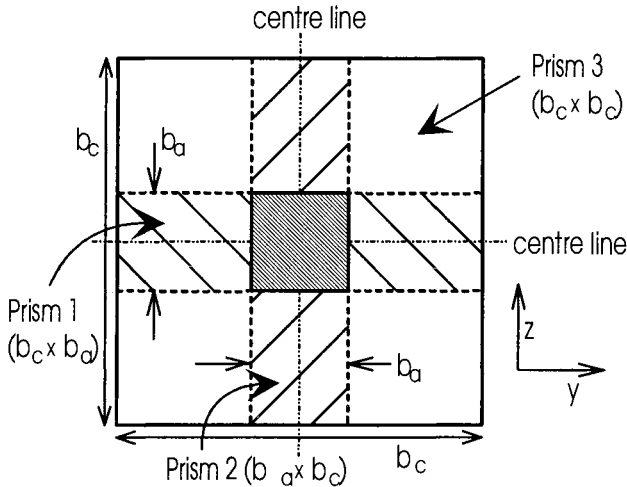
Fig. 11.17 Concentric square prism and patch load

The resistance to the strip load of the same area as Prism 2 in Fig. 11.17 is P_{strip}. The resistance to the strip load of the area of Prism 1 is also P_{strip}, as the dimensions are the same. Hence applying the reciprocal relationship of Eq. 11.32 gives

$$P_{patch} = \frac{P_{strip}}{2} \qquad (11.48)$$

Equation 11.47 is based on the additive relationship and Eq. 11.48 is based on the reciprocal relationship. The same strength P_{patch} is therefore achieved when

$$b_c = 4b_a \qquad (11.49)$$

which is only slightly greater than the width required for the minimum strength P_{min} in Eq. 11.27. A comparison of Eqs. 11.47 and 11.48 shows that when $b_c > 4b_a$ the reciprocal relationship predicts a larger strength than the additive relationship. Hence the reciprocal relationship tends to be an upper bound to the strength, except at small effective widths when it tends to be conservative.

Example 11.8 Local resistance using additive relationship

The mechanical shear connector in Fig. 11.8 has been analysed for two-dimensional splitting in Examples 11.1, 11.4 and 11.6 for an effective width of 4 m, 2 m, 1 m and 0.54 m; where the latter effective width is the width required for the minimum splitting strength P_{min}. The two-dimensional splitting strengths came to 1984 kN, 1093 kN, 673 kN and 550 kN.

The same composite beams were analysed in Example 11.7 using the reciprocal relationship, to allow for three-dimensional dispersal of the load, and the analyses gave splitting strengths of 3002 kN, 1621 kN, 952 kN and 691 kN which, as would be expected, are all greater than the two-dimensional strengths quoted in the previous paragraph. The increase in strengths were thus 51%, 48%, 41%, and 26%.

The additive technique for allowing for three-dimensional splitting is now applied to the same composite beams. Equation 11.40 applies to all the specimens. The next step is to determine the factor K_s from either Eqs. 11.38 or 11.42. As $h_c < 3h_a$, Eq. 11.42 applies, giving $K_s = 4.71$. Let us now consider the 4 m wide slab. From Eq. 11.37, $V = 0.041K_s = 0.193$. Hence the three-dimensional splitting strength is 19.3% greater than the two-dimensional splitting strength. Applying this technique to all four slabs gives splitting strengths of 2368 kN, 1478 kN, 1058 kN and 935 kN. The increases in strength are thus 19%, 45%, 57% and 70%. It can be seen that the greatest percentage increase in strength occurs at low effective widths, which is to be expected as the size of Prism 2 in Fig. 11.6(a) approaches the size of Prism 1 as b_c reduces. Furthermore, as the width of the slab increases, the effect of vertical dispersal diminishes, being only 19% when the width of the slab is 4m. These trends have been confirmed by experiments (Oehlers 1989). *It is also worth noting that the results from the reciprocal relationship in the previous paragraph do not have the same trend, and should therefore only be used as a guideline. The reciprocal analysis was included to complete the picture on splitting.*

The effect of three-dimensional dispersal on global splitting can be allowed for by using an effective height as defined by Eq. 11.39. For example, it was shown in the previous paragraph that $V = 19.3\%$ for the 4 m wide slab, which means that the two-dimensional strength is increased by 19.3% due to the vertical dispersal. This can be allowed for in both the local and global analysis of two-dimensional splitting by simply increasing the height of the connector by 19.3%, that is by applying Eq. 11.39 where Q is defined in Eq. 11.36. Hence, in this example $h_v = 95.4$ mm. So the two-dimensional analyses for both local and global splitting such as Eqs. 11.7, 11.11, 11.12, 11.21 and 11.22 can be applied by substituting h_v for h_a. For example, in the global analysis of splitting due to point loads in Example 11.2, the step change in the shear flow to cause splitting will be 1.193 x 827 = 987 N/mm, and in Example 11.3 the variable component of the shear flow to cause splitting is 1.193 x 0.526 = 0.628 N/mm^2. It should be

noted that h_v may be greater than h_c, which is satisfactory because h_v is only an effective height.

11.3.8 EQUIVALENT PRISM

11.3.8.1 *General*

In many composite beams, the concrete element is not rectangular but may have sloping sides and haunches as shown in Figs. 1.8(d) and 1.11(b). The research previously described on the local and global splitting of rectangular concrete elements must therefore be adapted to allow for non-rectangular concrete elements (Oehlers and Park 1994).

11.3.8.2 *Local splitting*

(a) Effective sides

In composite beams with shallow haunches as shown in Fig. 11.18, or with sloping sides as in Fig. 11.19, the width, or effective width of the slab as described in Section 11.3.4, varies at the level of the splitting zone. Hence Eq. 11.7 cannot be used directly to determine the splitting strength of these prisms.
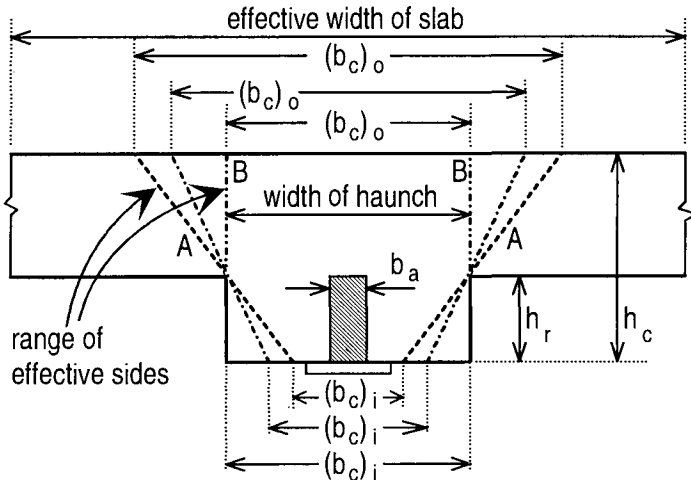
Fig. 11.18 Range of effective sides

Intuitively the engineer would expect that when the depth of the haunch $h_r \to 0$ in Fig. 11.18, then the splitting strength P_{split} would depend on the effective width of the slab. Furthermore when $h_r \to h_c$, then P_{split} would depend on the width of the haunch. Similarly it would be expected that when the slope of the side $\theta \to 0$ in Fig. 11.19, then P_{split} is a function $(b_c)_i$ and when $\theta \to 90°$ then P_{split} is a function of the effective width.
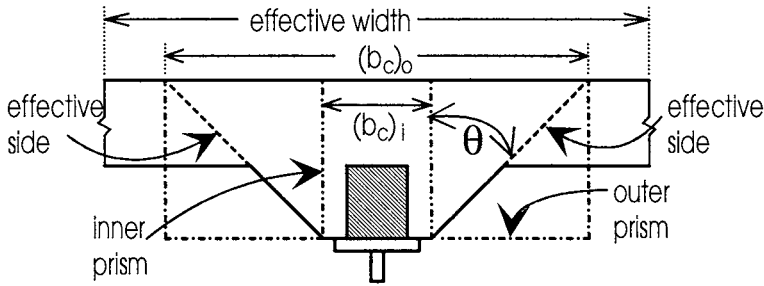
Fig. 11.19 Effective sides

Consider the two types of prisms shown in Fig. 11.20. Both cross-sections can be defined by an outer rectangular prism of width $(b_c)_o$ and height h_c, and an inner rectangular prism of width $(b_c)_i$ and the same height h_c, as shown. It can be seen that the inner and outer prisms enclose the sloping portion of the haunch. The strength of the inner prism $(P_{split})_i$ can be determined from Eqs. 11.7 and 11.39 using the dimensions of the inner rectangular prism, and so can the strength of the outer prism $(P_{split})_o$ from the dimensions of the outer rectangular prism. When $\theta = 0$ then $(P_{split})_i$ is correct and when $\theta = 90°$ then $(P_{split})_o$ is correct. We therefore know the strength at the extremities of the slope, that is at $\theta = 0$ and at $\theta = 90°$, and so we need to know how the strength varies between these extremities. Experiments (Oehlers and Park 1994) on shear connectors encased in prisms of the shapes shown in Fig. 11.20 demonstrated that the variation in strength between these extremities was linearly dependent on the slope θ, when measured in degrees. Hence the splitting strength of a concrete element with sloping sides $(P_{split})_\theta$ is given by the following linear interpolation

$$\left(P_{split}\right)_\theta \;=\; \left(P_{split}\right)_i + \left(\left(P_{split}\right)_o - \left(P_{split}\right)_i\right)\frac{\theta}{90} \tag{11.50}$$

where θ is measured in degrees, and where $\theta = 0$ the strength is that of the inner prism, and where $\theta = 90°$ the strength is that of the outer prism.

When the shape of the cross-section does not have one of the standard configurations in Fig. 11.20, then effective sides can be used to generate these standard sections and their associated inner and outer prisms as in Fig. 11.18. Whenever these effective sides fall within the sides of the slab cross-section, they will underestimate the splitting resistance and hence can be used in design. There can be an infinite number of effective sides that will generate an infinite number of cross-sections and it is left to the engineer to choose the one that gives the greatest splitting resistance $(P_{split})_\theta$, for use in design. In general, only the two extreme values of effective sides have to be checked, such as effective sides A and B in Fig. 11.18.
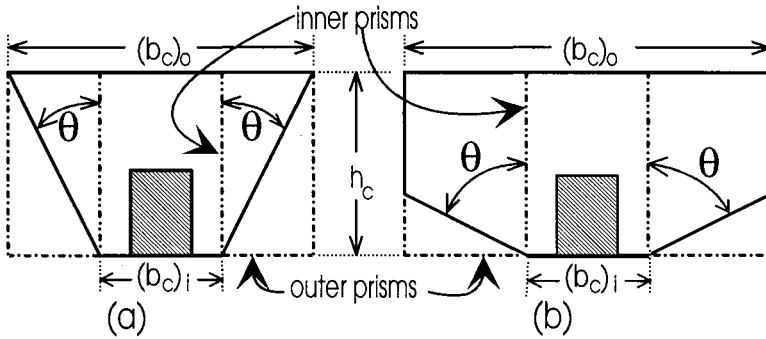
Fig. 11.20 Standard sections

In choosing the effective sides as in Fig. 11.18, it is necessary to comply with the bounds of the splitting analysis. Hence for patch loads

$$(b_c)_i \geq 3b_a \tag{11.51}$$

that can be obtained from Eq. 11.40, and for two lines of connectors then

$$((b_c)_i)_{two} \geq 2b_a \tag{11.52}$$

from Eq. 11.44.

Dove-tail trough profiles can be analysed in a similar fashion by ensuring that θ in Fig. 11.21 is always positive; positive being defined as the rotation of the slope that causes the cross-sectional area of the effective prism to increase. Prisms that are not symmetrical about the vertical axis, as in Fig. 11.22, can be made symmetrical with the use of an effective side as shown.

(b) Effective height

In the analysis of deep beams or deep haunches, it is necessary to restrict the height of the prism for use in the splitting analyses, as discussed in Section 11.3.7.3(b). Hence an upper limit to the height of the prism, or an effective height $(h_c)_e$ as shown in Fig. 11.22, can be derived from Eq. 11.43 and is given by

$$(h_c)_e \leq 4.5h_a \tag{11.53}$$

When $h_c < 4.5h_a$, then h_c is used in the analysis.

(c) Equivalent prism

In summary, in determining the splitting resistance of a concrete element, it is first necessary to define the effective shape of the concrete element that is suitable for analysis. This is achieved by using effective widths, effective sides and effective

heights. This effective shape will be referred to as the *equivalent prism* for analysis, and examples are shown hatched in Figs. 11.21 and 11.22.
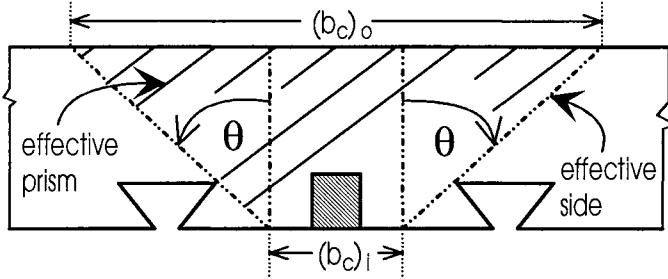
Fig. 11.21 Dove-tail trough profiles
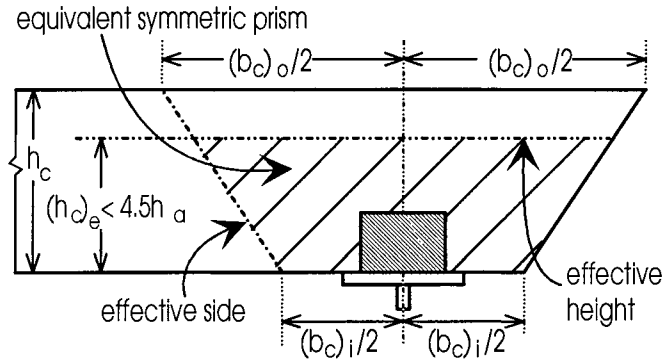
Fig. 11.22 Equivalent prism

11.3.8.3 *Global splitting*

In order to analyse global splitting in concrete elements with non-rectangular cross sections, it is necessary to determine the effective width $(b_c)_\theta$ of an equivalent rectangular prism that has a splitting resistance of $(P_{split})_\theta$.

From Eqs. 11.7, 11.36 and 11.39

$$\left(P_{split}\right)_\theta = \frac{0.6(b_c)_\theta f_{cb}}{K_d} h_a \left(1 + K_d \pi K_s \frac{b_a}{(b_c)_\theta}\right) \tag{11.54}$$

and rearranging Eq. 11.54 gives

$$\frac{(b_c)_\theta}{K_d} = \frac{\left(P_{split}\right)_\theta}{0.6 f_{cb} h_a} - \pi b_a K_s \tag{11.55}$$

and hence the effective width $(b_c)_\theta$ can be derived from an iterative solution.

Example 11.9 Local and global resistance of non-rectangular slab

The 4 m wide composite beam in Example 11.1 has the mechanical shear connectors shown in Fig. 11.8 that have a dowel strength of 1300 kN. It is necessary to include a 25 mm haunch as shown in Fig. 11.23 and the question is whether this will reduce the strength of the shear connection.

    The greatest slope θ of the effective sides occurs when the effective width of the internal prism is the narrowest allowable. From Eq. 11.51, the narrowest allowable effective width is $(b_c)_i$ = 540 mm. The effective side with the greatest slope is then drawn passing through the edge of the haunch as shown in Fig. 11.23. The effective width of the outer prism is therefore $(b_c)_o$ = 3300 mm. From Example 11.8, the splitting resistance of the inner prism is $(P_{split})_i$ = 935 kN. The splitting strength of the outer prism can be determined as $(P_{split})_o$ = 2054 kN. Hence from Eq. 11.50, $(P_{split})_\theta$ = 1962 kN as θ = 83°.

    Effective sides A in Fig. 11.23 forms the other extremity of the possible ranges of effective sides. In this case, the effective sides form a rectangular prism of 1 m width that, from Example 11.8, has a splitting resistance of 1058 kN. Bearing in mind that it is the equivalent prism with the maximum resistance that governs design, the splitting resistance is therefore given by effective sides B and so is equal to 1962 kN. This is still greater than the dowel strength of 1300 kN, and hence the haunch will not reduce the dowel strength.

    The equivalent width of a rectangular prism that has the same strength as $(P_{split})_\theta$ = 1962 kN can be derived from Eq. 11.55 as $(b_c)_\theta$ = 3100 mm. From Eq. 11.39, h_v = 99.4 mm. These dimensions can therefore be used in the global splitting analyses. For example, applying Eq. 11.11 with $h_a = h_v$ gives Δq_{split} = 1027 N/mm.

    Increasing the depth of the haunch from 25 mm to 50 mm in Fig. 11.23 reduces the splitting strength to 1339 kN, that is still slightly greater than the dowel strength of 1300 kN. Any further increase will reduce the dowel strength through splitting, unless of course there is adequate transverse reinforcement as described in Chapter 12.

11.4 Application

11.4.1 GENERAL

As discussed in Section 1.1.3, there is an enormous variety of mechanical shear connectors, some of these are shown in Fig. 1.5. Furthermore, there are very few limitations on the placement of these connectors. For example, the connectors could be placed in a line along the steel element as shown in Fig. 1.8(a), spread over the steel

flange as in (g), concentrated in groups as in the truss girder in Fig. 1.9(c), or placed in discontinuous lines in the stub girders in (b).
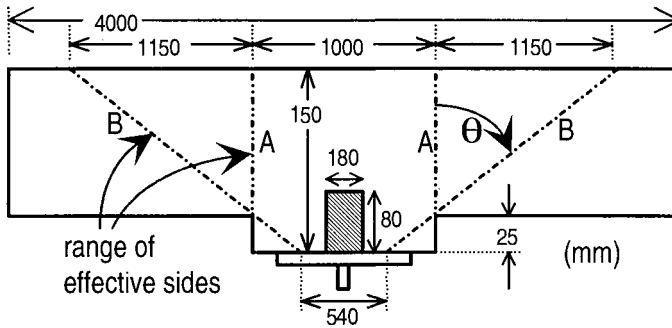
Fig. 11.23 Example 11.9 on splitting of haunched composite beams

Recommendations are now given for applying the procedures developed in Section 11.3 to most types of mechanical dowels and placement configurations. Values of the characteristic splitting resistances are also given for the design of individual and groups of connectors.

11.4.2 EQUIVALENT HEIGHT OF CONNECTOR

The procedures developed in Section 11.3 were derived theoretically and validated experimentally for patch loads acting on prisms. In this type of loading, the bearing pressure between the patch and the prism can be assumed to be fairly uniformly distributed over the area of the interface. For example, let the steel beam in Fig. 2.15 represent the patch and let the applied load 2F be uniformly distributed over the width 2h. Then it could be expected that the bearing pressure between the steel beam and the concrete element is fairly uniform. An alternative way of visualising the problem is that when the beam thickness d = 0, then the distribution of the interface pressure must be exactly equal to the uniform load applied to the patch.

In contrast to a patch load, a shear load is applied to a mechanical dowel connection at the base of the dowel and, as explained in Section 2.4.2, this is equivalent to a concentrated load at the mid-span of the steel beam as shown in Fig. 2.15; the steel beam on either side of the 'mid-span' represents a mechanical dowel with their base joined at mid-span. In this case, the distribution of the bearing pressure depends on the stiffness of the steel beam (that is the steel dowel) relative to that of the concrete medium. For example and as explained in Section 2.4.2, as d increases then e → h/2 and the bearing pressure tends to uniformity so that the splitting resistance of the dowel approaches that of the patch load of width 2h. Furthermore, as d → 0 then e → 0, hence the bearing pressure tends to be concentrated at the base of the connector and so the splitting resistance reduces which is equivalent to a patch load that is narrower than 2h.

It can thus be seen from the previous paragraph that the distribution of the interface bearing pressure depends on the aspect ratio d/h in Fig. 2.15. We will define the equivalent height of the connector as $h_{eq} = 2e$, where e is the eccentricity of the resultant force F in Fig. 2.15. For large values of d/h it would be expected that $h_{eq} = h = h_a$, where h_a is the height of the connector, and these connectors will be referred to as stiff connectors, so that

$$\left(h_{eq}\right)_{stiff} = h_a \tag{11.56}$$

Conversely for low values of d/h, $h_{eq} < h_a$ and these connectors will be referred to as flexible connectors.

In order to apply the splitting analyses in Section 11.3, it is necessary to determine the equivalent height of the connector through either experimental testing or non-linear finite element analyses. The equivalent height of stud shear connectors of height h_s and shank diameter d_{sh} and with an aspect ratio ($h_s/d_{sh} = h/d$) of approximately 5 was determined experimentally (Oehlers 1989) and is given by

$$\left(h_{eq}\right)_{stud} = 1.80d_{sh} \tag{11.57}$$

which means that the splitting resistance to a stud shear connector of shank diameter d_{sh} is equivalent to the splitting resistance to a stiff connector of width $b_a = d_{sh}$ and height $h_a = 1.80d_{sh}$. As h_{eq} is less than the height of the connector h_s, stud shear connectors can be categorised as flexible shear connectors.

Stud shear connectors are by far the most common form of shear connection and ample experimental splitting tests are available to determine the equivalent height (Oehlers 1989). This is not so with other types of mechanical connectors. However, in many cases a reasonable judgement can be made in estimating the equivalent height. Take for example the bar connector shown in Fig. 11.24. In general, the aspect ratio $h_a/d \approx 1$ so this could be considered to be a very stiff connector and therefore it would be expected that $h_{eq} = h_a$ as in Eq. 11.56. The remaining connectors in Fig. 11.24 may not be solid, as in the bar connector, but in general their aspect ratio $h_a/d \leq 1$ so these can also be defined as stiff connectors (Eurocode 4) and hence $h_{eq} = h_a$. It is also worth noting that it is suggested that the full width b_a of these connectors should be used in the splitting analysis as shown in (b).

All connectors except the 'bar' connector in Fig. 1.5 can be considered to be flexible connectors, and hence have an equivalent height that is less than the height of the connector. These equivalent heights should be determined experimentally, but until this evidence is available it is suggested that the results from stud shear connectors, that is Eq. 11.57, could be used as an initial guideline. For example and as a first approximation, it may be assumed that Eq. 11.57 can be applied directly to the bolted connections (b), (g) and (h) where d_{sh} would be the diameter of the bolt. For the channel connector in (c), it is suggested that as a first approximation

$$\left(h_{eq}\right)_{plate} = t_f + 1.8t_w \tag{11.58}$$

and this can also be applied to connectors (d) and (f).
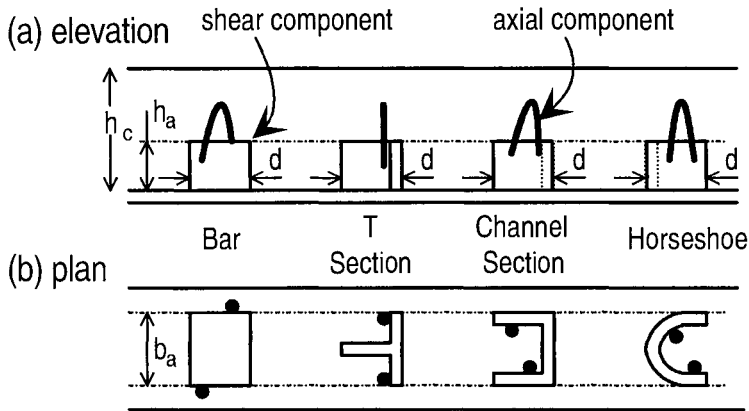
Fig. 11.24 Stiff connectors

11.4.3 CONNECTOR CONFIGURATIONS

It is difficult to define the transition between local and global splitting, and it is therefore necessary to check for both forms of splitting in all configurations of shear connectors (Oehlers 1989). In general, local splitting governs design when the effective width is small and global splitting when the effective width is large. We will define an *individual* connector as a single connector, a *group* of connectors as a concentration of laterally spaced individual connectors as shown in Fig. 11.25(a), a *block* of connectors as a concentration of groups of connectors in which the longitudinal spread $d_f \ll b_c$ as in (b), and a *line* of connectors when the longitudinal spread d_f is greater than or of the same order of magnitude as b_c.

Consider the group of connectors in Fig. 11.25(a). It is necessary to ensure that all combinations of connectors within this group do not cause splitting, such as the individual connectors, pairs of connectors and the whole group. The individual connector that is most likely to induce splitting is the connector with the smallest effective width of slab, which is No. 1 in (a) of breadth $(b_a)_1$ acting on prism of effective width $(b_c)_1$. Hence it is necessary to ensure that the dowel strength D_{max} does not exceed the splitting resistance of this prism. The pair of connectors to check would be Nos. 1 and 2 acting together of effective breadth $(b_a)_2$ acting on a prism of effective width $(b_c)_2$ and hence it is necessary to ensure that the splitting resistance of this prism is greater than $2D_{max}$. Finally, it is necessary to ensure that the splitting resistance to the whole group of effective breadth $(b_a)_3$ acting on a prism of effective width $(b_c)_3$ exceeds $3D_{max}$.

Consider the block of connectors in Fig. 11.25(b). Each group of three connectors, groups numbered 4, 5 and 6, induces a lateral tensile stress distribution in

front of the connectors of the same shape as that shown in Fig. 11.7(c), which has a peak stress f_{max} that lies close to the group of connectors that induced it. When $d_f \ll b_c$ as in Fig. 11.25(b), it can be assumed that the peak stresses from each group coincide and therefore all nine connectors act as one group. Hence it is necessary to ensure that the splitting resistance of the prism of width b_c in (b) that is subjected to a patch load of effective width b_a is greater than $9D_{max}$. It is worth noting that should splitting occur, then it will only affect the connectors on the boundaries of the group; the boundaries being defined by the connectors along the lines 1, 3, 4 and 6 in (b). This is because the shear connectors are connected to a rigid steel flange and so the shear connectors laterally restrain the concrete element within their boundaries, as they themselves are restrained from lateral movement relative to each other by the steel flange. Therefore splitting will not occur within the connector boundaries.
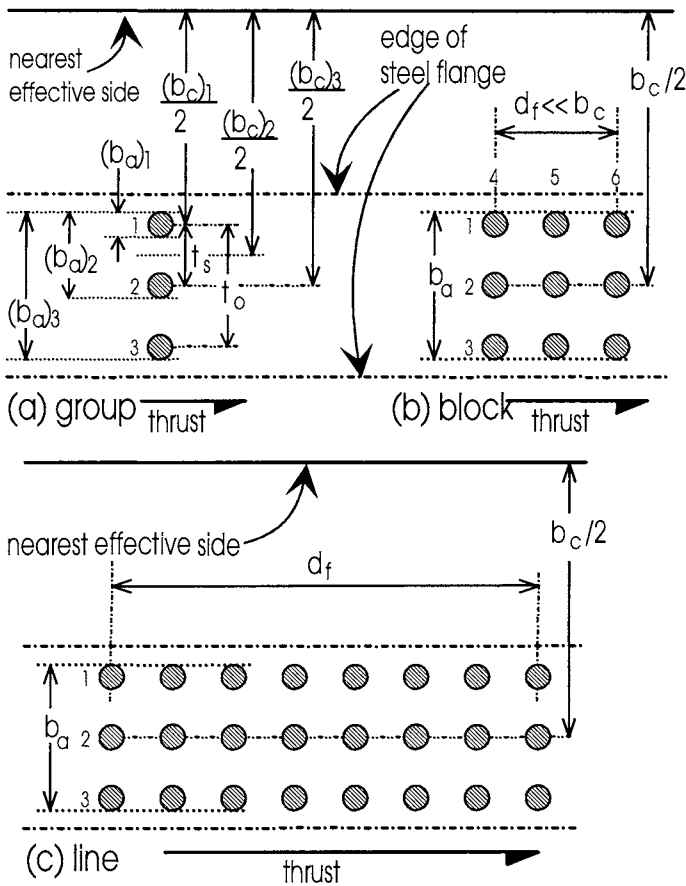
Fig. 11.25 Arrangement of connectors

Consider the line of connectors in Fig. 11.25(c). The individual connectors along lines 1 and 3 will have to be checked for splitting as the splitting zone along line 1 is not laterally restrained by the connectors. Groups of connectors will have splitting

zones that lie within the boundaries of the connectors and as this region is laterally restrained through the steel flange it is not necessary to check for the splitting resistance to these groups. When d_f is of the same order of magnitude as b_c, it is not necessary to analyse all the connectors as though they were acting as a block, since it would be extremely conservative to assume that all the lateral tensile stress zones coincide. However, it will be necessary to check for global splitting for a shear flow of width b_a in (c) acting on a concrete element of width b_c.

11.4.4 TRANSVERSE FLEXURE

Transverse flexure, as shown in Fig. 11.26, induces lateral stresses that are directly in line with the lateral stresses induced by splitting and therefore have to be incorporated into the design procedure.
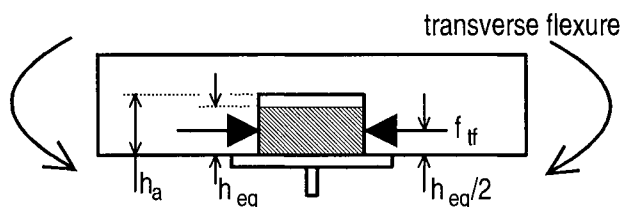
Fig. 11.26 Transverse flexure

Splitting occurs near the base of the connector where the dowel load is concentrated. The depth of the splitting is approximately equal to the equivalent height of the connector h_{eq}, as defined in Section 11.4.2, and so as a first approximation it will be assumed that the flexural stress at the mid-depth of the splitting zone f_{tf} in Fig. 11.26 should be used in the analysis of splitting. This flexural stress can be determined from rigid plastic analysis if the concrete slab is near its maximum strength or it can be determined from linear elastic analysis at low loads. However, it will be shown that in general it is not necessary to determine this stress.

The effect of lateral flexural stresses on the splitting strength can simply be allowed for by using an equivalent tensile strength $(f_{cb})_{eq}$ in the splitting equations, such that

$$\left(f_{cb}\right)_{eq} = f_{cb} - f_{tf} \tag{11.59}$$

where f_{tf} is positive when the lateral flexural stress in the splitting zone is tensile. This sign convention is in agreement with that defined for shear flow in Section 11.3.3.2.

For composite beams with limited side cover to the connectors such as L-beams and beams with deep haunches, the flexural stress at the splitting zone can be assumed to be negligible so that $(f_{cb})_{eq} = f_{cb}$ in Eq. 11.59. Similarly when the load applied to the composite beam does induce transverse flexure, as would occur if the load was applied immediately above the steel element in Fig. 11.26, then $(f_{cb})_{eq} = f_{cb}$.

When the load applied to the composite beam induces transverse hogging or negative moments over the steel element, then large flexural compressive stresses occur in the splitting zone that are of the same order of magnitude as the compressive cylinder strength f_c, so that $(f_{cb})_{eq} \approx f_c$ in Eq. 11.59. Hence splitting is unlikely to occur.

Finally, when transverse sagging or positive moments occur in the slab over the steel element, then flexural cracking along the splitting zone will occur at an early stage of loading so that $(f_{cb})_{eq} = 0$ in Eq. 11.59. This situation can occur when parallel composite beams do not deflect the same amount. After splitting, the dowel strength and behaviour of the mechanical shear connectors will be defined by the post-splitting behaviour as described in Chapter 12.

11.4.5 CHARACTERISTIC STRENGTHS

11.4.5.1 *General equations*

Consider the formula for the characteristic strength of ductile connectors in Eq. 2.30. When both sides of the equation are divided by the mean strength P_m, the ratio of the characteristic strength to the mean strength $C = P_{ch}/P_m$ is given by

$$C = 1 - \frac{1.64 K_{cov}}{\sqrt{n}} \qquad (11.60)$$

where $K_{cov} = D_p/P_m$ is the standard deviation divided by the mean (that is the coefficient of variation), the constant 1.64 is the number of standard deviations from the mean at which the 5% confidence limit occurs, and n is the number of connectors that can be assumed to fail as a group. Splitting is a brittle mechanism of failure when there is no transverse reinforcement. In this case the connectors cannot be assumed to fail as a group and therefore it is necessary to assume that n = 1 in Eq. 11.60, that is we are dealing with the characteristic strength of an individual connector. However, where there is sufficient transverse reinforcement, as described in Chapter 12, then splitting is a ductile behaviour and n can be made equal the number of shear connectors in a shear span.

From experimental tests on the splitting of prisms (Oehlers and Johnson 1981; Oehlers 1989), the coefficient of variation in Eq. 11.60 was found to be

$$\left(K_{cov}\right)_{split} = 0.150 \qquad (11.61)$$

The splitting resistances in Section 11.3 are based on the two-dimensional splitting resistances of prisms that are themselves directly dependent on the height of the connector h_a. A convenient method of allowing for the scatter of splitting resistances is to use an adjusted height of the connector $(h_a)_{ch}$ to allow for the scatter of results, where

$$\left(h_a\right)_{ch} = h_a C \qquad (11.62)$$

It was shown in Section 11.3.7.3(a) and in Eq. 11.39 that the height of the connector can also be adjusted to allow for vertical dispersal and hence combining Eqs. 11.39 and 11.62 and using h_{eq}, from Section 11.4.2, instead of h_a, gives an effective height for design or analysis purposes h_{eff} as

$$h_{eff} = h_{eq} QC \tag{11.63}$$

Hence for design purposes h_{eff} can be substituted for h_a in all the two-dimensional splitting equations in Sections 11.3.2 to 11.3.6.

11.4.5.2 Characteristic strengths

(a) One mechanism of failure

Most standard design procedures are based on one mechanism that causes failure. For example, the design philosophy may assume that the design limit state is reached as soon as splitting occurs. Then in order to ensure a 1 in 20 probability of failure, it is necessary to base the design on the 5% characteristic strength $C_{5\%}$, that can be derived by inserting Eq. 11.61 into Eq. 11.60 to give

$$C_{5\%} = 1 - \frac{0.25}{\sqrt{n}} \tag{11.64}$$

that can be used in Eq. 11.63 for design.

(b) Two mechanisms of failure

An alternative approach is to require two mechanisms of transferring the longitudinal shear to fail before the design limit state is reached. For example, the cross section of the concrete element can be dimensioned so that the design limit state can be reached before splitting occurs. Furthermore, sufficient transverse reinforcement can be used as described in Chapter 12, so that if splitting should occur prematurely, then the post splitting strength also exceeds the strength required for the design limit state.

If a two mechanism to failure approach is applied, then it is not necessary to base the design on the 5% (1 in 20) probability of each mechanism failing, as the probability of both mechanisms occurring would be 1 in 400. Instead, design should be based on a 1 in $\sqrt{20}$ (22.4%) probability of occurrence for each mechanism, so that the probability of both of them occurring is 1 in 20. The 22.4% confidence limit occurs at 0.76 standard deviations. Substituting 0.76 for 1.64 in Eq. 11.60 and using the coefficient of variation in Eq. 11.61 gives

$$C_{22\%} = 1 - \frac{0.11}{\sqrt{n}} \tag{11.65}$$

It is suggested that a two mechanism approach should be used wherever possible. However, it is not necessary to ensure that both mechanisms have the same probability of failure just as long as the combined probability is 1 in 20.

11.4.6 FUNDAMENTAL SPLITTING EQUATIONS

The fundamental equation for local splitting, Eq. 11.7, can be written in the following form to allow for the equivalent height and characteristic strength.

$$\left(P_{split}\right)_{ch} = \frac{0.6 b_c h_{eff} \left(f_{cb}\right)_{eq}}{K_d} \tag{11.66}$$

Similarly, the fundamental equations of global splitting, Eqs. 11.9 and 11.20 can be written in the form

$$f_d = \frac{K_d q}{h_{eff}} \tag{11.67}$$

and

$$f_r = \frac{dq}{dx}\left(\frac{b_c \pi K_d}{16 h_{eff}}\right) \tag{11.68}$$

where

$$\sum f_r + \sum f_d \leq \left(f_{cb}\right)_{eq} \tag{11.69}$$

that is the stresses are summed for each of the components of dq/dx and q shown in Fig. 11.10.

Example 11.10 Characteristic local resistance to angle connections

The angle connector in Fig. 1.5(f) is part of an L-beam and is encased in a concrete slab of depth 130 mm and tensile strength $f_{cb} = 3$ N/mm². The connector has a width $b_a = 120$ mm and plate thickness of 8 mm. Let us consider the minimum local splitting resistance of the slab to this connector.

From Section 11.3.6 and Eq. 11.27, the minimum splitting resistance occurs when $b_c = 360$ mm. From Eq. 11.58, the equivalent height of this connector is $h_{eq} = 22.4$ mm. From Eq. 11.53, the effective height of the slab $(h_c)_e = 4.5 h_{eq} = 101$ mm. The dimensions of the shear connection have now been defined. As the connector is part of an L-beam, the lateral flexural stresses can be ignored so that from Eq. 11.59, $(f_{cb})_{eq} = f_{cb} = 3$ N/mm².

We need to determine the effective height h_{eff} in Eq. 11.63 in order to allow for vertical dispersal (the parameter Q) and to allow for the characteristic strength (the C parameter). The vertical dispersal parameter Q can be derived from Eqs. 11.36 and 11.37. From Eq. 11.19, $K_d = 0.142$. As $h_c > 3 h_{eq}$, K_s can be derived from Eq. 11.38 giving $K_s = 7.44$. Hence V = 1.10 and Q = 2.10.

Let us first consider the case of a connector in a concrete element that does not have sufficient transverse reinforcement to make the splitting failure ductile. In this case, the failure of the weakest shear connection will precipitate failure of the other shear connections and hence it is necessary to design for the 5% characteristic strength of an individual connector. Hence from Eq. 11.64, $C = 0.75$ when $n = 1$. As V and Q have already been derived, from Eq. 11.63 $h_{eff} = 35.3$ mm. Applying $h_{eff} = 35.3$ mm to Eq. 11.66 gives the characteristic splitting resistance to an individual connector as 162 kN. If we assumed that there was sufficient transverse reinforcement, then Eq. 11.65 could be applied, which would increase the characteristic strength of an individual connector to 192 kN. If we now assumed that there were 20 connectors in a shear span so that $n = 20$ in Eq. 11.65, then the characteristic strength would increase to 212 kN which is only slightly less than the mean strength of 217 kN that can be derived by substituting $C = 1$, that is $n = \infty$ in either Eqs. 11.64 or 11.65.

Example 11.11 Local resistance to blocks of stud shear connectors in open truss girder

In the open truss girder in Fig. 1.9(c), the connectors are concentrated in blocks as shown. It is necessary to have sixteen 19 x 100 stud shear connectors in each block in four rows and four lines and as close to each other as possible. The characteristic dowel strength of all sixteen connectors is 1920 kN and the concrete slab has a compressive strength of $f_c = 30$ N/mm² and tensile strength of $f_{cb} = 2.7$ N/mm². The height of the slab $h_c = 125$ mm and the effective breadth of the prism on which the block of connectors act is $b_c = 4000$ mm. There are four blocks of connectors per shear span.

The minimum lateral spacing for stud shear connectors is given in Section 2.4.6.1 as $4d_{sh}$. Therefore as there are four lines of connectors, the minimum effective width of the block $b_c = 13d_{sh} = 247$ mm. The minimum longitudinal spacing is given in Section 2.4.6.1 as $5d_{sh}$ and as there are four rows of connectors, the minimum spread of the block, d_f in Fig. 11.25(b), is $d_f = 16d_{sh} = 304$ mm. As $d_f \ll b_c$, all 16 connectors can be assumed to act as one.

A similar procedure to that outlined in Example 11.10 is followed. From Eq. 11.57, $h_{eq} = 1.80d_{sh} = 34.2$ mm. As $h_c < 4.5h_{eq}$ (Eq. 11.43), $(h_c)_e = h_c = 125$ mm from Eq. 11.53. From Eq. 11.38, $K_s = 6.93$; from Eq. 11.19, $K_d = 0.280$; from Eq. 11.37, $V = 0.377$; from Eq. 11.36, $Q = 1.38$ and hence from Eq. 11.63, $h_{eff} = 47.1C$.

Suppose there is plenty of transverse reinforcement to maintain the dowel strength after splitting. Then C can be derived from Eq. 11.65 with $n = 4$, as there are four blocks of connectors per shear span, to give $C = 0.945$ and hence an effective height of $h_{eff} = 44.5$ mm. Substituting this value for h_{eff} into Eq. 11.66 as well as $(P_{split})_{ch} = 1920$ kN, which is the total force exerted by all the connectors, gives the lateral tensile stress as $(f_{cb})_{eq} = 5.03$ N/mm². If the lateral flexural stress is zero, that is $f_{tf} = 0$ in Eq. 11.59, then the equivalent tensile strength $(f_{cb})_{eq} = f_{cb} = 2.7$ N/mm² and splitting will occur as the lateral splitting stress is greater. The engineer will then have

to ensure using the procedures described in Chapter 12 that there is sufficient transverse reinforcement so that the post-splitting stress is equal to the dowel strengths. However, if the applied load is uniformly distributed over the slab so that lateral flexural compressive stresses are induced in the splitting zone, then there is a good chance that $(f_{cb})_{eq} \rightarrow f_c$ so that splitting is unlikely to occur.

11.5 Stud shear connectors

11.5.1 GEOMETRIC DIMENSIONS

It is now worth looking at stud shear connections by themselves as they are the commonest form of shear connection. The first step in the design procedure is to define the effective dimensions of the stud shear connection and these are summarised in Fig. 11.27 where reference to the appropriate equation or section is given. All of these dimensions except c_{do} were developed from the preceding analyses on splitting.

Fig. 11.27 Effective dimensions of stud shear connection
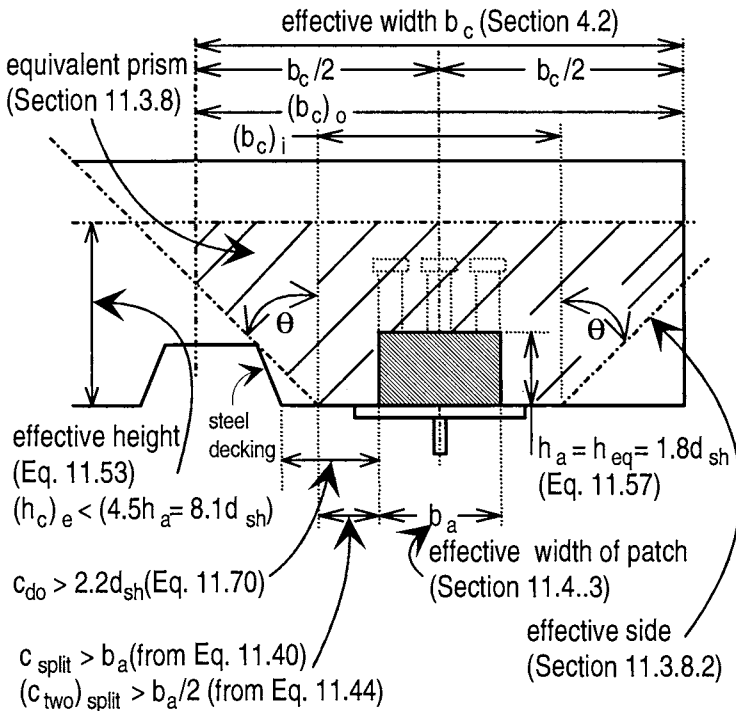
The minimum side cover requirement

$$c_{do} \geq 2.2 d_{sh} \tag{11.70}$$

has been introduced to ensure that the dowel strength of the stud shear connection can be achieved when splitting does not occur. It has been shown in Section 2.4, that the dowel strength of a connector depends on the triaxial restraint to the concrete in the compression zone adjacent to the connector. The ability of the slab to impose this triaxial restraint will depend on the side cover, and it may be expected that even if splitting is prevented a minimum side cover requirement is necessary to ensure sufficient triaxial restraint. The minimum side cover of $2.2d_{sh}$ in Eq. 11.70 was derived from the satisfactory performance of stud shear connectors in tests (Oehlers and Park 1994) and is close to the code minimum requirements (Eurocode 4 1994).

It is worth emphasising the distinction between c_{do} and c_{split} in Fig. 11.27. The dimension c_{do} is the actual side cover and a minimum value of which is specified in order to ensure that the dowel strength is reached. The side dimension c_{split} is a theoretical dimension for the splitting analyses and a minimum dimension of which is specified that signifies a bound of the splitting theory.

11.5.2 SPLITTING ANALYSIS

The effective dimensions of the stud shear connection in Fig. 11.27 have been defined. The three-dimensional problem is then simplified to a two-dimensional problem of that of a concentric patch load acting on a prism as shown in Fig. 11.28. The local splitting strength of each rectangular prism can be derived from Eq. 11.66 and hence the actual splitting strength from Eq. 11.50; methods of converting the results for global splitting are discussed in Section 11.3.8.3.
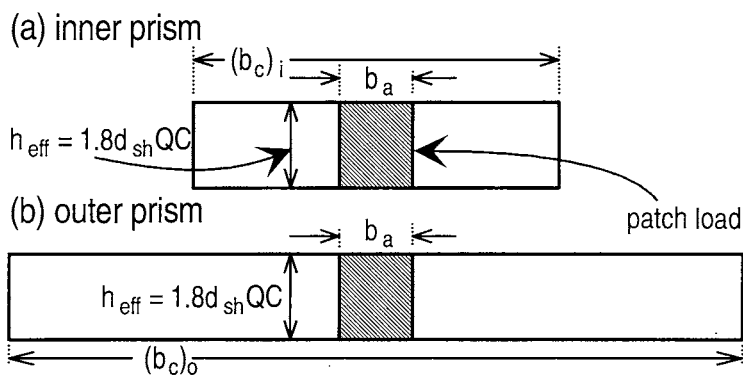
Fig. 11.28 Splitting analysis

The constant C in the effective height dimension h_{eff} in Fig. 11.28 defines the characteristic strength and is given by Eqs. 11.64 or 11.65, depending on the design philosophy that is being used. The constant Q, in the effective height dimension h_{eff}, defines the beneficial effect of vertical dispersal and is given by Eqs. 11.36 and 11.37 where K_s in Eq. 11.37 is given by either Eqs. 11.38 or 11.42 depending on the height of the slab. The parameter K_s was determined experimentally from push tests with stud shear connectors (Oehlers 1989) and it was suggested that a value of 10 be used

in design. It was found that K_s in Eq. 11.38 underestimated the beneficial effects of the vertical dispersal (Oehlers 1993) and that a better estimate would be to use

$$(K_s)_{3h_a \le h_c \le 4.5h_a} = \left(\left(1 - \frac{h_a}{2h_c} \right)^2 \frac{h_a}{2h_c} \right)^{-1}$$

(11.71)

A comparison of Eqs. 11.38 and 11.71 shows that at most Eq. 11.38 underestimates K_s by 35%, the difference reducing to zero at $h_c = h_a = 1.8d_{sh}$. The effect on the splitting strength is quite small bearing in mind that K_s affects the proportional increase in the splitting strength due to vertical dispersal as given by Eq. 11.36. Substituting $h_a = h_{eq} = 1.8d_{sh}$ in Eq. 11.71 gives

$$(K_s)_{5.4d_{sh} \le h_c \le 8.1d_{sh}} = \left(\left(1 - \frac{0.9d_{sh}}{h_c} \right)^2 \frac{0.9d_{sh}}{h_c} \right)^{-1}$$

(11.72)

Assuming a linear variation from $h_c = 3h_a$ to $h_c = h_a$ gives the following variation in K_s

$$(K_s)_{h_a \le h_c \le 3h_a} = 13.0 \left(1 - \frac{h_a}{h_c} \right)$$

(11.73)

which is equivalent to Eq. 11.42. Substituting $h_a = 1.8d_{sh}$ gives

$$(K_s)_{1.8d_{sh} \le h_c \le 5.4d_{sh}} = 13.0 \left(1 - \frac{1.8d_{sh}}{h_c} \right)$$

(11.74)

11.5.3 GENERAL ANALYSIS PROCEDURES

11.5.3.1 *General*

For most stud shear connections $h_c > 5.4d_{sh}$ so that K_s in Eq. 11.72 normally applies and so this version of K_s will be used in the following general analysis equations. It will also be assumed that the lateral flexural stresses are negligible so that f_{cb} controls design, and it will be assumed that for normal density concrete $f_{cb} = 0.5\sqrt{f_c}$ (as given by Eq. 2.7) and for lightweight concrete the reduction factor in Eq. 13.5 can be used if required.

11.5.3.2 *Single line of stud shear connectors*

For a single line of connectors such as line 1 in Fig. 11.25(a), $b_a = d_{sh}$ and from Eq. 11.66 the splitting resistance is given by

$$P_{one} = 1.7 \left(\left[\left(1 - \frac{0.9d_{sh}}{h_c} \right)^2 \frac{0.9d_{sh}}{h_c} \right]^{-1} + \frac{b_c}{d_{sh}\left(1 - \dfrac{d_{sh}}{b_c}\right)^2} \right) Cd_{sh}^2 \sqrt{f_c} \qquad (11.75)$$

where the characteristic parameter C is given by either Eqs. 11.64 or 11.65 depending on the design philosophy, and where the units are in N and mm as the $\sqrt{f_c}$ is proportional to the tensile strength of the concrete.

The minimum splitting strength occurs at $c_{split} = b_a = d_{sh}$ in Fig. 11.27 and can be derived from Eq. 11.28 as

$$\left(P_{min}\right)_{one} = 1.7 \left(\left[\left(1 - \frac{0.9d_{sh}}{h_c} \right)^2 \frac{0.9d_{sh}}{h_c} \right]^{-1} + \frac{27}{4} \right) Cd_{sh}^2 \sqrt{f_c} \qquad (11.76)$$

where the units are in N and mm.

11.5.3.3 *Two lines of stud shear connectors*

For a double line of stud connectors such as lines 1 and 2 in Fig. 11.25(a), $b_a = t_s + d_{sh}$, where t_s = lateral spacing of connectors. The splitting resistance against these two connectors acting together is given by

$$P_{two} = 1.7 \left(\left[\left(1 - \frac{0.9d_{sh}}{h_c} \right)^2 \frac{0.9d_{sh}}{h_c} \right]^{-1} + \frac{b_c}{(t_s + d_{sh})\left(1 - \dfrac{t_s + d_{sh}}{b_c}\right)} \right) C(t_s + d_{sh})d_{sh}\sqrt{f_c}$$

$$(11.77)$$

The minimum splitting strength occurs at $c_{split} = b_a/2 = (t_s + d_{sh})/2$ and is given by

$$\left(P_{min}\right)_{two} = 1.7 \left(\left[\left(1 - \frac{0.9d_{sh}}{h_c} \right)^2 \frac{0.9d_{sh}}{h_c} \right]^{-1} + 4 \right) C(t_s + d_{sh})d_{sh}\sqrt{f_c} \quad (11.78)$$

where the units are in N and mm.

11.5.3.4 *More than two lines of stud shear connectors*

For more than two lines of connectors such as the connectors between lines 1 and 3 in Fig. 11.25(a), $b_a = t_o + d_{sh}$, where t_o = lateral spacing between the outer lines of

connectors. The splitting resistance to this group of connectors acting together is given by

$$P_{more} = 1.7 \left(\left[\left(1 - \frac{0.9d_{sh}}{h_c}\right)^2 \frac{0.9d_{sh}}{h_c} \right]^{-1} + \frac{b_c}{(t_o + d_{sh})\left(1 - \frac{t_o + d_{sh}}{b_c}\right)^2} \right) C(t_o + d_{sh})d_{sh}\sqrt{f_c}$$

(11.79)

The minimum splitting strength occurs at $c_{split} = b_a = t_o + d_{sh}$ and is given by

$$(P_{more})_{min} = 1.7 \left(\left[\left(1 - \frac{0.9d_{sh}}{h_c}\right)^2 \frac{0.9d_{sh}}{h_c} \right]^{-1} + \frac{27}{4} \right) C(t_o + d_{sh})d_{sh}\sqrt{f_c}$$

(11.80)

where the units are in N and mm.

11.5.4 DETAILING RULES FOR MINIMUM COVER

As an example of the application of the splitting theory, detailing rules will be developed for the minimum cover for individual connectors of dowel strength D_{max} in slabs with rectangular cross-sections.

From Eq. 2.7, it will be assumed that $f_{cb} = 0.5\sqrt{f_c}$. The splitting resistance of an individual connector is given by Eq. 11.66 and we need to ensure that $(P_{split})_{ch}$ is greater than or equal to the dowel strength of the shear connection in a composite beam D_{max} as given by Eq. 2.37. As we are dealing with minimum cover requirements, the lateral flexural stresses on the splitting zone can be assumed to be zero, so that in Eq. 11.66 the equivalent tensile strength $(f_{cb})_{eq} = f_{cb} = 0.5\sqrt{f_c}$. The lateral dispersal factor K_d is given by Eq. 11.19 with $b_a = d_{sh}$ and $b_c = 2c_{split} + d_{sh}$ where c_{split} is the side dimension of the prism. The height of most stud shear connectors is greater than $4d_{sh}$ and the concrete cover to the top of the stud is usually greater than or about equal to d_{sh}. Therefore the height of the slab h_c will usually be greater than $5d_{sh}$, so that vertical dispersal factor K_s in Eq. 11.72 should be used in deriving h_{eff} in Eq. 11.66. It will be assumed that there is plenty of transverse reinforcement so that characteristic strength parameter C in Eq. 11.65 should be applied. As we are dealing with a rectangular concrete prism $c_{split} = c_{do} \doteq$ the side cover required. Including all of these parameters into Eq. 11.66 gives

$$D_{max} \leq 1.7 \left(\left[\left(1 - \frac{0.9d_{sh}}{h_c}\right)^2 \frac{0.9d_{sh}}{h_c} \right]^{-1} + \frac{2c_{do} + d_{sh}}{d_{sh}\left(1 - \frac{d_{sh}}{2c_{do} + d_{sh}}\right)^2} \right) d_{sh}^2 \sqrt{f_c} \left(1 - \frac{0.11}{\sqrt{n}}\right)$$

(11.81)

where the units are in N and mm as the $\sqrt{f_c}$ is the tensile strength of the concrete. By making the inequality into an equality, this equation could be solved iteratively to determine the minimum cover that is required. This is the most accurate method of analysis but it is obviously too cumbersome for routine design.

Consider the characteristic strength parameter in Eq. 11.81 that is also given in Eq. 11.65. When $n = 10$, $C_{22\%} = 0.97$ and so even with only a few shear connectors in a shear span it can be assumed that $C = 1$. For most slabs h_c is at least equal to $6d_{sh}$ or $7d_{sh}$, so that the vertical dispersal parameter in Eq. 11.81 and also shown in Eq. 11.72 can be taken to be equal to 10 which is the value determined experimentally (Section 11.5.2). Substituting these values into Eq. 11.81 and re-arranging gives

$$\frac{c_{do}}{d_{sh}} \geq \left(1 - \frac{d_{sh}}{2c_{do} + d_{sh}}\right)^2 \left(\frac{0.29 D_{max}}{d_{sh}^2 \sqrt{f_c}} - 5\right) - 0.5 \tag{11.82}$$

which is slightly easier to solve for the minimum cover requirement c_{do} but still requires an iterative procedure.

A further simplification of Eq. 11.81 can be made by considering the horizontal dispersal parameter $(1 - d_{sh}/(2c_{do} + d_{sh}))^2$. From Eq. 11.70, a minimum value of c_{do} is $2.2d_{sh}$ which gives a minimum value of this dispersal parameter as 0.66 and a maximum value of unity that occurs when $(b_c = 2c_{do} + d_{sh}) \gg d_{sh}$. Hence a conservative approach would be to assume that this horizontal dispersal factor is equal to unity, giving

$$\frac{c_{do}}{d_{sh}} \geq \frac{0.29 D_{max}}{d_{sh}^2 \sqrt{f_c}} - 5.5 \tag{11.83}$$

so that the minimum cover can now be determined directly.

A further simplification would be to assume that the dowel strength in a beam is given by Eq. 2.37. We will also assume that $f_u = 500$ N/mm² which is about the minimum requirement in most national standards, $E_s = 200$ kN/mm² and a conservative approach to design against splitting would be to base the design on the mean dowel strength, that is $n = \infty$ in Eq. 2.37. Furthermore, if normal density concrete is being used then E_c in Eq. 2.37 is given by Eq. 2.15. Substituting gives

$$\frac{c_{do}}{d_{sh}} \geq 12.8 f_c^{0.05} - 5.5 \tag{11.84}$$

where f_c is in N/mm².

A final simplification can be made by considering that range of $f_c^{0.05}$ in Eq. 11.84. For f_c between 25 and 50 N/mm² this parameter only varies from 1.17 to 1.22. This small variation is because both the dowel strength and the splitting resistance

increase with increases in the concrete strength. A conservative design approach would be to use 1.22 to give

$$\frac{c_{do}}{d_{sh}} \geq 10.0 \tag{11.85}$$

so that the minimum cover requirement is $10d_{sh}$.

Example 11.12 Side cover requirement for single stud shear connector

A 19 mm stud shear connector with tensile strength of $f_u = 500$ N/mm² is encased in concrete of $f_c = 30$ N/mm². Determine the minimum side cover if the slab is rectangular.

     From Eq. 11. 85, $c_{do} \geq 190$ mm. From Eq. 11.84, $c_{do} \geq 184$ mm. From Eq. 11.83, $c_{do} \geq 183$ mm and from Eq. 11.82, $c_{do} \geq 162$ mm. The simplification of Eq. 11.85 is thus conservative.

Example 11.13 Local resistance to stud shear connections in a haunched beam

Consider the stud shear connection in the deep haunch in Fig. 11.29. A 20x100 mm stud is embedded in concrete of $f_c = 40$ N/mm².

     The dimensions of the equivalent prism in Fig. 11.29 are derived from the bounds shown in Fig. 11.27. The effective side to be used in design is in line with the side of the haunch in Fig. 11.29 as using effective sides within this region will lead to reduced splitting resistances, and it is the maximum splitting resistances that controls design. The splitting resistance $(P_{split})_{ch}$ of the inner and outer prisms is given by Eq. 11.75. For the inner prism $(P_{split})_i = 92C$ kN and for the outer prism $(P_{split})_o = 131C$ kN. Hence from Eq. 11.50, the splitting resistance of the haunched slab $(P_{split})_\theta = 105C$ kN.

     Let us assume that adequate transverse reinforcement cannot be placed within the haunch. Splitting will be brittle and so it would be necessary to base design on the 5% characteristic splitting resistance of an individual connection. For n = 1 in Eq. 11.64, $C_{5\%} = 0.75$ and hence $(P_{split})_\theta = 79$ kN.

     If adequate transverse reinforcement can be placed within the haunch in accordance with Chapter 12 so that the dowel strength can be maintained after splitting, then two mechanisms are available to transfer the shear so that $C_{22\%}$ in Eq. 11.65 can be used. If the number of connectors in a shear span n = 20, then $C_{22\%} = 0.98$ and so $\left(P_{split}\right)_\theta = 102$ kN which is very close to the mean strength of 105 kN. If it is necessary to prevent splitting at service loads, then the analysis in the previous paragraph applies so that the maximum dowel load at service loads must not exceed 79 kN.

effective height $f_c = 40 \text{ N/mm}^2$

20x100 $\theta = 30°$ 125

inner prism

outer prism

162 200

65

(mm)

75 75 94
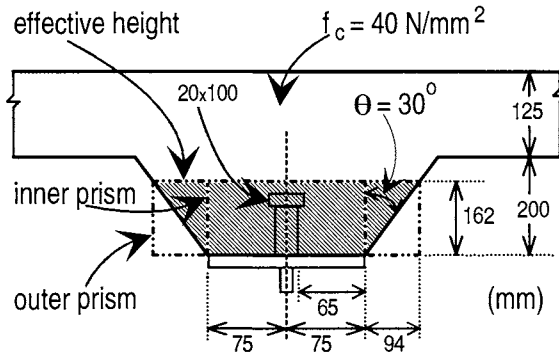
Fig. 11.29 Haunched beam

Example 11.14 Local resistance to stud shear connections in composite slab with parallel ribs

Consider the trough formed by the steel decking in Fig. 11.30. The effective dimensions of this connection are given by the bounds shown in Fig. 11.27 from which it can be seen that the full depth of the slab can be used in the analysis. The two effective sides A and B in Fig. 11.30 should be considered in the analysis, however only the calculations for side A will be given as this is the effective side that gives the greatest splitting resistance. The splitting action of the individual connectors and that of both connectors acting as one has to be considered.

For the single connector, the equivalent prism concept will be applied as represented in Fig. 11.22. It has simply to be assumed that the section to the left of the centre line of the single connector in Fig. 11.30 is the mirror image of the section to the right. For the effective side A, the width of the inner prism is 260 mm and that of the outer prism 560 mm. Following the same procedure as in Example 11.13, $(P_{split})_\theta$ = 144C kN. For the effective side B in Fig. 11.30, the outer prism occurs when $(c_{split})_{min} = d_{sh}$ and has a width of 950 mm. The strength of the outer prism is given by Eq. 11.75 and the strength of the inner prism which is also the minimum splitting strength is given by Eq. 11.76. From these, the strength of the haunch can be derived as $(P_{split})_\theta$ = 167C kN. Therefore the equivalent prism that is defined by side B controls design as this has the greater splitting resistance, that is $(P_{split})_\theta$ = 167C kN.

For the double line of connectors, Eqs. 11.77 and 11.78 control the analysis. For side B, $(P_{split})_i = (P_{min})_{two}$ = 317C kN, $(P_{split})_o$ = 453C kN and so $(P_{split})_\theta$ = 385C kN. However, it should be remembered that $(P_{split})_\theta$ = 385C kN is the resistance to two connectors and hence the load per connector is a half, that is 193C kN. As this is greater than the strength of the individual connectors of 167C kN, there is no need to check side A as it is the larger of the two strengths that controls the analysis.

The splitting resistance is therefore given by $(P_{split})_\theta$ = 167C kN and is determined by the strength of the individual connectors. If the steel decking can be

assumed to act as transverse reinforcement then $C_{22\%}$ in Eq. 11.65 could be used in the analysis. Even for small numbers of connectors in a shear span $C_{22\%} \rightarrow 1$, so that the dowel load to cause splitting will be close to 167 kN.
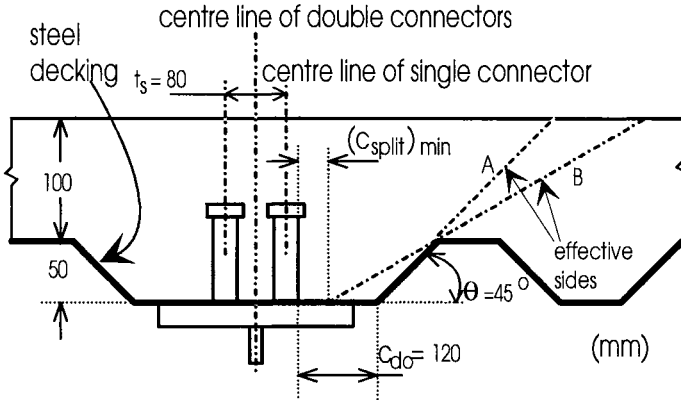
Fig. 11.30 Composite slab

Example 11.15 Stud shear connection cover in composite beam with composite slab

Consider the case of a composite beam made with the steel decking shape and slab depth shown in Fig. 11.30. It may be necessary to provide detailing rules for the cover c_{do} to ensure that the dowel strength of the connector D_{max} can be reached without splitting.

As has been discussed in Example 11.14, the effective side B in Fig. 11.30 where $(c_{split})_{min} = d_{sh}$ and the splitting resistance to an individual connector controls design. However, using this effective side to formulate detailing rules leads to a complex function as the slope of the effective side varies with the cover c_{do}. A simpler and conservative assumption is to use effective side A at a fixed angle $\theta = 45°$. The strength of the inner and outer prisms can be determined from Eq. 11.75 in terms of c_{do} and d_{sh}. Using the assumptions discussed in Section 11.5.4 that $K_s = 10$ and $C = 1$, it can be derived from Eq. 11.50 that

$$\frac{c_{do}}{d_{sh}} \geq \frac{0.23 D_{max}}{d_{sh}^2 \sqrt{f_c}} - \frac{62}{d_{sh}} - 4.4 \qquad (11.86)$$

Using the same assumptions as those used in deriving Eqs. 11.84 and 11.85 gives a further simplification as

$$\frac{c_{do}}{d_{sh}} \geq 7.9 - \frac{62}{d_{sh}} \qquad (11.87)$$

For the connection used in Example 11.12, Eq. 11.87 requires a minimum cover of 4.6d_{sh} compared with 10d_{sh} from Eq. 11.85 when the side of the slab is vertical. This comparison serves to emphasise the beneficial effect of a sloping side as compared with that of a vertical side.

11.5.5 TRANSVERSE RIBS

The design rules derived in this chapter can be applied to composite beams with composite slabs in which the ribs of the steel decking are parallel to the steel element of the composite beam, as shown in Fig. 1.11(b) and also shown in Fig. 4.4 with $\theta = 0$. When the ribs are transverse to the span of the composite beam as in Fig. 1.11(c) and Fig. 4.4 with $\theta = 90°$, then splitting may still occur but the problem is complicated by the action of local flexural stresses acting on the splitting plane and by the void formed by the rib. The problem is complex and in general the strength of the shear connection in transverse ribs is derived empirically.

The general trend in the design procedures is to apply a reduction factor to the dowel strength of the stud shear connection in a solid slab. For example, the following reduction factor R_{rib} is given in draft Eurocode 4 (Johnson 1994)

$$R_{rib} = \frac{0.7b_h}{\sqrt{N}h_r}\left(\frac{h_s}{h_r}-1\right) \leq 1.0 \tag{11.88}$$

where N is the number of connectors in a rib, h_r is the height of the rib, h_s is the height of the stud and b_h is approximately the mean width of the haunch between the ribs. Empirical equations of this type should be used with caution and only well within the bounds of the tests from which they were derived. As an example, Eq. 11.88 should only be applied for studs (Johnson and Anderson 1993) with a diameter $d_{sh} \leq 20$ mm, the tensile strength of the stud f_u should be assumed not to be greater than 450 N/mm^2, and $R_{rib} \leq 0.8$ when $N \geq 2$.

When θ in Fig. 4.4 lies between 0 and 90°, it would be reasonable to assume a linear transition between the splitting resistances of a longitudinal and transverse haunch. Let $(P_{split})_i$ be the stud shear connection strength when $\theta = 90°$ as given by the other sections of this chapter and Chapter 12. Let $(P_{split})_o$ be the stud shear connection strength when $\theta = 90°$ as given by Eq. 11.88. Then the strength of the shear connection $(P_{split})_\theta$ when the ribs are at an angle θ as in Fig. 4.4 is given by Eq. 11.50.

11.6 References

Eurocode 4 (1994) Part 1.1: Design of composite steel and concrete structures. DD ENV 1994-1-1: 1994. Draft for development.

Gilbert, R.I. and Mickleborough, N.C. (1990) *Prestressed Concrete*, Unwin Hyman, London.

Jayas, B.S. and Hosain, M.U. (1988). "Behaviour of headed studs in composite beams: push-out tests", Canadian Journal of Civil Engineering, Vol.5, No.20, 240-253.

Johnson, R.P. (1994). *Composite Structures of Steel and Concrete,* 2nd edn, Blackwood Scientific Publications, U.K.

Johnson, R.P. and Anderson, D. (1993). *Designers' Handbook to Eurocode 4 Part 1.1: Design of Composite Steel and Concrete Structures.* Thomas Telford, London.

Johnson, R. P. and Oehlers, D. J. (1981). "Analysis and design for longitudinal shear in composite T-beams", Proceedings Institution of Civil Engineers, London, Part 2, Vol.71, 989-1021.

Johnson, R. P. and Oehlers, D. J. (1982). "Design for longitudinal shear in composite L-beams", Proceedings Institution of Civil Engineers, London, Part 2, Vol.73, 147-170.

Leonhardt, F., (1964). *Prestressed Concrete, Design and Construction,* 2nd edn, Wilhelm Ernst and sohn, Berlin-Munich.

O'Brien, D. K. (1986). "Shear failure of diagonally cracked reinforced concrete beams by ripping of the concrete ", M.Sc. Thesis, University College, Cork, National University of Ireland.

Oehlers, D.J. (1989). "Splitting induced by shear connectors in composite beams", Journal of Structural Engineering, ASCE,, Vol. 115, No.2. Feb., 341-362.

Oehlers, D.J. (1993). "Detailing rules for the side cover to stud shear connectors to prevent splitting", Research Report R106, Dept. of Civil and Env. Engng, University of Adelaide, Australia.

Oehlers, D. J. and Johnson, R. P. (1981). "The splitting strength of concrete prisms subjected to surface strip or patch loads." Magazine of Concrete Research, Vol.33, No.116, 171-179.

Oehlers, D. J. and Park, S. M. (1994). "Shear connection in haunched composite beams with sloping sides", Journal of Structural Engineering, ASCE Vol. 120, No. 7, 2227-2232.

Teraszkiewicz, J.S. (1968). "Static and fatigue behaviour of simply supported and continuous composite beams of steel and concrete", Ph.D. Thesis, University of London.

Timoshenko, S.P. and Goodier, J. N. (1970). *Theory of elasticity,* 2nd edn, McGraw Hill Book Co., New York.

Toprac, A.A. and Dale, G.E. (1967). "Composite beams with a hybrid Tee steel section", Journal of the Structural Division, ASCE, No.ST5, 309-322.

Trahair, N.S. and Bradford, M.A. (1991). *The Behaviour and Design of Steel Structures*, revised 2nd edn., Chapman and Hall, London.

Williams, A. (1979). "The bearing capacity of concrete loaded over a limited area." Technical Report 526 (Publication 42.526), Cement and Concrete Association, Wexham Springs, U.K..

12 Post Cracking Dowel Strength

12.1 Introduction

It has been shown in Section 2.4.2 that the dowel strength D_{max} of mechanical shear connectors depends on the triaxial restraint to the concrete in the bearing zone shown in Fig. 2.14(a). If this triaxial restraint to the bearing zone is maintained, then the dowel strength D_{max} is the maximum shear strength of the shear connection. When a longitudinal crack forms through this bearing zone, the triaxial restraint to the bearing zone is then provided by any transverse reinforcement that crosses the crack. The post-cracking dowel strength D_{crack} therefore depends on the amount and position of the transverse reinforcement and in general is less than the dowel strength in uncracked concrete D_{max}.

Not all longitudinal cracks in the concrete element of a composite beam affect the dowel strength. When transverse flexural forces in the concrete element cause hogging or negative moments over the steel element of the composite beam, as shown in Fig. 11.26, then flexural cracking will occur above the bearing zone, so that these longitudinal cracks will not affect the dowel strength. In fact, transverse negative moments will increase the dowel strength by applying transverse compressive stresses to the bearing zone, but this beneficial effect has not been quantified. Conversely, transverse sagging or positive moments will induce longitudinal flexural cracks at the bottom of the slab, through the bearing zones of the shear connections, so these flexural cracks will reduce the dowel strength to D_{crack}. Furthermore, as cracking through longitudinal splitting (Chapter 11) always starts at the base of mechanical shear connectors, then the post-splitting dowel strength is always given by D_{crack}. In the remainder of this chapter we will refer to longitudinal cracking due to splitting as described in Chapter 11, however it is worth bearing in mind that the results are also applicable to longitudinal cracking induced by negative transverse flexural moments.

The effect of transverse reinforcement on longitudinal cracking and hence the dowel strength is described in qualitative terms in Section 12.2. Quantitative analysis techniques are then given in Section 12.3 for straight transverse reinforcing bars, and in Section 12.4 for transverse reinforcing bars that are hooped around stud shear connections that have limited side cover. Further rules for distributing the transverse reinforcement that is required to resist the longitudinal shear forces in the concrete element are given in Chapter 13. It is worth noting that the same transverse reinforcement can be used to maintain the post-cracking dowel strength as well as maintain the longitudinal shear strength; hence it is *not* required to add the reinforcement in Chapter 12 to that required in Chapter 13.

12.2 Qualitative behaviour due to transverse reinforcement

12.2.1 GENERAL

The effect of transverse reinforcement in uncracked sections is described in Section 12.2.2 in terms of both the splitting resistance of the slab and the dowel strength of the shear connection. The effect of transverse reinforcement on the post-splitting or post-cracking behaviour is then described in Section 12.2.3, where it is shown how the transverse reinforcement affects crack propagation, the dowel strength and the ductility, and where detailing rules are also given for the anchorage of the transverse reinforcement.

12.2.2 PRE-SPLITTING EFFECT

12.2.2.1 *Splitting resistance*

Let r_t be the percentage of transverse reinforcement that crosses the lateral splitting zone shown in Fig. 11.5(a) and let n be the modular ratio of the steel to concrete elastic moduli, that is E_s/E_c. Then from transformed sections, as described in Section 6.4.1, the proportional increase in the area of the lateral zone due to the transverse reinforcement is $(n-1)r_t$. For example, if $r_t = 1\%$ and $n = 7$, then the transverse reinforcement increases the area of the lateral zone by 6%. As the resistance to splitting is proportional to the area of the lateral zone (Section 11.3.2), it can be seen that the increase in the splitting resistance due to the transverse reinforcement is not significant and hence can be ignored in practice.

12.2.2.2 *Dowel strength*

The qualitative effect of transverse reinforcement on the dowel strength in longitudinally uncracked concrete has been determined using finite element models of shear connections such as that shown in Fig. 12.1 (Johnson and Oehlers 1981). In these analyses, inclusions of varying size, position and stiffness were simulated to determine their effect on the dowel strength. The change in the dowel strength due to the insertion of a single stiff inclusion or a void are shown as proportional changes in Fig. 12.1. The stiff inclusions can be considered to be equivalent to transverse reinforcement crossing the direction of thrust of the connector. Placing reinforcement within the bearing zone of the shear connection increased the strength from 0.4% to 32%, depending on the position and size of the stiff inclusion.

There would appear to be two mechanisms by which the dowel strength is increased. The reinforcing bar restrains the concrete that is sandwiched between the connector and the bar and hence increases its compressive strength. Furthermore, the connector can literally bear onto the reinforcing bar that then acts as a steel beam on a concrete foundation as illustrated in Fig. 2.15. The latter bearing mechanism occurred in the dowel failure in the push specimen in Fig. 12.2, where it can be seen that the middle of the exposed reinforcing bars is deformed at its centre in line with where the stud shear connectors were.
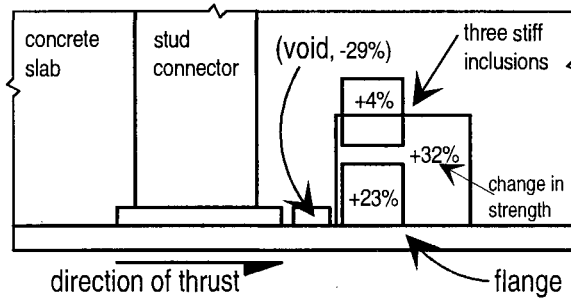
Fig. 12.1 Dowel strength with voids and inclusions

Fig. 12.2 Dowel failure through bending

A further understanding (Johnson and Oehlers 1981) of the dowel action can be drawn from the results in Fig. 12.1. Placing a void in the bearing zone next to the weld collar of the stud shear connector in Fig. 12.1 was found to reduce the dowel strength by 29%, and this result emphasises the importance of compacting the concrete around the base of connectors. Furthermore, the stiff inclusions can be considered to represent aggregate particles that in practice will occur at random positions relative to the connector, and hence cause large variations in the strengths of the individual connectors. The random variation in the individual strengths emphasises the importance of basing the strength of connectors on the mean of a group, as given by Eq. 2.30, and not on the characteristic strength of an individual connector. Finally, it would appear to be reasonable to assume that the dowel strength depends on the

aggregate stiffness as voids reduce the strength and stiff inclusions increase the strength, and hence it can be inferred that using a lightweight aggregate will reduce the dowel strength in contrast to a stiff aggregate that increases the dowel strength even though the compressive strengths f_c are the same.

12.2.3 POST-SPLITTING BEHAVIOUR

12.2.3.1 *Crack propagation*

When a composite beam is subjected to a stationary concentrated load, experimental research has shown (Johnson and Oehlers 1981) that the transverse reinforcement can prevent a longitudinal split from propagating or even reaching the surface of the slab and becoming visible.

The mechanism by which longitudinal splitting cracks propagate (Johnson and Oehlers 1981; Oehlers 1989) is illustrated in qualitative terms in Fig. 12.3. Let us first consider a composite beam that does not have transverse reinforcement, and which is subjected to a uniform shear flow given by the rectangular distributions (1) and (2) in Fig. 12.3(a) that are discontinuous at positions A, B and C. The distribution of the lateral stresses has been described in Section 11.3.3.3 and illustrated in Fig. 11.12, and is shown again in Fig. 12.3(b). The rectangular shear flow distribution (1) in (a) induces the lateral stress distributions marked (1) at both positions A and B in (b). The rectangular shear flow distribution (2) in (a) induces the lateral stress distributions marked (2) at both B and C in (b). Summation of these lateral stress distributions leaves a tensile stress distribution (1) at A and a compressive stress distribution (2) at C. Let us assume that the maximum lateral tensile stress f_d is sufficient to cause splitting of the concrete and let us also assume that the dowel strength reduces to zero where there is a split. The split will first occur at position A in (b) and extend from A to A'. The stress distribution will then change in shape (Oehlers and Johnson 1981) to that marked (4) to accommodate the split but still be at a maximum of f_d at the crack tip which now represents the discontinuity in the shear flow. There is therefore nothing to prevent this crack from propagating along the length of the beam.

Now consider the case of a slab with transverse reinforcement, so that we can now assume that the shear flow does not reduce to zero in regions of a split but can be transferred across the crack by the mechanism described in Section 2.5. For convenience, let us assume that the cracked region extends from A to B in Fig. 12.3 so that the crack tip is now at B, and let us also assume that the shear flow in this region has a linear variation from q at the crack tip at B to zero where cracking first started at A, as shown by the shear flow distribution (3) in (a). The lateral stresses induced by this varying component of the shear flow have been determined in Section 11.3.3.5 and are shown in Fig. 11.13, and are also shown as the compressive distribution (3a) at B in Fig. 12.3(b) and the tensile distribution (3b) between A and B. Superposing the lateral stress distributions due to shear flows (3) and (2) in (a) gives the tensile stress distribution (3b) between A and B in (b) and the compressive stress distribution (2) at C. It can be seen that the lateral tensile stress f_r at the crack tip, that is now at B, is much less than the maximum compressive stress f_d at C which was also equal to the original lateral tensile stress at A when cracking had not occurred. Because the presence of the transverse reinforcement allows shear flow in the cracked

region, the tensile splitting stress at the crack tip has reduced from f_d when the crack tip was at A to f_r when the crack tip is at B. Therefore, the shear flow will have to be increased to propagate the splitting crack in regions of transverse reinforcement, and hence transverse reinforcement acts as crack arresters.
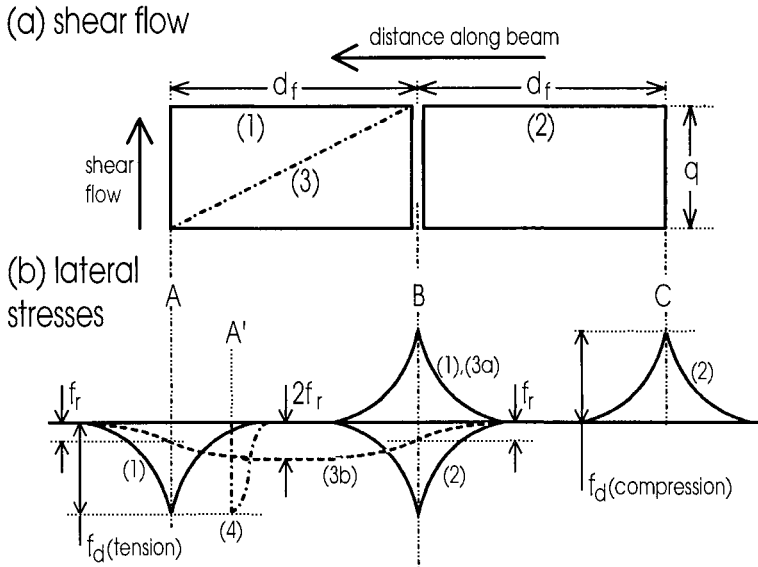
Fig. 12.3 Propagation of splitting crack

It can be seen that transverse reinforcement restricts the extent of cracking in a composite beam subjected to stationary loads. However, in a composite beam that is subjected to a longitudinally moving point load, such as a wheel, there is always a discontinuity in the shear flow at the position of the point load, such as at C in Fig. 11.11(b). Hence the split will move with the point load along the length of the beam and will not be affected nor restricted by the presence of transverse reinforcement as has been shown experimentally (Johnson and Oehlers 1981).

12.2.3.2 Dowel strength

It was shown in the previous Section that when splitting occurs in a concrete element without transverse reinforcement, then the split propagates along the length of the element causing the concrete element to separate as in Fig. 11.1. In effect, the triaxial restraint to the bearing zone of the shear connector has reduced to zero so that the dowel strength D_{max} is also zero. When transverse reinforcement crosses the splitting plane, the reinforcement then provides lateral restraint to the bearing zone and hence the dowel strength does not reduce to zero but depends on the amount and position of the transverse reinforcement.

An example of dowel failure after longitudinal cracking through splitting in a slab with transverse reinforcement is shown in Fig. 12.4. The plate to which the studs were welded is shown on the right of the photograph. It can be seen that the studs

have fractured above the weld collar and a large volume of concrete has crushed in the bearing zones adjacent to each connector. The failure mode is similar to that associated with dowel failure in longitudinally uncracked concrete, as shown in Fig. 2.20, except that the concrete compressive failure zone is more extensive when splitting has occurred. This is to be expected as the split reduces the triaxial restraint, that is now provided by the transverse reinforcement, which in turn reduces the compressive strength of the concrete in the bearing zone and hence more concrete crushes.

Fig. 12.4 Dowel failure through fracture

Dowel failure is not always associated with fracture of the connector but is also associated with bending of the connector as shown in Fig. 12.2. In this example, splitting and the lack of transverse reinforcement has caused extensive compressive failure of the concrete. Compressive failure of the concrete at the base of the connector, such as in Fig. 2.14(a), causes the bearing zone to rise. Hence in Fig. 2.14(b), the eccentricity e_2 of force F_2 increases, causing the flexural forces on the connector to increase and eventually bend the connector, as shown in Fig. 12.2.

In summary, the dowel mechanism in both longitudinally cracked slabs with transverse reinforcement and in uncracked slabs is the same. The longitudinal crack simply has the effect of reducing the compressive strength of the concrete and the effective reduction in the compressive strength depends on the transverse reinforcement. Therefore, the connector behaves as if it were encased in weaker concrete, that is the crack reduces the effective values of f_c and E_c and hence $(D_{max})_{beam}$ in Eq. 2.37.

12.2.3.3 *Ductility*

Transverse reinforcement is very important in ensuring a ductile shear-connection behaviour. When transverse reinforcement is not present, then the strength reduces immediately splitting or longitudinal cracking occurs, and so the shear connection exhibits a brittle behaviour such as the load/slip curve D in Fig. 1.13.

Experimental research has shown that even small amounts of transverse reinforcement will allow a gradual reduction in the dowel strength with slip (Oehlers 1989, Li and Cederwall 1991). Larger amounts of reinforcement can be used to maintain the dowel strength at the splitting strength over large slips (Li and Cederwall 1991), and even larger amounts can be used to increase the strength above that of the splitting strength (Oehlers and Park 1992) as shown by curve E in Fig. 1.13. In general, these experimental results with transverse reinforcement have shown that with a reasonable amount of transverse reinforcement the slip capacity is greater than that associated with shear connectors in uncracked concrete.

12.2.3.4 *Anchorage of transverse reinforcement*

It was shown in Section 12.2.2.2 that the transverse reinforcement affects the dowel strength by confining the concrete adjacent to the reinforcing bar or by allowing the connector to bear onto the bar. Both mechanisms do not require the reinforcing bar to be fully anchored, that is anchored sufficiently to achieve its yield strength. It has been suggested (Li and Cederwall 1991, Oehlers and Park 1992) that it is the stiffness of the transverse reinforcement, and not the strength, that affects the dowel strength of the shear connection and this conclusion has been confirmed experimentally (Oehlers and Johnson 1981, Li and Cederwall 1991, Oehlers and Park 1992).

Li and Cederwall (1991) measured the strains in the transverse reinforcing bars that crossed the bearing zones of stud shear connections. Their tests showed that the strains in the reinforcement at the maximum achieved dowel loads varied from 200×10^{-6} to 1000×10^{-6} and then increased as the dowel load reduced with the slip of the connector. It is suggested as a guideline that there should be sufficient anchorage to the transverse reinforcement on either side of the longitudinal crack to maintain a strain of about 1300×10^{-6}, that is a stress of about 250 N/mm^2, in order to achieve the required dowel strength of the shear connection. Methods for determining this dowel strength are given in the next section.

It is worth stressing and repeating that equilibrium techniques for the anchorage zone design of post-tensioned members, in which fully anchored tension steel is provided to resist the lateral tensile forces, should not be applied to mechanical shear connectors because of the very high compressive stresses that are induced. Hence it is not necessary to anchor fully the transverse reinforcement in order to achieve the dowel strength of the shear connection. However, it is also worth bearing in mind that the transverse reinforcement required in Chapter 13 to transfer the longitudinal shear forces has to be fully anchored as it relies on a different mechanism of failure.

12.3   Straight reinforcing bars

12.3.1 GENERAL

In this section we will deal with the effect of straight reinforcing bars that cross the crack plane as shown in Fig. 12.2. It will be assumed that the transverse reinforcement is anchored on either side of the crack according to Section 12.2.3.4. The following analysis rules were developed empirically (Oehlers and Park 1992) from push tests with stud shear connections. However, it is felt that these rules can, at the very least, be used as a guideline for other types of mechanical shear connectors and so they have been written in a general form.

12.3.2 POST-CRACKING DOWEL STRENGTH

The post-cracking dowel strength of a mechanical shear connector D_{crack} is given by

$$D_{crack} = D_{max}\left(0.60 + \frac{3.0A_r s_s}{h_{eq}^2}\right)$$
(12.1)

where D_{max} is the dowel strength in uncracked concrete, A_r is the area of the transverse reinforcement per unit longitudinal length of the crack plane, s_s is the longitudinal spacing of a longitudinal line of shear connectors as shown in Fig. 12.5, and h_{eq} is the equivalent height of the connector as given by Eqs. 11.56 to 11.58. The 95% characteristic strength occurs when the constant 0.60 in Eq. 12.1 is replaced by 0.55.
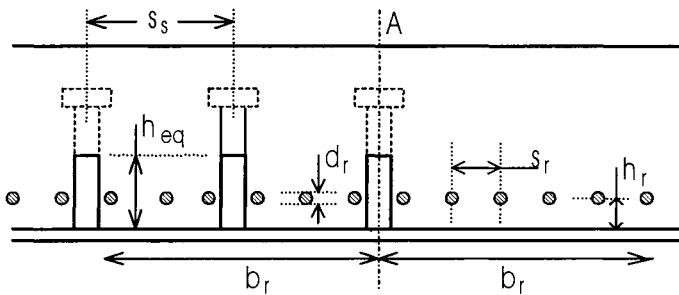
Fig. 12.5 Distribution of transverse reinforcement

Equation 12.1 can be applied when

$$A_r \geq \frac{0.02h_{eq}^2}{s_s}$$
(12.2)

that therefore defines a minimum amount of transverse reinforcement. The maximum post-cracking dowel strength that was achieved in the experiments was $0.9D_{max}$. However, it is suggested that Eq. 12.1 can be applied up to D_{max}, as any errors in this

extrapolation will only lead to a slight change in the flexural strength of the composite beam. Therefore

$$D_{crack} \leq D_{max} \tag{12.3}$$

12.3.3 DETAILING RULES FOR TRANSVERSE REINFORCEMENT

In order to ensure that the reinforcing bars are in a position to restrain the concrete in the bearing zone, the following detailing rules have to be adhered to.

Very large diameter bars at very large spacings will not have the same confining effect as a larger number of smaller bars, and hence it is necessary to ensure that

$$d_r \leq 0.4h_{eq} \tag{12.4}$$

where d_r is the diameter of the reinforcing bar. Furthermore and in order to enhance the confining effect to the bearing zone of the shear connection, it is necessary to restrict the bar to a region close to the bearing zone so that

$$h_r \leq 1.7h_{eq} \tag{12.5}$$

where h_r is the distance of the bar from the base of the shear connection as shown in Fig. 12.5. Finally in order to produce uniform confinement to the concrete around the shear connection, it is necessary to spread the reinforcement over a distance b_r on either side of each connector as shown for connector A in Fig. 12.5, where

$$b_r \geq 11h_{eq} \tag{12.6}$$

Example 12.1. Dowel strength in cracked slab with straight bars

A composite beam has two lines of 19 mm stud shear connectors with a longitudinal spacing of 200 mm. The dowel strength of the shear connectors in uncracked concrete $D_{max} = 120$ kN. It is necessary to allow for flexural cracking or splitting.

The design for each line of connectors is the same, so that the same transverse reinforcement can be used to cross each longitudinal cracking plane. One possible design approach is to place sufficient transverse reinforcement so that the dowel strength is unchanged after splitting or longitudinal cracking. Substituting into Eq. 12.1, $h_{eq} = 34$ mm (Eq. 11.57), $s_s = 200$ mm and $D_{crack} = D_{max}$ gives $A_r = 0.78$ mm that is the cross-sectional area of reinforcing bar per unit longitudinal length of the splitting plane. The area of reinforcement $A_r = 0.78$ mm is greater than the minimum requirement of 0.12 mm from Eq. 12.2. From Eq. 12.4, $d_r \leq 14$ mm so 10 mm diameter bars will be used. Dividing the area of the reinforcing bar by $A_r = 0.78$ mm gives a longitudinal spacing of bars in the slab, s_r in Fig. 12.5, of 101 mm. From Eq. 12.5, the bars must be placed within a distance $h_r \leq 58$ mm from the soffit of the slab. Furthermore, from Eq. 12.6, the bars must be spread over a distance of at least $b_r =$

376 mm in front of and behind each connector. It must be emphasised that A_r is not the area required per connector but the area required in the slab.

It is worth noting the effect of halving the longitudinal spacing of the stud shear connectors s_s from 200 mm to 100 mm. According to Eq. 12.1, the area of reinforcement A_r must be doubled in order to ensure the same confining effect per connector. Hence, the 10 mm reinforcing bars would have to be spaced at 50 mm in order to achieve the maximum dowel strength.

12.4 Hooped reinforcing bars

12.4.1 GENERAL

When shear connectors have limited side cover, it may be difficult if not impossible to anchor the transverse reinforcement on both sides of a splitting plane as required in the previous section on straight bars and as also required in Chapter 13. An alternative technique is to hoop the reinforcement around the connector as shown in Fig. 12.6. After splitting, such as along the plane C-C, the hoop forms a cone of concrete around the outer connector as shown in (b) that confines the concrete around the outer connector and in particular around the bearing zone A adjacent to the outer connector. Therefore, the hoop provides the post-splitting lateral restraint to the concrete that is required for the post-cracking dowel strength D_{crack} to be achieved. Furthermore, the hoop transfers the shear across shear planes such as B-B, and so that this form of reinforcing is also an alternative method to that described with straight bars in Chapter 13.

Failure of a push specimen with hooped reinforcement is shown in Fig. 12.7. The concrete surrounding the inner connector only shows a relatively small amount of damage commensurate with dowel failure in uncracked concrete that is shown in Fig. 2.20. Experimental research (Johnson and Oehlers 1982) has found that the dowel strength of this inner connector in Fig. 12.7 is unaffected by the split when the reinforcement is hooped as shown, and hence the maximum dowel strength D_{max} can be used to determine the strength of this inner shear connection. However, it can be seen that there is substantial damage to the concrete surrounding the outer connector, and it is the strength of this outer shear connection that is the subject of this section. The following design and analysis procedures (Johnson and Oehlers 1982) were developed from experimental and computer modelling of stud shear connections with hooped reinforcement, and hence should only be used as a guideline for other types of mechanical shear connectors.

12.4.2 POST-CRACKING DOWEL STRENGTH

It has been shown in Section 2.4.2 and illustrated in Fig. 2.14(b) that the dowel strength of a shear connection is highly sensitive to the eccentricity e of the shear force F. Increasing the eccentricity e increases the flexural forces at the base of the connector and hence reduces the dowel strength of the shear connection. It can

therefore be expected that the post-cracking dowel strength D_{crack} is inversely proportional to the cover to the hooped reinforcement at the base of the connector, that is c_b in Fig. 12.6(b). Experimental research (Johnson and Oehlers 1982) has shown this to be true, where the variation in the dowel strength with cover is given by

$$D_{crack} = D_{max}\left(1.6 - \frac{0.4\left(c_b + \frac{h_r}{2}\right)}{d_{sh}}\right)$$

(12.7)

where D_{max} is the dowel strength in uncracked concrete as given by Eq. 2.37, h_r is the depth of the hooped reinforcement as shown in Fig. 12.6(b), d_{sh} is the diameter of the shank of the stud and where

$$D_{crack} \leq D_{max}$$

(12.8)
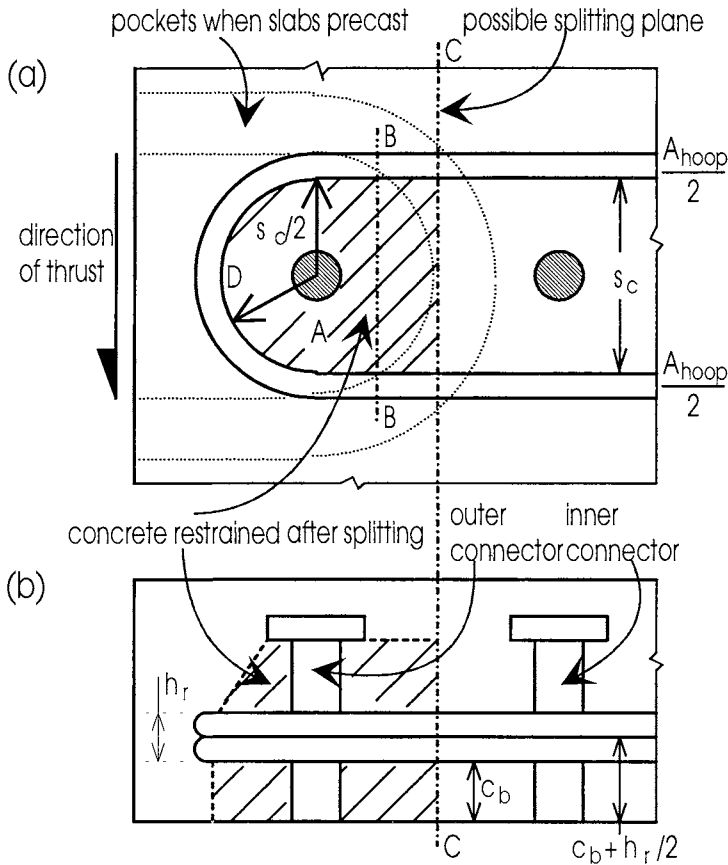
Fig. 12.6 Hooped reinforcement in a composite L-beam

Fig. 12.7 Concrete failure with hooped reinforcement

12.4.3 DETAILING RULES FOR TRANSVERSE REINFORCEMENT

To achieve the post-cracking dowel strength of Eq. 12.7, the hooped reinforcement must comply with the following details.

The following equation ensures that the hooped reinforcement is stiff enough to triaxially restrain the concrete in the bearing zone at A in Fig. 12.6(a).

$$A_{hoop} \geq \frac{0.9 s_c^2}{n}\left(\frac{D_{crack}}{D_{max}} - 0.4\right)$$ (12.9)

where A_{hoop} is the cross-sectional area of both arms of the hooped reinforcement as shown in (a), $D_{crack} \leq D_{max}$, n is the modular ratio E_s/E_c and

$$s_c \geq 3d_{sh}$$ (12.10)

In order to prevent the hooped reinforcement from yielding through axial loads in the reinforcement, it is necessary to ensure that

$$A_{hoop} f_{yr} \geq 0.24 s_c^2 f_c$$ (12.11)

where f_{yr} is the yield stress of the hooped reinforcement and f_c is the compressive cylinder strength of the concrete. It should be noted that as it is necessary for the reinforcement to reach its yield strength, the hooped reinforcement has to be fully anchored.

Finally in order to prevent the concrete crushing within the bend of the hoop, in region D in Fig. 12.6(a), when the hooped reinforcement has yielded, it is necessary to ensure that

$$h_r \geq 0.16 s_c \tag{12.12}$$

Example 12.2. Transfer of shear and confinement of concrete using hooped reinforcement

The shear connection in Example 12.1 is used in a composite L-beam so that the transverse reinforcement cannot be fully anchored on either side of the splitting plane or on either side of the shear plane defined in Chapter 13. Hence it is necessary to use hooped reinforcement. We will assume that the dowel strength of the shear connection is $D_{max} = 120$ kN, the diameter of the shank of the stud $d_{sh} = 19$ mm, a minimum cover to the reinforcement of $c_b = 20$ mm is required, the modular ratio of the steel and concrete is n = 7, and the cylinder strength of the concrete is $f_c = 30$ N/mm^2.

Let us design the shear connection so that the dowel strength is unchanged after cracking, that is $D_{crack} = D_{max}$. This design will also ensure that the longitudinal shear strength of the concrete element, as required in Chapter 13, is adequate. From Eq. 12.7, $(c_b + h_r/2) = 1.5 d_{sh} = 28.5$ mm, where the parameter $(c_b + h_r/2)$ is the distance from the centroid of the hooped reinforcement to the soffit of the slab as shown in Fig. 12.6(b). As it is a requirement that $c_b = 20$ mm, $h_r/2 \leq (28.5-20) = 8.5$ mm, that is $h_r \leq 17$ mm.

From Eq. 12.10, the minimum value of $s_c = 3 d_{sh} = 57$ mm, so we will use $s_c = 70$ mm to allow for some fabrication tolerance. From Eq. 12.9, $A_{hoop} = 378$ mm^2 which is the area of both arms of a hoop. If we were to use two reinforcing bars as shown in Fig. 12.6(b), then we would require, from $A_{hoop} = 378$ mm^2, two 12 mm bars and hence $h_r = 24$ mm which is greater than the allowable value of 17 mm that was calculated in the previous paragraph. Therefore we will have to use one bar of diameter 16 mm (where $A_{hoop} = 402$ mm^2) so that $h_r = 16$ mm. From Eq. 12.11, $f_{yr} \geq 93$ N/mm^2 so that mild steel bars can be used, and from Eq. 12.12 $h_r \geq 11.2$ mm so that the 16 mm bar will suffice; the latter two requirements rarely govern design.

It is worth noting that when $D_{crack} = 0$ in Eq. 12.7 then $(c_b + h_r/2) = 4 d_{sh}$. Most stud shear connectors have a height of $4 d_{sh}$ or $5 d_{sh}$, and hence placing the hoop around the head of the connector will simply not work. It is also worth noting that this form of construction can be used when the slabs are precast (Johnson and Oehlers 1982), in which case pockets would be left in the slab as indicated in Fig. 12.6(a). The dowel strength of the shear connection can then be substantially increased by filling the pockets with concrete that has a much greater strength than that of the precast slab.

12.5   References

Johnson, R. P. and Oehlers, D. J. (1981). "Analysis and design for longitudinal shear in composite T-beams ", Proceedings, Institution of Civil Engineers, London, Part 2, Vol. 71, 989-1021.

Johnson, R. P. and Oehlers, D. J. (1982). "Design for longitudinal shear in composite L-beams ", Proceedings, Institution of Civil Engineers, London, Part 2, Vol. 73, 147-170.

Li, A. and Cederwall, K. (1991.). "Push test on stud connectors in normal and high strength concrete", Report 91:6, Chalmers Tekniska Hogskola, Institutionen For Konstruktionsteknik Betongbyggnad, Goteborg, Sweden.

Oehlers, D.J. (1989). "Splitting induced by shear connectors in composite beams ", Journal of Structural Engineering, ASCE, Vol. 115, No. 2, 341-362.

Oehlers, D. J. and Johnson, R. P. (1981). "The splitting strength of concrete prisms subjected to surface strip or patch loads ", Magazine of Concrete Research, Vol. 33, No. 116, 171-179.

Oehlers, D. J. and Park, S. M. (1992). "Shear connectors in composite beams with longitudinally cracked slabs ", Journal of Structural Engineering, ASCE, Vol.118, No.8, 2004-2022

13 Longitudinal Shear

13.1 Introduction

Mechanical shear connectors in composite beams impose concentrated loads on the concrete element of the composite beam, as shown schematically in Fig. 1.14(b). In order to disperse the shear flow that is induced by these concentrated loads, the slab is subjected to both transverse tensile stresses, that can cause longitudinal splitting, and to shear stresses, that can induce a herringbone formation of cracks. The slab has therefore to be designed separately to resist both splitting forces as well as shear forces, and the latter is the subject of this chapter.

To understand the philosophy behind shear transfer, let us first briefly reiterate the philosophy behind splitting as described in Chapters 11 and 12, where it was shown that it is necessary to distinguish between the local lateral stress distribution in the slab induced by the individual shear connectors and the global lateral stress distribution in the whole slab that is induced by all the shear connectors. Each individual connector causes a local distribution of lateral tensile and compressive stresses that depends on the position of the connector relative to the ends of the slab. Connectors near the ends of the slab induce stress distributions shown in Fig. 11.7(a) and those remote from the ends induce the stress distributions shown in (c). When the slab is very narrow, as in the L-beam in Fig. 1.8(e) or the haunch in (d), then the local lateral stress distributions from each connector do not overlap and analysis is based on the local stress distribution.

For most geometrise of slabs, the local lateral stress distributions overlap and so the distribution of lateral stresses now depends on the global distribution of the shear flow. As an example and for the stub girder with a uniform distribution of the shear flow in Fig. 11.12, the lateral stresses peak at the ends of the stub girder as shown. Furthermore, it can be seen that the global distribution of the lateral stresses, shown in Fig. 11.12(b), are completely different from the local distribution of the individual connectors that induced them and which are shown in Fig. 11.7(c). Hence the engineer cannot use the local distribution but must deal with the global distribution.

Let us now consider the longitudinal shear transfer. The dispersal of the concentrated load from each mechanical shear connector induces lateral tensile stresses and shear stresses that can cause cracking as shown in Fig. 1.14(b). One way of differentiating between analyses that deal with splitting and those that deal with the longitudinal shear is that splitting is concerned with lateral equilibrium, whereas shear is concerned with longitudinal equilibrium. Furthermore, in splitting we have to deal with the local lateral equilibrium when the slabs are narrow and with global lateral equilibrium when the slabs are wide; however in shear we only deal with the global longitudinal equilibrium. For example, if the individual mechanical shear connector shown in Fig. 1.14(b) is replaced by the longitudinal plate rib shear connector in Fig. 2.27, then the longitudinal shear forces are no longer transmitted as individual

concentrated loads but as a global uniform longitudinal shear force acting along the length of the beam, as shown in Fig. 11.12, that has to be resisted by the slab.

It is worth noting that the longitudinal shear force varies along the width of the slab, having a maximum value of $qd_f/2$ at section E-H in Fig. 11.12, less at section C-D and zero at section A-B. It is also worth noting that longitudinal cracks, whether they are induced by splitting or flexural cracking, can reduce the dowel strength of the connector, as described in Chapter 12, as they traverse the triaxial compression zone and hence reduce the compressive strength of the concrete. However, the herringbone formation of cracks shown in Fig. 1.14(b) can be assumed not to affect the dowel strength as they occur to the sides of the connector and hence do not traverse the triaxial compression zone.

13.2 Shear flow planes

The first step of the analysis procedure is to identify possible longitudinal shear failure planes. Consider the shear plane at section A in Fig. 13.1(a) where a longitudinal shear force V acts on the slab over a length L as shown. The area of the shear plane A is $L(L_p)_A$, where (L_p) will be defined as the length of the perimeter of the shear plane which in this case is equal to the depth of the slab. In analysis, it is easier to deal with the longitudinal shear force per unit length, $q = V/L$, hence the area over which q acts is $L(L_p)_A/L = (L_p)_A$. The length of the perimeter of the shear plane L_p is therefore an important parameter as it is the area of the shear plane over which the shear flow force q acts.

Further examples of shear planes, as defined by their perimeter lengths, are shown in Fig. 13.1. The perimeter length can extend from one surface of the slab to the other as in sections A, B and E or it can encompass a group of shear connectors by starting and finishing at the same slab surface as in sections C, D, F, G, and H. It is not necessary to consider shear planes that intersect the shear connectors as in section I, as the dowel acts as a reinforcing bar crossing the shear plane and therefore substantially increasing the shear strength of this plane.

13.3 Shear flow forces

Having defined a shear flow plane, it is necessary to determine the shear flow force that acts on this plane. As an example, consider the slab in Fig. 11.12(b) where the shear flow force applied to the slab is $q_t = q/2$. The total shear force $F_t = q_t d_f = qd_f/2$ that is acting along the shear flow plane E-H, is transferred into the concrete slab and results in an axial compressive force of an equal magnitude of $F_t = qd_f/2$ at section A-C-I that has a cross-sectional area A_{conc}. As we are ignoring shear lag, we can assume that the slab is subjected to a uniform compressive stress $\sigma_a = F_t/A_{conc}$ at section A-C-I. In order to determine the shear flow along plane C-D, it is necessary to consider the free body A-B-C-D that has a cross-sectional area of slab A_{free} at section A-C. The shear force F_f along C-D is equal to the axial compressive stress along A-C times the cross-sectional area, that is $F_f = \sigma_a A_{free}$. Substituting $\sigma_a = F_t/A_{conc}$ gives $F_f =$

$F_t A_{free}/A_{conc}$. Now dividing by d_f, the shear flow force q_f at any longitudinal shear plane is therefore given by

$$q_f = \frac{A_{free}}{A_{conc}} q_t \qquad (13.1)$$

where q_t is the shear flow force applied to the slab by the shear connection, A_{conc} is the cross-sectional area of the concrete slab and A_{free} is the cross-sectional area of the free body that does not contain the shear connectors. The distribution of the shear flow is therefore in proportion to the cross-sectional area of the free body formed by cutting the slab along the shear flow plane.
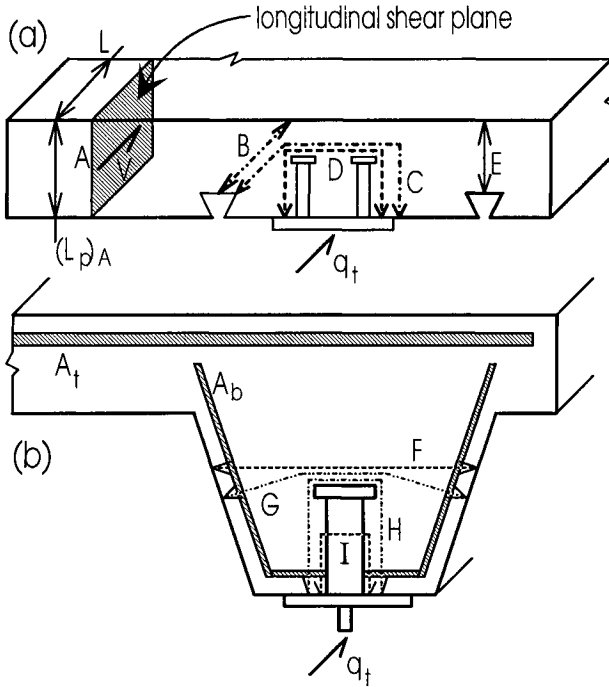
Fig. 13.1 Shear plane perimeters

As a further example consider the composite beam in Fig. 13.2 that is subjected to a longitudinal shear flow at the steel/concrete interface of q_t as shown, and in which the total cross-sectional area of the concrete slab is A_{conc}. The shear flow at section A is $(A_A/A_{conc})q_t$, as A_A is the cross-sectional area of the free body that does not contain the shear connector. On the other hand, the shear flow at section B is $((A_{conc}-A_B)/A_{conc})q_t$ as A_B is the cross-sectional area of the free body that contains the connectors.
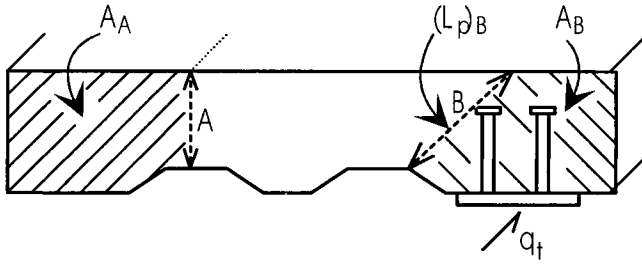
Fig. 13.2 Area of free bodies

13.4 Shear flow strengths

13.4.1 GENERAL EQUATIONS

The concrete element has to transfer the longitudinal shear flow forces in regions of uncracked concrete, in regions where the concrete has a herringbone formation of cracks and in regions where there are longitudinal cracks that have been induced by transverse flexural forces or longitudinal splitting. Experimental research by Mattock et al (Hofbeck, Ibrahim, and Mattock 1969, Mattock and Hawkins 1972) described in detail in Section 2.5, has shown that the shear plane is weakest when there is a longitudinal crack and so most design procedures assume that the shear plane is cracked.

The shear strength of a cracked plane is developed in Section 2.5.4.1 and the characteristic failure stresses are given by Eqs. 2.46 to 2.48. In analysis or design, it is more convenient to deal with shear flow strengths, that is the shear strength per unit longitudinal length of the shear plane, and this can be done by multiplying Eqs. 2.46 to 2.48 by the perimeter length of the shear plane L_p to give

$$Q_{ch} = 0.66 f_{ct} L_p + 0.8 A_{tr} f_{yr} + 0.8 F_{nf} \tag{13.2}$$

when both

$$0.8 \left(A_{tr} f_{yr} + F_{nf} \right) \geq 0.53 f_{ct} L_p \tag{13.3}$$

and

$$Q_{ch} \leq 0.3 f_c L_p \tag{13.4}$$

where Q_{ch} is the characteristic shear flow strength, A_{tr} is the area of the transverse reinforcement that is crossing the shear plane per unit longitudinal length of the shear plane, F_{nf} is the algebraic sum of the of the normal forces to the shear plane per unit length and in which compression is taken as positive.

It may be more convenient to express the shear flow strengths in Eqs. 13.2 to 13.4 purely in terms of the cylinder strength f_c. For normal density concrete, Eq. 2.6 can be used to convert the tensile strength f_{ct} to a cylinder strength f_c. The effect of lightweight concrete is allowed for in the draft Eurocode 4 (1994) by multiplying both the term containing f_{ct} in Eq. 13.2 and the term f_c in Eq. 13.4 by a reduction factor for lightweight concrete η where

$$\eta = 0.3 + 0.7\frac{\rho}{24} \tag{13.5}$$

and where the density of the concrete ρ is measured in kN/m^3.

13.4.2 SHEAR PLANE THROUGH DEPTH OF SLAB

A shear plane that traverses the full depth of the slab such as at sections A, B and E in Fig. 13.1(a) is shown in Fig. 13.3. In this example, even though the top portion of the shear plane is in tension and the bottom is in compression, the resultant force across the shear plane $F_{nf} = 0$ so that Eq. 13.2 becomes

$$Q_{ch} = 0.66 f_{ct} L_p + 0.8(A_t + A_b) f_{yr} \tag{13.6}$$

where A_t is the area of the top transverse reinforcement that crosses the shear plane per unit length of shear plane, A_b is the area of the bottom reinforcement and where the reinforcement is fully anchored on both sides of the shear plane. If the reinforcement is not fully anchored then the term $A_t f_{yr}$ or $A_b f_{yr}$ is the strength of the anchorage of the respective reinforcement.
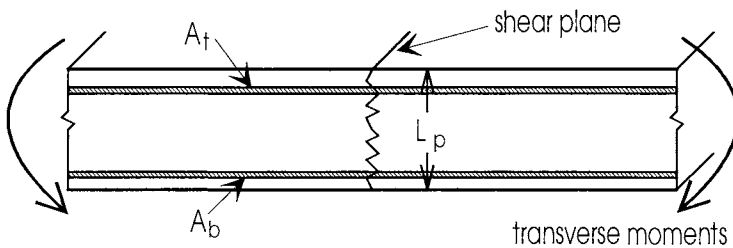
Fig. 13.3 Full depth shear planes

In composite beams with profiled slabs, the profiled sheeting can be assumed to act as bottom transverse reinforcement of area A_b when the ribs of the sheet are transverse to the beam as in Fig. 1.11(c) (Johnson 1994). As with transverse reinforcing bars, the profiled sheet has to be fully anchored on either side of the shear plane, otherwise the strength depends on the anchorage which in turn depends on the bond strength of the profiled ribs as described in Section 2.6.5. In contrast, profiled sheeting with ribs in line with the steel element as in Fig. 1.11(b) are assumed not to act as transverse reinforcement as the ribs can open out as in Fig. 2.29(a).

Example 13.1. Shear strength of planes through depth of slab

A composite L-beam is shown in Fig. 13.4(a) where all the dimensions and forces are in N and mm unless otherwise stated. The top transverse reinforcement consists of reinforcing bars of strength $f_{yr} = 400$ N/mm² and with a cross sectional area of 0.5% of that of the cross-sectional area of the slab. The bottom transverse reinforcement consists of steel decking that is continuous over the steel beam and transverse to the steel beam as shown in (b). The profiled sheet is 1.2 mm thick, has a yield strength of 550 N/mm², and the bond between the profile sheet and the concrete is 0.54 N/mm² and only acts along the rib. Let us consider the shear plane through the depth of the slab at section A in (a), that is just to the left of the connectors.

If the slab were solid, then the length of the perimeter of the shear plane L_p would be the depth of the slab $h_c = 130$ mm. However, allowance must be made for the voids in the slab enclosed by the profile ribs as shown in Fig. 13.4(b). The perimeter length L_p is really the area of the shear plane per unit length, so that we need to determine an equivalent depth of a solid slab with the same cross-sectional area as the existing slab. This can be found by considering a section between ribs such as the hatched region B in (b). The equivalent depth can simply be determined by dividing the area of region B by the longitudinal length of 200 mm to give an equivalent depth of solid slab of 122.5 mm. Hence $L_p = 122.5$ mm.

The length of the profile sheet that bounds region B in Fig. 13.4(b) is 190 + 67 + 67 + 50 = 374 mm and so the cross-sectional area of profile sheeting per rib is 374x1.2 = 449 mm². Therefore the area per unit longitudinal length A_b = 449/200 = 2.24 and the strength per unit length is $A_b f_{yr} = 1234$ N/mm. This is the maximum transverse force that can be applied to the sheeting when it is fully anchored, that is when it has full shear connection so that it can reach its yield strength.

The strength of the anchorage of the profiled sheeting at section A in Fig. 13.4(a) is the bond strength over the shorter span of 1.2 m. The bond force is assumed to occur only along the rib, so that the bond force per rib is simply the length of the rib L in (a) multiplied by the contact perimeter length of the rib which is 67 + 67 + 50 = 184 mm, and then multiplied by the bond strength of 0.54 N/mm² and this comes to 100L N/mm. Therefore the bond strength per unit longitudinal length is 100L/200 = 0.5L N/mm. Equating the bond strength of 0.5L with the yield strength of 1234 N/mm gives an anchorage length of 2468 mm that is required for full anchorage, that is for full shear connection. As the actual length is only 1200 mm, the lateral strength of the profile sheet $A_b f_{yr} = (1200/2468)\times 1234 = 600$ N/mm.

It will be assumed that the top reinforcement at section A in Fig. 13.4(a) is fully anchored. The area per unit length A_t is 0.5% of the depth of 130 mm, that is 0.65 mm, so that the strength per unit longitudinal length $A_t f_{yr} = 260$ N/mm.

Because the shear plane lies through the full depth of the slab, the resultant normal force $F_{nf} = 0$ and Eq. 13.6 can be used to derive the longitudinal shear flow strength. The interface interlock component $0.66 f_{ct} L_p = 192$ N/mm and the dowel action component $0.8(A_t + A_b) f_{yr} = 688$ N/mm, so that the characteristic shear flow strength $Q_{ch} = 880$ N/mm. Let q_t be the shear flow force imposed by the shear

connectors, so that q_t is the shear flow at the interface between the steel element and the concrete slab. As the shear connectors are grouped in pairs, $q_t = 2D_{max}/s$ where s is the longitudinal spacing of the connectors and $D_{max} = 140$ kN is the given dowel strength of one shear connector. From Eq. 13.1, the shear flow force at shear plane A is $q_f = (1.2/4)q_t$; substituting $q_t = 2D_{max}/s$ and $Q_{ch} = 880$ for q_f gives $s_{min} = 96$ mm, which is the minimum longitudinal spacing of the connectors. Therefore any spacings less than this minimum value will cause longitudinal shear failure at the full depth shear plane A in Fig. 13.4.

The bounds of Eq. 13.2, as given by Eqs. 13.3 and 13.4, must also be satisfied. The left hand term in Eq. 13.3 has already been calculated as 688 N/mm and the right hand term comes to 154 N/mm, so this minimum reinforcement requirement is satisfied. The maximum strength limit is given by Eq. 13.4 and as the shear flow strength $Q_{ch} = 880$ N/mm is less than $0.3f_cL_p = 1286$ N/mm, this limit is also satisfied.

It was shown in Section 2.5.4.1 that the mean shear strength can be derived from Eq. 13.2 by replacing the factor 0.66 by 1.1. This will increase the shear flow strength due to interface interlock from 192 N/mm to 319 N/mm and leave the dowel action component unchanged at 688 N/mm. Therefore, the mean shear flow strength in a longitudinally cracked plane is 1007 N/mm which is 14% greater than the characteristic shear flow strength. It was also shown in Section 2.5.4.2 that for a longitudinally uncracked plane in the positive or sagging region of a slab, a lower bound to the mean shear strength can be derived by replacing 0.66 by 1.4. This will increase the interface interlock component to 406 N/mm and the mean strength to 1094 N/mm. Hence the mean longitudinal shear strength of an uncracked plane is at least 24% greater than the characteristic shear strength of a cracked plane.

13.4.3 SHEAR PLANES ENCOMPASSING SHEAR CONNECTORS

An example of a shear plane that encompasses the shear connectors is shown in Fig. 13.5. The strength depends on the height of the shear plane h_p relative to the depth of the concrete slab h_c, and so a certain amount of engineering judgement must be used in the analysis.

For example, let us assume that the top steel is fully yielded at a tensile force of $A_t f_{yr}$ as shown, and that the height h_p is only slightly less than the height of the top reinforcement h_t. Therefore, the shear plane will be subjected to a compressive force of $F_{nf} = A_t f_{yr}$ on either side of the shear plane as shown, so that the total compressive force acting on the shear plane is $2A_t f_{yr}$. The only transverse reinforcement crossing the shear plane in this example is the bottom steel, but this crosses the shear plane twice so that the area resisting the shear is $2A_b$. Substituting into Eq. 13.2 gives the following strength.

$$Q_{ch} = 0.66 f_{ct} L_p + 0.8(2A_b) f_{yr} + 0.8(2A_t) f_{yr} \qquad (13.7)$$

If there is a possibility that longitudinal shear failure can occur before the top steel has yielded in flexure, then the third term $0.8(2A_t)f_{yr}$ should be ignored, as it is in most national standards.
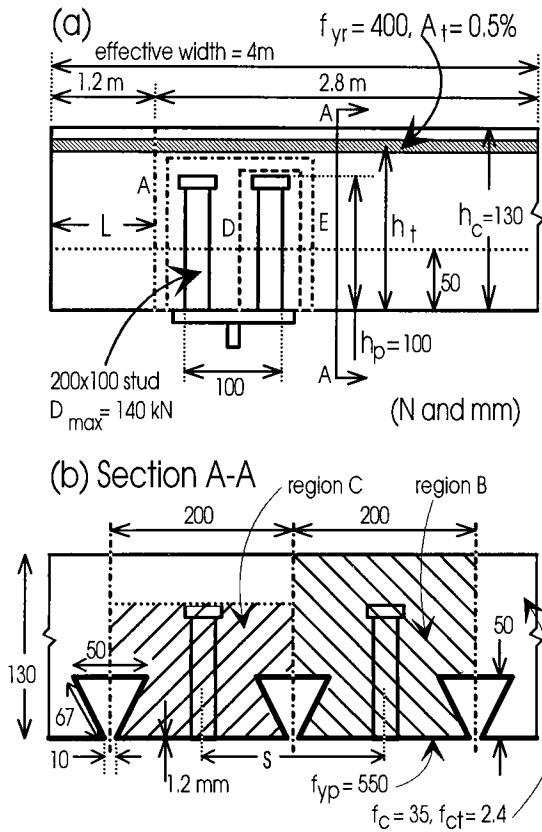
Fig. 13.4 Examples 13.1 and 13.2 on the longitudinal shear strength
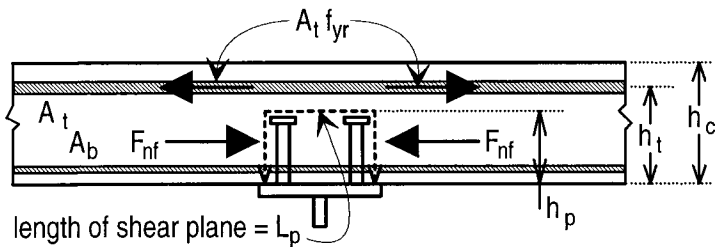
Fig. 13.5 Shear planes encompassing connectors

If the slab is now subjected to transverse positive sagging moments that are sufficient to cause the bottom steel to yield in tension, then F_{nf} is now tensile of magnitude $2A_b f_{yr}$, so that Eq. 13.7 becomes

$$Q_{ch} = 0.66 f_{ct} L_p + 0.8(2A_b) f_{yr} - 0.8(2A_b) f_{yr} = 0.66 f_{ct} L_p \qquad (13.8)$$

and the strength reduces considerably in this unusual but possible case of transverse positive flexure. Furthermore, if $h_p << h_c$ in Fig. 13.5 and transverse negative or hogging moments are being applied, then only part of the compressive force F_{nf} in Fig. 13.5 will act on the part of the shear plane of height h_p, and so any beneficial effect of F_{nf} should be ignored. Hence the third term on the right hand side of Eq. 13.7 can be ignored giving

$$Q_{ch} = 0.66 f_{ct} L_p + 0.8(2A_b) f_{yr} \qquad (13.9)$$

which is the strength when the transverse moment is zero. In addition, when the shear planes fall within a haunch as in Fig. 13.1(b), then the normal force F_{nf} across the shear plane can be assumed to be zero giving Eq. 13.9.

Example 13.2. Shear strength of planes encompassing the shear connectors

As a continuation of Example 13.1, let us consider the shear flow planes that encompass the shear connectors in Fig. 13.4(a). It has already been shown in Example 13.1 that $A_t f_{yr} = 260$ N/mm and $A_b f_{yr} = 600$ N/mm at shear plane A, and as shear plane A is adjacent to the connectors these values apply to the shear planes that encompass the shear connectors.

Failure can occur in a shear plane that encompasses a single connector such as D in Fig. 13.4(a) or in a shear plane that encompasses a pair of connectors as in E. The height of the shear plane $h_p = 100$ mm is the same in both cases. The effective height of the shear plane can be derived by considering the hatched region C in Fig. 13.4(b). Using the same procedure as outlined in Example 13.1 gives an effective height $h_p = 92.5$ mm.

The shear plane D in Fig. 13.4(a) must resist the shear flow forces due to a single connector, whereas shear plane E must resist the shear flow forces due to two lines of connectors. In shear plane D the perimeter length $L_p = 92.5 + 92.5 + 20 = 205$ mm, so that the shear flow force per unit perimeter length, that is the shear stress, is $\tau_D = D_{max}/205$. In shear plane E, $L_p = 285$ mm and hence the shear flow force per unit perimeter length is $\tau_E = 2D_{max}/285 = D_{max}/142$. As the shear stress $D_{max}/142 > D_{max}/205$, shear plane E, with $L_p = 285$ mm, will fail first and hence this failure plane controls design.

The cross-sectional area of the slab encompassed by shear plane E in Fig. 13.5(a) is much less than the cross-sectional area of the slab A_{conc}. Therefore, the area of the free body outside the shear plane $A_{free} \rightarrow A_{conc}$ in Eq. 13.1, so that it can be

assumed that the shear flow force in shear plane E which is $q_f = q_t = 2D_{max}/s$ where s is the longitudinal spacing of the connectors.

The maximum shear flow strength of shear plane E occurs when there is transverse hogging or negative moments that are of sufficient magnitude to cause the top steel to yield. We will assume that h_p is only slightly less than the height of the top reinforcement h_t, so that all of the normal compressive force is applied to the shear plane. Therefore, the maximum shear flow strength is given by Eq. 13.7 where the interface interlock term $0.66f_{ct}L_p = 446$ N/mm, the dowel term $0.8(2A_b)f_{yr} = 960$ N/mm, and the interface friction term $0.8(2A_t)f_{yr} = 416$ N/mm, and this gives a shear flow strength of $Q_{ch} = 1822$ N/mm. The minimum longitudinal spacing of the pairs of connectors is therefore given by $s_{min} = 2D_{max}/Q_{ch} = 154$ mm.

When no transverse moments are acting, then the friction term in Eq. 13.7 is zero so that Eq. 13.9 gives the shear flow strength. This equation also applies when $h_p \ll h_c$, as all of the normal force cannot be assumed to act on the shear plane. From Eq. 13.9, $Q_{ch} = 1406$ mm, so that the minimum spacing is now 199 mm.

The minimum shear flow strength occurs when sagging moments are applied that are of sufficient magnitude to cause the bottom steel to either yield or achieve its maximum tensile stress when bond controls design as in this example. The shear strength is given by Eq. 13.8, where it can be seen that shear is only transferred by the interface interlock that comes to $Q_{ch} = 446$ N/mm and which requires a minimum spacing of 628 mm.

13.5 References

Eurocode 4 (1994) Part 1.1: Design of composite steel and concrete structures. DD ENV 1994-1-1: 1994. Draft for development.

Hofbeck, J.A., Ibrahim, I.O. and Mattock, A.H. (1969). "Shear transfer in reinforced concrete ", Journal of the American Concrete Institute, Feb., 119-128.

Mattock, A.H. and Hawkins, N.M. (1972). "Shear transfer in reinforced concrete recent research ", Precast Concrete Institute Journal, March-April, 55-75.

Johnson R.P. (1994). *Composite Structures of Steel and Concrete : Volume 1.* 2nd edition, Blackwood Scientific Publications, U.K.

14   Embedment Forces

14.1   Introduction

An assumption that is generally made in the analysis of composite beams is that the curvature in the concrete element is always the same as the curvature in the steel element as shown in Fig. 1.23. This can be achieved when there is no separation at the steel/concrete interface of the standard form of composite beam that is shown in Fig. 1.1. Therefore, the shear connection in the composite beam has to be constructed to resist both tensile and compressive forces that are normal to the steel/concrete interface. These forces can cause the shear connectors to pull out of the concrete slab and this is the subject of this chapter.

The normal forces across the concrete-slab/steel-beam interface will be referred to as axial forces as they occur in the direction of the axis of the shank of stud shear connectors. Axial compressive forces can be resisted by bearing of the slab onto the flange of the steel element and hence rarely, if ever, pose a problem. In contrast, axial tensile forces can cause separation between the steel and concrete elements and hence the shear connectors have to be constructed to resist these tensile forces. In profiled rib connectors, the sheet is deformed into a shape that can directly resist axial tension, such as the dove-tail or re-entrant profile in Fig. 1.6(a) or the L-shaped profile in (c). The axial tensile force at the steel-rib/concrete interface is uniformly spread over the length of the rib and hence rarely causes any problem, although trapezoidal ribs as in (b) do tend to separate from the concrete element.

Mechanical shear connectors are also formed into a shape that can resist axial tensile forces as shown in Fig. 1.5. For example, the head of the stud connector in (a), the top flange of the channel in (c) and the horizontal reinforcing bar in the angle connector in (f) are there to resist axial tensile forces. Furthermore unlike rib connectors, these axial tensile forces are not distributed along a line, but apply concentrated 'point' loads to the slab and are therefore more likely to cause embedment cracking of the type shown in Fig. 1.14(a).

The distribution of axial forces in composite beams and push specimens is discussed in the following section. The remaining sections deal with the behaviour of stud shear connections as there is very little research on other types of shear connectors.

14.2   Embedment forces

14.2.1 PUSH SPECIMENS

It was shown in Section 2.4.3 that the shear strength of shear connectors in push-tests is strongly influenced by the axial force across the steel/concrete interface (Oehlers 1990). Teraszkiewicz (1965) showed experimentally that the strength of push-tests in

which the base is free to slide, as in Fig. 2.16(c), is substantially less than in push-tests in which the base is fixed as in (e). This reduction in shear strength is due to the change in the resultant axial force across the interface from compression when the base is fixed to a zero resultant, but with tension in the studs, when the base can slide. Teraszkiewicz recorded reductions in the shear strength of headed studs of up to a third when the base was free to slide, and almost a half when both the base was free to slide and when the head was removed from the stud.

14.2.2 GLOBAL DISTRIBUTION IN BEAMS

14.2.2.1 *General*

The magnitude of embedment forces in composite beams is generally considerably less than in push-tests because of the difference between the external restraints in the two systems.

The vertical forces on a section of a composite beam is shown in Fig. 14.1. The following well known relationship between the applied load and the rate of change in the shear force can be derived from equilibrium of the concrete element.

$$\left(w - r\right) \;=\; \frac{dV_c}{dx} \tag{14.1}$$

where w is the applied load per unit length, r is the axial line force per unit length and V_c is the shear force in the concrete element. Re-arranging Eq. 14.1 gives the following variation in the axial force along the length of the beam.

$$r \;=\; w - \frac{dV_c}{dx} \tag{14.2}$$
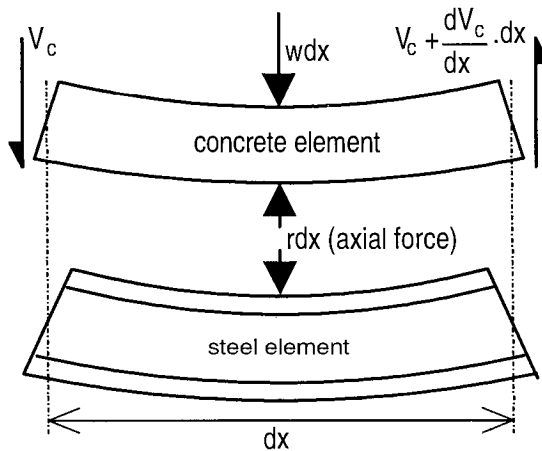
Fig. 14.1 Vertical forces in composite beam

Let us consider a simply supported composite beam. If the concrete slab is infinitely stiff, then all of the applied load will be resisted by the concrete slab so that $w = dV_c / dx$ and hence, from Eq. 14.2, the axial interface force is zero. Conversely, if the concrete slab is very flexible, relative to the stiffness of the steel beam, then all the load would be resisted by the steel beam so that $dV_c / dx = 0$ and hence the axial force is compressive and equal to the applied load. Hence, the global axial force will always be compressive and have a maximum value that is equal to that of the applied load. A similar logic can be used when the gravity load wdx is hung onto the bottom flange of the steel element in Fig. 14.1. In this case the axial load will be tensile and vary from zero to w. Therefore, the global axial force depends on the relative stiffness of the steel and concrete elements and the method of applying the loads.

14.2.2.2 *Uniformly distributed load*

The results of a finite element analysis of the axial interface forces in a simply supported composite beam (Raleigh 1984) is shown in Fig. 14.2. Line A is the distribution of axial forces when a uniformly distributed line load of magnitude w is applied to the composite beam. As the rate of change of the vertical shear force is constant, line A lies dV_c / dx below the line of magnitude w. It can be seen that the axial forces are uniform, as given by Eq. 14.2, except at the boundary of the supports where a large compressive force is required to balance the uniformly distributed line load of (w-r) on the slab.
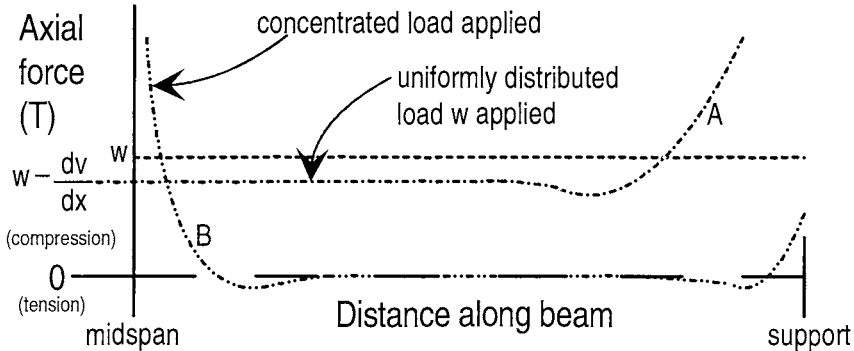
Fig. 14.2 Axial force distribution

There is a very close analogy between the axial stress distribution at the steel/concrete interface and the lateral stress distribution associated with splitting and which has been described in Chapter 11. This is because the vertical dispersal of the concentrated load imposed on the slab by the shear connectors will induce vertical 'splitting' stresses that are in the same direction as the axial forces. This analogy allows a qualitative description of the global and local distribution of axial forces.

It was shown in Chapter 11 that the concentrated force from each mechanical shear connector has to be dispersed both horizontally and vertically. Let us consider the distribution of the lateral forces shown in Fig. 11.13(b) that were induced by the horizontal dispersal of the concentrated loads in a stub girder. The varying shear flow

in (a) is the same as in a simply supported beam with a uniformly distributed load, so that the lateral stress distribution in (b) would be induced by the connectors on one half of the simply supported beam, where point E is the mid-span and point H is near the support. The shear flow on the left hand side of the mid-span would be a mirror image of that of the right hand side, so that superposing the lateral stress distributions from both halves of the beam would give a uniform distribution throughout the span of magnitude $2f_r$, except in regions close to the supports.

The vertical dispersal of the connector loads would also produce lateral stresses of the same distribution but these would be normal to the concrete/steel interface and are therefore equivalent to the axial forces. Hence the dV_c / dx component in the global axial force distribution of Eq. 14.2 and shown in Fig. 14.2 is equivalent to the global lateral stress distribution in splitting shown in Fig. 11.13(b).

14.2.2.3 *Point load*

When a concentrated load is applied at mid-span to a simply supported beam, the axial interface force distribution is given by line B in Fig. 14.2. The axial stress is zero except near both the supports and midspan, as given by Eq. 14.2 and by the analogy with splitting as shown in Fig. 11.12 for the case of uniform shear flow. The tensile and compressive axial interface force distribution near midspan of the beam in Fig. 14.2 can be considered to consist of the interface compressive stresses induced by the concentrated load above this region and the tensile 'splitting' stresses at E in Fig. 11.12(b).

14.2.3 LOCAL DISTRIBUTION IN BEAMS

It was shown in Section 14.2.2 that the global axial interface force distribution is analogous to the global lateral stress distribution induced by splitting forces. It was also shown in Chapter 11 on splitting that the global lateral stress distributions were formed by superposition of the local lateral stress distributions from each connector, that is the stress distributions in Figs. 11.7(a) and (c). Hence within this global axial force distribution are the local axial force distributions due to the vertical dispersal of the concentrated load from each connector.

Local variations in the axial interface force distributions are also caused by shear deformations in the composite beam. For example, the shear deformation around web openings in composite beams, as shown in Fig. 15.9, can cause the steel element to separate from the concrete element. Furthermore, the post buckling tension field action of slender webs with transverse stiffeners in composite beams can exert axial tensile forces on the shear connectors. Local variations in the axial force distributions are also induced by lateral distortional buckling as explained in the U-frame action in Chapter 10.

14.3 Axial embedment strength

When an axial tensile load is applied to a stud shear connector it can cause the stud to pull out of the slab forming a cone around the stud as in Fig. 14.3. Alternatively, the axial load can cause the shank of the stud to neck and fracture at the axial tensile strength of the shank of the stud, that is $A_{sh}f_u$ where A_{sh} is the cross-sectional area of the shank of the stud and f_u its tensile strength.

Fig. 14.3 Axial embedment failure

The tensile failure plane in Fig. 14.3 is often assumed to be conical with the dimensions shown in Fig. 14.4(a) (McMackin, Slutter and Fisher 1973). McMackin and his colleagues used the surface area of this conical failure plane as the major parameter in deriving the following axial embedment strength.

$$f_{emb} \;=\; \frac{X_{emb}}{A_{sh}} \;=\; \frac{1.88\sqrt{f_c}\,h_{sh}\left(h_{sh}+d_{hd}\right)\eta}{d_{sh}^2} \tag{14.3}$$

where the units are in N and mm, f_{emb} is the axial tensile stress in the shank of the stud that is required to form a conical failure plane, X_{emb} is the axial load to cause this failure, A_{sh} is the cross-sectional area of the shank of the stud, f_c is the compressive cylinder strength of the concrete, η is a factor that allows for lightweight concrete and it is suggested that Eq. 13.5 can be used, and the remaining dimensions are defined in Fig. 14.4(a). It is not clear from the research report (McMackin, Slutter and Fisher 1973) whether Eq. 14.3 is the mean or characteristic value. Equation 14.3 is applicable when

$$f_{emb} \;\le\; f_u \tag{14.4}$$

otherwise shank failure at $A_{sh}f_u$ will occur prior to cone failure.
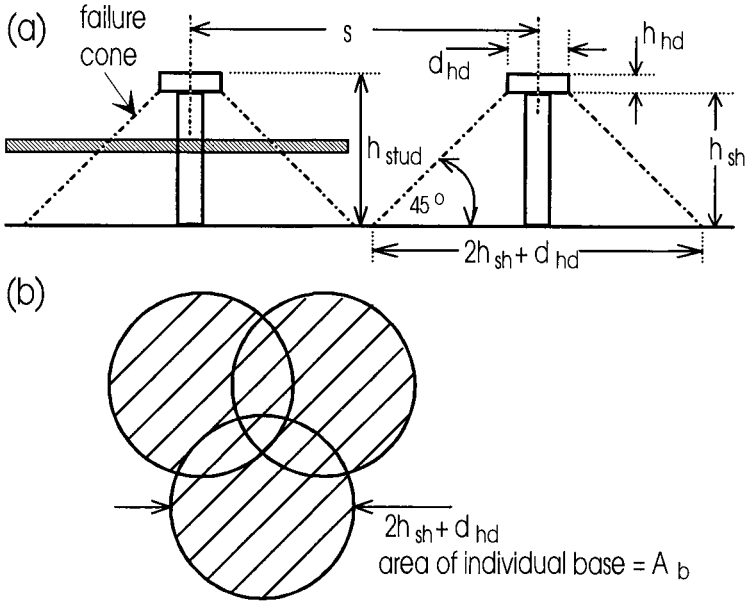
Fig. 14.4 Conical failure planes

For most stud shear connectors, the thickness of the head of the stud $h_{hd} = 0.5d_{sh}$ in Fig. 14.4(a) and the width of the head $d_{hd} = 1.5d_{sh}$. Substituting these values into Eq. 14.3 and also substituting the height of the stud as a proportion of the shank diameter $h_{stud} = nd_{sh}$ gives

$$f_{emb} = \frac{X_{emb}}{A_{sh}} = 1.88\sqrt{f_c}(n-0.5)(n+1)\eta \qquad (14.5)$$

where the units are in N and mm and n is the height of the stud as a proportion of its shank diameter. Equation 14.5 can be simplified to the following lower bound strength of

$$f_{emb} \approx \frac{X_{emb}}{A_{sh}} = 1.88\sqrt{f_c}n^2\eta \qquad (14.6)$$

where the units are N and mm and which clearly shows that the axial embedment strength is proportional to the square of the height of the stud.

Example 14.1 Embedment strength

A 19x100 mm stud shear connector with a tensile strength of $f_u = 500$ N/mm² and stiffness $E_s = 200$ kN/mm² is embedded in normal density concrete with a compression strength of $f_c = 35$ N/mm² and stiffness $E_c = 30$ kN/mm².

From Eq. 14.5, the axial embedment strength $X_{emb} = 94$ kN which is an axial stress of $f_{emb} = 331$ N/mm^2. Substituting $f_{emb} = f_u = 500$ N/mm^2 into Eq. 14.5 gives n $= 7.0$ and hence increasing the height of the stud to $h_{stud} = 7.0d_{sh} = 133$ mm would ensure that shank failure occurred before a conical failure cone.

14.4   Shear embedment strength

When a shear load is applied to a stud shear connector as shown in Fig. 2.14(b), the deformation of the stud causes the head to rotate in an anticlockwise direction, which may cause the concrete to crack in region G (Ollgaard et al 1971). The tensile crack in region G will allow further rotation of the head and increase the stresses at the critical region of the steel failure zone at B and hence reduce the shear strength of the shear connector. In some cases, the tensile crack can circumvent the stud producing a typical shear embedment failure cone as shown in Fig. 14.5.

Fig. 14.5 Shear embedment failure

Experimental research has shown that short studs have a lower shear strength than long studs. However the variation in the shear strength with height has never been quantified experimentally but has been recognised in some national standards. For example, the British Bridge Code (BS5400: Part 5:1979) gives the strength of 19x100 mm stud shear connectors as 14% to 18% stronger than 19x75 mm connectors depending on the strength of the concrete.

The results of a finite element analysis of stud shear connectors with varying heights (Johnson and Oehlers 1981) are shown in Fig. 14.6. It can be seen that the

increase in strength with height of stud is initially fairly rapid and then constant at about n = 9. It is interesting to note that at n = 7 the strength is 98% of the maximum attainable strength which is in agreement with the results from axial embedment failure where it was shown in Example 14.1 that the optimum height is about the same at $7d_{sh}$. The strength of 19x100 mm studs (n = 5.3) in Fig. 14.6 is 10% greater than the strength of 19x75 mm studs (n = 4), which is less than the 14% to 18% predicted by the British Bridge Code.
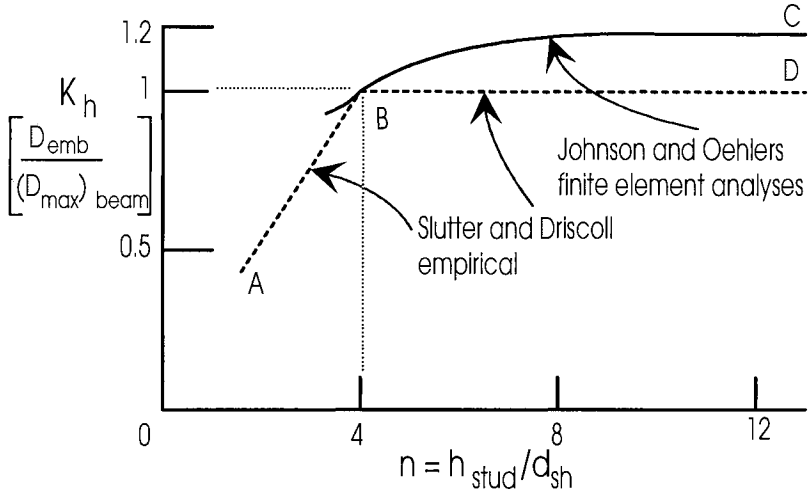
Fig. 14.6 Shear embedment strength

From experimental tests, Slutter and Driscoll (1962) proposed the bilinear variation in strength, A-B-D in Fig. 14.6, that assumes that the strength remains constant when n ≥ 4. This does not allow for the difference in strength between 19x75 mm and 19x100 mm connectors, so it is suggested that as a guideline the variation in the longitudinal shear strength that allows for shear embedment failure D_{emb} can be assumed to follow the line A-B and then the curve B-C.

The longitudinal shear strength of stud shear connectors in composite beams, which is given as $(D_{max})_{beam}$ in Eq. 2.37, was derived from experimental tests on 19x75 mm studs by Ollgaard et al (1971), and hence studs with longer height to diameter ratios can be assumed to be stronger. Point B in Fig. 14.6 corresponds to Ollgaard's specimens and hence $D_{emb} = (D_{max})_{beam}$ at this level. If we define K_h as the ratio between the shear strength D_{emb} and the shear strength of connectors with a height of $h_{stud} = 4d_{sh}$ then

$$D_{emb} = K_h(D_{max})_{beam} \tag{14.7}$$

where D_{emb} is the shear strength that allows for variations in shear embedment strength, K_h can be derived from line A-B-C in Fig. 14.6 and $(D_{max})_{beam}$ can be derived from Eq. 2.37.

14.5 Interaction between shear and axial forces

14.5.1 GENERAL

When a stud shear connector in a push-test is subjected to a shear load, the stud is subjected to a complex distribution of forces. An indication of the distribution of these forces was derived from a finite element analysis (Johnson and Oehlers 1981) and are shown in Fig. 14.7(a) where the force F_{exp} should be ignored. In this finite element analysis, a stud shear connector in a push specimen (of the type shown in Fig. 2.16 with the base restrained as in (e)) was subjected to a shear load of F_{shear} as shown in Fig. 14.7(a). The shear connection was loaded by applying a longitudinal displacement to the steel flange along F-F in (a), so that there was slip between the concrete and steel elements but there was not any separation.
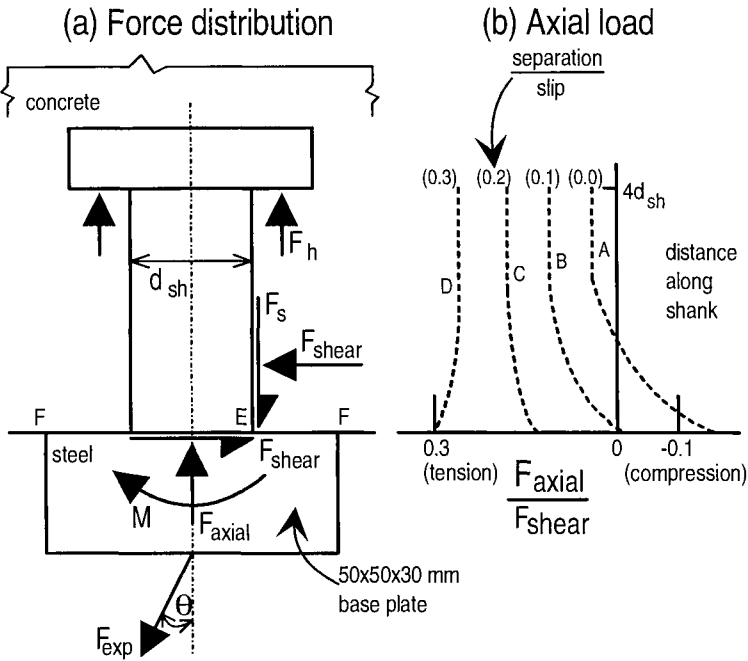
Fig. 14.7 Axial loads on stud shear connectors

It can be seen in Fig. 14.7(a) that the head of the stud is subjected to an axial tensile force F_h, as expected by the deformation described in Section 14.4. However the shank of the stud is subjected to a shear force F_s, so that the axial force in the shank changes from a tensile value of F_h at the head to compression value of F_{emb} at the base. Hence the critical failure region at E in (a) is subjected to the beneficial effect of axial compression. The distribution of the axial force along the axis of the stud F_{axial} is shown as line A in (b).

The effect of axial forces on the shear connection was simulated by applying a constant ratio of downward displacement to the steel flange (separation) to longitudinal displacement (slip), but still ensuring the flange was parallel to the soffit of the concrete so that it did not rotate. The results for different separation to slip ratios (Oehlers 1980) are shown in Fig. 14.7(b). It can be seen that as the axial separation increases, the tensile force at the head of the stud increases and hence the probability of embedment failure increases. Furthermore, the axial force at the base of the stud changes from compression in line A to tension in line D. The critical tensile failure region at E in (a) is therefore more likely to fail when axial tensile forces are applied.

Externally applied axial tensile forces will therefore weaken the shear connection at the base of the stud and further weaken the shear connection by inducing embedment failure. It is therefore necessary to determine the interaction between shear and axial forces, that is the combination of applied axial loads X_a and applied shear load D_a that causes the shear connector to fail. We already know the two extremities of this failure envelope, that is points A and B in Fig. 14.8. At point A, $D_a = D_{emb}$ which is given by Eq. 14.7 as $X_a = 0$. Furthermore, point B can be derived from Eq. 14.3 as $X_a = X_{emb}$ when the shear force is zero. The failure envelope between these points is determined from experimental data in the following sections. However they should only be used as guidelines as none of the research is based on axial strengths in composite beams.
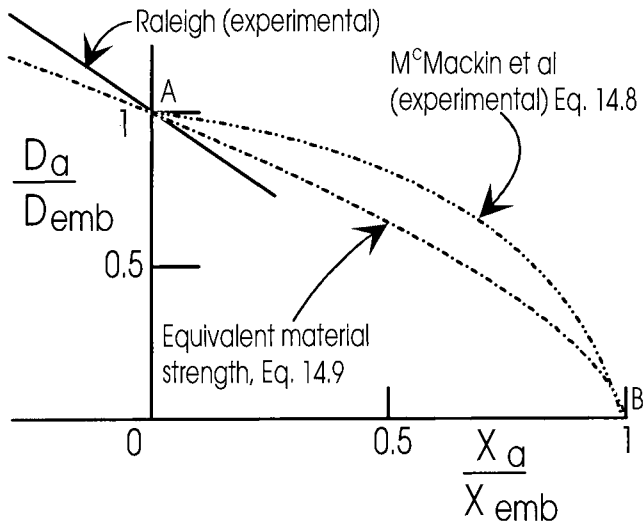
Fig. 14.8 Shear - Axial failure envelope

14.5.2 PULL TESTS

The fundamental research on the interaction between shear and axial loads was performed by McMackin, Slutter and Fisher (1973). They welded stud shear connectors to square base plates that were 50x50x13 mm and cast these into large concrete blocks as shown in Fig. 14.7(a). The specimens were then loaded at fixed

inclinations, such as F_{exp} at an angle θ, until they failed. The failure envelope was derived by testing at angles of 0, 30° and 60°, whereas the pure shear condition at $\theta = 90°$ was determined from the results of conventional push tests by Ollgaard et al (1971).

The following elliptical interaction curve was found to give the best fit to the test data.

$$\left(\frac{D_a}{D_{emb}}\right)^{\frac{5}{3}} + \left(\frac{X_a}{X_{emb}}\right)^{\frac{5}{3}} \;=\; 1 \tag{14.8}$$

where D_a and X_a are the combination of shear and axial loads required to cause failure when the shear connection has pure shear and pure axial strengths of D_{emb} and X_{emb}. The failure envelope is plotted in Fig. 14.8 and shows a fairly weak interaction between shear and axial loads.

As with all push or pull tests the results have to be interpreted with caution to allow for the difference between the restraints in these specimens and those in beams. A finite element analysis of the pull-test (Raleigh 1984) showed that allowing the base plate in Fig. 14.7(a) to rotate freely moved the maximum principal tensile stress from the critical region at E, at the base of the plate, to a position approximately $1.5d_{sh}$ from the base which is in agreement with experimental results by Thurlimann (1959). Furthermore, the magnitude of the maximum principal stress was halved implying an increase in the strength. It is felt that the small base plate used in the pull specimens used to derive Eq. 14.8 would allow a reasonable degree of rotation, and so it is suggested that these results should be viewed as an upper bound, bearing in mind that it is correct at the extremities of the failure envelope.

14.5.3 PUSH TESTS

An attempt was made to determine the failure envelope directly from push tests (Oehlers and Johnson 1987, Raleigh 1984). The standard type of push specimen was made statically determinate as shown in Fig. 14.9. Tensile axial forces were induced in the stud shear connectors by placing the knife edge supports to the sides of the steel element as shown. Whereas, compressive axial forces were induced in the connectors by placing the knife edge supports below the steel element and by replacing the strut with a tie.

The results of a linear regression analysis of Raleigh's experimental results (1984) is shown in Fig. 14.8. The scatter was large and the specimens were only tested over a small range of axial loads, and therefore the results are not suitable for quantitative analyses. However, they do show a very strong interaction between axial loads and shear and that the beneficial effect of axial compressive forces is the same as the detrimental effect of axial tensile forces. Furthermore, the tests also showed that axial forces did not reduce the ductility of the connector, but may have increased the ductility when axial tensile forces were applied as these induced substantial deformation of the stud through necking before failure.
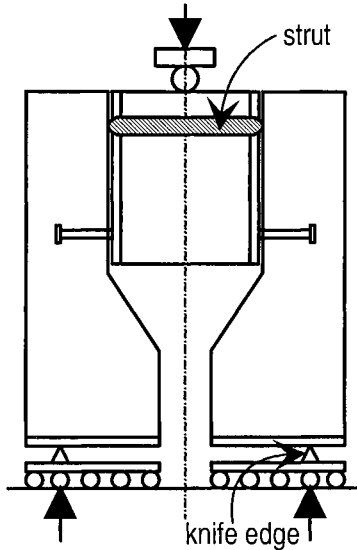
Fig. 14.9 Statically determinate push test

The results are important in qualitative terms because they show that the reduction in strength due to local axial tensile forces can be balanced by the increase in strength due to the local compressive axial forces, because the ductility of the shear connectors can redistribute the shear load from weaker to stronger regions. Hence the average axial force in a beam should control design, unless the local axial tensile forces are severe enough to cause embedment failure before longitudinal shear failure of the connectors. It is therefore suggested that as most composite beams are loaded from above, and hence there is a net compressive force across the interface as shown in Fig. 14.2, the effects of axial forces can be ignored.

It is not so easy to deal with severe variations of axial forces as might occur in regions with web openings as described in Section 14.2.3. In these regions it may be necessary to deal with the forces in individual connectors, or alternatively to include transverse reinforcement in order to ensure that the system remains ductile after conical cone failure so that the longitudinal shear can be redistributed.

14.5.4 EQUIVALENT MATERIAL STRENGTH

An alternative method of visualising the effect of axial forces is to assume that they affect the dowel strength of the shear connector by changing the material tensile strength of the shear connector. For example, if an axial tensile stress $\sigma_a = X_a/A_{sh}$ is applied that is equal to the tensile strength of the stud material f_u, then the shear connection will fail under pure axial loads so that the dowel strength is zero. This is equivalent to $f_u = 0$ in Eq. 2.37, or the equivalent tensile strength $(f_u)_{eq} = f_u - \sigma_a = 0$. To allow for pure axial embedment failure at stresses f_{emb} that are less than f_u, as given

in Eq. 14.3, the equivalents tensile strength can be given in the following form for use in the parameter $(D_{max})_{beam}$ in Eq. 14.7.

$$\left(f_u\right)_{eq} = \left(1 - \frac{\sigma_a}{f_{emb}}\right) f_u \qquad (14.9)$$

where σ_a is negative for compressive axial stresses. The expression can therefore be used to quantify the effects of both tensile and compressive axial forces on the dowel strength of stud shear connectors as shown in Fig. 14.8. It can be seen that it forms a lower bound to McMackin's failure envelope.

Example 14.2 Shear strength of stud shear connections subjected to axial loads

Continuing the analysis of the 19x100 mm stud shear connector in Example 14.1, let us assume that the shear connector is subjected to an axial load of $X_a = 20$ kN.

From Eq. 2.37, the mean dowel strength $(D_{max})_{beam} = 113$ kN which would be the strength of a 19x75 mm stud shear connection. The strength of a 19x100 mm connector can be derived from Eq. 14.7 and Fig. 14.6 where $K_h = 1.1$ to give $D_{emb} = 124$ kN. From McMackin's procedure in Eq. 14.8, a tensile axial load of 20 kN reduces the shear strength to $D_a = 118$ kN. Furthermore, from the equivalent material strength procedure of Eq. 14.9, a tensile axial load of 20 kN would reduce the shear strength to $D_a = 106$ kN, however a compressive axial load of 20 kN would increase the shear strength to 140 kN.

14.6 Detailing

When the spacing of a pair of stud shear connectors, s in Fig. 14.4(a), is greater than the width of the base of the failure cone of $2h_{sh} + d_{hd}$, then the failure planes do not intersect. In this case, the axial force required to induce embedment failure in both connectors is the embedment strength of two connectors and this will remain constant while $s \geq 2h_{sh} + d_{hd}$. When the spacing $s = 0$, then the embedment strength of both connectors is that of one connector. Hence the embedment strength reduces when the failure cones intersect.

As a rule of thumb, it can be assumed that the axial force required to induce embedment failure is proportional to the area of slab encompassed by the failure cones. For example, if the area of the base of a cone is A_b as shown in Fig. 14.4(b) and the total area of slab encompassed by the bases of the three connectors is A_t, then the embedment strength of each connector would reduce by a factor of $A_t/3A_b$.

Transverse reinforcement can be placed through the possible failure cones as shown in Fig. 14.4(a). This may not necessarily increase the embedment strength but would probably allow a ductile failure and permit redistribution of the load.

14.7 References

BS5400: Part 5 (1979). *Steel, Concrete and Composite Bridges. Part 5. Code of Practice for Design of Composite Bridges.* British Standards Institution, London.

Johnson, R. P. and Oehlers, D. J. (1981). "Analysis and design for longitudinal shear in composite T-beams", Proceedings, Institution of Civil Engineers, London, Part 2, Vol. 71, 989-1021.

McMackin, P.J., Slutter, R.G. and Fisher, J.W. (1973). "Headed steel anchor under combined loading", Engineering Journal, American Institute of Steel Construction, second quarter, 43-53.

Oehlers, D.J. (1980). Stud shear connectors for composite beams. Ph. D. Thesis, University of Warwick, Department of Engineering, March.

Oehlers, D.J. (1990). "Method of estimating the fatigue endurances of stud shear connectors", IABSE Proceedings P-145/90, November, Zurich.

Oehlers, D.J. and Johnson, R.P. (1987). "The strength of stud shear connections in composite beams", The Structural Engineer, Vol. 65B No.2, 44-48.

Ollgaard, J.O, Slutter, R.G. and Fisher, J.W. (1971). "Shear strength of stud connectors in lightweight and normal-weight concrete", Engineering Journal, AISC, April, 55-64.

Raleigh, J.R. (1984). Axial loads in stud shear connections in composite beams. M.Eng.Sc. Thesis, University College Cork, National University of Ireland, .

Slutter, R. G. and Driscoll, G. C. (1962). "Test results and design recommendations for composite beams", Lehigh University, Fritz Engineering Laboratory, Report No. 279. 10, January.

Teraszkiewicz, J.S. (1965). "Tests on stud shear connectors", Road Research Laboratory Technical Note No. 36, Crowthorne, U.K., December.

Thurlimann, B. (1959). "Fatigue and static strength of stud shear connectors", Journal of American Concrete Institute, Vol. 30, 1287-1302.

15 Composite Beams with Service Ducts

15.1 Introduction

It is a convenient practice to insert openings in the webs of composite beams, as shown in Fig. 1.9(a), to allow for the passage of services since it allows the overall floor heights to be reduced. It is fairly obvious that removal of part of the web of the steel element will reduce the shear and flexural strengths of the composite beam at the openings, as these strengths depend on the axial strength of the steel element as described in Chapter 7. However, the removal of part of the web may also affect the transfer of the longitudinal shear through the connectors, and hence may also affect the strength of the composite beam at other sections as well as at the web opening.

The mechanism by which the composite beam with an opening resists both flexural and shear forces is fairly complex. However, the solution requires a full grasp of rigid plastic principles, and hence is an ideal problem for the reader in order to consolidate his or her understanding of Chapter 7, which should be read before continuing with this chapter. Furthermore, the analysis procedure for a composite beam with a web opening as in Fig. 1.9(a) can be applied to the analysis of composite stub girders in (b) and has similarities to the analysis of composite truss girders in (c) and (d).

15.2 Analysis philosophy

The fundamental if not classical research on composite beams with web openings has been carried out separately by Redwood (Redwood and Wong 1982, Redwood and Poumbouras 1983 and 1984, Cho and Redwood 1986) and Darwin (Darwin 1984, Darwin 1988, Narayanan 1988). We will follow here the fundamental principles advocated by both research workers. However, the general procedures described in the following are more closely aligned to those of Darwin, but differ in the treatment of shear on the yield properties of the steel.

Consider the composite beam shown in Fig. 1.1(a). Let us assume that a duct with an opening of length a_o is required to the left of mid-span as shown in Fig. 1.9(a). The composite beam over the length a_o of the opening is shown in Fig. 15.1(a) where the moment on the left hand side of the duct is lower than that on the right hand side in this beam. The following subscripts will be used when referring to the parts of this composite beam: ℓ for the low moment end; h for the high moment end; t for the top T-section shown in (b); and b for the bottom T-section. The depth of the top T-section will be denoted by h_t, that of the service duct as h_o, and that of the bottom T-section as h_b, and the applied moment and shear at the centre of the duct as M_a and V_a as shown in (a). As a first assumption, we will assume that the shear V_a is constant along the length of the duct. We will denote the applied moment at the low moment end of the duct as $(M_a)_\ell$ and that at the high moment end as $(M_a)_h$.
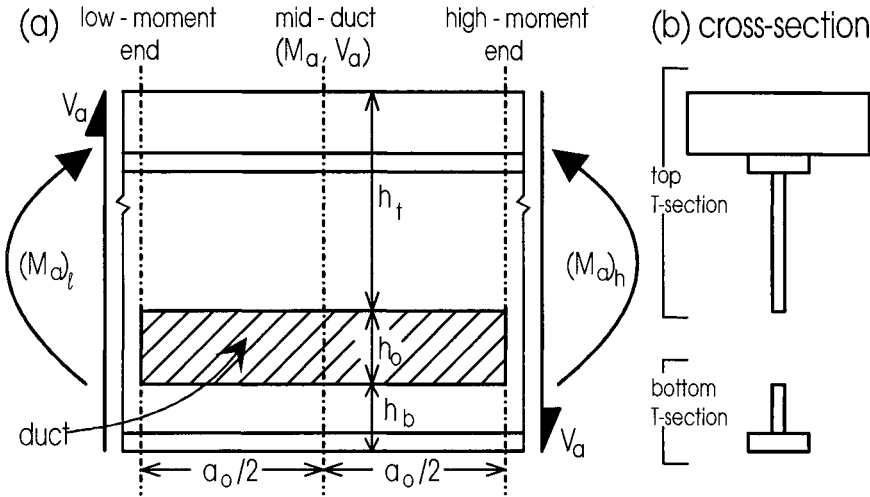
Fig. 15.1 Applied stress resultants

The applied moments and shear forces at each end of the duct in Fig. 15.1(a) impose local internal stress resultants as shown in Fig. 15.2, where at each T-section an axial force F, a shear force V and a moment M act. For example, on the right hand side of the duct, the applied moment $(M_a)_h$ in Fig. 15.1(a) is comprised of the local moments in Fig. 15.2 of M_{th} and M_{bh} as well as the composite moment Fh_1, where from horizontal equilibrium $F_b = F_t = F$. Furthermore, the applied shear load V_a in Fig. 15.1(a) is comprised of the shear resisted by the top T-section V_t, in Fig. 15.2, and the shear resisted by the bottom T-section V_b.
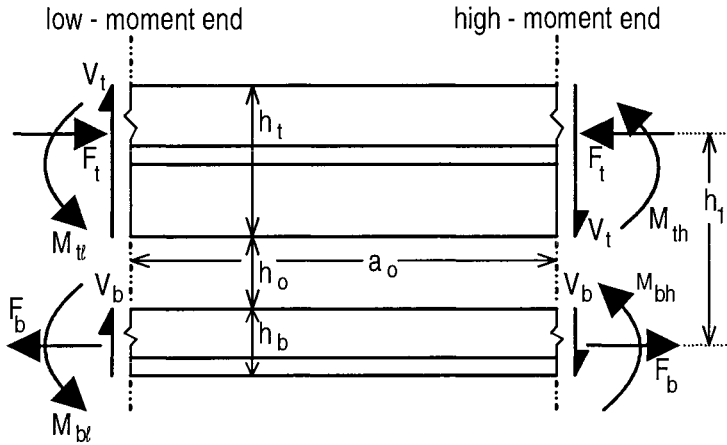
Fig. 15.2 Local internal stress resultants

The distribution of the local internal stress resultants in Fig. 15.2 is difficult to define for combinations of applied moment M_a and shear force V_a. In order to find a

solution, researchers have based the strength on what will be referred to as the *pure flexural capacity* M_{pur}, the *pure shear capacity* V_{pur}, and an empirically derived failure envelope for a section subjected to shear and flexure that is based on M_{pur} and V_{pur}. The *pure flexural capacity* of the composite section at the duct is simply the flexural capacity of the section when vertical shear is not present, that is $V_t = V_b = 0$ in Fig. 15.2. Hence it is also the theoretical maximum flexural capacity and its derivation is given in Section 15.3.

The *pure shear capacity* will be defined as the maximum shear force that can be transferred across a web opening that is situated in a region of low applied moment. It can be seen in Fig. 15.2 that each T-section is subjected to three stress resultants such as F_t, V_t and M_{th} at the high moment end of the top T-section. In order to maximise the shear capacity V_t, it is necessary to minimise the other stress resultants F_t and M_{th} and this can be achieved by assuming that the top T-section and the bottom T-section in Fig. 15.2 do not act compositely, so that the composite moment $F_t h_1 = 0$, that is $F_t = 0$. One way of visualising the problem is that the moments M_{th} and $M_{t\ell}$ are now local moments that are required to form a mechanism to transfer the shear V_t across the duct. In general, the local moments M_{th} and $M_{t\ell}$ are in the same direction as shown in Fig. 15.2, so that a point of contraflexure, that is a point of zero moment, exists within the region of the duct, so that we are dealing with a region in which the moment distribution is at its lowest but never zero throughout. The pure shear capacity is the sum of the shear capacities of both the top and bottom T-sections and methods for determining the pure shear capacity are given in Section 15.4.

Finally, and in order to determine the flexural and shear capacity of the composite beam at the duct, a failure envelope is defined in Section 15.5 that is based on both the *pure shear* and *pure flexural* capacities.

15.3 Pure flexural capacity

A composite beam with a web opening that is under pure flexure is shown in Fig. 15.3. The flexure causes compression in the top fibres of the concrete element and possibly tensile cracking in the bottom fibres as shown, depending upon the position of the neutral axis. It will be assumed that the curvature κ in both the top steel T-section and in the concrete element is the same and that a slip strain ds/dx may occur at the concrete-steel interface as shown. It will also be assumed that the geometric proportions of the beam around the duct are such that the curvature in the top composite T-section is the same as that in the bottom steel T-section, and that the strain profile in the bottom steel T-section is simply an extension of that of the top steel T-section as shown. Hence we are assuming that the dimension h_o does not vary through the length of the duct and that no slip strain exists between the two steel strain profiles as shown. The pure flexural capacity can therefore be determined from rigid plastic analysis as described in Section 7.3.

It was shown in Section 7.5 that the flexural capacity of a composite beam varies along its length and therefore in theory it is necessary to ensure that the flexural capacity along the length of the beam exceeds the applied moment, but in practice this

is seldom done except for unusual beams or loading conditions. However when a duct is placed in a beam, it can cause rapid changes in strength along the length of the beam. Therefore, it is necessary to check the strength of the beam at critical cross-sections such as the low moment end at section B in Fig. 15.4, the high moment end at C and the position of maximum moment at D.
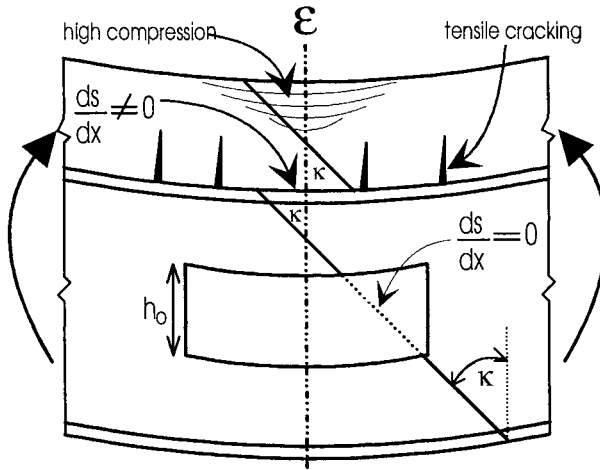
Fig. 15.3 Composite beam subjected to flexure
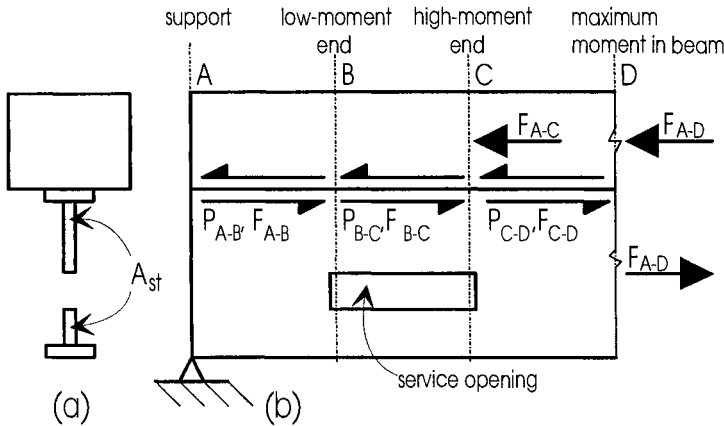
Fig. 15.4 Axial force distribution

Consider the beam in Fig. 15.4(b). Let us assume that the composite beam was first designed without a duct such that the moment capacity exceeded the applied moment at the position of maximum moment at D. The beam could have been designed at D for full shear connection with the neutral axis in either the concrete element or the steel element (Section 7.3.1), or it could have been designed with

partial shear connection with neutral axes in both elements (Section 7.3.2). In all cases, design would have been based on all of the connectors being fully loaded. Hence both the total axial force in the concrete element at section D as well as the total axial force in the steel element at D, which will be referred to as F_{A-D}, will equal the strength of the shear connectors over the shear span A-D (P_{A-D}), that is $F_{A-D} = P_{A-D}$ at section D.

Let us now assume that a service opening is now inserted in the web as shown in Fig. 15.4(b) and that the total cross-sectional area of steel remaining in the steel element is A_{st} as shown in (a), so that the axial strength of the steel element at the duct is now $A_{st}f_y$. If at section C in (b), the axial strength of the steel element $A_{st}f_y$ is greater than the strength of the shear connectors in the shear span A-C (P_{A-C}), then the steel element is partly in tension and partly in compression. Therefore the force in the concrete element F_{A-C} remains at P_{A-C}, so that the distribution of the connector forces in the beam is unchanged.

Conversely, if $A_{st}f_y < P_{A-C}$ in Fig. 15.4(b) then the steel element will be fully yielded in tension, so that the maximum force in the concrete element and hence the force in the shear connectors will reduce from P_{A-C} to $A_{st}f_y$. The connectors in the shear span A-C are therefore not fully loaded, but it would be reasonable to assume that they are uniformly loaded over the shear span A-C, that is the load on each connector is $\left(A_{st}f_y / P_{A-C}\right)D_{max}$ where D_{max} is the strength of the shear connector. The flexural capacity at section C has therefore reduced, not only because of the reduction in the cross-sectional area of the steel element, but also because the force in the shear connectors has also reduced.

If $A_{st}f_y < P_{A-C}$ at C in Fig. 15.4(b), then the force in the concrete element at D has also reduced, thereby reducing the flexural capacity at the position of maximum moment. Furthermore, if $A_{st}f_y < P_{A-C}$ at C, then the force in the shear connectors in shear span A-B F_{A-B} will be $\left(A_{st}f_y/P_{A-C}\right)P_{A-B}$, where P_{A-B} is the strength of the shear connectors in the shear span A-B. Therefore, the flexural capacity at B will be less than if the connectors were fully loaded. It can now be seen how the presence of a duct can affect the flexural capacity of the composite beam along its whole length and that the most important critical section is at the high moment end of the duct.

The statement of the analysis in terms of variables is fairly cumbersome, and so is illustrated in the following by examples.

Example 15.1. Pure flexural capacity when connectors fully loaded

The composite beam in Fig. 15.5 was initially designed for full shear connection at midspan in order to support a concentrated load. It was decided to insert a duct at a quarter span and at the centre of the web of the steel element as shown. It is required to determine the pure moment capacity at all critical sections. Units of N and mm are used in Fig. 15.5 unless shown otherwise.

Position of maximum moment

The analysis for the flexural capacity at mid-span, Section D in Fig. 15.5, is summarised in Fig. 15.6 and follows the procedures outlined in Section 7.3.1.3 and outlined in Fig. 7.4.

Step 1: The axial strengths P of the rectangular components of the composite beam are listed in Fig. 15.6(b).

Step 2: The next step is to find the level of the neutral axis, that is the rectangular element of the cross-section in Fig. 15.6(a) through which the neutral axis passes. Referring to Figs. 1.20(b) and (e), it can be seen that when there is full shear connection, all the forces above the neutral axis are compressive and all the forces below are tensile. The same applies to the neutral axis in the steel element in (h) where there is partial shear connection, because the tensile strength of the concrete is assumed to be zero. We appear to be looking for a position or level in the section where the compressive force above is equal to the tensile force below, but it must be emphasised that we are really looking for a neutral axis level where the sum of the compressive forces equals the sum of the tensile forces. This is worth bearing in mind as it will be shown in Section 15.4.4.3 that the forces on either side of the neutral axis in the steel element are not always of one sign. As the strength of the concrete element (P_{conc} = 3825 kN in Fig. 15.6(b)) is greater than the strength of the steel element (P_{steel} = 2830 kN), the neutral axis N-A must lie in the concrete element as shown in (c).

Step 3: Having determined that the neutral axis lies in the concrete element, we now know that the force in the concrete element, F_{A-D} in Fig. 15.4(b), is equal to the axial strength of the steel element P_{steel} = 2830 kN. This is also the strength of the shear connection P_{A-D}, in shear span A-D, as we have assumed that the beam has been designed with full shear connection at mid-span. Hence at section D, where η_{max} = 1, the force in the concrete element F_{A-D} = P_{A-D} = P_{steel} = 2830 kN as shown in Fig. 15.6(e). The depth of the neutral axis n in (d) and (a) can be determined by equating the strength in this concrete element to F_{A-D}, that is $1000n0.85f_c = 2830 \times 10^3$ N, giving n = 111 mm.

Step 4: We now know the magnitude and position of all the axial forces acting on the section as shown in Fig. 15.6(e) and (f) where h_F is the distance of the axial force from the top fibre. Taking moments about any convenient level, such as the top fibre, gives a moment capacity of M_{fsc} = 1118 kNm. As we are designing for full shear connection, the strength of the shear connection in each shear span of the beam in Fig. 15.5(a), $P_{A-D} = P_{steel}$ = 2830 kN.

High moment end

The analysis for the pure flexural capacity at the high moment end of the duct at section C in Fig. 15.5(a) is summarised in Fig. 15.7.

We will assume that the shear connectors are uniformly distributed along the shear span A-D in Fig. 15.5(a) of the beam, so that the degree of shear connection at C

is $\eta_C = 4.4/8 = 0.55$. Hence, the strength of the shear connectors in the shear span A-C is 0.55 x 2830 = 1557 kN. This is shown in Fig. 15.7(b) as the maximum force that can be applied to the concrete element. The strength of the steel element (2330 kN) is still greater than the maximum force that can be applied to the concrete element (1557 kN), even though there is an opening in the duct, so the connectors are still fully loaded in the shear span A-C in Fig. 15.5(a). A comparison of the axial strengths in Fig. 15.7(b) shows that the neutral axis in the steel element lies in the top flange as shown in (c). Because in this example the steel element with the duct is symmetrical, a quicker solution is to use the equivalent stress system in (d), where the resultant forces are shown in (e). From horizontal equilibrium, the equivalent compressive force in the top flange is 2330 - 1557 = 773 kN, and hence the depth of the equivalent compressive stress field n = 7.7 mm. The position of the resultant forces from the top fibre h_F is shown in (f). Hence from (e) and (f), the moment capacity at the high moment end $M_{psc} = 881$ kN.

It is worth noting that if the duct region is represented as a free body, then the forces shown in Fig. 15.7(e) are the external forces that are required to maintain the equilibrium of this free body. In these analyses, the direction of the applied moment is obvious, but it will be shown later in the analysis of the pure shear capacity that the direction of the moment can reverse and hence it is important that this convention is adhered to.

Low moment end

The connectors in shear span A-C in Fig. 15.5 have been shown to be fully loaded so that those in shear span A-B are also fully loaded. Hence at the low moment end of the duct at section B in Fig. 15.5, $\eta = 3.6/8 = 0.45$ so that the strength of the shear connectors in the shear span A-B is 0.45 x 2830 = 1274 kN. The analysis procedure for the low moment end of the duct follows the same procedure as that of the high moment which is shown in Fig. 15.7. Substituting 1274 kN for 1557 kN in (b) gives the axial strengths at the low moment end, and following the analyses represented by (c) to (f) gives a moment capacity at the low moment end of $M_{psc} = 853$ kN.

Example 15.2. Pure flexural capacity when connectors partially loaded

When a duct is near the position of maximum moment or when the duct is very large, the presence of the duct can reduce the flexural capacity along the full length of the beam.

Consider the composite beam in Fig. 15.8 which is the same as that in Fig. 15.5 except that the duct has been moved closer to the position of maximum moment. From Example 15.1, the strength of the shear connectors in shear span A-D in Fig. 15.8 is $P_{A-D} = 2830$ kN and these are distributed uniformly over the shear span. Therefore the strength of the shear connectors in shear span A-C is $P_{A-C} = 2618$ kN and that in A-B is $P_{A-B} = 2335$ kN. Furthermore from Example 15.1, the axial strength of the steel element at the duct is 2330 kN.

The critical section to consider within the duct is at C in Fig. 15.8, where the strength of the shear connectors in the shear span relative to that of the axial strength of the steel element is the highest. The maximum axial force in the steel element is 2330 kN, which occurs when all of the steel element is fully yielded in tension. Therefore, the maximum force that can be applied to the shear connectors in shear span A-C is F_{A-C} = 2330 kN which is lower than the strength of these shear connectors of P_{A-C} = 2618 kN. Therefore the connectors in shear span A-C are not fully loaded and have a force in them of F_{A-C} = 2330 kN as shown in Fig. 15.8. The force in the concrete element F_{conc} is also equal to the force in the connectors, so that F_{conc} = 2330 kN as shown. The force in the concrete element has therefore reduced from 2618 kN to 2330 kN due to the presence of the duct and therefore the flexural capacity at section C will also have reduced. As the force in the shear connection, the steel element and the concrete element are known, the flexural capacity can be determined using the partial interaction procedure outlined in Example 15.1 and described in Section 7.3.2.

The connectors in shear span A-C in Fig. 15.8 are not fully loaded, but it would be reasonable to assume that they are uniformly loaded along the shear span, so that the force in the shear connectors in shear span A-B would be (6.6/7.4) x 2330 = 2078 kN. Therefore at section B, F_{conc} = 2078 kN and hence the force in the concrete element has reduced from 2335 kN to 2078 kN and hence the flexural capacity at C will also have reduced due to the presence of the duct.

The connectors in the shear span C-D in Fig. 15.8 are unaffected by the duct and so will be fully loaded; the strength of these connectors is (0.6/8) x 2830 = 212 kN. As the force in the shear connectors in shear span A-C is 2330 kN, the maximum force that can be applied to the shear connectors in A-D is 2330 + 212 = 2542 kN. The force in the concrete has therefore reduced from 2830 kN to 2542 kN, thereby reducing the flexural capacity at D.
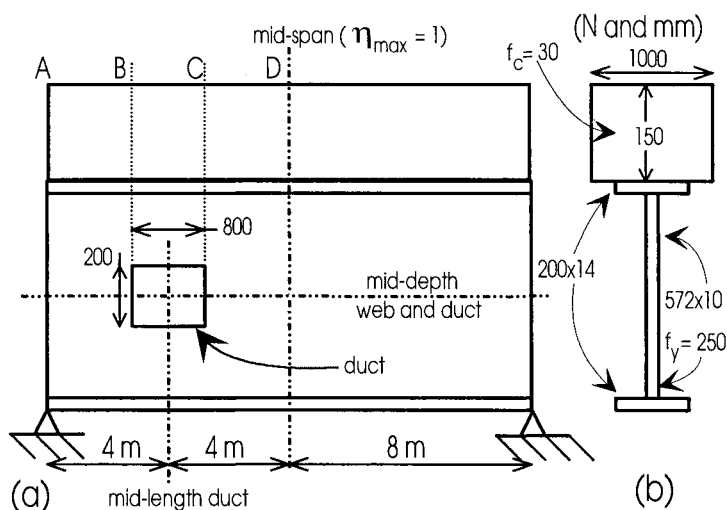
Fig. 15.5 Beam with web opening
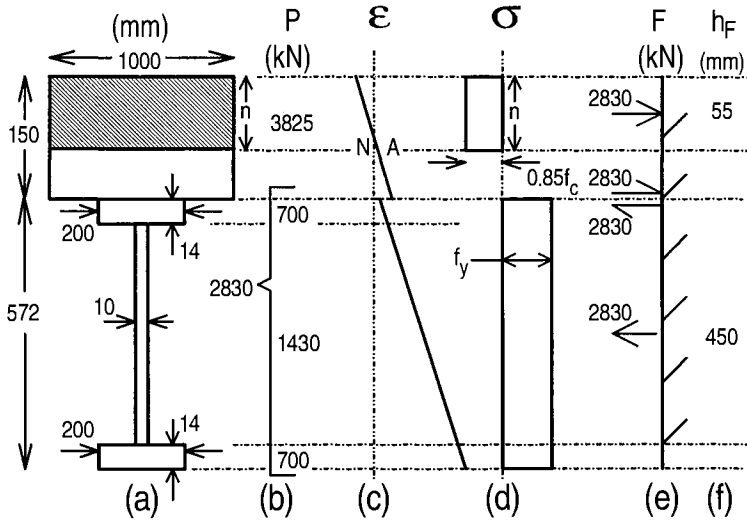
Fig. 15.6 Example 15.1: Capacity at maximum moment position
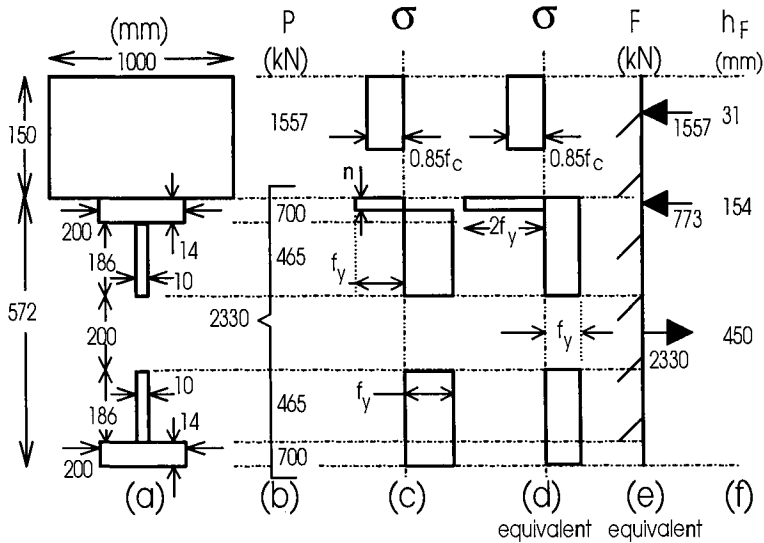
Fig. 15.7 Example 15.1: Flexural capacity at high moment end

$P_{A\text{-}B} = 2335$ kN $\quad P_{A\text{-}C} = 2618$ kN $\quad P_{A\text{-}D} = 2830$ kN
$F_{A\text{-}B} = 2078$ kN $\quad F_{A\text{-}C} = 2330$ kN $\quad F_{A\text{-}D} = 2542$ kN
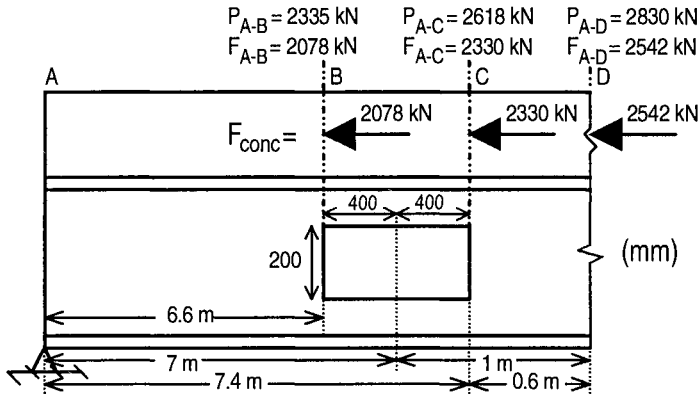
Fig. 15.8 Example 15.2: Large duct at or near position of maximum moment

15.4 Pure shear capacity

15.4.1 GENERAL

The deformation of a composite section subjected to high shear forces and low moments is shown in Fig. 15.9(a). The deformation and forces induced by this system are described in Section 15.4.2. The shear capacity of the bottom steel T-section in Fig. 15.9(b) is then derived in Section 15.4.3, that of the top composite T-section in (b) in Section 15.4.4 and the resultant pure shear capacity in Section 15.4.5.
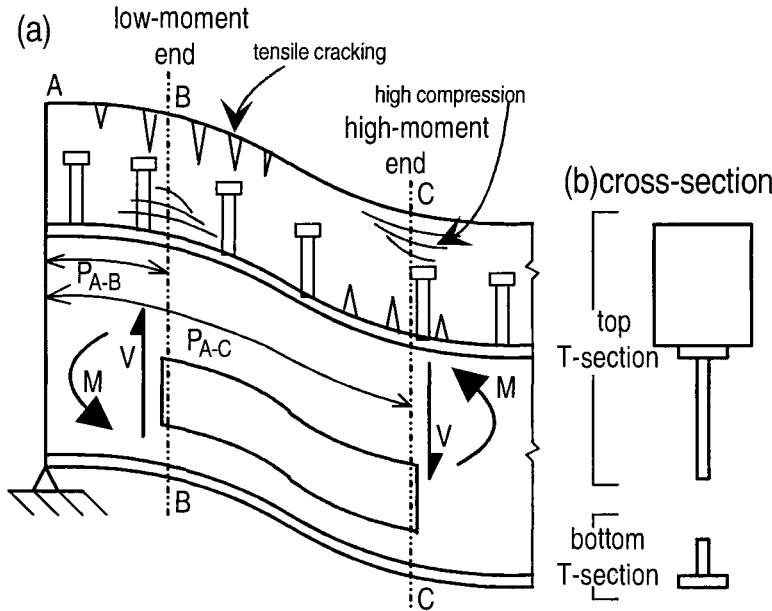
Fig. 15.9 Shear deformation

15.4.2 BASIC BEHAVIOUR

15.4.2.1 *Deformation*

The shear deformation in Fig. 15.9(a) can visualised as the deformation of a continuous composite beam near a point of contraflexure. The shear force V is transferred across the duct by both the bottom steel T-section and the top composite T-section. Each T-section is assumed to deform independently.

The shear deformation at the high moment end of the top composite T-section, at section C in Fig. 15.9(a), causes the concrete in the top fibres of the concrete slab to go into compression and the bottom fibres to crack in tension as shown. The deformation, and hence analysis of this section, is therefore the same as the positive region of a composite beam. The resultant axial force in the concrete element, F_{conc} at C, therefore acts in the top region of the slab and is in equilibrium with the force in the shear connectors between section C and the support of the beam at section A.

The shear deformation at the low moment end of the top composite T-section, at B in Fig. 15.9(a), causes the concrete in the top fibres of the concrete element to crack in tension. However, the force in the connectors between sections A and B have still to be transferred into the concrete element at section B, and hence the bottom fibres must be in compression as shown. It is worth noting that between sections B and C, the axial force in the concrete element F_{conc} moves from the bottom fibres of the slab at B to the top fibres at C. Therefore the force F_{conc} has a vertical component which will induce tensile separation between the concrete element and the steel element of the top composite T-section. These tensile forces are resisted by vertical axial tensile forces in the shear connectors that can induce embedment failure as described in Chapter 14.

15.4.2.2 *Equilibrium*

The stress resultants shown in Fig. 15.9(a) can be considered to consist of the local stress resultants shown in Fig. 5.10 that have been separated into the four components in blocks (a) to (d) at the four 'corners' of the service duct. For example, block (d) is applicable to the top T-section at the high moment end. It is assumed in this analysis that the top composite T-section does not act compositely with the bottom steel T-section so that the resultant axial force in each T-section is zero, that is F = 0 in Figs. 15.2 and 15.10. Non-composite action also means that the curvatures in the T-sections are not the same. Hence each T-section is assumed to resist the shear forces separately.

Consider firstly the bottom steel T-section in Figs. 15.10(a) and (b), the cross-section of which is shown in Fig. 15.9(b). The T-section can be considered to be a free body as in Fig. 15.11(b) so that the forces shown are the external forces that are required to maintain equilibrium of the free body. Hence from moment equilibrium at the right hand end

$$V_b a_o \quad = \quad M_{b\ell} + M_{bh} \tag{15.1}$$

It can be seen that the shear forces V_b induce a couple $V_b a_o$ that must be in equilibrium with the end moments $M_{b\ell}$ and M_{bh}. As the shear force increases, the local moments $M_{b\ell}$ and M_{bh} also have to increase to maintain equilibrium. The problem is to find the maximum shear load that will cause the whole section to yield through the action of the shear stresses and flexural stresses, and this can be done using rigid plastic analysis techniques as described in Section 7.5.3. Increasing the duct length a_o in Eq. 15.1 reduces the maximum shear load that can be applied, as it increases the magnitude of the local moments that are required to maintain equilibrium.
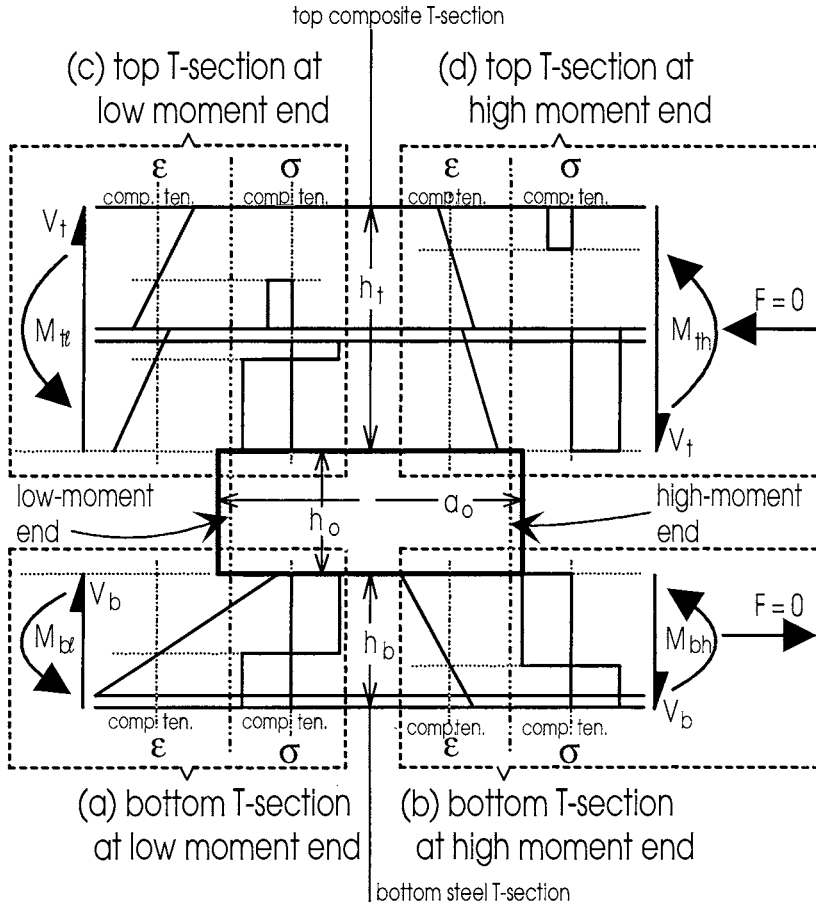
Fig. 15.10 Local stress resultants

Now consider the top composite T-section in Figs. 15.10(c) and (d) with the cross-section shown in Fig. 15.9(b). For equilibrium of the external forces shown in Fig. 15.11(a)

$$V_t a_o \quad = \quad M_{t\ell} + M_{th} \tag{15.2}$$

As in the bottom steel T-section, the problem is to find the maximum shear load that will cause the section to fully yield using the principles of rigid plastic analysis. However, in this case we are dealing with a composite section. The stress and strain distribution at the high moment end in Fig. 15.10(d) follows the standard convention for positive or sagging regions. However, the distribution at the low moment end at (c) is unusual, as the lower fibres of the concrete element are in compression. Furthermore, this latter form of stress distribution in (c) requires a very large slip strain.
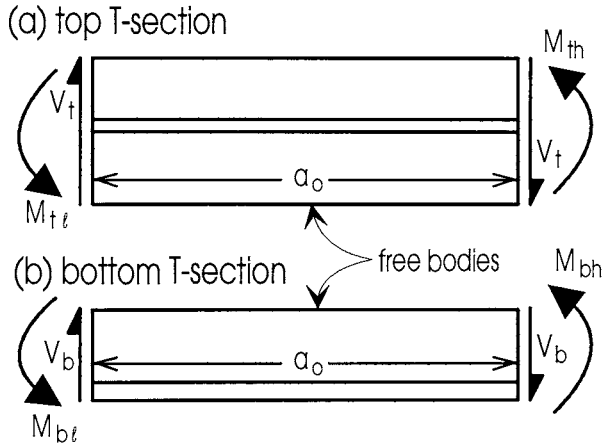
Fig. 15.11 Equilibrium of T-sections

To complete the equations of equilibrium, from Fig. 15.10

$$V = V_t + V_b \tag{15.3}$$

where V is the total shear load as shown in Fig. 15.9 and V_t and V_b are the local shear loads shown in Fig. 15.10.

15.4.2.3 *Iterative solution*

To find the pure shear capacity, it is necessary to determine the combination of shear stresses and flexural stresses that will cause the whole cross-section to yield. We will use von Mises' maximum distortional energy theory in Section 2.2 to allow for the effect of shear on the yield strength as described in Section 7.5.3. Because of the non-linearity of the problem, an iterative solution will be used to find the pure shear capacity.

Re-arranging Eq. 15.1 for the bottom steel T-section gives

$$V_b = \left(M_{b\ell} + M_{bh} \right) \frac{1}{a_o} \tag{15.4}$$

which is shown as the linear variation in Fig. 15.12 where $V = V_b$ and $\sum M = M_{b\ell} + M_{bh}$. Therefore the correct solution lies on the straight line at a slope of $1/a_o$. The procedure used is to first guess a reasonable value for the maximum shear strength such as V_{g1}. By knowing the shear force V_{g1} that is acting on the section, the maximum moment capacity $\left(M_{b\ell} + M_{bh}\right)_{V_{g1}}$ can be calculated as will be shown in Section 15.4.3 and the result plotted as in Fig. 15.12. If the result does not intersect the straight line as shown in this example, then a better value of the shear strength such as V_{g2} can be used and the procedure repeated. The analysis quickly converges to the pure shear capacity of the bottom T-section $(V_b)_{pur}$ as shown. Exactly the same procedure can be applied to determine the pure shear capacity of the top composite T-section $(V_t)_{pur}$. The pure shear capacity of the section V_{pur} being the sum of $(V_b)_{pur}$ and $(V_t)_{pur}$.
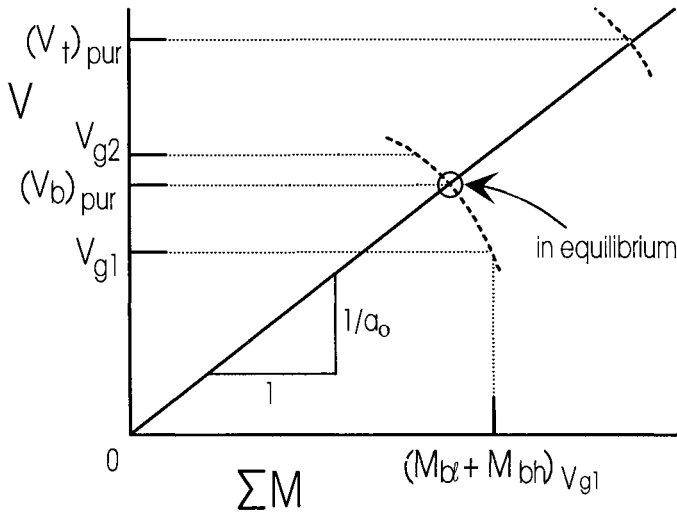
Fig. 15.12 Iterative solution

15.4.3 BOTTOM T-SECTION

15.4.3.1 *General*

It is a very simple procedure to derive the pure shear capacity of the bottom T-section as it is a non-composite steel section. The analysis procedure is illustrated in Fig. 15.13 and follows the general procedure that has been described in Section 7.5.3. Let us start by considering a section at the high moment end of the bottom T-section in Fig. 15.10(b) where the moment M_{bh} is causing compressive strains in the top fibre as shown.
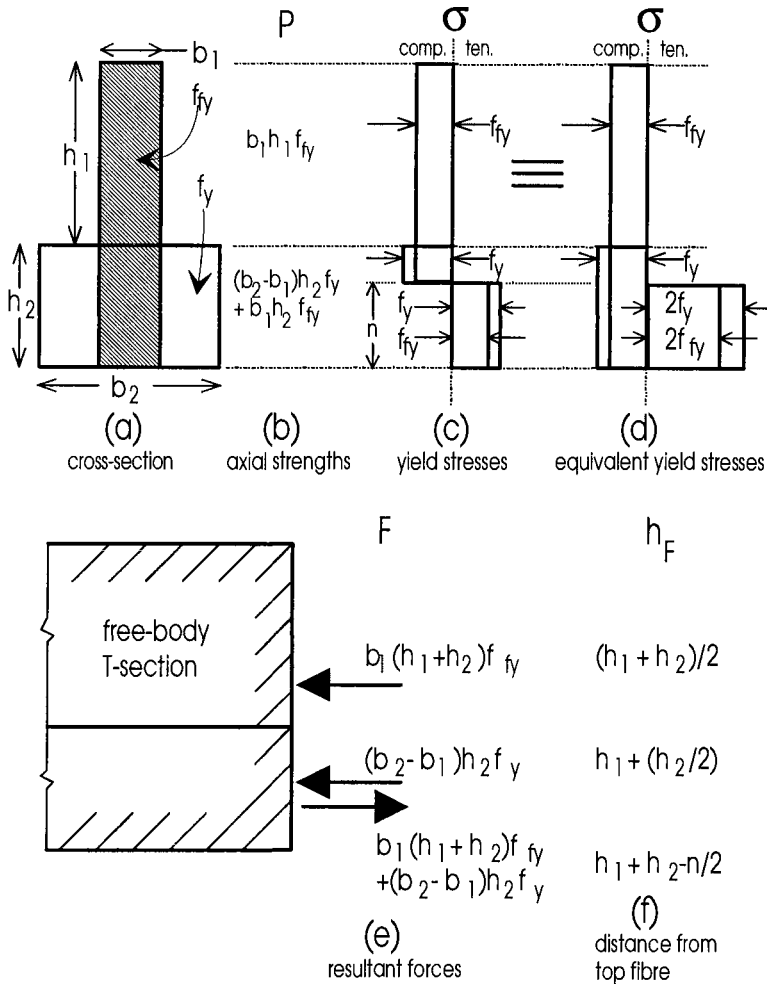
Fig. 15.13 Analysis for pure shear capacity of bottom T-section

15.4.3.2 *High moment end*

The first step is to make an educated guess of the pure shear capacity. This can be done by considering the material shear capacity of the section. It is assumed that the web resists all the shear forces. The area of the web, shown in Fig. 15.13(a), has a depth h_1+h_2 and width b_1. The shear stress to cause yielding is given by Eq. 2.4 as $f_y / \sqrt{3}$, so that the maximum shear capacity derived purely from a material point of view V_{mat} and ignoring the flexural mechanisms required to transfer the shear is given by

$$V_{mat} = \frac{f_y}{\sqrt{3}}(h_1 + h_2)b_1 \tag{15.5}$$

Some proportion of V_{mat} can be used as a first guess say V_g.

The next step is to derive the axial strengths of the rectangular elements in Fig. 15.13(a) as listed in (b). The area of the flange of width b_2-b_1 and depth h_2 is unaffected by the shear forces and so has a yield strength of f_y. The shear forces are assumed to be uniformly distributed over the web, so that the mean shear stress τ_w is given by

$$\tau_w = \frac{V_g}{(h_1 + h_2)b_1} \tag{15.6}$$

Therefore the flexural stress to cause yield in the presence of shear f_{fy} can be derived from Eq. 7.12, and hence the axial strength of the web is as given in (b).

Having derived the axial strengths, the next step is to determine the rectangular element in which the neutral axis lies. This can be done by comparing the axial strength, in Fig. 15.13(b), of the rectangular element of area h_1b_1 in (a) with that of the rectangular element of area h_2b_2. Let us assume in this example that $b_1 h_1 f_{fy} < (b_2 - b_1)h_2 f_y + b_1 h_2 f_{fy}$, in (b), so that the strength of the upper rectangular element in (a) is less than that of the lower element which means that the neutral axis lies within the lower rectangular element.

Let us define the distance from the neutral axis to the bottom fibre as n so that the real stress distribution will be given by Fig. 15.13(c), where the top fibres are in compression because we are dealing with the high moment end, that is M_{bh} in Fig. 15.10(b). This real stress distribution in Fig. 15.13(c) can be used to derive the forces within the system and hence the moment capacity, or alternatively the equivalent stress system in (d) can be used as it simplifies the analytical procedure. Using the equivalent stress system in (d) and equating the compressive forces to the tensile forces gives

$$b_1(h_1 + h_2)f_{fy} + (b_2 - b_1)h_2 f_y = b_1 n(2f_{fy}) + (b_2 - b_1)n(2f_y) \tag{15.7}$$

which can be solved to determine the position of the neutral axis depth n in (d).

Having determined the position of the neutral axis, the stress distribution in Fig. 15.13(d) is now fully defined, so that the resultant forces from this stress distribution can now be determined as in (e) and their position relative to the top fibre as in (f). We are considering equilibrium of the bottom steel T-section in Figs. 15.10(a) and (b), so we need to know the magnitude and direction of the external forces acting on this section. This can be visualised by cutting the section at the ends of the duct at sections B and C in Fig. 15.9(a) to form the free body shown in Fig. 15.11(b), where the stress resultants are the external stress resultants that have to be imposed on the free body to maintain the internal stresses and deformations. The forces in Fig. 15.13(e) have therefore been drawn as the external forces to the free body.

The moment capacity can now be derived by taking moments about a convenient axis which in this case will be at the top fibre. Hence the moment capacity

at the high moment end $(M_{bh})_{Vg}$ is the algebraic summation of the product of the force, in Fig. 15.13(e), and lever arm, in (f). In this case the moment will act in an anti-clockwise direction, because we have assumed that the top fibre strains are in compression as shown by the strain profile corresponding to M_{bh} in Fig. 15.10(b).

We now know that when we apply a shear load V_g to the T-section, the remaining material strength of the section will allow us to apply a maximum moment of $(M_{bh})_{Vg}$. To determine whether the T-section in Fig. 15.11(b) is in equilibrium we also need to determine the moment capacity $M_{b\ell}$ at the low moment end.

15.4.3.3 *Low moment end*

If the cross-section at the low moment end of the bottom T-section in Fig. 15.10(a) is the same as at the high moment end, then the moment capacity at the low moment end will be the same as at the high moment end. Hence for the same imposed shear force V_g, $(M_{b\ell})_{Vg} = (M_{bh})_{Vg}$ which has already been determined in the previous section. This is because we are dealing with a non-composite section made from a material which is assumed to have identical compressive and tensile characteristics.

It is worth noting that because the end moments, shown in Fig. 15.11(b), are of equal magnitude but of opposite direction, a point of contraflexure exists mid-way between the ends of the bottom T-section.

15.4.3.4 *Equilibrium*

We can now plot the point $(V_{g1}, (M_{b\ell} + M_{bh})_{V_{g1}})$ in Fig. 15.12, to determine whether the stress resultants are in equilibrium, that is whether the point lies on the line at a slope of $1/a_o$. The procedure can be repeated until the stress resultants are in equilibrium, to give us the maximum shear force than can be applied to the bottom T-section $(V_b)_{pur}$.

Example 15.3. Pure shear capacity of bottom steel T-section

The pure shear capacity of the bottom T-section in the composite beam in Fig. 15.5 is determined. The analysis of the high moment end is given in Fig. 15.14 and follows the steps illustrated in Fig. 15.13.

From Eq. 15.5, the maximum shear load based on material strengths is $V_{mat} = 289$ kN. It is the shear strength of the T-section when the length of the duct $a_o = 0$. For example in Eq. 15.1, when $a_o = 0$ then $V_b a_o = 0$, hence the flexural forces $M_{b\ell} + M_{bh} = 0$, so that only the shear load V_b exists to induce yielding in the steel. The pure shear capacity is therefore less than 289 kN and as a first guess we will assume that it is $V_g = 100$ kN. Hence from Eq. 15.6, the mean shear stress is $\tau_w = 50$ N/mm^2 and from Eq. 7.12 the flexural stress to cause yield in the presence of shear is $f_{fy} = 235$ N/mm^2.

The cross-section of the T-section is shown in Fig. 15.14(a) and the axial strengths in (b). As the strength of the top rectangular element (437 kN) is less than

that of the bottom rectangular element (698 kN), the neutral axis must lie in the bottom rectangular element as shown in (d). The equivalent yield stress distribution in (d) assumes that the whole section is fully yielded in compression and that the section below the neutral axis is also subjected to tensile stresses of twice the yield stress. Hence the summation of these stresses gives the true stress distribution. Equating the forces as in Eq. 15.7 gives the position of the neutral axis as n = 11.4 mm from the bottom fibre.

The resultant forces are shown in Fig. 15.14(e). The compressive force in the web over the full depth of 200 mm is 470 kN and acts at a distance of 100 mm from the top fibre as shown in (f). The compressive force in the remainder of the steel section is 665 kN and acts at mid-depth of the flange at 193 mm from the top surface. The tensile forces below the neutral axis are of equal magnitude to the compressive forces and act at n/2 from the bottom fibre which is 194.3 mm from the top fibre. Taking moments gives the moment capacity as $(M_{bh})_{100kN}$ = 45 kNm when a shear load of V_g = 100 kN is applied. The moment capacity at the low moment end is the same so $(M_{b\ell})_{100kN}$ = 45 kNm

From Fig. 15.5, a_o = 0.8 m, and from equilibrium of the free body shown in Fig. 15.11(b), the couple induced by the shear load $V_b a_o$ = 80 kNm and this is resisted by a moment of $(M_{b\ell} + M_{bh})_{100kN}$ = 90 kNm. Hence the system is not in equilibrium with regard to Eq. 15.1. The results are also plotted as point A in Fig. 15.15 and also plotted is the equilibrium line from Eq. 15.4. It can be seen that the shear load can be increased. A further calculation at V_g = 150 kN gives $(M_{b\ell} + M_{bh})_{150kN}$ = 83 kNm and this is plotted as point B. The intersection of a line between points A and B with the equilibrium line (at a slope of 1.25) therefore occurs at $(V_b)_{pur}$ ≈ 110 kN. Although not required, the remainder of the curve is plotted in Fig. 15.15. At point C, the shear load is zero and the sum of moments is 96 kNm. At point D, the maximum shear load of 289 kN is applied so that the web is fully yielded and hence the moment resistance is only provided by the flange.
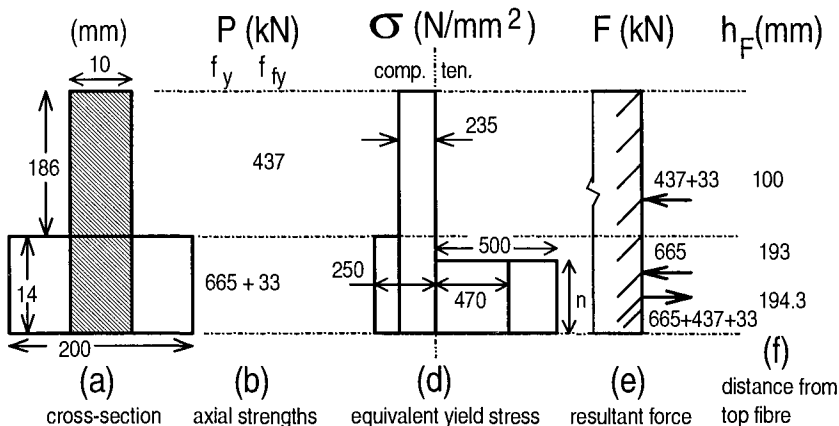
Fig. 15.14 Example 15.3: Pure shear capacity of bottom T-section
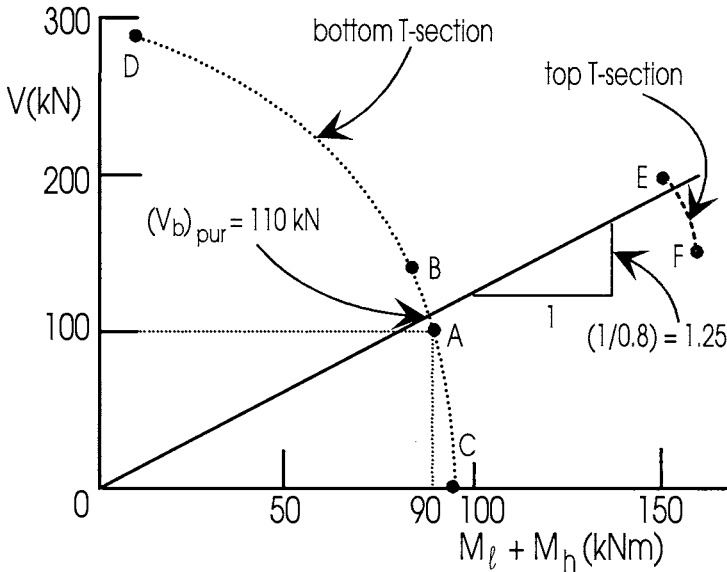
Fig. 15.15 Pure shear capacity of beam in Fig. 15.5

15.4.4 TOP T-SECTION

15.4.4.1 *General*

Derivation of the pure shear capacity of the top T-section such as in Figs. 15.10(c) and (d) is more complex than that of the bottom T-section because we are now dealing with a composite section. The high moment end at (d) will be dealt with first in Section 15.4.4.2 as this section often affects the strength at the low moment end. The behaviour at the low moment end at (c) is dealt with in Section 15.4.4.3 where it will be shown that we are dealing with an unusual stress and strain distribution, as shown in (c), that can cause reversals in the resisting moments.

15.4.4.2 *High moment end*

Consider the high moment end of the top composite T-section at section C in Fig. 15.9(a). At section C, the strength of the shear connectors in shear span A-C will be referred to as P_{A-C}. The deformation and stresses in this section are shown in Fig. 15.10(d) and the cross-section at Fig. 15.16(a).

As in the analysis of the bottom steel T-section in Section 15.4.3, the first step is to make an informed guess of the pure shear capacity. A conservative approach to the analysis would be to assume that the concrete element of area $b_3 h_3$ in Fig. 15.16(a) does not directly resist the vertical shear stresses, so that the vertical shear stresses are only resisted by the steel web of area $b_1(h_1+h_2)$, as in the analysis of the bottom steel T-section. Therefore, the theoretical maximum shear load $V_{material}$ is given by Eq. 15.5.

This can be used to make the informed guess of the pure shear capacity V_g, the mean shear stress τ_w from Eq. 15.6 and hence from Eq. 7.12 the flexural stress to cause yield in the presence of shear f_{fy}.
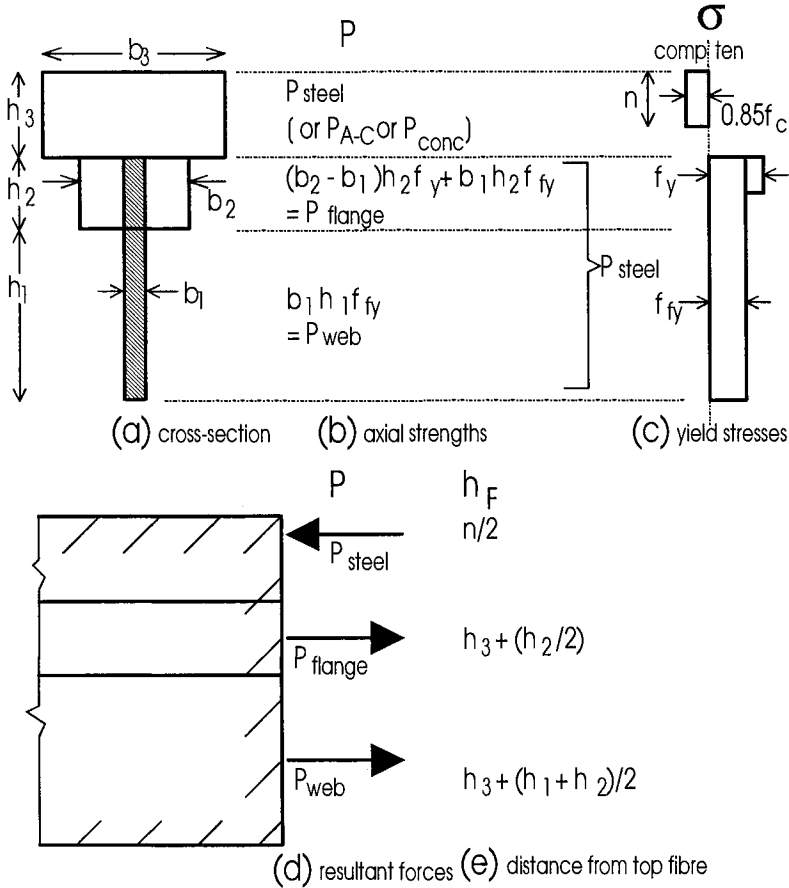
Fig. 15.16 Composite T-section at high moment end

The axial strength of the steel element $P_{steel} = P_{flange} + P_{web}$ can now be determined as shown in Fig. 15.16(b). The force in the concrete element F_{conc} is the minimum of the strength of the concrete element $P_{conc} = 0.85f_cb_3h_3$, the strength of the steel element P_{steel}, and the strength of the shear connectors P_{A-C} in the shear span A-C in Fig. 15.9(a). Rarely will P_{conc} control design in a composite T-section, so that F_{conc} is usually governed by P_{A-C} or P_{steel} depending on the position of the duct along the length of the composite beam. We will assume in this example that $P_{steel} < P_{A-C}$, so that the resultant force in the concrete element $F_{conc} = P_{steel}$ and, therefore, the resultant force in the steel element $F_{steel} = P_{steel}$ and the resultant in the shear connectors $F_{A-C} = P_{steel}$.

As we are assuming in this example that $P_{steel} < P_{A-C}$, the shear connectors in the shear span A-C in Fig. 15.9(a) will not be fully loaded so that we are now dealing with a section that has full shear connection. The fact that the shear connectors are not fully loaded in shear span A-C will not affect the capacity at section C, as this has full shear connection, but will affect the capacity at the low moment end at section B which will have partial shear connection. In the analysis of the low moment end at section B, we will assume that the connectors are uniformly loaded along the shear span A-C with a total force of P_{steel}. Hence the force in the connectors in shear span A-B, F_{A-B}, is given by

$$F_{A-B} = P_{A-B} \frac{P_{steel}}{P_{A-C}} \tag{15.8}$$

where P_{A-B} is the strength of the shear connectors in shear span A-B in Fig. 15.9(a). The shear force F_{A-B} in the connectors is also the resultant axial force in the concrete element and the resultant axial force in the steel element at section B.

Having determined the axial strengths in Fig. 15.16(b), the next step is to determine the rectangular element in (a) though which the neutral axis passes. As a conventional strain distribution exists at the high moment end, as shown in Fig. 15.10(d), we can derive the neutral axis by using the standard procedure of determining the level at which the compressive strength above the neutral axis is equal to the tensile strength below. In this example in Fig. 15.16, the neutral axis will lie in the concrete element, as we have assumed that P_{steel} controls design, and so the stress distribution is as shown in (c). The depth of the neutral axis n can be derived by equating $P_{steel} = 0.85 f_c b_3 n$.

Having defined the stress distribution, the magnitude and position of the resultant forces can be derived as in Fig. 15.16(d) and (e) and hence the moment capacity can be determined by the algebraic summation of the products of (d) and (e). This will give the moment capacity M_{th} in Fig. 15.11(a) that is in an anti-clockwise direction which we will define as positive.

Example 15.4. Local moment capacity to resist shear at high moment end of composite T-section

The local flexural capacity, that is available to resist shear, of the top composite T-section at the high moment end in Fig. 15.5(a) is determined. The analysis is summarised in Fig. 15.17 and follows the procedure outlined in Fig. 15.16.

Since the cross-section of the steel element in Fig. 15.17(a) is the same as that of the bottom steel T-section, shown in Fig. 15.14(a), the maximum material shear capacity of the two sections is the same so that $V_{mat} = 289$ kN from Example 15.3 or Eq. 15.5. As the pure shear capacity of the bottom T-section was found to be 110 kN in Example 15.3, we will choose a starting value between 110 kN and 289 kN, say $V_{g1} = 200$ kN. From Eq. 15.6, $\tau_w = 100$ N/mm^2 and from Eq. 7.12, $f_{fy} = 180$ N/mm^2. The axial strengths of the steel component can now be derived and are listed in Fig. 15.17(b) where it can be seen that $P_{steel} = 1025$ kN.

From Example 15.1, the strength of the shear connectors required for full shear connection is 2830 kN. The composite beam in Fig. 15.5(a) was designed with full shear connection at mid-span and with a uniform distribution of shear connectors, so that the degree of shear connection at section C is $\eta = 4.4/8 = 0.55$. Therefore, the strength of the shear connectors in shear span A-C is $P_{A-C} = 0.55 \times 2830 = 1557$ kN. This is shown in Fig. 15.17(b) as a possible force in the concrete element. The axial strength of the concrete element, $P_{conc} = 3825$ kN, and that of the steel element, $P_{steel} = 1025$ kN, are also shown as possible forces. The minimum of these three forces, $P_{steel} = 1025$ kN, controls the analysis, so that the steel is fully yielded in tension as shown in (c). The resultant forces and their positions are given in (d) and (e), leading to an anti-clockwise moment capacity of $M_{th} = +179$ kNm.

It is worth determining at this stage of the analysis the force in the shear connectors in shear span A-B in Fig. 15.5, as this force is required for the following analysis at the low moment end. The force in the connectors in shear span A-C in Fig. 15.5 is equal to the resultant force in the concrete element as well as the resultant force in the steel element, that is $F_{A-C} = F_{conc}$ (in Fig. 15.17(b)) = 1025 kN. This is less than the strength of the shear connectors over the same shear span A-C which is $P_{A-C} = 1557$ kN. Therefore the connectors in the shear span A-C are not fully loaded, however we will assume that they are uniformly loaded. Hence the force in the connectors in the shear span A-B is $F_{A-B} = (3.6/4.4) \times 1025 = 839$ kN, as the shear span A-B is 3.6 m and the shear span A-C is 4.4 m.
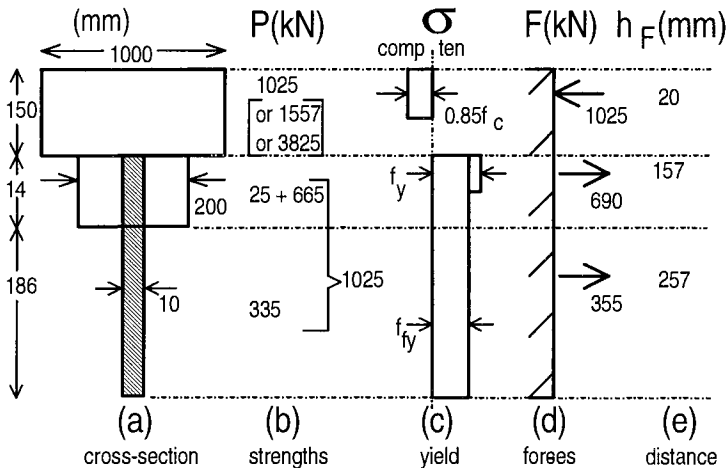
Fig. 15.17 Example 15.4: Pure shear capacity of top T-section at high moment end

15.4.4.3 *Low moment end*

Consider the low moment end of the top composite T-section at section B in Fig. 15.9(a). The deformation of this section produces an unusual distribution of stresses

and strains as shown in Fig. 15.10(c). The distributions are different from the familiar hogging and sagging distributions in composite beams, already described in Chapter 7, because part of the concrete element must always be in compression in order to resist the thrust from the connectors in the shear span A-B in Fig. 15.9(a). The curvature of the top T-section at B requires the strain profile in Fig. 15.10(c) in which there is a large slip strain at the concrete/steel interface.

The analysis of the section is described diagramatically in Fig. 15.18. The axial strengths of the steel element in (b) are determined in the same way as the axial strengths at the high moment end, that has been described in the previous section. The maximum force that can be applied to the concrete element, F_{conc}, is the minimum of the four possible forces shown adjacent to the concrete element in (b), these are: the strength of the steel element P_{steel}; the strength of the concrete element P_{conc}; the strength of the shear connectors P_{A-B} in shear span A-B in Fig. 15.9; and the maximum force in the connectors F_{A-B} in shear span A-B when the connectors are not fully loaded, as described in the previous section and given by Eq. 15.8. In this example, which is a continuation of the example described in the previous section, we will assume that F_{A-B} controls the analysis, because P_{steel} controlled the analysis at the high moment end.

The strain profile required for the deformations induced at the low moment end in Fig. 15.9(a) is shown in Fig. 15.18(c) and this produces the stress profile in (d). The lower fibres of the concrete element are in compression in order to resist the thrust from the shear connectors. The bottom fibres of the steel element are also in compression so that the tensile component is sandwiched between the two compressive components. Therefore, the position of the neutral axis cannot be derived using the standard procedure of finding a level at which the strength above is equal to the strength below, because the strength above may be a combination of tensile and compressive strengths. Instead it is necessary to compare the strengths of the elements which are likely to go into compression with those which are likely to go into tension. For example, if $F_{A-B} > P_{steel}$, then all the steel will have yielded in tension, so that the force in the shear connectors in shear span A-B in Fig. 15.9 will be P_{steel}. This is unlikely to occur unless the steel section at the low moment end is smaller than that at the high moment end. Much more likely to occur is when $F_{A-B} < P_{steel}$ in Fig. 15.18(b), then the neutral axis must lie in the steel element. Furthermore, if $(F_{A-B} + P_3) > (P_1 + P_2)$, then the neutral axis must lie in the web as shown in (c). Alternatively, if $(F_{A-B} + P_3) < (P_1 + P_2)$, then the neutral axis must lie in the flange.

Let us assume in this example in Fig. 15.18 that the neutral axis in the steel element lies in the flange as shown in (c), then the stress distribution is as shown in (d) which is equivalent to the stress distribution in (e). Equilibrium of the forces in (e) gives

$$F_{A-B} + P_{steel} = P_1 + b_1(h_1 + h_2 - n)2f_{fy} \tag{15.9}$$

which can be solved to first determine the position of the neutral axis n, then the resultant forces and their position in (f) and (g), and hence the magnitude and direction of the resisting moment $M_{t\ell}$ in Fig. 15.11(a).
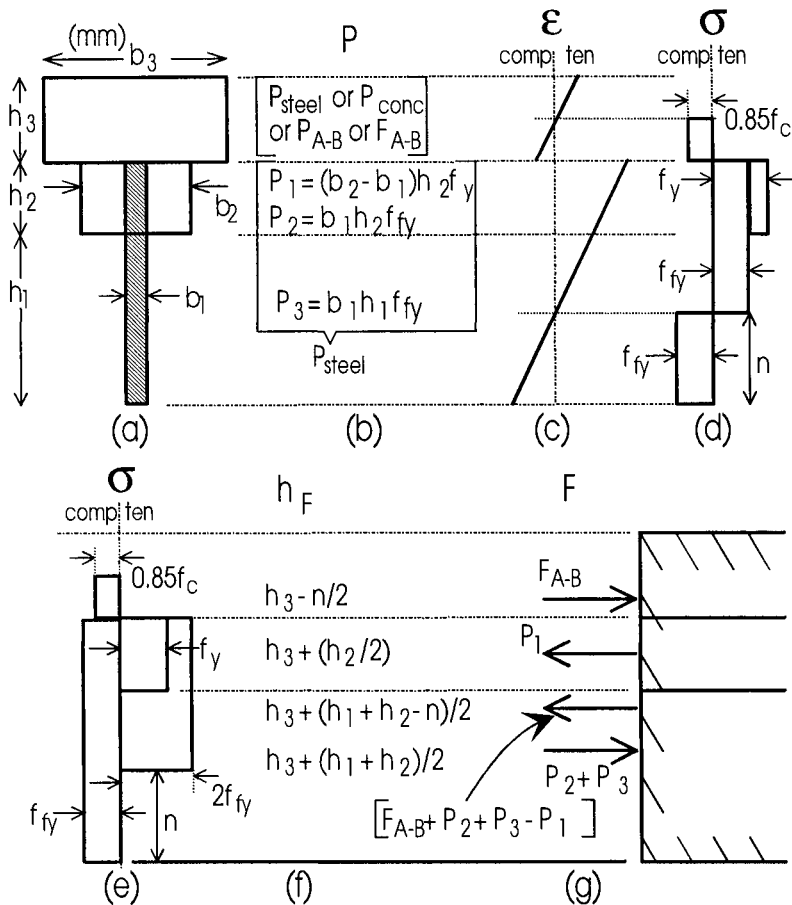
Fig. 15.18 Composite T-section at low moment end

The direction of the resisting moment derived from Fig. 15.18 (f) and (g) can vary. For example, consider a section at the low moment end of a duct that is close to the supports, so that the force in the connectors F_{A-B} in Fig. 15.18(b) can be assumed to be zero. This situation is shown in Fig. 15.19(a). As there are no compressive forces in the concrete, the strain in the concrete can be fully tensile as shown so that the concrete is cracked through its depth. The resisting moment $M_{t\ell}$, shown as a couple in the force profile F in (a), acts in an anti-clockwise direction (positive). Therefore the resisting moment $M_{t\ell}$ in Fig. 15.11(a) is acting in the same direction as that at the high moment end M_{th}, and so it increases the resistance to $V_t a_0$ and hence increases the shear capacity.

Consider a duct in which the low moment end is at a section in which F_{A-B} (in Fig. 15.18(b)) = P_{steel}, in which case the stress distribution is as shown in Fig. 15.19(b). In this case, all of the steel must be in tension in order to maintain

equilibrium with the compressive force in the concrete that resists the thrust of the shear connectors. The curvature of the section must be the same as that shown in Fig. 15.18(c), in order to accommodate the deformations at this section. This can be accomplished with the strain profile shown in Fig. 15.19(b) in which there is a very large slip-strain to allow all the steel to be in tension. The resultant forces are shown in the force profile F in (b) and these induce a clockwise (negative) resisting moment. The resisting moment $M_{t\ell}$ in Fig. 15.11(a) is therefore in an opposite direction to that shown, so that the secondary moment that resists $V_t a_o$ is reduced to $M_{th} - M_{t\ell}$, and hence in this situation $M_{t\ell}$ reduces the shear capacity as it acts in the opposite direction to M_{th}.
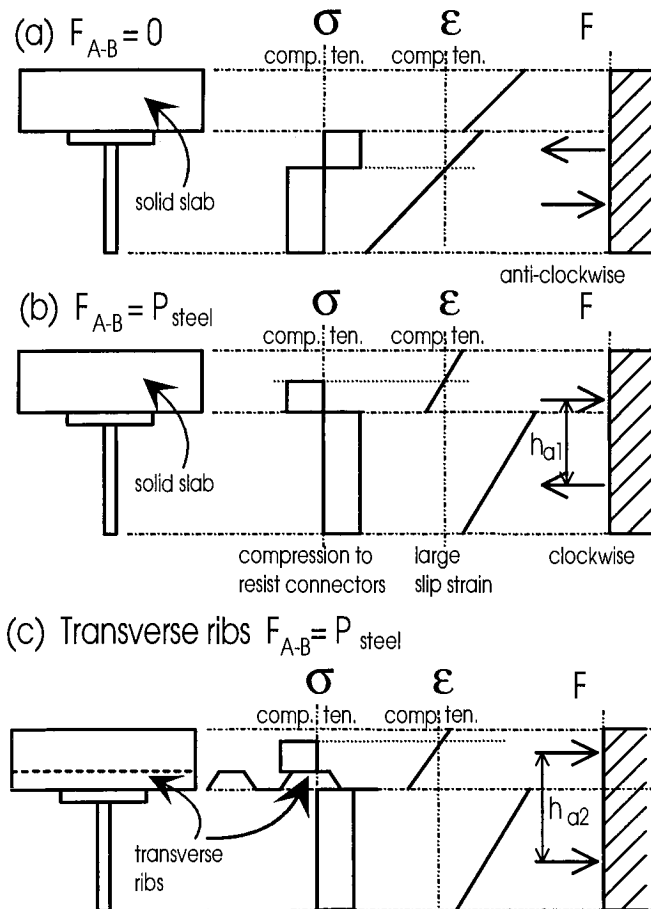
Fig. 15.19 Resisting moment

It is also worth noting the effect of the presence of transverse ribs in the concrete element, as shown in Fig. 15.19(c). Let us consider the case of $F_{A-B} = P_{steel}$ in both (b) and (c). The compressive zone must lie above a rib as shown in Fig. 15.19(c). The rib therefore increases the lever arm from h_{a1} in the composite beam

with a solid slab in (b) to h_{a2} for the composite beam with the transverse steel decking in (c). Therefore, the transverse ribs have increased the lever arm, thereby increasing the negative resisting moment described in the previous paragraph and hence reduces the resistance to shear.

Example 15.5. Local moment capacity to resist shear at low moment end of composite T-section

The local flexural capacity available to resist shear at the low moment end of the composite T-section in Fig. 15.5 is derived. This is a continuation of the analysis in Example 15.4 in which $V_g = 200$ kN.

     The analyses are shown in Fig. 15.20 and follow the procedures outlined in Fig. 15.18. The axial strengths in Fig. 15.20(b) were derived in Example 15.4 where F_{conc} = 839 kN is the force on the shear connectors in shear span A-B in Fig. 15.5. As F_{conc} (839 kN) is less than P_{steel} (1025 kN), the neutral axis must lie in the steel element. As $F_{conc} + P_3$ (1174 kN) is greater than $P_1 + P_2$ (680 kN), the neutral axis must lie in the web. Therefore, this section has the strain profile shown in Fig. 15.18(c) and the equivalent stress distribution in (e) where n can be derived from Eq. 15.9, which gives the resultant forces in Fig. 15.20(d) that act at the distance (c) from the top fibre. The resulting moment resistance from (c) and (d) gives a moment capacity of 27 kNm that acts in a clockwise direction, that is $M_{t\ell} = -27$ kNm as it acts in the opposite direction to that shown in Fig. 15.11(a).
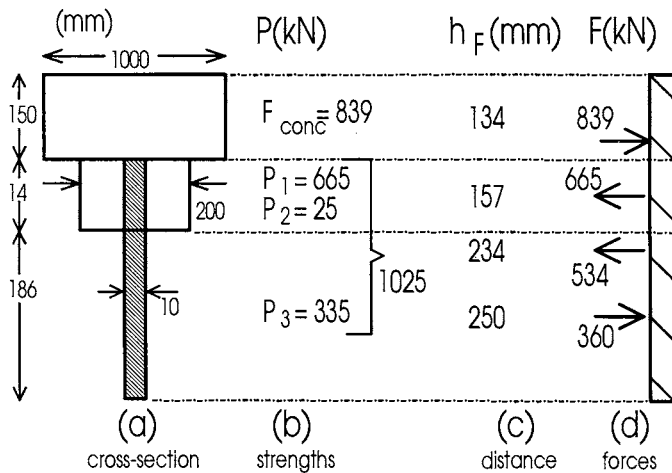
Fig. 15.20 Example 15.5: Pure shear capacity of top T-section at low moment end

15.4.4.4 *Equilibrium*

Having derived the flexural capacity at the high moment end, M_{th} in Fig. 15.11(a), and at the low moment end, $M_{t\ell}$, for a specific shear force V_t, it is necessary to ensure that

the system is in equilibrium, that is it satisfies Eq. 15.2 as described in Section 15.4.2.2. If the system is not in equilibrium, then a better estimate of the pure shear capacity has to be made using the iterative procedure described in Section 15.4.2.3, which entails plotting the results on a graph such as in Fig. 15.12.

Example 15.6. Pure shear capacity of top composite T-section

We will continue the analysis of the top composite T-section of the composite beam in Fig. 15.5.

From Example 15.4, $M_{th} = +179$ kNm as it acts in an anti-clockwise direction as in Fig. 15.11(a). From Example 15.5, $M_{t\ell} = -27$ kNm as it acts in a clockwise direction. The shear load used in these analyses was $V_g = 200$ kN and the length of the duct $a_o = 0.8$ m. The couple induced by the shear forces is therefore $V_g a_o = 160$ kNm and the resisting moments is $M_{th} + M_{t\ell} = 179 - 27 = 152$ kNm. So the system is not quite in equilibrium, and the results have been plotted in Fig. 15.15 as point E. An analysis of the section at $V_g = 150$ kN, gives $M_{th} = +188$ kNm and $M_{t\ell} = -28$ kNm, so that the sum of moments is 160 kNm and this is plotted as point F. The intercept with the equilibrium line occurs at $(V_t)_{pur} \approx 190$ kN.

It is worth noting here that the pure shear capacity of the bottom steel T-section was found in Example 15.3 to be 110 kN, whereas the top composite T-section is 190 kN. In this example, the steel element in both the top and bottom T-sections is identical so that the increase in strength of 80 kN, from 110 kN to 190 kN, is due to the composite action. It is also worth remembering that it was assumed that the concrete element did not resist any vertical shear stresses directly, so that the increase in the shear capacity is due to the increase in the flexural capacity due to the composite action. Furthermore, because M_{th} does not equal $M_{t\ell}$ the point of contraflexure does not lie at the mid-length of the duct, as in the bottom T-section, but can lie outside the region of the duct, further emphasising the point that the two T-sections are assumed to act separately when subjected to vertical shear forces.

15.4.5 PURE SHEAR CAPACITY

The pure shear capacity of the composite beam at a duct V_{pur} is simply the summation of the pure shear capacities of the bottom T-section $(V_b)_{pur}$, from Section 15.4.3, and the top T-section $(V_t)_{pur}$, from Section 15.4.4.

Example 15.7. Pure shear capacity of composite beam at service duct

We will now complete the analysis of the top composite T-section of the composite beam in Fig. 15.5.

From Example 15.3, $(V_b)_{pur} = 110$ kN and from Example 15.6, $(V_t)_{pur} = 190$ kN, therefore the pure shear capacity of the composite beam over the whole length of the duct is $V_{pur} = 300$ kN.

15.5   Interaction between shear and flexure

The method for determining the pure flexural capacity at the high moment end of the duct $(M_h)_{pur}$ and at the low moment end of the duct $(M_\ell)_{pur}$ has been described in Section 15.3, and the method for determining the pure shear capacity at the high moment end $(V_h)_{pur}$ and at the low moment end $(V_\ell)_{pur}$ has been described in Section 15.4. Therefore, we know two points of the failure envelope for the composite beam at both the high moment end and at the low moment end of the service duct, that is point A in Fig. 15.21 where the flexural capacity is M_{pur}, because the shear force is zero, and at point B where the shear capacity is V_{pur}, because the composite flexural force is zero. Between points A and B, where there is an interaction between the shear and flexural forces, we will refer to the moment capacity as M_{int} and to the shear capacity as V_{int} as shown.
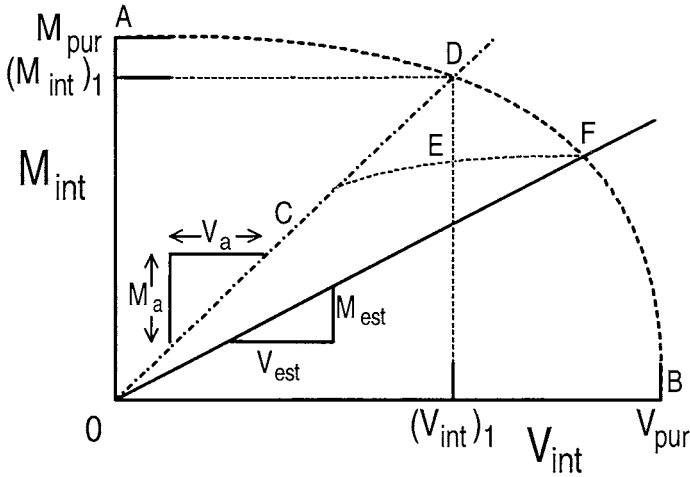
Fig. 15.21 Interaction between shear and flexure

The failure envelope defined by M_{int} and V_{int} in Fig. 15.21 is difficult to determine theoretically. Darwin (1988) showed experimentally that the interaction between the shear forces and the flexural forces is very weak and proposed the following failure envelope

$$\left(\frac{M_{int}}{M_{pur}}\right)^3 + \left(\frac{V_{int}}{V_{pur}}\right)^3 = 1 \tag{15.10}$$

which is shown in Fig. 15.21. Redwood and Poumbouras (1984) proposed a different failure envelope that also assumed a weak interaction, and because the interaction is very weak it does not really matter which is used in the analysis. The interaction in

many national steel standards is also often represented as a weak relationship, often of three straight lines.

For a statically determinate beam, the ratio M_a/V_a between the applied moment M_a and the applied shear force V_a, at the section being considered, is constant. Therefore as the beam is loaded, the applied forces follow line C in Fig. 15.21 so that we require to determine the intercept of the failure envelope with the load line C, that is the coordinates $(V_{int})_1$ and $(M_{int})_1$ at point D, where

$$\frac{M_{int}}{V_{int}} = \frac{M_a}{V_a} \tag{15.11}$$

Re-arranging Eq. 15.10 and substituting Eq. 15.11 gives

$$M_{int} = M_{pur}\left[\frac{\left(\dfrac{M_{pur}}{V_{pur}}\right)^3}{\left(\dfrac{M_a}{V_a}\right)^3}+1\right]^{-\frac{1}{3}} \tag{15.12}$$

which can be used to derive the reduced flexural capacity directly.

For statically indeterminate beams, the ratio M_a/V_a will vary once redistribution of the applied moment occurs through material non-linearity as was discussed in Chapter 9, and which is shown by the curve E in Fig. 15.21. In this case, an iterative procedure will have to be applied. For example, the ratio of the applied stress resultants will have to be estimated such as $M_a/V_a = M_{est}/V_{est}$ in Fig. 15.21. Applying this ratio to Eq. 15.12 will give M_{int}. The applied shear load to give an applied moment M_{int} can then be determined if the amount of redistribution is known, and the ratio of these stress resultants can compared with the original estimate of M_{est}/V_{est} to see if it was correct. If not, a new ratio can be assumed and the procedure repeated.

Example 15.8. Flexural capacity at service duct

Let us now complete the analysis of the composite beam in Fig. 15.5.

Consider the high moment end of the duct at section C in Fig. 15.5. The beam is subjected to a point load at mid-span, so that $M_a/V_a = 4.4$ m. From Example 15.1, $M_{pur} = 881$ kNm; and from Example 15.7, $V_{pur} = 300$ kN. Substituting these values into the square bracket in Eq. 15.12 gives 0.92, that is the flexural capacity is 92% of the pure flexural capacity M_{pur}, which comes to $M_{int} = 808$ kNm. Hence the shear force has reduced the flexural capacity by 8%.

Consider finally the low moment end of the duct at section B in Fig. 15.5 where the ratio $M_a/V_a = 3.6$ m. From Example 15.1, $M_{pur} = 853$ kNm; and from Example 15.7, $V_{pur} = 300$ kN. Substituting into the square bracket in Eq. 15.12 gives

0.88, that is the shear force has reduced the flexural capacity by 12% so that $M_{int} =$ 746 kNm.

15.6 Detailing

The procedures described in this Chapter are based on rigid plastic flexural analyses. Detailing rules are therefore required to allow for the effects of local buckling and stress concentrations, and these are provided elsewhere in detail by Darwin (1988) and Patrick and Poon (1989).

Distortion of the steel web around the duct is restricted by placing limits on the shape and size of the duct relative to the depth of the web of the steel element. Local buckling is prevented by placing limits to the slenderness of the web and can also be eliminated by stiffening the opening. The effect of load concentrations is reduced by ensuring that the duct is not too close to supports, applied concentrated loads and adjacent ducts. Separation of the concrete element from the top steel T-section, as described in Section 15.4.2.1 is restricted by requiring a minimum number of shear connectors and a minimum amount of longitudinal reinforcing bars in the region of the duct.

15.7 References

Cho, S.H. and Redwood, R.G. (1986). "The design of composite beams with web openings", Structural Engineering Series No. 86-2, Department of Civil Engineering and Applied Mechanics, McGill University, Montreal, Canada, June.

Darwin, D. (1984). "Composite beams with web openings", Proceedings National Engineering Conference, AISC, Tampa, Florida, U.S.A, March.

Darwin, D. (1988). "Draft -Design of steel and composite beams with web openings", American Iron and Steel Institute, U.S.A..

Narayanan, R. (1988). *Steel-Concrete Composite Structures, Stability and Strength*, Elsevier Applied Science, London.

Patrick, M. and Poon, S.L. (1989). *Composite Beam Design and Safe Load Tables.* Australian Institute of Steel Construction, Sydney.

Redwood, R.G. and Poumbouras, G. (1983). "Tests of composite beams with web holes", Canadian Journal of Civil Engineering, Vol. 10, No. 4, 713-21.

Redwood, R.G. and Poumbouras, G. (1984). "Analysis of composite beams with web openings", Journal of Structural Engineering, ASCE, Vol. 110, No. 9, 1949-58.

Redwood, R.G. and Wong, P.P.K. (1982). "Web holes in composite beams with steel deck", Proceedings 8th Canadian Structural Engineering Conference, Canadian Steel Construction Council, Vancouver, February.

16   Composite Profiled Slabs and Profiled Decking

16.1   Introduction

In Parts 3, 4 and 5 of this book, we have dealt primarily with one-way composite T-beams, consisting usually of a steel I-section element which is composite with a fairly narrow concrete slab. In bridges, it is usual to construct the narrow concrete element with conventional formwork which is stripped after the concrete has cured, so that its soffit is flat. A slab in a building is one for which the thickness is usually an order of magnitude less than the geometric dimensions such as length and slab width, and these are generally constructed by using light-gauge cold formed steel profiled decking as the soffit, as in Fig. 1.3(c).

Composite profiled slabs constructed from profiled decking have two major advantages over slabs with off-form soffits. Firstly, the decking provides permanent and integral formwork for the slab during construction, so that it is not necessary to strip the timber forms as would be required for a flat soffit slab. The ribs in the sheeting provide a reasonably high flexural rigidity, so that the construction loads consisting largely of the wet concrete can be resisted without falsework, making access to the storey below freely available. Moreover, because the sheeting has a typical thickness of only 1.0 or 1.5 mm, the stud shear connectors can be welded directly through the sheeting onto the flange of the steel I-section element.

The second major advantage of composite profiled slabs accrues to their composite behaviour under live loading. Once the concrete has hardened, the steel decking acts as tensile reinforcement to the concrete slab, thereby eliminating or reducing greatly the need for conventional tensile reinforcement. Lighter fabric or mesh reinforcement is only needed for slab shrinkage control and for fire. Composite profiled slabs have reduced thicknesses over their reinforced concrete counterparts, so that dead loads are reduced, with consequent smaller column sizes needed was well as smaller foundation loads.

The ribs of the profiled decking may be parallel to the steel element, as shown in Fig. 1.11(b), in which case we have one-way composite action. However, it is more usual to place the ribs orthogonal to the steel element, since it is desirable for economy to have the latter more widely spaced. For this case, which is shown in Figs. 1.9(d) and 1.11(c) and considered in the remainder of this chapter, the composite action is two-way, and bending in the plane of the web of the steel I-section element is resisted by the composite T-beam, while bending orthogonal to the web of the I-section element is resisted by the action of the composite slab. Of course, it is also possible for the ribs of the profiled sheeting to be placed skew to the steel I-section element, as shown in Fig. 4.5.

Although the structural system of using thin profiled decking for the soffit of composite slabs is now both widespread and extremely simple to implement in

practice, research into the various aspects of the system has been far from exhaustive, with the range of parameters over which the mainly empirical design rules are applicable being somewhat limited. This chapter aims to describe the fundamental behaviour of a composite profiled slab system, by considering firstly aspects germane to the steel decking during the construction phase. Included in this are the material behaviour of the sheeting and its response to wet concrete loading. The main behavioural aspects of the composite slab are its interaction with the concrete, and this was touched on in Section 1.1.2. Composite beam behaviour in the direction of the steel element has been the subject of much of this book, and the modifications of predictions of behaviour that are needed for composite profiled slabs where the composite action is orthogonal to the steel element are discussed. Finally, the response to fire, which is of great importance in office building application, is touched upon.

16.2   Behaviour of steel decking during construction loading

16.2.1   GENERAL

Profiled steel decking is made from thin cold formed steel of thicknesses typically 1.0 or 1.5 mm. Trapezoidal profiles, with typical dimensions in Fig. 16.1(a) are most often deployed, but dove-tail profiles as in (b) may also be used. Dove tails may also be cold rolled into the flanges of trapezoidal profiles, as in (a). The profiles are embossed, as shown in Fig. 1.6, in order to achieve composite slab action between the steel sheeting and the concrete by shear bonding.
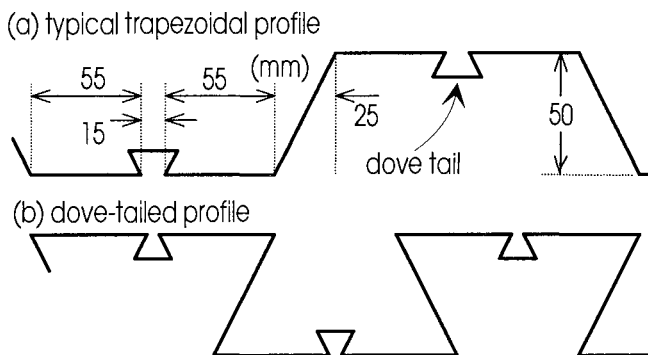
Fig. 16.1 Decking profiles

16.2.2   MATERIAL PROPERTIES

16.2.2.1   *Constitutive relationship*

Profiled steel sheeting is manufactured by cold rolling thin steel plate into a cold formed shape: either trapezoidal, dove tailed or L-shaped, as in Figs. 1.6 and 16.1. The constitutive stress versus strain relationship, needed for determining the response of the sheeting to construction loading, differs from that usually observed for mild

steel (as discussed in Section 2.2) which is applicable to the steel element of a composite beam. In addition, the stamping or rolling of embossments into the profiled steel sheeting has a measurable effect on its stress-strain response in much the same way that residual stresses affect mild steel shapes.

Tensile coupons of cold formed sheeting typically have a linear stress-strain curve, of modulus E_s, over a substantial loading range. Rather than exhibiting a well-defined yield point, as with mild steel, the stress-strain curve becomes nonlinear and rounded past the limit of proportionality, as shown in Fig. 16.2. The difficulty in quantifying the limit of proportionality means that a proof stress f_{yp} is taken as the yield stress of the material. The proof stress is obtained by constructing a line of slope E_s, parallel to the linear region but starting at a strain ε_{yp} usually equal to 0.002, and recording the stress f_{yp} where the line intersects the nonlinear material stress-strain curve. For profiled sheeting, this proof stress at 0.2% offset is quite commonly $f_{yp} = 550$ N/mm^2.
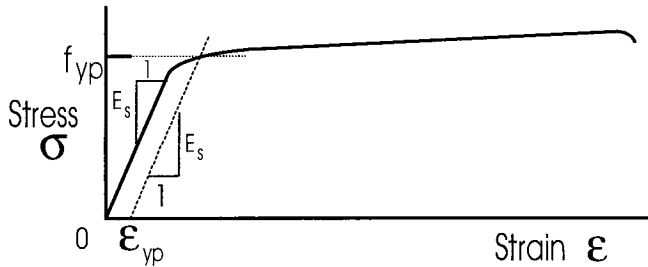
Fig. 16.2 Actual stress-strain curve

The strain versus stress relationship may be represented by the well-known constitutive law developed by Ramberg and Osgood (1943). It has the form

$$\varepsilon = \frac{\sigma}{E_s} + \varepsilon_{yp}\left(\frac{\sigma}{f_{yp}}\right)^n \tag{16.1}$$

The constant n in Eq. 16.1 describes the shape of the curve at the knee, with a value of n = 25 being appropriate for profiled sheeting.

Equation 16.1 describes the strain ε as a function of the stress σ, when in fact it is more desirable for analysis to have stress as a function of strain. A tri-linear stress versus strain representation developed by Uy and Bradford (1994a) for cold formed steel sheeting with $f_{yp} = 550$ N/mm^2 and n = 25 was found to give a simple stress versus strain representation of the Ramberg-Osgood relationship. This representation may be written as

$$\sigma = 200,000\,\varepsilon \qquad 0 \le \varepsilon \le 0.0025 \tag{16.2a}$$

$$\sigma = 500 + 22{,}222\,\varepsilon \qquad 0.0025 \le \varepsilon \le 0.00475 \qquad (16.2b)$$

$$\sigma = 550 + 5667\,\varepsilon \qquad 0.00475 \le \varepsilon \le 0.019 \qquad (16.2c)$$

where the units and in N and mm and with fracture of the tensile coupon occurring at a stress $f_u = 630$ N/mm^2 corresponding to a strain of 0.019. The tri-linearization is shown diagrammatically in Fig. 16.3.
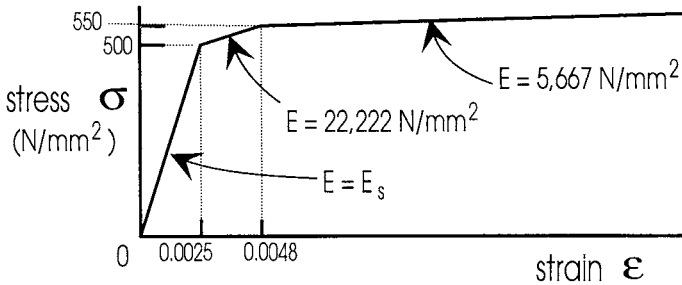
Fig. 16.3 Tri-linear stress-strain curve

16.2.2.2 *Residual strains and stresses*

Residual stresses are present in cold formed steel sheeting, and are caused mainly by the cold-bending effect during the forming process (Yu 1973). Due to the difference in the manufacturing process of a hot-rolled and cold formed steel member, the residual stresses can be quite different.

Weng and Pekoz (1990) undertook an extensive experimental study of residual stresses in cold formed steel members. From this study an idealised distribution pattern of residual strains in a cold formed channel section was obtained, as illustrated in Fig. 16.4. It can be seen that the residual strains vary through the thickness of the sheet, with those in compression on the outer surface being approximately of the same magnitude as those in tension on the inner surface. Thus if membrane behaviour is being considered, as would generally be the case with profiled sheeting used in composite slabs, it can be assumed that the residual strains have little effect on the behaviour (Uy and Bradford 1994a).

16.2.3 WET CONCRETE LOADING

16.2.3.1 *General*

In profiled composite slabs, the loading of the sheeting by the wet concrete may produce the most critical design loading. If there is no falsework under the sheeting, which is usual, then the floor span between the steel elements is governed primarily by the ability of the profiled sheeting to resist the weight of the wet concrete. Because fairly large strains are attainable in tension, as illustrated by the constitutive model of Section 16.2.2.1 and Fig. 16.2, it is the buckling of the compression portions of the profiled sheeting that govern its behaviour under wet concrete construction loading.
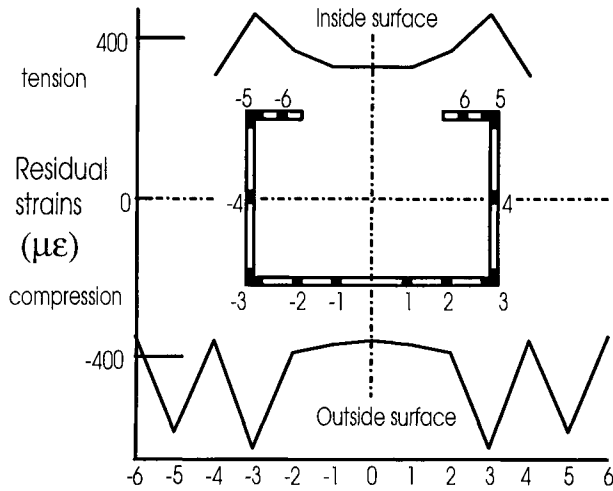
Fig. 16.4 Residual cold formed strain pattern (after Weng and Pekez 1990)

16.2.3.2 *Linear material response*

Under the loading caused by the wet concrete, the moment versus curvature response of the sheeting is initially fairly linear with a stiffness E_sI, where I is the second moment of area of the profiled sheeting about its neutral axis. Because the top surface of the concrete remains horizontal, ponding may occur as shown in Fig. 16.5(a) producing a nonlinearity which should be considered in design unless the loading is small. In addition, the loaded sheeting may develop a curvature orthogonal to its ribs, as shown in (b).

At reasonably low levels of wet concrete loading, the nonlinearities caused by ponding and edge deflections may be ignored in design. The deflection of the sheeting may thus be calculated from the stiffness E_sI by treating the one-way bending action of the sheeting across the I-section elements as that of a continuous beam subjected to a uniformly distributed load.

Ponding effects may be included approximately if a computer stiffness analysis of the sheeting is being undertaken. For this, the first order deflections at A and C in Fig. 16.5(a) obtained using a stiffness E_sI can be used to determine additional concentrated loads per unit width at these points caused by ponding of the wet concrete. Considering the distribution of the uniformly distributed load along the sheeting, the additional load per unit length at quarter points A can be approximated by $3L\,\delta_A\,\gamma_{conc}\,/\,8$ and at midspan C by $L\delta_C\gamma_{conc}\,/\,4$, where δ_A is the quarter point deflection and δ_C is the midspan deflection, and γ_{conc} is the specific gravity of the wet concrete. The first order computer analysis is re-run with these additional loads to determine the new deflections $\delta_A{}'$ and $\delta_C{}'$ at points A and C. The analysis then iterates until, usually after one or two steps, the deflections at A and C converge.

(a) ponding deflection

(b) orthogonal curvature
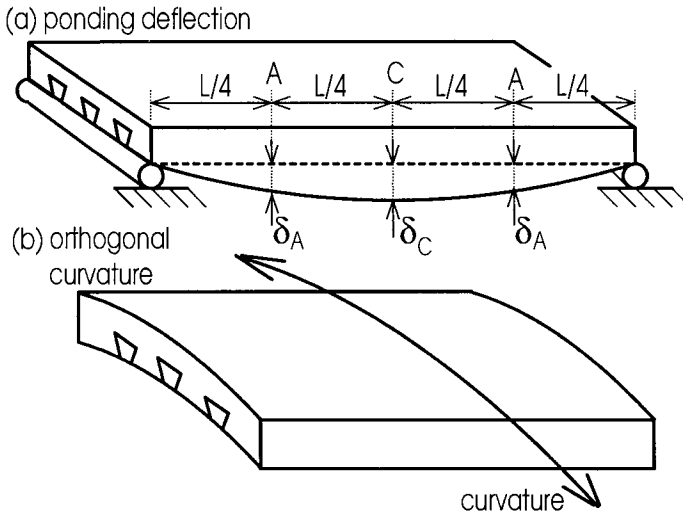
Fig. 16.5 Wet concrete deformations of profiled sheeting

Of course, additional deflections caused by the deformations of the centreline of the steel I-section element must also be included. For typical beam spans and typical slab spans, the deflection of the slab relative to the beam is greater than that of the beam relative to a horizontal datum.

16.2.3.3 *Nonlinear response*

The wet concrete loading causes tensile stresses to develop in the soffit of the sheeting in the positive bending region between supports. On the other hand, compressive stresses develop in the flanges of the ribs in positive bending regions, so that the compressive flanges may be susceptible to local buckling, as shown in Fig. 16.6(a). Over an internal support, the sheeting is subjected to hogging bending, so that the soffit flange of the profile may buckle locally, as in (b).

Because the sheeting is both thin and generally has a high yield stress, the local buckling is elastic. Unlike lateral-torsional buckling or lateral-distortional buckling that was treated in Chapter 10, elastic local buckling does not represent a strength limit state, and the sheeting can carry further load, but with a stiffness reduced below $E_s I$, until the ultimate strength is attained when the maximum stress in the locally buckled profile reaches its yield stress f_{yp}. The load versus deflection response of the sheeting in the more advanced stages of wet concrete loading is thus nonlinear.

The ability of a thin plate, such as the flanges of profiled steel sheeting, to carry load beyond that to cause initial local buckling is due to a benign post-locally buckled response. The elastic postbuckling behaviour of steel elements was described in Section 5.2.2, and is reiterated here. After local buckling, the stresses in the plate

are subjected to a redistribution, with those in the less stiff central region of the plate being reduced and those toward the supported edges of the plate increasing to maintain equilibrium, as in Fig. 16.7(a). The postbuckled stress redistribution, which is a consequence of nonlinear finite deflection plate behaviour, continues with increasing load until the maximum stress at the edge reaches yield and the ultimate strength of the plate is reached. If the plate contains initial geometric imperfections, then the stress redistribution takes place after the commencement of loading, but is greatest after the theoretical local buckling stress has been passed.
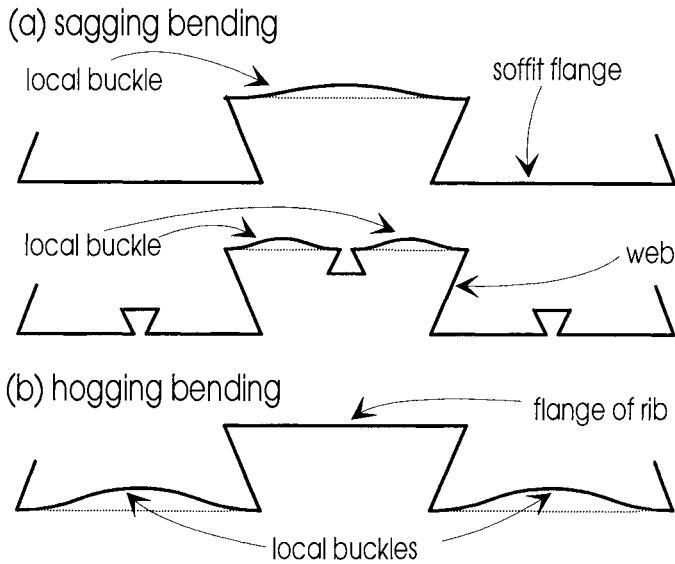
Fig. 16.6 Local buckling of profile under construction load
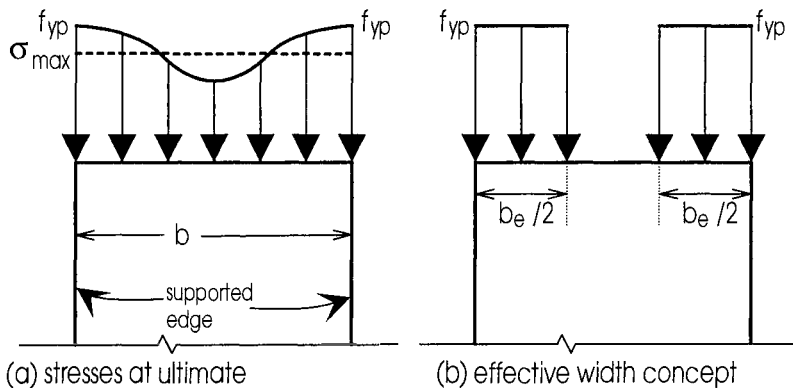
Fig. 16.7 Effective width of supported plate

Postbuckling analyses of plates are difficult, and it is common to use the effective width concept first proposed by von Karman (1910) and discussed in Section 5.2.2. For a supported plate, as in Fig. 16.7(a), the maximum stress at the edge, f_{yp}, is assumed to be constant over an effective width b_e, as in (b), with the central less-stiff portion of the plate being unstressed. Note that the effective width concept for post-local buckling is not the same as that for shear lag, that was treated in Chapter 4.

A semi-empirical expression for b_e for a cold formed profile was proposed by Winter (1969). Based on Winter's proposals, a suitable expression for b_e for a cold formed steel sheet may be taken as

$$b_e = \frac{857t}{\sqrt{\sigma}} \left(1 - \frac{187t}{b\sqrt{\sigma}}\right) \leq b \tag{16.3}$$

in which σ is the average stress in N/mm^2 determined from a linear analysis and t is the plate thickness. The stiffness of the profiled sheeting E_sI' is then obtained from the reduced second moment of area of the profile with a reduced geometry comprising of flanges of effective widths b_e. Since b_e decreases as the stress σ calculated linearly from the loading increases, the stiffness E_sI' decreases with additional load in the postbuckled range and the load-deflection response becomes increasingly nonlinear.

The webs of the profile are subjected to bending stresses, and the reduction in the postbuckled stiffness of supported bending elements is not large (Bradford 1985). Because of this, the webs of the profiled sheeting may be assumed to be fully effective.

16.2.3.4   Ultimate strength

The effective width formulation in Eq. 16.3 was really only derived to produce the effective width at ultimate, with the stress σ_{max}, applied over the full width b, being replaced by the yield stress applied over the ultimate effective width $(b_e)_{ult}$ in Fig. 16.7(a), that is when $\sigma = f_{yp}$ in Eq. 16.3. Hence the postbuckled *stiffness* based on b_e at a stress $\sigma \leq f_{yp}$ is only approximate, whereas the *strength* based on $(b_e)_{ult}$ when $\sigma = f_{yp}$ in Eq. 16.3 is accurate.

When the profile is in a positive bending region, the effective second moment of area $(I')_{sag}$ is calculated using $(b_e)_{ult}$ for the top flange of the profile, with the remainder of the sheeting being treated as fully effective. In a negative region where the profiled sheeting is continuous over the I-section element, the effective second moment of area $(I')_{hog}$ is calculated using $(b_e)_{ult}$ for the bottom flange of the profile, with the remainder of the sheeting being treated as fully effective. The lesser of the elastic section moduli $(Z')_{sag}$ and $(Z')_{hog}$, calculated from $(I')_{sag}$ and $(I')_{hog}$

respectively, may conservatively be used to calculate the sagging and hogging cross-sectional strengths $\left(M_p\right)_{sag}$ and $\left(M_p\right)_{hog}$, from

$$\left(M_p\right)_{sag} = f_{yp} \left(Z'\right)_{sag} \tag{16.4}$$

and

$$\left(M_p\right)_{hog} = f_{yp} \left(Z'\right)_{hog} \tag{16.5}$$

These cross-sectional strengths based on an 'elastic' analysis form the basis of a plastic analysis of the profiled sheeting subjected to wet concrete loading.

For example, consider the profiled sheeting spanning three I-beams as shown in Fig. 16.8. If ponding is neglected, each span can be analysed plastically as a propped cantilever of length L with positive and negative plastic moments $\left(M_p\right)_{sag}$ and $\left(M_p\right)_{hog}$ respectively, and subjected to a uniformly distributed load of intensity w. The ultimate value of w for plastic failure, w_{ult}, can thus be derived by adapting the method of Section 9.2.4.3 as

$$w_{ult} = \frac{8}{L^2}\left[\left(M_p\right)_{sag} + 0.46c\left(M_p\right)_{hog}\right] \tag{16.6}$$

We saw in Section 9.3 for composite beams that plastic analysis is generally applicable when the sagging hinge is the last plastic hinge to form. However, in profiled sheets the negative hinge is not able to allow large rotations at $\left(M_p\right)_{hog}$, unlike a steel I-section. Because of this, the capacity of the hogging hinge that permits the sagging hinge to form is $c\left(M_p\right)_{hog}$. Based on experiments by Bryan and Leach (1984), a support rotation of 2 to 3 degrees can be achieved with c = 0.5 as a lower bound in Eq. 16.6.
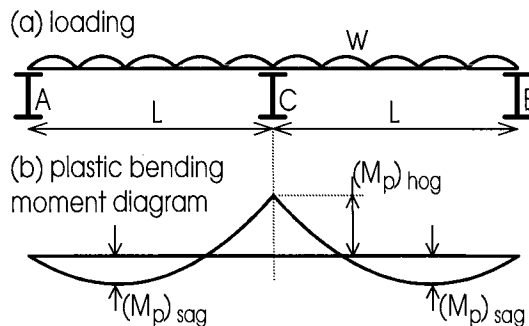
Fig. 16.8 Ultimate behaviour of profiled decking under construction load

Example 16.1 Resistance of profiled sheet to construction loads

The profiled trough shown in Fig. 16.1(a) has a proof stress of $f_{yp} = 550$ N/mm^2, is continuous over two spans as shown in Fig. 16.8 of 4m and is subjected to a construction load of $w = 4$ kN/m^2.

The maximum moment from an elastic analysis is $M_{max} = 8$ kNm per metre width at the internal support. For the strength calculation, from Eq. 16.3 with $\sigma = 550$ N/mm^2 and b = 55 mm, $b_e = 42.9$ mm < b. Hence from the effective section shown in Fig. 16.9, $\bar{y} = 22.0$ mm and I = 835×10^3 mm^4/m, producing $(Z')_{sag} = (Z')_{hog} = 835 \times 10^3/22.0 = 38.0 \times 10^3$ mm^3/mm. Substitution into Eqs. 16.4 and 16.5 gives $\left(M_p\right)_{sag}$ and $\left(M_p\right)_{hog} = 20.9$ kNm/m. From Eq. 16.6, using c = 0.5, the ultimate load to cause plastic failure is $w_{ult} = 12.8$ kN/m^2 which is greater than $w = 4$ kN/m^2, so the strength criterion is satisfied.

For serviceability, the average stress at ultimate over the effective area is $\sigma = 8 \times 10^6/38.0 \times 10^3 = 211$ N/mm^2. We can then use this stress in Eq. 16.3 for a stiffness approximation, giving $b_e = 57.4$ mm $\approx$ b, so $\bar{y} = 25$ mm and I = 980×10^3 mm^4/mm. It is worth noting that as $Z_{sag} = Z_{hog} = 980 \times 10^3/25 = 39.2 \times 10^3$ mm^3/m which gives $\sigma = 8 \times 10^6/39.2 \times 10^3 = 204$ N/mm^2, then using Eq. 16.3 for serviceability results in a fully effective section. Assuming now that the spans conservatively are simply supported and that the service load is 4/1.3 = 3 kN/m, say, then $\delta = (5/384) \times 3 \times 4000^4/2 \times 10^5 \times 980 \times 10^3 = 51$ mm which is approximately (span/80). This deflection is quite high, and the ponding deformation should be included in a second order analysis as described in Section 16.2.3.2.
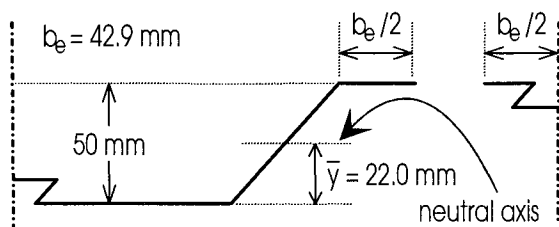
Fig. 16.9 Effective Section in Example 16.1

16.3 Composite slab behaviour

16.3.1 FLEXURAL STRENGTH

16.3.1.1 *General*

Continuous composite slabs as shown in Fig. 16.10 are often designed as simply supported and additional reinforcement is placed over the supports to restrict crack widths. This section will deal with the simply supported case, although it is possible to design the slabs as continuous using the theory described in Chapters 7 and 9 on rigid plastic analysis and moment redistribution respectively.
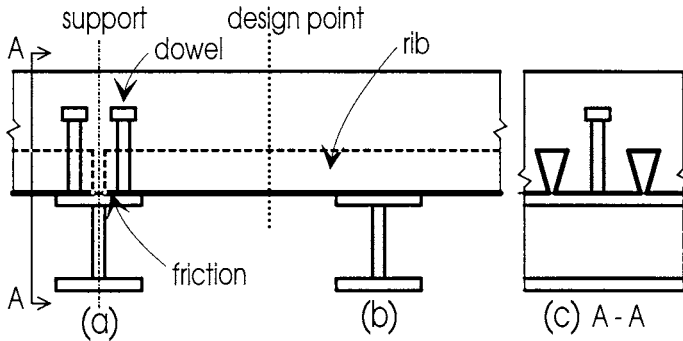
Fig. 16.10 Shear connection in composite slabs

Chapter 7 dealt with the rigid plastic analysis of standard forms of composite beams in which the concrete element was above the steel element as shown in Fig. 1.8. In this form of construction, the strain profile in the concrete element does not overlap with the strain profile in the steel element as shown in Fig. 1.23. Therefore, the position of the neutral axis can be determined by simply equating the compressive force above the neutral axis to the tensile force below as in Fig. 7.3(e). This technique ensures that the resultant force in the concrete element is equal to the resultant force in the steel element, which in turn is equal to the resultant force in the shear connectors F_{shear} as shown in (f). For example and in Case 1 in Fig. 1.20, the resultant force in the concrete element, the resultant force in the steel element and the resultant force in the shear connectors is equal to the strength of the steel element P_{steel}. However, in Case 3 for partial shear connection, it is equal to the strength of the shear connection P_{shear}.

In other forms of composite beams such as those shown in Fig. 1.7, the strain profile in the concrete element can overlap with the strain profile in the steel element as in Fig. 16.11(b) and (e), so that the technique of determining the neutral axis by equating the strength above to the strength below may not always work. Instead, it is necessary to ensure that the three resultant forces, that is the resultant force in the steel element, in the concrete element and in the shear connectors are equal. This technique of determining the neutral axis or axes from the shear

connection forces can be applied to all shapes of composite slabs as well as to all forms of composite beams.
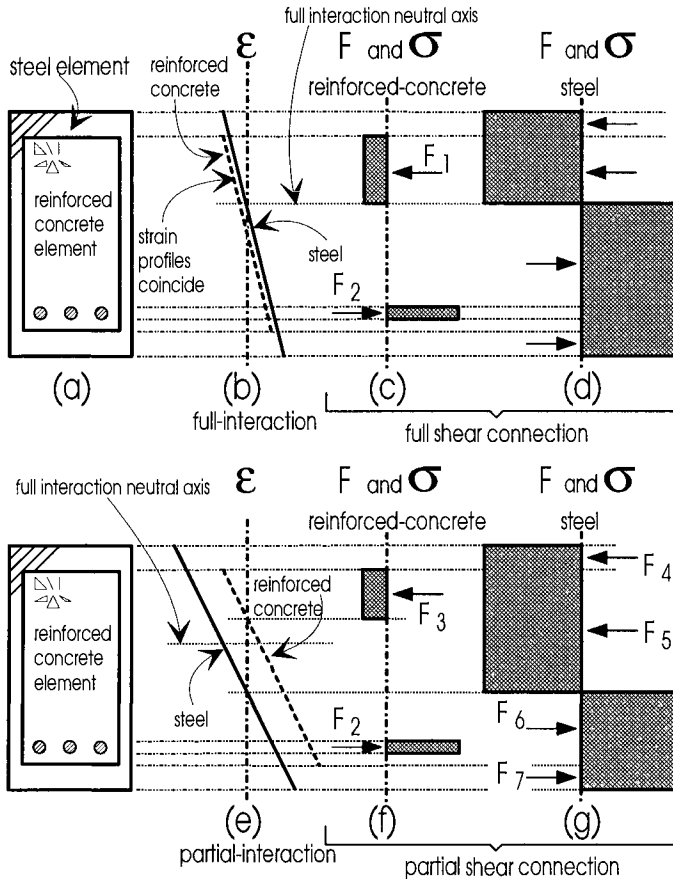
Fig. 16.11 Overlap of strain profiles

16.3.1.2 *Shear connection forces*

The shear connection in a composite slab can be provided by friction at the supports where the profiled sheet is sandwiched between the concrete element and the flange of the steel beam as shown in Fig. 16.10(a), although this transfer of shear is generally ignored in practice. Very often, stud shear connectors are welded through the metal decking onto the steel flange in order to provide the shear connection for the main composite beam. These connectors also provide shear connection to the composite slab, because interface slip of the profile slab is restricted by the sheet bearing onto the stud (Eurocode 4 1994). However, the main source of shear connection is provided by the ribs themselves as described in Section 2.6. It will be assumed in the following analyses that the shear connection exhibits ductile characteristics with unlimited slip, so that it will not be necessary to check for fracture of the shear connection as described in Chapter 8.

(a) Full interaction and full shear connection

Let us first assume that the strength of the shear connection in the composite beam in Fig. 16.11(a) is very strong so that we are dealing with full shear connection. In order to calculate the flexural capacity from rigid plastic analysis, we need to determine the strain profile in both the steel element and the concrete element, that is the position of both of the neutral axes in (e).

In the composite beam with the strain profile in Fig. 1.23(a) that has no interaction, the two elements are acting separately, so that the flexural strength of the composite beam is the sum of the flexural strengths of the individual elements. In a composite beam with full interaction with the strain profile in (b), the two elements are acting together, so that the strength of the composite section is greater than that of the beam with no interaction. It can therefore be seen that a loss of interaction can and generally does weaken a beam, and that the greatest strength of a composite beam occurs when there is full interaction, that is when the reinforced concrete and steel strain profiles in Fig. 16.11(e) coincide as in (b).   Hence, full interaction is synonymous with full shear connection. As the neutral axes in the reinforced concrete and steel elements coincide in (b), we can simply use the technique of equating the force above the neutral axis with the force below to determine the position of the neutral axis in (b). The forces in the individual elements are shown in (c) and (d) and also shown is the stress distribution. The resultant force in the reinforced concrete element in (c) is (F_1 - F_2) and is equal to the magnitude of the resultant force in the steel element in (d) which in turn is equal to the force in the shear connection F_{fsc}. Hence F_{fsc} is the strength of the shear connection that is required for full shear connection and can be derived by assuming full interaction.

(b) Partial interaction and partial shear connection

When the strength of the shear connection is less than that required for full shear connection, then we have a composite beam with partial shear connection. It can be seen in Case 3 in Fig. 1.20, that partial shear connection is always associated with two neutral axes and hence a slip strain must always be present as in Fig. 16.11(e). Partial shear connection is therefore synonymous with partial interaction.

If the strength of the shear connection F_{psc} in the beam in Fig. 16.11(a) is less than that required for full shear connection F_{fsc}, then the resultant force in the reinforced concrete element, in the steel element and in the shear connection is F_{psc}. Therefore, for beams with partial shear connection, the strength of the shear connection F_{psc} can be used to determine the positions of the neutral axes and hence the flexural strength of the composite structure.   As an example, consider the reinforced concrete element in (a).   The position of the neutral axis for full shear connection in (b) is shown in (e).   When the strength of the shear connection is reduced so that there is partial shear connection, the neutral axis for the reinforced concrete element will rise as in (e). The position can be determine by finding the level in (f) where F_3 - F_2 = F_{psc}. The position of the neutral axis in the steel element can be determined in the same way, by finding the position where the sum of forces in (g) is

equal to F_{psc}. The flexural capacity can then be determined by taking moments of the forces F_2 to F_7 in (f) and (g) about any convenient axis.

16.3.1.3 *Composite slabs with full shear connection*

(a) Neutral axis above profiled sheet

When the neutral axis lies above the profiled sheet as often occurs in composite slabs with shallow profiles, the composite slab can be treated in the same way as a reinforced concrete slab. Figure 16.12 shows the procedure for determining the flexural capacity of the slab per rib, where b_r in (a) is the lateral spacing of the ribs, h_r is the distance from the top compressive fibre to the centroid of the profiled sheet, A_p is the cross-sectional area of the profile over a width b_r, and f_{yp} in (c) is the yield strength of the profile sheet. The resultant force in the concrete, the resultant force in the profile and the resultant force in the shear connection is $A_p f_{yp}$.
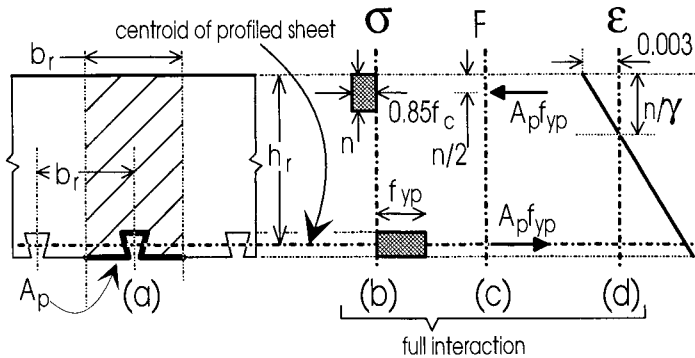
Fig. 16.12 Shallow profiles

In order to achieve full shear connection, the strength of the shear connection over the length of the rib between the design point and the beam support must be greater than $A_p f_{yp}$, where the strength of the rib shear connection can be derived from Section 2.6. Maintaining the analogy with a reinforced concrete member, it may be necessary to ensure that the steel yields before the concrete crushes and this can be achieved by either limiting the depth of the neutral axis to no more than $h_r/2$ (BS5950 1982) or using the γ factor described in Section 2.3.2 and Eq. 2.17 and illustrated in Fig. 16.12(d).

Example 16.2 Full shear connection strength of composite slab with shallow profiles

A simply supported composite slab with a shallow profile is shown in Fig. 16.13(a) where all the dimensions are in N and mm unless stated otherwise. The profile sheet is 1 mm thick and is produced in 300 mm widths. The sheets are joined by lapping the ribs so that the L-ribs can be assumed to be 2 mm thick as shown.

A full shear connection rigid plastic flexural analysis is shown in Fig. 16.13(b) for a 300 mm width of slab, so that we are determining the flexural strength of the slab per rib. The cross-sectional area of the profiled sheet per rib is $A_p = 480$ mm^2 and from considering the first moment of area, the centroid is 15 mm from the soffit as shown. The axial strength of the profile sheet $P_{steel} = A_p f_{yp} = 192$ kN which is considerably less than the axial strength of the concrete above the profile of 536 kN, and hence the neutral axis must lie above the steel element. The force $P_{steel} = 192$ kN therefore controls design as shown in (b), from which can be determined the depth of the rectangular stress block in the concrete of n = 25 mm. Because the steel element is uniformly stressed, the resultant axial force in the steel element occurs through the centroid and hence the lever arm between axial forces is 103 mm which produces a flexural capacity of the composite slab per rib of 19.7 kNm. It is also worth noting that in order to attain the full shear connection flexural capacity, the strength of the rib shear connection between the design point and the support must be at least 192 kN.

If the composite slab is being treated as a reinforced concrete slab then it should, in theory, be necessary to ensure that yielding occurs prior to crushing of the concrete by checking for compatibility. The γ factor in Eq. 2.17 and explained in Section 2.3.2 can be used to determine the true neutral axis as shown in the analysis in Fig. 16.13(c). If the concrete is assumed to crush at a strain of 0.003, then the minimum strain in the profile sheet is 0.004 which is considerably higher than the yield strain of the steel of 0.002 and hence the composite beam will attain its flexural capacity of 19.7 kNm. This type of compatibility calculation is rarely done in composite beams or slabs, but it is worth noting that the real neutral axis in (c) is not the same as that assumed in the rigid plastic analysis in (b).
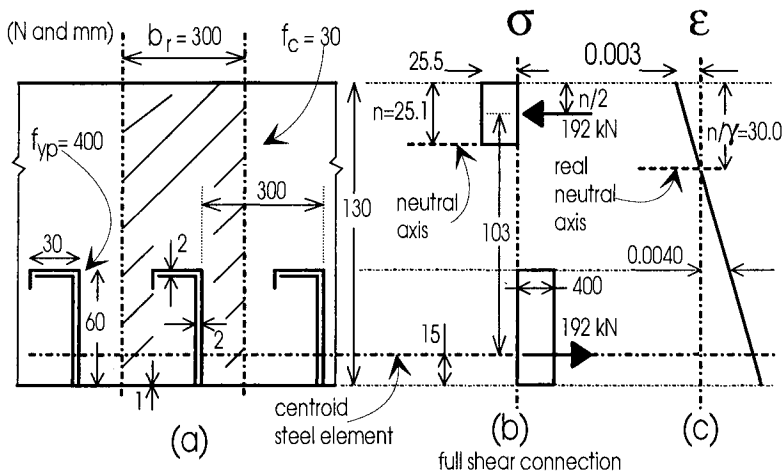
Fig. 16.13 Example 16.2: Concrete slab with shallow profiles

(b) Neutral axis within profiled sheet

Composite slabs with deep profiled sheets as in Fig. 16.14(a) can be treated as the equivalent composite beam in (b), where b_r is the lateral spacing of the profiles, b_t is the width of the top element of the profile, b_b is the width of the bottom element, t is the profile thickness, t_h is the horizontal width of the inclined profile, b_h is the average width of the haunch and A_r is the total area of the reinforcing bars per rib. Composite slabs are unlikely to have reinforcing bars in the sagging or positive regions as in (a) but these have been included to clarify the analysis technique.
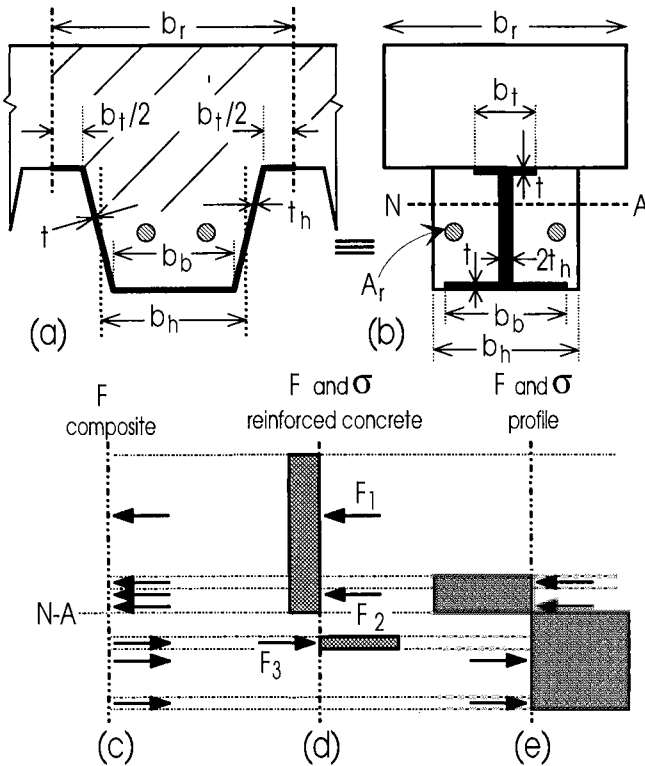
Fig. 16.14 Deep profiles

The position of the neutral axis can now be determined by equating the compressive strength above the neutral axis to the tensile strength below, as shown in Fig. 16.14(c), where the tensile strength of the concrete is assumed to be zero. Taking moments of these forces about any convenient level gives the flexural capacity, and the resultant of the forces in either the reinforced concrete element in (d) or the steel element in (e) will give the shear connection strength required for full shear connection.

When the neutral axis lies within the steel element, then it will be necessary to ensure that local buckling of the profile sheet does not reduce the flexural capacity

as explained in Section 16.3.1.5. Alternatively and as a lower bound, the profiled sheet in compression can be ignored in the analysis.

Example 16.3 Full shear connection strength of composite slab with deep profiles

A composite slab with deep profiles is shown in Fig. 16.15(a) where the units are in N and mm. The lateral spacing of the ribs $b_r = 330$ mm and the sheet thickness is 2 mm.

     The composite slab in Fig. 16.15(a) is equivalent to the composite beam in (b). The axial strength of each rectangular element of the beam is shown in (c), where it should be noted that the concrete strengths are the compressive strengths and that the tensile strength of the concrete is assumed to be zero. From inspection of the axial strengths in (c), it can be deduced that the neutral axis lies in the top flange of the steel element and therefore we can ignore the haunched area of the concrete of width 190 mm. Equating the axial strength above the neutral axis to the axial strength below the neutral axis produces the distribution of forces in (d). The distance of these resultant axial forces from the top fibre is shown in (e). In the top flange of the steel element in (d), the compressive force of 39 kN lies just above the tensile force of 61 kN, but because the flange is only 2 mm thick it can be assumed in the calculations that these forces act at the same level at 50 mm from the top fibre as shown in (e). Taking moments about the top fibre using (d) and (e) produces a flexural capacity of 27.9 kNm.

     From Fig. 16.15(d), the resultant force in the steel element is 351 kN which is both the resultant force in the concrete element and also the strength of the shear connection required for full shear connection.
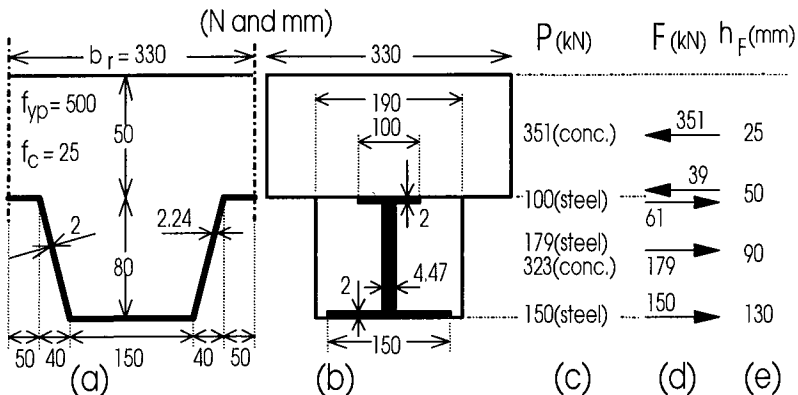
Fig. 16.15 Example 16.4: Composite slabs with deep profiles

16.3.1.4 *Composite slabs with partial shear connection*

The full interaction analysis described in Section 16.3.1.3 gives the strength of the shear connection between the design point and the support in Fig. 16.10 that is

required for full shear connection. When the strength of the shear connection is less than that required for full shear connection, we have to resort to a partial interaction analysis technique in which there are two neutral axes, in order to determine the flexural capacities. The starting point in the analysis is therefore the force in the shear connection F_{psc}, which is now known as it is the strength of the shear connection, and which is also the resultant force in each element of the composite slab.

Let us consider the reinforced concrete element in the composite slab in Fig. 16.14(b). The position of the neutral axis in the reinforced concrete element of the composite beam can be determined by considering the axial strengths of the reinforced concrete element alone. The neutral axis in the reinforced concrete element in (d) occurs when the resultant force is F_{psc}, that is $F_1 + F_2 + F_3 = F_{psc}$. Hence, the position and magnitude of the forces in the reinforced concrete element are now known. The same procedure can be applied to the steel element in (e) in order to find the position and magnitude of a distribution of forces in the steel element in which the resultant axial force is F_{psc}. Knowing the position of the resultant forces, the flexural capacity can be determined by taking moments of the forces in (d) and (e) about any convenient axis.

Example 16.4 Partial shear connection strength of composite slab

It was shown in Example 16.3, that the composite slab in Fig. 16.15(b) requires a shear connection strength of 351 kN per rib in order to achieve its maximum flexural capacity. Let us assume that the available shear connection strength is 175 kN, that is we have nearly a 50% degree of shear connection.

As we are dealing with partial shear connection, the shear connection strength of 175 kN is the starting point of our analysis, which is shown in Fig. 16.16 and where the units are in kN and mm. The basic principle is that the resultant force in the concrete element is equal to the resultant force in the steel element, which is equal to the strength of the shear connection. It is therefore necessary to look at the steel and concrete elements separately. The resultant compressive force in the concrete element is 175 kN and occurs 12 mm from the top fibre as shown in (b). Consider now the steel element by itself. The neutral axis can be determined by finding the level at which the resultant tensile force is 175 kN and this occurs when the neutral axis is 12 mm from the top flange of the steel element, and this gives the magnitude and distribution of forces shown in (d) and (e). Taking moments of the forces in both elements about the top fibre using (b), (d) and (e) results in a flexural capacity of 25.4 kNm.

If we assume that the profile sheet cannot take compressive forces because the local buckling strength is low, then the only parts of the steel element that are in tension are active as shown in Fig. 16.16(f). The sum of the tensile forces in the steel element must still be 175 kN as in (g), so the depth of the web in tension can be determined as 11 mm. Hence, the position of the resultant forces can be found, as in (h). The force in the concrete element is unchanged, as in (b). Taking moments about the top fibre using (b), (g) and (h) gives a flexural capacity of 20.5 kNm, which is 81% of the capacity in the previous analysis that ignored local buckling.
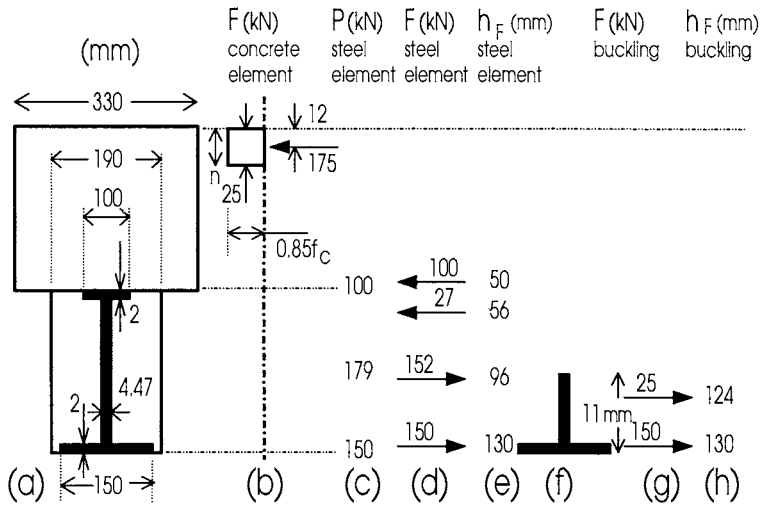
Fig. 16.16 Example 16.3: Deep profiles with partial shear connection

16.3.1.5 *Local buckling*

Local buckling of thin steel sheeting that was discussed in Chapter 5 may take place when the steel is subjected to compressive stresses. Such situations occur in the negative region of the composite profiled slab, or in the top flange of a trapezoidal or dove-tailed rib when the rib is deep enough relative to the slab thickness to force the neutral axis to lie below the top flange of the rib. If full composite action is to occur in these regions, then local buckling should be prevented, although after the onset of local buckling there may be partial composite action. On the other hand, if a rigid plastic analysis is to be undertaken, then it is important that the yield stress f_{yp} of the profiled sheet is readily attainable before local buckling.

The mode of local buckling, which will be discussed further in Section 17.2.2, is governed by the fact that the concrete acts as a rigid medium, and restrains the buckles so that they may only form away from the concrete, as in Fig. 16.17. This has the effect of increasing the buckling stress above that to cause local buckling of unrestrained thin plates.

The local buckling of plates in uniform compression restrained by a concrete medium has been considered by Wright (1993), Oehlers, Wright and Burnet (1994) and Uy and Bradford (1994b). The study by Uy and Bradford used the finite strip method (see Section 10.2.1.3), and was able to model the elastic stiffness provided by the ribs. In all the above studies, the chemical bond between the concrete and steel was assumed to be small, and ignored in calculating the local buckling stress.

(a) Section A-A

concrete element

sheeting buckles away

(b)

A←⌐

A←⌐
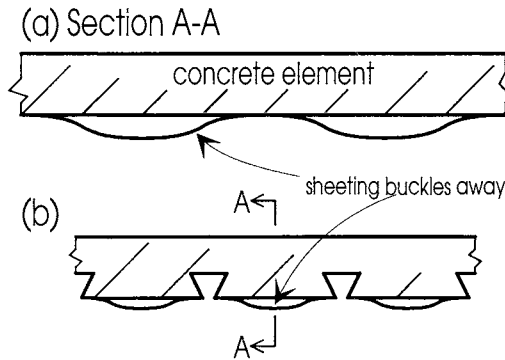
Fig. 16.17 Buckling mode in profiled slab

Elastic local buckling takes place at a stress $\sigma_{o\ell}$ given by

$$\sigma_{o\ell} = k \frac{\pi^2 E_s}{12(1-v_s^2)} \frac{1}{(b/t)^2} \tag{16.7}$$

where b is the plate width between longitudinal supports and t is the plate thickness. Equation 16.7 was also stated in Chapter 5 as Eq. 5.2. The local buckling coefficient k in Eq. 16.7 depends on the restraints provided to the edges of the plate, and was determined by Uy and Bradford (1994b) for a number of restraint cases for an elastic thin steel plate restrained by a rigid concrete core. Under uniform compression, if the ribs provide rigid or clamped edges, then k is approximately 10.2, while if the unloaded edges are simply supported, then k is approximately 5.5. This latter case provides a conservative approximation, so that local buckling will not occur before the yield stress f_{yp} is reached provided the modified plate slenderness $(b/t)\sqrt{f_{yp}/550}$ is less than 45, where f_{yp} is in N/mm^2. This conservative limit is obtained by setting $\sigma_{o\ell} = f_{yp}$ in Eq. 16.7.

　　If a rigid plastic analysis is to be undertaken, then the inelastic response of the profiled sheeting must be included in the buckling analysis so that local buckling does not occur before the section strength is reached. Inelastic local buckling with a rigid restraint was considered by Uy and Bradford (1994a), in which the stress-strain relationship of Eqs. 16.2 was used in their inelastic finite strip treatment. The study considered a number of restraint conditions, with clamped and simply supported unloaded edges being the most important, as they are limiting cases of the restraint provided to the sheeting by the ribs. Limiting modified plate slendernesses $(b/t)\sqrt{f_{yp}/550}$ of 30 for a cold formed plate with simply supported edges and 35 for a plate with clamped edges were suggested. These limits were found to permit the full proof stress f_{yp} to be obtained, as well as strains of at least twice the proof strain ε_{yp}, thereby allowing the strains in the steel shown in Figs. 16.11(b) and (e) to be realised.

Example 16.5 Local buckling of profile sheet in a composite beam

In the composite slab with a deep profile shown in Fig. 16.15 and considered in Example 16.4, the width of the top flange of the profile is 50 x 2 = 100 mm. The modified slenderness of this plate is thus $(100/2)\sqrt{500/550} = 47.6$. Since this value is greater than the suggested conservative limit of 30 and the clamped limit of 35, it may be prudent to ignore the compressive portions of the profile as was done in Example 16.4.

Similarly, if the slab considered in Example 16.2 and shown in Fig. 16.13(a) is to be considered in the negative region, the ultimate hogging strength can only be used if the soffit bottom flange does not buckle before yielding. Since its modified slenderness is $(300/1)\sqrt{400/550} = 256$, it clearly cannot be considered in the hogging strength calculation, and this leads to the common assumption of ignoring the sheeting in regions of negative bending. Of course, the L-ribs can be included, as these are prevented from buckling by the concrete element.

16.3.2   VERTICAL SHEAR STRENGTH

The vertical shear strength of composite slabs is often determined from procedures, as in BS5950 (1982), that are based on the empirically derived rules developed by Zsutty (1968) that are used to determine the vertical shear strength of reinforced concrete beams. The profiled sheet is assumed to act as tension reinforcement, and it will therefore be necessary to ensure that it is fully anchored on either side of the shear failure plane. This anchorage can be achieved by the longitudinal shear strength due to friction, rib shear connection or the sheet bearing against the stud as shown in Fig. 16.10(a), or it can simply be achieved by continuity of the profiled sheet over the support as in (b).

In general, the vertical shear strength rarely controls design, and the shear strength for a composite slab with a specific profile is often determined empirically. Experimental studies (Patrick and Bridge 1992) have shown that it is very difficult to induce vertical shear failure in a composite slab; short shear spans are prone to flexural failure induced by longitudinal shear failure of the shear connection whereas long shear spans are prone to flexural failure of the composite slab. Furthermore, experiments (Luo 1993) on simply supported reinforced concrete beams with steel plates glued to their soffits and extending the full length of the beam and over the supports, which is analogous to the composite slab in Fig. 16.10(a), showed that the increase in the vertical shear strength due to the plate was much greater than the increase in strength predicted by Zsutty (1968) for the same amount of reinforcing bars. Hence, it may be expected that the profiled sheet is at least as effective as reinforcing bars in resisting shear just as long as the sheet is fully anchored.

16.4   Composite beams with composite slabs

16.4.1   GENERAL

The profiled sheet in a composite slab that is part of a composite beam affects the composite beam action in many ways, by changing the shape of the section, acting as reinforcing bars and affecting the dowel strength of the mechanical shear connectors in the composite beam.   The magnitude of these effects depends on the type of profiled sheet and is best left to the engineering judgement of the designer.

16.4.2   CROSS-SECTION OF COMPOSITE BEAM

The composite slab in a composite beam that incorporates steel decking alters the cross-sectional shape of the composite beam as described in Section 4.3 and shown in Figs. 4.4 and 4.6. In general, the sheet is ignored in deriving the flexural strength of the composite beam from rigid plastic analyses.

16.4.3   ACTION AS TRANSVERSE REINFORCEMENT

The profiled sheet can be assumed to act as transverse reinforcement to the composite beam, however the effectiveness as transverse reinforcement is a matter of engineering judgement.

As an example, it was shown in Chapter 13 on *longitudinal shear* that profiled sheets with the ribs transverse to the steel element of a composite beam, as in Fig. 1.11(c), could be assumed to act as transverse reinforcement. When the sheet is fully anchored across the shear plane, the full strength of the profiled sheet can be used in deriving the longitudinal shear strength. However, when the sheet is not fully anchored, then the longitudinal shear strength depends on the anchorage strength. A similar analogy can be made with the *post-splitting dowel strength* in Chapter 12, where the profiled sheet can also be assumed to act as transverse reinforcement. In this case, the anchorage length required for post-splitting action was shown in Chapter 12 to be much less than that required for the longitudinal shear, as it is the stiffness not the strength of the profile sheet that affects the post-splitting dowel strength. Hence, the profile sheet should be quite effective in maintaining the dowel strength of the mechanical shear connectors after longitudinal cracking.

When the profiled ribs are parallel with the steel element as in Fig. 1.11(b), then it was assumed in Chapter 13 on *longitudinal shear* that the profiled sheet was not effective as transverse reinforcement because the ribs could open out as in Figs. 2.28 and 2.29(a). This assumption can also be applied to the *post-splitting dowel strength* in Chapter 12. However, it is suggested that when L-shaped ribs are used, as in Fig. 1.6(c), then the profiled sheet can be assumed to act as transverse reinforcement for *longitudinal shear* and for the *post-splitting dowel strength*, as this rib is unlikely to open out as it is virtually fully encased by the concrete. Similarly, it could be expected that re-entrant ribs as in (a) will be fairly effective in anchoring the profiled sheet, particularly for the *post-splitting dowel strength*.

16.4.4   DOWEL STRENGTH OF MECHANICAL SHEAR CONNECTORS

The ribs of the profiled sheets that are transverse to the composite beam can be expected to act as voids and dense inclusions in the concrete element as described in Section 12.2.2.2. It would be expected that when the L-shaped ribs, in Fig. 1.6(c), are close to mechanical shear connectors they would increase the dowel strength by acting as stiff inclusions, whereas re-entrant ribs in (a) that are close to the mechanical shear connectors will act as voids and hence reduce the dowel strength.

Large transverse ribs, such as the trapezoidal ribs in Figs. 1.9(d) and 1.11(c), have been found experimentally to reduce the dowel strength of the mechanical shear connectors as described in Section 11.5.5. Furthermore, large longitudinal ribs in Fig. 1.11(b) can induce splitting as described in Chapter 11 and hence they can affect the dowel strength as described in Chapter 12.

16.5   Fire resistance

16.5.1   GENERAL

At elevated temperatures, the steel element in a composite member experiences reductions in its strength and stiffness. This has led to reduced design loads being specified for the fire limit state, and is of particular importance for composite profiled slabs. Fire limit states also assume that the composite structure will be inadequate for routine use after the event of a fire. This is both conservative and uneconomical, and does not provide a true understanding of the structural behaviour. Because of this, researchers have tried to evaluate the contribution of the steel to the structural strength at elevated temperatures. Consideration of composite members at the elevated temperatures produced by fire is therefore a necessary requirement for a limit states analysis. Composite members should be designed to be able to maintain their strength throughout severe temperatures, or their behaviour at elevated temperatures should be clearly understood.

16.5.2   LOCAL BUCKLING

Local buckling may occur in a composite slab in negative regions adjacent to the supporting I-section elements. Because the concrete acts as a rigid medium, the steel profile may only buckle away from this concrete core as discussed in Section 16.3.1.5, and not in the typical mode shown in Fig. 16.6.

Local buckling may be precipitated at elevated temperatures as both the elastic modulus $E_s(T)$ and the yield stress of the profile $f_{yp}(T)$ at a temperature T are reduced. Based on tests, an accepted expression for $E_s(T)$ is (Uy and Bradford 1995)

$$E_s(T) = R_{ET}(T) E_s(20) \tag{16.8}$$

where $E_s(20)$ is the elastic modulus at 20°C, and the modulus reduction factor $R_{ET}(T)$ is

$$R_{ET}(T) = 1 + \frac{T}{2000 \, \ell n \, (T/1100)} \tag{16.9}$$

when 0°C ≤ T ≤ 600°C, and

$$R_{ET}(T) = \frac{690 \, (1 - T/1000)}{T - 53.5} \tag{16.10}$$

when 600°C < T ≤ 1000°C. Similarly, a close approximation to the yield stress $f_{yp}(T)$ is

$$f_{yp}(T) = R_{yT}(T) \, f_{yp}(20) \tag{16.11}$$

where $f_{yp}(20)$ is the yield stress of the sheeting at 20°C, and the reduction factor $R_{yT}(T)$ is

$$R_{yT}(T) = 1 - \frac{T - 300}{500} \leq 1 \tag{16.12}$$

where T is the temperature in degrees C.

The elastic local buckling stress of the profiled sheeting in a region of negative bending is obtained from Eqs. 5.2 and 16.7 as

$$\sigma_{o\ell}(20) = \kappa \frac{\pi^2 E_\sigma(20)}{12 \left(1 - v_\sigma^2\right)} \left(\frac{t}{\beta}\right)^2 \tag{16.13}$$

where t is the thickness of the sheeting, b is its width between longitudinal supports, v_s is Poisson's ratio for steel and k is the elastic local buckling coefficient. For a simply supported plate, it is well-known that k = 4, but when the simply supported plate is restrained by a rigid medium, then it was shown in Section 16.3.1.5 that k is increased to about 6. At elevated temperatures, the local buckling stress $\sigma_{o\ell}(T)$ can be obtained in the elastic range as (Uy and Bradford 1995)

$$\sigma_{o\ell}(T) = \sigma_{o\ell}(20) \frac{E_s(T)}{E_s(20)} \tag{16.14}$$

and in the inelastic range as

$$\sigma_{o\ell}\left(T\right) \;=\; \sigma_{o\ell}\left(20\right)\frac{f_{yp}\left(T\right)}{f_{yp}\left(20\right)} \tag{16.15}$$

where in the inelastic range the temperature scaling is based on the yield stress rather than the elastic modulus.

Uy and Bradford (1995) developed an inelastic finite strip analysis of local buckling at elevated temperatures of profiled steel troughs in contact with a concrete slab, and the results of their study showed that buckling is elastic for typical trough girders at temperatures up to 600°C. They pointed out that, somewhat paradoxically, the limiting width to thickness ratios as discussed in Section 5.2.4 which categorise the slender classification of Section 5.3.2.5 actually increase at elevated temperatures. This occurs because of the variation of the yield stress and elastic modulus, as well as the local buckling stress, with temperature.

The strength of profiled sheeting in profiled composite slabs at elevated temperatures in the post-locally buckled domain has not yet been properly addressed. However it is suggested that, if local buckling has not occurred, the strength and stiffness of the profiled slab be obtained from the constitutive properties in Eqs. 16.8 to 16.12. If the sheeting has buckled locally, then the contribution of the steel sheeting can conservatively be ignored.

16.5.3 THE FIRE ENGINEERING METHOD

The Steel Construction Institute (1988) has developed the more rational procedure called the 'Fire Engineering Method' to calculate the amount of slab reinforcement needed for a given fire resistance period. The capacity of the cross-section is calculated taking into account the temperatures throughout the section and the reduced strength of the sheeting, as discussed in Section 16.5.2, as well as of the concrete and conventional reinforcement. Typically, the reduced plastic moments are 50 to 60% of the ultimate moments calculated from Chapter 7 or Section 16.3 at 400°C.

The capacity of a profiled composite slab subjected to fire depends quite substantially on the conventional reinforcement, as this is normally well-insulated from the effects of the fire. The Fire Engineering Method requires additional conventional reinforcing if resistance periods or fire ratings greater than 90 minutes are required, and it places lower bounds on slab thicknesses. For example, trapezoidal profiles require a minimum slab depth of 140 mm for spans between I-section elements of up to 3.6 m, while the corresponding slab depth for a dovetail profile is 135 mm. These recommendations are based on a loading of 6.7 kN/m^2. Further guidelines are given in a CIRIA special publication (CIRIA 1986).

16.6   References

Bradford, M.A. (1985). "Local and post-local buckling of fabricated box members", Civil Engineering Transactions, Institution of Engineers, Australia, Vol. CE27, No. 4, 391-396.

Bryan, E.R. and Leach, P. (1984). "Design of profiled sheeting as permanent formwork", CIRIA Technical Note No. 116.

BS5950: Part 4: (1982). *British Standard. Structural use of Steelwork in Buildings. Part 4. Code of Practice for Design of Floors with Profiled Steel Sheeting*, British Standards Institution, London.

Construction Institute Research and Information Association (1986). "Data sheet: Fire resistance of composite slabs with steel decking", CIRIA Special Publication No. 42.

Eurocode 4: (1994). *Design of Composite Steel and Concrete Structures. Part 1.1 General Rules and Rules for Buildings*. DDENV 1994-1-1: 1994 Draft for development.

Luo, W. (1993). "Strengthening of post-tensioned and reinforced concrete beams by bonding external steel plates", M.Eng.Sc. Thesis, The University of Adelaide, Department of Civil and Environmental Engineering.

Oehlers, D.J., Wright, H.D. and Burnet, M.J. (1994). "Flexural strength of profiled beams", Journal of Structural Engineering, ASCE, Vol. 120, No. 2, 378-393.

Patrick, M. and Bridge, R.Q. (1992). "Design of composite slabs for vertical shear, composite construction in steel and concrete II", Proceedings of an Engineering Foundation Conference, Trout Lodge, Missouri, June, 304-322.

Ramberg, W. and Osgood, R. (1943). "Description of stress-strain curves by three parameters", NACA Technical Note No. 902.

Steel Construction Institute (1988). *Fire Resistance of Composite Slabs with Steel Decking*. SCI, Ascot.

Uy, B. and Bradford, M.A. (1994a). "Inelastic local buckling behaviour of thin steel plates in profiled composite beams", The Structural Engineer, Vol. 72, No. 16, 259-267.

Uy, B. and Bradford, M.A. (1994b). "Slenderness limits for thin steel plates restrained by concrete", Australian Structural Engineering Conference 1994, Sydney, 613-618.

Uy, B. and Bradford, M.A. (1995). "Local buckling of composite elements at elevated temperatures", Journal of Constructional Steel Research, to appear.

von Karman, T. (1910). "Festigkeitsprobleme in machinebau", Encyk. der Math Wiss, Vol. 4, Part 4, Art. 27.

Weng, C.C. and Pekoz, T. (1990). "Residual stresses in cold formed steel members", Journal of Structural Engineering, ASCE, Vol. 116, No. 5, 1611-1625.

Winter, G. (1969). "Thin-walled structures - Theoretical solutions and test results", Preliminary Publication of Eighth Congress, IABSE, New York.

Wright, H.D. (1993). "Buckling of plates in contact with a rigid medium", The Structural Engineer, Vol. 71, No. 12, 209-215.

Yu, W.W. (1973). *Cold-Formed Steel Structures*, McGraw-Hill, New York.

Zsutty, T.C. (1968). "Beam shear strength prediction by analysis of existing data", ACI Journal, Proc. Vol. 65, No. 11.

17 Composite Profiled Beams

17.1 Introduction

In Chapter 16, we saw that profiled steel sheeting made of cold formed steel may be used as permanent and integral formwork for composite slabs. These slabs provided many advantages such as reduced slab depths and reduced construction times as propping and stripping were virtually eliminated. Composite profiled slabs are provided with longitudinal shear connection for the slab through embossments on the ribs, and are supported by steel I-section elements with longitudinal beam shear connection usually provided between the slab and I-section through stud shear connectors. Thus composite T-beams utilising composite profiled slabs are used primarily for steel framed building construction, and the composite action is double, as in Figs. 1.11(b) and (c).

Concrete framed construction has until recently been traditionally undertaken using plywood formwork for all structural elements, and so no inherent advantages have been achievable during the construction phase. This has been overcome by the development of *composite profiled beams* (Oehlers 1993, Uy 1995) which, in a similar way to profiled composite slabs, employ a permanent formwork system consisting of profiled sheeting for concrete framed construction, as shown in Figs. 1.10(b) and (d). The steel profiled sheeting provides permanent and integral formwork to the soffit and sides of the reinforced concrete beam, with which it acts compositely.

This chapter outlines the behaviour of composite profiled beams, which are a new form of composite construction hitherto researched most extensively by the authors of this book. The behaviour of the hollow steel trough or box girders into which the wet concrete is poured is considered firstly in Section 17.2, and it will be seen that local buckling effects are crucial in their behaviour and design. Once the concrete has hardened, we have composite behaviour, and the remaining sections will consider the behaviour of the composite profiled beams with respect to flexure, shear, local buckling, time-dependent deflections and fire.

17.2 Behaviour of profiled trough girders

17.2.1 GENERAL

In the first stage of the construction of a composite profiled beam, the profiled steel sheeting is fabricated into fully braced open trough girders, as shown in Fig. 17.1. The trough section is then placed on site with a minimum of additional propping or support, with the concrete being poured to form a composite profiled beam as shown in Fig. 17.2. Because the steel sheeting is thin, local instability may affect the behaviour even before the concrete has been poured.
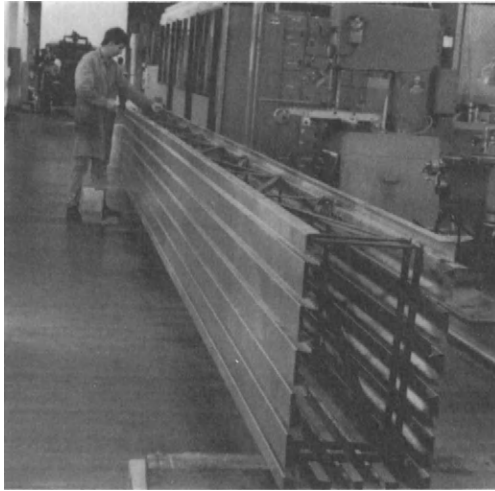
Fig. 17.1 Trough girder

Fig. 17.2 Composite profiled beam

Three basic types of profiled sheet configuration have been investigated for utilisation in composite profiled beam construction. They are the re-entrant L rib profile shown in Fig. 1.6(c), the dove-tailed rib profile shown in (a) and the trapezoidal rib profile shown in (b). During the construction phase, trough girders fabricated from these profile types must be able to support their own weight and the self weight of the adjacent slab soffit profiled sheeting and construction loads. The empty thin-walled trough section when undergoing sagging bending is then subjected to linearly varying compression in the upper part of the beam, and thus local instability caused by high localised compressive stresses may occur.

17.2.2   INITIAL LOCAL BUCKLING

17.2.2.1   *Analysis*

The prediction of local buckling may be based on the classical methods for plates in bending and plates in compression Using this approach, the local buckling of a plate assembly may be analysed approximately by assuming that the plate elements are hinged along their common boundaries, so that each plate acts as if simply supported along its common boundaries and free along any unconnected boundary. The elastic critical stress of each plate is determined using the appropriate buckling stress, and the lowest of these is used as an approximation for the local buckling stress of the plate assembly. This approximation is conservative, since the rigidity of the joints between the plate elements causes all plates to buckle simultaneously at a stress intermediate between the lowest and highest critical stresses of the individual plate elements.

The elastic buckling stress $\sigma_{o\ell}$ of a thin steel plate may be written in the form of Eq. 5.2, repeated here as

$$\sigma_{o\ell} = k \frac{\pi^2 E_s}{12(1-v_s^2)(b/t)^2} \frac{1}{} \tag{17.1}$$

where t is the plate thickness, b is the plate width and k = 4 for a simply supported plate in uniform compression and k = 0.425 for a plate outstand simply supported along one edge and free along the other edge. Equation 17.1 thus forms the basis for an approximate analysis of the plates in a thin-walled steel trough girder.

The conservatism of the preceding approximate analysis can be overcome by utilising the matrix stiffness methods of structural analysis. For local buckling, the semi-analytical finite strip method described in Section 10.2.1.3 for distortional buckling may be used. In this method, the component plates are discretised into a number of prismatic strips, as shown in Fig. 17.3 for a re-entrant L profiled trough. A typical finite strip, as shown in Fig. 17.4, is assumed to be subjected to a linearly varying end stress of

$$\lambda\sigma = \lambda\sigma_1 + \lambda(\sigma_2 - \sigma_1)x/b \tag{17.2}$$

where σ_1 and σ_2 are the initially applied edge stresses and λ is the buckling load factor. In an analogous manner to that described in Section 10.2.1.2 and following the standard matrix stiffness techniques for the finite strip method outlined by Cheung (1976), the stiffness matrix $[K^e]$ and the stability matrix $\lambda[G^e]$ for each strip may be developed, and these are assembled into the respective stiffness and stability matrices [K] and λ [G] for the folded plate structure. Local buckling will then occur when

$$([K] - \lambda[G])\{Q\} = \{0\} \tag{17.3}$$

where {Q} is the vector of buckling displacements and rotations at the nodal lines joining the finite strips.
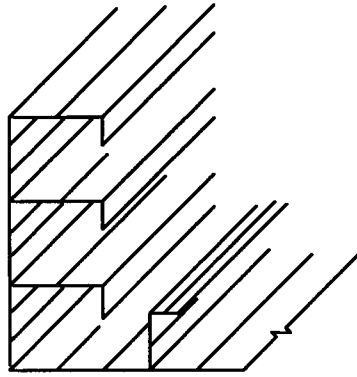
Fig. 17.3 Finite strip discretisation
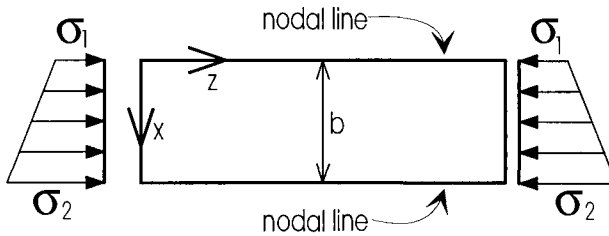
Fig. 17.4 Finite strip and edge stresses

Clearly the vector {Q} must be nonzero if we are going to have buckling displacements, so the nontrivial solution to Eq. 17.3 is

$$\mid [\,K\,] - \lambda_{cr}[\,G\,]\mid \;=\; 0 \tag{17.4}$$

which is the same as Eq. 10.3, where λ_{cr} is the critical value of the load factor λ that makes the determinant in Eq. 17.4 vanish. It can be determined by the method described in Section 10.2.1.2.

Once the local buckling stress $\sigma_{o\ell}$ has been determined by the finite strip method, the buckling coefficient k in Eq. 17.1 may be determined. Since the plate slendernesses b/t are large and the proof yield stress f_{yp} of the cold formed sheeting is quite high, being typically 550 N/mm^2, the buckling mode will invariably be elastic as $\sigma_{o\ell}$ will be much less than f_{yp}. The trough girder is therefore neither plastic nor compact (Section 5.2.4) and so cannot be designed plastically.

17.2.2.2   *Behaviour*

The semi-analytical finite strip method described in Section 17.2.1.1 has been used by Uy and Bradford (1993a) to study the local buckling response of the three profiles shown in Fig. 17.3. Each of the troughs was subjected to a linearly varying stress distribution throughout the depth. In this study, a maximum compressive stress of 1 kN/mm^2 was arbitrarily applied to the top fibre, and the stress distribution so defined was multiplied by the buckling eigenvalue λ_{cr} after the solution of the eigenproblem in Eq. 17.4 to obtain the stress distribution at elastic local buckling.

   The buckling stress is dependent on the half-wavelength of the local buckle L, so a plot such as that in Fig. 17.5 may be made close to the local buckling nadir. A polynomial interpolation may therefore be used to determine the minimum local buckling stress from calculated points close to the nadir.
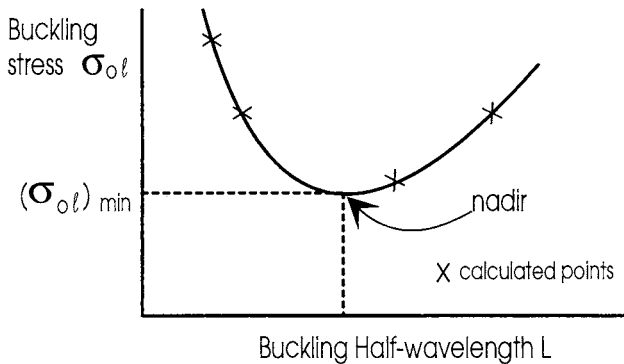
Fig. 17.5 Typical local buckling Garland Curve

   Plots of the local buckling coefficient k in Eq. 17.1 have been derived by Uy and Bradford (1993a) for various rib geometries, configurations and trough sizes. It was found that trapezoidal ribs were the most effective rib type for delaying the onset of local buckling. When the rib thickness is doubled, as would occur when the sheets are overlapped, then the value of the local buckling coefficient is almost doubled. This would be expected as the rib acts as a stiff supporting stiffener to the web, which in turn provides greater resistance to local buckling (Bradford 1989). Additionally, increasing the width of the empty trough girder had only a slight effect on the value of the local buckling coefficient.

17.2.3   POSTBUCKLING

The phenomenon of post-local buckling was introduced in Section 5.2.2, and applied to profiled steel sheeting subjected to wet concrete loads in Section 16.2.3.3. In a hollow trough girder, the elastic local buckling explained in Section 17.2.2 does not represent the ultimate strength of the trough, and the benign redistribution of the stresses after initial local buckling allows for larger loads to be carried than that to cause initial local buckling. The load-carrying capacity of the trough is exhausted

once the most highly stressed portions yield, or when the postbuckled deflections exceed serviceability limits.

Post-local buckling depends on nonlinear effects, so that the analysis is made difficult because the stiffness matrices are nonlinear. Azhari and Bradford (1995) included the nonlinear thin plate membrane strains (Timoshenko and Woinowsky-Krieger 1959) in their finite strip modelling of the problem, and derived stiffness relationships of the type

$$([K_0] + [K_1])\{Q\} = \{F_0\} + \{F_1\} \tag{17.5}$$

where $\{Q\}$ is the vector of postbuckled deformations, $[K_0]$ and $\{F_0\}$ are matrices dependent on the initial out-of-flatness of the thin plates, $\{F_1\}$ is a load vector resulting from the applied bending strains and $[K_1]$ is a stiffness matrix which is a quadratic function of the deformations $\{Q\}$. Consequently, Eq. 17.5 is nonlinear, and it was solved in the formulation of Azhari and Bradford by recourse to the well-known Newton-Raphson method.

Azhari, Uy and Bradford (1994) tested two thin-walled profiled trough girders in the postbuckling range, and obtained very good agreement with the finite strip postbuckling theory. In the latter method, at a given value of the curvature κ the postbuckled stress distribution was established, and this was integrated over its lever arm to obtain the moment M. The postbuckled stiffness S^* was then calculated from $S^* = M/\kappa$. In the postbuckled range of structural response, the stiffness S^* decreases below its initial value of $S = M/E_sI$. For an I-section beam, the minimum value of S^*/S is about 0.74 (Bradford 1983, Azhari and Bradford 1995) while it was found in a parameter study using the finite strip method that the minimum value of S^*/S for a profiled trough girder was close to 0.83. This difference may be attributed to the monosymmetry of the trough, where much less of the web is subjected to compression than occurs in an I-section beam. It is thus possible to obtain the maximum deflection of a profiled trough girder by analysing it with a linear stiffness E_sI, and increasing the deflection by 1/0.83 or 120%.

Example 7.1 Deflection of trough girder

The re-entrant L trough girder shown in Fig. 17.6 of thickness t = 1.0 mm is considered with and without a 25x25x5 equal angle bracing truss. The girder is subjected to a construction load of 1.2 kN/m and spans 6 m.

It is easy to establish that the neutral axis depth $\bar{y}$ and second moment of area I for the braced trough are 204 mm and 43.6×10^6 mm^4 respectively, and for the unbraced trough are 229 mm and 32.2×10^6 mm^4. The linear deflections $(5/384)wL^4/E_sI$ are 2.3 mm or L/2580 for the braced girder, and 3.1 mm or L/1900 for the unbraced girder. These may be increased by 120% due to postbuckling to obtain upper bound deflections.

The local buckling charts in Uy and Bradford (1993a) suggest a local buckling coefficient of k = 74 for the trough of Fig. 17.6. Thus from Eq. 17.1 with v_s = 0.3 and b = 400 mm, the elastic buckling stress $\sigma_{o\ell}$ = 83.6 N/mm^2. The stresses in the top of the trough can be obtained from the maximum moment wL^2/8 of 5.4 kNm as 25.3 N/mm^2 if the trough girder is braced and 38.4 N/mm^2 if it is unbraced. These stresses are well below both the local buckling and yield stresses, and so the stiffness reduction of 0.83 does not need to be applied.
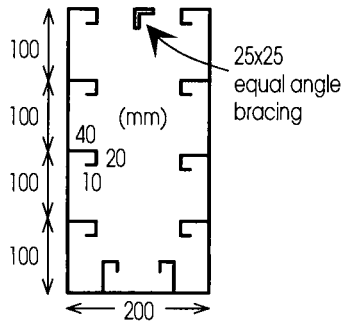
Fig. 17.6 Re-entrant L trough girder

17.2.4 REMEDIAL MEASURES

Based on the finite strip parameter study undertaken by Uy and Bradford (1993a), several remedial measures may be proposed to increase the local buckling capacity of an empty profiled trough girder. The local buckling stress may be increased by increasing the rib thickness where overlapping does not occur, and decreasing the vertical spacing of the ribs, particularly where high compressive stresses exist. Profiled rib shapes that have a large amount of continual directional change of the plates in the cross-section such as trapezoidal or dove-tailed ribs have higher local buckling stresses.

Both theory and tests have shown that the local buckling half-wavelength L in Fig. 17.5 at the minimum buckling stress is of the order of 20% of the trough depth. While the figure shows that the local buckling stress may be increased by enforcing a shorter buckling half-wavelength L in Fig. 17.5, bracing of the top of the trough more closely along its length as in Fig. 17.7 may prove impractical because of the close spacing required. An alternative is to tack weld the profiled sheeting used as the soffit for the composite slab to the top of the trough girder at close intervals to decrease the buckling half-wavelength at the top of the trough.
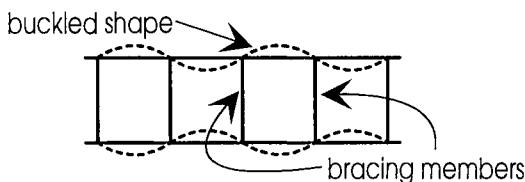
Fig. 17.7 Plan on top of trough girder

17.3   Composite profiled beams in flexure

17.3.1   GENERAL

After the concrete has been poured into the empty trough and cured, the steel sheeting and concrete will act compositely. The flexural analysis of composite profiled beams is similar to that of composite profiled slabs that was described in Chapter 16. It was shown in Section 16.3.1.2 and illustrated in Fig. 16.11(b) and (e) that the strain profile in the reinforced concrete element overlapped the strain profile in the steel element. Hence full shear connection is synonymous with full interaction, so that the neutral axis, and hence the strength, is determined by equating the compressive strength above the neutral axis to the tensile strength below the neutral axis. Furthermore, it was shown that partial shear connection is synonymous with partial interaction, so that the neutral axes in these beams can be determined by ensuring that each element is in equilibrium with the shear connection strength. The same procedure can also be applied to composite profiled beams.

A composite profiled beam is shown in Fig. 17.8(a). The composite action between the open profiled trough section, or box beam, and the reinforced concrete element it encases, as in (a), is described in the following section, where standard forms of rigid plastic analysis are used. A more refined and different approach to the same problem is described in Section 17.3.3, where standard procedures for reinforced concrete beam analysis are combined with standard procedures for composite beam analysis.

The ribs of the steel decking in profiled slabs are shaped so that they can be clipped together. Therefore, large areas of profiled shuttering can be formed by simply joining together individual segments of profiled sheet. The same procedure can be applied to composite profiled beams, where virtually any shape and size of the cross-section can be constructed by clipping together narrow segments of profiled sheet. This form of construction, where the rib joints are clipped together, is different from the open box girder technique described in the previous paragraph, since the joints between the sheet segments are free to slide in the longitudinal direction. The ramifications that this has on the composite action are described in Section 17.3.4.

An important consideration in the behaviour of composite profiled beams is the possibility of local buckling in the compressive and shear regions of the member. The buckle differs in its nature from that in the empty trough, as the

concrete element forms a rigid restraining medium and prevents the buckle from forming into the concrete. The buckled shape is thus not of a sine-type curve, but rather is of a sine squared shape. This characteristic increases the buckling resistance, and is considered more fully in Section 17.5.
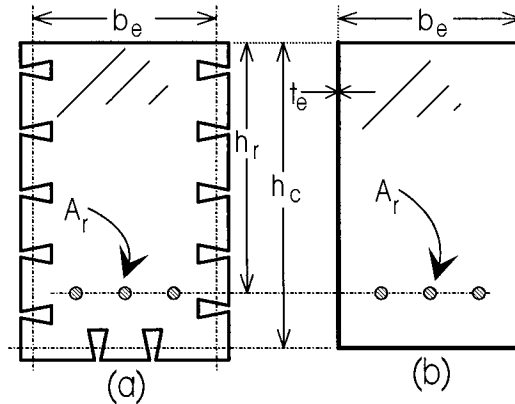
Fig. 17.8 Composite profiled beam

17.3.2   OPEN BOX BEAM

17.3.2.1   *Full shear connection*

The behaviour of the side profiles of the composite profiled beam shown in Fig. 17.8(a) differs in many ways to that of the soffit profiles in composite profiled slabs that were discussed in Chapter 16. For example, the side profiles are just as effective in both the positive and negative regions of continuous beams, whereas the soffit profile is only effective in positive regions.

The ribs in the side profiles in Fig. 17.8(a) have two main purposes. They firstly ensure vertical compatibility by tying the reinforced concrete element and hence ensure that the curvature in both elements is the same, and secondly they transmit the longitudinal shear between the two elements. The behaviour of side profiles can best be illustrated by considering the action of the side profiles themselves as shown in Fig. 17.9(a). For ease of discussion in the following analyses on full shear connection, we will combine the outer side elements, such as those of thickness t, so that we are dealing with an inner element and an outer element of thickness 2t.

(a) Symmetrical and homogeneous beam with full depth plates

Let us consider a composite beam with side plates as in Fig. 17.9(a) and (b) in which the materials of the elements exhibit rigid plastic properties, and each material has identical properties in tension and compression. The side plates are placed central to the mid-depth of the beam as shown in (a) and (b) so that by symmetry the neutral axis is at the mid-depth as shown in (c). The force and stress distribution for the inner element can be derived from rigid plastic analysis, and are shown in (d).

Because of symmetry, the compressive force above the neutral axis F_1 is equal to the tensile force below the neutral axis, and hence the resultant force in the inner element is zero. Because of this, the resultant longitudinal bond force that is applied to the inner element is also zero. Exactly the same argument can be applied to the outer plate element to give the result in (e) where the resultant force is also zero. Hence, this homogeneous and symmetrical form of structure does not require any longitudinal shear strength to achieve the flexural capacities of the elements which can be determined from (d) and (e).
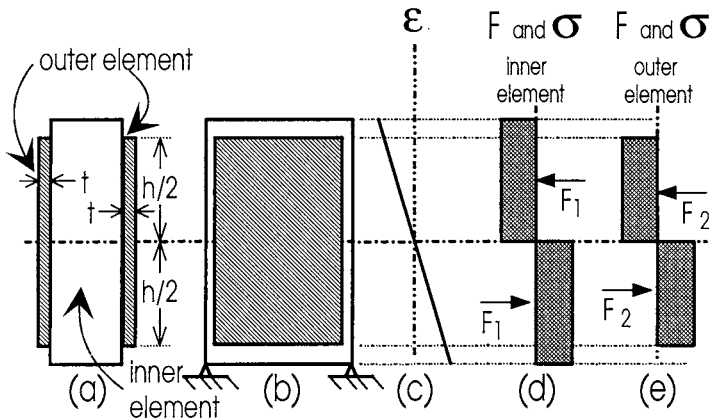
Fig. 17.9 Symmetrical elements

It is worth noting that if both elements in the beam in Fig. 17.9(b) are displaced equally in the vertical direction by the applied loads, then there is no need for any type of bond between the inner and outer elements. However, if the load is applied directly to the inner element, then the applied load is transferred to the outer elements through the profile ribs, as described in Section 17.4, which is another principal reason for having the ribs.

(b) Symmetrical and homogeneous with plates split

Let us now consider the same composite beam as in Fig. 17.9 but with the plate divided in half, as in Figs. 17.10(a) and (b). We are still dealing with full interaction as shown in (c) and as the beam is still symmetric the neutral axis is still at mid-depth. The upper outer element in (a) will be fully yielded in compression with a resultant force of F_2 as shown in (e), as the whole element is above the neutral axis. Therefore, the resultant force in the shear connection between the upper outer element and the inner element is also F_2. Similarly, the lower outer element will be fully yielded in tension as in (f) inducing a resultant force in the shear connection of equal magnitude but opposite direction to the shear force induced by the upper outer element in (e). The inner element is therefore subjected to equal and opposite shear forces of magnitude F_2, so that the resultant of the longitudinal shear forces acting on the inner element is zero and therefore the resultant force in the inner element is still zero, as shown in (d). It can thus be seen by comparing the stress distributions that

the flexural strengths of the composite beams in Figs. 17.9 and 17.10 are identical, but the beam with a split plate requires a shear connection strength of $2F_2$ per shear span, whereas the beam with the unsplit plate requires no longitudinal shear connection.
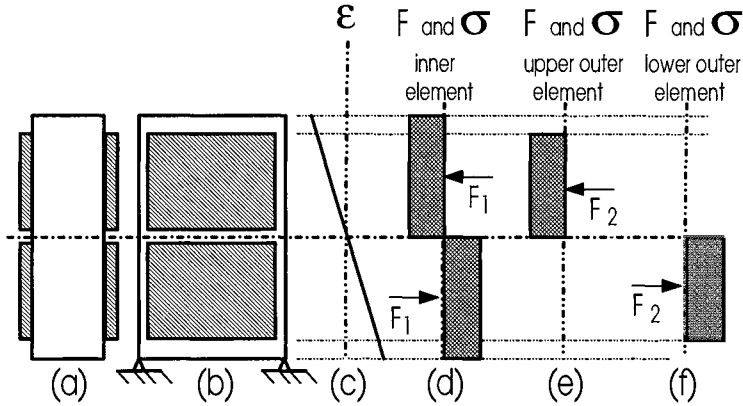
Fig. 17.10 Outer element split

One of the fundamental principles of composite rigid plastic analysis is that the magnitude of the resultant force in each element and in the shear connection is equal. This principle applies perfectly well when there are only two elements, but has to be used with caution when dealing with more than two elements. It may be better to state the principle as the resultant force in an element, the resultant force in the remainder of the structure and the resultant shear connector force between the element and the remainder of the structure are of equal magnitude. Hence the resultant force in the upper outer element in Fig. 17.10(e) is equal to F_2, the resultant force in the remainder, that is (d) and (f), is also F_2, and the resultant shear connection force between the upper outer element and the remainder of the structure is F_2.

(c) Non-homogeneous and non-symmetrical

Consider now a reinforced concrete element that is sandwiched between two steel plates as shown in Fig. 17.11(a) where there is full interaction between the elements as shown in (c). The level of the neutral axis can be determined by equating the compressive strength of the concrete and any steel above the neutral axis with the tensile strength of the steel and reinforcement below the neutral axis. The resultant force in both elements, $F_1 - F_2$ in (d) and $F_4 - F_3$ in (e), have the same magnitude and is also the resultant force in the shear connection.

Example 17.2 Full shear connection strength

For analysis purposes, the geometry of a composite profiled beam such as that shown in Fig. 17.8(a) can be simplified to the idealised version shown in (b) (Oehlers,

Wright and Burnet 1994). The effective thickness of the profiled sheet t_e is such that the cross-sectional area of the idealised profiled sheet in (b) is the same as the area of the sheet in (a). The effective depth h_c can be taken to the centroid of the soffit profiles, as the moment within these profiles is minimal due to their shallow depth. The effective width b_e can be chosen so that the area of concrete in (a) is the same as that in (b). The distance h_r is measured to the depth of the reinforcing bars of total area A_r.

The shear connection strength of the bond between the reinforced concrete element and the profiled-sheet element is the shear strength of all the rib connectors, that is the rib shear connection strength between the design point and the point of contraflexure. It will be shown in Section 17.4 that the position of the bond force and therefore the ribs does not affect the flexural capacity of the composite beam, but does affect the vertical shear forces within the steel element and concrete element.

An idealised composite profiled beam is shown in Fig. 17.12(a) and a full shear connection analysis is shown in (b), (c) and (d), where the units are N and mm unless stated otherwise. The forces shown in (d) for the profiled sheet are the sum of the forces in both side sheets, so that we are dealing with a single 6 mm sheet thickness for the side profiles whereas the soffit profile remains at 3 mm.

The first step in the analysis is to determine the neutral axis depth n in Fig. 17.12(b) by equating the compressive strength of the concrete and profile above the neutral axis to the tensile strength of the profile and reinforcing bars below the neutral axis. This produces n = 212 mm, as shown in (b). The distribution of axial forces for each of the elements is as shown in (c) and (d), where the bracketed number is the distance of the force from the top fibre. Taking moments of the axial forces in (c) and (d) about the top fibre, for convenience, produces the full shear connection flexural capacity as $M_{fsc} = 853$ kNm. The bond strength required for full shear connection is the resultant of the forces in either (c) or (d), and this is calculated as $P_{fsc} = 1079$ kN. Hence the total strength of the rib shear connection between the design point and the point of contraflexure, or the nearest support in the case of a simply supported beam, must be at least 1079 kN in order to achieve the maximum flexural capacity.

If it is found that the distance between the ribs in Fig 17.8(a) is too large to prevent buckling, then the effective section approach could be used to reduce the effective thickness t_e of the profiled sheet above the neutral axis. A lower bound to the strength would be to ignore the profile sheet that is in compression, and this analysis is shown in Figs. 17.12(e), (f) and (g). As the compression steel is ignored, more concrete must go into compression and so the neutral axis drops to 275 mm in (e). The flexural capacity is now 757 kNm, that is an 11% reduction from the previous analysis. However, the bond strength required has increased substantially to 1567 kN, which is a 45% increase.
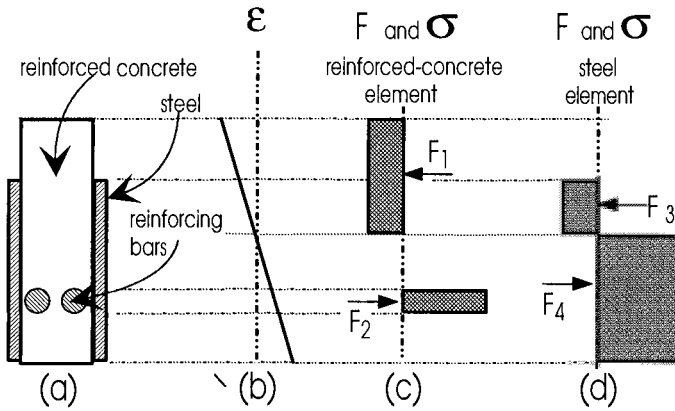
Fig. 17.11 Non-symmetry
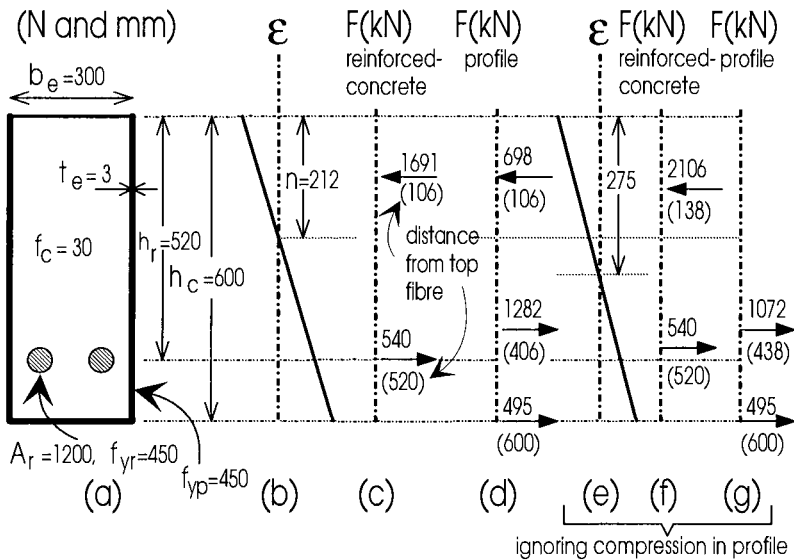
Fig. 17.12 Example 17.2: Full shear connection

17.3.2.2 *Partial shear connection*

The analysis procedures described in the previous section can be used to determine the strength of the shear connection that is required for full shear connection. When the actual strength of the shear connection in the shear span of the beam is less than that required for full shear connection, then the beam has partial shear connection and hence the beam exhibits partial interaction. An example of the strain profile for a beam with partial shear connection is shown in Fig. 16.11(e). The strain profiles are parallel because the curvatures are the same in both elements, and hence the slip

strain and therefore the slip between elements is the same throughout the depth of the beam.

The composite beam in Fig. 17.11(a) is now analysed with partial shear connection in Fig. 17.13. With full shear connection and full interaction, the strain profiles in the reinforced concrete element and the steel element coincide as shown in (b), and loss of interaction causes the strain profiles to separate as shown in (c) and (d), and ensuring that the resultant force within each element is equal to the shear connection strength. The flexural capacity can now be determined by taking moments of the forces in (c) and (d) about any convenient level.
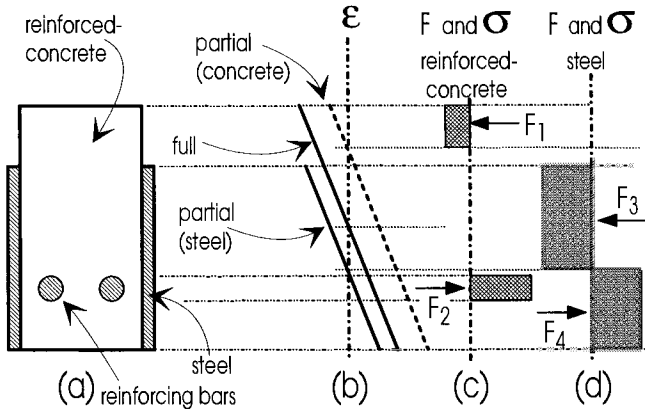
Fig. 17.13 Partial shear connection

Example 17.3 Partial shear connection strength

The composite beam in Example 17.2 and in Fig. 17.12(a) has been re-analysed in Fig. 17.14 with a 50% degree of partial shear connection. The forces are in kN, the distances in mm and the bracketed number is the distance of the force from the top fibre. It has also been assumed that the profiled sheet will not buckle locally.

From Example 17.2, the full shear connection strength $P_{fsc} = 1079$ kN, therefore the 50% shear connection strength is $P_{50\%} = 540$ kN. The neutral axis position of the reinforced concrete element in Fig. 17.13(b) can be determined by equating the algebraic sum of the compressive forces above the neutral axis and the tensile forces below the neutral axis to the bond strength of $P_{50\%}$ as shown in Fig. 17.14(b). The same procedure can be applied to the profile element as in (c). The moments of the forces in (b) and (c) give a partial shear connection flexural strength of $M_{50\%} = 812$ kNm. Hence a 50% reduction in the shear connection strength, from that of the full shear connection strength, has reduced the flexural capacity by only 5%, from $M_{fsc} = 853$ kNm in Example 14.2 to 812 kNm.

When there is no longitudinal shear strength, that is there is a degree of shear connection of zero, then the reinforced concrete element and the profiled element act as individual beams. The flexural strengths of the individual beams can be determined using the procedure outlined in Fig. 17.14. However, in this case the algebraic sum of the forces will equate to zero. The flexural capacity of the reinforced concrete beam can be calculated as 262 kNm, and that of the profiled beam as 427 kNm, producing a total moment capacity of $M_{0\%}$ = 689 kNm which is only 19% less than the flexural capacity with full shear connection (Example 14.2).
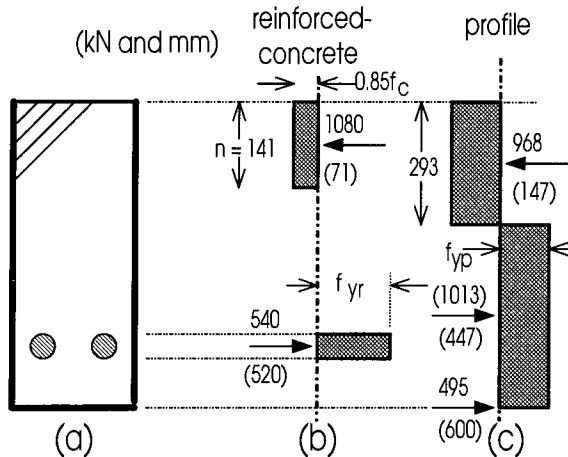
Fig. 17.14 Example 17.3: 50% partial shear connection

It can be seen from Example 17.3 that, unlike composite profiled slabs, the flexural capacity of profiled beams is not highly dependent on the bond strength. It is also noteworthy that experimental research (Oehlers 1993, Uy and Bradford 1995a) has shown that the ductility of the profiled beam is on a par with the ductility of the reinforced concrete element acting by itself, and that a profiled beam is more ductile than a reinforced concrete beam of the same strength.

17.3.3   REFINED MODEL

17.3.3.1   *General*

The analyses of composite profiled slabs in Chapter 16 and the profiled beams in the previous Section 17.3.2 are based on *rigid plastic theory*. The steel element is assumed to have the stress-strain relationship O-A-B in Fig. 2.2 of unlimited ductility, and the concrete is assumed to have the stress-strain relationship A-F-G in Fig. 2.8 that also has unlimited ductility. An example of an analysis is shown in Fig. 16.11 where it can be seen in (c) and (d) that the neutral axes occur just below the compression zones. It is normal practice to use this approach in steel beam and composite beam design. However, in reinforced concrete design, it is more common

to use the stress-strain relationship A-B-C-D-E in Fig. 2.8 in order to allow for the nonlinearity and limited ductility of the concrete.

The composite section in Fig. 16.11(a) can be considered to consist of a steel element that encases a reinforced concrete element. Therefore, a more refined analysis (Oehlers, Wright and Burnet 1994) would be to treat the steel element as a steel beam with the stress-strain relationship O-A-B in Fig. 2.2 and the reinforced concrete element as a reinforced concrete beam where the concrete has the stress-strain relationship A-B-C-D-E in Fig. 2.8 Hence, when the area of the steel element tends to zero, the analysis reverts to that of a reinforced concrete beam.

A full interaction analysis and hence a full shear connection analysis of an idealised composite profiled beam is shown in Fig. 17.15. The analysis procedure follows exactly the same procedure as outlined in Section 17.3.2, except that only the part of the concrete in the compression zone of depth n/γ has compressive stresses as shown in (c), where γ is the neutral axis factor given by Eq. 2.17. The neutral axis is derived using the standard procedure of equating the compressive strength above the neutral axis to the tensile strength below the neutral axis. Having derived the neutral axis, the stress distributions in each element in (c) and (d) are now known, so the flexural capacity with full shear connection can be determined, which will be slightly less than that derived using the standard rigid plastic analysis approach. The bond strength for full shear connection can then be derived from the resultant force in either of the elements in (c) or (d).
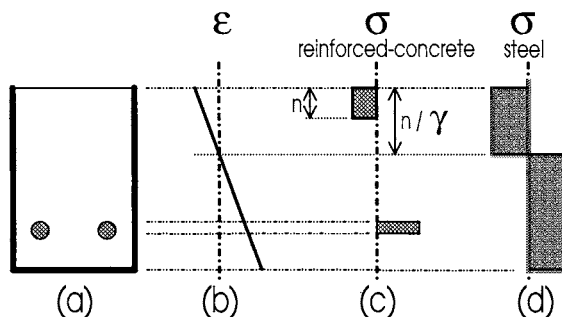
Fig. 17.15 Full shear connection

When the bond strength for full interaction cannot be achieved, then the analysis reverts to the standard partial shear connection analysis where the neutral axis in each element is determined by ensuring that the resultant force in each element is equal to the bond force.

17.3.3.2 *Analysis*

The idealised section shown in Fig. 17.16(a) will be analysed using this refined model. However, a slightly different approach (Oehlers, Wright and Burnet 1994) will be used that clarifies the relationship between full and partial shear connection analyses.
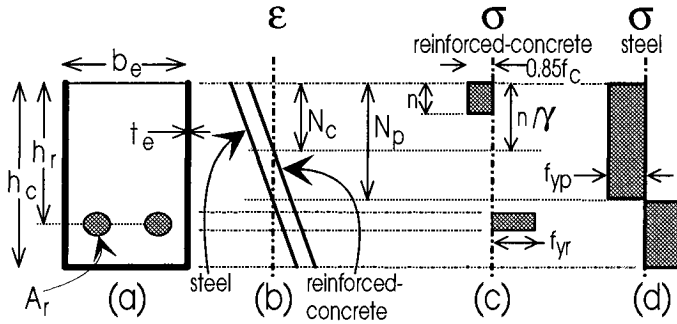
Fig. 17.16 Partial shear connection

(a) Axial strengths

The axial strength of the reinforcing bars in Fig. 17.16(a) of area A_r and yield strength f_{yr} is given by

$$P_r = A_r f_{yr} \qquad (17.6)$$

The axial strength of the profiled sheet with the dimensions shown in (a) and yield strength f_{yp} is given by

$$P_p = t_e(2h_c + b_e)f_{yp} \qquad (17.7)$$

and the axial strength of the longitudinal shear connection is

$$P_b = NLQ_r \qquad (17.8)$$

where N is the number of profiled ribs in the profiled-beam cross-section, Q_r is the longitudinal shear strength of a rib per unit length, and L is the length of the shear span from the design point to the point of contraflexure such as the support of a simply supported beam.

(b) Neutral axes

For the case of partial shear connection as shown in Fig. 17.16(b), the depth to the neutral axis in the reinforced concrete element N_c is given by

$$N_c = \frac{P_r + P_b}{0.85 f_c \gamma b_e} \qquad (17.9)$$

where f_c is the compressive cylinder strength of the concrete. The depth to the neutral axis in the profiled element N_p is given by

$$N_p = \frac{P_p - P_b}{4t_e f_{yp}} \tag{17.10}$$

(c) Partial shear connection

Having determined the positions of the neutral axes in Fig. 17.16(b), the stress profiles in (c) and (d) are now known, and hence the resulting forces and the moment capacity M_{psc} with a partial shear connection strength of P_b can be determined as

$$M_{psc} = t_e f_{yp}(h_c^2 + b_e h_c - 2N_p^2) + P_r h_r - \frac{0.85 f_c b_e \gamma^2 N_c^2}{2} \tag{17.11}$$

(d) Full shear connection

The partial interaction and partial shear connection flexural strength of Eq. 17.11 is only applicable when the strength of the shear connection is less than that required for full shear connection $(P_b)_{fsc}$. This strength can be determined by equating the neutral axis depths in both elements in Eqs. 17.9 and 17.10 to give

$$(P_b)_{fsc} = \frac{0.85 f_c \gamma b_e P_p - 4t_e f_{yp} P_r}{0.85 f_c \gamma b_e + 4t_e f_{yp}} \tag{17.12}$$

Substituting $(P_b)_{fsc}$ for P_b in Eqs. 17.9 and 17.10 and inserting these values into Eq. 17.11 gives the flexural capacity for full shear connection. It can be seen that full shear connection is thus simply a special case of partial shear connection.

(e) No shear connection

No shear connection is also only a special case of partial shear connection. The flexural capacity with no shear connection can be determined by substituting $P_b = 0$ into Eqs. 17.9 and 17.10 and inserting these into Eq. 17.11 for the flexural capacity with no shear connection.

Example 17.4 Flexural capacity using Refined Model

The composite profiled beam in Fig. 17.12(a) and Example 17.2 is to be re-analysed for full shear connection using the 'refined' approach.

From Eq. 2.17, $\gamma = 0.836$ and hence from Eq. 17.12, $(P_b)_{fsc} = 944$ kN. The neutral axis depths are $N_c = N_p = 232$ mm (Eqs. 17.9 and 17.10), so that from Eq. 17.11, $M_{fsc} = 850$ kNm which is only a fraction smaller than that derived from rigid plastic analysis of 853 kNm (Example 17.2). This technique is useful since N_c in Fig. 17.16(b) can then be used to ensure that yielding of the reinforcing bars occurs before the concrete crushes in the reinforced concrete element.

17.3.4   CLIPPED JOINTS

17.3.4.1   *Full shear connection*

When the profiled section of a composite profiled beam is formed by clipping narrow segments of profiled sheet together as was described in Section 17.3.1, then it is necessary to ensure equilibrium of each segment of the profiled section. The analysis for full shear connection and full interaction is shown in Fig. 17.17 for a composite profiled beam that has been constructed with five levels of segments as shown in (a). Each of the joints at the ribs is free to slide in the longitudinal direction.
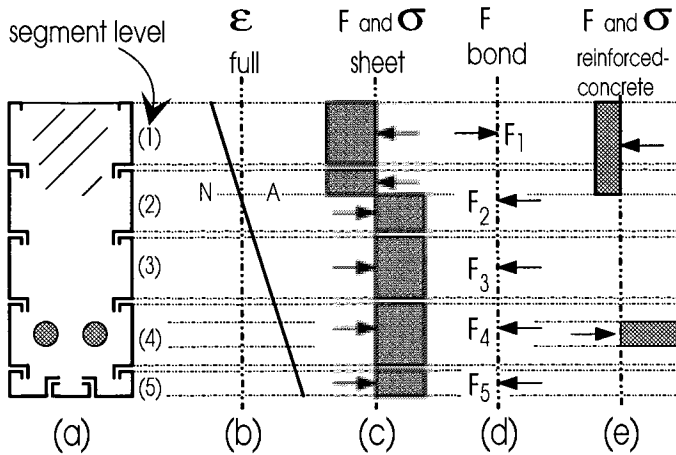
Fig. 17.17 Profiled beam with full shear connection

The first step in the analysis is to determine the level of the neutral axis in Fig. 17.17(b), where the compressive strength of the concrete and sheet above the neutral axis is equal to the tensile strength of the sheet and the reinforcing bars below the neutral axis. Having determined the level of the neutral axis, the distribution of stresses and forces within each segment of the profiled sheet can be determined as shown in (c) as well as the distribution within the reinforced concrete element in (e), and these can be used to determine the flexural capacity of the section with full shear connection. It can be seen in (c) and (e) that a full shear connection and a full interaction analysis ensures that the maximum lever arm exists between the elements in compression and tension which maximises the flexural capacity of the composite beam.

The resultant axial force in each of the profiled segments can be determined from the stress distribution in Fig. 17.17(c) and is shown in (d). The second segment down at level 2 requires only a relatively small bond force as the segment is partly in tension and partly in compression. The resultant forces in (d) are therefore the longitudinal shear connection strength of each segment that is required

for full shear connection of that segment, and the algebraic sum of these forces is the resultant axial force in the reinforced concrete element in (e).

Example 17.5 Full shear connection analysis of profiled beam with clipped joints

The composite beam in Example 17.2 and Fig. 17.12(a) has been re-analysed as a clipped profiled beam in Fig. 17.18 where the dimensions are in mm. The analysis for full shear connection in (b), (c) and (d) is exactly the same as in Example 17.2 and Fig. 17.12 However, the axial forces in Fig. 17.12(d) have now been distributed amongst the segments as in Fig. 17.18(d).

    The resultant force in each segment in Fig. 17.18(d) is the bond force required for full shear connection in that segment. Hence, the summation of the magnitudes of these forces, and not the algebraic summation, is the bond force required for full shear connection, and this comes to $(P_{fsc})_{clip}$ = 2065 kN which is much higher than the bond strength required for the box section in Example 17.2 of P_{fsc} = 1079 kN. Because of this, clipped joints require a much greater bond strength than rigid continuous joints in order to achieve the same full shear connection flexural capacity.
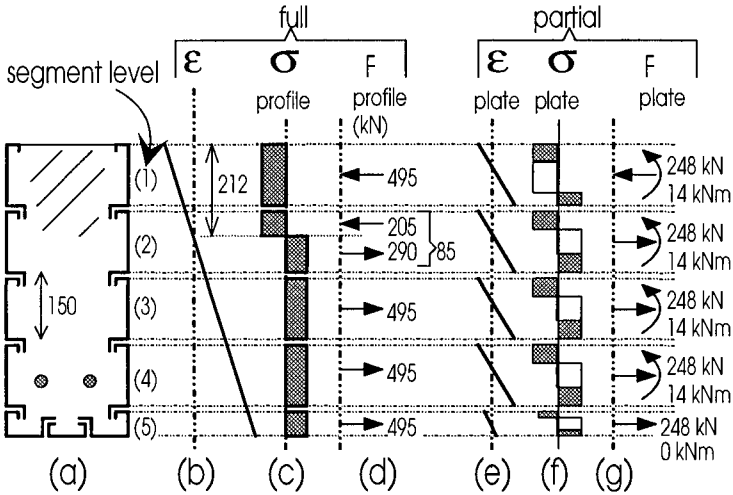
Fig. 17.18 Examples 17.5 and 17.6: Clipped joints

17.3.4.2 *Partial shear connection*

If any of the five shear connection strengths required in Fig. 17.18(d) cannot be achieved, then the full shear connection neutral axis position in (b) must change to accommodate the resulting changes in the axial forces. Hence, a slip strain is induced between the strain profile in the reinforced concrete element and the strain profiles in the profiled segments. We are, therefore, dealing with a state of partial interaction and hence partial shear connection.

The composite beam shown in Fig. 17.17 is re-analysed in Fig. 17.19 with partial shear connection instead of full shear connection. Let us assume that the longitudinal shear strength is not sufficient to sustain any one of the bond forces F_1, F_3, F_4 or F_5 in Fig. 17.17(d) that are required for full shear connection. However, it is sufficient to sustain the relatively small bond force F_2 at level 2. Because of the reduction in the bond force due to partial shear connection, the resultant axial force in the reinforced concrete element will be less than that required for full shear connection. Hence the neutral axis in the reinforced concrete element moves up, as shown in Fig. 17.19(b), so that there is less concrete in compression as in (c). For convenience, the curvatures for full and partial interaction in (b), that is the slope of the strain profiles, are drawn equal but in reality they will be different.
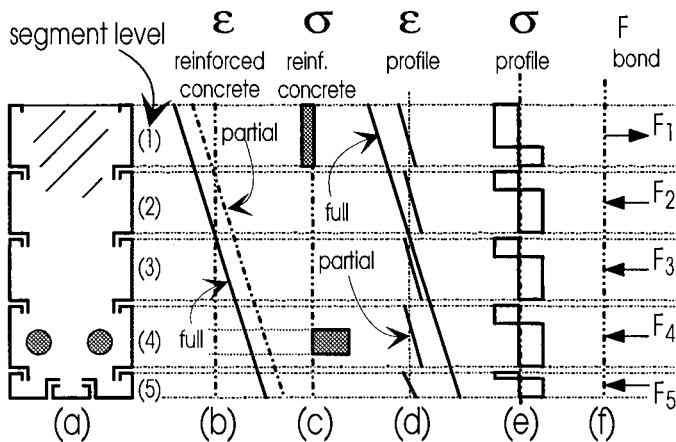
Fig. 17.19 Profiled beam with partial shear connection

The reduction in the bond strength has also to be accommodated by movement of the strain profiles in the profiled segments (Burnet and Oehlers 1995). At level 1 in Fig. 17.19(a), the strain profile must move to the right as shown in (d), such that part of the segment is in tension as in (e), so that the resultant compressive axial force in the segment is now equal to the bond force F_1 as shown in (f). The bond force F_1 is the strength of the shear connection in the segment at level 1. At levels 3, 4 and 5, the strain profile must move to the left to induce the stress distributions in (e), and hence the bond forces in (f). It can be seen that the strain profiles move just sufficiently enough to ensure equilibrium with the bond strength. For example, the strain profile at level 4 in (d) could move further to the left to induce a resulting compressive force in the profile and hence reverse the bond force at level 4 in (f), but this is theoretically incorrect as it would reduce the flexural capacity of the composite beam.

It is not obvious what will happen to the segment at level 2 in Fig. 17.19(a) where it was assumed that the lower bond force of does not exceed the longitudinal bond strength, and therefore a state of full shear connection would appear to exist.

For a state of full shear connection to exist, we also require a state of full interaction. It is shown in (b) that the strain profile in the reinforced concrete element will move relative to the full interaction position when there is a loss of shear connection in the beam. Therefore, the strain profile in the reinforced concrete element at level 2 in (b) will not be in line with the strain profile of the profiled segment at level 2 in (d). A state of partial interaction thus exists at level 2, and therefore a state of partial connection exists, even though the segment at level 2 appeared to be in a state of full shear connection. The strain profile at level 2 therefore moves to accommodate the bond strength. If it is unclear which way the strain profile will move, that is whether the resultant force in the element should be compressive or tensile, then the correct position is the one that maximises the flexural strength of the composite beam.

Example 17.6 Partial shear connection analysis of a beam with clipped joints

The composite beam in Example 17.5 and in Figs. 17.18(a) to (d) is re-analysed with a 50% degree of shear connection. The properties of the beam are given in Fig. 17.12(a). The assumed distribution of strain is shown in Fig. 17.18(e), the stresses in (f) and the stress resultants in (g).

The resultant axial forces in all five segment levels in Fig. 17.18(g) have the same magnitude of 248 kN, that is 50% of the full shear connection strength of 495 kN as shown in (d). The moments in all four side segments have the same magnitude of 14.0 kNm, but it has been assumed that the moment in the soffit segment is zero as the depth of this segment is very small. The algebraic sum of the forces in (g) is 744 kN, and this is the resultant axial force in the reinforced concrete element. Hence in the reinforced concrete element there is a tensile force in the reinforcing bars of 540 kN acting at 520 mm from the top fibre, as well as a compressive force in the concrete of $540 + 744 = 1284$ kN acting 84 mm from the top fibre. As all the stress resultants are now known, the moment capacity with 50% shear connection can be calculated as $M_{50\%} = 637$ kNm. If the stress profile at level 2 in Fig. 17.18(f) was changed to that at level 1 then the flexural capacity would drop to 593 kNm, confirming that the original assumption was correct.

The analysis can be repeated for zero shear connection, in which case the resultant axial force in Fig. 17.18(g) would be zero and the magnitude of the moment would be 18.6 kNm. The flexural capacity with zero shear connection then comes to $M_{0\%} = 336$ kNm which is only slightly greater than that of the reinforced concrete beam acting by itself of 262 kNm (Example 17.3).

17.4 Vertical shear in composite profiled beams

In the analysis of the standard form of composite beam in Chapter 7, it was shown that the position at which the longitudinal shear was transferred does not affect the flexural capacity. For example in Fig. 7.3(f), the longitudinal shear at the interface in which there are equal and opposite components does not contribute to the flexural capacity, as the resulting moment of these forces is zero. However, the position of

the resultant bond force does affect the distribution of the vertical shear forces between the elements of the composite beam.

Let us consider the profiled beam in Fig. 17.20(a) where each side profiled sheet is continuous through the depth, that is it is not formed by clipping. Analysis of the composite section at the design point shown in (b) will produce the stress distribution in the profile as shown in (c). This is equivalent to the stress resultants in (d) that consist of a moment M_p and an axial force F_{shear} at some arbitrary level. Now let us consider horizontal equilibrium of the profile by itself. The axial force F_{shear} at the design point shown in (d) must be balanced by a shear force at the plate-concrete interface of equal magnitude F_{shear} and opposite direction, as shown in (b). The position of the resultant shear force depends on the distribution of rib shear connectors, and let us assume that it acts at an eccentricity Δ from the resultant axial force at the design point as shown. The plate is therefore subjected to a moment due to M_p and $F_{shear}\Delta$. In order to maintain rotational equilibrium, vertical shear forces have to be induced at the plate-concrete interface, the resultants of which have been shown in (b) as V_{shear} acting at a distance L apart. Hence

$$V_{shear}L \;=\; M_p + F_{shear}\Delta \tag{17.13}$$

The stress resultants M_p and F_{shear} are constant and let us assume that L is also constant. Hence V_{shear} depends on Δ, that is the vertical shear forces depend on the position of the resultant longitudinal shear force Δ even though Δ does not affect the flexural capacity (Oehlers and Ahmed 1995).
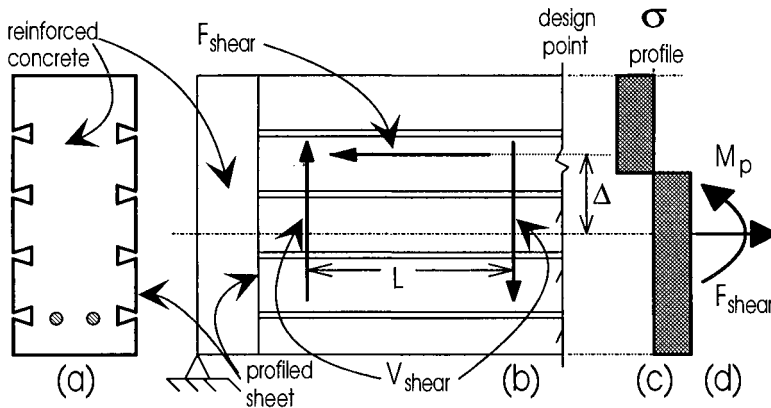
Fig. 17.20 Vertical shear in steel element

If the load is applied directly to the reinforced concrete element, then the vertical shear in the profiled sheet V_{shear} is transmitted into the profiled sheet by the rib shear connectors. Hence, the rib shear connectors have three main functions, they must be able to transfer longitudinal shear as well as vertical shear, and prevent separation between the steel and concrete elements. It is also worth noting that

experimental research has shown (Oehlers 1993, Bradford and Kyakula 1994) that side profiles can substantially increase the shear strength and ensure ductile shear failure, provided that the profiles do not buckle in shear.

17.5   Local buckling in composite profiled beams

17.5.1   GENERAL

It was outlined in Section 16.3.1.5 that when the concrete has hardened in a composite profiled slab, local buckling of the steel sheeting was forced to occur away from the rigid concrete slab, which acts as a restraining medium. While this was primarily of importance for slabs in regions of negative bending and with deep ribs, it is very important in composite profiled beams because the side profiles are subjected to bending stresses.

In a similar manner to the analysis of Section 16.3.1.5, Uy and Bradford (1994a) deployed the finite strip method to analyse local buckling in the sheeting of composite profiled beams in the elastic range of structural response. This analyses was subsequently extended into the inelastic domain (Uy and Bradford 1994b), so that recommendations could be made regarding plastic design of composite profiled beams.

17.5.2   ELASTIC BEHAVIOUR

The finite strip theory was calibrated against a series of so-called 'local buckling push tests' by Uy (1995). These consisted of thin cold formed plates loaded eccentrically to simulate axial stress and bending, while being restrained in small concrete blocks. The finite strip method was then applied to study parametrically the elastic buckling of several composite profiled beams with varying rib geometries. Local buckling coefficients were obtained, and the proof yield stress f_{yp} was set equal to $\sigma_{o\ell}$ in Eq. 17.1 to obtain limiting values for the modified slendernesses $(b/t)\sqrt{f_{yp}/550}$, where b is the distance between the ribs. When the top profile is anchored rigidly into the top of the concrete element by a bend in the profile to form a horizontal top plate as shown at the top surface of the beam in Fig. 17.17(a), yielding will occur before elastic local buckling when the modified slenderness $(b/t)\sqrt{f_{yp}/550}$ is less than 64 for a re-entrant L profile; 63 for a dove-tailed profile and 54 for a trapezoidal profile. It can be seen that although the trapezoidal profile is efficient for the empty trough or box girder, it loses its local buckling efficiency when full composite action is considered.

17.5.3 INELASTIC BEHAVIOUR

The width to thickness ratios obtained in the previous Section 17.5.2 give limits on the *slender* classification of a composite profiled beam, but they will allow local buckling to occur before the full plastic moment is attained. Therefore, for a rigid plastic analysis to be applicable, inelastic buckling in the compression zones can only

take place after the ultimate strength of the profile steel has been reached, in much the same way as for a steel I-section member analysed plastically (Trahair and Bradford 1991). In order to address this situation, Uy and Bradford (1994b) modified their finite strip method to handle inelastic effects, using the Ramberg-Osgood stress-strain relationship in Eq. 16.2. The calculation of the buckling stress is more difficult than for the elastic case, as an incremental and iterative scheme must be deployed to consider the spread of plasticity.

The finite strip method was validated by tests undertaken by Uy (1995), and limits were placed on the modified slenderness of the profile web between ribs $(b/t)\sqrt{f_{yp}/550}$. These may be approximated linearly as

$$(b/t)\sqrt{f_{yp}/550} = \lambda_1 + \alpha(\lambda_2 - \lambda_1) \tag{17.14}$$

where α is the stress gradient shown in Fig. 17.21(b) for the composite profiled beam with the buckle shown in (a), and λ_1 and λ_2 are the limiting slenderness values. For a plate with clamped unloaded sides, $\lambda_1 = 35$ and $\lambda_2 = 20$, while if the unloaded sides are simply supported, then $\lambda_1 = 30$ and $\lambda_2 = 20$. Since there is not a great deal of difference between the calculated slendernesses for these two restraint cases, the simply supported unloaded edge case provides a conservative and reasonably accurate prediction for a web profile between rib attachments.
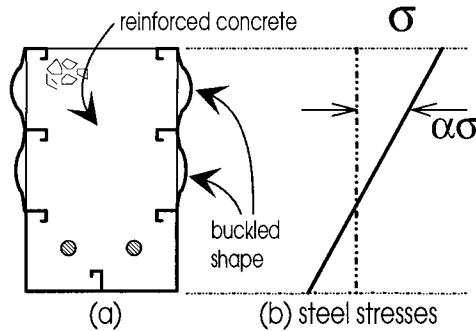
Fig. 17.21 Stress gradient in restrained plates

17.6 Ductility

As was mentioned in Section 17.3.2.2, one of the structural advantages that accrues to composite profiled beams is the increased ductility of a beam over its reinforced concrete counterpart that has the same ultimate strength. This was highlighted in experiments undertaken by Uy and Bradford (1995a) where two composite profiled beams and two reinforced concrete beams were tested under two-point loading to simulate a region of uniform bending. In accordance with the ultimate strength theory of Section 17.3, all beams were designed to have the same flexural strength, so that a valid comparison could be made.

Figure 17.22 shows schematically the moment-curvature results that were obtained theoretically and in tests. It can be seen that the initial stiffness is higher for the profiled beams than for the reinforced concrete beams, and that the curves for the profiled beams become more rounded in the advanced stages of loading. The increased ductility afforded by the composite profiled beams is obvious, and the redistribution of bending moments required in a plastic analysis of continuous beams that was discussed in Chapter 9 is attainable, provided that premature local buckling can be controlled. Conservatively, if local buckling does take place, then the buckled profile sheeting can be ignored.
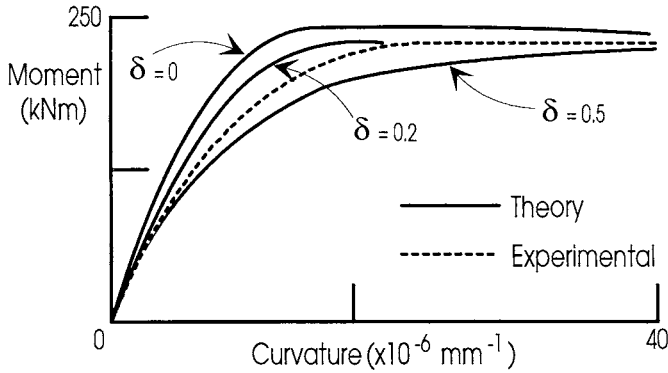
Fig. 17.22 Moment-curvature response

In order to quantify the various parameters in a composite profiled beam that affect its ductility, Uy and Bradford (1995b) undertook a theoretical study that was calibrated against the tests outlined in the previous paragraph. This analysis is similar to that undertaken by Uy and Bradford (1993b), and discussed in Chapter 9, and the results of this are outlined in the following. The cross-sectional analysis used two strain profiles, and the slip strain between the steel sheeting and the concrete was quantified in terms of a non-dimensional slip strain parameter δ, such that the slip strain was given by $\varepsilon_s = \delta \kappa d_{ss}$, where κ is the curvature and d_{ss} is the depth of the centroid in the steel sheeting below the top fibre. The stress-strain curve for the steel was obtained from Eq. 16.2, while that for the concrete was the CEB-FIP curve of Eqs. 2.11 to 2.13. with E_c given by Eq. 2.15. Schematic results for the moment versus curvature response are shown in Fig. 17.22 for a range of slip parameters δ. As has been discussed previously throughout this book, the ductility increases as the degree of interaction decreases but the ultimate strength is reduced.

Several other parameters were varied in the study based on the theoretical model of Uy and Bradford (1995b). The results of these are outlined in the following.

(a) Effect of profile yield stress f_{yp}

The effect of the profile yield stress was determined by using values typically available for cold formed steel, that is 250, 350, 450 and 550 N/mm^2. The effect of increasing the yield stress is an increase in strength, with reduced ductility as the ultimate curvature is reduced.

(b) Effect of concrete strength f_c

Concrete strengths of 25, 28, 32, 35 and 40 N/mm^2 were used in the study, and it was found that increasing the concrete compressive strength reduced the ductility significantly, while increasing the strength and stiffness. This well-known property of reinforced concrete is discussed more fully in Warner, Rangan and Hall (1989).

(c) Effect of concrete tensile strength f_t

The tensile strength of concrete f_t was represented using the range quoted by Gilbert (1988). This may be written as $f_t = k_t \sqrt{f_c}$, where k_t was taken as 0, 0.6, 0.85 and 1.1. Increasing the tensile strength substantially increases the stiffness and strength at service loads, and there is no penalty on strength and ductility at ultimate conditions.

(d) Effect of tensile reinforcing area A_{rt}

As with a reinforced concrete beam (Warner, Rangan and Hall 1989), increasing the area of tensile reinforcement greatly increases the stiffness and strength of a composite profiled beam, and reduces its ductility significantly.

(e) Effect of compressive reinforcing area A_{rc}

Increasing the compressive reinforcing area results in an increase in stiffness, strength and ductility. Hence if the strength needs to be increased by the addition of tensile reinforcement, then compressive steel bars may have to be added to maintain the level of ductility, in much the same way as for conventional reinforced concrete construction.

(f) Effect of profiled sheeting thickness t

The study varied the cold formed sheeting gauge thickness for those commonly available, namely t = 0.75, 1.0, 1.25 and 1.5 mm. As would be expected, the strength and stiffness are greatly increased, but the reduction in ductility somewhat minor as some of the sheeting is in the compressive zone as well as the tensile zone of the beam.

17.7   Service load behaviour

As with the service load behaviour discussed in Chapter 6, the time-dependent effects of creep and shrinkage of the concrete element may affect substantially the response of a composite profiled beam at service loads. Short-term deflections can be obtained from the moment versus curvature response that may be generated in the way described in Section 17.6. Long-term time-dependent deflections are of importance, and may be obtained by the approximate methods for unpropped or propped construction outlined in Section 6.4. The analyses of T-beams and of composite profiled beams are similar, but it should be noted that the creep coefficient ϕ and shrinkage strain ε_{sh} will be quite dissimilar for the two beam types, owing to the restraint afforded to the egress of moisture by the sheeting in composite profiled beams.

Uy and Bradford (1994c) tested two composite profiled beams and two reinforced concrete beams of the same calculated ultimate strength to compare their performance under long-term loading. It was found, both in their tests and in a theory based on the Age-Adjusted Effective Modulus Method described in Section 2.3.3, that composite profiled beams perform more favourably than their reinforced concrete counterparts in regard to long-term deformations. This is to be expected, since the steel sheeting reduces the creep coefficient and shrinkage strain.

One important aspect germane to composite construction with thin-walled sheeting acting compositely with a rigid concrete medium was the occurrence of long-term local buckling. This occurs because the time-dependent response of the concrete sheds load into the sheeting, in the same way as it sheds load into reinforcing bars in reinforced concrete construction (Gilbert 1988). This phenomenon was observed in the tests of Uy and Bradford, and a mathematical model to predict this has been proposed (Uy and Bradford 1995c) in which the time-dependent strains induced in the sheeting are inputted into the finite strip local buckling model. This local buckling in the time domain may therefore result in a loss of composite action, and the engineer should use his or her judgement to detail the design so as to prevent local buckling of the profiled sheeting in regions of high compressive stress. Thus, the limits on b/t ratio proposed in Section 17.5.2 may have to be reduced. It is felt, though, that this is probably not necessary, as the b/t limits in this section prevent local buckling before yielding, while local buckling induced by creep and shrinkage is a service load phenomenon that takes place at stresses well below the yield stress f_{yp}. In conclusion, as b/t is inversely proportional to $\sqrt{\sigma_{o\ell}}$ for elastic buckling, provided the yield limits of Section 17.5.3 are satisfied, it is unlikely that time-dependent local buckling will occur.

17.8   Behaviour under fire

The reduction in strength and stiffness of steel at elevated temperatures is detrimental to steel encased concrete composite structures, so that the response of composite profiled beams to fire is of importance, particularly as these members are proposed for office building construction. The behaviour has been studied most with regard to

concrete-filled tubular columns (Chapter 18), where the concrete core must carry the load during a fire as these members are invariably unreinforced. This is not so important for composite profiled beams, where reinforcing bars are usually provided in addition to the profile steel element.

The analysis of structural members experiencing elevated temperatures, such as those caused by a fire, are outlined in a suite of national standards for concrete, steel and composite construction. These standards usually suggest different load combinations than those adopted for strength or serviceability limit states.

Recommendations have yet to be proposed for composite profiled beams in fire, although we saw in Section 16.5.3 that the 'Fire Engineering Method' has been suggested for composite profiled slabs. However, a number of tests have been undertaken on composite structures with a thin steel skin, and design rules could be based on the measured behaviour in the tests. For example, Schmidt and Lehmann (1986) undertook tests on the fire resistance of composite deck slabs. Various rib configurations were used and a very extensive test series was carried out to ascertain the period of time which the profiled composite slabs could resist with the applied design fire load. A similar series of tests was undertaken by Cooke, Lawson and Newman (1988) for the fire behaviour of profiled steel sheet floors. Both studies considered simply supported and continuous slab, and used a furnace to heat the specimens using the standard fire curve as outlined in various technical publications, such as those of the CSIRO (1991).

Fire testing is prohibitive in cost, and Uy and Bradford (1995c) undertook a finite strip study to determine the degradation in the local buckling strength of the thin steel sheeting in contact with a rigid concrete core. The analysis was described more fully in Section 16.5.2, and is of particular use in composite profiled beam construction as the model was for plates in bending as would occur in the side shuttering. Although tangible design recommendations are yet to be formulated, the buckling stresses in Uy and Bradford's charts can be used to ascertain the contribution that the steel shuttering makes to the strength of a composite profiled beam at elevated temperatures.

17.9　　References

Azhari, M. and Bradford, M.A. (1995). "The use of bubble functions for the post-local buckling of plate assemblies by the finite strip method", International Journal for Numerical Methods in Engineering, Vol. 38, No. 6, 955-968.

Azhari, M., Uy, B. and Bradford, M.A. (1994). "Local and post-local buckling of cold formed steel trough girders", Fifth International Conference on Steel Structures, Jakarta, 17-24.

Bradford, M.A. (1983). *Buckling of Beams with Flexible Cross-Sections*, Ph.D. Thesis, The University of Sydney.

Bradford, M.A. (1989). "Buckling of longitudinally stiffened plates in bending and compression", Canadian Journal of Civil Engineering, Vol. 16, No. 5, 607-614.

Bradford, M.A. and Kyakula, M. (1994). "Shear strength of profiled composite beams", Civil Engineering Transactions, Institution of Engineers, Australia, Vol. CE36, No. 2, 173-179.

Burnet, M.J. and Oehlers, D.J. (1995). "Reinforced concrete beams constructed using profiled sheets as permanent and integral shuttering", EASEC-5 Conference, Gold Coast, Australia.

Cheung, Y.K. (1976). *Finite Strip Method in Structural Analysis*, Pergamon Press, Oxford.

Cooke, G.M.E., Lawson, R.M. and Newman, G.M. (1988). "Fire resistance of composite deck slabs", The Structural Engineer, Vol. 66, No. 16, 253-267.

CSIRO (1991) "Fire protection in buildings", Report TR 91/1, CSIRO Division of Building, Construction and Engineering, Sydney.

Gilbert, R.I. (1988). *Time Effects in Concrete Structures*, Elsevier, Amsterdam.

Oehlers, D.J. (1993) "Composite profiled beams", Journal of Structural Engineering, ASCE, Vol. 119, No. 4, 1085-1100.

Oehlers, D.J. and Ahmed, M. (1995). "Design procedures for bolting steel plates to the sides of reinforced concrete plates", International Conference on Structural Stability and Design, Sydney.

Oehlers, D.J., Wright, H.D. and Burnet, M.J. (1994). "Flexural strength of profiled beams", Journal of Structural Engineering, ASCE, Vol. 120, No. 2, 379-393.

Schmidt, H. and Lehmann, R. (1986). "New concept for economic and fire-resistant profiled sheet floor", IABSE Colloquium on Thin Walled Metal Structures in Building, Stockholm, 443-450.

Timoshenko, S.P and Woinowsky-Krieger, S. (1959). *Theory of Plates and Shells*, McGraw-Hill, New York.

Trahair, N.S and Bradford, M.A. (1991). *The Behaviour and Design of Steel Structures*, revised 2nd edn., Chapman and Hall, London.

Uy, B. (1995). *Profiled Composite Beam Construction*, Ph.D. Thesis, The University of New South Wales, Sydney.

Uy, B. and Bradford, M.A. (1993a) "Local buckling of trough girders composed of an assemblage of profiled steel sheets", UNICIV Report R-317, School of Civil Engineering, The University of New South Wales.

Uy, B. and Bradford, M.A. (1993b) "Cross-sectional deformation of prestressed composite beams", Structural Engineering Review, Vol. 5, No. 1, 63-70.

Uy, B. and Bradford, M.A. (1994a). "Slenderness limits for thin steel plates when restrained by concrete", Australasian Structural Engineering Conference 1994, Sydney,. 613-618.

Uy, B. and Bradford, M.A. (1994b). "Inelastic local buckling of thin steel plates in profiled composite beams", The Structural Engineer, Vol. 72, No. 16, 259-267.

Uy, B. and Bradford, M.A (1994c). "Service load tests on profiled composite and reinforced concrete beams", Magazine of Concrete Research, Vol. 46, No. 166, 29-33.

Uy, B. and Bradford, M.A. (1995a) "Ductility and member behaviour of profiled composite beams: experimental study", Journal of Structural Engineering, ASCE, Vol. 121, No.5, 876-882.

Uy, B. and Bradford, M.A (1995b). "Ductility and member behaviour of profiled composite beams: analytical study", Journal of Structural Engineering, ASCE, Vol.121, No.5, 883-889.

Uy, B. and Bradford, M.A. (1995c). "Local buckling of cold formed steel in composite structural elements at elevated temperatures", Journal of Constructional Steel Research, to appear.

Warner, R.F., Rangan, B.V. and Hall, A.S. (1989). *Reinforced Concrete*, 3rd edn., Longman Cheshire, Melbourne.

18   Composite Columns

18.1   Introduction

Composite columns are a very important application of composite construction, and they find widespread use, particularly in high-rise office buildings. The general term 'composite column' refers to any compression member in which a steel element acts compositely with the concrete element, so that both elements resist compressive forces. There is a wide variety of column types of various cross-section, but the most commonly used and studied are the *encased I-section* shown in Fig. 1.2(a) and in Fig. 18.1, and the *concrete-filled steel tube* shown in Figs. 1.7(c) and (d) and in Fig. 18.2.
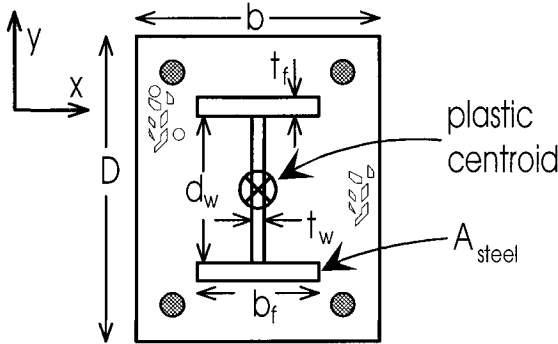
Fig. 18.1 Encased column
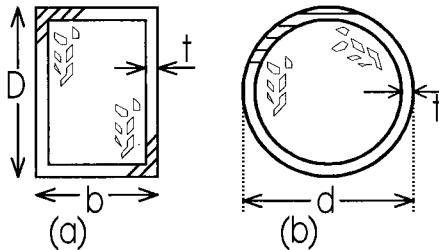
Fig. 18.2 Concrete-filled steel tubes

Steel I-section elements were initially encased with concrete for the purpose of fire protection, but the increase in strength afforded by the concrete was not quantified until the 1950's (Faber 1956, Stevens 1959). Since then, research and application of composite columns has advanced, and they have now found widespread application in the construction industry over the last decade. The attraction for

438

composite columns is that the expensive steel skeleton can be constructed first, and this can support the dead loads and construction loads. Subsequent concreting increases the capacity greatly, and the composite column which develops when the concrete hardens is suitable for resisting additional live loading as well as dead loads. Hence composite columns reduce substantially the amount of expensive steel required to support a given design load, while the dimensions of the column are smaller than those of a reinforced concrete column of the same strength, thereby increasing the available floor space. The advantages that accrue to the construction process itself are obvious.

As we saw in Section 1.3.2, short or stocky columns fail by squashing, and their strength depends on the component material strengths, namely f_c for the concrete and f_y for the steel. Additionally, stocky concrete-filled tubes are also susceptible to local buckling of the outer skin, and this is of importance in the very thin-walled tubes which are nowadays often used in office building construction. Long or slender columns are susceptible to instability or overall buckling effects, and we saw in Section 1.3.4 that there are two approaches for quantifying the strength of these columns. Firstly, the column may be designed along the same lines as that for a reinforced concrete member (Warner, Rangan and Hall 1989), as in Fig. 1.26 and used in some national concrete-based design standards. On the other hand, a strength versus slenderness curve similar to that used in steel design such as the Perry curve (Trahair and Bradford 1991) and introduced in Section 1.3.4.2 and shown in Fig. 1.28 is often favoured, and is presented in some national steel standards used for composite design. As we shall see in Section 18.2.3.4, a combination of both methods has been proposed for eccentrically loaded composite columns, and this correlates well with test results.

This chapter discusses the fundamental behaviour of doubly-symmetric encased columns and concrete-filled steel tubes which find the most widespread use in practice. Included are predictions of the ultimate strength and behaviour under service loads which is governed by the creep and shrinkage of the concrete. Based on their fundamental behaviour, some methods of predicting the response of composite columns are discussed, and some design recommendations are proposed.

18.2   Encased columns

18.2.1   GENERAL

Encased columns, as in Fig. 18.1, are usually doubly-symmetric with respect to the steel I-section element and concrete encasement. They are generally loaded eccentrically about the major (x) axis or minor (y) axis, although more generally they may be bent biaxially about both axes. Analyses, however, are usually for uniaxial bending, and then an interaction equation is used for the biaxial bending.

Stocky encased columns are governed by their *section strength*, which is the capacity of the cross-section to resist the applied axial loads and flexural forces that is based purely on the material strength at a section. Slender encased columns are

governed by what can be termed their *member strength*, reflecting the fact that instability is dependent not only on the material properties of both strength and stiffness, but also on the geometric properties of the whole member and not just the section. Under service loads the time-varying effects of creep and shrinkage serve to increase the deformation of composite columns that are subjected to sustained loads.

Generally, steel, reinforced concrete and composite columns tend to behave in a similar way. Stocky columns are axially stiff, and are controlled, as noted, by the cross-section or section strength. Slender columns are less stiff axially, and the well known "$P - \delta$ effect" (Trahair and Bradford 1991) results in the bending moments in them being amplified by the axial force as described in Section 1.3.4.1 and illustrated in Fig. 1.27. The emphasis in the design of reinforced concrete columns is placed on *section strength*, with reduction factors being applied to account for the $P - \delta$ effect which causes an amplification of moments in more slender columns, so that the *member strength* may also be predicted. In steel design, however, the emphasis is placed on failure by instability in the form of member or flexural buckling, since steel members subjected to axial loads are more likely to fail by instability than reinforced concrete members, and because the range of slendernesses over which *section strength* governs is only small. Composite steel-concrete columns are intermediate between reinforced concrete columns and steel columns. The *section strength* is governed by factors similar to those governing reinforced concrete columns, but composite columns are quite often more slender than reinforced concrete columns, so that a *member strength* representation of failure is more appropriate. These considerations are discussed in Sections 18.2.2 and 18.2.3 following, while the service load behaviour of encased composite columns under sustained service loads is discussed in Section 18.2.4.

18.2.2   SHORT COLUMNS

18.2.2.1   *Section strength*

The general principles of rigid plastic analysis given in Chapter 7 are also applicable in theory to calculating the section strength. Figure 18.3(a) shows an encased I-section element that is bent about the major (x) axis whose neutral axis lies at a depth n_a below the top reference fibre as in (b). It is also assumed that there is full interaction with only one strain profile. The concrete encases the whole of the I-section in (a) and therefore, as was discussed in Section 2.3.2, it is unlikely that all of the steel element will have fully yielded before the concrete crushes at a strain of 0.003. Hence it is necessary to use the γ factor in Eq. 2.17 to determine the real neutral axis position n_a and hence the strain distribution at failure as in (b), as compared with determining just the depth of the rectangular stress block in a rigid plastic analysis. The stress distribution in the steel element is therefore assumed to have an elastic-plastic distribution as in (d) which can be derived from the strain distribution in (b), in contrast to the concrete element that is assumed to be rigid plastic as in (c) with a yield stress of $0.85f_c$.
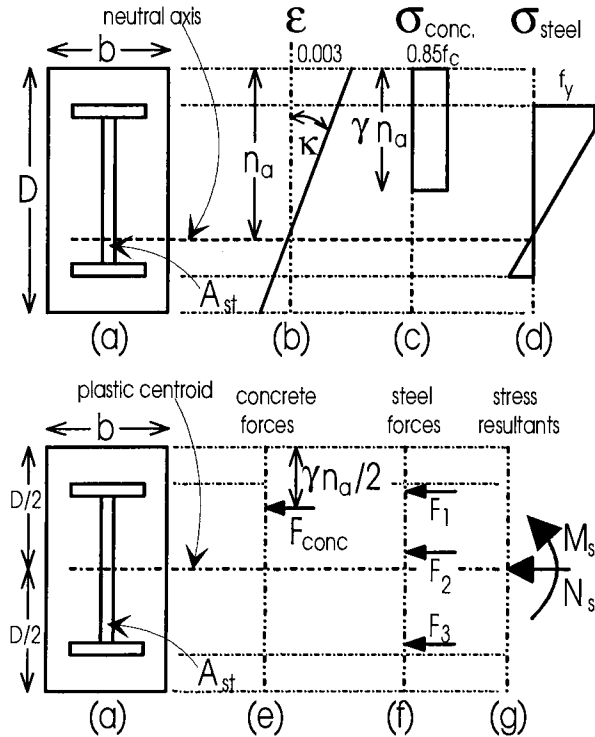
Fig. 18.3 Analysis of doubly symmetric section

Let us suppose that the neutral axis is positioned n_a below the top fibre, and that the ultimate concrete strain is 0.003 as shown in Fig. 18.3(b). As the concrete is fully stressed as in (c), the resultant force in the concrete element F_{conc} is positioned $\gamma\, n_a/2$ below the top fibre as in (e), and is given by

$$F_{conc} = 0.85 f_c \gamma n_a b \qquad (18.1)$$

where b is the width of the concrete element in (a). Because the curvature in the steel element is $\kappa = 0.003/n_a$ in (b), we may calculate the strain distribution in (b), stresses in the steel element in (d) and hence forces in the top flange F_1, web F_2 and bottom flange F_3 as in Fig. 18.3(f). Note generally that the top flange and some portion of the web will be at yield as shown in (d). Since the forces F_1, F_2 and F_3 act at the centroids of their stress blocks over their respective areas, the depths to these forces below the top fibre may be conveniently obtained, and taking the moments of these forces about the top fibre produces the moment M_{top}. Of course, any reference fibre may be used, and in general we finally relate the moment about the reference fibre to that at the plastic centroid. From equilibrium, the axial force in the cross-section N_s in (g) is the algebraic summation

$$N_s = F_{conc} + F_1 + F_2 + F_3 \tag{18.2}$$

Therefore, the moment M_s in (g) at the plastic centroid, which is also at the elastic centroid in this doubly symmetric case, can be derived from statics and is given by

$$M_s = M_{top} + \frac{N_s D}{2} \tag{18.3}$$

It is worth noting that the condition of pure compression is a limiting case of this analysis when $n_a \rightarrow \infty$. We then have the squash load of the composite column N_0 given by

$$N_o = 0.85 f_c (bD - A_{steel}) + f_y A_{steel} \tag{18.4}$$

since at the strain of 0.003 the steel will have yielded when $f_y \leq 600$ N/mm^2, which will generally be the case.

The failure envelope of (M_s, N_s) in Fig. 18.3(g) may be generated by varying the neutral axis depth n_a, and this has the form shown in Figs. 1.26 and 18.4. When the eccentricity e_0 about the plastic centroid of the axial force N_s in Eq. 18.2 is zero, a condition of concentric axial compression exists and the compressive strength N_0 in Fig. 18.4 may be calculated from Eq. 18.4. At the other extreme, when $e_0 \rightarrow \infty$, the section will be subjected to pure bending, and the moment capacity M_0 in Fig. 18.4 can be obtained accurately from the elastic-plastic analysis technique described previously, or approximately but fairly accurately from the rigid plastic techniques described in Chapter 7. For a given value of M_s/N_s, that is an eccentricity e_0 of loading as shown in Fig. 18.4(a), a value of n_a may be assumed and $(M_s)_1$ and $(N_s)_1$ calculated, producing an eccentricity $e_1 = (M_s)_1/(N_s)_1$ as shown. If e_1 differs significantly from the original given e_0, a new value of n_a must be assumed and an iterative procedure followed. This is clearly suitable for computer programming, but approximations have been derived and are discussed in Section 18.2.2.2.

A similar analysis of a composite cross-section may also be undertaken when the section is bent about its minor axis. An indicative failure envelope is shown in Fig. 18.4(b).

It is worth noting that although the composite failure envelope represented as an interaction diagram between M_s and N_s is similar to that for reinforced concrete columns, the same general assumptions are not always applicable to both. The concept of balanced failure in a singly or doubly reinforced concrete column is not the same as that for composite columns. For example, the balanced failure condition in reinforced concrete where concrete crushing occurs simultaneously with steel yielding in tension defines closely the point of maximum moment. However, this is not the case for composite columns, and in fact the simultaneous failure mode does not appear to be of particular interest in composite columns.
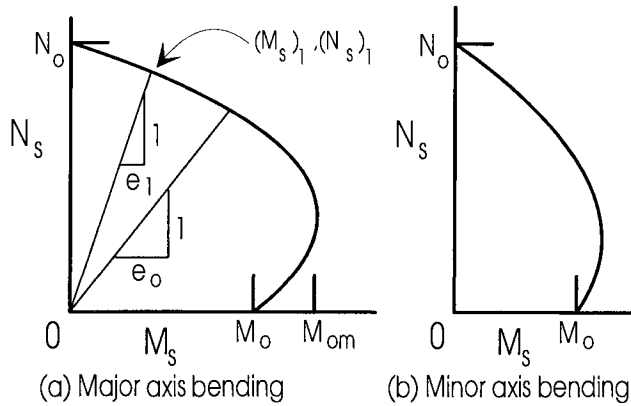
Fig. 18.4 Short column interaction curves

Example 18.1 Section strength from first principles

Consider the encased section shown in Fig. 18.5(a) where the dimensions are in mm and $f_c = 30$ N/mm^2 and $f_y = 250$ N/mm^2, so $\varepsilon_y = 250/200 \times 10^3 = 0.00125$. When the neutral axis depth n_a lies at infinity, we have the concrete stress block shown in (b) and steel stress block shown in (c). Noting that $A_{steel} = 16{,}000$ mm^2 gives the squash load $N_o = 15{,}067$ kN from Eq. 18.4.

Suppose now that the neutral axis is at mid-depth, that is $n_a = 450$ mm as in Fig. 18.5(d). From Eq. 2.17, $\gamma = 0.836$ so that the depth of the concrete stress block in (e) is $0.836 \times 450 = 376$ mm, and the force F_{conc} from Eq. 18.1 is $F_{conc} = 4797$ kN and acts at $376/2 = 188$ mm from the top fibre as shown in (g) where the bracketed number is the distance from the top fibre in mm. Note that in deriving Eq. 18.1 we have ignored the area of the steel inside the concrete area of depth γn_a. The strain on the inside face of the steel flange at failure is $(350/450) \times 0.003 = 0.00233 > \varepsilon_y$, so all of the flange has yielded as in (f). Hence from symmetry, $F_1 = -F_3 = 300 \times 15 \times 250$ N = 1125 kN as shown in (g). The force F_{2t} in the portion of the web above the neutral axis is 640 kN, and clearly again by symmetry the force in the web below the neutral axis, F_{2b}, is -640 kN. Figure 18.5(g) shows the forces acting on the section in kN, with the dimensions in brackets being the depths of the forces below the top fibre in mm. The moment $M_{top} = -178$ kNm can be obtained by taking the moments of these forces about the top fibre. Since $F_1 = -F_3$ and $F_{2t} = -F_{2b}$, $N_s = 4797$ kN, and so M_s in Eq. 18.3 is $-178 + 4797 \times 900 \times 10^{-3}/2 = 1980$ kNm. This point (1980, 4797) on the strength interaction curve in Fig. 18.4(a) corresponds to an eccentricity of $e_1 = (1980/4797) \times 1000 = 413$ mm.
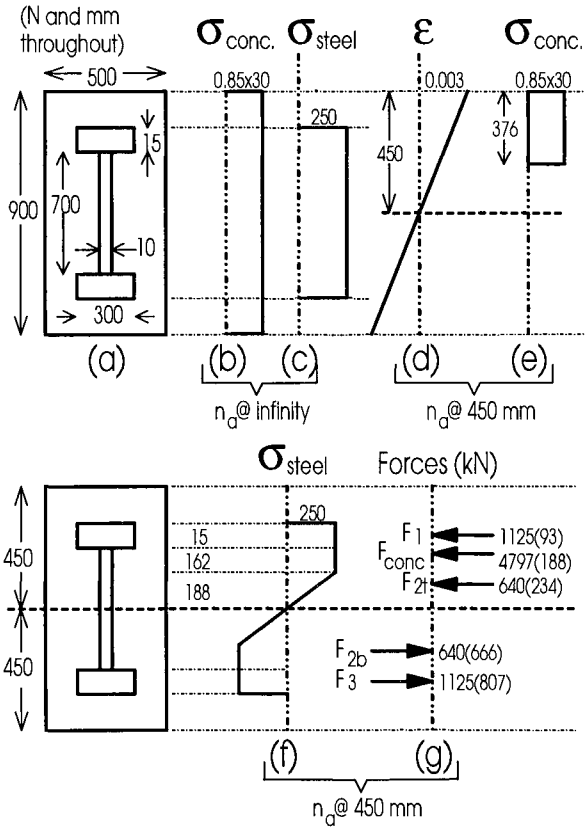
Fig. 18.5 Example 18.1 on section strength from first principles

18.2.2.2 *Design recommendations*

There are a number of design proposals that can be used to establish the load-moment strength interaction relationship in lieu of using an accurate computer program. Among these are the proposals of Basu and Somerville (1969), Wakabayashi (1976), Rotter (1982) and the work of Roik, Bergmann (1989) and others that has appeared in Eurocode 4 (1994). The simplified method of Wakabayashi and that of the Eurocode are given in the following.

(a) Wakabayashi's method

This method provides the simplest equations for the ultimate strength failure envelope. For this, the strengths of the concrete and steel elements are found independently, and are then superimposed. Of course, superposition is not structurally valid since the materials are not elastic and the interaction between the steel and concrete is ignored. The method requires the easily calculated squash load of the concrete given by

$$N_{conc} = 0.85 f_c A_{conc} \tag{18.5}$$

and the squash load of the steel given by

$$N_{steel} = f_y A_{steel} \tag{18.6}$$

as well as the combined squash load

$$N_o = N_{conc} + N_{steel} \tag{18.7}$$

and the full plastic moment of the steel element that can be determined from Chapter 7 as in Example 7.1 or from

$$M_{ps} = f_y S \tag{18.8}$$

where S is the plastic modulus of the steel element.

The superposition method is shown in Fig. 18.6. When the axial force N_s lies in the range $0 \leq N_s \leq N_{conc}$, then the moment capacity is given by

$$M_s = M_{ps} + \frac{0.85 f_c b D^2}{8}\left[1 - \left(\frac{2N_s}{N_{conc}} - 1\right)^2\right] \tag{18.9}$$

The first term M_{ps} on the right hand side of Eq. 18.9 is the steel contribution and is shown as line A_2 in Fig. 18.6, the second term which is the concrete contribution is shown as line A_1 and the superposition of these gives the strength interaction line A_3. However, if the axial force N_s lies in the range $N_{conc} \leq N_s \leq N_o$ then

$$M_s = M_{psN} \tag{18.10}$$

where M_{psN} is the full plastic moment of the steel element when carrying an axial load in the steel element of $N_s - N_{conc}$. The derivation of M_{psN} is illustrated in Fig. 18.7 where the central stress block in (b) of area A_1 resists the axial loads $N_s - N_{conc}$ leaving the outer elements of equal strength to resist the moment $M_{PsN} = F_1 h_1$ as shown in (c). The variation of the flexural capacity with axial load in the steel element is shown as line B_1 in Fig. 18.6. The axial strength of the concrete element is N_{conc} and is shown as line B_2. Superposition of B_1 and B_2 gives the strength interaction line B_3. This strength interaction line may be expressed with close accuracy using a well-known interaction equation (Trahair and Bradford 1991) as

$$M_{psN} = 1.18\left(1 - \frac{N_s - N_{conc}}{N_s}\right)M_{ps} \leq M_{ps} \tag{18.11}$$

which reduces to

$$M_{psN} = \left(\frac{1.18N_{conc}}{N_s}\right) M_{ps} \leq M_{ps} \qquad (18.12)$$
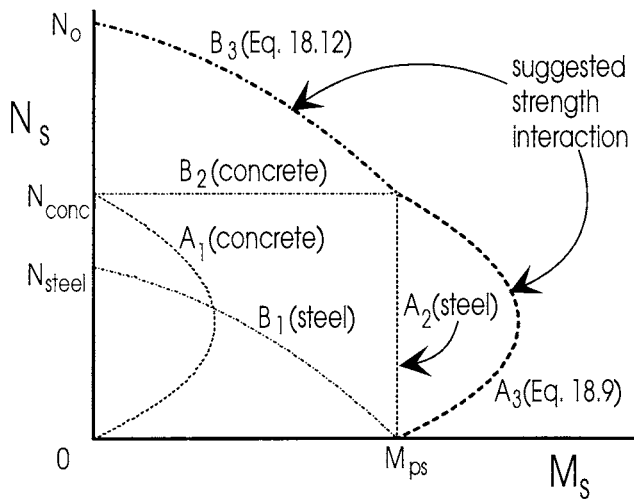
Fig. 18.6 Superposition method of Wakabayashi
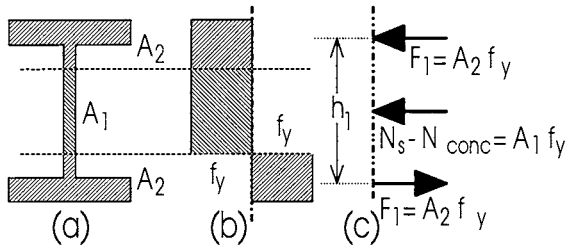
Fig. 18.7 Moment capacity of steel element with axial load

As mentioned earlier, the method lacks a logical structural basis, but it allows three points to be established on the interaction curve reasonably well. These are M_0 in Fig. 18.4 when $N_s = 0$ which corresponds with M_{ps} in Fig. 18.6 and hence can be determined from Eq. 18.8, M_s at an axial force of $N_{conc}/2$ in Fig. 18.6 which from Eq. 18.9 is the point of maximum moment and corresponds with M_{om} in Fig. 18.4(a), and the squash load N_0. The pure moment M_0 is underestimated because the interaction between the steel and concrete is ignored. The axial load corresponding to the condition of maximum moment is represented reasonably accurately, but the moment itself is overestimated as the steel is assumed to be fully plastic although the

strains in the concrete throughout the depth are not large enough to allow this condition to be approached. The squash load is, of course, accurately represented.

Example 18.2 Wakabayashi's approximate method for the section strength

The composite column of Example 18.1 is subjected to a load N_s = 4797 kN that was calculated for the neutral axis at mid-depth. The squash load N_{conc} in the concrete is 11,067 kN from Eq. 18.5, and this uses A_{conc} = bD - A_{steel}. The axial force thus lies in the range $0 \leq N_s \leq N_{conc}$. From Chapter 9, the plastic section modulus for the steel element may be calculated as S = 4.44×10^6 mm^3, so M_{ps} = 1110 kNm. Thus in Eq. 18.9, M_s = 2378 kNm. This load is close to the condition of maximum moment ($N_{conc}/2$ in Eq. 18.9), so it can be seen from Example 18.1 that the moment is indeed overestimated by 2378/1980 or 20%.

(b) Eurocode method

The method adopted by Eurocode 4 approximates the interaction diagram shown in Fig. 18.8(a) by the polygon AECDB shown. For doubly-symmetric I-sections, the point E can be omitted on this polygon because the variation between A and C can be assumed linear for doubly-symmetric sections. In order to calculate the vertices of the polygon, the stress distributions and neutral axes given in Figs. 18.8(b) to (e) are used, and it is a simple matter to take the moments of the idealised plastic stress blocks around the plastic centroid to obtain M_s, and to sum the axial forces of the plastic stress blocks to obtain N_s. Explicit equations for the neutral axis parameter h_n in Fig. 18.8 are given in the Eurocode.

Point A in Fig. 18.8(a) is the squash load N_o and the appropriate stress distribution for its derivation is shown in (b). Point B in (a) is the pure flexural capacity M_o and its derivation is shown in (c), where h_n is the distance of the neutral axis above the plastic centroid, for this pure flexure condition. The derivation of M_o follows the rigid plastic principles for full shear connection that are outlined in both Chapters 7 and 17. Point C in (a) occurs when the neutral axis is now h_n below the plastic centroid as shown in (d), and the resulting axial force N_{om} is the integral of the unhatched stress distribution over the areas over which they act. It is worth noting that the analysis for point C follows the rigid plastic principles for partial shear connection analysis of the concrete element or the steel element of the profiled beams in Chapter 17, as the axial force N_{om} in (d) is equivalent to the strength of the shear connection in a profiled beam. Point D in (a) is the position of maximum moment M_{om} and the distribution of stresses at which it occurs is shown in (e), where the neutral axis lies at mid-depth and the axial force is half of that at point C.
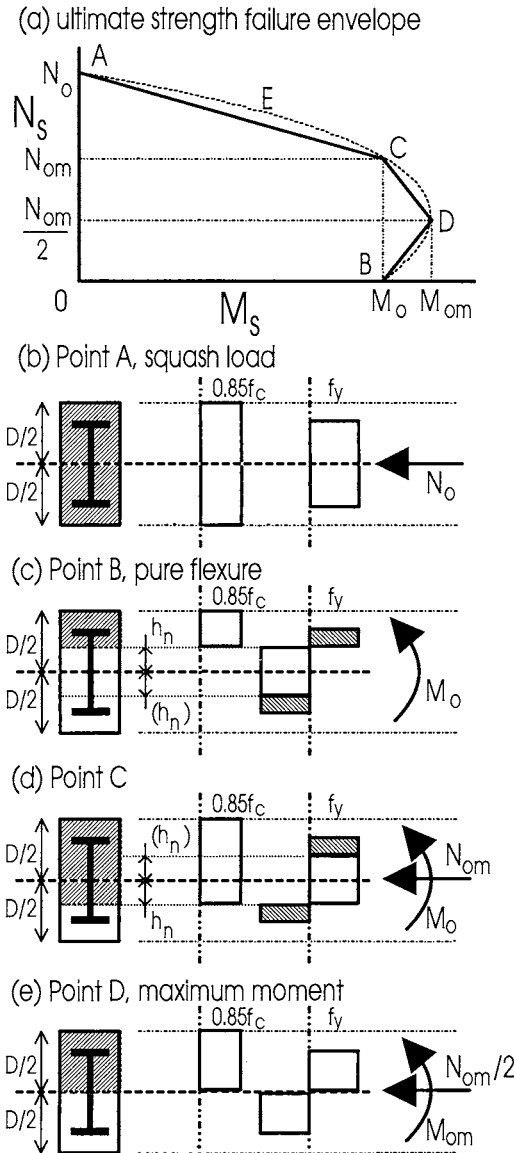
Fig. 18.8 Eurocode 4 proposal

(c) Roik and Bergmann's approach

The Eurocode method described in the previous section and illustrated in Fig. 18.8 is based on the following ingenious solution developed by Roik and Bergmann (1989). The solution can only be applied to a cross-section that is symmetrical about the axis of bending, which is often the case. Furthermore, it can be applied to a section with any number of materials just as long as the materials can be assumed to exhibit rigid plastic properties, that is when they are strained they are either fully yielded or not

Point B, pure flexure
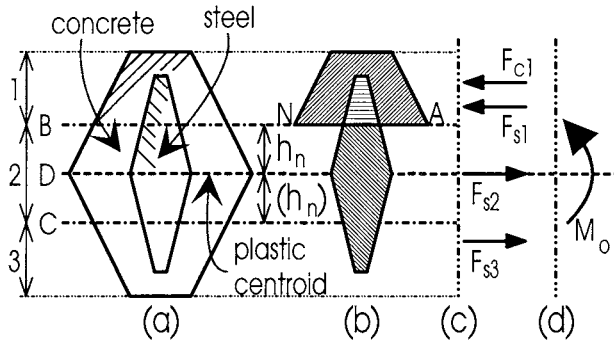
Roik and Bergamann's point C
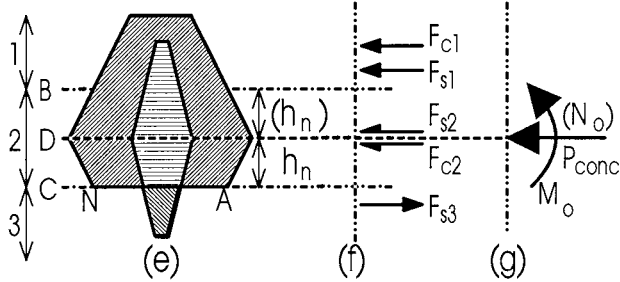
Point D, maximum moment
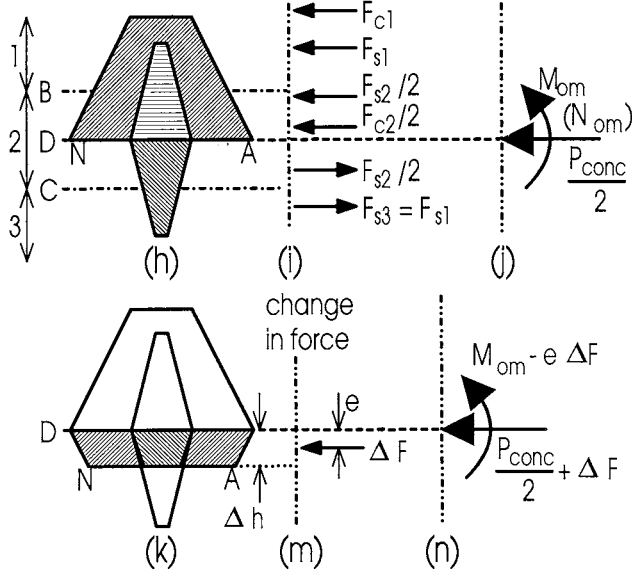
Fig. 18.9 Roik and Bergmann's column interaction points

stressed at all. The procedure will be illustrated for the cross-section in Fig. 18.9(a) that is symmetrical about axis D so that the plastic centroid also lies at D. The section has two rigid plastic materials consisting of the steel element, which is assumed to be fully yielded in tension and compression at f_y as shown in Fig. 7.1, and a concrete element which is assumed to be fully yielded in compression at $0.85f_c$ as shown in Fig. 7.1, but to have zero tensile strength. In this example, the steel element is encased by the concrete element although the same solution is also applicable when the steel encases the concrete.

Let us first consider point B in Fig. 18.8(a) which is the pure flexure capacity. The distribution of stress is shown in Fig. 18.9(b) where the stress above the neutral axis position N-A is compressive. Therefore below the neutral axis, only the steel element is stressed in tension as the concrete is cracked in tension and is therefore assumed to have zero stress. The neutral axis position h_n above the plastic centroid can be determined by equating the compressive strength of the steel and concrete above the neutral axis to the tensile strength of the steel below the neutral axis. For convenience we will divide the section into the three regions shown in (a), that is region 2 that lies within the distance h_n on either side of the plastic centroid, region 1 which is further than h_n above the plastic centroid and region 3 that is further than h_n below the plastic centroid. The resultant force in the concrete in each of these is shown in (c). For example, the force F_{c1} is the resultant force in the concrete in region 1 and acts at the centroid of the concrete region, whereas F_{s1} is the resultant force in the steel element in this region and acts at the centroid of the steel in this region. Taking moments of the resultant forces in (c) gives the pure flexural capacity M_o in (d).

By symmetry about the D axis in Fig. 18.9(b), the resultant force in the steel element in region 2, that is F_{s2}, acts through the plastic centroid as shown. Furthermore by symmetry, the compressive force in the steel element in region 1 is the same magnitude as the tensile force in the steel element in region 3, so that

$$| F_{s3} | = | F_{s1} | \tag{18.13}$$

As we are dealing with a case of pure flexure, the sum of the resultant forces is zero and hence

$$F_{c1} + F_{s1} \quad = \quad F_{s2} + F_{s3} \tag{18.14}$$

Substituting Eq. 18.13 into Eq. 18.14 produces

$$F_{c1} \quad = \quad F_{s2} \tag{18.15}$$

and moreover by symmetry,

$$F_{c3} \quad = \quad F_{c1} \tag{18.16}$$

then from Eqs. 18.15 and 18.16

$$F_{c1} \quad = \quad F_{c3} \quad = \quad F_{s2} \tag{18.17}$$

The next step in the procedure is to consider point C in Fig. 18.8(a) where the moment capacity about the plastic centroid is the same as the pure flexural capacity M_o but where there is a resultant axial load N_{om}. The analysis of this section is shown in Figs. 18.9(e) and (f). It can be seen in (c) that F_{s2} does not contribute to the moment capacity about the plastic centroid as it acts through the centroid. Therefore, only the three resultant forces F_{c1}, F_{s1} and F_{s3} contribute to M_o when the moment is taken about the plastic centroid. It is therefore necessary to find a position of the neutral axis N-A in (e) where only these three resultant forces, F_{c1}, F_{s1} and F_{s3}, contribute to the moment capacity about the plastic centroid in order to ensure that the moment capacity remains at M_o. This can only be achieved when the neutral axis is h_n below the plastic centroid for pure flexural capacity as shown in (b). This is because when the neutral axis moves from levels B to C in (e), that is it traverses region 2, the change in the stress distribution in region 2 is symmetric about the plastic centroid as shown. Therefore, the resultant changes in force in region 2, that is F_{s2} and F_{cs} in (f), act through the centroid and therefore do not contribute to the moment capacity about the plastic centroid.

The resultant force in Fig. 18.9(c) is zero as we are dealing with pure flexure. As the moment capacity M_o is the same in (c) and (f), any changes in the resultant forces from distribution (c) to (f) is due to the externally applied axial force N_o in (g). In the concrete element in region 2 in (e), the resultant force changes from zero in (c) to a compressive force of F_{c2} in (f) and hence an applied compressive force of magnitude F_{c2} is required to cause this change. However in region 2, the resultant force in the steel element changes from tension of magnitude F_{s2} in (c) to compression of the same magnitude in (f), so the applied compressive force that is required to cause this change is $2F_{s2}$. Because of this, the applied axial load N_o in (g) that is required to cause the change from (c) to (f) and which occurs in conjunction with M_o is given by

$$N_o \quad = \quad 2F_{s2} + F_{c2} \tag{18.18}$$

Substituting into Eq. 18.18 the relationships $F_{s2} = F_{c1}$ and $F_{s2} = F_{c3}$ from Eq. 18.17 gives

$$N_o \quad = \quad F_{c1} + F_{c2} + F_{c3} \quad = \quad P_{conc} \tag{18.19}$$

where P_{conc} is the axial compressive strength of the concrete element. It can be seen from this simple and ingenious solution that the axial load in combination with M_o that is required to cause failure is equal to the compressive strength of the whole of the component that has zero tensile strength, that is the compressive strength of the concrete section P_{conc}.

The final vertex to be determined is at D in Fig. 18.8(a) where the moment has a maximum value of M_{om}. We will assume that the neutral axis occurs at the plastic centroid as shown in Fig. 18.9(h) and leave the proof of this assumption until later. The distribution of the resultant forces above and below the plastic centroid is shown in (i). By symmetry, the steel component in region 2 is subjected to tensile and compressive forces of equal magnitude $F_{s2}/2$ and furthermore $F_{s3} = F_{s1}$. Hence the summation of the forces in (i) gives

$$N_{om} = F_{c1} + F_{c2}/2 = P_{conc}/2 \qquad (18.20)$$

which is half of the compressive strength of the concrete section. The moment capacity at this axial load M_{om} can be derived by taking moments of the forces in (i) about the plastic centroid. It is now necessary to determine whether this is the maximum moment.

Let us now consider the change in the force distribution ΔF when the neutral axis is just below the plastic centroid as shown at the distance Δh in (k). The changes in the stress distribution occur within the hatched region in (k). The concrete stress increases from zero to $0.85f_c$ and the steel stress changes by a magnitude of $2f_y$ as it goes from tension to compression. Integrating these changes in the stress distribution over the areas over which they act gives the resultant compressive force ΔF at an eccentricity e below the plastic centroid. Therefore, the change in the neutral axis position causes the original axial force of $P_{conc}/2$ in (j) to increase by ΔF as shown in (n). Furthermore, the moment due to ΔF in (m) acts in the opposite direction to M_{om} in (j) so that the moment capacity reduces by $e\Delta F$ as shown in (n). Because of this, a downward shift in the neutral axis causes a reduction in the moment capacity. A similar argument can be applied when moving the neutral axis upwards by Δh, in which case ΔF in (m) occurs above the plastic centroid at an eccentricity e and is in an opposite direction as the change in force is tensile. Therefore, an upward shift in the neutral axis causes the axial load to reduce by ΔF and the moment capacity also to reduce by $e\Delta F$. In conclusion, a movement of the neutral axis away from the plastic centroid will cause a reduction in the moment capacity and hence the maximum moment must occur when the neutral axis is at the plastic centroid.

Example 18.3 Eurocode method for section strength

Let us consider again the composite column that was analysed in Examples 18.1 and 18.2. Point D in Fig. 18.8(a) and (e) corresponds to the case in Example 18.1 where $n_a = D/2$, but note that the concrete stress block in the Eurocode method is stressed to $0.85f_c$ throughout the depth n_a, and not through the depth $\gamma\, n_a$. The force N_s is thus $N_{conc}/2$, where N_{conc} is in Eq. 18.5, producing $(N_s)_D = 5534$ kN. For the case of $N_s = 4797$ kN treated in Examples 18.1 and 18.2, we must therefore consider the line BD in Fig. 18.8(a). At point D, depicted in (e), $M_s = M_{ps} + 0.85f_cbD^2/8$, giving $M_s = 2629$ kNm. Note that the maximum moment that occurs at point D is the same as that predicted in Wakabayashi's formulation in Eq. 18.9.

Consider now the neutral axis to be at a depth n_a from the top fibre in Fig. 18.8(c). The compressive force in the concrete F_{conc} is thus $0.85 \times 30 \times 500 \times n_a \times 10^{-3} = 12.75 n_a$ kN, where n_a is in mm. The neutral axis height h_n in Fig. 18.8(c) is thus $h_n = 450 - n_a$, so that the net tensile force in the plastic steel is thus $2 h_n \times 10 \times 250 \times 10^{-3} = 5(450 - n_a)$ kN. Since the net compression at point B is zero, equating these forces yields $n_a = 129$ mm. Figure 18.10 shows the forces in the plastic stress blocks in kN and their distances in mm from the plastic centroid in brackets.

The moment M_0 is thus $2 \times 1425 \times 357 + 1645 \times 386$ kNmm or 1652 kNm. Interpolating linearly between (1652, 0) and (2629, 5534) to produce $(M_s, 4797)$ gives $M_s = 2553$ kNm. In comparison with the solution of Example 18.1, the rigid plastic Eurocode approach thus overestimates the moment by 2553/1980 or 29%.
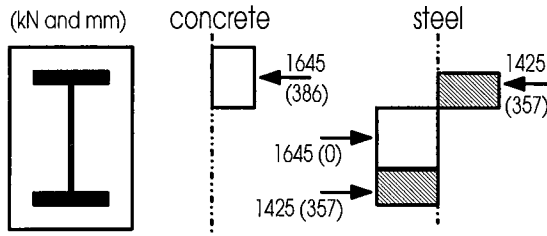
Fig. 18.10 Example 18.3 on Eurocode method for section strength

18.2.2.3 *Allowance for shear*

As we saw in Chapter 7, rigid plastic analyses must be modified for the effects of shear. A composite column subjected to a moment gradient will experience a shear force, and this shear is assumed to be resisted by the web of the steel I-section element.

Consequently, in the Wakabayashi and Eurocode predictions, the web yield stress must be reduced below its strength f_y. It was shown in Section 7.5.3.2 that an appropriate reduced yield stress for the web is given by

$$f_{py} = \sqrt{f_y^2 - 3\tau_w^2} \qquad (18.21)$$

where

$$\tau_w = \frac{V}{d_w t_w} \qquad (18.22)$$

where V is the shear load. Equations 18.21 and 18.22 are based on the von Mises yield criterion (Chapter 2), and the assumption that the shear yield stress τ_w in the web of the steel element is uniform.

18.2.3   SLENDER COLUMNS

18.2.3.1   *General*

Composite columns are clearly intermediate between steel and reinforced concrete columns. However, the design philosophy for each of these two structural members is fundamentally different. Steel columns are treated as "concentric" in that they are loaded through their centroids, but with due allowance being made for residual stresses, initial out-of-straightness and slight eccentricities of the load. The basis of the design of steel columns is *instability* or buckling, and any moments which act at the ends of the column are then incorporated by reducing the axial load by way of an interaction equation.

The approach for reinforced concrete columns is quite different than that for steel columns in that the loads are considered to be eccentric to the centroid. The failure is generally, but not always, attributable to *cross-section material failure*, and is based on the cross-section interaction curve shown in Figs. 18.4 and 18.8(a). The main difficulty, as we have seen, is the amount of algebraic work required to derive this curve accurately.

Because of the similarity of composite columns to both steel and concrete columns, there has been a great deal of debate by researchers as to which approach should be adopted. Short or stocky composite columns are clearly governed by cross-section failure, while long or slender columns are prone to buckling. Perhaps the most logical treatment to date is that provided by the Eurocode, where we will see in Section 18.2.3.4 that the behaviour of composite columns can best be treated by a combination of both approaches.

18.2.3.2   *Steel approach*

The theory of the failure of steel columns is rather complex, and only a description of the mechanism is given here. The reader is referred to standard texts such as Trahair and Bradford (1991) for a fuller treatment.

Consider the column shown in Fig. 18.11 which has an initial geometric out-of-straightness of total magnitude δ_o which follows a sine curve, as shown. When the column is initially straight, the internal moment in the buckled configuration is (Hall 1984) $-EId^2u/dz^2$. The differential equation for buckling is clearly, from equilibrium

$$-EI\frac{d^2u}{dz^2} \quad = \quad Nu \tag{18.23}$$

and for nontrivial buckling displacements u, the solution to this differential equation yields

$$N_{oc} = \frac{\pi^2 EI}{L^2} \qquad\qquad (18.24)$$

and

$$u = \delta \sin \pi z / L \qquad\qquad (18.25)$$

The buckling load N_{oc} in Eq. 18.24 is the familiar Euler load for a straight elastic column, and Eq. 18.25 shows that the column buckles as a sine curve with an undetermined magnitude of the central deflection δ. Simply stated, a straight elastic column will remain straight under the action of a concentric load N until the buckling load N_{oc} is reached as shown in Fig. 18.12. Of course, if N_{oc} is greater than the squash load N_{steel}, the short steel column will squash before yielding.
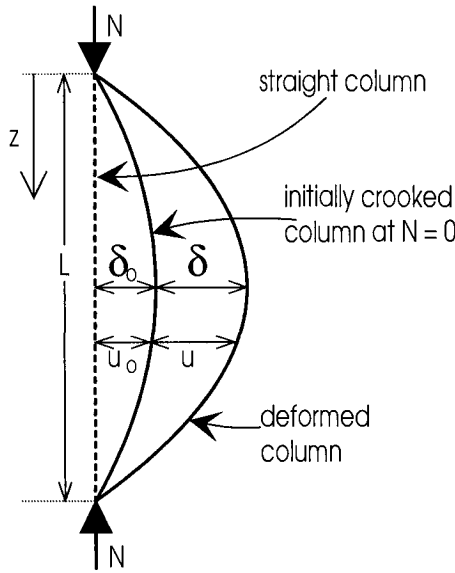
Fig. 18.11 Geometrically imperfect column
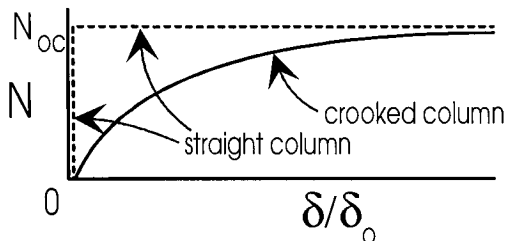
Fig. 18.12 Deformation of crooked elastic column

The Euler buckling concept is clearly a simplification. Let us consider again the column in Fig. 18.11 which as a geometric out-of-straightness $u_0 = \delta_0 \sin \pi z / L$. The differential equation in the bent position is now

$$-EI\frac{d^2u}{dz^2} = N(u+u_o) \tag{18.26}$$

and the solution of this equation that satisfies u(o) = u(L) = 0 is the deflected shape given by Eq. 18.25, but where

$$\frac{\delta}{\delta_o} = \frac{N/N_{oc}}{1-N/N_{oc}} \tag{18.27}$$

Equation 18.27 clearly indicates that δ is not of indeterminate magnitude, but increases with the onset of loading N. This relationship is shown in Fig. 18.12, where $\delta = 0$ when N = 0, and $\delta \to \infty$ as $N \to N_{oc}$.

The analysis so far has only been for elastic behaviour. In the bent position, a compressive bending stress of $N(u+u_0)/Z$ will occur on the concave side of the member, and a tensile bending stress of the same magnitude will be present on the convex side, where Z is the section modulus. If we set the maximum compressive stress in the bent column equal to the yield stress f_y, then

$$f_y = \frac{N}{A_{steel}} + \frac{N(\delta+\delta_o)}{Z} \tag{18.28}$$

If N_L is the limiting load to cause first yield in Eq. 18.28, then substituting Eq. 18.27 into Eq. 18.28 and solving for N_L produces a quadratic equation that gives

$$\frac{N_L}{N_{steel}} = \xi - \sqrt{\xi^2 - N_{oc}/N_{steel}} \tag{18.29}$$

where N_{steel} is the squash load $f_y A_{steel}$ and where

$$\xi = \frac{1+(1+\eta)N_{oc}/N_{steel}}{2} \tag{18.30}$$

and

$$\eta = \frac{\delta_o B}{2r^2} \tag{18.31}$$

in which Z is written as 2I/B, where B is the member width measured transverse to the axis of buckling, and r is the radius of gyration $\sqrt{I/A}$.

Equations 18.29 to 18.31 define what is commonly called the "Perry curve" as shown in Fig. 18.13, where the abscissa $\lambda = \sqrt{N_{steel}/N_{oc}}$ is a measure of the slenderness. It is clear that the Perry curve provides a transition from the squash load N_{steel} at $\lambda = 0$ to the Euler load N_{oc} as $\lambda \rightarrow \infty$. The constant η in Eq. 18.31 is known as the imperfection parameter, and its basis is empirical as we do not generally know δ_0 explicitly and the assumption $Z = 2I/B$ does not necessarily hold. The validity of Eqs. 18.29 to 18.31 has been established from a wealth of experimental data, provided that η is adjusted suitably to fit the tests that also incorporate residual stresses. Because of this, the suite of limit states steel codes uses column strengths N_L based on the Perry curve, but several curves are defined by assigning values of η empirically based on tests. For example, the Eurocode 3 expresses Eqs. 18.29 to 18.31 as

$$N_L = \chi N_{steel} \tag{18.32}$$

where χ is a reduction factor dependent on both the slenderness λ and the section type. The Eurocode 3 gives four buckling curves, labelled a to d, and shown schematically in Fig. 18.14. Curve 'a' has the highest strength, and corresponds to members with low imperfection levels such as annealed columns. Curve 'd' has the least strength, and is used for members with substantial residual stresses. The intermediate curves 'b' and 'c' are used for the most commonly encountered steel members, and are chosen on the basis of test data.
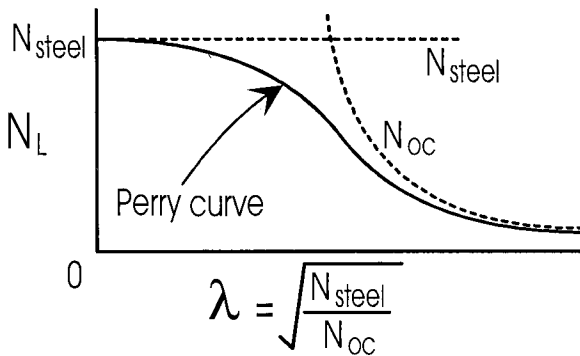
Fig. 18.13 Perry curve

18.2.3.3 *Reinforced concrete approach*

In the analysis of steel columns in Section 18.2.3.2, we determined the strength of a compression member that was nominally concentrically loaded. In reinforced concrete design, the column is considered to be subjected to end moments, as shown in Fig. 18.15(a). Of course, if a steel column is subjected to end moments, then its capacity must be reduced, but this was not considered in Section 18.2.3.2 since it is not relevant to the design of composite columns treated in Section 18.2.3.4 following.
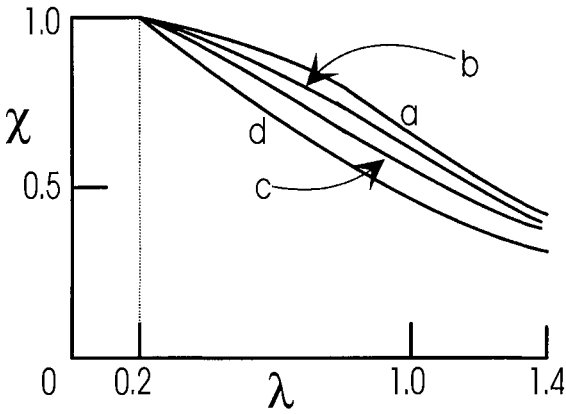
Fig. 18.14 Eurocode 3 column curves
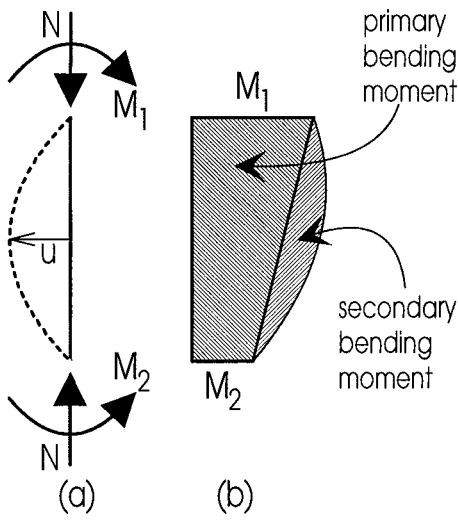
Fig. 18.15 Bending moment diagram

Figure 18.15(a) shows the bending moment diagram along the column. The line joining M_1 to M_2 is known as the primary bending moment diagram. This moment causes bending deflections u, so that an additional secondary moment Nu is generated, as shown. For an elastic column subjected to end moments M and βM, where $-1 \leq \beta \leq 1$ and β is positive for single curvature, then it may be shown (Trahair and Bradford 1991) that the maximum moment M_m is

$$M_m = M \sqrt{1 + \left(-\beta \cos ec\pi \sqrt{\frac{N}{N_{oc}}} + \cot \pi \sqrt{\frac{N}{N_{oc}}} \right)^2} \qquad (18.33)$$

when $\beta > \cos \pi \sqrt{N/N_{oc}}$, and that the maximum moment is at the end of the member, that is

$$M_m = M \qquad (18.34)$$

when $\beta < \cos \pi \sqrt{N/N_{oc}}$, where N_{oc} is the Euler load. Of course, these equations are not valid for a general reinforced concrete member owing to such nonlinearities as cracking. A suitable approximation for the maximum moment is

$$M_m = \delta_b M \qquad (18.35)$$

where M is the maximum first order or applied moment and

$$\delta_b = \frac{k_m}{1 - N/N_c} \qquad (18.36)$$

in which

$$k_m = 0.6 + 0.4\beta \geq 0.4 \qquad (18.37)$$

is a factor to account for the moment gradient and N_c is the buckling load for a concentrically loaded column. The buckling load is not equal to the Euler load N_{oc} as the concrete is not linearly elastic, and so the flexural rigidity EI must be modified. One such modification given in Warner, Rangan and Hall (1989) is to write

$$N_c = \frac{\pi^2}{L^2} 200 d M_{ub} \qquad (18.38)$$

where d is the effective depth of the reinforced concrete member and M_{ub} is its moment at balanced failure (Section 18.2.2.1), as shown in Fig. 18.16.

The design procedure for a reinforced concrete column is to draw the cross-sectional strength envelope shown in Fig. 18.16. This procedure is much simpler algebraically than for a composite column, as each individual reinforcing bar is at a discrete point in the section and is not continuous as for a composite column. If the column is subjected to a load N of maximum eccentricity e_0, so that the maximum first order moment is $M = Ne_0$, a line is drawn on the load-moment graph in Fig. 18.16 at a slope of $1/e_0$. At each value of N, the amplification factor δ_b in Eq. 18.36 is calculated, so that points corresponding to (M_m, N) may be plotted, as shown. This loading line is continued until it intersects the cross-section strength curve, and the maximum load N_s is then read off. The more slender is the column, then the lower is

the value of N_c, so that the amplification factor δ_b in Eq. 18.36 is increased. Of course, if $N > N_c$, then the column will fail by instability or buckling before the cross-sectional strength is reached, as shown in Fig. 18.16.
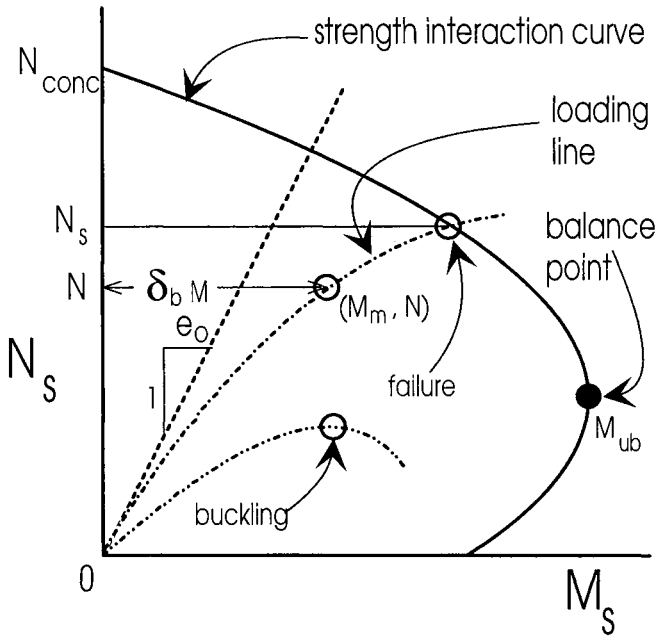
Fig. 18.16 Loading lines for reinforced concrete column

18.2.3.4 *Design recommendations for composite columns*

As was mentioned earlier, many researchers have traditionally advocated the design of composite columns using either the steel or reinforced concrete principles that were described in Sections 18.2.3.2 and 18.2.3.3 respectively. A logical design procedure has been adopted by Eurocode 4, and is described in this section as a design recommendation. Basically, it uses the steel approach to calculate the buckling load of a concentrically loaded column, and modifies this to handle end moments by applying the reinforced concrete approach.

It is firstly necessary to calculate the critical load N_{crit}. This is written in the Euler form

$$N_{crit} = \frac{\pi^2 (EI)_e}{L^2} \tag{18.39}$$

The 'effective elastic flexural stiffness' $(EI)_e$ about the axis of bending is expressed as

$$(EI)_e = E_s I_s + 0.8 E_c I_c \tag{18.40}$$

where I_c is the second moment of area about the centroid of the uncracked concrete element. The factor 0.8 in Eq. 18.40 is based partly on test data. Note that in Eq. 18.40 we have ignored the presence of any reinforcing steel, in order to simplify the explanation of the procedure.

The modified slenderness λ is calculated from

$$\lambda = \sqrt{\frac{N_o}{N_{crit}}} \qquad (18.41)$$

where N_0 is the squash load given in Eq. 18.4 and N_{crit} is the critical load in Eq. 18.39. The concentric strength N_c is then given by writing Eq. 18.32 as

$$N_c = \chi N_o \qquad (18.42)$$

where χ is obtained from the slenderness λ and from curve 'b' in Fig. 18.14 of Eurocode 3 if the encased column is bent about the major axis, or the lower curve 'c' of Eurocode 3 if the encased column is bent about the minor axis.

Second order effects are included in the design at this stage by multiplying the largest first order moment by an amplification factor δ_b, which is similar to that of Eq. 18.36, but is represented as (Eurocode 4 1994)

$$\delta_b = \frac{k_m}{1 - N / N_{crit}} \qquad (18.36)$$

where N_{crit} is as in Eq. 18.39 and

$$k_m = 0.66 + 0.44\beta \geq 0.44 \qquad (18.43)$$

which is similar to Eq. 18.37.

The way in which bending actions are incorporated is best illustrated with reference to Fig. 18.17, which shows the load-moment strength envelope for the section which is derived in the manner discussed in Section 18.2.2. The abscissa has been non-dimensionalised as M_s/M_0 and the ordinate as N/N_0. In this way, we can express the capacity reduction factor χ. Having determined χ in Eq. 18.42 from the Eurocode curve that appears in Fig. 18.14, we can plot point B in Fig. 18.17 on the interaction curve that represents the column failure when subjected to a compression χN_0 without any applied or primary bending moment M. Using the argument of Johnson (1994), the moment AB in the figure would represent the maximum bending moment caused by the axial load that is the bending due to the second order effects, just prior to failure of the column. This secondary bending moment is assumed to be proportional to the applied axial load N and therefore increases along the path O-B as A-B is the secondary moment at failure. The ordinate of the design load N is given by

$$\chi_d \ = \ \frac{N}{N_o} \tag{18.44}$$

as shown in Fig. 18.17. At axial load χ_d the secondary moment is represented by the length CE that is the intersection of χ_d with O-B. The bending resistance of axial load χ_d is thus CF, so that resistance EF is available for the secondary bending moment. Hence $\delta_b M$ must not be greater than EF, where M is the maximum applied bending moment at the end of the beam and δ_b, from Eq. 18.36, is the amplification factor for the applied moment.
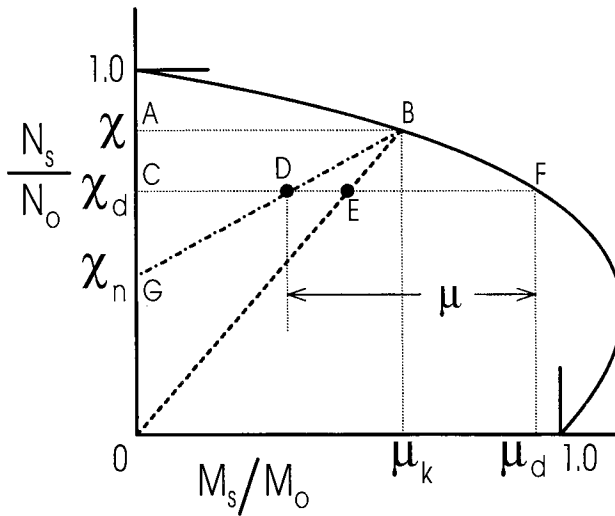
Fig. 18.17 Design procedure for compression and bending

At a given level of axial load, the secondary moment reduces as the moment gradient β decreases below 1.0 until, in fact, it disappears when the member is bent in or close to double curvature. To allow for the reduction in the secondary moment, the line OEB is thus replaced by the line GDB, where G has the non-dimensional ordinate

$$\chi_n \ = \ \chi(1-\beta)/4 \ \leq \ \chi_d \tag{18.45}$$

The reduction in the second order moment with β thus increases the bending resistance from EF to DF. Clearly when $\beta = 1$ in Eq. 18.45, $\chi_n = 0$ and the second order effect is maximised, so point G moves to the origin O.

The bending capacity is thus measured by the distance μ in Fig. 18.17. If point B has non-dimensional coordinates (μ_k, χ) and F has coordinates (μ_d, χ_d) then

$$\mu = \mu_d - \mu_k \left(\frac{\chi_d - \chi_n}{\chi - \chi_n} \right) \tag{18.46}$$

Because of the unconservative assumption that the concrete stress block is fully plastic to the neutral axis, the capacity measure μ is reduced by 10% in the Eurocode. Thus, the bending resistance is

$$M_s = 0.9\mu M_o \tag{18.47}$$

It is worth noting that if the factor 0.9 is applied to Wakabayashi's method in the strength envelope generated in Example 18.2, then this model overestimates the moment by only 8% and the Eurocode based method in Example 18.3 overestimates the moment by 16%.

Note also that the magnification of the loading line due to the secondary effects takes place at the outset, where the design moments are magnified by δ_b. This differs from the reinforced concrete approach where δ_b is applied to the first order moment at all points along the loading line.

Example 18.4 Eurocode method for member strength

Consider the column section shown in Fig. 18.5(a) and whose section strength was analysed by the Eurocode method in Example 18.3. The section strength is plotted non-dimensionally in Fig. 18.18 by dividing the abscissa by $M_o = 1652$ kNm and the ordinate by $N_o = 15,067$ kN. Suppose that the column is subjected to a moment M at one end and M/2 at the other end, so that $\beta = 0.5$, and that its effective length is L = 25 m. We will assume that $E_c = 25$ kN/mm^2 and that the design load is N = 6000 kN applied at the centroid.

The section properties may be determined readily as $I_s = 861 \times 10^6$ mm^4 for the steel element and $I_c = 30.4 \times 10^9$ mm^4 for the concrete element, so that from Eq. 18.40 with $E_s = 200$ kN/mm^2, $(EI)_e = 780 \times 10^{12}$ Nmm^2 and so $N_{crit} = 12,320$ kN from Eq. 18.39. The modified slenderness for the column from Eq. 18.41 is $\lambda = \sqrt{15,067/12.320} = 1.105$. By interpolating linearly from curve 'b' of Eurocode 3, $\chi = 0.532$. The coordinates of the point on the strength envelope corresponding to χ, B in Fig. 18.17, are $(\mu_k, \chi) = (1.345, 0.532)$ as shown in Fig. 18.18. For the 6000 kN design load, $\chi_d = 6000/15,067 = 0.398$ in Eq. 18.44. The coordinates of the point F in Fig. 18.17, shown in Fig. 18.18, are thus $(\mu_d, \chi_d) = (1.545, 0.398)$. Also from Eq. 18.45, the ordinate of point G in Fig. 18.17 is $\chi_n = 0.532 \times (1 - 0.5)/4 = 0.0065$. Thus from Eq. 18.46, $\mu = 1.545 - 1.345(0.398 - 0.0065)/(0.532 - 0.0065) = 0.543$. The maximum *second order* moment that can be resisted at this load from Eq. 18.47 is $M_s = 0.9 \times 0.543 \times 1652 = 807.3$ kNm. Note that this is the second order moment, which must be divided by δ_b in Eq. 18.36 to give the first order or applied moment that can be resisted.
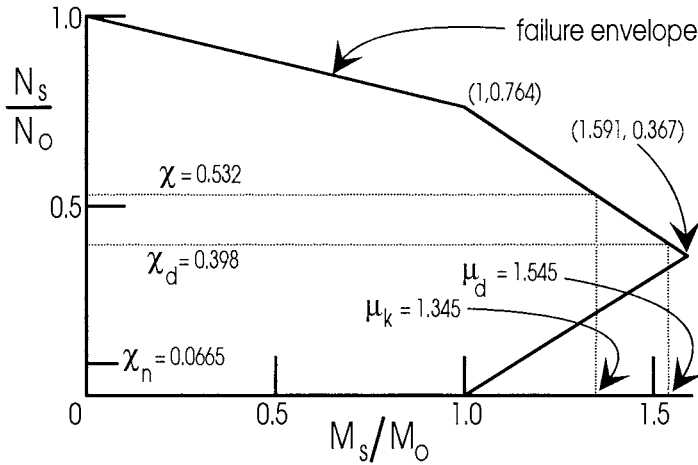
Fig. 18.18 Example 18.4

If the composite column is also subjected to bending about the minor axis, a condition of biaxial bending exists. For design, the Eurocode procedure described in the previous section is again followed, except that χ_y for bending about the y axis is determined from Eurocode curve 'c' in Fig. 18.14. The moments M_x and M_y about the x and y axes must satisfy

$$M_x \leq 0.9\mu_x M_{ox} \tag{18.48}$$

and

$$M_y \leq 0.9\mu_y M_{oy} \tag{18.49}$$

where M_{ox} and M_{oy} are the full plastic moments about the x and y axes, and μ_x and μ_y are obtained for bending about the x and y axes. In addition to satisfying Eqs. 18.48 and 18.49, the linear interaction equation

$$\frac{M_x}{\mu_x M_{ox}} + \frac{M_y}{\mu_y M_{oy}} \leq 1 \tag{18.50}$$

must also hold. The provisions of Eqs. 18.40 to 18.42 are illustrated in Fig. 18.19.
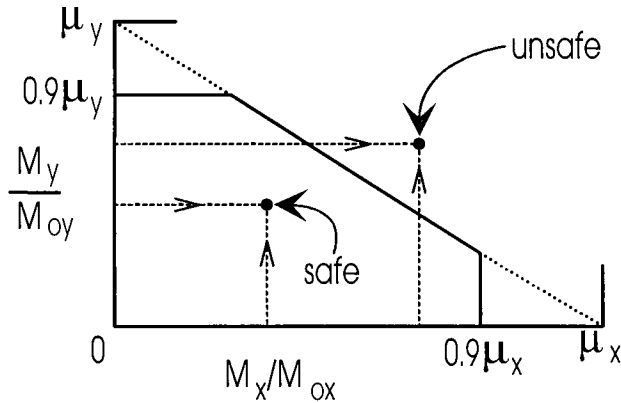
Fig. 18.19 Linear biaxial bending interaction

18.2.4   LONG-TERM BEHAVIOUR

18.2.4.1   *General*

The effects of creep and shrinkage that were discussed in Chapter 2 may have a substantial effect on the service load behaviour of encased I-section composite columns that are subjected to sustained dead loads. The composite column behaves in a similar fashion to a reinforced concrete column, but the behaviour is markedly different from a concrete-filled steel tube where the egress of moisture from the concrete is inhibited by the steel skin. There appears to be very little research into the time-dependent behaviour of composite columns subjected to the effects of sustained service loads apart from that reported by Bridge (1979) and Bradford and Gilbert (1990).

This sub-section outlines the mechanism of the behaviour of encased I-sections in the time domain. Following this, a design proposal is suggested that may be used with the Eurocode-based method described in Section 18.2.3.4.

18.2.4.2   *Behaviour*

As was described in Chapter 2, the analysis of concrete elements subjected to creep and shrinkage is limited to what may be termed "linear elastic" behaviour, although this is really a misnomer as the concrete cracks and the creep response is not strictly elastic. Figure 18.20(a) shows a portion of a composite column that is subjected to an eccentric axial load, so that it has assumed a bent position at its midlength. The compressive stresses on the concave side are clearly larger than those on the convex side, and for simplicity we will assume that the stress distribution is linear. Creep occurs under sustained loading, so that greater creep strains will occur on the concave side than on the convex side, with the effect that the curvature will be increased under a sustained service load, since the strain gradient in Fig. 18.20(b) is increased.
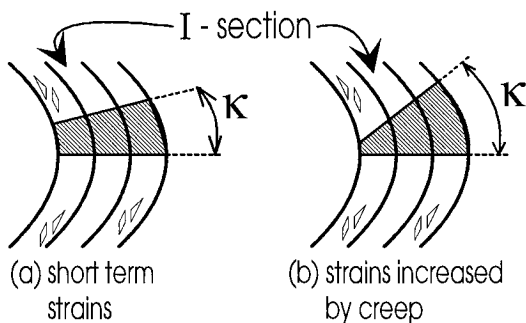
Fig. 18.20 Curvature increase due to creep

Because the lateral deformation depends on the curvature, the effect of a sustained service load that induces creep strains will be to increase the lateral deflection of the column, and subsequently the $P-\delta$ effect is accentuated. This may lead to reduced design loads under sustained dead loading, and may even lead to instability or *creep buckling* when the lateral deflections approach infinity.

In a reinforced concrete column, the effective flexural rigidity EI used in the buckling representation of Eq. 18.38 is determined by writing

$$EI = \frac{200dM_{ub}}{1+\beta_d} \tag{18.51}$$

where β_d is a term intended to allow for the effects of creep. It is written in Warner, Rangan and Hall (1989) as

$$\beta_d = \frac{G}{G+Q} \tag{18.52}$$

where G is the sustained dead load and Q is the short term live load. Clearly under only dead loading, $\beta_d = 1$, while if the load is only a short term sustained load, $\beta_d = 0$. Hence the critical load N_c in Eq. 18.38 is reduced by the effects of creep, so that the amplification factor δ_b for second order effects is increased. As pointed out in Warner, Rangan and Hall, there is really no logical basis for Eqs. 18.51 and 18.52, although they produce the desired effect in terms of the amplification of the first order moment due to creep.

18.2.4.3 *Design recommendation*

A comprehensive study of the behaviour of encased composite columns in the time domain was undertaken by Bradford and Gilbert (1990). The analysis was for a column with equal end eccentricities e_o, although similar conclusions to this study were obtained by Gilbert and Bradford (1990) for a reinforced concrete column under unequal end eccentricity.

In the method of Bradford and Gilbert, the moment magnifier δ_b was expressed in the form of Eq. 18.36, but with $k_m = 1$ as the end moments were equal, and for short term loading

$$N_{crit} = \frac{\pi^2 \Omega (EI)_c}{L^2} \tag{18.53}$$

in which $(EI)_c$ is the modulus transformed to the uncracked concrete cross-section and Ω is a factor to allow for cracking of the concrete. Using regression analysis, and based on a suggestion by Rangan (1989) and Gilbert and Bradford (1990) for reinforced concrete columns, the reduction factor Ω was expressed empirically as

$$\Omega = 0.43 + 0.14 \left(\frac{e_b}{e_o} \right) \tag{18.54}$$

where e_o is the eccentricity of the applied load and e_b is the ratio of the maximum moment on the strength interaction diagram to the value of the axial compressive load that exists at this point. For long-term loading, the effective modulus $(EI)_c$ in Eq. 18.53 was replaced by $(EI)_c/(1+\phi)$ based on an analysis using the Age-Adjusted Effective Modulus Method (Section 2.3.3), where ϕ is the creep coefficient at the time being considered. The effect of $\Omega(EI)_c$ is thus equivalent to Eq. 18.40 and used in the Eurocode-based prediction.

Although the factor 0.8 in Eq. 18.40 was intended in some ways to account for creep, a suitable design recommendation based on the Eurocode approach described in Section 18.2.3.4 is to determine N_{crit} in Eq. 18.31 using

$$(EI)_e = E_s I_s + \frac{0.8 E_c I_c}{1+\phi} \tag{18.55}$$

where ϕ is the creep coefficient at the time considered. The remainder of the procedure follows the Eurocode approach.

18.3   Concrete-filled steel tubes

18.3.1   GENERAL

An increasingly popular trend in composite columns is to fill steel tubes with a concrete core. Both the steel and concrete contribute to the strength, but the steel tube provides triaxial confinement in much the same way as stirrups in reinforced concrete columns. As we saw in Section 18.1, the main advantage in deploying concrete-filled tubes, however, is the advantage that the system has in the construction sequence. The steel tubes can be designed to resist construction loads, and then sequential concreting of the tubes can progress from the lower stories while the upper stories are

being formed. This procedure has been found to speed up considerably the construction time for a multi-storey building (Webb and Peyton 1990).

There are a few structural considerations that must be borne in mind when comparing and contrasting the fundamental behaviour of encased columns and concrete-filled steel tubes. Firstly, concrete-filled tubes are susceptible to local buckling of the steel skin, which in many cases is very thin. The second point pertains to the triaxial confinement provided by the tube to the expansion of the concrete core in compression, and it has been found that this confinement enhances considerably the strength of a short column, but is insignificant in slender columns. Thirdly, the steel skin inhibits the egress of moisture that contributes to creep and shrinkage effects, so research into monitoring the time-dependent deformations of concrete-filled tubes has indicated a reduced creep and shrinkage-induced response. Finally, as was pointed out in Section 18.1, the main reason for the initial adoption of encased columns was for fire protection of the steel. This does not occur with filled steel tubes, which must generally be coated with additional fire-resisting material to obtain the desired fire rating. In addition, small holes are often drilled into the steel skin to allow steam to escape when the encased concrete core is heated in a fire, thereby reducing the possibility of explosive failure caused by pressurised steam generated from the comparatively moist concrete.

18.3.2   SHORT COLUMNS

18.3.2.1   *Confinement*

In a short concentrically loaded concrete-filled steel tube, the concrete core of the column is subjected to a confining stress, and as a result the column can carry considerably larger axial forces than if the concrete was unconfined. The results of triaxial tests on concrete have illustrated this, where concrete subjected to a lateral confining pressure can carry a greater axial load than unconfined concrete. Of course, this is utilised in reinforced concrete construction where spirally reinforced columns provide a lateral stress that increases the axial load carried by the concrete core. However, the behaviour of an axially loaded steel tube filled with concrete will vary according to the method in which the ends of the member are loaded. Essentially, there are three fundamentally different methods of applying the loading, and these are discussed below.

(a) Load the steel and not the concrete

This condition of loading may not increase the axial load capacity of the column above that of the steel tube alone, because the Poisson's effect causes the steel tube to separate from the concrete once the adhesive chemical bond between the concrete and steel has been exceeded. The column will generally fail at the maximum load which the hollow steel tube alone can carry, but the concrete core may tend to delay the column local buckling, as is discussed in Section 18.3.2.3. Tests carried out by Gardner and Jacobson (1968) showed that loading the steel alone did not increase the failure load much above that for a hollow steel tube.

(b) Load the concrete and not the steel

This condition is known as the Lohr principle (Lohr 1934), with the steel acting as an encasement. In principle, this is the most favourable loading method as the steel does not resist axial load, but only provides a confining stress to the concrete in an analogous manner to a spirally reinforced concrete column. However, since there is some adhesion between the steel and concrete, the condition is hard to attain as some axial load is produced in the steel.

(c) Load the steel and concrete

This is the method most often encountered in practice, and it may be enforced by welding stud shear connectors to the inside of the steel tube where practicable. If the steel is axially stressed in compression as well as circumferentially because of the expansion of the concrete, it will be subjected to a state of biaxial stress (Section 2.2) which, in accordance with the von Mises' yield criterion, will reduce the yield stress in the circumferential direction. This has the effect of lowering the confining effect, and hence reduces the maximum load on the concrete. The reduction in the confining effect is offset, though, since the steel now carries some of the compressive force, thereby increasing the load-carrying capacity of the column.

There are many methods for analysing the behaviour of short, concrete-filled steel tubes. In the so-called "equilibrium method" (Cai and Jian 1984) shown in Fig. 18.21, the reduced stress in the concrete, f_{cr} may be written in terms of f_c as

$$f_{cr} \;=\; f_c \left[1 + \frac{1}{32}\left(\frac{\sigma_r}{f_c}\right)^{\!\frac{1}{3}} + 2\frac{\sigma_r}{f_c} \right] \qquad (18.56)$$

where σ_r is the radial lateral confining pressure. The yielding of the steel tube is governed by von Mises' criterion (Section 2.3.2), which may be written in terms of the stresses in Fig. 18.21 as

$$\sigma_1^{\,2} + \sigma_1\sigma_2 + \sigma_2^{\,2} \;=\; f_y^{\,2} \qquad (18.57)$$

By ignoring the contribution of σ_r in the von Mises treatment as being negligible for the steel, the concentric capacity N_u of the concrete-filled tube can be written as

$$N_u \;=\; A_{conc}\,f_c \left[\left\{ 1 + \frac{1}{32}\left(\frac{\sigma_r}{f_c}\right)^{\!\frac{1}{3}} + 2\frac{\sigma_r}{f_c} \right\} + \sqrt{\phi^2 - 3\left(\frac{\sigma_e}{f_c}\right)^{\!2}} \; - \frac{\sigma_r}{f_c} \right] \qquad (18.58)$$

where

$$\phi = \frac{A_{steel}f_y}{A_{conc}f_c} \tag{18.59}$$

If we now minimise N_u in Eq. 18.58 with respect to σ_r, that is to set $dN_u / d\sigma_r = 0$, the concentric capacity can be approximated by

$$N_u = A_{conc}f_c(1+\beta\phi) \tag{18.60}$$

where

$$\beta = 0.21+\frac{1}{\sqrt{\phi}} \tag{18.61}$$

and ϕ is as in Eq. 18.59.
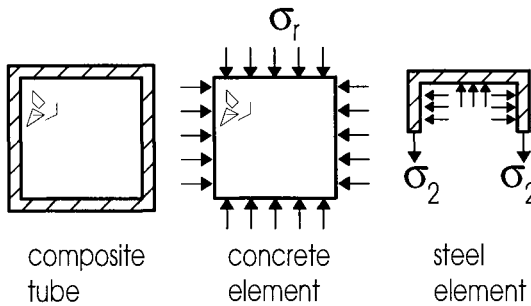
Fig. 18.21 Stresses acting on concrete and steel elements

Example 18.5 Squash load of concrete-filled steel tube

The cross-section shown in Fig. 18.2(a) with D = 500 mm, b = 300 mm and t = 5 mm has strengths f_c = 40 N/mm^2 and f_y = 350 N/mm^2. The cross-sectional properties are A_{conc} = (300-10)x(400-10) = 113,100 mm^2 and A_{steel} = 300x400 - 113,100 = 6900 mm^2. Hence from Eq. 18.59, ϕ = 0.534 and β = 1.58 from Eq. 18.61. Substituting into Eq. 18.60 gives N_u = 8341 kN.

If we now assume no confinement, that is that the concrete is stressed to $0.85f_c$ and that the steel is at full yield, then N_u = 0.85x40x113,100 + 350x6900 = 6260 kN. The confinement effect, based on the equilibrium principle, is thus an enhancement of 8341/6260 or 33%.

Elastic and plastic theories have also been deployed to calculate the section strength of a concrete-filled steel tube with confinement. It has been found that there are some disparities between the results of the theories, and the shape of the cross-

section, namely rectangular or circular. Because we are generally concerned with more slender members, and because experiments (Tomii, Matsui and Sakimo 1973) suggest that microcracking in the concrete can reduce the triaxial effect below that of Eq. 18.60, Chen and Atsuta (1976) and Bradford (1991) have conservatively suggested that the effective strength of concrete in a steel casing should not exceed $0.85f_c$, so that Eq. 18.4 can be used as the concentric strength of a steel tube. The strength of the steel, however, may have to be reduced for the effects of inelastic local buckling, and this is discussed in Section 18.3.2.3.

18.3.2.2 Section strength

An analysis of a cross-section subjected to compression and bending, such as that shown in Fig. 18.22, may be undertaken using the same principles as explained in Section 18.2.2.1 for an encased I-section column. The behaviour of the column is similar to that of Fig. 18.4 at ultimate.
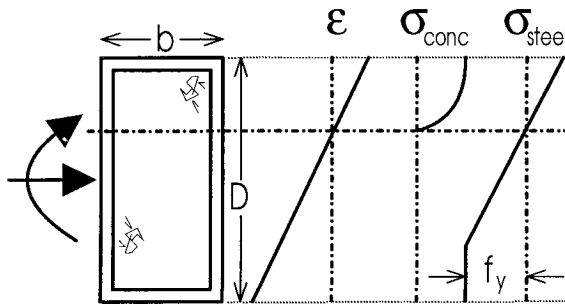
Fig. 18.22 Concrete-filled steel tube

 An analysis of a rectangular concrete-filled steel tube subjected to an eccentric loading was undertaken by Bradford (1991) using first principles. This analysis was simplified into an empirical design rule, which is outlined in the following procedure for obtaining the strength interaction diagram. Although intended for rectangular tubes, it is felt, without extensive analysis, that it is also applicable with slight modification to circular tubes.

 The starting points in the analysis are the squash load N_0 given in Eq. 18.4 and the moment under pure bending, approximated as

$$M_o \;=\; f_y Z_s + \frac{A_{steel}}{2} f_y \left(\frac{D}{2} - \frac{t f_y}{1.7 f_c} \right) \tag{18.62}$$

The interaction strength envelope of points (M_s, N_s) is then obtained from the expression

$$\frac{M_s}{M_o} = 1 + 2\left(\frac{N_s}{N_o}\right) - 3\left(\frac{N_s}{N_o}\right)^{\alpha} \tag{18.63}$$

where the index α is obtained from the cross-section property ζ as

$$\alpha = 1.0 + 0.5\zeta \tag{18.64}$$

in which

$$\zeta = \frac{0.85 f_c A_{conc}}{f_y A_{steel}} \tag{18.65}$$

It should be reiterated that the basis of Eqs. 18.62 to 18.65 is empirical.

18.3.2.3   *Local buckling of steel tube*

Because the steel tube is usually thin, it may be subjected to the effects of local buckling. As for the steel sheeting treated in the local buckling of profiled composite slabs in Chapter 16 and profiled composite beams in Chapter 17, the concrete core acts as a restraining medium, so that the local buckling coefficient is greater than that for the empty tube alone, as illustrated in Fig. 5.13.

The local buckling may be elastic or inelastic. Elastic buckling takes place before the critical stress σ_{cr} in Eq. 5.2 reaches the yield stress f_y and then there may be a benign post-local buckling effect, as was discussed in Section 5.2.2 On the other hand, crushing of the concrete at ultimate generally takes place at a strain of 0.003, so it is important for the steel skin to be able to resist this strain. This strain may not be attainable in the steel because of inelastic local buckling at a strain greater than $\varepsilon_y = f_y/E_s$.

Most design recommendations base the limiting width to thickness ratios for the steel element on test results, or on the provisions of theoretically derived limits for hollow tubes. The problem has been treated analytically by Uy and Bradford (1994) for both concentric and eccentric compression using the finite strip method, where the concrete core restrains buckling of the steel skin. For a rectangular column, elastic local buckling will take place for width to thickness ratios b/t greater than $1500/\sqrt{f_y}$ and inelastic buckling for b/t ratios greater than $470/\sqrt{f_y}$, where f_y is expressed in N/mm^2.

The post-local buckling reserve may be included in the design. Hence, the capacity N_o in Eq. 18.4 may be written when the steel buckles locally as

$$N_o = 0.85 f_c A_{conc} + f_y (A_{steel})_{eff} \tag{18.66}$$

where the effective steel area $(A_{steel})_{eff}$ may be obtained from the effective widths b_e of the steel plates. For a rectangular column with slight geometric imperfections, the effective width ratio may be written as (Yamaki 1959)

$$b_e / b \;=\; 1.0 \qquad\qquad 0 \le \omega \le 0.5 \qquad\qquad (18.67)$$

$$b_e / b \;=\; 1.055 - 0.11\omega \qquad 0.5 \le \omega \le 0.8 \qquad (18.68)$$

$$b_e / b \;=\; 1.159 - 0.24\omega \qquad 0.8 \le \omega \le 1.2 \qquad (18.69)$$

$$b_e / b \;=\; 1.08 - 0.175\omega \qquad 1.2 \le \omega \le 1.6 \qquad (18.70)$$

$$b_e / b \;=\; 1.0 - 0.125\omega \qquad 1.6 \le \omega \le 2.0 \qquad (18.71)$$

where

$$\omega \;=\; f_y / \sigma_{cr} \qquad\qquad\qquad\qquad (18.72)$$

For a concentrically loaded rectangular composite tube, the elastic local buckling coefficient for the steel skin is (Uy and Bradford 1994) $k = 10.31$. Hence substituting for σ_{cr} in Eq. 5.2 produces

$$\omega \;=\; 537 x 10^{-9} f_y \left(\frac{b}{t}\right)^2 \qquad\qquad (18.73)$$

which makes use of the material properties $E_s = 200$ kN/mm^3 and $v_s = 0.3$.

Example 18.6 Local buckling in concrete-filled tube

In the concrete-filled steel tube shown in Fig. 18.2(a) with D = 500 mm, b = 300 mm and t = 5 mm and analysed in Example 18.5, b/t for the longer side is 80 and for the shorter side is 60. Hence $(\omega)_{long} = 1.208$ and $(\omega)_{short} = 0.677$ from Eq. 18.73, so $(b_e)_{long} = 347$ mm and $(b_e)_{short} = 294$ mm, giving $(A_{steel})_{eff} = 6410$ mm^2. The capacity including local buckling is thus, from Eq. 18.66, $N_o = 6089$ kN. This represents a reduction of 6089/6260 or 3%.

18.3.3   SLENDER COLUMNS

The analysis of slender concrete-filled steel tubes is similar in principle to that of encased I-sections, and either a steel approach with suitable reductions for the bending, or a reinforced concrete approach may be adopted. For rectangular tubes, Bradford (1995) used a concrete-based approach, whereby Eq. 18.53 was used in the moment amplification, with the cracking parameter Ω given by Eq. 18.54. In this method, the loading line, including the magnifier δ_b in Eq. 18.36, was extended to

intersect the cross-section strength envelope derived in Section 18.3.2.2. A transcendental equation was then developed to obtain the maximum load N_u at this point of intersection, which was found to agree very well with the test results of Bridge (1976) and Shakir-Khalil and Zeghiche (1989).

In lieu of the use of these specialised treatments, a rational design procedure similar to that outlined in Section 18.2.3.4 may be used (Eurocode 4 1994). The capacity reduction factor χ is found in the same way as for encased columns, but with a squash load of N_o that is given in Eq. 18.66. This is slightly different than the squash load for an encased column, and is introduced to incorporate the effects of local buckling. Because concrete-filled hollow sections are more ductile than encased sections, the Eurocode recommends the use of the highest column curve, curve 'a' in Fig. 18.14. The moment capacity may then be found by the geometric construction in the strength interaction diagram outlined in Section 18.2.3.4.

18.3.4   LONG-TERM BEHAVIOUR

The behaviour of concrete-filled steel tubes when undergoing creep and shrinkage caused by a sustained load is different from that of encased I-section columns. The main difference is attributable to the reduction in the moisture loss that is directly related to the creep and especially shrinkage properties. Thus, while the analytical techniques, such as the Age-Adjusted Effective Modulus Method (Section 2.3.2) are applicable to both types of composite column, the creep and shrinkage properties are different. It is also worth noting that, in the time-domain, load is shed into the steel. This has relatively little effect in encased I-sections, but for steel tubes with very thin walls the time-induced load shedding may increase the compression in the steel markedly, and thus precipitate local buckling. This latter phenomenon has been alluded to by a few researchers (Webb and Peyton 1990, Terrey, Bradford and Gilbert 1994), but its influence is still to be quantified.

Recently, Terrey, Bradford and Gilbert (1994) undertook a series of experiments to measure the creep and shrinkage response of concrete in thin circular steel tubes. It was concluded that the moisture loss that takes place in these tubes may be very small or eliminated totally, with a consequent reduction in the effects of creep and shrinkage. In these tests, plain concrete cylinders were tested in a creep rig and found to have a long-term creep coefficient in the range $\phi^*(\tau)$ of 2.15 to 2.3. The long-term creep coefficient for the concrete in the concrete-filled tubes, on the other hand, was found to have a final creep coefficient $\phi^*(\tau)$ in the range of 1.15 to 1.25, representing a reduction in the order of 60% in the final creep coefficient due to the prevention of the egress of moisture. The tests also confirmed that the shrinkage strains are negligible when compared with those of a plain concrete specimen. When small holes are drilled into the tubes for fire control, as was noted earlier, these creep coefficients and shrinkage strains may increase, but they would vary nonuniformly through the cross-section of the concrete core.

A service load analysis was undertaken for a rectangular concrete-filled steel tube (Bradford and Gilbert 1992), in which a sustained load was applied

eccentric to the plastic centroid of the column. The Age-Adjusted Effective Modulus Method was used, and a reinforced concrete design approach was adopted for the composite column. Using this, the moment amplification factor δ_b in Eq. 18.36 was used, but the critical load N_{crit} was represented in the form given in Eq. 18.53, with Ω taken as being the same as in Eq. 18.54. In order to account for creep, the transformed stiffness $(EI)_c$ used in deriving N_{crit} was divided by $1+\phi$, where ϕ is the creep coefficient at the time under consideration. Hence a suitable design procedure based on the Eurocode approach is to adopt the same method for encased columns, that is to base $(EI)_e$ on Eq. 18.55. Because the creep coefficient is less for concrete-filled tubes than for encased I-section columns, the reduction in N_c is greater for the encased columns.

18.4   References

Basu, A.K. and Somerville, W. (1969). "Derivation of formulae for the design of rectangular composite columns", Proceedings of the Institution of Civil Engineers, London, Supplementary Volume, 233-280.

Bradford, M.A. (1991). "Design of short concrete-filled RHS sections", Civil Engineering Transactions, Institution of Engineers, Australia, Vol. CE33, No. 3, 189-194.

Bradford, M.A. (1995). "Design strength of slender concrete-filled rectangular steel tubes", American Concrete Institute Structural Journal, to appear.

Bradford, M.A. and Gilbert, R.I. (1990). "Time-dependent analysis and design of composite columns", Journal of Structural Engineering, ASCE, Vol. 116, No. 2, 3338-3357.

Bradford, M.A. and Gilbert, R.I. (1992). "Non-linear time-dependent behaviour of slender concrete-filled rectangular steel columns", Proceedings of the Institution of Civil Engineers Structures and Buildings, Vol. 94, 179-186.

Bridge, R.Q. (1976). "Concrete-filled steel tubular columns", Civil Engineering Transactions, Institution of Engineers, Australia, Vol. CE18, No. 2, 127-133.

Bridge, R.Q. (1979). "Composite columns under sustained load", Journal of the Structural Division, ASCE, Vol. 105, No. ST3, 563-576.

Cai, S-H. and Jiao, C (1984). "Ultimate strength of concrete-filled tube columns", Proceedings of Engineering Foundation Conference on Composite Construction in Steel and Concrete, ASCE, 702-710.

Chen, W.F. and Atsuta, T. (1976). *Theory of Beam-Columns - Vol. 1: In-Plane Behaviour and Design*, McGraw-Hill, New York.

Eurocode 4 (1994). *Design of Composite Steel and Concrete Structures*. DDENV 1994-1-1, Draft for development.

Faber, O. (1956). "Savings to be effected by the more rational design of cased stanchions as a result of recent full size tests", The Structural Engineer, March, 88-109.

Gardner, N.J. and Jacobson, E.R. (1968). "Structural behaviour of concrete filled steel tubes", Proceedings, American Concrete Institute, Vol. 65, No. 1, 66-69.

Gilbert, R.I. and Bradford, M.A. (1990). "Design of slender reinforced concrete columns for creep and shrinkage", Second International Conference on Computer Aided Analysis and Design of Concrete Structures, Zell am See, Austria, 739-748.

Hall, A.S. (1984). *An Introduction to the Mechanics of Solids,* John Wiley, Sydney.

Johnson, R.P. (1994). *Composite Structures of Steel and Concrete:* Volume 1, 2nd edn., Blackwell Scientific Publications, U.K.

Lohr, W.S. (1934). "Concrete encased in steel shells proposed", Engineering News Record, Vol. 113, 760-762.

Rangan, B.V. (1989). "Lateral deflection of slender reinforced concrete columns under sustained load", American Concrete Institute Structural Journal, Vol. 86, No. 6, 660-663.

Roik, K. and Bergmann, R. (1989). "Eurocode 4: composite columns", Report EC4/6/89, University of Bochum, June.

Rotter, J.M. (1982). Lecture 3 of *Composite Structures of Steel and Concrete*, Postgraduate Course, School of Civil and Mining Engineering, The University of Sydney.

Shakir-Khalil, H. and Zeghiche, J. (1989). "Experimental behaviour of concrete-filled rolled rectangular hollow-section columns", The Structural Engineer, Vol. 67, No. N19/3, 346-353.

Stevens, R.F. (1959). "Encased steel stanchions and BS449", Engineering, October, 376-377.

Terrey, P.J., Bradford, M.A. and Gilbert, R.I. (1994). "Creep and shrinkage in concrete-filled steel tubes", Proceedings of the Sixth International Symposium on Tubular Structures, Melbourne, 293-298.

Tomii, M., Matsui, C. and Sakino, K. (1973). "Concrete filled steel tube structures", Tokyo Regional Conference, IABSE-ASCE Tall Buildings Conference, Tokyo.

Trahair, N.S. and Bradford, M.A. (1991). *The Behaviour and Design of Steel Structures*, revised 2nd edn., Chapman and Hall, London.

Uy, B., and Bradford, M.A. (1994). "Local buckling of composite steel-concrete rectangular columns", Fifth International Conference on Steel Structures, Jakarta, 313-322.

Wakabayashi, M. (1976). "A proposal for design formulas for composite columns and beam-columns", Second International Colloquium on Stability, Tokyo, 65-87.

Warner, R.F., Rangan, B.V. and Hall, A.S. (1989). *Reinforced Concrete*, 3rd edn., Longman Cheshire, Melbourne.

Webb, J. and Petyon, J.J. (1990). "Composite concrete filled steel tube columns", Structural Engineering Conference, The Institution of Engineers, Australia, Adelaide, 181-185.

Yamaki, N. (1959). "Postbuckling behaviour of rectangular plates with small initial curvature loaded in edge compression", Journal of Applied Mechanics, Vol. 26, No. 3, 407-414.

19 Fatigue Degradation of Composite Bridge Beams

19.1 Introduction

The repeated application of loads to bridges, due to the traversal of vehicles, causes cracks to initiate and propagate that may eventually lead to a reduction in the strength of the structure. It is therefore necessary to ensure that the strength of the structure is always greater than the maximum applied load during the whole of the design life of the structure and not just at the start. All of the previous chapters on structural analysis have dealt with the static strength of a structure, that is the strength of a structure that has not been subjected to a large number of load applications. In this chapter, we will be dealing with the remaining or residual strength of a structure that has been subjected to a large number of load applications, that is fatigue loads.

A system for quantifying the large variety and frequency of fatigue loads is first described in Section 19.2. These loads are converted into stress resultants in Section 19.3 and then combined with the fatigue material properties in Chapter 3 to form a general fatigue analysis equation in Section 19.4. It is shown that the general fatigue equation can be adapted to determine the reduction in strength of a component due to fatigue loading and this is referred to as the *crack propagation approach*, or it can be simply based on the endurance, as in existing standard S-N fatigue design, and this is referred to as the *crack initiation approach*. The general fatigue analysis procedure is then applied in both a design mode and an assessment mode to non-welded components in Section 19.5 to illustrate the *crack initiation approach*, to welded stud shear connectors in Section 19.6 to illustrate the *crack propagation approach*, and then to welded steel components in Section 19.7 to illustrate both approaches.

The symbol q will be used to denote the *shear flow force*, that is the longitudinal force per unit length that is resisted by the mechanical dowel action or friction. Whereas the symbol Q will be used to denote the *shear flow strength*, that is the longitudinal shear strength of the component per unit length which is a material property.

19.2 Applied loads

19.2.1 GENERAL

A bridge must be able to resist the maximum possible overload, or design load, that has a very low probability of occurrence, such as once in the lifetime of the structure. The bridge must also be resistant to the damage caused by the enormous number of load applications by the traversal of vehicles that can occur several times a minute, that is fatigue loads.

It is normal design practice to ensure that the factored strength of the structure, that is termed the design strength, is always greater than the factored maximum

overload, that is the design load. However, it is also normal practice to base the damage caused by the fatigue loads on the unfactored working loads, but then to reduce the probability of failure by using characteristic fatigue material properties. Hence, fatigue analyses are usually based on unfactored working loads and because we are dealing with working loads the stress resultants are usually determined from linear elastic analyses.

19.2.2 FATIGUE LOADS

19.2.2.1 *Frequency*

Hundreds of millions of vehicles, if not a billion vehicles, may traverse a bridge over its design life. A bridge may be subjected to vehicles that range in weight from cars of a few kN to commercial vehicles weighing 4000 kN. It was shown in Section 3.2.4, that the damage due to fatigue is proportional to F^{m_e}, where F is the force in the component and m_e is the exponent of the endurance equation that has a value of 3 or greater. Because of this, the damage due to the fatigue forces induced by heavy vehicles will be much greater than those incurred by a lighter vehicle. Hence and in order to simplify the problem, it is normal practice to only consider the fatigue damage due to the traversal of commercial vehicles and to ignore the fatigue damage due to lighter vehicles such as cars.

We will refer to the number of load traversals that a component is subjected to as T and the commercial vehicles that induce fatigue damage as *fatigue vehicles.*

Example 19.1. Load traversals

A three lane highway may be subjected to 2 million traversals per year of commercial vehicles in the slow lane (BS5400 1980) and 1.5 million traversals per year in the adjacent lane, and the bridge may be required to last 120 years. Hence, a component in a beam that is loaded from both lanes will be subjected to T = 2x120 = 240 million load traversals from fatigue vehicles in the slow lane and 180 million from the adjacent lane, giving a total of 420 million load traversals.

19.2.2.2 *Standard fatigue vehicles*

The shapes of the commercial vehicles may range from vehicles with two axles at a 4 m spacing to vehicles with eighteen axles spread over 50 m. In order to determine the damage caused by the fatigue loads, it is necessary to calculate the magnitude and frequency of the range of cyclic stresses induced in the component by each fatigue vehicle that traverses the bridge. Linear elastic analyses are usually used to determine the cyclic stresses. Therefore, it will only be necessary to determine the ranges and frequencies of cyclic stress that are induced in the component by each shape of commercial vehicle, as variations in the weight can be allowed for by using the principle of superposition.

The problem of determining the cyclic stresses is often simplified by the use of *standard fatigue vehicles*. A *standard fatigue vehicle* is a standard shape of the axle distribution of a vehicle, such as shown in Fig. 19.1 (BS5400 1980), that can be assumed to represent the variety of shapes of all the commercial vehicles that traverse the bridge. The shape of the *standard fatigue vehicle* is chosen to impose the same fatigue damage as the various shapes of the fatigue vehicles. If it is felt that one shape of *standard fatigue vehicle* cannot represent all the shapes of the fatigue vehicles, then several *standard fatigue vehicles* can be used where each *standard fatigue vehicle* represents a group of the fatigue vehicles. Therefore, instead of having to determine the range and frequencies of the cyclic stresses when each shape of fatigue vehicle crosses the bridge, it will only be necessary to do the analysis for each *standard fatigue vehicle*.
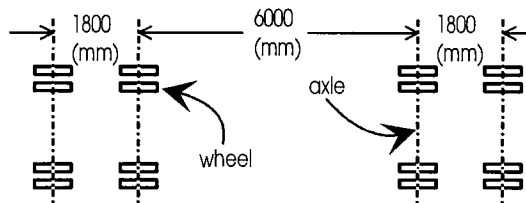
Fig. 19.1 Shape of standard fatigue vehicle

It is worth bearing in mind, and it is also shown in the following section, that the actual weight of the *standard fatigue vehicle* is not important. Any convenient weight can be chosen for analysis, such as a vehicle with sixteen wheels as in Fig. 19.1 with a load of 20 kN per wheel, giving a total weight of 320 kN (BS5400 1980). The weight of the standard fatigue vehicle will be referred to as W_{SFV}.

19.2.2.3 *Load spectrums*

Each standard fatigue vehicle represents a group of fatigue vehicles of varying weights that either have the same shape as the standard fatigue vehicle or produce the same fatigue damage. It is useful practice to represent the variation in the fatigue vehicle weights as a proportion of the weight of the standard fatigue vehicle. This is shown as W in column 2 in Table 1 where there are i weights of fatigue vehicles as shown in column 1. The weight of a fatigue vehicle at level x is therefore $W_x W_{SFV}$.

The probability of occurrence of each weight of vehicle at each of the i levels in Table 1 is given as B in column 3, such that the summation of B is equal to unity. Therefore, the number of fatigue traversals at level x is $B_x T$, where T is the total number of load traversals from all of the fatigue vehicles. Columns 2 and 3 in Table 1 are often referred to as a *load spectrum*.

Example 19.2. Frequency of fatigue loads

Let us assume that the weight of the standard fatigue vehicle is $W_{SFV} = 320$ kN and that the load spectrum is given by columns 2 and 3 in Table 2, which is similar to that applied to a British motorway or highway (BS5400 1980). Furthermore, the structure

in which the component is located is subjected to T = 240 million applications of load traversals from the slow lane during its design life of 120 years.

From Table 2, the weights of the fatigue vehicles range from 6.5x320 = 2080 kN at level 1 to 0.2x320 = 64 kN at level 6. The number of load traversals at level 1 for the vehicle of weight 2080 kN is B_1T = 4800 which is just over three per month. However, the number of load traversals for the lightest fatigue vehicle of weight 64 kN at level 6 is 144 million which is just over two per minute.

Table 1 Format of load spectrum

Level (x)	Weight (W)	Probability (B)	B W^m
(1)	(2)	(3)	(4)
1	W_1	B_1	$B_1W_1{}^m$
2	W_2	B_2	$B_2W_2{}^m$
i-1	W_{i-1}	B_{i-1}	$B_{i-1}W_{i-1}{}^m$
i	W_i	B_i	$B_iW_i{}^m$
		$\sum=1$	$L_f = \sum BW^m$

Table 2 Load spectrum

Level	W	B	BW^3 welded components		BW^4 non-welded components		$BW^{5.1}$ stud shear connectors		BW^{20} concrete	
(1)	(2)	(3)	(4)	(4a)%	(5)	(5a)%	(6)	(6a)%	(7)	(7a)%
1	6.5	0.00002	0.006	2	0.036	9	0.280	25	363×10^6	97
2	5.0	0.00010	0.013	5	0.063	15	0.367	32	10×10^6	3
3	2.0	0.01000	0.080	29	0.160	39	0.343	30	0	0
4	1.0	0.13988	0.140	51	0.140	34	0.140	12	0	0
5	0.5	0.25000	0.031	11	0.016	4	0.007	1	0	0
6	0.2	0.60000	0.005	2	0.001	0	0.000	0	0	0
		$\Sigma=1$	$\Sigma=0.274$		$\Sigma=0.415$		$\Sigma=1.14$			

19.2.3 OVERLOADS

We will define an overload as a load that occurs so infrequently that its contribution to fatigue damage can be ignored. However, it is necessary to ensure that the structure can resist this peak load throughout the whole of the design life. The maximum design

load that a structure is subjected to is an example of an overload that induces the maximum forces within the structure.

19.3 Cyclic stress resultants

19.3.1 GENERAL

The fatigue loads and overloads have to be converted to stress resultants. The normal procedure for doing this is to use a linear full-interaction analysis that allows for variations in the material properties due long-term and short-term loads, as described in Section 6.4, and for propped and unpropped construction as described in Section 6.5.

The use of a linear analysis is appropriate for the fatigue loads as we are dealing with working or serviceability loads. Furthermore, bridges are often designed to remain elastic when the overload is applied. A full interaction analysis is generally used because of its simplicity. However, a full interaction analysis, that is an analysis that ignores the slip of the shear connectors in a composite beam, tends to overestimate the shear flow forces on the mechanical shear connectors at the concrete-slab/steel-beam interface, but tends to underestimate the stress resultants within the concrete slab and within the steel beam.

The full interaction behaviour is first described. This is then followed by a qualitative description of the partial interaction behaviour, that allows for the slip and incremental set of the mechanical shear connectors as described in Section 3.4.2.

19.3.2 FULL INTERACTION BEHAVIOUR

19.3.2.1 *General*

The purpose of this section is only to illustrate the effect of the distribution of the stress resultants on the fatigue damage, and in particular the effect of the concrete-slab/steel-beam interface friction on the fatigue damage to mechanical shear connectors in a composite beam. Therefore, only basic elementary analysis techniques will be used, only the simplest of structures, that of a simply supported beam will be considered, and only shear forces and in particular shear flow forces will be dealt with.

19.3.2.2 *Longitudinally moving point load*

First consider the case of a fatigue vehicle that can be represented by a single point load or axle of weight V that traverses a simply supported beam as shown in Fig. 19.2(a). The beam has a constant cross-section throughout its length L. As we are dealing with a linear full interaction analysis, Eq. 1.9 can be used to convert the vertical shear forces to the longitudinal shear flow forces q that cause the fatigue damage. Hence, the shape of the envelope of the maximum shear flow forces that occur along the length of the beam will be the same as the shape of the vertical shear force envelope. Therefore, the shear flow force envelope consists of two parallel lines at a

spacing of q_v as shown in Fig. 19.2(a), where q_v is the shear flow force due to a vertical shear force of V.
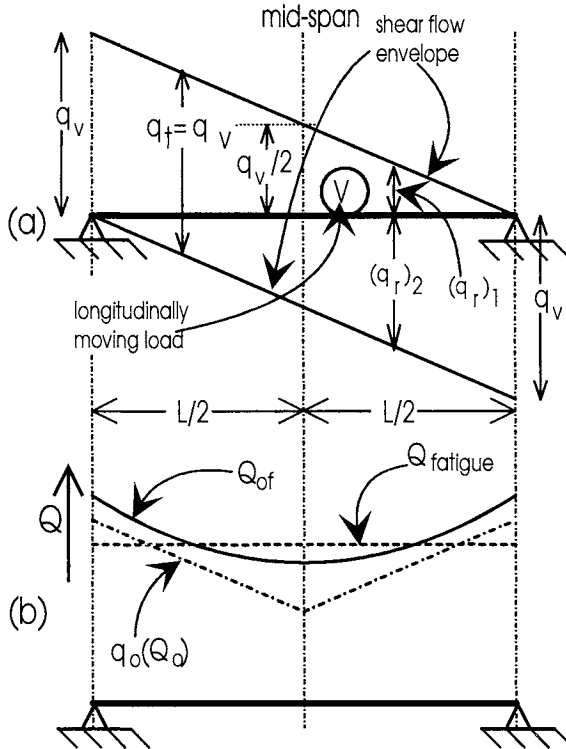
Fig. 19.2 Shear flow for single axle

It can be seen in Fig. 19.2(a) that the range of the total cyclic shear flow force q_t remains constant at a magnitude at q_v throughout the length of the beam, and that q_t is a reverse cyclic load except at the supports where it is uni-directional. Now the damage due to fatigue forces in welded components depends on the total cyclic range q_t because of the presence of residual stresses. Hence in welded components, the fatigue damage will be constant throughout the length of the beam.

The uni-directional component of the total range of the cyclic load q_t is shown as $(q_r)_1$ and $(q_r)_2$ in Fig. 19.2(a) and varies from q_v at the supports to $q_v/2$ at mid-span. In structures without residual stresses such as some non-welded components, the fatigue damage depends on the uni-directional range. Hence, the fatigue damage in these structures will be much greater at the supports than at mid-span.

The peak of the cyclic load is at a maximum value of q_v at the supports and reduces to $q_v/2$ at mid-span, so that the mid-span of the beam can withstand a greater reduction in strength due to fatigue damage than the supports.

19.3.2.3 *Longitudinally moving vehicle*

(a) Influence line diagrams

Influence line diagrams can be used to determine the variation of the loads at a design point of the beam when a combination of axles traverses the beam. To illustrate the technique, let us consider a standard fatigue vehicle that has two axles as shown in Fig. 19.3(a); the longitudinal spacing of the axles is L/4, and each axle, the front axle marked A and the back axle marked B, weighs V. The standard fatigue vehicle traverses a beam of span L (as shown in (b)) from the left to the right, and it is necessary to determine the variation of the cyclic forces at the design point marked D that is at the quarter span.

Let us first determine the variation of the cyclic forces due to the weight V acting on only the back axle B so that the front axle does not have a load. When the front axle is at the support at point C in Fig. 19.3(c), the shear force throughout the beam is zero as shown. When the back axle is just to the right of C as in (d), then the shear force adjacent to the support is V and remains at zero over the rest of the beam. The distribution of the shear forces when the back axle is just to the left of the design point at D and then just to the right of the design point are shown in (e) and (f). The standard fatigue vehicle is moved along the rest of the beam in (g) to (i).

An influence line diagram shows the variation of the forces at a design point for all positions of the applied load along the length of the beam. For convenience, we will define the position of this standard fatigue vehicle in terms of the position of its front axle. When the front axle is at position C, the shear force at the design point at D is zero as shown in Fig. 19.3(c), and so point 1 in the influence line diagram in Fig. 19.4(b) is at zero shear. When the front axle is at D as in Fig. 19.3(d), then the shear force at the design point is still zero as shown by point 2 in Fig. 19.4(b). When the front axle is just to the left of E in Fig. 19.3(e), so that the back axle is just to the left of the design point, then the shear force at the design point is V/4 which is point 3 in 19.4(b). Moving the vehicle just to the right of E in Fig. 19.3(f) changes the direction of the shear at the design point and increases it to 3V/4 which is point 4 in 19.4(b). Further movement along the beam produces a linear reduction in the shear flow as shown by points 5 to 7 in (b). The shear force at the design point being zero when the front of the vehicle is at point H which is a distance of L/4 beyond the end support.

An influence line diagram based on the position of the front axle can also be determined for the case when the front axle is only loaded as shown in Fig. 19.4(c). Summing (b) and (c) gives the influence line for a beam with both axles loaded as shown in (d), where it can be seen that the influence line diagram extends over a greater length than the span. Design point D is therefore subjected to the variation of the vertical shear force in (d) when a standard fatigue vehicle traverses the beam.

(b) Equivalent ranges of cyclic forces

The variations of the force in an influence line diagram have to be converted to a set of equivalent cyclic forces that produce the same fatigue damage. One of several conversion procedures is the *reservoir method* (BS5400 1980). This method consists
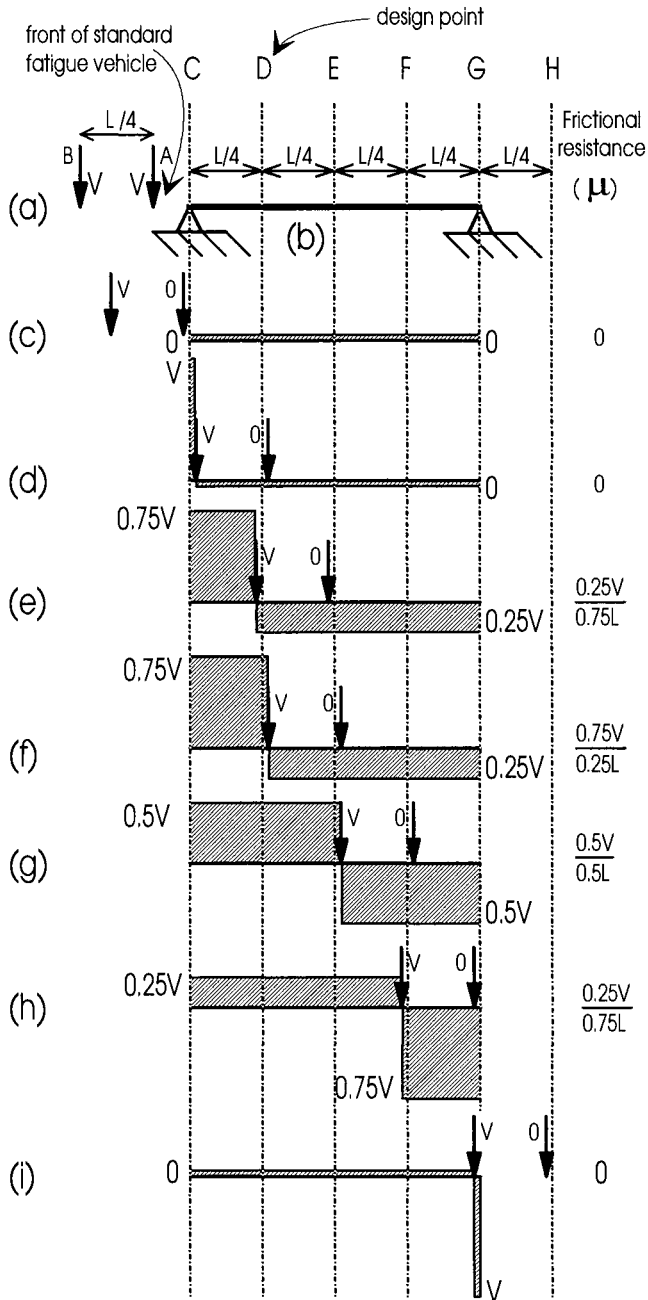
Fig. 19.3 Influence line analysis

of drawing a pair of influence line diagrams that are adjacent to each other as shown in Fig. 19.5. The upper part of the influence line diagram will be referred to as positive and the lower part as negative. The range of the cyclic load to be used in the analysis depends on whether fatigue damage is caused by the total reverse range or the uni-directional range, bearing in mind that it is the tensile stresses and not the compressive stresses that cause fatigue damage.
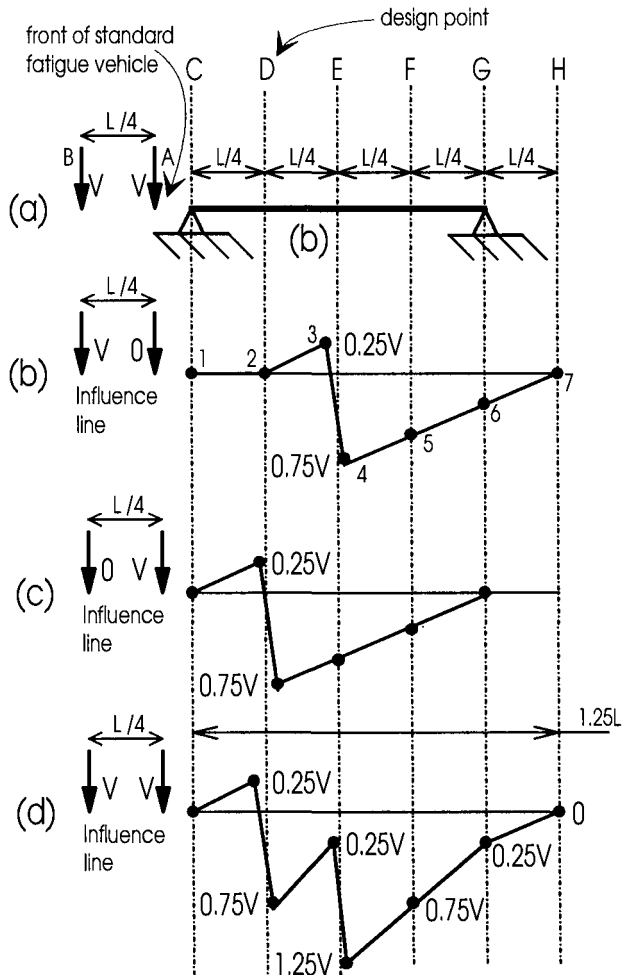
Fig. 19.4 Influence lines

When the fatigue damage depends on the total or reverse range of force, then the positive and negative parts of the influence line diagram must be used together as shown in Fig. 19.5(a). In the *reservoir method* of cyclic counting, the diagram in (a) can be considered to be the cross-section of a reservoir and the method requires that the reservoir is emptied but always drained from the lowest point. The depth from the reservoir surface to the drainage point is the equivalent cyclic range which in this case

is R_1. The remaining pockets of water are then drained from their lowest points until the reservoir is empty. In this case there is only one other cyclic range of R_2.
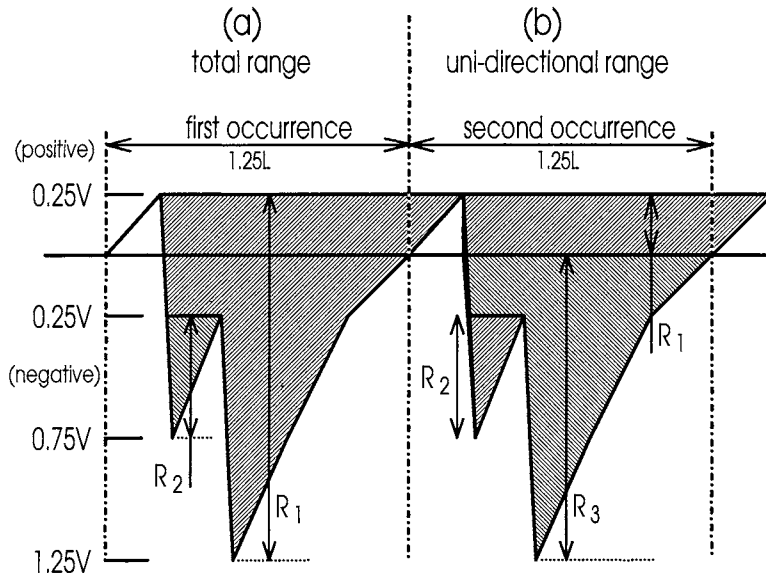
Fig. 19.5 Equivalent ranges using reservoir method

When the fatigue damage depends on the uni-directional range of the force, then the positive and negative parts of the influence line diagram must be considered separately as shown in Fig. 19.5(b). In this case, there are three ranges of cyclic load as shown and only the ranges that induce tensile stresses will cause fatigue damage.

Example 19.3. Equivalent ranges of cyclic loading using reservoir method

The two axle vehicle in Fig. 19.3(a) is replaced with a four axle vehicle. Each axle imposes a force of V and is spaced uniformly at a distance L/4. Determine the equivalent cyclic shear forces.

The influence line diagram for this problem is shown in Fig. 19.6 and was developed from the procedure described in Fig. 19.3. The reservoir method is shown for the reverse range of force. The lowest drainage point occurs at -1.5V and the depth of the water at this level is 1.75V, so that the maximum equivalent cyclic range is 1.75V and only occurs once. Draining the reservoir from this point leaves three pockets of water and draining these gives three ranges of magnitude V, 0.75V and 0.5V and each has a frequency of one.
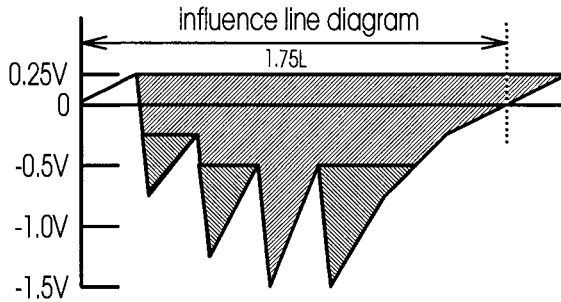
Fig. 19.6 Example 19.3: Equivalent ranges

19.3.2.4 *Frictional force at steel-concrete interface*

Frictional forces at the concrete-slab/steel-beam interface increase both the degree of interaction and the degree of shear connection between the concrete and steel elements of the composite beam. Under working loads, the frictional forces also reduce the shear flow forces on the mechanical shear connectors and hence help to extend the fatigue design life of the structure. It is suggested that the beneficial effects of friction at the interface should not be used in designing new structures but only in assessing the performance of existing structures.

(a) Longitudinally moving point load

The simply supported composite beam in Fig. 19.7(a) of length L is subjected to a single axle load of magnitude V. The axle load is positioned so that the left hand shear span is of length L_1 and has a shear load V_1, and the right hand shear span is of length $L_2 = L - L_1$ and has a shear load of $V_2 = V - V_1$. The shear flow force at the concrete-element/steel-element interface in the shear span of length L_1 can be derived from Eq. 1.9 and will be denoted by q_1. Hence, the longitudinal shear force in the shear span of length L_1 is $(F_{max})_1 = q_1 L_1$ which is also the resultant force in the concrete element as shown in Fig. 19.8.

As the load is applied to the top surface of the concrete beam as shown in Fig. 19.7(a), the load paths must cross the concrete-element/steel-element interface to reach the supports. The force that is perpendicular or normal to the interface in shear span L_1 is therefore V_1 and that in the shear span L_2 is V_2. Hence, the maximum longitudinal frictional resistance in shear span L_1 is $(P_{fric})_1 = \mu V_1$, where μ is the coefficient of friction between a steel and concrete interface that is subjected to cyclic loads and may be taken at about 0.7 (Singleton 1985). Similarly, the maximum frictional resistance in the shear span of length L_2 is $(P_{fric})_2 = \mu V_2$.

Equilibrium of the concrete element in the shear span of length L_1 is shown in Fig. 19.8. The longitudinal force in the concrete element $(F_{max})_1$ is resisted by the frictional force F_{fric} that has a maximum value of $(P_{fric})_1 = \mu V_1$ which is the frictional resistance. The longitudinal shear force in the mechanical shear connectors is $(F_{dowel})_1$ which has a maximum value of D_{max} per connector which is the dowel strength of the

mechanical shear connectors as described in Section 2.4, however it will be assumed that this strength will not be achieved in this instance as we are dealing with cyclic service loads. Hence, the cyclic force on the shear connectors that causes fatigue damage F_{dowel} is given by

$$F_{dowel} = F_{max} - F_{fric} \qquad (19.1)$$

Fig. 19.7 Frictional resistance envelope

We do know the frictional resistance P_{fric}, that is the maximum frictional force that could be applied, but it is necessary to determine the actual frictional force F_{fric} in Eq. 19.1 that is being applied. The problem is complicated by the fact that the mechanical dowel shear connectors require longitudinal slip before they resist shear, whereas the mechanism of friction does not require slip to resist shear. However, we do know that when slip does occur then the full frictional resistance $F_{fric} = P_{fric}$ is being achieved and hence we do know the frictional force and hence the dowel force when slip occurs.

Fig. 19.8 Dowel forces

The simplest solution to Eq. 19.1 is to assume that the frictional resistance P_{fric} is uniform throughout the shear span, that is the normal force V_1 in Fig. 19.8 is uniformly spread along the shear span. Therefore, all of the frictional resistance has to be overcome before the slip that is needed to load the mechanical shear connectors can occur. This will give the greatest benefit by providing the greatest reduction in the mechanical shear connector dowel loads. Replacing F_{fric} in Eq. 19.1 with P_{fric} and converting the forces to shear flows with the help of Eq. 1.9, gives the shear flow forces that act on the mechanical connectors by the equation.

$$\left(q_{dowel}\right)_n \;=\; V_n\left(\frac{A_{conc}\,\bar{y}_{conc}}{I_{nc}} - \frac{\mu}{L_n}\right) \tag{19.2}$$

where $(q_{dowel})_n$ is the shear flow force on the connectors in a span designated n of length L_n, V_n is the vertical shear force in shear span n, A_{conc} is the cross-sectional area of the concrete element as shown in Fig. 19.7(b), $\bar{y}_{conc}$ is the distance between the centroid of the concrete element and the centroid of the transformed concrete section of the composite beam, and I_{nc} is the second moment of area of the transformed concrete section.

Equation 19.2 assumes that the longitudinal shear flow force can cause slip throughout the length of the shear span, so that all of the available frictional resistance is being used. If the frictional resistance can prevent slip over part of the shear span, particularly in the region adjacent to the axle load where the normal force may be expected to be greatest, then the frictional force F_{fric} will not reach the frictional resistance P_{fric}. In this case Eq. 19.2 will overestimate the beneficial effect due to friction and lead to an unconservative analysis.

When the axle load is close to a support, then the length of the shear span L_n $\rightarrow 0$ in Eq. 19.2 so that the frictional resistance tends to infinity. Therefore, the friction resists all the shear flow in the short shear span. The mechanical shear connectors are then not loaded because they are unable to slip, and so the analysis in this situation will not be unconservative. When the axle load is near mid-span, the

vertical shear force, and hence the normal force that provides the frictional resistance in the shear spans, is at its lowest. There is, therefore, a greater probability that the friction resistance will be exceeded and so the beam is likely to gain the full benefit of the friction as defined by Eq. 19.2. The more axle loads there are on the beam, the more uniformly distributed will be the frictional forces and the more likelihood of Eq. 19.2 being correct. And finally, it would be a simple procedure to include the normal force due to the dead weight of the concrete slab resting on the steel-beam, which would not only increase the frictional resistance but would also be uniformly distributed and hence increase the probability that Eq. 19.2 is not unduly unconservative. If more accurate analyses are required, then the engineer could resort to the partial interaction analyses procedures described in Section 19.3.3 that could easily be adapted to allow for friction.

Equation 19.2 can be used to derive the effect of friction on the shear flow force envelope and an example of the analysis is shown in Fig. 19.7(c). Line A is the envelope for the applied loads as given by the first term on the right hand side of Eq. 19.2, whereas line B is the frictional resistance as given by the second term of $\mu V_n/L_n$ in Eq. 19.2. The relative positions of these lines depends on the cross-sectional properties and the coefficient of friction μ. The shaded area encompassed by both lines is the shear flow force on the connectors and therefore the upper and lower portions would have to be added to determine the reverse cyclic load. It can be seen that the greatest benefit due to friction occurs in the region adjacent to the supports and the least benefit occurs at mid-span.

(b) Longitudinally moving vehicles

The frictional resistance parameter $\mu V_n/L_n$ in Eq. 19.2 can also be plotted as an influence line diagram. In this case, we are in effect plotting the pressure distribution at the interface, that is V in Fig. 19.8. This pressure will always be compressive and hence, unlike the shear flow influence line which reverses in direction or sign when a load crosses the design point, the frictional resistance influence line diagram will be the same sign throughout the length of the beam.

The influence line diagram for the frictional resistance within the beam in Fig. 19.3(b) with the axle loads in (a) and at design point D, can be derived from the vertical shear force distributions in (c) to (i). The frictional resistance at the design point is shown on the right of each figure and is plotted in Fig. 19.9(a). When the fatigue vehicle is as shown in Fig. 19.3(e), that is the back axle is just to the left of the design point at D, then the vertical shear force at the design point is V/4. This is also the normal force across the interface of the shear span of length 3L/4 that contains the design point, and so the frictional resistance is $\mu(V/3L)$ as shown on the right hand column which is in terms of μ. When the front of the vehicle moves just to the right of position E as shown in (f), then the shear force changes in magnitude and direction at the design point but the normal force remains compressive and only changes in magnitude to 3V/4. The normal force is spread over a length L/4 and so the frictional resistance is $\mu(3V/L)$. These resistances are shown as points 1 and 2 in Fig. 19.9(a).

The influence line for the frictional resistance with the back axle only loaded is shown in Fig. 19.9(b). The influence lines in (a) and (b) can be combined as in (c) to give the resulting influence line diagram of the frictional resistances for the standard fatigue vehicle. Equation 19.2 can now be used to combine the influence line diagram for the vertical shear in Fig. 19.4(d) with the influence line diagram for the frictional resistance in Fig. 19.9(c). For example, when the front axle is just to the left of position E in Fig. 19.3(e), the vertical shear force is V/4 as shown just left of position E in Fig. 19.4(d), and the frictional resistance is $(4\mu V)/(3L)$ which is shown just to the left of position E in Fig. 19.9(c). Hence, the shear flow force in the shear connectors at the design point can be derived from q_{dowel} in Eq. 19.2. Moving the vehicle just to the right of position E will increase the vertical shear force to 5V/4 (just to the right of position E in Fig. 19.4(d)) and also increase the frictional resistance to $4\mu V/L$ (just to the right of position E in Fig. 19.9(c)).
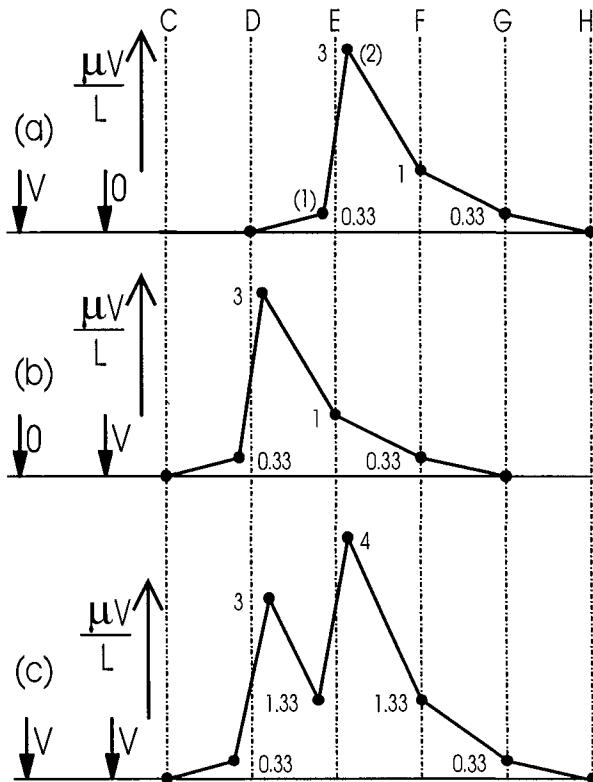
Fig. 19.9 Frictional resistance influence line diagram

19.3.3 PARTIAL INTERACTION BEHAVIOUR

19.3.3.1 *General*

The full interaction analyses described in the previous section tends to overestimate the shear flow forces in the mechanical shear connectors and underestimate the stress resultants in both the steel element and the concrete element. A more accurate estimation of the stress resultants in all three components can be obtained from computer models that allow for the static and dynamic non-linearity in the load/slip characteristics of the mechanical shear connectors (Murray 1988).

The local effects of the non-linearity of the load/slip characteristics of stud shear connectors on the behaviour of individual connectors has already been described in Section 3.4. It was shown that the non-linearity due to both the change in path and incremental set has the following effects: it redistributes the shear load in groups of connectors from weaker to stronger connectors; induces a fatigue limit in the beam; reduces the fatigue life in propped construction; and increases the fatigue life when an overload is applied. In this section, we will deal with the global effects of the non-linear behaviour of stud shear connectors, that is the effect of the non-linearity in the shear connection on the shear flow force distribution along the length of a beam.

19.3.3.2 *Computer models*

Computer models have different degrees of sophistication depending in particular on their ability to simulate the material properties. A full interaction analysis, which can be considered to be the least sophisticated of models, assumes that the shear connector stiffness is infinite as shown by the load/slip curve $K = \infty$ in Fig. 2.18. An improvement would be to assume that the connectors have a constant spring stiffness K when loaded and unloaded so that the loading and unloading paths are identical. Both of these methods are linear elastic analyses. However, the former is a full interaction analysis whereas the latter is a partial interaction analysis; a full interaction analysis being a special case of a partial interaction analysis with $K \rightarrow \infty$.

A further improvement in the computer model would be to allow for the change in path between loading and unloading as shown in Fig. 3.8. In this case, the connector would have either a uni-linear load/slip path O-C, or a bi-linear path O-B-A or a trilinear path O-B-A-C. A final improvement in the material simulation would be to allow for the incremental set that is induced by each cycle of load, as described in Section 3.4.2.4 and in Eq. 3.11, that is the lateral displacement in the load/slip path from B-A to G-F in Fig. 3.8 when a cycle of load is applied. Both of these changes cause non-linearity, as the secant stiffness of the shear connection now varies.

When the direction of span of the composite beam is perpendicular to the direction of traversal of the standard fatigue vehicle, then the composite beam in the computer model can be considered to be subjected to longitudinally stationary but cyclic loads as described in the following section. This is similar to standard fatigue tests on composite beams in the laboratory where the beam is subjected to cyclic loads at a specific point or points (Toprac 1965). When the standard fatigue vehicle moves along the length of the beam, then the computer model must be able to simulate

longitudinally moving cyclic loads and also allow for the spectrum of loads (Murray 1988) as described in Section 19.3.3.4. The following sections describe the results of computer simulations that allow for both the change in the loading path and the incremental set.

19.3.3.3 *Longitudinally stationary cyclic loads*

In order to gain a qualitative understanding of the fatigue behaviour, let us consider a simply supported composite beam, with a uniform distribution of stud shear connectors along its span and in which the cyclic load is applied at mid-span.

(a) Minimum of applied cyclic load is zero

The beam is subjected to an applied cyclic load in which the minimum of the applied cyclic load F_m is zero. This is equivalent to unpropped construction where the steel beam resists the dead load and where the composite action, and hence the mechanical shear connectors, only resists the live cyclic load. The results of a computer simulation are shown in Fig. 19.10 (Oehlers and Singleton 1986) where F_p is the shear load on the shear connectors at the peak of the applied cyclic load. In this case F_p is also equal to the range of load as the minimum of the cyclic load $F_m = 0$. The endurance E_{beam} in Fig. 19.10 is the number of cycles for the first connector to fail and N is the number of applied cycles.
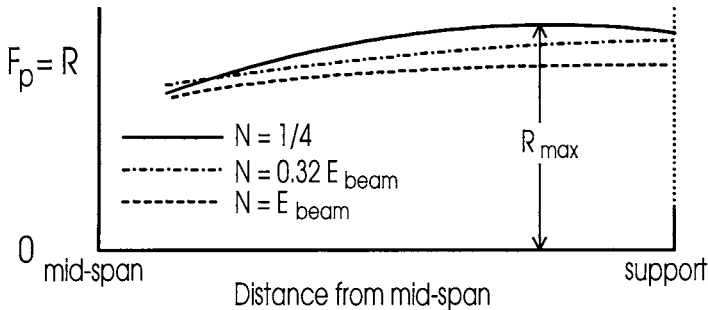
Fig. 19.10 Peak of shear flow at stages of design life

The distribution of the shear flow forces at different stages N of the beam endurance E_{beam} is shown in Fig. 19.10. The distribution of the shear flow ranges when the cyclic load is first applied is shown as line N = 1/4 as a quarter of a cycle has been applied. Inserting the maximum of these cyclic ranges R_{max} into the connector endurance Eq. 3.12 would give the fatigue life of the beam if the distribution of the shear flow did not change with time or number of cycles. However, the fatigue set induced by cyclic loading, given by Eq. 3.11, reduces the shear connector stiffnesses and hence reduces the total longitudinal shear force on the connectors, so that the mean range of load on the connectors also reduces. As the fatigue set is proportional to R^{m_a}, as shown in Eq. 3.11 where $m_a \approx 5$, heavily loaded connectors near the supports will attract a greater set at an early stage and shed their loads to lightly loaded connectors near mid-span. This redistribution makes the shear flow more uniform and

may also increase the shear loads on the connectors near mid-span as shown by the distribution at $N = 0.32E_{beam}$. The overall effect of the incremental set induced by fatigue loading is to reduce the range of loads on the shear connectors and make the distribution more uniform as at $N = E_{beam}$. Both of these effects will reduce the probability of failure.

Figure 19.11 shows the variation of the log of the endurance of the beam E_{beam} with the log of the range of the cyclic load R_{max}, where R_{max} is the maximum range when first loaded as shown in Fig. 19.10. Figure 19.11 is analogous to the E-R curves for the experimentally determined endurance of shear connectors, as shown in Fig. 3.3 and Eq. 3.12 which are a fatigue material property of the shear connectors. However, in this case we are dealing with the endurance of the beam which depends on the redistribution between shear connectors. The variation of the beam endurance that is derived from the shear flow forces when first loaded is shown as line $N = 1/4$ in Fig. 19.11; the variation in the endurance is linear as the incremental set does not affect the shear flow on first loading. When incremental set is allowed for in the computer model, then the endurance of the beam increases as shown by line $F_m = 0$. However, the slope of the line increases suggesting that the beam is more susceptible to fatigue damage from higher loads as will be explained in Section 19.4.4.

$\log_{10} E_{beam}$

$\log_{10} R_{max}$

$N = 1/4$
$F_m = 0$ unpropped
$F_m = 0.1F_p$ propped
$F_m = 0$ and initial overload
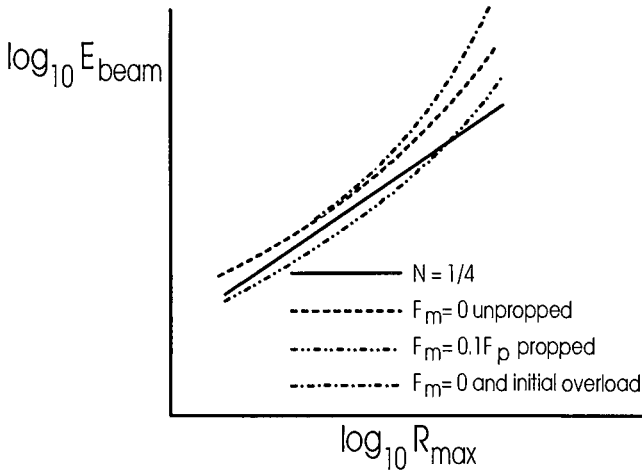
Fig. 19.11 Fatigue life of composite beam

(b) Minimum of cyclic load greater than zero and overloads

When the minimum of the applied cyclic load $F_m \neq 0$, then this is equivalent to propped construction where the composite action resists both the dead and live loads. The endurance of the beam when the minimum of the cyclic load $F_m = 0.1F_p$ is shown in Fig. 19.11, and in most cases it is less than that anticipated from a linear partial interaction analysis as given by line $N = 1/4$. Furthermore, the application of an initial overload will increase the endurance of the beam as given by line $'F_m = 0$ and initial overload'. The former reduction in strength and the latter increase in strength is due

to the change in the load-slip path and the mechanism by which it occurs is explained in Section 3.4.2.

19.3.3.4 *Longitudinally moving cyclic loads*

In order to illustrate the effect of longitudinally moving loads on composite beams, a computer model of a 12 m simply supported beam with a uniform distribution of 19 mm stud shear connectors was subjected to a longitudinally moving load (Oehlers and Carroll 1987). The stiffness and number of connectors were such that when the load was applied at mid-span, the total force in the connectors from the linear partial interaction analysis was 85% of that from the linear full interaction analysis. The distributions of the shear flow force envelopes are shown in Fig. 19.12 where F_p is the maximum force on the connector and D_{max} is the static strength of the shear connector.

The shear flow envelope for the linear full interaction analysis shown in Fig. 19.12 has the familiar shape of parallel sides with a constant reverse range and varying peak load, that is lines A are more or less parallel and their vertical separation is virtually the same throughout the length of the beam. This distribution would induce uniform fatigue damage throughout the length of the beam. However, it is worth noting that the connectors at the supports would not be able to sustain as much fatigue damage as those at mid-span because of the larger maximum shear forces F_p at the supports.
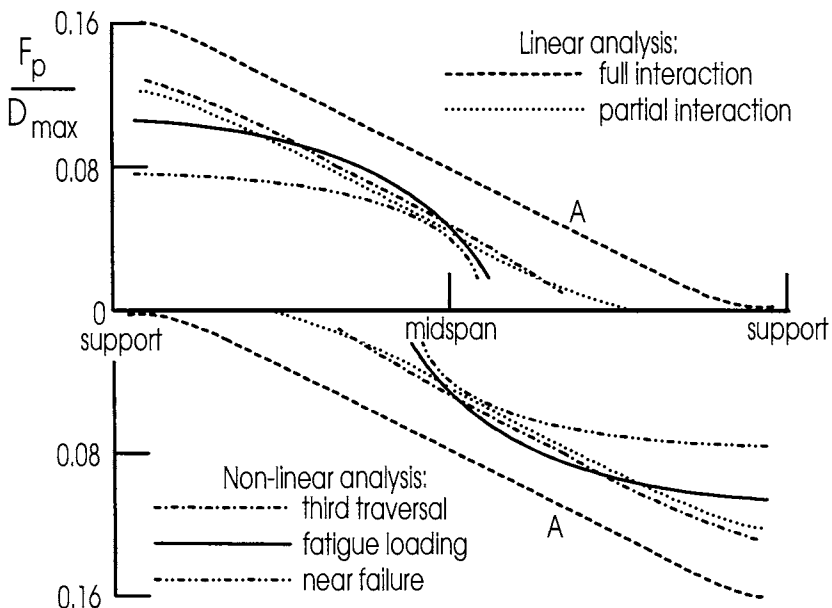
Fig. 19.12 Shear envelope 12 m beam

Allowing the connectors in the full interaction analysis to slip but to remain linear elastic would give the linear partial interaction envelope shown in Fig. 19.12. Hence, slip produces a fairly constant reduction in the shear flow envelope as can be seen by the vertical separation between the full and partial linear analyses. In the linear partial interaction analysis, the range of the shear flow near mid-span is still constant and reverse as occurred in the linear full interaction analysis, but as the supports are approached the range becomes uni-directional and increases to its largest value at the supports. This would suggest that the supports are susceptible to fatigue failure because the rate of fatigue damage would be greatest at the supports (as this depends on the range) and because the fatigue damage that can be sustained would be the smallest at the supports (as this depends on the peak load).

As soon as the traffic load starts to traverse the beam, the connectors follow a bi- or tri-linear load-slip path and never behave as in a linear partial interaction analysis where the connector stiffnesses are assumed to be constant. This change in the load-slip path of the connectors as the fatigue vehicle traverses the beam, leads to a variation along the beam of the connector stiffnesses. This stiffness variation causes local increases in the shear flow, and hence an overall increase in the shear flow envelope as shown by the 'third traversal' in the non-linear analysis in Fig. 19.12.

The mechanism by which the shear flow envelope increases throughout the span during the first few traversals of the fatigue vehicle can be understood by comparing the behaviour of a connector near the support with the behaviour of a connector further from the support. It can be seen in Fig. 19.2(a) that the largest shear flow force of magnitude q_V exist at the supports and that the shear flow forces reduce to a minimum value of $q_V/2$ at mid-span. Therefore, the connectors near the supports will be subjected to a larger slip than the connectors further from the support. Let us assume that the connectors near the supports follow the path O-A in Fig. 19.13 and then unload along A-B. The connectors further from the support will be subjected to a lower shear flow force, and hence will follow the path O-C in Fig. 19.13 and then unload along C-D. After the first traversal, the secant stiffness of the connector near the support is less than that of the connector further from the support because the permanent set O-B is greater than the permanent set O-D as shown in Fig. 19.13. For example, it can be seen at the shear force F in Fig. 19.13 that the secant stiffness of the connector further from the support is greater than that of the connector near the support. Therefore, in the next traversal and when both connectors in Fig. 19.13 lie in the same shear span, the connectors near the support will attract less load than anticipated and those further from the support, and which are nearer to the point of application of the load, will attract more load. It is this local increase in shear load due to the change in path that increases the shear flow envelope during the initial traversals as shown in Fig. 19.12.

Fatigue loading then causes, through the incremental set described in Section 3.4.2.4(a), an overall reduction in the total shear force as shown by the line marked 'fatigue loading' in Fig. 19.12. However, redistribution to lightly loaded connectors may cause a local increase in the shear force envelope above that of the linear partial interaction analysis. It can be seen that the range of cyclic loading is now predominantly uni-directional with a very small amount of reverse cyclic loading near mid-span.
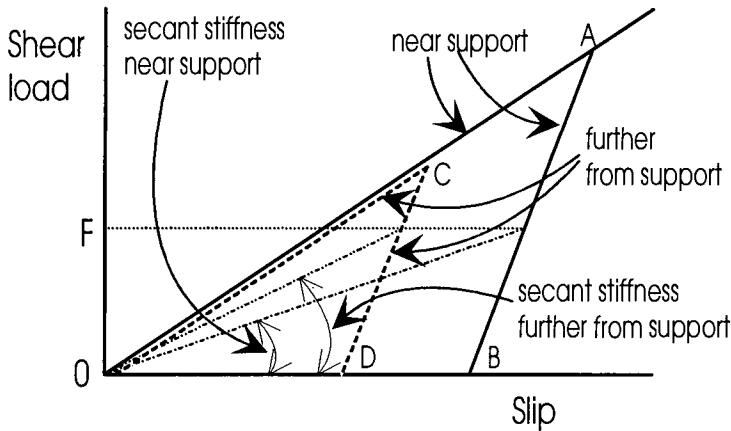
Fig. 19.13 Load-slip paths

It is to be expected that the properties of a composite beam will change substantially during the initial stages of its design life due to the effects of creep and shrinkage, and this phenomenon also occurs in other forms of construction and in particular reinforced concrete beams. However, it can be seen in Fig. 19.12 that the stress resultants in a composite beam are continually changing during the whole of its design life due to the gradual increase in the incremental set and this behaviour is unique to composite beams.

The non-linear partial interaction behaviour depends to a large extent on the ratio of the span of the beam to the diameter of the shear connector. Increasing the length of the 12 m beam to 48 m without changing the number of connectors increased the ratio of the partial to full interaction shear forces from 85% to 95%. Therefore, the difference between the shear flow envelopes for a linear full and a linear partial interaction analysis was quite small as shown in Fig. 19.14. The simulations of longitudinally moving traffic loads showed that the shear envelope after the third traversal was very close to that of the linear full interaction analysis, and further fatigue loadings caused the shear force in some connectors to exceed that derived from a full interaction analysis.

19.3.3.5 *Reduction in endurance due to propped construction*

It was shown in Section 19.3.3.3(b) and illustrated in Fig. 19.11 that propped construction can reduce the endurance of the shear connections in a beam by increasing the range of the cyclic load on the shear connection. This reduction in endurance is due to the change in path of the load-slip curve of the connection during cyclic loading, as explained in Section 3.4.2.1 and illustrated in Fig. 3.8.

Consider a design point in a linear elastic composite beam with partial interaction. When a load W is applied to the beam, the connections at the design point will slip s. The W-s response will be linear as shown in Fig. 19.15 for 'partial interaction' because, as stated previously, we are dealing with linear elastic behaviour.

When the composite beam is first loaded, the connections will slip along a path such as O-A in Fig. 3.8 of constant stiffness K_{si}. The partial-interaction W-s response in Fig. 19.15, shown at an angle α, can thus be derived either from computer simulations or from the partial interaction theory described in Section. 6.3 using a connection stiffness of K_{si}. When the applied load W is removed from the beam, the connectors will follow a path such as A-B-O in Fig. 3.8. When the slip is less than B, the shear connectors will be unloaded and thus they will have zero stiffness and we will be dealing with a case of zero interaction. This is shown as the W-s zero-interaction response at an angle β in Fig. 19.15, that can also be derived from computer simulations or linear elastic theory.
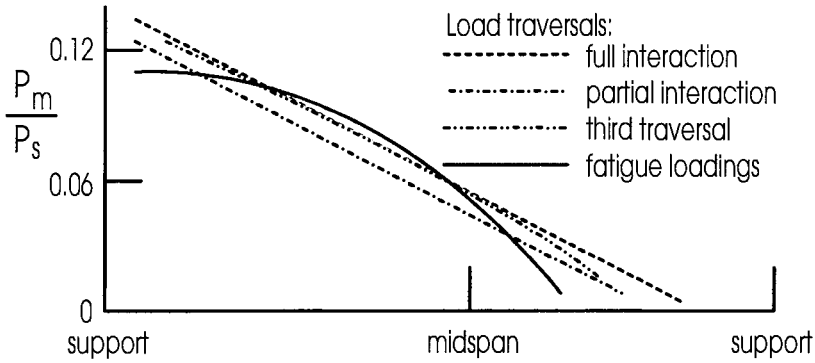
Fig. 19.14 Shear envelope 48 m beam
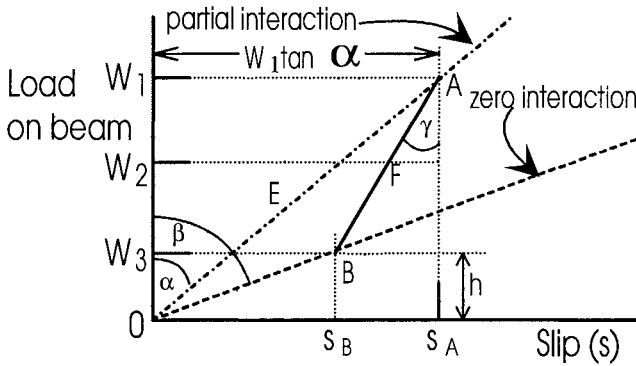
Fig. 19.15 Propped construction

Let us now consider the behaviour of the beam at the design point when first loaded. The beam follows the path O-E-A in Fig. 19.15 where $s \propto W$. Furthermore, as we are assuming that the connection stiffness is constant at K_{si}, the force on the connector $F \propto s$. Therefore, the force on the connector F is directly proportional to the load applied to the beam W so that $F = \lambda W$ where λ is the constant of proportionality. If W_2 is the minimum of the cyclic load that is applied to the beam,

the force on the connector at this beam load is λW_2, and if W_1 is the maximum of the cyclic beam load then the force on the connector is λW_1. Hence the range of load that is applied to the connector on first loading is given by

$$R_{linear} \quad = \quad \lambda\left(W_1 - W_2\right) \tag{19.3}$$

and this would be the range if the connector stayed on the path 0-A in Fig. 3.8 or was assumed in the analysis to stay on this path as in a linear partial interaction analysis.

On unloading the beam at A in Fig. 19.15, the force on the connector falls to zero at B, where there is zero interaction, and stays at zero force along O-B. On re-loading, the beam follows the path O-B-A. Points B and A can be determined as will be illustrated in the following example with stud shear connectors, however, we will assume a linear interpolation between these known points as shown. At B the force on the connector is zero and at A the force is λW_1. Therefore, the range of load on the connector when a range of load of W_1-W_2 is applied to the beam is given by

$$R_{non-linear} \quad = \quad \frac{AF}{AB}\left(\lambda W_1\right) \quad = \quad \frac{W_1 - W_2}{W_1 - h}\left(\lambda W_1\right) \tag{19.4}$$

where $h = W_1\left(\tan\alpha - \tan\gamma\right)/\left(\tan\beta - \tan\gamma\right)$ and the angle γ is shown in Fig. 19.15. Thus from Eqs. 19.3 and 19.4, the magnification of the range of load M due to propped construction is given by

$$M \quad = \quad \frac{R_{non-linear}}{R_{linear}} \quad = \quad \frac{1}{1 - \dfrac{h}{W_1}} \quad = \quad \frac{\tan\beta - \tan\gamma}{\tan\beta - \tan\alpha} \tag{19.5}$$

This magnification factor is correct when the minimum of the cyclic applied load W_2 in Fig. 19.15 is greater than the applied load W_3 that is required to cause the connectors to reload at point B after cyclic loading. When $W_2 = 0$ the cyclic range is the same on both paths 0-E-A and 0-B-A which is the case for unpropped construction.

The only unknown in Eq. 19.5 is the angle γ which is a function of the unloading path of the connector, that is A-B in Fig. 3.8. It was shown in Section 2.4.6.2 for stud shear connectors, that the unloading stiffness K_{tc} in Fig. 3.8 is $2.8K_{si}$. Hence if s_A is the slip at A and s_B is the slip at B then $s_B = 0.643s_A$. These values are shown in Fig. 19.15 and hence define γ and therefore the magnification factor M in Eq. 19.5, which for stud shear connectors comes to

$$M_{stud} \quad = \quad \frac{1}{1 - 0.643\dfrac{\tan\alpha}{\tan\beta}} \tag{19.6}$$

where α and β is defined in Fig. 19.15 and can be determined from linear elastic analyses of the composite beam.

19.3.4 FORCE SPECTRUM

The non-linear computer models described in the previous section are capable of simulating a composite beam throughout its whole fatigue life and for all variations in load, and hence are ideal for assessment purposes (Murray 1988).

In general, the linear full interaction and linear partial interaction models will give a conservative design or assessment of the shear connectors, that is they will overestimate the forces. A convenient method for categorising the stress resultants in linear analyses is the *force spectrum* shown in Table 3. Column 2 lists the magnitude of the ranges of the cyclic stress resultants R that are induced by a single traversal of the standard fatigue vehicle. Whereas column 3 lists the frequencies of these ranges f, that is the number of times a magnitude of range of the stress resultant occurs during a single traversal of the standard fatigue vehicle. Hence, the *force spectrum* lists the frequency and magnitude of the ranges of cyclic stress resultants that occur at a design point when the standard fatigue vehicle moves across the bridge. In contrast to the *load spectrum* in Section 19.2.2.3 that lists the probabilities of occurrence and the weights of the fatigue vehicles.

Table 3 Format of force spectrum

Level (k)	Range (R)	frequency (f)	f R^m
(1)	(2)	(3)	(4)
1	R_1	f_1	$f_1 R_1{}^m$
2	R_2	f_2	$f_2 R_2{}^m$
Z-1	R_{Z-1}	f_{Z-1}	$f_{Z-1} R_{Z-1}{}^m$
Z	R_Z	f_Z	$f_Z R_Z{}^m$
			$F_f = \sum fR^m$

Example 19.4. Force spectrum with and without frictional resistance

A standard fatigue vehicle consisting of two axles is moved across a simply supported beam as shown in Fig. 19.3(a). It is required to determine the force spectrum with and without the beneficial effects of the frictional resistance and at a design point that is at a quarter span from a support. The load imposed by an axle of the standard fatigue vehicle $V = 180$ kN and the longitudinal spacing of the axles is 8 m. The cross-sectional properties of the composite beam are such that in Eq. 19.2 $A_{conc}\, \bar{y}/\, I_{nc} = K = 0.5 \times 10^{-3}$ mm^{-1}. The span of the beam is 32 m and the coefficient of friction between the steel element and the concrete element is $\mu = 0.7$. As the axle spacing of the standard fatigue vehicle is a quarter of the span of the beam and as the design point is at a quarter span, the analyses given in Figs. 19.3 and 19.4 on shear flow forces and those in Fig. 19.9 on frictional shear flow resistances apply directly to this problem. The results of these analyses are summarised in Table 4.

The vertical shear forces at the design point induced by the traversal of a standard fatigue vehicle have already been derived in Fig. 19.4(d). Multiplying these vertical shear forces by $K = A_{conc} \bar{y} / I_{nc}$ gives the shear flow force at the design point which is listed as q_{flow} in row 1 in Table 4 and which is given in terms of KV. Substituting the beam property $K = 0.5 \times 10^{-3}$ gives the shear flow forces in row 2. These shear flow forces would also be the shear flow forces on the connectors when the frictional resistance is zero or ignored in the analysis, which is usually the case when designing new structures. Using the reservoir method of cyclic counting, that is illustrated in Fig. 19.5(a), for the shear flow forces in row 2 of Table 4 gives two ranges of cyclic load of 135 N/mm and 45 N/mm, each of which occurs once during a single traversal of the standard fatigue vehicle. Therefore, in terms of the force spectrum in Table 3: $R_1 = 135$ N/mm and $f_1 = 1$; and $R_2 = 45$ N/mm and $f_2 = 1$.

The frictional shear flow resistance is given by the term $\mu V_n / L_n$ in Eq. 19.2 and these resistances have already been derived in Fig. 19.9(c) and are listed as Q_{fric} in row 3 in Table 4. Substituting the actual values for μ, V and L gives the frictional shear flow resistance in row 4. Unlike shear flow forces, the frictional shear flow resistances do not depend on the direction of the vertical shear forces at the design point, but only on the normal force across the steel/concrete interface, which in this example always remains compressive and hence has been shown as positive throughout row 4. The frictional shear flow resistance in row 4 resists the shear flow forces in row 2, no matter what the direction or sign of the shear flow forces. Hence, the modulus of row 4 must be subtracted from the modulus of row 2 to obtain the shear flow force resisted by the mechanical shear connectors q_{dowel} in row 5. The shear flow force q_{dowel} in row 5 must have the same sign as q_{flow} in row 2. However, q_{dowel} can reduce in magnitude to zero when $|Q_{fric}| \geq |q_{flow}|$. The results in row 5 can be used to plot an influence line diagram from which the cyclic ranges can be derived from the reservoir method, giving the following force spectrum that incorporates the beneficial effect of friction: $R_1 = 118$ N/mm and $f_1 = 1$; and $R_2 = 39$ N/mm and $f_2 = 1$. These results can then be used to assess the performance of an existing composite bridge beam.

Table 4 Influence lines at quarter-span

	Design point	C	D		E		F		G		H
(1)	q_{flow} (KV) (q_{dowel} without friction)	0	+0.25	-0.75	-0.25	-1.25	-0.75	-0.75	-0.25	-0.25	0
(2)	q_{flow} (N/mm)	0	+22.5	-67.5	-22.5	-113	-67.5	-67.5	-22.5	-22.5	0
(3)	Q_{fric} (μV/L)	0	0.33	3	1.33	4	1.33	1.33	0.33	0.33	0
(4)	Q_{fric} (N/mm)	0	1.3	11.8	5.3	15.8	5.3	5.3	1.3	1.3	0
(5)	q_{dowel} N/mm (with friction)	0	+21.2	-55.7	-17.2	-96.7	-62.2	-62.2	-21.2	-21.2	0

19.4   Fatigue analysis

19.4.1   GENERAL

Most fatigue procedures are based on the endurance of a structure, that is the fatigue procedure ensures that the structure can withstand cyclic serviceability loads during its design life. Therefore, these existing fatigue procedures use accumulated used-life laws as described in Section 3.2.3. These laws which are shown in Eq. 3.3, only consider the number of cycles of the serviceability load to failure E_e and the number of cycles that have occurred N and hence ignore the strength of the structure during its design life. However, the primary aim of an engineer is to ensure that the strength of a structure is sufficient during its design life to resist the occasional overload, that is the reduction in strength due to fatigue cyclic serviceability loads does not prevent the occasional design overload from being resisted. There would, therefore, appear to be a contradiction between the function of existing fatigue procedures and the requirements of engineers.

The fatigue analysis that is developed in this section is based on the variation of the strength of a structure that is subjected to fatigue loads, that is the residual strength envelope. However, it will be shown that the standard endurance based fatigue procedures are a special case of residual strength based endurance procedures. Residual strength envelopes are first defined and then these are used to develop a general fatigue equation for analysis that determines the distribution of fatigue damage; fatigue damage being now defined as the reduction in the strength of the component due to cyclic loading. The general fatigue analysis equation is then applied in both a design mode for new structures and an assessment mode for existing structures.

19.4.2   LINEAR RESIDUAL STRENGTH ENVELOPES

19.4.2.1 *Varying strength accumulated damage laws*

As discussed in Section 3.3.3, all residual strength envelopes or failure envelopes, such as those shown in Fig. 3.4, can be idealised as a set of linear failure envelopes as shown in Fig. 3.5. Let us consider the Stage 2 residual strength envelope shown in Fig. 3.5 where the strength reduces linearly with the number of cycles or load applications. Equation 3.4 defines the Stage 2 residual strength envelope where N_b is the number of applications of a range of cyclic load that has an asymptotic endurance E_a and P_c is the residual strength of a component with an initial strength prior to cyclic loading of P_{prop}.

The linear residual strength failure envelope of Eq. 3.4 can be rearranged into the following accumulated damage law.

$$\sum \frac{N_b}{E_a} \;=\; 1 - \frac{P_c}{P_{prop}} \tag{19.7}$$

Therefore, an accumulated damage law is simply a residual strength envelope. Furthermore, it can be seen that the accumulated damage law of Eq. 19.7 is based on

the reduction in strength and so the term *fatigue damage* now applies to the reduction in strength due to fatigue loads.

19.4.2.2 *Constant strength accumulated damage laws*

When $P_{prop} \rightarrow \infty$ in Fig. 3.5, the failure envelope tends to the vertical so that we are now dealing with the Stage 3 failure envelope which is shown. As this failure envelope is vertical, the points E_a, E_r and E_e in Fig. 3.5 coincide, and furthermore as the failure envelope is still linear Eq. 19.7 still applies. Substituting $P_{prop} \rightarrow \infty$ and $E_a = E_e$ into Eq. 19.7 gives the following Stage 3 accumulated damage law.

$$\sum \frac{N_b}{E_e} = 1 \qquad\qquad (19.8)$$

where E_e is the experimentally derived endurance.

Equation 19.8 is Miner's accumulated damage law (1945) that is used in most standard fatigue procedures. Miner based his law on the summation of endurances, however it can be seen that this law is a special but extreme case of an accumulated damage law that is based on a linear residual strength envelope.

19.4.2.3 *Linear accumulated damage laws*

Accumulated damage laws that are based on linear failure envelopes are a convenient mathematical model as they can easily cope with fatigue damage due to variable loads and due to variable sequences of loadings. For example, consider the linear failure envelope marked A in Fig. 19.16 which is the failure envelope for a components subjected to a constant range of cyclic load R_1. It can be seen that applying one cycle of load of range R_1 after a block of N_1 cycles causes the same reduction in strength ΔP_c as applying one cycle of load after a block of N_2 cycles. Hence the fatigue damage, that is the reduction in strength per cycle, is the same throughout the fatigue life $(E_a)_1$.

Let us assume that when the range of the cyclic load is reduced from R_1 to R_2, then the asymptotic endurance increases from $(E_a)_1$ to $(E_a)_2$ in Fig. 19.16. Therefore, the same component has the linear failure envelope marked A when the range is R_1 and the linear failure envelope marked B when the range is R_2. It can be seen in Fig. 19.16 that if N_3 cycles at range R_1 are applied then the reduction in strength is $(\Delta P_c)_3$, or alternatively if N_4 cycles at range R_2 are applied then the reduction in strength would be $(\Delta P_c)_4$. If N_3 at R_1 cycles are first applied, then the strength reduces to $P_{prop}-(\Delta P_c)_3$ which is point C; if N_4 cycles at R_2 are then applied, the strength reduces to $P_{prop}-$ $(\Delta P_c)_3-(\Delta P_c)_4$ which is point D. Alternatively if N_4 cycles of range R_2 are applied first, then the strength reduces to point E and then the application of N_3 cycles at R_1 would also reduce the strength to point D.

It can, therefore, be seen from the previous paragraph that when uni-linear failure envelopes are used as in A and B in Fig. 19.16, the sequence of loading does not affect the fatigue damage, which would not be true if for instance a quadratic failure envelopes were used (Ghosh 1995). An alternative way of visualising this

problem is to plot non-dimensionally the abscissa in Fig. 19.16 in terms of the of the asymptotic endurance E_a. Then the failure envelopes A and B will coincide, that is the same linear failure envelope will apply for all ranges on the component. Therefore, a single non-dimensional uni-linear failure envelope can be used to describe the variation of the fatigue damage for all ranges of cyclic loads on a component. Hence, the combination of loads and the sequence of fatigue cyclic loads will not affect the fatigue damage.
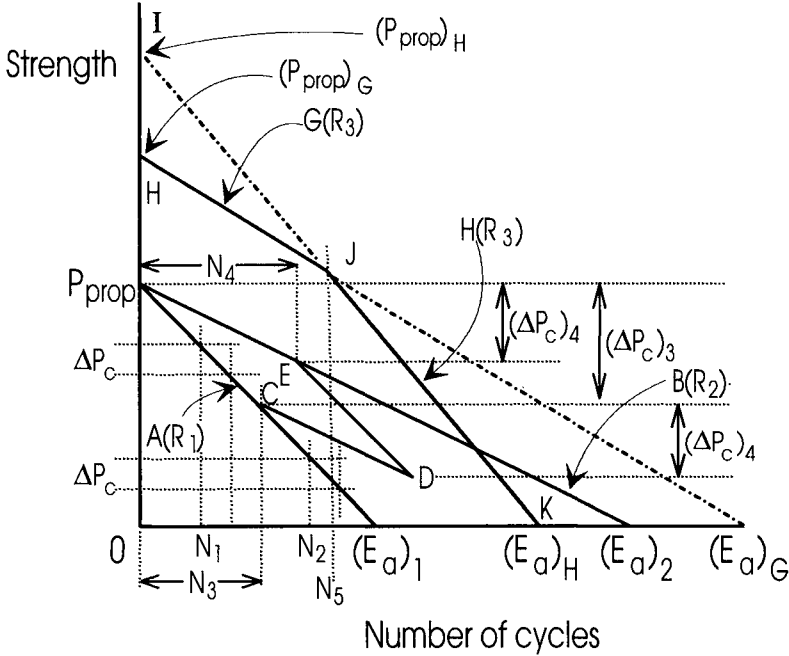
Fig. 19.16 Linearisation and sequence of loading

Let us consider the case when a bi-linear failure envelope is required to simulate the real failure envelope as shown by the failure envelope consisting of the parts G and H in Fig. 19.16. The uni-linear failure envelope G, that is defined by $(P_{prop})_G$ and $(E_a)_G$, can be used to quantify the fatigue damage until the strength has reduced to point J at the intersection of the uni-linear regions. When the strength is less than that at point J, then the uni-linear failure envelope H, that is defined by $(P_{prop})_H$ and $(E_a)_H$, can be used to predict the fatigue damage. Hence, the sequence of loading does not affect the analysis within a uni-linear region of the failure envelope but it does affect the analysis when going from one uni-linear region to another.

19.4.3 GENERAL ANALYSIS FATIGUE EQUATION

19.4.3.1 *Fatigue material properties*

In order to derive a general analysis fatigue equation, we will use the following generic form of the accumulated damage laws of Eqs. 19.7 and 19.8

$$\sum \frac{N}{E} \;=\; A \tag{19.9}$$

Therefore, the variable A is either equal to $1-P_c/P_{prop}$ which represents a variation in the residual strength or $A = 1$ which represents a constant residual strength during the design life. Furthermore, the endurance E is either equal to the asymptotic endurance E_a or the experimental endurance E_e.

We will also use the following generic form of the endurance Eqs. 3.2 and 3.7

$$E \;=\; C\left(\frac{R}{X}\right)^{-m} \tag{19.10}$$

where the constant of the endurance equation C is either equal to $10^{H_e-2D_e}$ or $10^{H_a-2D_a}$ and the exponent m is either equal to m_a or m_e depending on whether we are dealing with the asymptotic endurance or the directly derived experimental endurance.

It is convenient in fatigue assessment and design to state the range of the stress resultant R as a proportion of a parameter X as shown in Eq. 19.10. For example, the endurance of stud shear connectors in Eq. 3.14 is a function of the range of load on a connector R as a proportion of the static strength of the shear connector prior to fatigue loading D_{max}, so that for stud shear connectors $X = D_{max}$ in Eq. 19.10. As a further example, the endurance of fillet welds is often assumed to be dependent on the shear stress τ, so that the endurance equation for the weld would take the form of Eq. 19.10 but with $R = \tau$ and $X = 1$, and this form is convenient for the assessment of existing welds. However in the design of new fillet welds, it is easier to work in terms of the shear flow force q acting over a transverse length of weld L, so that q/L can be used to replace R/X in Eq. 19.10 when designing new welds.

19.4.3.2 *Stress resultants*

In order to illustrate the development of the general analysis fatigue equation, let us make the following simple assumptions. The composite beam is subjected to a total of T traversals of fatigue vehicles and that the fatigue vehicles can be represented by the geometry of one standard fatigue vehicle. The traversal of the standard fatigue vehicle produces two ranges of the stress resultant of magnitude R_1 at a frequency of f_1 and R_2 at f_2, so that we are dealing with the first two levels of the force spectrum in Table 3. There are only two weights of fatigue vehicles, so that we are dealing with only the first two levels of the load spectrum in Table 1, such that in column 3 the probabilities $B_1 + B_2 = 1$ and the weights of the fatigue vehicles in column 2 are either W_1 or W_2 times the weight of the standard fatigue vehicle.

In this very simple example, we are dealing with four ranges of the stress resultants that are W_1R_1, W_1R_2, W_2R_1 and W_2R_2. Furthermore, the total number of times these stress resultants that occur during the T traversals of the fatigue vehicles is B_1Tf_1, B_1Tf_2, B_2Tf_1 and B_2Tf_2 which are listed in the same sequence as the former list

of stress resultants; for example, the stress resultant W_1R_1 occurs B_1Tf_1 times and W_1R_2 occurs B_1Tf_2 times.

19.4.3.3 *Fatigue damage*

Let us consider the fatigue damage due to the cyclic range W_1R_1. The range in terms of the parameter X is W_1R_1/X. Substituting this range into Eq. 19.10 gives the endurance

$$E_{first} \ = \ CW_1^{-m}R_1^{-m}X^m \tag{19.11}$$

where E_{first} is the fatigue endurance for the first of the cyclic ranges W_1R_1.

The number of cycles of the first range W_1R_1 has been shown to be $N_{first} = B_1Tf_1$. Substituting N_{first} and E_{first} into the accumulated damage law of Eq. 19.9 gives

$$A_{first} \ = \ C^{-1}\left(B_1W_1^m\right)\left(f_1R_1^m\right)TX^{-m} \tag{19.12}$$

where A_{first} is the fatigue damage due do the first of the cyclic ranges W_1R_1.

The procedure described previously can be repeated for the remaining three cyclic ranges of W_1R_2, W_2R_1 and W_2R_2 to give the following fatigue damage terms.

$$A_{second} \ = \ C^{-1}\left(B_1W_1^m\right)\left(f_2R_2^m\right)TX^{-m} \tag{19.13}$$

$$A_{third} \ = \ C^{-1}\left(B_2W_2^m\right)\left(f_1R_1^m\right)TX^{-m} \tag{19.14}$$

$$A_{fourth} \ = \ C^{-1}\left(B_2W_2^m\right)\left(f_2R_2^m\right)TX^{-m} \tag{19.15}$$

Summing the fatigue damage in Eqs. 19.12 to 19.15, for all four ranges of cyclic load, gives the analysis fatigue equation for this simple problem as

$$A \ = \ T\left(B_1W_1^m + B_2W_2^m\right)\left(f_1R_1^m + f_2R_2^m\right)X^{-m}C^{-1} \tag{19.16}$$

where A is the total fatigue damage.

19.4.3.4 *General analysis fatigue equation*

The parameter $\left(B_1W_1^m + B_2W_2^m\right)$ in Eq. 19.16 can be obtained from the first two levels of the load spectrum in Table 1, as shown in the first two levels of column 4; bearing in mind that $B_1 + B_2 = 1$ in column 3 because in this analysis there are only two levels. This fatigue parameter will be referred to as the *load constant* and will be denoted by the symbol L_f. The load constant L_f can be derived from the following equation

$$L_f \ = \ \sum_{x=1}^{x=i}\left(B_xW_x^m\right) \tag{19.17}$$

when there are i levels in the load spectrum as shown in Table 1. The derivation of L_f is also shown in column 4 of Table 1.

The fatigue parameter $\left(f_1 R_1^m + f_2 R_2^m\right)$ in Eq. 19.16 will be referred to as the *force constant* F_f and can be obtained from the first two levels of the force spectrum in Table 3, as shown in the first two levels of column 4. The fatigue parameter can be derived from the equation

$$F_f \;=\; \sum_{k=1}^{k=z}\left(f_k R_k^m\right) \tag{19.18}$$

when there are z levels in the force spectrum as in column 1 in Table 1.

Substituting L_f and F_f into Eq. 19.16 gives the following general analysis fatigue equation.

$$X^{-m} \;=\; \frac{AC}{\displaystyle\sum_{y=1}^{y=j}\left(TF_f L_f\right)_y} \;=\; \frac{AC}{T_1\left(F_f\right)_1\left(L_f\right)_1 + T_2\left(F_f\right)_2\left(L_f\right)_2 \ldots\ldots + T_j\left(F_f\right)_j\left(L_f\right)_j} \tag{19.19}$$

The parameter TFL quantifies the fatigue damage that the component is subjected to. For convenience in the fatigue analysis, we will define a *fatigue zone* as a period of T_y traversals of fatigue vehicles during which both F_f and L_f are constant. As the analysis is based on a linear failure envelope, the sequence at which the *fatigue zones* occur does not affect the overall damage as explained in Section 19.4.2.3, so that the fatigue damage due to each *fatigue zone* can be summed as shown in Eq. 19.19 where there are j zones.

19.4.4 FATIGUE DAMAGE PARAMETER

19.4.4.1 *Distribution of fatigue damage*

(a) Fatigue vehicle traversals T

The fatigue damage parameter $TF_f L_f$ in Eq. 19.19 can be used to distinguish the circumstances that have a significant contribution to the fatigue damage. It is fairly obvious from Eq. 19.19 that the fatigue damage is directly proportional to the number of fatigue vehicle traversals T, so that doubling the number of fatigue vehicle traversals will simple double the amount of fatigue damage.

(b) Load constant L_f

The load constant L_f in Eq. 19.17 is derived by summing the values of the local load constants $(BW^m)_x$ at each level x of the load spectrum, as shown in column 4 of Table 1. Therefore, the percentage contribution to the fatigue damage of each level can be

derived by dividing the local load constant $(BW^m)_x$ at each level by the sum of all the local load constants, that is the total load constant L_f.

Example 19.5. Distribution of fatigue damage within a load spectrum

The load spectrum in columns 2 and 3 of Table 2 is an example of a load spectrum for a freeway or highway. It is worth noting that the probability of occurrence B in column 3 can increase by four orders of magnitude from level 1 to level 6, whereas the proportional weight of the vehicle W in column 2 only increases by one order of magnitude and in the reverse direction from level 6 to level 1. However because the fatigue damage is proportional to BW^m, it is not obvious from columns 2 and 3 at which level most of the fatigue damage occurs. Derivation of the total load constant L_f and the local load constants $(BW^m)_x$ at each level for four different values of the fatigue exponent m are shown in columns 4 to 7.

Let us start with welded steel components in which the fatigue exponent m = 3. The distribution of the local load constants is listed in column 4 and sums to L_f = 0.274. The local load constants $(BW^m)_x$ are listed as a proportion of L_f in column 4a. It can be seen in column 4a that the greatest contribution to fatigue damage of 51% occurs at level 4 where the weight of the fatigue vehicle is equal to that of the standard fatigue vehicle, that is W = 1.0 in column 2. Furthermore levels 3 to 5, where W ranges from 2.0 to 0.5 and where $\sum B$ at these levels is 0.4, contribute 91% of the fatigue damage. It can, therefore, be seen that welded components in bridge structures are susceptible to fatigue damage from frequent but relatively light commercial vehicles. It is worth noting that at level 6, where W = 0.2 and which is equivalent to a six tonne commercial vehicle, the contribution to the fatigue damage is very small at 2% even though the probability of occurrence B is very high at 60%. It is also worth noting that if a weight restriction is placed on the bridge that prevents level 1 and 2 vehicles from crossing, then this would only reduce the fatigue damage by 2% + 5% = 7% which would only increase the fatigue life by a factor of $(1-0.07)^{-1} = 1.08$ which is hardly worth implementing.

In column 5 in Table 2, the fatigue exponent m = 4 which is applicable to non-welded steel components. The greatest contribution to the fatigue damage now occurs at a higher level at level 3. Levels 2 to 4, where W ranges from 1.0 to 5.0 and where $\sum B$ is 0.15, contribute 88% of the fatigue damage. Furthermore, placing a weight restriction to eliminate the first two levels will reduce the fatigue damage by 24%. It can be seen that increasing m increases the contribution to the fatigue damage from the heavier vehicles that occur less frequently.

When m = 5.1 in column 6 in Table 2, which is a value used for welded stud shear connectors as in Eq. 3.14, the first three levels which contain the heaviest vehicles contribute 87% of the fatigue damage, even though the probability of occurrence at these levels is only 0.01. Eliminating the first two levels by placing a weight restriction on the bridge would reduce the fatigue damage by 57% which would substantially increase the design life by a factor of $(1-0.57)^{-1} = 2.3$. When m = 20 in column 7 which is an approximate value for concrete, then only the very heavy vehicles at level 1 contribute to the fatigue damage.

(c) Force constant F_f

The contribution of the force constant to the fatigue damage can be viewed in the same way as the contribution of the load constant. Instead of dealing with $(BW^m)_x$ at each level of the load spectrum in Table 1 we are now dealing with $(fR^m)_k$ at each level of the force spectrum in Table 3.

Example 19.6. Distribution of fatigue damage within a force spectrum

In Example 19.4, a standard fatigue vehicle with two axles traversed a bridge and induced two ranges of shear flow force of $R_1 = 135$ N/mm and $R_2 = 45$ N/mm. Each range only occurred once so that $f_1 = f_2 = 1$. Let us consider the distribution of the fatigue damage within this force spectrum.

Let $m = 3$ for a welded steel component. The contribution to the fatigue damage from the first range is $f_1R_1{}^m = 135^3$ and that from the second range is $f_2R_2{}^m = 45^3$. Hence, the proportion of the fatigue damage contributed by the first range is $135^3/(135^3+45^3) = 96.4\%$ and that of the second range is 3.6%. It can be seen that the contribution to the fatigue damage by the second range is minuscule. This is because the fatigue damage is proportional to R^3 and also because the frequencies of the two ranges are the same, that is the change in the fatigue damage due to a reduction in the range is not compensated by an increase in the frequency Unlike the fatigue damage distribution in the load spectrum, where the probabilities of low loads is much higher than those of high loads which tends to even out the fatigue damage in the spectrum, in this case the probabilities of occurrence, that is the frequencies, are the same and in general they are of the same order of magnitude.

When $m = 5.1$ for welded stud shear connectors, the contribution to the fatigue damage due to the second range reduces to $45^{5.1}/(135^{5.1}+45^{5.1}) = 0.4\%$ and hence can be ignored in practice. This is the reason why some design procedures are based on only the maximum range. It was also shown in Example 19.4 that the frictional resistance reduced the shear flow force on the shear connectors from 135 N/mm to 118 N/mm. Therefore, the fatigue damage with frictional resistance as a proportion of the fatigue damage without frictional resistance is $118^{5.1}/135^{5.1} = 50\%$, hence the frictional resistance would double the design life of the shear connectors at this design point.

19.4.4.2 *Fatigue zones*

In applying the general analysis fatigue equation, it is necessary to define and determine all the fatigue zones. A fatigue zone has already been defined as the number of fatigue vehicle traversals T_y in which both the force constant F_f and the load constant L_f are unchanged. For each change in F_f or L_f, a new fatigue parameter $(TF_fL_f)_y$ has to be determined and then these can be simply added together to determine the overall fatigue damage. It can be seen that it is a very simple procedure to allow for variations in L_f and F_f during the fatigue design life.

There are a variety of reasons for changes in the force spectrum and hence for changes in F_f. For example, a single force spectrum could be derived for the traversal of the standard fatigue vehicle in all of the lanes that affect the design point. This can be achieved by moving the standard fatigue vehicle across each lane in turn and so producing an influence line diagram for each lane, from which a single force spectrum can be derived. Alternatively a separate force spectrum can be derived for the traversal of the standard fatigue vehicle in each lane. If it is felt that one standard fatigue vehicle cannot be used to represent the geometry of all the fatigue vehicles, then several standard fatigue vehicles may have to be used and a force spectrum will have to be derived for each standard fatigue vehicle in each lane. Furthermore, the shapes of the fatigue vehicles may change during the design life of the bridge and so it may be necessary to change the shape of the standard fatigue vehicle and hence the force spectrum with time. Upgrading of the bridge may change its structural properties and hence change the stress resultants within the bridge which will require the formation of another force spectrum.

The load spectrum is also subject to change. A load spectrum will be required for each standard fatigue vehicle and may also be required for each standard fatigue vehicle in each lane if the distribution of fatigue vehicles varies from lane to lane. The distribution of fatigue vehicles on a bridge may change with time and this variation with time can be represented by several load spectrums. If weight restrictions are placed on a bridge, then this can be allowed for with a new load spectrum.

19.4.4.3 *Adaptation of fatigue zone*

The fatigue parameters $(TF_f L_f)_y$ in Eq. 19.19 can be adapted to suit the problem under consideration in order to simplify the design or assessment procedure. However simplifying the general analysis fatigue equation, does tend to hide the fundamental principles or assumptions on which the analysis is based. In order to illustrate the simplification procedures let us consider Eq. 19.19 but with only one load constant and one force constant.

(a) Simplification procedure

It was shown in Example 19.6 that often the maximum range of the stress resultant in the force spectrum R_{max} contributes to the vast majority of the fatigue damage, so that the force constant F_f can be replaced by R_{max}^m. A further simplification is to assume that the load spectrum for all bridges is the same and therefore the load constant L_f is a constant value $(L_f)_{const}$. A final simplification is to assume that all the bridges are to be designed for the same number of fatigue vehicle traversals T_{const}. Substituting these values into Eq. 19.19 gives

$$X^{-m} = \frac{AC}{T_{const} R_{max}^m \left(L_f\right)_{const}} \tag{19.20}$$

If this equation were to be used in a design mode, then it would only be necessary for the engineer to ensure that

$$R_{max} \leq \left(\frac{ACX^m}{T_{const}(L_f)_{const}} \right)^{\frac{1}{m}} \qquad (19.21)$$

where R_{max} is the maximum range from the traversal of the standard fatigue vehicle.

(b) Standard fatigue vehicle approach

An alternative approach would be to base the whole design procedure on the traversal of standard fatigue vehicles. In order to do this, it is necessary to determine the number of traversals of the standard fatigue vehicles T_{SFV} that produces the same fatigue damage as the traversals T of the fatigue vehicles. Equating the fatigue damage from the fatigue vehicles to the fatigue damage from the standard fatigue vehicles gives

$$TF_f L_f \ = \ T_{SFV} \ F_f \ L_{SFV} \qquad (19.22)$$

where L_{SFV} is the load constant for a load spectrum with only standard fatigue vehicles, and where the left hand side of the equation relates to the fatigue vehicles and the right hand side to the standard fatigue vehicles.

The force constants F_f on both sides of Eq. 19.22 have the same value as both are derived from the traversal of the standard fatigue vehicle. If a load spectrum comprises of only one weight of vehicle and that vehicle has the same weight as the standard fatigue vehicle, then the load spectrum only consists of one level i = 1 where $W_1 = 1$ and $B_1 = 1$, and so from Eq. 19.17 $L_{SFV} = 1$. Therefore from Eq. 19.22, $T_{SFV} = TL_f$ which is the equivalent number of standard fatigue vehicles that induces the same fatigue damage as all the fatigue vehicles.

Hence, the general fatigue equation becomes

$$X^{-m} \ = \ \frac{AC}{T_{SFV}F_f} \ \approx \ \frac{AC}{T_{SFV}R_{max}^m} \qquad (19.23)$$

when $F_f \approx R_{max}^m$.

(c) Experimentally determined stress resultants

The fatigue parameter $(TF_f L_f)_y$ can also be used to determine the fatigue damage when the stress resultants are determined experimentally. For example, strain gauges could have been used to measure the cyclic stresses in a component over a period of a week to produce an influence line diagram of the cyclic stresses. The reservoir approach could then be used to convert the influence line diagram to a force spectrum that contained all the ranges of stress over a period of a week.

The way to visualise this problem is to assume that a standard fatigue vehicle took a week to traverse the bridge and induce all the ranges of stress in the force spectrum. Using Eq. 19.18, the force constant F_f can be derived from the force spectrum. As the load spectrum only consists of only a standard fatigue vehicle then L_f

= 1, as in the previous section (b). The number of fatigue vehicles T in the fatigue parameter would in this case be a number of weeks as the force spectrum was determined over a period of one week.

(d) Equivalent range

As the accumulated damage law is based on a linear failure envelope as explained in Section 19.4.2.3, variable cyclic ranges can be converted to a single constant range that produces the same fatigue damage. For example, the fatigue damage term $(TF_f L_f)_y$ can be written in the following form

$$T\left(\sum_{k=1}^{k=z}\left(f_k R_k^m\right)\right)L_f \;=\; \left(T\sum_{k=1}^{k=z}f_k\right)R_{equiv}^m L_f \tag{19.24}$$

where the $f_k R_k^m$ term is the force constant from Eq. 19.18 and the term $T\sum f_k$ is the number of cycles of all the stress resultant that the design point is subjected to during T fatigue vehicle traversals. Therefore R_{equiv} is the equivalent constant cyclic range of the stress resultant that produces the same damage as the variable cyclic load when applied the same number of times as the number of variable cyclic loads.

Alternatively, the equivalent range of the stress resultant that causes the same fatigue damage as the variable cyclic load when applied the same number of times as the number of traversals of the fatigue vehicles T is given by the following equation.

$$\left(R_{equiv}\right)_T \;=\; \left(\sum_{k=1}^{k=z}\left(f_k R_k^m\right)\right)^{\frac{1}{m}} \tag{19.25}$$

19.4.5 CRACK PROPAGATION APPROACH

19.4.5.1 *General crack propagation fatigue equation*

Equation 19.19, which is the general analysis fatigue equation, was developed for the generic form of the accumulated damage law shown in Eq. 19.9 and for the generic form of the endurance equation as in Eq. 19.10. Equation 19.19 can now be applied specifically to the Stage 2 residual strength failure envelope in Fig. 3.5 (Oehlers, Ghosh and Wahab 1995) that is defined by Eq. 19.7 .

Comparing Eq. 19.9 with 19.7, it can be seen that $A = 1 - P_c/P_{prop}$ and that $E = E_a$, where the asymptotic endurance E_a is given in the form of Eq. 3.7. Therefore, comparing Eq. 19.10 with Eq. 3.7, gives $m = m_a$ and $C = 10^{H_a - 2D_a}$. Substituting these values into Eq. 19.19 gives

$$X^{-m_a} = \frac{\left(1 - \dfrac{P_c}{P_{prop}}\right)10^{H_a - 2D_a}}{\displaystyle\sum_{y=1}^{y=j}\left(T\big(F_f = f(R)\big)L_f\right)_y} \tag{19.26}$$

where $F_f = f(R)$ in the denominator on the right hand side of the equation is there to remind the reader that the force constant F_f is a function of the range of the cyclic stress resultant R.

Equation 19.26 will be referred to as the general crack propagation fatigue equation as it assumes an immediate reduction in strength when cyclic loads are applied. How the variables in this equation are defined depends on whether the equation is being used to design new structures or to assess the performance of existing structures.

19.4.5.2 *Design mode*

When used in a design mode, the general crack propagation fatigue equation of Eq. 19.26 has the following form

$$X^{-m_a} = \frac{\left(1 - \dfrac{P_o}{P_{of}}\right)10^{H_a - 2D_a}}{\displaystyle\sum_{y=1}^{y=j}\left(T\big(F_f = f(R)\big)L_f\right)_y} \tag{19.27}$$

where P_o is the force exerted by the maximum overload, that is the factored design load, and P_{of} is the strength required to resist the maximum overload after the anticipated reduction in strength due to fatigue loads. Therefore, P_{of} is the strength of the structure when it is first built, that is its static strength prior to cyclic loading, and P_o is the force exerted by the maximum design load and is therefore the strength the structure must have at the end of its design life in order to resist the maximum overload. The difference in strength $P_{of} - P_o$ is the reduction in strength due to fatigue damage during the design life.

Example 19.7. Design equation for stud shear connections using crack propagation approach

Equation 19.27 can be applied to the design of stud shear connectors in composite bridge beams (Oehlers 1995). It is convenient in the design and assessment of shear connectors in composite beams to deal with the shear flows. We will define the shear flow force q in the beam as the longitudinal shear force per unit length, and the shear flow strength Q of the beam as the longitudinal shear strength per unit length. By comparing the generic endurance of Eq. 19.10 with the endurance of stud shear connectors in Eq. 3.14, it can be seen that the parameter X is the static strength of a stud shear connector prior to cyclic loading D_{max}. In the design mode $D_{max} = P_{of}$ in

Eq. 19.27, that is the strength of the shear connection when the structure is first built. Hence substituting q and Q as appropriate for the stress resultants P in Eq. 19.27 gives

$$Q_{of}^{-m_a} = \frac{\left(1 - \dfrac{q_o}{Q_{of}}\right)10^{H_a - 2D_a}}{\sum\limits_{y=1}^{y=j}\left(T\left(F_f = f(q_r)\right)L_f\right)_y} = \frac{\left(1 - \dfrac{q_o}{Q_{of}}\right)10^{H_a - 2D_a}}{T_1\left(F_f\right)_1\left(L_f\right)_1 + T_2\left(F_f\right)_2\left(L_f\right)_2 + ...}$$

(19.28)

where q_r is the spectrum of the range of the shear flow force when the standard fatigue vehicle traverses the bridge, q_o is the maximum shear flow force induced by the maximum overload and Q_{of} is the shear flow strength that the component must have when it is first built, so that it can resist q_o at the end of its design life after the fatigue damage due to q_r.

Consider the following design problem. All the fatigue vehicles on the bridge can be represented by two standard fatigue vehicles SFV_1 and SFV_2. The design point on the beam is only subjected to loads from one lane. The fatigue vehicles represented by SFV_1 have a load spectrum that has a load constant $(L_f)_1$ and these fatigue vehicles traverse the structure T_1 times during the design life. The standard fatigue vehicle SFV_1 induces a force spectrum when it is traversed across the lane that has a force constant $(F_f)_1$. Similarly for SFV_2, we have T_2, $(F_f)_2$ and $(L_f)_2$.

The parameters m_a and $10^{H_a - 2D_a}$ in Eq. 19.28 are fatigue material properties that can be derived from a stud shear connection endurance equation such as Eq. 3.14. Furthermore, q_o in Eq. 19.28 is the maximum shear flow force at the design point due to the maximum overload, that is the factored design load. Therefore, the only unknown quantity in Eq. 19.28 is Q_{of} which is the strength required when the structure is first built, and this can be derived by an iterative solution as the equation is non linear.

Example 19.8. Application of crack propagation design equation

Equation 19.28 will be applied to the very simple problem shown in Fig. 19.2(a). The effect of the frictional shear flow resistance will be ignored. Let us assume that the fatigue vehicles and the maximum design overload can be represented by the traversal of single axle vehicles. Moving the maximum design vehicle across the beam gives the variation of the shear flow force q_o in (b) which is at a maximum at the supports and half that value at mid-span. This is also the minimum shear flow strength Q_o the structure must have in order to resist the occasional maximum design load.

The total range of the cyclic load q_r is constant as shown by the shear flow envelope in Fig. 19.2(a) where $q_r = q_t$ is constant, so that the fatigue damage is constant throughout the length of the beam. Equation 19.28 can now be applied at successive design points along the beam in order to derive the variation of Q_{of} in Fig.

19.2(b), which is the variation of the shear flow strength when the structure is first built. The increase in the required strength from Q_o to Q_{of} is the increase in strength that is required to allow for fatigue damage.

It can be deduced from an endurance equation such as Eq. 3.14 that fatigue damage is proportional to $(q_r / Q_{of})^{m_a}$. The range $q_r = q_t$ in Fig. 19.2(a) is constant throughout the length of the beam whilst q_o and therefore Q_{of} is a maximum at the supports as shown in (b). Therefore the largest value of $(q_r / Q_{of})^{m_a}$, and hence the greatest fatigue damage, occurs at mid-span. This is the reason why $Q_{of} - q_o$, that is $Q_{of} - Q_o$, is a minimum at the supports and a maximum at mid-span.

The interaction between the strength and the fatigue damage in this crack propagation approach is clearly shown in Fig. 19.2(b). The beam must have at least the distribution of strength given by Q_o in order to resist the static maximum overload. If there are no fatigue vehicles then from Eq. 19.28, the variation of Q_{of} in Fig. 19.2(b) will be the same as that of Q_o. However, any fatigue loading will require an increase in the strength from Q_o to Q_{of}.

It is worth noting that because the fatigue damage is proportional to $(q_r / Q_{of})^{m_a}$, a small increase in Q_{of} will provide a substantial reduction in the damage parameter $(q_r / Q_{of})^{m_a}$. Conversely, a substantial increase in the anticipated fatigue damage will only require a relatively small increase in the initial strength. For example, let us represent the fatigue damage as FD as shown in the following equation.

$$\left(\frac{q_r}{Q_{of}} \right)^{m_a} = FD \tag{19.29}$$

We may wish to increase the fatigue damage by a factor of ten by, for example, applying ten times the original number of fatigue vehicles. Therefore, the fatigue damage per cycle must reduce by a factor of ten and this can be achieved by increasing the original strength from Q_{of} to $(Q_{of})_{10}$ such that

$$\left(\frac{q_r}{\left(Q_{of} \right)_{10}} \right)^{m_a} = \frac{FD}{10} \tag{19.30}$$

Substituting FD in Eq. 19.29 into Eq. 19.30 and $m_a = 5.1$, from Eq. 3.14, gives

$$\left(Q_{of} \right)_{10} = 10^{\frac{1}{m_a}} Q_{of} = 1.57 Q_{of} \tag{19.31}$$

Therefore, in order to resist a tenfold increase in the fatigue damage, it would only be necessary to increase the initial static strength by 57%.

19.4.5.3 Assessment mode

The assessment mode of Eq. 19.26 has the following form

$$X^{-m_a} = \frac{\left(1 - \frac{P_{res}}{P_{st}}\right)10^{H_a - 2D_a}}{\sum_{y=1}^{y=j}\left(T\left(F_f = f(R)\right)L_f\right)} \tag{19.32}$$

where P_{res} is the residual or remaining strength after cyclic loading and P_{st} is the strength at the start of the fatigue life, that is prior to cyclic loads.

Example 19.9. Assessment of stud shear connections using crack propagation approach

Using the same procedure as that described in Example 19.7, the following equation has been developed for the assessment of shear flows on stud shear connectors

$$Q_{st}^{-m_a} = \frac{\left(1 - \frac{Q_{res}}{Q_{st}}\right)10^{H_a - 2D_a}}{\sum_{y=1}^{y=j}\left(T\left(F_f = f(q_r)\right)L_f\right)_y} = \frac{\left(1 - \frac{Q_{res}}{Q_{st}}\right)10^{H_a - 2D_a}}{T_1\left(F_f\right)_1\left(L_f\right)_1 + T_2\left(F_f\right)_2\left(L_f\right)_2 + \ldots} \tag{19.33}$$

where Q_{res} is the remaining or residual shear flow strength at the design point after cyclic loading, and Q_{st} is the shear flow strength at the start of the fatigue loading and which is equal to Q_{of} in the design mode in Eq. 19.28. It can be seen in Eq. 19.33 that there is a linear variation of the residual strength Q_{res} with fatigue damage.

The application of Eq. 19.33 is illustrated in Fig. 19.17. At a design point, the shear flow strength of the shear connectors prior to cyclic loading is Q_{st}, which is shown as point A. This is the strength of the shear connectors when the beam was first constructed. The strength required to resist the maximum overload or design load is shown as Q_o on the ordinate and the beam has already been subjected to N_2 traversals of fatigue vehicles. The load constant is shown as L and the force constant as F in Fig. 19.17.

During the first T_1 traversals, the load spectrum and force spectrum remained constant giving a load constant of L_a and a force constant of F_a in Fig. 19.17. These values can be inserted into Eq. 19.33 as the first fatigue zone $(TF_fL_f)_1 = T_1F_aL_a$ to give Q_{res} which is shown as point B in Fig. 19.17.

After the first T_1 traversals in zone 1 and during the next T_2 traversals in zone 2, the weights of the commercial vehicles were allowed to increase. However, it was found that the same standard fatigue vehicle could still represent the commercial vehicles, that is the fatigue vehicles. As the standard fatigue vehicle is unchanged, the

force constant remains unchanged at F_a during the next T_2 traversals, as shown in Fig. 19.17. Furthermore, changing the weights of the fatigue vehicles will change the load spectrum so that the load constant is now L_b during the T_2 traversals. Therefore, the second fatigue zone is $(TF_fL_f)_2 = T_2F_aL_b$. Inserting the first plus second fatigue zone into Eq. 19.33, will give the residual strength at point C in Fig. 19.17 which is the strength at the present time when N_2 applications have occurred.

The end of the fatigue life will be reached when the residual strength Q_{res} reduces to the strength required to resist the maximum overload Q_o. This will occur after a further T_x fatigue vehicle traversals during which it will be assumed that the fatigue constant and the load constant remain unchanged at F_a and L_b, as shown in Fig. 19.17. Substituting $Q_{res} = Q_o$ and a third fatigue zone $(TF_fL_f)_3 = T_xF_aL_b$ into Eq. 19.33 will give the number of fatigue vehicle traversals T_x that will reduce the strength to Q_o which is point F in Fig. 19.17.

If the engineer decides that the future fatigue life of T_x traversals is not long enough, then a weight restriction could be placed on the bridge. This would change the load spectrum by removing some of the higher weight levels so that the load constant is now L_c in zone 3 in Fig. 19.17. A weight restriction would not affect the force spectrum, so that the force constant would remain at F_a. The third fatigue zone in Eq. 19.33 would now be $(TF_fL_f)_3 = T_3F_aL_c$. Inserting the three fatigue zones and $Q_{res} = Q_o$ into Eq. 19.33 will give the future endurance T_3 when there is a weight restriction.

From the previous calculation, remedial work will not be required until a further T_3 fatigue vehicles have traversed the bridge. Let us assume that the bridge is strengthened only after a further T_3 fatigue vehicle traversals, so that we are now at point D in Fig. 19.17 where the residual strength is just sufficient to resist the design load q_o, and that the strengthening procedure reduces the shear flow forces by 10%. Reducing the shear flow forces by 10% will reduce the shear flow force q_o due to the maximum overload so that the strength required to resist the maximum overload $Q_o* = 0.9Q_o$ as shown. This will allow the shear connectors to resist a greater amount of fatigue damage, that is their strength can now reduce by a further 10%. The 10% reduction in the shear flow forces will also reduce the cyclic ranges q_r by 10% and hence their fatigue damage. This will reduce the force constant of Eq. 19.18 by a factor of $(1-10\%)^{ma}$ to give a new force constant F_b in zone 4 in Fig. 19.17. It will be assumed that the weight restriction is removed after strengthening so that the load spectrum reverts back to the original value of L_b. The fourth fatigue zone in Eq. 19.33 would now be $(TF_fL_f)_4 = T_4F_bL_c$ and substituting $Q_{res} = 0.9Q_o$ will give the future endurance T_4.

19.4.6 CRACK INITIATION APPROACH

19.4.6.1 *General crack initiation equation*

The generic form of the general analysis fatigue equation of Eq. 19.19 can be used to develop the Stage 3 residual strength failure envelope in Fig. 3.5. Comparing Eq. 19.9

with Eq. 19.8 gives A = 1 and E = E_e, and comparing Eq. 19.10 with Eq. 3.2 gives $C = 10^{H_e - 2D_e}$ and m = m_e. Substituting these values into Eq. 19.19 gives the following general Stage 3 fatigue equation.

$$X^{-m_e} = \frac{10^{H_e - 2D_e}}{\sum\limits_{y=1}^{y=j}\left(T\left(F_f = f(R)\right)L_f\right)_y} = \frac{C}{\sum\limits_{y=1}^{y=j}\left(T\left(F_f = f(R)\right)L_f\right)_y} \qquad (19.34)$$

This equation will be referred to as the general crack initiation fatigue equation as it assumes that there is no reduction in strength until rapid failure immediately after E_e cycles, which is the assumption used in most national design standards or codes.
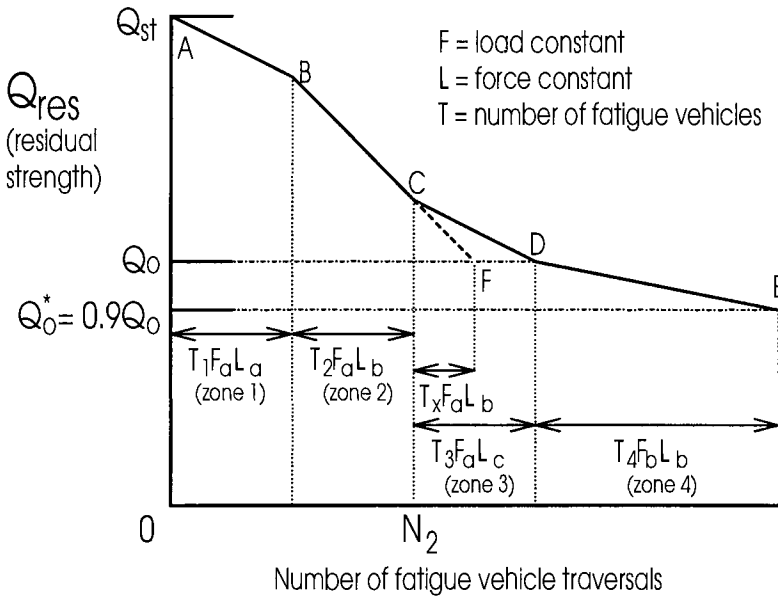
Fig. 19.17 Fatigue assessment using crack propagation approach

19.4.6.2 *Design mode*

It is a very simple procedure to use Eq. 19.34. All that is needed are the fatigue material properties and the fatigue damage term. It is worth noting that Eq. 19.34 is independent of the strength of the component.

Unlike the crack propagation approach where there is a close interaction between the strength and the fatigue damage, the crack initiation approach assumes that the strength and the fatigue damage are independent. It is, therefore, necessary for the engineer to determine in separate calculations the strength required to resist the maximum design load and the strength required to resist the fatigue damage due to the serviceability loads. The maximum of these two strengths will then govern the design.

Example 19.10. Design equations for welds using crack initiation approach

Equation 19.34 can be applied to the design of fillet welds and as with stud shear connectors it is convenient to work in terms of shear flow forces q. The endurance of fillet welds is usually given in the form of Eq. 3.2 where R is the range of the shear stress τ, so that the equation is dimensionally incorrect and therefore the constant of the equation will depend on the units used. Let W be the width of the throat of the weld, therefore $\tau = q/W$ and hence $R = \tau = q_r/W$ in Eq. 3.2 which becomes

$$\left(E_e\right)_{ch} = 10^{H_e - 2D_e}\left(\frac{q_r}{W}\right)^{-m_e} \tag{19.35}$$

Comparing Eq. 19.35 with Eq. 19.10 gives $R = q_r$ and $X = W$, so that the general crack initiation equation of Eq. 19.34 can be written in the following form specifically for welded joints.

$$W^{-m_e} = \frac{10^{H_e - 2D_e}}{\sum\limits_{y=1}^{y=j}\left(T\left(F_f = f(q_r)\right)L_f\right)_y} = \frac{10^{H_e - 2D_e}}{\left(TF_fL_f\right)_1 + \left(TF_fL_f\right)_2 + \cdots\cdots} \tag{19.36}$$

The fatigue material properties, that is the fatigue exponent m_e and the fatigue constant $10^{H_e - 2D_e}$ in Eq. 19.36, can be derived from most national standards which give the endurance in the form of Eq. 3.2. The fatigue parameter in the denominator on the right hand side of Eq. 19.36 can be derived in the usual way from the force spectrum, the expected load spectrum and the expected frequency of loading. This leaves the size of the weld W as the only unknown in Eq. 19.36 that can now be derived directly. The size of the weld W is the size required to resist the fatigue damage due to the serviceability loads imposed by the traversal of the fatigue vehicles.

Example 19.11. Application of crack initiation design approach

The crack initiation approach of Eq. 19.34 can be applied to the very simple problem shown in Fig. 19.2(a). This problem has already been dealt with in Example 19.8 using the crack propagation approach and in terms of shear flows in the shear connectors .

Equation 19.34 can be adapted for stud shear connectors using either of the forms of the endurance equations for stud shear connectors given by Eqs. 3.16 and 3.17. For example by comparing Eq. 19.10 with Eq. 3.17, it can be seen that the parameter R/X in Eq. 19.10 is equivalent to R/D_{max} in Eq. 3.17. However in terms of shear flows, R/D_{max} is equivalent to $q_r/Q_{fatigue}$, where $Q_{fatigue}$ is the shear flow strength of the shear connection that is required to resist the fatigue damage. Therefore in Eq. 19.34, $R = q_r$ which is the range of the cyclic shear flow forces, and $X = Q_{fatigue}$. Substituting these values for R and X into Eq. 19.34 gives the following crack initiation fatigue equation for stud shear connectors.

$$Q_{fatigue}^{-m_e} = \frac{10^{H_e - 2D_e}}{\sum\limits_{y=1}^{y=j} \left(T\left(F_f = f(q_r) \right) L_f \right)_y} \qquad (19.37)$$

As the fatigue vehicles consist of a single axle as shown in Fig. 19.2(a), the total range of the cyclic load is constant throughout the length of the beam as shown in (a). Therefore, the fatigue damage term in Eq. 19.37 is also constant along the beam which means that $Q_{fatigue}$ is also constant along the length of the beam as shown in Fig. 19.2(b).

The engineer is now required to compare the strengths required to resist the fatigue load $Q_{fatigue}$ with the strength required to resist the maximum design load Q_o in Fig. 19.2(b). The upper bound of these two distributions will define the distribution of the shear connection to be used in the beam. It can be seen in (b) that Q_o is more likely to control design at the supports than at mid-span. When the fatigue loading is low, that is $Q_{fatigue}$ falls below the minimum value of Q_o at mid-span, then the static design based on the maximum overload will control design. Conversely when $Q_{fatigue}$ is greater than the maximum value of Q_o at the supports, then fatigue will control design. It can be seen that there is no direct interaction between strength and fatigue damage in the crack initiation approach as compared with the crack propagation approach where there is a direct interaction.

19.4.6.3 *Assessment mode*

Equation 19.34 can also be used to assess the performance of existing structures. As in the design mode described in the previous section, the crack initiation approach has a very limited use as there is no direct interaction between strength and fatigue damage.

Example 19.12. Assessment of welds using crack initiation approach

Equation 19.36 in Example 19.10 can also be used to assess the performance of a weld in an existing structure. In this case, the size of the weld W in Eq. 19.36 is known. If for example, the first fatigue term $(TF_f L_f)_1$ is the damage that has already occurred, then the second fatigue term $(TF_f L_f)_2$ will be the damage that will occur. Hence T_2, in the second fatigue term, can be derived to give the future endurance.

In theory, rapid failure will occur immediately after a further T_2 fatigue vehicles have traversed the bridge. If this future endurance is not considered sufficient, then the endurance could be extended by placing a weight restriction on the bridge which would change the load constant L_f in the second fatigue zone. Alternatively, the structure could be strengthened to reduce the shear flow forces q_r which would change the force constant F_f in the second fatigue zone.

The main limitation to the crack initiation approach is that it is based purely on the fatigue damage because there is no interaction between the strength and fatigue

damage. For example, if the analysis described previously had shown that all of the available fatigue life T had been used but the structure is still standing, then the engineer would find it difficult assess the effect of remedial work using the crack initiation approach. Furthermore, this approach does not give guidance to the engineer on the effect of the fatigue damage of increasing the maximum design load.

19.5   Non-welded steel components

19.5.1 GENERAL

The fatigue analysis of non-welded steel components will be used to illustrate the crack initiation approach in both the design mode for new structures and in the assessment mode for existing structures. It is worth noting that in non-welded steel components the fatigue exponent m $\approx$ 4, in comparison with welded components that are dealt with in Section 19.7 where m $\approx$ 3 and in comparison with welded stud shear connectors in Section 19.6 where m $\approx$ 5.

The characteristic experimentally derived fatigue endurance of a non-welded steel component $(E_e)_{ch}$ is often given in national standards in the following form

$$\left(E_e\right)_{ch} \quad = \quad C\sigma^{-m_e} \tag{19.38}$$

where σ is the range of the cyclic stress, and where it is often assumed that the fatigue exponent m_e = 4 in non-welded steel components. The coefficient C of the endurance equation defines the characteristic endurance. For example at 2 standard deviations, that is at a 2.3% probability of failure, $C = 10^{H_e-2D_e}$ as shown in Eq. 3.2 and illustrated in Fig. 3.3. Alternatively, for a 5% probability of failure that occurs at 1.64 standard deviations $C = 10^{H_e-1.64D_e}$. Equation 19.38 is dimensionally incorrect so that the coefficient C varies with the units that are being used.

19.5.2 DESIGN MODE

For convenience in design, Eq. 19.38 can be written in the following form.

$$\left(E_e\right)_{ch} \quad = \quad C\left(\frac{\left(\dfrac{\sigma}{\sigma_{max}}\right)}{\sigma_{max}^{-1}}\right)^{-m_e} \tag{19.39}$$

where σ_{max} is any constant value of stress.

By comparing Eq. 19.39 with Eq. 19.10, it can be seen that R = σ/σ_{max} and $X = \sigma_{max}^{-1}$. Substituting these values into Eq. 19.34 and rearranging gives

$$\sigma_{max} = \left(\frac{C}{\sum\limits_{y=1}^{y=j} \left(T\left(F_f = f\left(\frac{\sigma}{\sigma_{max}} \right) \right) L_f \right)_y} \right)^{\frac{1}{m_e}}$$ (19.40)

For design purposes, it is convenient to make σ_{max} equal to the maximum range of the cyclic stress at the design point when the standard fatigue vehicle traverses the bridge. The force constant F_f is now in terms of a non-dimensional ratio σ/σ_{max}.

The non-dimensional ratio σ/σ_{max} in Eq. 19.40 is very convenient for design, as this ratio can be determined without knowledge of the cross-sectional properties of the composite beam. For example if we were dealing with flexural stresses, then from the well known linear elastic flexural equation the flexural stress $\sigma = My/I$. Therefore, the ratio $\sigma/\sigma_{max} = M/M_{max}$ and Eq. 19.40 becomes

$$\sigma_{max} = \left(\frac{C}{\sum\limits_{y=1}^{y=j} \left(T\left(F_f = f\left(\frac{M}{M_{max}} \right) \right) L_f \right)_y} \right)^{\frac{1}{m_e}}$$ (19.41)

where M is the cyclic range of moment at the design point and M_{max} is the maximum cyclic range of moment that is induced by the standard fatigue vehicle. The force constant F_f in Eq. 19.18 can now be determined from a force spectrum in which $R = M/M_{max}$ so that this force constant can be determined without prior knowledge of the cross-sectional properties of the beam.

The right hand side of Eq. 19.41 can be visualised as a 'fatigue' stress because it is derived from the fatigue loads and the fatigue material properties and can be determined without prior knowledge of the cross-sectional properties of the beam. The left hand side of Eq. 19.41 is the range of the maximum cyclic stress at the design point due to M_{max}, that is due to the maximum cyclic moment induced by the standard fatigue vehicle. Therefore, the engineer is required to choose a cross-section in which σ_{max} induced by M_{max} on the left hand side of Eq. 19.41 is less than the 'fatigue' stress on the right hand side.

Example 19.13. Design of non-welded steel component

Equation 19.41 will be applied to the fatigue design of the tension flange of a composite bridge beam. The fatigue material properties for non-welded steel components can be obtained from national standards and it will be assumed that in Eq. 19.38 the exponent $m_e = 4$ and the constant $C = 1.0 \times 10^{15}$ when the units are in N and mm. The design point being considered is subjected to loads from only one lane, 300 million fatigue vehicles will traverse this lane during the design life, and the fatigue

vehicles can be represented by one standard fatigue vehicle and by the load spectrum in Table 2.

It will be assumed that moving the standard fatigue vehicle across the beam will only induce one cyclic range of moment. Therefore $M/M_{max} = 1$ in Eq. 19.41, and hence $F_f = 1$ from Eq. 19.18. From Eq. 19.17 and column 5 in Table 2, $L_f = 0.415$ and from the specifications in the previous paragraph $T = 300 \times 10^6$. Substituting these values into Eq. 19.41 gives $\sigma_{max} = 53$ N/mm^2. Hence a cross-sectional property must be chosen such that the standard fatigue vehicle does not exert a range of cyclic stress at the design point that is greater than 53 N/mm^2. The structure has still to be designed to resist the static maximum design load and the greater strength requirement of the fatigue and static analysis will govern the design.

19.5.3 ASSESSMENT MODE

When assessing the performance of an existing structure, the cross-sectional properties of the beam are known so that it may be convenient to work directly in terms of the cyclic stresses induced by the standard fatigue vehicle σ. Comparing Eq. 19.38 with Eq. 19.10 gives $R = \sigma$ and $X = 1$. Substituting these values into Eq. 19.34 and rearranging gives

$$ C = \sum_{y=1}^{y=j} \left(T\big(F_f = f(\sigma)\big) L_f \right)_y = \left(TF_f L_f\right)_1 + \left(TF_f L_f\right)_2 + \ldots \qquad (19.42)$$

The fatigue material property C on the left hand side of the equation is the maximum fatigue damage that the material can withstand and the right hand side of the equation is the fatigue damage that has occurred.

Example 19.14. Assessment of non-welded steel component

Equation 19.42 can be used to assess the performance of the tension flange in Example 19.13. The fatigue material properties were given as $C = 1.0 \times 10^{15}$ and $m_e = 4$. The bridge has been subjected to the load spectrum of fatigue vehicles in Table 2 and two hundred million fatigue vehicles have already traversed the bridge. Furthermore, the traversal of the standard fatigue vehicle induces only one range of cyclic stress of 55 N/mm^2.

The first fatigue zone $(TF_f L_f)_1$ in Eq. 19.42 can represent the fatigue damage that has already occurred. Hence $T_1 = 200 \times 10^6$, the load constant $(L_f)_1 = 0.415$ (derived in column 5 of Table 2) and $(F_f)_1 = 55^4$. Therefore $(TF_f L_f)_1$ in Eq. 19.42 becomes 0.76×10^{15} and the remaining resistance to fatigue damage is $(TF_f L_f)_2 = C - (TF_f L_f)_1 = (1.0 - 0.76) \times 10^{15} = 0.24 \times 10^{15}$. The second fatigue zone $(TF_f L_f)_2$ in Eq. 19.42 can now be assumed to represent future damage. Equating this to the remaining resistance to fatigue damage of 0.24×10^{15} will give the future endurance $T_2 = 64 \times 10^6$ fatigue vehicle traversals. If it is anticipated that the lane will be subjected to 5 million fatigue vehicle traversals per year, then the expected remaining design life is approximately 15 years, that is 64/5 years.

If the anticipated future endurance of 15 years is considered to be inadequate, then the endurance can be extended by placing a weight restriction on the bridge. It can be seen in column 5(a) of Table 2 that the first two levels of the load spectrum produce 24% of the fatigue damage. Placing a weight restriction that prevents fatigue vehicles at these two levels would produce a load spectrum that consists of only levels 3 to 6. The probabilities in column 3 between and including levels 3 to 6 should then be proportionately adjusted so that they sum to unity. However, as the probabilities at levels 1 and 2 are very small, the distribution of probabilities can be left as they are. The load factor of the load spectrum with the weight restriction comes to 0.3165 (the sum of levels 3 to 6 in column 5) which is 76% of the original value of 0.415 as the fatigue damage has been reduced by 24%. The weight restriction does not affect the force spectrum which will remain at 55^4. Substituting these values into the second fatigue zone will give $T_2 = 83 \times 10^6$.

An alternative approach for extending the endurance is to strengthen the structure. If remedial work reduces the stresses by 10%, then the force constant reduces to $(F_f)_2 = (0.9 \times 55)^4$. Strengthening the structure does not affect the load constant which remains at $(L_f)_2 = 0.415$. Substituting these values into the second fatigue zone gives $T_2 = 97 \times 10^6$. A more direct mathematical approach would be to realise that the fatigue damage reduces by a factor of 0.9^4 so that the endurance increases to $(64/0.9^4) \times 10^6 = 97 \times 10^6$. Placing the weight restriction as well as strengthening the beam will make $(L_f)_2 = 0.3165$ and $(F_f)_2 = (0.9 \times 55)^4$ and the combined effect will increase the future endurance to $T_2 = 127$ million fatigue vehicle traversals.

19.6   Welded stud shear connectors

19.6.1 GENERAL

The design and assessment of stud shear connectors in composite bridge beams will be used to illustrate the crack propagation approach to fatigue analysis. The following procedures will first deal with shear flow forces and shear flow strengths. These shear flows will then be converted to the forces on individual stud shear connectors and to the characteristic strengths of individual connectors that are loaded in groups of size n.

19.6.2 DESIGN MODE

The general design equation for stud shear connectors has already been developed in Eq. 19.28. Inserting the material properties from the asymptotic endurance of Eq. 3.14 into Eq. 19.28 gives the following fatigue design equation in terms of the shear flow forces q and the shear flow strengths Q that occur along the line of the stud shear connectors at the steel-element/concrete-element interface.

$$\left(Q_{of} = f(n)\right)^{-5.1} = \frac{\left(1 - \dfrac{q_o}{\left(Q_{of} = f(n)\right)}\right)10^{3.12-\frac{0.70}{\sqrt{n}}}}{\displaystyle\sum_{y=1}^{y=j}\left(T\left(F_f = f(q_r)\right)L_f\right)_y} = \frac{\left(1 - \dfrac{q_o}{\left(Q_{of} = f(n)\right)}\right)10^{3.12-\frac{0.70}{\sqrt{n}}}}{T_1\left(F_f\right)_1\left(L_f\right)_1 + T_2\left(F_f\right)_2\left(L_f\right)_2 + ...}$$

(19.43)

A composite beam can be divided into a finite number of design regions where the shear flow forces and the shear flow strengths can be assumed to be constant. A specific position within these regions has already been referred to as a design point. Hence q_r in Eq. 19.43, which is a spectrum of the total range of the cyclic shear flow forces induced by the traversal of the standard fatigue vehicle, is assumed to be constant over the design region. The parameter q_o in Eq. 19.43 is the maximum uni-directional shear flow force that is induced by the maximum design load or overload and it is necessary to ensure that the shear flow strength Q is always greater that q_o during the whole design life. The parameter Q_{of} is the characteristic shear flow strength of the stud shear connectors that is required when the structure is first built, which will be greater than the strength Q_o required to resist the maximum overload q_o in order to allow for the reduction in strength due to the fatigue damage induced by the ranges of the cyclic shear flow forces q_r.

The characteristic shear flow strength of the stud shear connectors, that is Q_{of} in Eq. 19.43, can be derived from Eq. 2.37. The characteristic strength is a function of the parameter $\left(4.3 - 1.1/\sqrt{n}\right)$ in Eq. 2.37, where n is the number of connectors in the shear span between the design point and the nearest support or within a region of the beam where the connectors can be assumed to fail as a group. The endurance parameter $10^{(3.12-0.70/\sqrt{n})}$ in Eq. 19.43 is also a function of n as it defines the characteristic asymptotic endurance as given in Eq. 3.14. Hence Eq. 19.43 is based on the characteristic strength and characteristic endurance of stud shear connectors, both of which depend on the number of shear connectors n in the shear span and hence on the position of the design point along the length of the beam.

Example 19.15. Design of stud shear connections based on mean material properties

Let us first consider a design that is based on the mean endurances and mean strengths (Oehlers, Ghosh and Wahab 1995) and we will only design the connectors at one design point on the beam.

A design based on the mean endurance can be achieved by inserting n = ∞ into Eq. 19.43 so that the endurance parameter becomes $10^{3.12}$. A full-interaction linear elastic analysis has shown that the maximum design load on the bridge exerts a uni-directional shear flow force at the design point of $q_o = 1200$ N/mm which is the static strength requirement Q_o. The bridge is to be subjected to T = 300x10^6 fatigue vehicle traversals. The fatigue vehicles can be represented by the load spectrum in Table 2 that has a load constant for stud shear connectors (where m = 5.1 in column 6) of $L_f = 1.14$. The traversal of the standard fatigue vehicle induces the force spectrum in Table 5, so that the force constant for stud shear connectors, in which m = 5.1, is given in

column 6 as $F_f = 1.27 \times 10^{11}$. Inserting these values into Eq. 19.43 and rearranging gives the following equation in which the units are in N and mm.

$$Q_{of} = 1733 \left(1 - \frac{1200}{Q_{of}} \right)^{-\frac{1}{5.1}}$$

(19.44)

As Eq. 19.44 is non linear, it can be solved iteratively by finding a value of Q_{of} such that the left hand side is equal to the right hand side. As Q_{of} is always greater than Q_o, a value of Q_{of} should first be chosen that is greater than Q_o which in this case is 1200 N/mm. The iterative procedure converges rapidly giving $Q_{of} = 2070$ N/mm.

The static strength of stud shear connectors in composite beams is given by Eq. 2.37. Let us assume that after inserting the geometric and material properties for a 19x100 mm stud shear connection into Eq. 2.37, the characteristic static strength is given by

$$D_{max} = 25000 \left(4.3 - \frac{1.1}{\sqrt{n}} \right)$$

(19.45)

where the units are in N and mm. The mean static strength is obtained by inserting n = ∞ to give $D_{max} = 107500$ N. The shear force on a connector is equal to the product of the shear flow and the longitudinal spacing when there is only one line of connectors. Hence the required longitudinal spacing of the connectors at the design point is $107500/2070 = 52$ mm when there is a single line of connectors.

Table 5 Force spectrum

Level	q_r (N/mm)	f	fq_r^3 welded components	(4a)%	fq_r^4 non-welded components	(5a)%	$fq_r^{5.1}$ stud shear connectors	(6a)%
(1)	(2)	(3)	(4)	(4a)%	(5)	(5a)%	(6)	(6a)%
1	150	1	3.37×10^6	84	506×10^6	95	1.25×10^{11}	98
2	50	4	5.00×10^5	13	25×10^6	5	1.85×10^9	2
3	20	16	1.28×10^5	3	3×10^6	0	6.91×10^7	0
			$\Sigma = 4.00 \times 10^6$		$\Sigma = 534 \times 10^6$		$\Sigma = 1.27 \times 10^{11}$	

Example 19.16. Design of stud shear connections based on characteristic material properties

Let us continue the analysis in Example 19.4 of a 32 m beam with the loading configuration in Fig. 19.3(a) and (b). The units of N and mm will be used throughout unless stated to the contrary.

The stress resultants at the design point D in Fig. 19.3(a) which is at a quarter span were determined in Example 19.4. The results of the analyses for determining points on the influence line diagrams have already been summarised in Table 4 in terms of the shear flow forces on the shear connectors, and for analyses both with a without the benefit of interface friction. The shear flow forces that were derived from these analyses are given in column 3 of Table 6 and are in units of N and mm. Rows 1 and 2 contain the ranges of the shear flow forces on the connectors when friction is ignored, that is $(q_r)_1$ = 135 N/mm and $(q_r)_2$ = 45 N/mm. Row 3, with F_{max} = 113 N/mm, is the maximum uni-directional shear flow force exerted on the connectors by the standard fatigue vehicle which is derived from the maximum shear flow force in row 2 in Table 4.

The analyses that have been described in the previous paragraph for the design point at a quarter span at D in Fig. 19.3(b) have been repeated for a design point at the support at C and also for a design point at mid-span at E. The influence line diagrams are given in Tables 7 and 8 and the results from the influence line diagrams are listed in columns 2 and 4 in Table 6. By comparing the results in the rows 1 to 3, that ignore the beneficial effect of friction, it can be seen that the maximum cyclic range and the maximum uni-directional force on the shear connectors occurs at the supports.

It will be assumed in the following fatigue analyses that the maximum shear flow force, that is exerted by the maximum design load on the bridge, is nine times the maximum force exerted by the standard fatigue vehicle. Therefore q_o in row 4 of Table 6 is nine times the value of F_{max} in row 3 and it is also the minimum static strength requirement Q_o. Each range of shear flow force in rows 1 and 2 only occurred once during the traversal of the standard fatigue vehicle. Hence for example, the force spectrum for the design point at a quarter span consists of $(q_r)_1$ = 135 N/mm and $(q_r)_2$ = 45 N/mm with f_1 = f_2 = 1. The force constant F_f has been determined from Eq. 19.18 with m = 5.1 and is given in row 5 of Table 6. The force constant which is proportional to the fatigue damage is the same at the quarter-span and half-span but more than twice as much at the supports. It is also worth noting that the contribution of the lower range $(q_r)_2$ in row 2 to the force constant F_f in row 5 ranges from 0.005% to 4% and so the contribution to the fatigue damage of the lower range can be ignored. The bridge is to be subjected to T = 400x10^6 traversals of fatigue vehicles that have the load spectrum in Table 2, so that the load constant for stud shear connectors is L_f = 1.14 as in column 6. The static strength of the stud shear connectors is given by Eq. 19.45.

In the fatigue design procedure, the beam will be divided into the three regions shown in Fig. 19.18. We will assume that the distribution of connectors in region C will be the same as that required at design point C and similarly for regions D and E. The characteristic endurance and the characteristic strength of the shear connection depend on the number of connectors n between the design point and the support as shown in Eqs. 19.43 and 19.45. Therefore, the distribution of the shear connectors depends on the relative position of the design point from the support and hence it is convenient to start the design procedure at the support.

The number of connectors n_1 in region C in Fig. 19.18, that is adjacent to the supports, is not known at this stage. It will, therefore, be assumed as a first approximation that n $\rightarrow \infty$, so that we will at first be dealing with the mean strengths and endurances. Substituting into Eq. 19.43, $q_0 = 1418$ from row 4 and column 2 of Table 6, n $\rightarrow \infty$, T = 400x10^6, $L_f = 1.14$ and $F_f = 161$x10^9 from row 5 in Table 6, gives $Q_{of} = 1920\left(1-\left(1418/Q_{of}\right)\right)^{-0.196}$ from which $Q_{of} = 2310$ N/mm. From Eq. 19.45, when n $\rightarrow \infty$ then $D_{max} = 107.5$ kN. Therefore the number of connectors required in region C in Fig. 19.18 that is of length 4 m is $n_1 = (2310$x$4000)/107,500 = 86$. Repeating the analyses in this paragraph but now with n = 86 gives $Q_{of} = 2380$ N/mm and $n_1 = 91$. A further iteration would show that the solution has converged to the correct value. The strength of the shear connection that is required to resist the maximum design load is $Q_0 = 1418$ N/mm from row 4 of Table 6 and this strength has to be increased to $Q_{of} = 2380$ N/mm to allow for the reduction in strength due to the fatigue damage. It is also worth noting the small difference between $n_1 = 86$ which was based on the mean strength and $n_1 = 91$ which was based on the characteristic strength.

The procedure described in the previous paragraph can be repeated for design point D at a quarter-span in region D in Fig. 19.18. When n $\rightarrow \infty$, $Q_{of} = 1910$ N/mm and in the span I-D in Fig. 19.18 $n_2 = 71$. Therefore, the number of connectors between the design point D and the support is n = $n_1 + n_2 = 71 + 91 = 162$. Repeating the analyses with n = 162 gives $Q_{of} = 1950$ N/mm and $n_2 = 74$. It can be assumed that in Fig. 19.18 $n_3 = n_2 = 74$. We will repeat the whole design procedure for design point E in Fig. 19.18 at mid-span. When n $\rightarrow \infty$, $Q_{of} = 1790$ N/mm and $n_4 = 67$ in region E. Repeating the analysis with n = 91 + 74 + 74 + 67 = 306 gives $Q_{of} = 1820$ and $n_4 = 69$.

When the design is based on the mean strength and endurance, that is it is assumed that n $\rightarrow \infty$ in both the endurance equation Eq. 19.43 and the strength equation 19.45, then the number of connectors required in a half span is 295. When the design is based on the characteristic strength and endurance as in the previous analysis, then the number of connectors that are required in a half span is 308. The difference is very small and it would be pedantic to insist on the additional effort required for the analyses based on the characteristic strengths, bearing in mind the large scatter of results associated with fatigue analyses. It is, therefore, suggested that for bridges with large numbers of connectors that design could be based on the mean strengths and mean endurances.

It was assumed in these analyses that the number of connectors n in the region between the design point and the point of contraflexure could fail as a group. If it is felt that this cannot be achieved, particularly when the region is long, then it may be prudent to use a shorter region adjacent to the design point. For example, the characteristic properties could be based on the number of connectors adjacent to the design point within a length of beam equal to its depth.
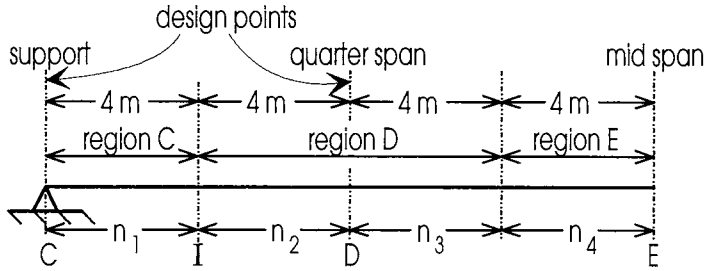
Fig. 19.18 Example 19.16: Design of stud shear connectors

Table 6 Shear flows

(1)	Support (N and mm) (2)	Quarter-span (N and mm) (3)	Mid-span (N and mm) (4)
No Friction:			
(1) $(q_r)_1$	158	135	135
(2) $(q_r)_2$	23	45	45
(3) F_{max}	158	113	68
(4) q_o	1418	1013	608
(5) F_f (x10^9)	161	74	74
With Friction:			
(6) $(q_r)_1$	97	118	124
(7) $(q_r)_2$	56	39	34
(8) F_{max}	97	97	62
(9) F_f (x10^9)	14	37	48
(10) Q_{of} and Q_{st}	2380	1950	1820
(11) Q_{res}	2310	1537	1101

19.6.3 ASSESSMENT MODE

The general assessment equation for stud shear connectors is given in Eq. 19.33. Inserting the material values from Eq. 3.14 and basing the assessment on the mean endurance so that n $\rightarrow \infty$ gives the assessment equation as

$$Q_{st}^{-5.1} = \frac{\left(1 - \dfrac{Q_{res}}{Q_{st}}\right)10^{3.12}}{\sum_{y=1}^{y=j}\left(T\left(F_f = f(q_r)\right)L_f\right)_y} = \frac{\left(1 - \dfrac{Q_{res}}{Q_{st}}\right)10^{3.12}}{T_1\left(F_f\right)_1\left(L_f\right)_1 + T_2\left(F_f\right)_2\left(L_f\right)_2 + T_2\left(F_f\right)_2\left(L_f\right)_2 + ..}$$

(19.46)

where Q_{st} is the shear flow strength of the shear connectors when the structure is first built, that is at the start of the fatigue life, and Q_{res} is the residual strength after the fatigue damage due to the TF_fL_f terms.

Example 19.17. Assessment of stud shear connections and effect of remedial action

The bridge in Example 19.15 has been subjected to 200 million fatigue vehicle traversals. The remaining strength Q_{res} can be derived from Eq. 19.46 by substituting $Q_{st} = Q_{of} = 2070$ N/mm, $(F_f)_1 = 1.27 \times 10^{11}$ and $(L_f)_1 = 1.14$, as calculated in Example 19.15. Furthermore, $T_1 = 200 \times 10^6$ and the other two fatigue terms $(TF_fL_f)_1$ and $(TF_fL_f)_2$ in Eq. 19.46 are zero. This will give the remaining strength as $Q_{res} = 1490$ N/mm which is exactly two-thirds of the change in strength form Q_{st} to Q_o (where $Q_o = q_o = 1200$ N/mm from Example 19.15), which is to be expected as the number of fatigue vehicle applications is two-thirds the original design number of applications.

It was decided after the first 200 million fatigue vehicle traversals that it was necessary to increase the design life beyond the original design requirement of 300 million traversals by placing a weight restriction on the bridge. The first fatigue term $(TF_fL_f)_1$ in Eq. 19.46 is now complete and hence a second fatigue term $(TF_fL_f)_2$ has to be introduced. A weight restriction was considered that would eliminate the loads at level 1 in the load spectrum in Table 2. The remaining probabilities in column 3 in Table 2 have now to be increased in proportion so that they sum to one. However in this case, the change is minuscule as the probability at level 1 is very small. The new load constant can be determined from column 6 and comes to $(L_f)_2 = 1.14 - 0.28 = 0.86$ where the value 0.28 is obtained from level 1. As the forces within the structure that are induced by the standard fatigue vehicle are unchanged, $(F_f)_2 = (F_f)_1 = 1.27 \times 10^{11}$. The fatigue term $(TF_fL_f)_1$ is unchanged and represents the used life that has occurred. In order to determine the remaining endurance, we need to know when the residual strength reduces to that required to resist the maximum load and hence we can substitute $Q_{res} = Q_o = 1200$ N/mm. The remaining unknown term is T_2 which comes to 130 million. Hence placing a weight restriction on the bridge will extend the original design life of a further 100 million applications by 30 million applications, to a further 130 million applications.

Let us assume that the 130 million applications of fatigue vehicle traversals have been applied, so that the strength of the structure at the design point has reduced to Q_o and hence the second fatigue term $(TF_fL_f)_2$ in Eq. 19.46 has been fully applied. The structure is now strengthened to reduce by 20% the shear flow forces induced by both the fatigue vehicles and the maximum design overload. The shear flow forces could be reduced by welding a plate to the flange of the composite beam or by adding more shear connectors which would reduce the shear flow force per connector. Reducing the shear flow forces by 20% will reduce the shear flow strength that is required to resist the overload by 20%. Hence in Eq. 19.46, the minimum remaining strength that is required to resist the maximum overload is now $Q_{res} = 0.8Q_o = 960$ N/mm. Furthermore, as the shear flow forces q_r are now 80% of their previous value in Example 19.15, the force constant from Eq. 19.18 will now be $0.8^{5.1}(F_f)_2$ and hence $(F_f)_3 = 0.41 \times 10^{11}$. Let us assume that the weight restriction is removed so that $(L_f)_3$ reverts to $(L_f)_1$. By solving Eq. 19.46, the endurance T_3 becomes 251 million which is

the additional number of applications that can be applied to the structure because of the remedial work.

Example 19.18. Assessment of stud shear connections with friction effects

The shear connection in the 32m beam in Example 19.4 was designed in Example 19.16. The beam was designed for the traversal of 400 million fatigue vehicles and the design procedure ignored the beneficial effects of the shear flow transferred by friction. The results of the design are given in row 10 of Table 6, where Q_{of} and Q_{st} are the shear flow strengths required when the structure is first build.

The influence line diagram for the frictional resistance when the design point is at a the support is listed in row 4 of Table 7 and plotted in Fig. 19.19; the analysis follows the procedure outlined in Example 19.4 for the design point at a quarter span. It can be seen that the frictional resistance tends to infinity when an axle load is adjacent to the support. By comparing row 2 with row 5 in Table 7, it can be seen that the frictional resistance causes a very large reduction in the influence line diagram of shear flow forces on the shear connectors. The results from the influence line diagrams that allow for friction are summarised in rows 6 to 9 in Table 6 and these can be compared with the results in rows 1 to 5 where the frictional effect was ignored; the analysis at midspan is summarised in Table 8. From Table 6, it can be seen that the beneficial effect of friction is much greater at the supports than at mid-span. Friction reduces the peak of the cyclic load by 39% at the supports but by only by 8% at mid-span, and hence the connectors at the supports can withstand a much greater reduction in strength due to fatigue damage than those at mid-span. Furthermore, the maximum range of cyclic load is also reduced by 39% at the support and by 8% at mid-span, and so the rate of fatigue damage at the supports would be considerably less than originally anticipated. This reduction in the fatigue damage at the supports is represented by the reduction in the force constant in column 2 from 161×10^9 when friction is ignored to 14×10^9 when the beneficial effects of friction are allowed for.

Let us assume that the beam designed in Example 19.16 has been subjected to all of its original design quota of fatigue vehicle traversals of 400×10^6. If the beneficial effects of friction are ignored, then the bridge would theoretically have reached its design life such that $Q_{res} = Q_o$. However, it will now be assessed with the benefits of friction.

Equation 19.46 can be written in the following form for deriving the residual strength Q_{res}.

$$Q_{res} = Q_{st} - \left[10^{-3.12} Q_{st}^{-4.1} \sum_{y=1}^{y=i} \left(TF_f L_f \right)_y \right] \qquad (19.47)$$

where $T = 400 \times 10^6$, F_f has been derived from rows 6 and 7 in Table 6 bearing in mind that the frequencies of these ranges $f = 1$ and are listed in row 9, and $L_f = 1.14$ as in Example 19.16. The second term on the right hand side of Eq. 19.47 is the reduction

in strength due to the fatigue damage. Applying Eq. 19.47 to the three design points, gives a reduction in strength of 70 N/mm at the supports, a reduction of 413 N/mm at a quarter-span and a reduction in strength of 719 N/mm at mid-span. The residual strengths are listed in row 11 of Table 6 and it can be seen that in all cases they are much greater than the minimum strength requirement of $Q_o = q_o$ in row 4.

The residual endurance can also be determined from Eq. 19.47 by substituting $Q_o = q_o$ for Q_{res} and solving for T. In which case the shear flow resistance at the support has a remaining endurance of $T = 5469 \times 10^6$ fatigue vehicle traversals, the quarter-span has a remaining endurance of $T = 908 \times 10^6$, and at mid-span the remaining endurance is $T = 675 \times 10^6$.

Table 7 Influence lines at support

Design point	C	D		E		F		G		H
(1) q_{flow} (KV) (q_{dowel} without friction)	-1	-0.75	-1.75	-1.25	-1.25	-0.75	-0.75	-0.25	-0.25	0
(2) q_{flow} (N/mm)	-90	-67.5	-158	-113	-113	-67.5	-67.5	-22.5	-22.5	0
(3) Q_{fric} ($\mu V/L$)	∞	3	∞	4	4	1.33	1.33	0.33	0.33	0
(4) Q_{fric} (N/mm)	∞	11.8	∞	15.8	15.8	5.3	5.3	1.3	1.3	0
(q) Q_{dowel} N/mm (with friction)	0	-55.7	0	-96.7	-96.7	-62.2	-62.2	-21.2	-21.2	0
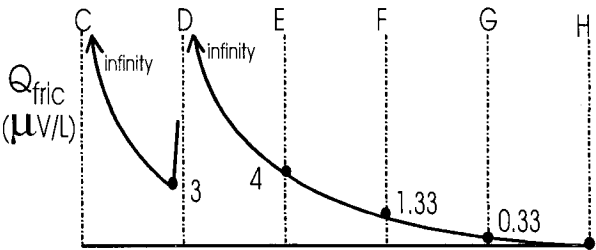
Fig. 19.19 Frictional resistance with design point at support

Table 8 Influence lines at mid-span

Design point	C	D		E		F		G		H
(1) q_{flow} (KV) (q_{dowel} without friction)	0	+0.25	+0.25	+0.75	-0.25	+0.25	-0.75	-0.25	-0.25	0
(2) q_{flow} (N/mm)	0	+22.5	+22.5	+67.5	-22.5	+22.5	-67.5	-22.5	-22.5	0
(3) Q_{fric} ($\mu V/L$)	0	0.33	0.33	1.33	1.33	1.33	1.33	0.33	0.33	0
(4) Q_{fric} (N/mm)	0	1.3	1.3	5.3	5.3	5.3	5.3	1.3	1.3	0
(5) q_{dowel} N/mm (with friction)	0	+21.2	+21.2	+62.2	-17.2	+17.2	-62.2	-21.2	-21.2	0

19.7 Welded steel components

19.7.1 GENERAL

Welded connections are usually designed using the crack initiation procedure and this will be illustrated in Section 19.7.2. However, the crack propagation approach is now being adapted for welded steel components (Oehlers, Ghosh and Wahab 1995) and the procedure being developed is outlined in Section 19.7.3 in mainly qualitative terms in order to give the reader an insight into future developments.

19.7.2 CRACK INITIATION APPROACH

The design and assessment of welded steel components can be based on the direct stress in the weld or in the material adjacent to the weld in which case the procedures developed for non-welded steel components in Section 19.5 can be applied. Alternatively, the analysis may be based on the shear flows in which case Eq. 19.36 is applicable.

Example 19.19. Design of weld using crack initiation approach

A type of weld is being designed in which national standards give the fatigue constant $10^{H_e-2D_e}$ in Eq. 3.2 as 3×10^{11}, where the units are in N and mm, and the fatigue exponent as $m_e = 4$. The design point is subjected to fatigue vehicle loads from two lanes. From lane 1: the design point is subjected to $T_1 = 200 \times 10^6$ fatigue vehicle traversals; the standard fatigue vehicle in lane 1 induces the force spectrum in Table 5 and the force constant for welds in column 4 where $F_f = 4.00 \times 10^6$; and the load spectrum in lane 1 is given in Table 2 and the load constant is $L_f = 0.274$ in column 4 where $m_e = 3$. From lane 2: the design point is also subjected to $T_2 = 150 \times 10^6$ fatigue vehicle traversals; the standard fatigue vehicle in lane 2 induces a force spectrum which is 20% less than that in Table 5 hence $(F_f)_2 = 0.8^3 \times 4.00 \times 10^6 = 2.05 \times 10^6$; and the load spectrum in lane 2 is the same as that in lane 1 so that $(L_f)_2 = (L_f)_1 = 0.274$. Substituting these values into Eq. 19.36 gives a required weld width of 10.0 mm.

19.7.3 CRACK PROPAGATION APPROACH

19.7.3.1 *General*

The stage 2 failure envelope in Fig. 3.5, on which the crack propagation approach of Section 19.4.5 is based, can be derived from theoretical modelling using fracture mechanics (Oehlers, Ghosh and Wahab 1995). As an example, the crack propagation approach will be developed for the classical problem of an infinitely wide plate with a centre crack to which a remote stress is applied, as this problem is the basis of many fracture mechanics procedures. It will be assumed that the centre crack is a flaw that has been produced by the welding technique.

19.7.3.2 *Infinitely wide plate*

(a) Stage 2 failure envelope

Irwin (1957) proposed the following stress intensity factor K_s to quantify the intensity of the stress field surrounding the crack tip in an infinitely wide plate with a remote stress σ.

$$K_s = \sigma\sqrt{\pi a} \tag{19.48}$$

where 'a' is the half length of the crack. Hence such a plate with a half crack size a_x will fracture when the applied stress σ_x satisfies the following equation.

$$K_c = \sigma_x\sqrt{\pi a_x} \tag{19.49}$$

where K_c is the critical stress intensity factor which is a material property. The rate at which the crack grows under constant amplitude cyclic loading can be derived from the equation that was proposed by Paris (1963) given by

$$\frac{da}{dN} = C_p(\Delta K_s)^{m_a} \tag{19.50}$$

which can be written in the following integral form to give the number of cycles N_f that are required for a crack of initial length $2a_i$ to propagate to a crack of length $2a_x$.

$$N_f = \int_{2a_i}^{2a_x} \frac{da}{C_p(\Delta K_s)^{m_a}} \tag{19.51}$$

where C_p is a material value, m_a is the exponent of the endurance equation such as that shown in Eq. 3.7 and ΔK_s is the range of the stress intensity factor induced by the cyclic load $\Delta\sigma$. We can derive from Eq. 19.48 that $\Delta K_s = \Delta\sigma\sqrt{\pi a}$ and from Eq. 19.49 that $a_x = K_c^2/(\sigma_x^2\pi)$. Substituting these values into Eq. 19.51 and integrating gives an equation for the failure envelope (Oehlers, Ghosh and Wahab 1995). The shape of this failure envelope varies according to the value of m_a.

When $m_a = 3$, the failure envelope derived from Eq. 19.51 is linear as shown by the stage 2 failure envelope in Fig. 3.5 and hence this linear failure envelope can be directly defined by the asymptotic endurance E_a and the initial fracture strength prior to cyclic loading P_{prop} as show. When $m_a = 3$ the asymptotic endurance E_a is given by

$$E_a = \frac{\sqrt{2}}{C_p\sqrt{\pi^3 a_i}}(\Delta\sigma)^{-3} \tag{19.52}$$

and the initial fracture strength P_{prop} by

$$P_{prop} = \frac{K_c}{\sqrt{\pi a_i}} \tag{19.53}$$

(b) General equation

By comparing Eq. 19.52 with Eq. 3.7, it can be seen that the fatigue constant in this fracture mechanics approach is given by

$$10^{H_a - 2D_a} = \frac{\sqrt{2}}{C_p \sqrt{\pi^3 a_i}} \tag{19.54}$$

Substituting this fatigue constant into the general crack propagation fatigue equation in Eq. 19.26 as well as substituting for P_{prop} in Eq. 19.53 and $m_a = 3$ gives

$$X^{-3} = \frac{\left(1 - \frac{P_c}{\left(\frac{K_c}{\sqrt{\pi a_i}} \right)} \right) \frac{\sqrt{2}}{C_p \sqrt{\pi^3 a_i}}}{\sum_{y=1}^{y=j} \left(TF_f L_f \right)_y} \tag{19.55}$$

It can now be seen that the stage two crack propagation approach can be applied directly to the classical problem of an infinitely wide plate with a through crack. This is because the fracture failure envelope for this problem is linear when m_a = 3. As Irwin's solution for the stress intensity factor in an infinitely wide plate in Eq. 19.48 is often used as the basis for the stress intensity factor in real components (Albrecht and Yamada 1977), as most national standards use m_a = 3 for welded components, and as it is generally accepted that most welded structures have initial cracks or welding flaws so that crack propagation occupies most if not all of the fatigue life (Maddox 1991), there is good reason to suggest that the crack propagation approach can be applied to real welded components.

(c) Design mode

In dealing with an infinitely wide plate of width B → ∞, it is convenient in design to deal with the force per unit width of plate q, that is q is the remote force on the plate over a unit length of the width of B. Hence q is analogous to shear flow. The infinitely wide plate has a thickness W and a crack of width $2a_i$ that penetrates the full thickness of the plate W. Therefore R/X in the generic form of the endurance equation in Eq. 19.10 is q/W so that X = W in Eq. 19.55. Substituting in Eq. 19.55 gives

$$W^{-3} \;=\; \frac{\left(1 - \dfrac{Q_o}{\left(\dfrac{K_c}{\sqrt{\pi a_i}}\right)W}\right)\dfrac{\sqrt{2}}{C_p\sqrt{\pi^3 a_i}}}{\displaystyle\sum_{y=1}^{y=j}\Big(T\big(F_f = f(q_r)\big)L_f\Big)_y} \tag{19.56}$$

where Q_o is the strength per unit width required to resist the maximum design overload, q_r is a spectrum of ranges of the cyclic force per unit width, and the parameter $(K_c W)/\sqrt{\pi a_i}$ in the numerator on the right hand side of Eq. 19. 56 is the fracture strength per unit width prior to cyclic loading.

Example 19.20. Design of wide plate using crack propagation approach

A very wide welded plate in a bridge structure is subjected to $T = 300 \times 10^6$ fatigue vehicle traversals. The fatigue vehicles can be represented by one standard fatigue vehicle that induces the force spectrum in Table 5 and the force constant in column 4 of $F_f = 4.00 \times 10^6$, and by the load spectrum in Table 2 and load constant in column 4 of $L_f = 0.274$. The maximum overload induces a force of $q_o = 1200$ N/mm. Furthermore, the plate has the material properties $K_c = 1500$ N/mm$^{3/2}$ and $C = 2.3 \times 10^{-13}$ and the welding procedure can restrict the half crack width to $a_i = 0.5$ mm. Equation 19.56 can now be solved for the plate thickness W which comes to 6.3 mm. This means that the overload stress must be limited to $1200/6.3 = 190$ N/mm^2 to allow the design life to be achieved, no matter how great the yield strength.

(d) Assessment mode

The stresses acting in a component can be determined directly in the assessment mode as the applied load and plate size are known. In which case, Eq. 19.55 can be written in the following form to give the remote stress to cause fracture $\sigma_{fracture}$.

$$1 \;=\; \frac{\left(1 - \dfrac{\sigma_{fracture}}{\left(\dfrac{K_c}{\sqrt{\pi a_{initial}}}\right)}\right)\dfrac{\sqrt{2}}{C_p\sqrt{\pi^3 a_{initial}}}}{\big(TF_f L_f\big)_1 + \big(TF_f L_f\big)_2 + \big(TF_f L_f\big)_3 + \dots} \tag{19.57}$$

where $a_{initial}$ is the initial crack size prior to cyclic loading.

From Eq. 19.49, $\sigma_x = K_c / \sqrt{\pi a_x}$ hence $\sigma_{fracture} = K_c / \sqrt{\pi a_{future}}$ where a_{future} is the crack size at $\sigma_{fracture}$. Substituting into Eq. 19.57 gives the size of the crack a_{future} after cyclic loading as follows.

$$1 = \frac{\left(1 - \sqrt{\dfrac{a_{initial}}{a_{future}}}\right)\dfrac{\sqrt{2}}{C_p\sqrt{\pi^3 a_{initial}}}}{\left(TF_f L_f\right)_1 + \left(TF_f L_f\right)_2 + \left(TF_f L_f\right)_3 + ...} \qquad (19.58)$$

which can be used to predict the crack growth. Furthermore Eq. 19.58 can be adapted in the following approximate form to predict the remote stress to cause local yield σ_{yield} in a plate with a finite width B.

$$1 = \frac{\left(1 - \sqrt{\dfrac{a_{initial}}{\dfrac{B}{2}\left(1 - \dfrac{\sigma_{yield}}{f_y}\right)}}\right)\dfrac{\sqrt{2}}{C_p\sqrt{\pi^3 a_{initial}}}}{\left(TF_f L_f\right)_1 + \left(TF_f L_f\right)_2 + \left(TF_f L_f\right)_3 + ...} \qquad (19.59)$$

where f_y is the yield strength of the steel.

In mild steel structures, the fracture strength $\sigma_{fracture}$ in Eq. 19.57 rarely controls design so that Eq. 19.57 is of little direct practical value. The significance of Eq. 19.57 is that it forms a linear failure envelope so that the sequence of cyclic loading within this linear failure envelope does not affect the rate of fatigue damage, and hence the fatigue damage terms can be added as shown in the equation. Furthermore, the significance of Eq. 19.57 is that it can be adapted to form a simple equation for predicting future crack sizes as in Eq. 19.58 which may be useful in quantifying inspection periods, or it can be adapted to predict when local yielding will occur as in Eq. 19.59.

19.7.3.3 *Real components*

In order to apply Eqs. 19.56 to 19.59 to real structures, it will be necessary to both linearise the real failure envelopes and to determine the initial crack sizes. The work described previously on the infinitely wide plate would suggest there is scope for linearisation.

An example of a fracture failure envelope for a real component is shown in Fig. 19.20. Once the fracture failure envelope is known, S-N data from national standards can be used to predict the initial fracture strength as shown by σ_{S-N}, and this can then be used to estimate initial crack sizes $a_{initial}$ (Ghosh, Oehlers and Wahab 1995). Hence this procedure can be used to convert S-N data into initial crack sizes for use in the crack propagation approach. The next step will be to linearise the failure envelope as shown in Fig. 19.20. Each of these idealised linear failure envelopes, referred to as bounds in Fig. 19.20, would be defined by its own asymptotic endurance and its own equivalent initial crack size.
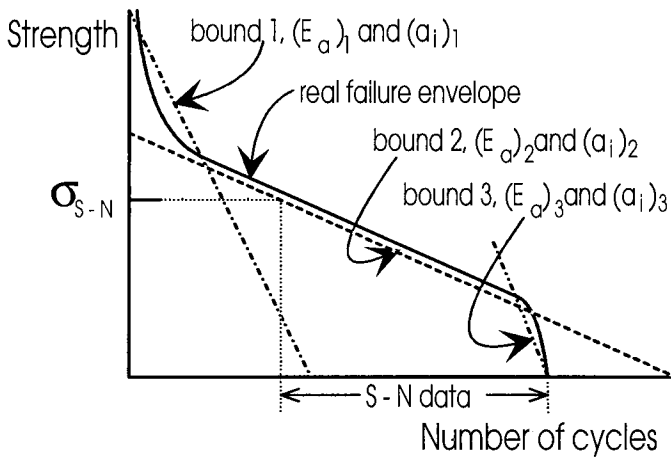
Fig. 19.20 Linearisation of failure envelope

19.8 References

Albrecht, P., and Yamada, K., (1977). "Rapid calculation of stress intensity factors." Journal of the Structural Division , ASCE, No. ST2, 377 - 389.

BS5400 : Part 10 : 1980. Steel, concrete and composite bridges, Part 10. Code of practice for fatigue. British Standards Institution, London.

Ghosh, A. (1995). Residual strength approach to the fatigue design and assessment of welded components. PhD thesis in preparation, Dept. of Civil and Env. Engng., University of Adelaide

Ghosh, A., Oehlers, D. J., and Wahab, M. A. "Linear fracture envelopes for fatigue assessment of welds." Submitted for publication in 1995.

Irwin, G. R. (1957). "Analysis of stresses and strains near the end of a crack traversing a plate." Transactions, ASME, Series E, Vol. 24, No. 3, Sept.

Maddox, S J. (1991). *Fatigue strength of welded structures.* Abington Publishing, Cambridge.

Miner, M.A. (1945) "Cumulative damage in fatigue." American Society of Mechanical Engineers. Transactions, Vol. 67.

Murray, K. J. (1988). The fatigue behaviour of composite bridge beams subject to a spectrum of highway loadings. Thesis submitted to the National University of Ireland for the degree of Master of Engineering Science.

Oehlers, D. J. (1995) "Design and assessment of shear connectors in composite bridge beams." Journal of Structural Engineering, ASCE, Vol. 121, No.2, 214-224.

Oehlers, D. J. and Carroll, M. A. (1987). "Simulation of composite beams subjected to traffic loads." Proceedings of an Engineering Foundation Conference, Composite Construction in Steel and Concrete, edited by Viest and Buckner. Published by the American Society of Civil Engineers (Henniker, U.S.A.). June, 450-459.

Oehlers, D. J., Ghosh A. and Wahab M. (1995) "A residual strength approach to fatigue design and analysis." Journal of Structural Engineering, to appear.

Oehlers, D. J. and Singleton, W. M. (1986). "The simulation of simply supported composite beams tested under fatigue loads." Proceedings, Institution of Civil Engineers, London, Part 2, Vol. 81, 647-657.

Paris, P. C. and Erdogan F. (1963). "A critical analysis of crack propagation laws." Journal of Basic Engineering Transactions ASME, 85, No. 4, 528

Singleton, W. M. (1985). The transfer of shear in simply supported composite beams subjected to fatigue loads. Thesis submitted to the National University of Ireland for the degree of Master of Engineering Science.

Toprac, A. A. (1965). "Fatigue strength of 3/4 inch stud shear connectors." Highway. Res. Rec., No. 103, 53-77.

Index